

Proceedings in Technology Transfer

Mokhtar Awang

Hussain H. Al-Kayiem

Ton C. Bor

Seyed Sattar Emamian *Editors*

Advances in Material Science and Engineering

Selected Articles from
ICMMPE 2022

 Springer

Proceedings in Technology Transfer

The book series “Proceedings in Technology Transfer” provides a valuable platform for researchers, practitioners, and policymakers to share their experiences and insights related to technology transfer. Our aim is to facilitate knowledge exchange between academic researchers and industry professionals, accelerating the introduction of new technologies and driving economic growth.

Our series publishes books and conference proceedings that focus on original research findings, best practice recommendations, emerging trends, and technology evaluations. The series covers all topics which explore the transfer of technology in various industry sectors that require innovations and economic growth.

Join us in advancing the technology transfer and its impact on innovation. Publish your proceedings with us and offer insights and expertise to professionals in your field.

Mokhtar Awang · Hussain H. Al-Kayiem ·
Ton C. Bor · Seyed Sattar Emamian
Editors

Advances in Material Science and Engineering

Selected Articles from ICMMPE 2022

Editors

Mokhtar Awang
Institute of Transport Infrastructure
Universiti Teknologi Petronas
Seri Iskandar, Perak, Malaysia

Ton C. Bor
Faculty of Engineering Technology
University of Twente
Enschede, The Netherlands

Hussain H. Al-Kayiem
University of Technology
Baghdad, Iraq

Seyed Sattar Emamian
Faculty of Engineering Technology
University of Twente
Enschede, The Netherlands

ISSN 2948-2321

ISSN 2948-233X (electronic)

Proceedings in Technology Transfer

ISBN 978-981-99-5317-2

ISBN 978-981-99-5318-9 (eBook)

<https://doi.org/10.1007/978-981-99-5318-9>

© The Editor(s) (if applicable) and The Author(s), under exclusive license
to Springer Nature Singapore Pte Ltd. 2024

This work is subject to copyright. All rights are solely and exclusively licensed by the Publisher, whether the whole or part of the material is concerned, specifically the rights of translation, reprinting, reuse of illustrations, recitation, broadcasting, reproduction on microfilms or in any other physical way, and transmission or information storage and retrieval, electronic adaptation, computer software, or by similar or dissimilar methodology now known or hereafter developed.

The use of general descriptive names, registered names, trademarks, service marks, etc. in this publication does not imply, even in the absence of a specific statement, that such names are exempt from the relevant protective laws and regulations and therefore free for general use.

The publisher, the authors, and the editors are safe to assume that the advice and information in this book are believed to be true and accurate at the date of publication. Neither the publisher nor the authors or the editors give a warranty, expressed or implied, with respect to the material contained herein or for any errors or omissions that may have been made. The publisher remains neutral with regard to jurisdictional claims in published maps and institutional affiliations.

This Springer imprint is published by the registered company Springer Nature Singapore Pte Ltd.
The registered company address is: 152 Beach Road, #21-01/04 Gateway East, Singapore 189721, Singapore

Paper in this product is recyclable.

Preface

This book highlights the recent research works on general mechanical engineering presented during the 8th International Conference on Mechanical, Manufacturing and Plant Engineering (ICMMPE 2022) held on November 24, 2022, in Kuala Lumpur, Malaysia. ICMMPE 2022 is a comprehensive conference covering various mechanical and manufacturing engineering topics. We believe that bringing these fields together creates a unique opportunity for collaboration between industry and academic researchers. This conference is also a chance to discuss existing challenges or problems that emerge in the industry, potentially and globally. This book is written by leading researchers and industry professionals. The conference participants submitted papers reflecting recent advances and address current issues in the fields of mechanical, manufacturing and plant engineering. The conference was intended to bring together the researchers and technologists working in 3 sections including; numerical studies, materials characterization and manufacturing processes. All articles have been blind peer-reviewed by highly reputable researchers from different universities around the world.

The organizing committee would like to express sincere appreciation to everybody who has contributed to the conference. Warmest thanks to the authors, reviewers, participants and to all the team of the organizers for their support and enthusiasm which granted success to the conference.

Contents

Analysis on the Efficiency of Logistics Companies in Malaysia Using Data Envelopment Analysis Model	1
<i>Pei Fun Lee, Weng Siew Lam, and Weng Hoe Lam</i>	
Evaluation of the Preference of Online Food Delivery Providers in Supply Chain Management with AHP Model	9
<i>Weng Siew Lam, Weng Hoe Lam, Chin Yap Hoh, and Shann Ying Wong</i>	
Performance Analysis of Courier Service Providers in Transportation Using TOPSIS Model	16
<i>Weng Siew Lam, Weng Hoe Lam, Ching Wen Heng, and Yen Shuang Tioh</i>	
A Fast Initial Response Double EWMA Chart for Process Mean	23
<i>Peh Sang Ng, Wai Chung Yeong, Irene Seok-Ching Yong, and Huai Tein Lim</i>	
Microstructural and Compositional Analyses of Resin Matrix Composites	31
<i>Mutiu Erinosh, Ester Angula, and Sam Shaanika</i>	
Stability Characteristics of Water/Diesel and Biodiesel Emulsions Under the Influence of Water Dosages	39
<i>Hasanain A. Abdul Wahhab, Hayder A. Dhahad, Mohammed A. Fayad, and Miqdam T. Chaichan</i>	
Prediction of a Diffusion Flame Characteristics with the Influence of Repulsive Electromagnetic Fields	50
<i>Hasanain A. Abdul Wahhab, Sameera S. Shijer, Mohammed A. Fayad, and Miqdam T. Chaichan</i>	
Design and Fabrication of a Livestock's Fodder Crusher	59
<i>Sam Shaanika, Mutiu Erinosh, and Ester Angula</i>	
Design of a Solar PV Water Pumping System for Small-Scale Farming Along the Calueque-Oshakati Canal in Namibia	66
<i>Sam Shaanika, Mutiu Erinosh, and Ester Angula</i>	
Effect of Cobalt Oxide Nanoparticles Additives to Water Hyacinth-Diesel Mixture Biofuel on the Performance and Emissions of Single CI Engine	73
<i>Raed A. Jessam, Elena Magaril, and Hasanain A. Abdul Wahhab</i>	

Design and Fabrication of a Solar-Powered Lawn Mower	85
<i>Mutiu Erinosh, Ester Angula, Sam Shaanika, and Oluwagbenga Johnson</i>	
Prediction of Surge/Swab Pressure in the Oil & Gas Industry: Effect of Process Parameters and Significance of Modeling	93
<i>Mohammad Yusuf, Syahrir Ridha, Shwetank Krishna, and Umar Nabil Sabo</i>	
Study the Behaviour of Chest Freezer Working with R134a and R600a Under Pull Down and Loading States	104
<i>Louay Abd Al-Azez Mahdi, Mohammed A. Fayad, Muna Kheder Jassim Al-Naamee, Miqdam Tariq Chaichan, Hasanain A. Abdul Wahhab, and Hayder Mohsin Ali</i>	
Effects of Arc Welding Current on the Mechanical Properties of Aluminium Plate Weldments	113
<i>Mutiu Erinosh, Ester Angula, and Sam Shaanika</i>	
Design of a Passive Dust Suppression System for the Coal Staithes	121
<i>Ester Angula, Mutiu Erinosh, Sam Shaanika, and Erasmus Shaanika</i>	
Design and Fabrication of a Hand Operated Sweeping Machine	129
<i>Mutiu Erinosh, Ester Angula, and Sam Shaanika</i>	
Study on Silica Content of Peat Soil and Concrete Reinforced Aluminium AA7075 Chips by Cold Compaction Method: Hardness and Physical Properties	138
<i>Nurul Farahin Mohd Joharudin, Noradila Abdul Latif, Mohammad Sukri Mustapa, Muhd Rizuan Rusli, Kamarul-Azhar Kamarudin, Wahyu Mulyo Utomo, Ahmed Sahib Mahdi, and Mohammed Hussein Rady</i>	
Numerical Modeling of an Open-Flow PV/T Cooling Collector	147
<i>Amged Al Ezzi, Hasanain A. Abdul Wahhab, and Raed A. Jessam</i>	
Impact Strength of Bio-Fibrous Concrete	156
<i>Rowena Richard, Samatar Hassan, Deshvinder Kaur, Badraan Abdalla, Saeed Cheema, Sook Kee, Hok Chai Yam, Abideen Ganiyu, Fadilat Ayeronfe, and Muyideen Abdulkareem</i>	
Dynamic Analysis of Floating Offshore Wind Turbine Subjected to Combined Deepwater Environmental Loads	163
<i>Ahmad Mahamad Al-Yacouby, Mohamad Azri bin Kamarulbahrin, and M. S. Liew</i>	

Continuum Modelling of Carbon Nanotube Composites: A Review	177
<i>N. Omar, Z. A. Rasid, and M. Z. Hassan</i>	
Investigation of Interfacial Behavior of SN100C and SN97C Solders with HASL Surface Finish Using Microwave Energy	198
<i>N. H. Noor Izza, M. A. Rabiatal Adawiyah, and O. Saliza Azlina</i>	
Potential Utilization of Acetylene as an Alternative Fuel in Petrol Engine	205
<i>O. L. Rominiyi, O. M. Ikumapayi, T. S. Ogedengbe, M. A. Akintunde, E. P. Nsien, and S. A. Afolalu</i>	
Development of a Filter-Based Fruit Preservation System via Refrigerating System	214
<i>Ojo P. Bodunde, Omolayo M. Ikumapayi, Rasaq A. Kazeem, Adebayo T. Ogundipe, Jesutoni R. Oluwafemi, Oritsetsolayemi O. Awani, and Vincent A. Balogun</i>	
Agro-Based Nano Coolant for Car Engines: Synthesis and Evaluation	230
<i>Sunday A. Afolalu, Omolayo M. Ikumapayi, Temitayo S. Ogedengbe, Abayomi Adegbenjo, Tien-Chien Jen, Adebayo T. Ogundipe, and Bernard A. Adaramola</i>	
Developing a Finite Element Model for Analysing Dissimilar Friction Stir Welding (FSW) of Al/Mg Alloys	241
<i>Bahman Meyghani, S. Emamian, and Mokhtar Awang</i>	
Vortex Induced Vibration of Free Span Pipeline – CFD Simulation	263
<i>Ahmad Mahamad Al-Yacoubby, Mohd Farid Bin Mizan, and M. S. Liew</i>	
Material Flow and Temperatures Prediction in Friction Stir Extrusion Process Using Smoothed Particle Hydrodynamics	275
<i>Venkata Somi Reddy Janga, Mokhtar Awang, and Eric J. Lee</i>	
Comparative Study of an Evacuated Tube with a Copper Heat Tube and a New Receiver for Air Heating by a Parabolic Trough Collector	285
<i>Ayad K. Khelif, Akram H. Abed, and Arshad A. Al Jalil</i>	
Characterization of Diamond-Like Carbon on WC and H13 Tool Steel to Improve the Wear Resistance of FSW Tool	294
<i>S. Emamian, M. Awang, and Bahman Meyghani</i>	
Optimization of Superhydrophobic Surface Preparation Using One-Step Immersion and Control Variate Method	312
<i>Shuai Zhang, Yong Chai Tan, Hui Xin Che, Vin Cent Tai, Yaw Yoong Sia, Shamini Janasekaran, and Walisijiang Tayier</i>	

Replacement of Solar Dish Collectors to Provide Heat in the Power Plant:
Case Study Malaysia 322
*Chen Rui Geach, Kamyar Mehranzamir, Ateeb Hassan,
Hadi Nabipour Afrouzi, Elammaran Jayamani,
and Seyed Morteza Alizadeh*

Modelling the Performance Efficiency of Construction Companies
in Malaysia Using Data Envelopment Analysis 332
Shun Jinn Lim, Weng Hoe Lam, and Weng Siew Lam

Analysis on the Performance of Technology Companies Using TOPSIS
Model 339
Kah Fai Liew, Weng Siew Lam, and Weng Hoe Lam

Diagnosis of Mycobacterium Tuberculosis via K-Means and Canny Edge
Detection 346
*Jia Wei Lim, Ting Rang Ling, Xin Hui Tsen, Sarah Jane Kho,
Hui En Lee, Patrick Guda anak Benjamin, Mong How Ooi,
and Hong Siang Chua*

Geo-tracing of Coffee Beans Using Metal Oxide Semiconductor Gas
Sensors Array 354
*Ashlee Jude Anak Nyaut, Hui En Lee,
Zehnder Jarroop Augustine Mercer, Sing Muk Ng, and Hong Siang Chua*

A Review of Common PV Array Configuration Schemes for Maximum
Output Power 361
*Lawrence Sii Ying Ting, Hadi Nabipour Afrouzi, Hong Siang Chua,
and Jubaer Ahmed*

A New Method for Image Encryption Using DNA Sequences and Hyper
Chaos 371
Mehrnaz Arian, Morteza Saberi Kamarposhti, and Ali Broumandnia

Cancer Detection in Digital Image Using Machine Learning Algorithms 379
*Yaser Darkaleh, Mahta Sadat Mirzazadeh Tekieh,
and Sima Aboulhassani Khajeh*

Author Index 387



Analysis on the Efficiency of Logistics Companies in Malaysia Using Data Envelopment Analysis Model

Pei Fun Lee, Weng Siew Lam^(✉), and Weng Hoe Lam

Department of Physical and Mathematical Science, Faculty of Science, Universiti Tunku Abdul Rahman, Kampar Campus, Jalan Universiti, Bandar Barat, 31900 Kampar, Perak, Malaysia
lamws@utar.edu.my

Abstract. The logistics industry plays an imminent role in the economic development in Malaysia. However, with operational and growth complexities, the logistics industry has been lagging due to unbearable costs. Data envelopment analysis (DEA), which is a linear programming model, has grown in popularity to study the efficiency of companies. Therefore, DEA is used to evaluate the performances of the 27 listed logistics companies in Malaysia from 2010–2021. This study found that only 33.33% of the companies are well-performing with the lowest efficiency level being 16.39%. From the optimal solution of DEA, this paper then offers insights to underperforming companies to improve based on the highest performing companies. This paper is also the pioneer in evaluating the performances of the listed logistics companies in Malaysia for the long run.

Keywords: Efficiency · Data Envelopment Analysis · Logistics Companies · Linear Programming Model

1 Introduction

Malaysia's diplomatic relations with a significant number of countries has opened up more markets for economic growth [1]. With this economic integration, the logistics industry serves as a major linkage between resources and markets through the extensive supply chain networks. However, according to a study [2] on the logistics performances in Asia Pacific, Malaysia fell behind with negative dynamics in infrastructure, transport organization and on time delivery. Given that Malaysia is an important logistics hub in ASEAN, it is imminent to boost the logistics industry to position the country strategically for the country's prosperity [3]. Besides contemporary logistics issues such as fuel prices, customer service and driver problems, logistics companies face fierce competition as they enhance digital connectivity integrating producer sites, warehouses, distribution centers, terminals and transport providers [4]. The procurement, adoption and management of equipment, information technology and human resources needed to augment the performances of the logistics industry require high financial efficacy. Moreover, there is heightened cost in transporting, storing, managing inventories and processing orders [5].

Therefore, this paper intends on investigating the performances of the listed logistics companies in Malaysia. Since the performances of the listed logistics companies involve a number of variables, with some variables acting as inputs while other variables serve to measure the outcomes of the companies, data envelopment analysis (DEA) model can then be used [6]. DEA involves linear programming model to assess the decision making units (DMUs) [7]. The DMUs in this study are the listed logistics companies in Malaysia. The performances are evaluated based on how efficient the listed logistics companies are in transforming the inputs to outputs. In short, the performances of the DMUs are measured based on efficiency scores. The efficiency scores are denoted by the weighted sum of outputs over the weighted sum of inputs [7–9]. For elevated performance, the efficiency has to be high, which then means that the outputs should be maximized while the inputs should be the least possible [10]. The highest efficiency in the DEA model developed by Banker et al. [11] is 100%. DMUs with the efficiency of 100% have attained the highest performance while DMUs with scores from 0% to below 100% are underperformed. Underperformed DMUs translate to the inability to fully utilize its inputs for the greatest outputs [12, 13]. DEA received wide recognition in assessing the efficiencies in banking [14, 15], healthcare [9, 16], hospitality [17, 18] and manufacturing [19, 20] industries.

The measurement of performances of the listed logistics companies in Malaysia with DEA model can then incorporate financial ratios. Financial ratios have been complemented by DEA in several studies to capture more information on the performances of the DMUs. The most common financial ratios used are current ratio (CR), debt ratio (DR), debt to equity ratio (DER), earnings per share (EPS), return on asset (ROA) and return on equity (ROE) [14, 21–25]. Therefore, the performances of the listed logistics companies in Malaysia will be examined based on multiple inputs and outputs in the DEA model [26–29]. CR, DR and DER are the inputs; EPS, ROA and ROE are the outputs.

A combination of logistics companies offering different services can be evaluated with DEA. Zheng et al. [30] covered the transportation, warehousing and postal companies when evaluating the efficiency of logistics companies in China with DEA model. Park and Lee [31] studied the logistics service providers in Korea with DEA with the inclusion of companies in shipping, air cargo and container terminals. The research contribution is to adopt factual data from the financial statements in the DEA model for the examination of the performances of listed logistics companies in Malaysia, which is often ignored. The results of this research could provide comprehensive and reliable understanding on the growth and development of the logistics industry in Malaysia. This would offer insights to policy makers, managements and market speculators to position their strategies to help enhance the logistics industry in Malaysia. Moreover, from the optimal solution of the DEA model, the highest performing logistics companies may act as benchmarks to the underperforming logistics companies, which allows the underperforming logistics companies to identify their potential areas of improvements. The introductory section will be followed by an overview of the DEA model, findings and a concluding section.

2 Data and Methodology

The formulation of the proposed framework is shown in Table 1.

Table 1. Proposed Framework to Evaluate the Performances of Logistics Companies.

	Items		
Objective	To evaluate the performance of listed logistics companies in Malaysia		
Inputs	CR	Outputs	EPS
	DR		ROA
	DER		ROE
DMUs	AIRPORT	HUBLINE	PRKCORP
	BHIC	ILB	SEALINK
	BIPORT	LITRAK	SEEHUP
	CJCEN	MAYBULK	SURIA
	COMPLET	MISC	SYSCORP
	FREIGHT	MMCCORP	TAS
	GCAP	NATWIDE	TASCO
	GDEX	POS	TNLOGIS
	HARBOUR	PDZ	TOCEAN

From Table 1, the inputs are CR, DR and DER and outputs are EPS, ROA and ROE. Table 1 also shows the 27 listed logistics companies in this paper. The performance is measured in terms of efficiency whereby it is the weighted sum of outputs over the weighted sum of inputs. The output-oriented BCC model is shown below [32, 33]:

$$\text{Maximize } h_q = \frac{\sum_{n=1}^m t_n y_{nq} - \mu_q}{\sum_{p=1}^s w_p x_{pq}} \quad (1)$$

Subject to

$$\frac{\sum_{n=1}^m t_n y_{nq} - \mu_q}{\sum_{p=1}^s w_p x_{pq}} \leq 1, q = 1, 2, 3, \dots, r \quad (2)$$

$$t_n \geq \varepsilon, n = 1, 2, 3, \dots, m \quad (3)$$

$$w_p \geq \varepsilon, p = 1, 2, 3, \dots, s \quad (4)$$

where

h_q = relative efficiency of DMU_q

m = number of outputs

t_n = weight of output n
 y_{nq} = degree of n output for DMU_q
 s = number of inputs
 w_p = weight of input p
 x_{pq} = degree of p input for DMU_q
 ε = positive values
 r = number of DMU s
 μ_q = free variables

Equation (1) aims at maximizing the efficiency of the particular DMU. Equation (2) limits the efficiency to range from 0% to 100%. t_n and w_p are the weights of the outputs and inputs in maximizing the efficiency of the DMU. After switching into the linear form, the LINGO optimization software is used to obtain the optimal solutions [33–35].

3 Result and Discussion

The performances, in terms of efficiency, of the listed logistics companies in Malaysia after being optimized with DEA model is tabulated in Table 2.

Based on the illustration in Table 2, listed logistics companies which attain 100.00% efficiency are efficient and ranked first in their performances. There are nine listed logistics companies with efficient performances, which are COMPLET, GDEX, HUBLINE, NATWIDE, POS, PDZ, PRKCORP, SYSCORP and TOCEAN because of the attainment of 100.00% efficiency. It also shows that these nine companies have managed to obtain the greatest outputs, given the fixed inputs. Since these nine companies are efficient, they are also the benchmarks for the other underperforming companies.

Conversely, 18 companies have been underperforming from 2010–2021 because their efficiencies are lower than 100.00%. In descending order (from higher performing to lower performing logistics companies), these 18 companies are SEALINK (99.13%), MISC (98.67%), ILB (97.62%), SURIA (96.06%), SEEHUP (85.51%), MAYBULK (83.60%), BHIC (83.54%), TNLOGIS (82.76%), TASC0 (80.09%), HARBOUR (79.41%), FREIGHT (78.91%), CJCEN (78.01%), MMCCORP (71.79%), AIRPORT (65.58%), TAS (62.27%), BIPORT (56.84%), LITRAK (47.04%), GCAP (16.39%). There is a wide difference among the performances of the listed logistics companies in Malaysia given that the efficiency level ranges from 16.39% to 100.00%. Therefore, there is a need for these underperforming companies to improve according to the benchmarks given in the optimal solution of the DEA model.

Table 3 offers a summary of the performances of the logistics companies in Malaysia based on the efficiencies. 33.33% of the logistics companies have the highest performances with efficiency level of 100.00%. This is in line with existing literatures with efficiency levels from 28.00% to 50.00% [14, 23, 36].

Table 4 presents the benchmarks for the underperforming companies.

From Table 4, the highest performing companies, which are COMPLET, GDEX, HUBLINE, NATWIDE, POS, PDZ, PRKCORP, SYSCORP and TOCEAN, make up the benchmarks. The 18 companies with efficiency levels below 100% can then benchmark these 9 highest performing companies. For example, AIRPORT can use PRKCORP, SYSCORP and TOCEAN as benchmarks to improve the performances. GCAP can

Table 2. Performances of the Listed Logistics Companies in Malaysia with DEA.

Companies	Efficiencies (%)	Rankings	Performances
AIRPORT	65.58	23	Inefficient
BHIC	83.54	16	Inefficient
BIPORT	56.84	25	Inefficient
CJCEN	78.01	21	Inefficient
COMPLET	100.00	1	Efficient
FREIGHT	78.91	20	Inefficient
GCAP	16.39	27	Inefficient
GDEX	100.00	1	Efficient
HARBOUR	79.41	19	Inefficient
HUBLINE	100.00	1	Efficient
ILB	97.62	12	Inefficient
LITRAK	47.04	26	Inefficient
MAYBULK	83.60	15	Inefficient
MISC	98.67	11	Inefficient
MMCCORP	71.79	22	Inefficient
NATWIDE	100.00	1	Efficient
POS	100.00	1	Efficient
PDZ	100.00	1	Efficient
PRKCORP	100.00	1	Efficient
SEALINK	99.13	10	Inefficient
SEEHUP	85.51	14	Inefficient
SURIA	96.06	13	Inefficient
SYSCORP	100.00	1	Efficient
TAS	62.27	24	Inefficient
TASCO	80.09	18	Inefficient
TNLOGIS	82.76	17	Inefficient
TOCEAN	100.00	1	Efficient

benchmark POS, PRKCORP and TOCEAN. PRKCORP acts as the benchmark for 14 underperforming companies while TOCEAN and SYSCORP are the benchmarks for 12 and 10 underperforming companies respectively.

Table 3. Summary of Performances of Listed Logistics Companies.

Items	Levels
Average efficiency (%)	83.82
Minimum efficiency (%)	16.39
Maximum efficiency (%)	100.00
Percentage of efficient organizations (%)	33.33
Percentage of inefficient organizations (%)	66.67%

Table 4. Benchmarks for Underperforming Companies.

Underperforming Companies	Benchmarks								
	COMPLET	GDEX	HUBLINE	NATWIDE	POS	PDZ	PRKCORP	SYSCORP	TOCEAN
AIRPORT	–	–	–	–	–	–	1	1	1
BHIC	–	–	1	–	–	–	–	1	–
BIPORT	1	–	–	–	–	–	1	–	1
CJCEN	1	–	–	–	1	–	1	–	1
FREIGHT	1	–	–	–	1	–	1	–	–
GCAP	–	–	–	–	1	–	1	–	1
HARBOUR	1	–	–	–	1	–	1	–	1
ILB	–	1	–	1	–	1	1	–	–
LITRAK	–	–	–	–	1	–	1	1	1
MAYBULK	–	–	–	–	–	1	–	–	1
MISC	–	–	–	–	–	–	1	1	1
MMCCORP	–	–	1	–	–	–	1	1	–
SEALINK	–	–	1	–	–	–	–	1	–
SEEHUP	–	–	–	–	1	–	1	1	1
SURIA	1	–	–	–	–	–	1	–	1
TAS	–	–	–	–	1	–	–	1	1
TASCO	–	–	–	–	1	–	1	1	1
TNLOGIS	–	–	1	–	1	–	1	1	–
Total	5	1	4	1	9	2	14	10	12

4 Conclusion

This paper has successfully evaluated the performances of the 27 listed logistics companies in Malaysia using DEA model from 2010–2021. Nine companies (33.33%), made up of COMPLET, GDEX, HUBLINE, NATWIDE, POS, PDZ, PRKCORP, SYSCORP and TOCEAN are the highest performing with efficiency level of 100.00%. GCAP has the lowest efficiency of below 20.00% and should benchmark the highest performing companies based on the optimal solution of DEA in improving their performances. This study is the pioneer in studying the long-term performances of listed logistics companies in Malaysia and has provided managerial and market insights on the performances of the companies over the past 12 years. This paper has also proven the strengths of DEA

in measuring the long-term efficiency of DMUs while the proposed framework can be applied in other markets.

References

1. Hong, M., Sun, S., Beg, R., Zhou, Z.: Malaysia's exports to China: does diplomatic relationship matter? *Econ. Pap. J. Appl. Econ. Policy* **39**(1), 72–88 (2020)
2. Nekhoroshkov, V.P., et al.: Logistics efficiency of APEC countries: diagnosis, interconnections and digital experience for Russia. *Transp. Res. Procedia* **61**, 118–124 (2022)
3. Nguyen, T., Nguyen, T., Zhang, J.: ASEAN logistics network model and algorithm. *Asian J. Shipp. Logist.* **37**, 253–258 (2021)
4. Saidi, S., Mani, V., Mefteh, H., Shahbaz, M., Akhtar, P.: Dynamic linkages between transport, logistics, foreign direct investment, and economic growth: empirical evidence from developing countries. *Transp. Res. Part A* **141**, 277–293 (2020)
5. Banomyong, R., Grant, D.B., Varadejsatitwong, P., Julagasigorn, P.: Developing and validating a national logistics cost in Thailand. *Transp. Policy* **124**, 5–19 (2022)
6. Kedžo, M.G., Lukač, Z.: The financial efficiency of small food and drink producers across selected European Union countries using data envelopment analysis. *Eur. J. Oper. Res.* **291**, 586–600 (2021)
7. Agüero-Tobar, M.A., González-Araya, M.C., González-Ramírez, R.G.: Assessment of maritime operations efficiency and its economic impact based on data envelopment analysis: a case study of Chilean ports. *Res. Transp. Bus. Manag.* (2022)
8. Bhatia, A., Mahendru, M.: Revenue efficiency evaluation of life insurance companies in India: identification of leaders and laggards. *Benchmarking Int. J.* (in Press)
9. Gandhi, A.V., Sharma, D.: Technical efficiency of private sector hospitals in India using data envelopment analysis. *Benchmarking Int. J.* **25**(9), 3570–3591 (2018)
10. Khoshroo, A., Izadikhah, M., Emrouznejad, A.: Energy efficiency and congestion considering data envelopment analysis and bounded adjusted measure: a case of tomato production. *J. Clean. Prod.* **328**(129639), 1–8 (2021)
11. Banker, R.D., Charnes, A., Cooper, W.W.: Some models for estimating technical and scale inefficiencies in data envelopment analysis. *Manag. Sci.* **30**(9), 1078–1092 (1984)
12. Tan, K.M., Kamarudin, F., Bany-Ariffin, A.N., Rahim, N.A.: Investigation on firm efficiency: evidence from selected Asia-Pacific countries. *Benchmarking Int. J.* **25**(8), 3062–3080 (2018)
13. Fancello, G., Carta, M., Serra, P.: Data envelopment analysis for the assessment of road safety in urban road networks: a comparative study using CCR and BCC models. *Case Stud. Transp. Policy* **8**, 736–744 (2020)
14. Kamel, M.A., Mousa, M.E., Hamdy, R.M.: Financial efficiency of commercial banks listed in Egyptian stock exchange using data envelopment analysis. *Int. J. Product. Perform. Manag.* (in Press)
15. Tamatam, R., Dutta, P., Dutta, G., Lessmann, S.: Efficiency analysis of Indian banking industry over the period 2008–2017 using data envelopment analysis. *Benchmarking Int. J.* **26**(8), 2417–2442 (2019)
16. Dixit, A., Routroy, S., Dubey, S.K.: Measuring performance of government-supported drug warehouses using DEA to improve quality of drug distribution. *J. Adv. Manag. Res.* (in Press)
17. Ang, S., Chen, M., Yang, F.: Group cross-efficiency evaluation in data envelopment analysis: an application to Taiwan hotels. *Comput. Ind. Eng.* **125**, 190–199 (2018)
18. Lado-Sestayo, R., Fernández-Castro, Á.S.: The impact of tourist destination on hotel efficiency: a data envelopment analysis approach. *Eur. J. Oper. Res.* **272**, 674–676 (2019)

19. Raval, S.J., Kant, R., Shankar, R.: Analyzing the lean six sigma enabled organizational performance to enhance operational efficiency. *Benchmarking Int. J.* **27**(8), 2401–2434 (2020)
20. Hahn, G., Brandenburg, M., Becker, J.: Valuing supply chain performance within and across manufacturing industries: a DEA-based approach. *Int. J. Prod. Econ.* **240**(108203), 1–12 (2021)
21. Mohtashami, A., Ghiasvand, B.M.: Z-ERM DEA integrated approach for evaluation of banks & financial institutes in stock exchange. *Expert Syst. Appl.* **147**(113218), 1–22 (2020)
22. Karimi, A., Barati, M.: Financial performance evaluation of companies listed on Tehran stock exchange: a negative data envelopment analysis approach. *Int. J. Law Manag.* **60**(3), 885–900 (2018)
23. Habib, A.M., Shahwan, T.M.: Measuring the operational and financial efficiency using a Malmquist data envelopment analysis: a case of Egyptian hospitals. *Benchmarking Int. J.* **27**(9), 2521–2536 (2020)
24. Venkadasalam, S., Mohamad, A., Sifat, I.M.: Operational efficiency of shipping companies: evidence from Malaysia, Singapore, the Philippines, Thailand and Vietnam. *Int. J. Emerg. Mark.* **15**(5), 875–897 (2020)
25. Martins, C., Vaz, C.B., Alves, J.M.A.: Financial performance assessment of branded and non-branded hotel companies. Analysis of the Portuguese case. *Int. J. Contemp. Hosp. Manag.* **33**(10), 3134–3156 (2021)
26. Bowlin, W.F.: Measuring performance: an introduction to data envelopment analysis (DEA). *J. Cost Anal.* **15**(2), 3–27 (1998)
27. Yannick, G.Z.S., Zhao, H., Thierry, B.: Technical efficiency assessment using data envelopment analysis: an application to the banking sector of Côte d’Ivoire. *Procedia Soc. Behav. Sci.* **235**, 198–207 (2016)
28. Ghondagsaz, N., Kordnaeij, A., Delkhah, J.: Operational efficiency of plastic producing firms in Iran: a DEA approach. *Benchmarking Int. J.* **25**(7), 2126–2144 (2018)
29. Vikas, B.R.: Efficiency evaluation of Indian oil and gas sector: data envelopment analysis. *Int. J. Emerg. Mark.* **14**(2), 362–378 (2019)
30. Zheng, W., Xu, X., Wang, H.: Regional logistics efficiency and performance in China along the Belt and Road Initiative: the analysis of integrated DEA and hierarchical regression with carbon constraint. *J. Clean. Prod.* **276**(123649), 1–15 (2020)
31. Park, H.G., Lee, Y.J.: The efficiency and productivity analysis of large logistics providers services in Korea. *Asian J. Shipp. Logist.* **31**(4), 469–476 (2015)
32. Mousa, M.E., Kamel, M.A.: An integrated framework for predicting the best financial performance of banks: evidence from Egypt. *J. Model. Manag.*, 1–23 (2021)
33. Lee, P.F., Lam, W.S., Lam, W.H.: Evaluation and improvement of the efficiency of logistics companies with data envelopment analysis model. *Eng. J.* **25**(6), 45–54 (2021)
34. Lam, W.S., Lam, W.H., Jaaman, S.H.: Portfolio optimization with a mean-absolute deviation-entropy multi-objective model. *Entropy* **23**(10), 1266 (2021)
35. Lam, W.H., Lam, W.S., Lee, P.F.: Optimizing the financial management of electronic companies using goal programming model. *J. Phys. Conf. Ser.* **2070**(012046), 1–11 (2021)
36. Chitnis, A., Mishra, D.K.: Performance efficiency of Indian private hospitals using data envelopment analysis and super-efficiency DEA. *J. Health Manag.* **21**(2), 279–293 (2019)



Evaluation of the Preference of Online Food Delivery Providers in Supply Chain Management with AHP Model

Weng Siew Lam, Weng Hoe Lam^(✉), Chin Yap Hoh, and Shann Ying Wong

Department of Physical and Mathematical Science, Faculty of Science, Universiti Tunku Abdul Rahman, Kampar Campus, Jalan Universiti, Bandar Barat, 31900 Kampar, Perak, Malaysia
whlam@utar.edu.my

Abstract. E-Commerce is well established nowadays as the whole world is accessible to the internet. Nowadays, people are busy with their working life and thus, they have a limited of time for dining. This trend creates an opportunity for online food delivery (OFD) market. The objective of this study is to propose a conceptual framework to analyze and determine the preference of OFD providers among Foodpanda, Uber Eats, DeliverEat and RunningMan Delivery in Malaysia with Analytic Hierarchy Process (AHP) Model. Besides, this study also aims to identify the priority of decision criteria in the selection of OFD providers with AHP model. The results of this study show that Foodpanda is the most preferred OFD provider, followed by RunningMan Delivery, Uber Eats and finally DeliverEat. Moreover, price, delivery time and variety of food have been identified as the top three influential decision criteria in the selection of OFD providers. This study is significant because it helps to identify the most influential decision criterion and also the most favorable OFD provider in Malaysia. This study can serve as a reference for those less favorable OFD providers to identify their potential improvements so that they can offer better services to their users in future.

Keywords: Analytic Hierarchy Process · E-Commerce · Online Food Delivery · Supply Chain Management · Preference

1 Introduction

Nowadays, many people are demanding for the online food delivery (OFD) service [1] because of the internet and technology [1]. Some restaurants use social media as well as online platform to promote and improve their businesses. Hence, a lot of restaurants are collaborating with OFD providers nowadays. Food variety, time of delivery, price, quality of website information as well as customer service have been identified as the important factors in the selection of OFD provider.

Online store plays an important role to increase the variety of products and services [2]. Dholakia and Zhao [3] mentioned that the good record of time delivery can improve the customer satisfaction. Hausman and Siekpe [4] found that the content of the online platform is important to the customers. Besides that, the quality of website

gives significant impact towards customer satisfaction [5]. The customers expect good service from the staff in food delivery process [6]. Service quality affects the customer satisfaction based on their expectation towards the services provided. Kedah and Ismail [1] mentioned that customer service is one of the key factors of the online food ordering services.

Selection of OFD providers is a multi-criteria decision making (MCDM) problem. The best decision alternative is determined by solving the MCDM problems including uncertainty in information sources that involve multiple decision criteria in the past studies [7–32]. Based on the past studies, there is no comprehensive study done on the preference of OFD providers with respect to multiple decision criteria in Malaysia with AHP model. Hence, this study aims to propose a conceptual framework to analyze and determine the preference of OFD providers and the top influential decision criteria in Malaysia with AHP model. AHP model has been studied in various areas such as the risk assessment of occupational health and safety in a manufacturing company [33], preference of coffee shop [34], rural housing ecological performance [35], insurance sector [36] and selection of supermarket [37]. AHP has also been incorporated to other decision making models for solving MCDM problems [38–41].

For the structure of the paper, Sect. 2 presents the data and methodology of this research. The empirical results and conclusion are presented in Sect. 4 and Sect. 5 respectively.

2 Data and Methodology

The proposed framework is presented in Table 1 to evaluate the preference of ODF.

Table 1. Proposed Framework to Evaluate the Preference of OFD

	Items
Objective	Evaluate the preference of OFD providers in Malaysia
Decision Criteria	C1: Price
	C2: Customer Service
	C3: Variety of Food
	C4: Delivery Time
	C5: Website Information Quality
Decision Alternatives	A1: Foodpanda
	A2: Uber Eats
	A3: DeliverEat
	A4: RunningMan Delivery

The proposed conceptual framework is illustrated with a case study in Kuala Lumpur, Malaysia. This research aims to identify the preference of OFD providers among the

customers in Kuala Lumpur, Malaysia based on the proposed conceptual framework using AHP model. The respondents provide the inputs as data-driven analysis in the preference of OFD providers in this study.

In this research, AHP model is employed to identify the weights of the decision criteria and decision alternatives as follows [42, 43].

1. Construct the hierarchical structure.
2. Collect data based on the relative scale of importance.
3. Build the pairwise comparison matrices as follows.

$$A = \begin{bmatrix} 1 & c_{12} & \cdots & \cdots & c_{1n} \\ 1/c_{12} & 1 & & & c_{2n} \\ \vdots & & \ddots & & \vdots \\ \vdots & & & \ddots & \vdots \\ 1/c_{1n} & \cdots & \cdots & \cdots & 1 \end{bmatrix} \tag{1}$$

c_{ij} denotes the level of preference of element i to element j .

4. Normalize the pairwise comparison matrices.
5. Find the weights of decision criteria and decision alternatives.
6. Check the consistency of the pairwise comparison matrix based on consistency ratio (CR) as follows:

$$CR = \frac{CI}{RI} \tag{2}$$

where CI denotes consistency index whereas RI denotes random index. The level of consistency in the pairwise comparison matrix is acceptable if the $CR \leq 0.10$.

3 Result and Discussion

The weights of decision criteria in the selection of OFD provider is shown in Fig. 1.

Based on Fig. 1, the weights of customer service, website information quality, price, delivery time and variety of food are 0.1564, 0.0963, 0.3273, 0.2538 and 0.1662 respectively. The results of this study shows that price is found to be the top influential decision criterion in the selection of OFD provider. The preference of OFD is followed by the time of delivery, food variety, customer service and quality of website information.

The weights of OFD providers with respect to each decision criterion is presented in Table 2.

Based on Table 2, Foodpanda is ranked at the top for all decision criteria based on the weights. This implies that Foodpanda is the most preferred OFD provider among the customers. After Food Panda, RunningMan Delivery excels other OFD providers in term of all decision criteria except website information quality and customer service. Uber Eats excels other OFD providers in term of website information quality and customer service. DeliverEat is ranked at the lowest in term of all decision criteria except price.

Figure 2 presents the final weights of OFD providers.

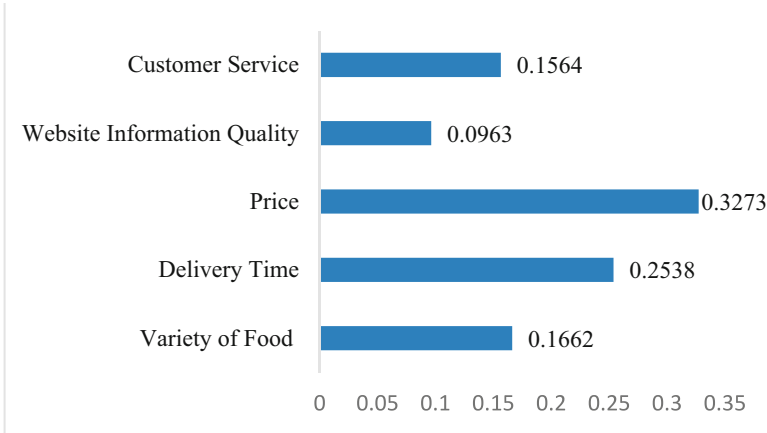


Fig. 1. Weights of decision criteria in the selection of OFD provider.

Table 2. Weights of OFD providers with respect to each decision criterion

OFD Provider	Variety of food	Delivery Time	Price	Website information quality	Customer service
RunningMan Delivery	0.2371	0.2329	0.2837	0.2021	0.2187
DeliverEat	0.1501	0.1534	0.2100	0.1631	0.1626
Uber Eats	0.2044	0.2053	0.2058	0.2119	0.2353
Foodpanda	0.4085	0.4084	0.3005	0.4228	0.3834

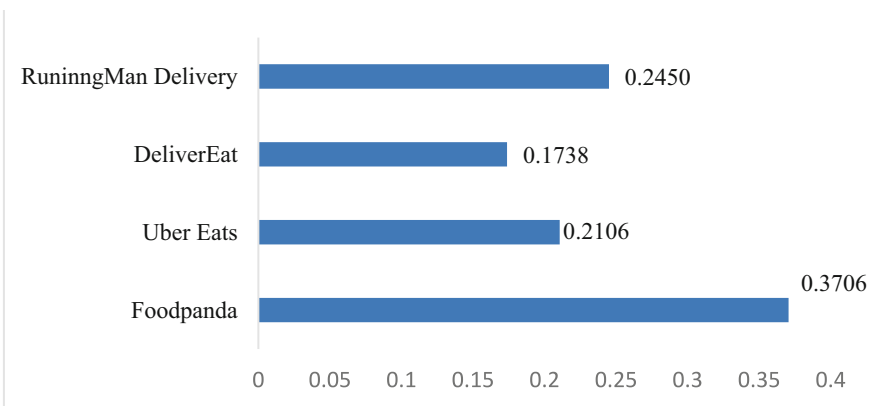


Fig. 2. Final weights of OFD providers

According to Fig. 2, the final weights of RunningMan Delivery, DeliverEat, Ubereats and FoodPanda are 0.2450, 0.1738, 0.2106 and 0.3706 respectively. FoodPanda obtains the highest weights among the OFD providers followed by RunningMan Delivery, Ubereats and finally DeliverEat. This implies that FoodPanda is the most preferred OFD provider by considering customer service, website information quality, price, delivery time and variety of food. It is because FoodPanda is ranked at the top for all decision criteria as presented in Table 2. The consistency ratio is 0.0058 and below 0.1000 which implies that result of this study is acceptable. Based on the findings of this study, price is found to be the top influential decision criterion in the selection of OFD providers. Therefore, the OFD providers should focus on a reasonable price for continuous improvement. Delivery time is the next priority of customer. The OFD providers are recommended to improve the reliability of delivery time by providing training to the staff. The OFD providers are recommended to work with various restaurants to serve more aged group efficiently [16]. In addition, the OFD providers can improve their tracking system to fulfill the customer demand effectively. For future research, the proposed conceptual framework can be applied in other countries by using AHP model.

4 Conclusion

This study aims to propose a conceptual framework to analyze and determine the preference of OFD providers among FoodPanda, Ubereats, DeliverEat and RunningMan Delivery using AHP model. Price is found to be the top influential decision criterion in the selection of OFD provider, followed by the time of delivery, food variety, customer service and quality of website information. Besides that, FoodPanda is the most preferred OFD provider followed by RunningMan Delivery, Ubereats and finally DeliverEat. This study helps to identify the top OFD provider and the preference of the decision criteria in the selection of OFD provider based on the proposed conceptual framework with AHP model. Furthermore, this study provides insights to other less favorable OFD providers such as Ubereats and DeliverEat to improve their services based on the top influential decision criteria.

References

1. Kedah, Z., Ismail, Y., Haque, A.A., Ahmed, S.: Key success factors of online food ordering services: an empirical study. *Malays. Manag. Rev.* **50**(2), 19–36 (2015)
2. Prasad, C.J., Aryasri, A.R.: Determinants of shopper behaviour in e tailing: an empirical analysis. *Paradigm* **13**(1), 73–83 (2009)
3. Dholakia, R.R., Zhao, M.: Effects of online store attributes on customer satisfaction and repurchase intentions. *Int. J. Retail Distrib. Manag.* **38**(7), 482–496 (2010)
4. Hausman, A.V., Siekpe, J.S.: The effect of web interface features on consumer online purchase intentions. *J. Bus. Res.* **62**(1), 5–13 (2009)
5. Belanche, D., Casalo, L.V., Guinaliu, M.: Website usability, consumer satisfaction and the intention to use a website: the moderating effect of perceived risk. *J. Retail. Consum. Serv.* **19**(1), 124–132 (2012)
6. Rashid, I.M.A., Abdullah, M.F.S., Yusuf, B.N.M., Shaari, M.S.: Impact of service and food quality on customer satisfaction among generation Y for the fast food restaurant in Malaysia. *J. Soc. Sci. Res.* **5**(2), 784–793 (2014)

7. Kilinc, C.C., Semiz, M., Katircioglu, E., Unusan, C.: Choosing restaurant for lunch in campus area by the compromise decision via AHP. *Int. J. Econ. Perspect.* **7**(2), 5–10 (2013)
8. Lam, W.H., Lam, W.S., Liew, K.F.: Performance analysis on telecommunication companies in Malaysia with TOPSIS model. *Indones. J. Electr. Eng. Comput. Sci.* **13**, 744–751 (2019)
9. Liew, K.F., Lam, W.S., Lam, W.H.: Financial network analysis on the performance of companies using integrated Entropy-DEMATEL-TOPSIS model. *Entropy* **24**(8), 1056 (2022)
10. Lam, W.S., Lam, W.H., Jaaman, S.H., Liew, K.F.: Performance evaluation of construction companies using integrated Entropy-Fuzzy VIKOR model. *Entropy* **23**(3), 320 (2021)
11. Lam, W.S., Liew, K.F., Lam, W.H.: Evaluation on the financial performance of the Malaysian banks with TOPSIS model. *Am. J. Serv. Sci. Manag.* **4**(2), 11–16 (2017)
12. Liew, K.F., Lam, W.S., Lam, W.H.: Financial analysis on the company performance in Malaysia with multi-criteria decision making model. *Syst. Sci. Appl. Math.* **1**(1), 1–7 (2016)
13. Liew, K.F., Lam, W.S., Lam, W.H.: An empirical evaluation on the efficiency of the companies in Malaysia with data envelopment analysis model. *Adv. Sci. Lett.* **23**(9), 8264–8267 (2017)
14. Lam, W.S., Liew, K.F., Lam, W.H.: Investigation on the efficiency of financial companies in Malaysia with data envelopment analysis model. *J. Phys. Conf. Ser.* **995**(1), 012021 (2018)
15. Lam, W.S., Chen, J.W., Lam, W.H.: An empirical study on the selection of fast food restaurants among the undergraduates with AHP model. *Am. J. Inf. Sci. Comput. Eng.* **2**(3), 15–21 (2016)
16. Lam, W.S., Liew, K.F., Lam, W.H.: An optimal control on the efficiency of technology companies in Malaysia with data envelopment analysis model. *J. Telecommun. Electron. Comput. Eng.* **10**(1), 107–111 (2018)
17. Hoe, L.W., Siew, L.W., Fai, L.K.: Improvement on the efficiency of technology companies in Malaysia with data envelopment analysis model. In: Badioze Zaman, H., et al. (eds.) *IVIC 2017. LNCS*, vol. 10645, pp. 19–30. Springer, Cham (2017). https://doi.org/10.1007/978-3-319-70010-6_2
18. Lam, W.S., Leong, W.B., Lam, W.H.: Selection of mobile network operator based on multi-criteria decision making model using analytic hierarchy process. *Math. Stat. J.* **1**(1), 12–18 (2015)
19. Lam, W.S., Bishan, R.S., Lam, W.H.: An empirical study on the mold machine-tool selection in semiconductor industry with analytic hierarchy process model. *Adv. Sci. Lett.* **23**(9), 8286–8289 (2017)
20. Lam, W.H., Din, M.A., Lam, W.S., Chen, J.W.: Evaluation on the performance of suppliers in Malaysia with TOPSIS model. *J. Fundam. Appl. Sci.* **10**(6S), 406–415 (2018)
21. Lam, W.S., Lam, W.H.: Strategic decision making in portfolio management with goal programming model. *Am. J. Oper. Manag. Inf. Syst.* **1**(1), 34–38 (2016)
22. Siew, L.W., Wai, C.J., Hoe, L.W.: Data driven decision analysis in bank financial management with goal programming model. In: Badioze Zaman, H., et al. (eds.) *IVIC 2017. LNCS*, vol. 10645, pp. 681–689. Springer, Cham (2017). https://doi.org/10.1007/978-3-319-70010-6_63
23. Lam, W.S., Liew, K.F., Lam, W.H.: Performance evaluation of construction companies in Malaysia with Entropy-VIKOR model. *Eng. J.* **25**(1), 297–305 (2021)
24. Lam, W.S., Chen, J.W., Lam, W.H.: Analysis on the preference of fast food restaurants with analytic hierarchy process model. *Int. J. Psychol. Cognit. Sci.* **3**(6), 72–76 (2017)
25. Lam, W.S., Liew, K.F., Lam, W.H.: Evaluation on the efficiency of healthcare companies in Malaysia with data envelopment analysis model. *SCIREA J. Math.* **1**(1), 95–106 (2016)
26. Lee, P.F., Lam, W.S., Lam, W.H.: Evaluation and improvement of the efficiency of logistics companies with data envelopment analysis model. *Eng. J.* **25**(6), 45–54 (2021)
27. Lam, W.S., Lam, W.H., Bakar, M.A., Lee, P.F.: Data driven decision analysis on the performance of electronic companies with TOPSIS model. *J. Adv. Inf. Technol.* **13**(1), 61–66 (2022)
28. Lam, W.S., Lam, W.H., Liew, K.F.: Data analysis on the performance of technology sector in Malaysia with Entropy-TOPSIS model. *Commun. Comput. Inf. Sci.* **886**, 194–203 (2018)

29. Lam, W.H., Lam, W.S., Jaaman, S.H., Lee, P.F.: Bibliometric analysis of information theoretic studies. *Entropy* **24**(10), 1359 (2022)
30. Lam, W.S., Liew, K.F., Lam, W.H.: Investigation on the performance of construction companies in Malaysia with Entropy-TOPSIS model. *Earth Environ. Sci.* **385**, 012006 (2019)
31. Lam, W.S., Lam, W.H., Jaaman, S.H.: Portfolio optimization with a mean-absolute deviation-entropy multi-objective model. *Entropy* **23**(10), 1266 (2021)
32. Liew, K.F., Lam, W.S., Lam, W.H.: Analysis on the library service quality with analytic hierarchy process model. *J. Phys. Conf. Ser.* **1706**, 012154 (2020)
33. Kokangul, A., Polat, U., Dağsuyu, C.: A new approximation for risk assessment using the AHP and Fine Kinney methodologies. *Saf. Sci.* **91**, 24–32 (2017)
34. Lam, W.S., Bakar, M.A., Lam, W.H., Chen, J.W., Ma, H.L.: Evaluation on the preference of coffee shops among undergraduate students with analytic hierarchy process model. *Int. J. Supply Chain Manag.* **7**(4), 209–215 (2018)
35. Zhe, Y.: The research on evaluation system of rural housing ecological performance based on the AHP system model. In: 2016 International Conference on Smart City and Systems Engineering (ICSCSE), pp. 254–256 (2016)
36. Khan, M., Bharathi, S.V., Londhe, B.R.: Ranking the critical buying factors of private health insurance using analytic hierarchy process. *Indian J. Sci. Technol.* **8**(S6), 35–42 (2015)
37. Lam, W.S., Bishan, R.S., Lam, W.H., Liew, K.F.: An empirical evaluation on the preference of supermarkets with analytic hierarchy process model. *J. Phys. Conf. Ser.* **995**(012037), 1–9 (2018)
38. Lam, W.S., Lam, W.H., Liew, K.F., Chen, J.W.: An empirical study on the preference of fast food restaurants in Malaysia with AHP-TOPSIS model. *J. Eng. Appl. Sci.* **13**, 3226–3231 (2018)
39. Lam, W.S., Bakar, M.A., Lam, W.H., Liew, K.F.: Multi-criteria decision making in the selection of mobile network operators with AHP-TOPSIS model. *J. Eng. Appl. Sci.* **12**, 6382–6386 (2017)
40. Lam, W.S., Lam, W.H., Liew, K.F., Bakar, M.A., Sim, J.X.: Analysis on the e-learning method in Malaysia with AHP-VIKOR model. *Int. J. Inf. Educ. Technol.* **11**(2), 52–58 (2021)
41. Lam, W.H., Lam, W.S., Liew, K.F., Wong, S.C.: Data driven decision analysis on the selection of course programmes with AHP-TOPSIS model. *Int. J. Supply Chain Manag.* **7**(4), 202–208 (2018)
42. Saaty, T.L.: Decision making with the analytic hierarchy process. *Int. J. Serv. Sci.* **1**(1), 83–98 (2008)
43. Lam, W.S., Lee, W.K., Lam, W.H.: Multi-criteria decision making in job selection problem using analytic hierarchy process model. *Math. Stat. J.* **1**(2), 3–7 (2015)



Performance Analysis of Courier Service Providers in Transportation Using TOPSIS Model

Weng Siew Lam, Weng Hoe Lam^(✉), Ching Wen Heng, and Yen Shuang Tioh

Department of Physical and Mathematical Science, Faculty of Science, Universiti Tunku Abdul Rahman, Kampar Campus, Jalan Universiti, Bandar Barat, 31900 Kampar, Perak, Malaysia
whlam@utar.edu.my

Abstract. Nowadays, the exponential growth of e-commerce has influenced the market of courier service providers. The sellers are increasing the parcels that need to be delivered every year, and this trend is expected to continue in the foreseeable future. In this competition environment, customer will choose the courier service provider that can provides the most satisfactory service. This study aims to propose a research framework to analyse and evaluate the performance of courier service providers in transportation using Technique for Order of Preference by Similarity to Ideal Solution (TOPSIS) model. This study indicates that the assurance and responsiveness are the influential decision criteria for the performance evaluation of courier service providers. Besides, GDEX outperforms Ninja Van and J&T Express as courier service providers in transportation based on the TOPSIS model.

Keywords: TOPSIS · Ideal solution · E-Commerce · Transportation · Ranking

1 Introduction

E-commerce is important in our daily lives nowadays. B2B and B2C businesses as well as online shopping are the important elements in e-commerce business. The rapid development of e-commerce provides opportunities and challenges to courier services companies. Courier service includes delivery of goods directly from the pick-up point to the clients [1].

Nowadays, customer expect for a fast and convenient delivery. Customer satisfaction is important in the courier services industry [2]. From the customers' perspective, if the courier service provider is not able to provide an efficient delivery, this will affect the customer satisfaction on the delivery service [3]. Service quality gives impact on the performance of a business as well as customer satisfaction. Assurance is one of the important criteria in delivery service [4]. Yee and Daud [5] mentioned that assurance affects the customer satisfaction in courier service industry. The company should provide an effective approach to serve the customers. Tracking technologies help the logistic companies in providing efficient courier services [6]. Responsiveness is important for sustaining competitive benefit based on customer demand [7]. Responsiveness measures

how well is the delivery service in term of flexibility, time as well as quality to the clients [8, 9].

Technique for Order of Preference by Similarity to Ideal Solution (TOPSIS) model aims to compare the decision alternatives to the negative ideal solution (NIS) and positive ideal solution (PIS). TOPSIS model is an effective decision tool for solving the multi-criteria decision-making (MCDM) problems such as evaluation of the fast food restaurants [10], mobile network operators [11], materials [12] and companies' performance [13, 14]. In solving MCDM problems, the best decision alternative is determined by considering multiple decision criteria [15–38]. TOPSIS model aims to identify the alternative that has the longest separation distance from the NIS and the shortest distance to the PIS. The ranking of the alternatives will be constructed according to their relative closeness to the ideal solution. Other approaches such as entropy has been incorporated into TOPSIS model for solving MCDM problems [39, 40]. Entropy has been considered into information theory due to the uncertainty in information sources [41, 42].

This study aims to propose a research framework to analyse and evaluate the performance of courier service providers in transportation using TOPSIS model. This study focuses on the important criteria such as assurance, convenience, and responsiveness. The organization of the paper is as follows. Section 2 presents the data and methodology of this study. The empirical results of this study are presented in Sect. 3. Section 4 concludes the paper.

2 Data and Methodology

The proposed framework is presented in Table 1 to evaluate the performance of courier service providers in transportation using TOPSIS model.

Table 1. Proposed Framework to Evaluate the Performance of Courier Service Providers using TOPSIS Model

	Items
Objective	To evaluate the performance of courier service providers in transportation
Decision Criteria	Assurance
	Convenience
	Responsiveness
Decision Alternatives	Ninja Van
	J&T Express
	Gdex

The proposed framework is illustrated with a case study in Perak, Malaysia. This study aims to evaluate the performance of courier service providers in transportation based on the proposed framework with TOPSIS model. The respondents provide the inputs as data-driven analysis of the weight of decision criteria for the performance

evaluation of courier service providers in this study. The TOPSIS model is presented as follows [43, 44]:

Step 1: Calculation of the weighted normalized decision matrix as follows:

$$v_{ij} = w_j \times r_{ij}, j = 1, 2, 3, \dots, n; i = 1, 2, 3, \dots, m \quad (1)$$

where w_j = weights of the criterion j and r_{ij} is the normalized decision matrix

Step 2: Computation of the alternatives' separation distance from the positive ideal solution, PIS (S^+) and negative ideal solution, NIS (S^-).

$$S_i^+ = \sqrt{\sum_{j=1}^n (v_j^+ - v_{ij})^2}, i = 1, 2, 3, \dots, m \quad (2)$$

$$S_i^- = \sqrt{\sum_{j=1}^n (v_j^- - v_{ij})^2}, i = 1, 2, 3, \dots, m, \quad (3)$$

where $v_j^+ = \{(\max v_{ij} | i \in I), (\min v_{ij} | i \in I')\}$ and $v_j^- = \{(\min v_{ij} | i \in I), (\max v_{ij} | i \in I')\}$

Step 3: Determination of the alternatives' relative closeness coefficient respect to the ideal solutions (s_{iw}).

$$s_{iw} = \frac{s_i^-}{(s_i^+ + s_i^-)}, 0 \leq c_i \leq 1, \quad (4)$$

Step 4: The decision alternatives are ranked according to their s_{iw} . The alternative with the largest value of s_{iw} will be the best decision alternative.

3 Result and Discussion

The weight of decision criteria for the performance evaluation of courier service providers is presented in Fig. 1.

As shown in Fig. 1, the weights of responsiveness, convenience and assurance are 0.4108, 0.1766 and 0.4126 respectively. The results of this study show that responsiveness and assurance are identified as the most influential decision criteria for the performance evaluation of courier service providers in this study. Table 2 presents the PIS and NIS for the decision criteria.

Based on the Table 2, the PIS for assurance, convenience and responsiveness is 0.2556, 0.1086 and 0.2511 respectively. On the other hand, the NIS for assurance, convenience and responsiveness is 0.2270, 0.0971 and 0.2296 respectively. Based on the TOPSIS model, the courier service providers can identify the potential improvement based on the ideal solution of PIS and NIS as presented in the Table 2.

Table 3 presents the separation distance of the courier service providers from the PIS (s_i^+) and NIS (s_i^-).

Based on Table 3, the separation distance from the PIS for Ninja Van, J&T Express and Gdex is 0.0372, 0.0337 and 0.0000 respectively. From here, it can be concluded that

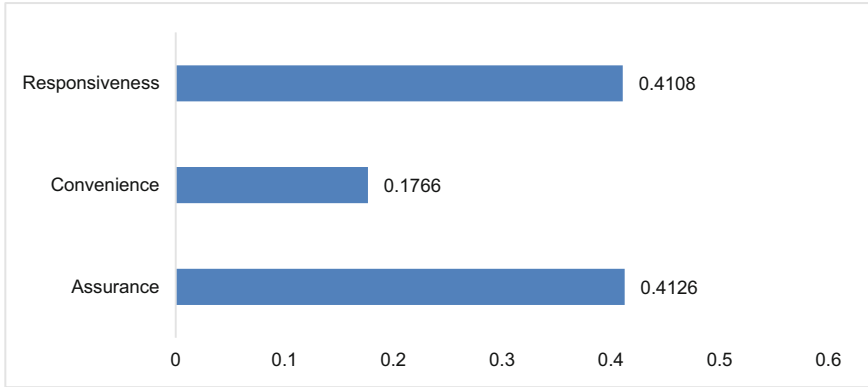


Fig. 1. Weight of decision criteria for the performance evaluation of courier service providers.

Table 2. PIS and NIS for the decision criterion

Decision Criteria	PIS	NIS
Assurance	0.2556	0.2270
Convenience	0.1086	0.0971
Responsiveness	0.2511	0.2296

Table 3. Separation distance of the courier service providers from the PIS (s_i^+) and NIS (s_i^-)

Courier service providers	s_i^+	s_i^-
Ninja Van	0.0372	0.0007
J&T Express	0.0337	0.0049
Gdex	0.0000	0.0375

Gdex is the closest and reaching the PIS. On the other hand, the separation distance from the NIS for Ninja Van, J&T Express and Gdex is 0.0007, 0.0049 and 0.0375 respectively. Therefore, Gdex is identified as a well-performed courier service provider because of the shortest distance to the PIS and farthest distance from the NIS.

Table 4 presents the overall performance of the courier service providers.

The overall performance of the courier service providers is determined based on the relative closeness to the ideal solution (s_{iw}). As shown in Table 4, s_{iw} of Ninja Van, J&T Express and Gdex is 0.0177, 0.1265 and 1.0000 respectively. Gdex obtains the highest value (1.0000) of s_{iw} among the courier service providers followed by J&T Express (0.1265) and finally Ninja Van (0.0177). This implies that Gdex obtains the first ranking and outperforms J&T Express and Ninja Van with respect to all decision criteria which

Table 4. Overall performance of the courier service providers

Courier service providers	Relative closeness to the ideal solution (s_{iw})	Ranking
Ninja Van	0.0177	3
J&T Express	0.1265	2
Gdex	1.0000	1

are assurance, convenience and responsiveness. It is because Gdex gives the shortest distance to the PIS and farthest distance from the NIS. Based on the findings of this study, responsiveness and assurance are identified as the most influential decision criteria for the performance evaluation of courier service providers. Therefore, the courier service providers should focus on the responsiveness and assurance factors for the continuous improvement.

4 Conclusion

This study aims to propose a research framework to evaluate the performance of courier service providers among Ninja Van, J&T Express and Gdex with TOPSIS model. The results of this study show that responsiveness and assurance are identified as the most influential decision criteria for the performance evaluation of courier service providers. Besides that, Gdex is the most performed courier service followed by J&T Express and finally Ninja Van. This study is significant because it helps to evaluate the performance of the courier service providers as well as the most influential decision criteria based on the proposed research framework with TOPSIS model. Furthermore, this study can serve as reference to other courier service providers such as J&T Express and Ninja Van to identify their potential improvements based on the ideal solution in this study.

References

1. Izzah, N., Rifai, D., Yao, L.: Relationship-courier partner logistics and e-commerce enterprises in Malaysia: a review. *Indian J. Sci. Technol.* **9**(9), 1–10 (2016)
2. Cheng, L.Y., Yang, C.C., Teng, H.M.: An integrated model for customer relationship management: an analysis and empirical study. *Hum. Factors Ergon. Manuf. Serv. Ind.* **23**(5), 462–481 (2013)
3. Chen, Y., Yu, J., Yang, S., Wei, J.: Consumer's intention to use self-service parcel delivery service in online retailing. *Internet Res.* **28**(2), 500–519 (2018)
4. Minh, N.H., Ha, N.T., Anh, P.C., Matsui, Y.: Service quality and customer satisfaction: a case study of hotel industry in Vietnam. *Asian Soc. Sci.* **11**(10) (2015)
5. Yee, H. L., Daud, D.: Measuring customer satisfaction in the parcel service delivery: a pilot study in Malaysia. *Bus. Econ. Res.* **1**(1) (2011)
6. Shamsuzzoha, A.H.M., Helo, P.T.: Real time tracking and tracing system: potentials for the logistics network. In: *Proceedings of the 2011 International Conference on Industrial Engineering and Operations Management*, pp. 22–24 (2011)

7. Sachdeva, A., Sharma, V., Garg, R.K., Singh, R.K.: Modelling of critical factors for responsiveness in supply chain. *J. Manuf. Technol. Manag.* **26**(6), 868–888 (2015)
8. Hasnan, N., Noordin, A., Osman, N.H.: Six main innovation issues: a case of service innovation of postal and courier services in Malaysia. *J. Technol. Manag. Bus.* **1**(1) (2014)
9. Al Rosyid, H., Setijadi, E., Nugroho, S.M.S.: Evaluating customer satisfaction and service quality using SERVQUAL model in the courier service delivery (CSD) provider (pilot study: Surabaya City, Indonesia). *IPTEK J. Proc. Ser.* **3**, 1–9 (2018)
10. Lam, W.S., Lam, W.H., Liew, K.F., Chen, J.W.: An empirical study on the preference of fast food restaurants in Malaysia with AHP-TOPSIS model. *J. Eng. Appl. Sci.* **13**, 3226–3231 (2018)
11. Lam, W.S., Bakar, M.A., Lam, W.H., Liew, K.F.: Multi-criteria decision making in the selection of mobile network operators with AHP-TOPSIS model. *J. Eng. Appl. Sci.* **12**, 6382–6386 (2017)
12. Bhattacharjee, P., Debnath, A., Chakraborty, S., Mandal, U.K.: Selection of optimal aluminum alloy using TOPSIS method under fuzzy environment. *J. Intell. Fuzzy Syst.* **32**, 871–876 (2017)
13. Lam, W.H., Lam, W.S., Liew, K.F.: Performance analysis on telecommunication companies in Malaysia with TOPSIS model. *Indones. J. Electr. Eng. Comput. Sci.* **13**, 744–751 (2019)
14. Liew, K.F., Lam, W.S., Lam, W.H.: Financial network analysis on the performance of companies using integrated Entropy-DEMATEL-TOPSIS model. *Entropy* **24**(8), 1056 (2022)
15. Lam, W.S., Lam, W.H., Jaaman, S.H., Liew, K.F.: Performance evaluation of construction companies using integrated Entropy-Fuzzy VIKOR model. *Entropy* **23**(3), 320 (2021)
16. Liew, K.F., Lam, W.S., Lam, W.H.: Financial analysis on the company performance in Malaysia with multi-criteria decision making model. *Syst. Sci. Appl. Math.* **1**(1), 1–7 (2016)
17. Lam, W.S., Liew, K.F., Lam, W.H.: Evaluation on the financial performance of the Malaysian banks with TOPSIS model. *Am. J. Serv. Sci. Manag.* **4**(2), 11–16 (2017)
18. Lam, W.S., Liew, K.F., Lam, W.H.: Investigation on the efficiency of financial companies in Malaysia with data envelopment analysis model. *J. Phys. Conf. Ser.* **995**(1), 012021 (2018)
19. Liew, K.F., Lam, W.S., Lam, W.H.: An empirical evaluation on the efficiency of the companies in Malaysia with data envelopment analysis model. *Adv. Sci. Lett.* **23**(9), 8264–8267 (2017)
20. Lam, W.S., Chen, J.W., Lam, W.H.: An empirical study on the selection of fast food restaurants among the undergraduates with AHP model. *Am. J. Inf. Sci. Comput. Eng.* **2**(3), 15–21 (2016)
21. Hoe, L.W., Siew, L.W., Fai, L.K.: Improvement on the efficiency of technology companies in Malaysia with data envelopment analysis model. In: Badioze Zaman, H., et al. (eds.) *IVIC 2017*. LNCS, vol. 10645, pp. 19–30. Springer, Cham (2017). https://doi.org/10.1007/978-3-319-70010-6_2
22. Lam, W.S., Liew, K.F., Lam, W.H.: An optimal control on the efficiency of technology companies in Malaysia with data envelopment analysis model. *J. Telecommun. Electron. Comput. Eng.* **10**(1), 107–111 (2018)
23. Lam, W.S., Leong, W.B., Lam, W.H.: Selection of mobile network operator based on multi-criteria decision making model using analytic hierarchy process. *Math. Stat. J.* **1**(1), 12–18 (2015)
24. Lam, W.S., Lee, W.K., Lam, W.H.: Multi-criteria decision making in job selection problem using analytic hierarchy process model. *Math. Stat. J.* **1**(2), 3–7 (2015)
25. Lam, W.H., Din, M.A., Lam, W.S., Chen, J.W.: Evaluation on the performance of suppliers in Malaysia with TOPSIS model. *J. Fundam. Appl. Sci.* **10**(6S), 406–415 (2018)
26. Lam, W.S., Bishan, R.S., Lam, W.H.: An empirical study on the mold machine-tool selection in semiconductor industry with analytic hierarchy process model. *Adv. Sci. Lett.* **23**(9), 8286–8289 (2017)

27. Siew, L.W., Wai, C.J., Hoe, L.W.: Data driven decision analysis in bank financial management with goal programming model. In: Badioze Zaman, H., et al. (eds.) *IVIC 2017. LNCS*, vol. 10645, pp. 681–689. Springer, Cham (2017). https://doi.org/10.1007/978-3-319-70010-6_63
28. Lam, W.S., Lam, W.H.: Strategic decision making in portfolio management with goal programming model. *Am. J. Oper. Manag. Inf. Syst.* **1**(1), 34–38 (2016)
29. Lam, W.S., Lam, W.H., Liew, K.F., Bakar, M.A., Sim, J.X.: Analysis on the e-learning method in Malaysia with AHP-VIKOR model. *Int. J. Inf. Educ. Technol.* **11**(2), 52–58 (2021)
30. Lam, W.H., Lam, W.S., Liew, K.F., Wong, S.C.: Data driven decision analysis on the selection of course programmes with AHP-TOPSIS model. *Int. J. Supply Chain Manag.* **7**(4), 202–208 (2018)
31. Lam, W.S., Liew, K.F., Lam, W.H.: Performance evaluation of construction companies in Malaysia with Entropy-VIKOR model. *Eng. J.* **25**(1), 297–305 (2021)
32. Lam, W.S., Chen, J.W., Lam, W.H.: Analysis on the preference of fast food restaurants with analytic hierarchy process model. *Int. J. Psychol. Cognit. Sci.* **3**(6), 72–76 (2017)
33. Lam, W.S., Liew, K.F., Lam, W.H.: Evaluation on the efficiency of healthcare companies in Malaysia with data envelopment analysis model. *SCIREA J. Math.* **1**(1), 95–106 (2016)
34. Lee, P.F., Lam, W.S., Lam, W.H.: Evaluation and improvement of the efficiency of logistics companies with data envelopment analysis model. *Eng. J.* **25**(6), 45–54 (2021)
35. Lam, W.S., Bishan, R.S., Lam, W.H., Liew, K.F.: An empirical evaluation on the preference of supermarkets with analytic hierarchy process model. *J. Phys. Conf. Ser.*, 012037 (2018)
36. Lam, W.S., Bakar, M.A., Lam, W.H., Chen, J.W., Ma, H.L.: Evaluation on the preference of coffee shops among undergraduate students with analytic hierarchy process model. *Int. J. Supply Chain Manag.* **7**(4), 209–215 (2018)
37. Lam, W.S., Lam, W.H., Bakar, M.A., Lee, P.F.: Data driven decision analysis on the performance of electronic companies with TOPSIS model. *J. Adv. Inf. Technol.* **13**(1), 61–66 (2022)
38. Liew, K.F., Lam, W.S., Lam, W.H.: Analysis on the library service quality with analytic hierarchy process model. *J. Phys. Conf. Ser.* **1706**, 012154 (2020)
39. Lam, W.S., Lam, W.H., Liew, K.F.: Data analysis on the performance of technology sector in Malaysia with Entropy-TOPSIS model. *Commun. Comput. Inf. Sci.* **886**, 194–203 (2018)
40. Lam, W.S., Liew, K.F., Lam, W.H.: Investigation on the performance of construction companies in Malaysia with Entropy-TOPSIS model. *Earth Environ. Sci.* **385**, 012006 (2019)
41. Lam, W.S., Lam, W.H., Jaaman, S.H.: Portfolio optimization with a mean-absolute deviation-entropy multi-objective model. *Entropy* **23**(10), 1266 (2021)
42. Lam, W.H., Lam, W.S., Jaaman, S.H., Lee, P.F.: Bibliometric analysis of information theoretic studies. *Entropy* **24**(10), 1359 (2022)
43. Yue, Z.: TOPSIS-based group decision-making methodology in intuitionistic fuzzy setting. *Inf. Sci.* **277**, 141–153 (2014)
44. Ou, Y., Yi, L., Zou, B., Pei, Z.: The linguistic intuitionistic fuzzy set TOPSIS method for linguistic multi-criteria decision makings. *Int. J. Comput. Intell. Syst.* **11**, 120–132 (2018)



A Fast Initial Response Double EWMA Chart for Process Mean

Peh Sang Ng¹(✉), Wai Chung Yeong², Irene Seok-Ching Yong³, and Huai Tein Lim¹

¹ Department of Physical and Mathematical Science, Faculty of Science,
Universiti Tunku Abdul Rahman, 31900 Kampar, Perak, Malaysia
psng@utar.edu.my

² School of Mathematical Sciences, Sunway University, 47500 Petaling Jaya, Malaysia

³ Centre for Internship Training and Academic Enrichment (CITrA), Universiti Malaya, Kuala Lumpur, Malaysia

Abstract. The performance of a control chart can be affected by an inefficient start-up setting and ineffective corrective action following an out-of-control condition. In this work, we proposed the double exponentially weighted moving average chart with fast initial response feature (FDEWMA) to monitor the process mean. The Monte Carlo simulation is used to evaluate the run length performance of the FDEWMA chart, in terms of the average run length (ARL), standard deviation of the run length (SDRL) and expected average run length (EARL). The proposed chart is then compared to the existing DEWMA chart without the fast initial response feature. Based on the simulation results, the shift detection ability of the proposed FDEWMA chart is enhanced and is shown to perform better than the DEWMA chart.

Keywords: Fast Initial Response · DEWMA chart · ARL · SDRL · EARL

1 Introduction

One of the main criteria that contributes to customer satisfaction and customer purchase loyalty is the quality of the product and services that is offered by the organizations. Thus, quality control is an important strategy for organizations to ensure good quality processes, and as a result to gain the competitive edge and business opportunities in the market.

Control chart is the most effective tool in Statistical Process Control to monitor and control the quality of any process [1]. The first control chart used in process monitoring is the Shewhart chart (also known as the \bar{X} chart), which was proposed by Walter A. Shewhart [2]. However, this \bar{X} chart is less sensitive in detecting small to moderate shifts. To address the drawback of the \bar{X} chart, the exponentially weighted moving average (EWMA) chart that is sensitive in small to moderate shifts detection is developed by Roberts [3]. To further detect the small shifts more efficiently, Zhang and Chen [4] proposed the double EWMA (DEWMA) chart. Results showed that the DEWMA chart surpasses the EWMA chart proposed by Roberts [3] for small shifts detection.

A process is statistically in control if it has a constant mean and variance throughout the process monitoring. This implies that if there is any start-up setting problems for the initiated control scheme or any ineffective corrective actions taken following the occurrence of assignable cause that result in off-target process mean, the process is declared as out-of-control. Hence, to increase the sensitivity of the chart in signaling an out-of-control situation when the process mean is off-target, the fast initial response (or known as head-start) feature was integrated into the CUSUM chart by Lucas and Crosier [5]. Worth noting that the effect of FIR feature on the performance of control chart is less pronounced if the process is in-control [5]. Subsequently, the FIR feature was integrated into one-sided EWMA chart by Lucas and Saccucci [6] and the results showed that the one-sided FIR EWMA chart gives better performance than the traditional EWMA chart in shift detection. To enhance the shift detection ability of the one-sided FIR EWMA chart proposed by Lucas and Saccucci [6], Steiner [7] proposed the time varying EWMA chart with FIR feature in process monitoring. Recently, Haq et al. [8] and Ng et al. [9] showed that their proposed charts with FIR feature outperform their corresponding traditional charts without FIR feature. With the salient feature of the FIR concept, the FIR feature is integrated into the DEWMA chart (named as the FDEWMA chart) in this paper.

In Sect. 2, the properties of the FDEWMA chart are discussed and the step-by-step to implement the FDEWMA chart is given. Section 3 explains the average run length (ARL), standard deviation of the run length (SDRL) and expected average run length (EARL) computations for the FDEWMA chart. The evaluation on the run length performance and the performance comparison between the proposed FDEWMA and existing DEWMA charts are made in this section as well. Lastly, the concluding remarks based on the observations found for the proposed FDEWMA chart and the possible future research are given.

2 The Properties of the FDEWMA Chart

Suppose we have a quality characteristic X under study that follows an independently and identically distributed normal distribution with in-control mean μ_0 and variance σ_0 , i.e., $X_i \sim N(\mu_0 + \delta\sigma_0, \sigma_0)$. Here, X_i are normal random variables for time $i \geq 1$, while δ is the standardized mean shift. If $\delta = 0$, then the process is in-control, otherwise the process has drifted (i.e., $\delta \neq 0$).

As claimed by Zhang and Chen [4], the performance of the DEWMA chart with equal smoothing constants, i.e., $\lambda_1 = \lambda_2$ is superior to the DEWMA chart with different smoothing constants, i.e., $\lambda_1 \neq \lambda_2$. Thus, in this paper, the FDEWMA chart with equal smoothing constants is proposed. The plotting statistic of the FDEWMA chart at time i , DE_i , is similar to that of the DEWMA chart by Zhang and Chen [4], is given as follows:

$$E_i = \lambda_1 \bar{X}_i + (1 - \lambda_1)E_{i-1}, 0 < \lambda_1 \leq 1,$$

$$DE_i = \lambda_2 E_i + (1 - \lambda_2)DE_{i-1}, 0 < \lambda_2 \leq 1, \text{ for } i = 1, 2, \dots, \quad (1)$$

where $E_0 = DE_0 = \mu_0$, \bar{X}_i is the average of the sample at time $i = 1, 2, \dots$, and λ_1 and λ_2 are the smoothing constants. The respective mean and variance of DE_i for the

DEWMA chart with $\lambda_1 = \lambda_2$ are derived as [4]

$$E(DE_i) = \mu_0 \quad (2)$$

and

$$\begin{aligned} \text{Var}(DE_i) = & \frac{\sigma_0^2 \lambda_1^4}{n(1 - (1 - \lambda_1)^2)^3} \left[1 + (1 - \lambda_1)^2 - (1 - \lambda_1)^{2i} (i^2 + 2i + 1) \right. \\ & \left. + (1 - \lambda_1)^{2(i+1)} (2i^2 + 2i - 1) - i^2 (1 - \lambda_1)^{2(i+2)} \right], \end{aligned} \quad (3)$$

respectively. Here, n is denoted as the sample size.

The time varying control limits of the FDEWMA chart at time i , i.e., the upper control limit (UCL_i), the center limit (CL_i) and the lower control limit (LCL_i) for the plotting statistic DE_i in Eq. (1) are given as

$$UCL_i = \mu_0 + kQ\sqrt{\text{Var}(DE_i)}, \quad (4a)$$

$$CL_i = \mu_0 \quad (4b)$$

and

$$LCL_i = \mu_0 - kQ\sqrt{\text{Var}(DE_i)}, \quad (4c)$$

respectively, where Q is defined as the fast initial response (FIR) feature by Steiner [7], and it is defined as follows:

$$Q = \left[1 - (1 - p)^{1+s(i-1)} \right]. \quad (5)$$

Here, p is an adjustable constant that is used to determine the proportion of distance from the first time period, while s is an adjustment parameter that can be calculated by using $\frac{1}{19} \left(-\frac{2}{\log(1-p)} - 1 \right)$. The combination $p = 0.5$ and $s = 0.3$ is recommended by Steiner [7] because it results in 50% head-start.

The implementation steps for the FDEWMA chart are described as below:

1. Specify the desired values of n , λ and the in-control ARL (ARL_0). Note that, since $\lambda_1 = \lambda_2$, then we let $\lambda = \lambda_1 = \lambda_2$.
2. Search for the value of k that gives the preliminarily specified ARL_0 .
3. Find the plotting statistic DE_i by using Eq. (1).
4. Calculate the values for the upper and lower control limits with Eqs. (4a) and (4c), respectively.
5. If $DE_i \in [LCL_i, UCL_i]$, the process is statistically in-control. In other words, if $DE_i > UCL_i$ or $DE_i < LCL_i$, the process is off-target at time i and corrective action is taken to remove the possible anomalies.

3 Computation and Comparisons of Run Lengths

The studies by Haq et al. [8], Ng et al. [9], Abbas et al. [10], Haq [11] and Hu et al. [12], all have employed the Monte Carlo simulation approach to compute the run length properties of their proposed methods. In like manner, the run length properties for both FDEWMA and DEWMA charts are computed using Monte Carlo simulation as well. Then, the run length comparisons between these two charts are made in terms of the ARL, SDRL and EARL. The ARL performance measure is employed to identify the average number of samples needed by a control chart to signal an off target process for a specific shift size, the SDRL is used to give the information on the stability of the ARL, while the EARL is used to determine the average number of samples needed to signal an out-of-control situation for an interval $(\delta_{\min}, \delta_{\max})$ shift sizes, where δ_{\min} and δ_{\max} are denoted as the upper and lower bounds of the shift sizes, respectively. Here, the ARL, SDRL and EARL values are computed using simulation (each run comprises of fifty thousand trials) with the assumption of the underlying process follows a normal distribution.

Similar to the DEWMA chart proposed by Zhang and Chen [4], we consider $ARL_0 = 200$, $n = 5$, $\lambda \in \{0.03, 0.05, 0.08, 0.10, 0.15, 0.20, 0.30, 0.50\}$ and $\delta \in \{0, 0.1, 0.2, 0.3, 0.4, 0.5, 1.0, 1.5, 2.0\}$ in this paper. Note that an extensive Monte Carlo search algorithm is used to search for the parameter k value that gives the desired ARL_0 of the FDEWMA chart. For example, when $\lambda = 0.03$, the parameter k value that gives an ARL_0 that is close to 200 is 1.7092 (see Table 1).

From Table 1, it is not surprising to observe that the out-of-control ARL (ARL_1) values of the FDEWMA chart decrease when δ increases. This is because a larger shift size can be detected quickly and thus the number of samples needed to detect the shift is lesser. On the other hand, the out-of-control SDRL ($SDRL_1$) values of the FDEWMA chart are also decreasing when δ increases. For instance, when $\delta = 0.1, 0.2, 0.3, 0.4, 0.5, 1.0, 1.5$ and 2.0 , the $(ARL_1, SDRL_1)$ values for the FDEWMA chart are obtained as $(32.820, 50.694)$, $(11.714, 16.589)$, $(5.846, 8.092)$, $(3.513, 4.551)$, $(2.408, 2.793)$, $(1.107, 0.405)$, $(1.006, 0.080)$ and $(1.000, 0.012)$, respectively (see Table 1). Furthermore, the $(ARL_1, SDRL_1)$ values of the FDEWMA chart increase when λ increases for $\delta \leq 1.5$. For instance, the $(ARL_1, SDRL_1)$ values of the FDEWMA chart for $\lambda = 0.03, 0.05, 0.08, 0.10, 0.15, 0.20, 0.30, 0.50$ are obtained as $(1.107, 0.405)$, $(1.129, 0.451)$, $(1.155, 0.499)$, $(1.168, 0.519)$, $(1.192, 0.553)$, $(1.210, 0.573)$, $(1.235, 0.591)$ and $(1.260, 0.598)$, respectively when $\delta = 1.0$ is considered in Table 1. This indicates that a larger λ tends to increase the number of samples to detect the mean shift and the spread in the run length distribution.

To have a fair comparison, the ARL_0 for the DEWMA chart is set to be 200 as well. From Table 1, we observe that the FDEWMA chart outperforms the DEWMA chart for all cases by having smaller $(ARL_1, SDRL_1)$ values, except for a few cases where the $SDRL_1$ values for the FDEWMA chart are slightly larger than that of the DEWMA chart. For example, when $\lambda = 0.05$, $\delta = 0.4$, the $(ARL_1, SDRL_1)$ values for the FDEWMA and DEWMA are $(3.961, 4.941)$ and $(5.722, 4.991)$, respectively.

The parameters used to compute the out-of-control EARL ($EARL_1$) values in Table 2 are similar to that of Table 1, except when the deterministic shift size δ is replaced by the interval shift size $(\delta_{\min}, \delta_{\max})$, such as $(\delta_{\min}, \delta_{\max}) = \{(0.1, 0.5), (0.5, 1.0), (1.0, 1.5)$,

Table 1. (ARL, SDRL) values for the DEWMA and FDEWMA charts with the corresponding parameter k when $n = 5$, $\lambda = \{0.03, 0.05, 0.08, 0.10, 0.15, 0.20, 0.30, 0.50\}$, $\delta = \{0.1, 0.2, 0.3, 0.4, 0.5, 1.0, 1.5, 2.0\}$ and $ARL_0 = 200$.

DEWMA		FDEWMA		DEWMA		FDEWMA	
$\lambda = 0.03$				$\lambda = 0.05$			
δ	$k = 1.5191$	$k = 1.7092$	$k = 1.705$	$k = 1.882$			
0	(200.028, 274.053)	(200.123, 360.683)	(200.082, 244.755)	(200.086, 321.386)			
0.1	(41.825, 47.880)	(32.820, 50.694)	(47.859, 50.240)	(38.386, 54.959)			
0.2	(15.362, 15.994)	(11.714, 16.589)	(17.383, 16.341)	(13.251, 17.309)			
0.3	(8.014, 7.971)	(5.846, 8.092)	(9.205, 8.298)	(6.603, 8.542)			
0.4	(4.989, 4.695)	(3.513, 4.551)	(5.722, 4.991)	(3.961, 4.941)			
0.5	(3.461, 3.067)	(2.408, 2.793)	(3.941, 3.304)	(2.668, 3.058)			
1.0	(1.321, 0.669)	(1.107, 0.405)	(1.422, 0.761)	(1.129, 0.451)			
1.5	(1.034, 0.190)	(1.006, 0.080)	(1.051, 0.231)	(1.008, 0.091)			
2.0	(1.001, 0.036)	(1.000, 0.012)	(1.003, 0.050)	(1.000, 0.013)			
$\lambda = 0.08$				$\lambda = 0.10$			
δ	$k = 1.8962$	$k = 2.06$	$k = 1.9893$	$k = 2.1478$			
0	(200.074, 225.027)	(200.062, 298.7)	(200.034, 218.458)	(200.086, 291.154)			
0.1	(54.091, 54.502)	(44.922, 61.722)	(57.407, 57.219)	(48.772, 66.072)			
0.2	(19.374, 16.876)	(14.971, 18.380)	(20.319, 17.384)	(15.890, 19.214)			
0.3	(10.268, 8.466)	(7.408, 8.932)	(10.773, 8.561)	(7.754, 9.097)			
0.4	(6.424, 5.144)	(4.383, 5.182)	(6.722, 5.188)	(4.556, 5.266)			
0.5	(4.434, 3.457)	(2.930, 3.264)	(4.662, 3.505)	(3.040, 3.323)			
1.0	(1.541, 0.852)	(1.155, 0.499)	(1.602, 0.892)	(1.168, 0.519)			
1.5	(1.075, 0.277)	(1.010, 0.103)	(1.090, 0.302)	(1.011, 0.109)			
2.0	(1.005, 0.067)	(1.000, 0.016)	(1.006, 0.077)	(1.000, 0.018)			
$\lambda = 0.15$				$\lambda = 0.20$			
δ	$k = 2.1668$	$k = 2.3071$	$k = 2.2905$	$k = 2.4215$			
0	(200.04, 211.057)	(200.062, 278.62)	(200.013, 207.009)	(200.01, 265.126)			
0.1	(65.464, 64.314)	(57.039, 75.594)	(71.860, 70.432)	(63.597, 83.726)			
0.2	(22.558, 19.251)	(17.621, 21.321)	(24.648, 21.449)	(19.309, 23.889)			
0.3	(11.644, 8.918)	(8.333, 9.524)	(12.387, 9.548)	(8.751, 10.093)			
0.4	(7.300, 5.296)	(4.841, 5.375)	(7.671, 5.454)	(5.011, 5.496)			
0.5	(5.057, 3.552)	(3.201, 3.384)	(5.319, 3.595)	(3.284, 3.399)			
1.0	(1.729, 0.959)	(1.192, 0.553)	(1.820, 0.995)	(1.210, 0.573)			
1.5	(1.124, 0.351)	(1.014, 0.123)	(1.152, 0.386)	(1.016, 0.132)			
2.0	(1.010, 0.100)	(1.000, 0.020)	(1.014, 0.118)	(1.000, 0.021)			
$\lambda = 0.30$				$\lambda = 0.50$			
δ	$k = 2.4689$	$k = 2.5869$	$k = 2.6749$	$k = 2.7834$			
0	(200.082, 202.98)	(200.01, 265.126)	(200.006, 201.922)	(200.152, 264.824)			
0.1	(84.589, 82.855)	(75.734, 99.205)	(106.688, 105.863)	(96.692, 129.563)			
0.2	(29.332, 26.683)	(22.857, 29.661)	(40.982, 39.157)	(31.148, 43.873)			
0.3	(14.126, 11.428)	(9.676, 11.733)	(18.915, 16.933)	(12.01, 17.022)			
0.4	(8.426, 6.121)	(5.261, 5.927)	(10.59, 8.655)	(5.876, 7.555)			
0.5	(5.736, 3.839)	(3.378, 3.452)	(6.772, 5.029)	(3.555, 3.946)			
1.0	(1.948, 1.025)	(1.235, 0.591)	(2.106, 1.068)	(1.260, 0.598)			
1.5	(1.199, 0.433)	(1.020, 0.145)	(1.265, 0.482)	(1.025, 0.160)			
2.0	(1.022, 0.147)	(1.001, 0.025)	(1.036, 0.187)	(1.001, 0.029)			

Table 2. EARL₁ values for the DEWMA and FDEWMA charts with the corresponding parameter k when $n = 5$, $\lambda = \{0.03, 0.05, 0.08, 0.10, 0.15, 0.20, 0.30, 0.50\}$, $(\delta_{\min}, \delta_{\max}) = \{(0.1, 0.5), (0.5, 1.0), (1.0, 1.5), (1.5, 2.0)\}$ and EARL₀ (in-control EARL) = 200.

		DEWMA		FDEWMA		DEWMA		FDEWMA	
		$\lambda = 0.03$				$\lambda = 0.05$			
δ_{\min}	δ_{\max}	$k = 1.5191$		$k = 1.7092$		$k = 1.705$		$k = 1.882$	
0.1	0.5	11.946		9.015		13.634		10.337	
0.5	1.0	2.039		1.504		2.278		1.599	
1.0	1.5	1.137		1.039		1.186		1.047	
1.5	2.0	1.012		1.002		1.018		1.002	
		$\lambda = 0.08$				$\lambda = 0.10$			
δ_{\min}	δ_{\max}	$k = 1.8962$		$k = 2.06$		$k = 1.9893$		$k = 2.1478$	
0.1	0.5	15.289		11.743		16.102		12.474	
0.5	1.0	2.537		1.699		2.663		1.746	
1.0	1.5	1.249		1.058		1.284		1.063	
1.5	2.0	1.028		1.003		1.035		1.003	
		$\lambda = 0.15$				$\lambda = 0.20$			
δ_{\min}	δ_{\max}	$k = 2.1668$		$k = 2.3071$		$k = 2.2905$		$k = 2.4215$	
0.1	0.5	17.929		13.97		19.523		15.292	
0.5	1.0	2.898		1.819		3.051		1.862	
1.0	1.5	1.357		1.074		1.413		1.082	
1.5	2.0	1.05		1.004		1.064		1.005	
		$\lambda = 0.30$				$\lambda = 0.50$			
δ_{\min}	δ_{\max}	$k = 2.4689$		$k = 2.5869$		$k = 2.6749$		$k = 2.7834$	
0.1	0.5	22.814		17.821		30.256		23.074	
0.5	1.0	3.268		1.91		3.654		1.957	
1.0	1.5	1.498		1.094		1.604		1.108	
1.5	2.0	1.088		1.006		1.124		1.008	

(1.5, 2.0)}. It is worth noting that the parameter k values in Table 2 for the case with interval shift size are set to be similar to that of Table 1 for the case with specific shift size, to ensure both cases have similar in-control performances. From Table 2, it is found that larger values of $(\delta_{\min}, \delta_{\max})$ result in a smaller EARL₁ value. For instance, when $\lambda = 0.05$ and $(\delta_{\min}, \delta_{\max}) = (0.1, 0.5), (0.5, 1.0), (1.0, 1.5)$ and $(1.5, 2.0)$ are considered for the FDEWMA chart, the EARL₁ values are 10.337, 1.599, 1.047 and 1.002, respectively. In addition, a larger value of λ tends to increase the EARL₁ values. For example, by considering the case $(\delta_{\min}, \delta_{\max}) = (1.0, 1.5)$ for the FDEWMA chart, the EARL₁ values for $\lambda = 0.03, 0.05, 0.08, 0.10, 0.15, 0.20, 0.30, 0.50$ are computed as 1.039, 1.047, 1.058, 1.063, 1.074, 1.082, 1.094, 1.108, respectively. In terms of comparison, FDEWMA chart also surpasses the existing DEWMA chart by having smaller EARL₁ values for all shift intervals and λ values. For example, when $(\delta_{\min}, \delta_{\max}) = (0.1, 0.5)$ and $\lambda = 0.03$ are considered in Table 2, the EARL₁ values for the FDEWMA chart is 9.015 as compared to 11.946 for the DEWMA chart.

4 Conclusion

A comprehensive understanding of the behavior of a control chart is important for the quality practitioners to ensure meaningful results are obtained. In control chart's implementation, the process may go out-of control in the beginning of the process monitoring (start-up quality problems) or due to ineffective corrective action to bring back the process mean to the target value after the occurrence of out-of-control situation. To address for all these problems, in this paper we integrate the FIR feature into the DEWMA chart for process monitoring. To evaluate the run length properties for the FDEWMA chart, the Monte Carlo simulation is used. By incorporating the effectiveness of the FIR feature in considering the occurrence of the off-target process, the sensitivity of the FDEWMA chart in shift detection increases by resulting in smaller ARL_1 and $EARL_1$ values for specific and interval shift sizes, respectively. The proposed FDEWMA chart is shown to result in remarkable improvement in shift detection as compared to the DEWMA chart without FIR feature.

This work can be extended to consider the auxiliary information concept in the plotting statistic of the FDEWMA chart. In addition, the FDEWMA chart in monitoring the process variance, or both process mean and process variance can be considered.

References

1. Teoh, W.L., Chong, J.K., Khoo, M.B.C., Castagliola, P., Yeong, W.C.: Optimal designs of the variable sample size chart based on median run length and expected median run length. *Qual. Reliab. Eng. Int.* **33**(1), 121–134 (2017)
2. Montgomery, D.C.: *Introduction to Statistical Quality Control*, 7th edn. Wiley, New York (2012)
3. Roberts, S.W.: Control chart tests based on geometric moving averages. *Technometrics* **1**(3), 239–250 (1959)
4. Zhang, L., Chen, G.: An extended EWMA mean chart. *Qual. Technol. Quant. Manag.* **2**(1), 39–52 (2005)
5. Lucas, J.M., Crosier, R.B.: Fast initial response for CUSUM quality-control schemes: give your CUSUM a head-start. *Technometrics* **24**, 199–205 (1982)
6. Lucas, J.M., Saccucci, M.S.: Exponentially weighted moving average control schemes: properties and enhancements. *Technometrics* **32**(1), 1–12 (1990)
7. Steiner, S.H.: EWMA control charts with time-varying control limits and fast initial response. *J. Qual. Technol.* **31**(1), 75–86 (1999)
8. Haq, A., Abidin, Z.U., Khoo, M.B.C.: An enhanced EWMA- t control chart for monitoring the process mean. *Commun. Stat. Theory Methods* **48**(6), 1333–1350 (2019)
9. Ng, P.S., Lau, Y.J., Lim, H.T., Yeong, W.C.: Fast Initial response for auxiliary information based EWMA chart for the process mean. In: Mahyuddin, N.M., Mat Noor, N.R., Mat Sakim, H.A. (eds.) *Proceedings of the 11th International Conference on Robotics, Vision, Signal Processing and Power Applications*. LNEE, vol. 829, pp. 677–683. Springer, Singapore (2022). https://doi.org/10.1007/978-981-16-8129-5_103

10. Abbas, N., Riaz, M., Does, R.J.: An EWMA-type control chart for monitoring the process mean using auxiliary information. *Commun. Stat. Theory Methods* **43**(16), 3485–3498 (2014)
11. Haq, A.: A new hybrid exponentially weighted moving average control chart for monitoring process mean. *Qual. Reliab. Eng. Int.* **29**(7), 1015–1025 (2013)
12. Hu, X., Qiao, Y., Zhou, P., Zhong, J, Wu, S.: Modified one-sided EWMA charts for monitoring time between events. *Commun. Stat. Simul. Comput.* <https://doi.org/10.1080/03610918.2021.1872632>



Microstructural and Compositional Analyses of Resin Matrix Composites

Mutiur Erinosh[✉], Ester Angula, and Sam Shaanika

Department of Mechanical and Metallurgical Engineering, University of Namibia, P.O. Box 3624, Ongwediva, Namibia
mutiuerinosh1@gmail.com

Abstract. Fiber reinforced composites can be categorized into diverse groups according to their matrices and these play a major role in the reinforcement. This paper presents the microstructural and the compositional analyses of resin matrix composites. The specimens produced were reinforcement fibre with mild steel metal chips, wood chips, granite particles and charcoal particles respectively. Each composite sample contains one strand of fibre and a fibre-resin composite was produce per set to serve as comparison to the particles reinforced composite samples. Good microstructures were observed in all the entire samples although there were some inhomogeneous mixtures in some of the structures. The wood chips reinforced particles composite sample formed long-pointed cluster, which was fairly distributed in the structure. The long-pointed worm-like clusters formed in the wood reinforced composite could promote the equally distribution of an applied load on the structure which can strengthens its mechanical properties with a prolonged lifespan. Most of compositions present in the entire samples have high tendencies for promoting the mechanical properties of the matrix composites.

Keywords: Composites · Glass fibre · Resin · Microstructure · XRF analysis

1 Introduction

The composites made from the commonly used fibre reinforcements such as aramid, carbon and glass-fibre applications are limited due to their low mechanical properties [1], however, there is need to enhance their mechanical properties by incorporating reinforcement particles such as synthetic reinforcements. In addition, the carbon and aramid fibres are used where more stiffness is required. The aramid fibre has strong heat resistance and mainly used for fire resisting clothing and bullet-proof [2]. Polymer resin is one of the synthetic resins that could be utilised as adhesive due to their lower shrinkage, and chemical characteristics [3]. A hyper composite plate structure composed of chopped glass fibre and carbon powder with polyester resin at different volume fractions was characterised under thermal and mechanical loading. It was found out that the addition of powder to the composite structure decreased the maximum deflection as a result of an increase in its young modulus, and by replacing the glass fibre used with carbon powder has enhanced the mechanical properties of the composite. The random distribution of

the powder in the matrix has stimulated the dispersion and the entire interface between the matrix and reinforcement material [4]. The mechanical properties of polymer matrix composites reinforced by nano silica particles and glass fibre were analysed. It was observed that the specimens reinforced with woven glass fibre gave higher ultimate tensile strength values than the specimens reinforced with chopped glass fibre and reported that the alignment and the length of the woven fibres have contributed to the equal distribution of the load along the length of the fibres [5]. Fibres are primarily categorised as natural or synthetic where natural fibres are made using natural source materials such as plants and animals while synthetic fibres are man-made from chemical compounds.

Figures 1 show the different form of natural fibres strand [6]. Natural fibres have excellent strength and stiffness due to the presence of cellulose, lignin, pectin, hemicelluloses, and waxes [7]. They are characterised with low density, biodegradability, easy availability, low cost and a non-abrasive nature [8].



Fig. 1. Commonly used natural fibres [6].

Glass fibre is the most used as it offers excellent resistance to impact, wear and friction and has good strength and durability [9]. Due to its lower cost, carbon and aramid are rarely used and only in applications where more stiffness is required. Carbon fibre exhibits high stiffness, chemical resistance, tensile strength and temperature tolerance while aramid fibre has vigorous heat resistance and is mainly used for fire-resisting clothing and bullet-proof [10]. Numerous research works have been conducted on glass fibre composites to enhance their applications during service but not many reviews on the microstructures have been established.

The main objective of this present research study is to characterise the natural fibre and particle reinforcements in a composite through its microstructure and to establish if there is a change in the compositional analysis using the XRF analyser.

2 Experimental Procedure

The general-purpose resin was used as the matrix throughout the experiment and it is an unsaturated transparent polyester resin. The resin was mixed with droplets of hardener. The specimen produced were reinforcement fibre with mild steel metal chips, wood chips, granite particles and charcoal particles. For each sample made, 25 ml of resin with a hardener and particles were added in a beaker, and thoroughly stirred for 5 min to achieve a homogeneous distribution of the reinforcement particles and solution. The homogeneous solution was first poured into the mold halfway and the fibre strand was positioned in the middle before adding the remaining solution. The samples were left to cure under standard atmospheric conditions and removed after they have hardened. This hardener is an amino polyamide which served as a catalyst and facilitated the molecular components bonding which was used to cure the composites by the process of polymerisation.

Three sets of samples were produced with metal chips, wood chips, granite particles, charcoal, fibre-resin only and hybrid particles respectively. The first set of samples had 5 drops of the hardener (5 DH), 10 drops of the hardener (10 DH) added to the second set, and 15 drops of the hardener (15 DH) added to the third set. In total, 18 samples were produced for characterization. The droplets of hardener was used in this research work since the hardener that came with the resin did not specify the mixing ratio, and this was done in order to evaluate if acting as a catalyst will have an effect on the composites. As a result of different hardener drops used in the preparing the samples, the first set with 5 droplets took 5 days to cure, the second set with 10 droplets took 3 days while 2 days to completely cure the 15 droplets of hardener. The metallographic samples were mounted in polyfast for microstructural examination and the XRF analyses were conducted for the composition. The surface morphologies of the composite specimen were analysed using the optical microscope and examined at 20X, 30X and 40X magnification respectively.

3 Results and Discussion

In order to characterise the studied composite materials, microstructural evaluation, and XRF analysis were conducted to better understand the structures as well as the compositional phases present.

The microstructures of the entire composite samples are explained in details in this section from the fibre-resin only to the particles reinforced composites. Figures 2 (a) to (c) depict the microstructures of the fibre-resin only composite samples with 5 drops of hardener (5 DH), 10 drops of hardener (10 DH) and 15 drops of hardener (15 DH) respectively while Figs. 2 (d) to (f) show the microstructures of the metal chips reinforced samples with 5 DH, 10 DH and 15 DH respectively.

The fibre-resin only reinforced composite samples bred an evenly distributed structure, and the thin fibre strand enhanced strong mechanical bond with the resin. Other regions of the samples had defects as a result of entrapped air, which caused the formation of voids and porosity. The metal chips reinforced composites have an evenly distributed microstructures as illustrated in Figs. 2 (d to f), closer to that of the fibre-resin only sample with defects and resin clusters in some regions of the structure. The

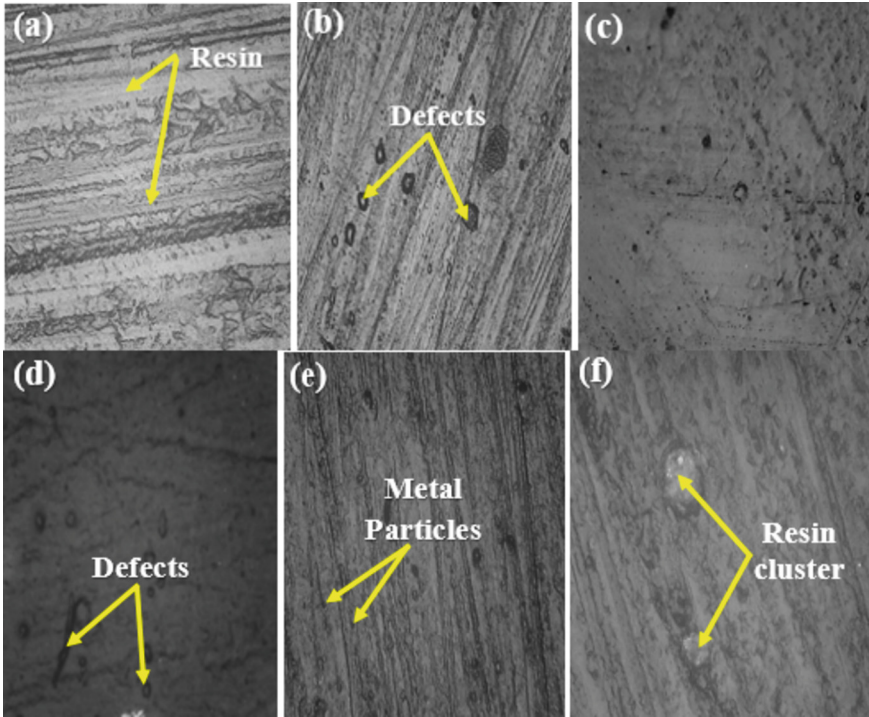


Fig. 2. (a to c) Microstructures of fibre-resin composite samples with 5 drops, 10 drops and 15 drops of hardener; (d to f) Microstructure of metal chips composite samples with 5 drops, 10 drops and 15 drops of hardener.

resin clusters are as a result of inhomogeneous mixture produced since the stirring was done using a stick. The formation could also be because of the particles choosing to settle in disperse areas of the samples due to difference in sizes and densities of the metal particles as some particles are in circular forms or entangled forms.

Figures 3 (a) to (c) present the microstructures of the wood chips reinforced composite samples with 5 DH, 10 DH and 15 DH, while Figs. 3 (d) to (f) show the microstructures of the granite chips reinforced samples with 5 DH, 10 DH and 15 DH respectively.

As shown in Fig. 3 (a), the wood chips reinforced particles composite sample formed long-pointed cluster fairly distributed in the structure. The particles are equiaxed in structure and swimming in the same direction. The long-pointed worm-like clusters of the particles promote the equally distribution of an applied load on the structure which strengthens its mechanical properties with a prolonged lifespan. The lightness and flexibility of the wood chips promoted the formation of a uniform mixture, forming a moderate structure. The granite-reinforced samples as shown in Figs. 3 (d) to (f) have light grey crystals in various location of the composites. Furthermore, the microstructures show the development of grains, which signify a completed polymerisation process. However, cluster of crystals were observed in some regions of the matrix.

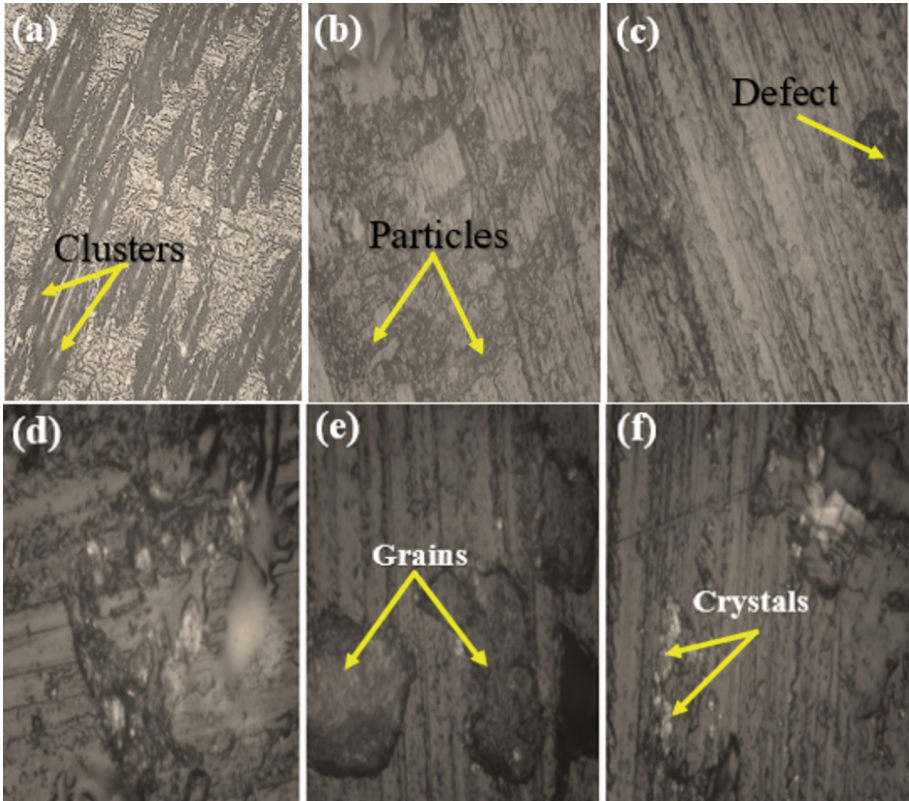


Fig. 3. (a to c) Microstructures of wood chips composite samples with 5 drops, 10 drops and 15 drops of hardener; (d to f) Microstructure of granite chips composite samples with 5 drops, 10 drops and 15 drops of hardener.

Figures 4 (a) to (c) present the microstructures of the charcoal chips reinforced composite samples with 5 DH, 10 DH and 15 DH, while Figs. 4 (d) to (f) show the microstructures of the hybrid chips reinforced samples with 5 DH, 10 DH and 15 DH respectively.

As depicted in Fig. 4 (c), the charcoal particles were more obvious in the reinforced composite sample forming clusters of resin and charcoal. The black phases represent the charcoal particles. Some elliptical grains were developed in the sample of Fig. 4 (b) where 10 drops of hardener was used. A homogeneous solution with fairly distributed charcoal particles were revealed in sample mixed 5 drops of hardener. The curing time has allowed the distribution of the particles in the matrix. Figure 4 (e) displays large area of resin only close to the interface regions with some dispersed anonymous particles. The hybrid reinforced composite exhibited uneven dispersion of the particles due to the differences in the densities of the mixed particles.

Table 1 shows the major elemental compositions present in the fibre-resin and particles reinforced composite samples.

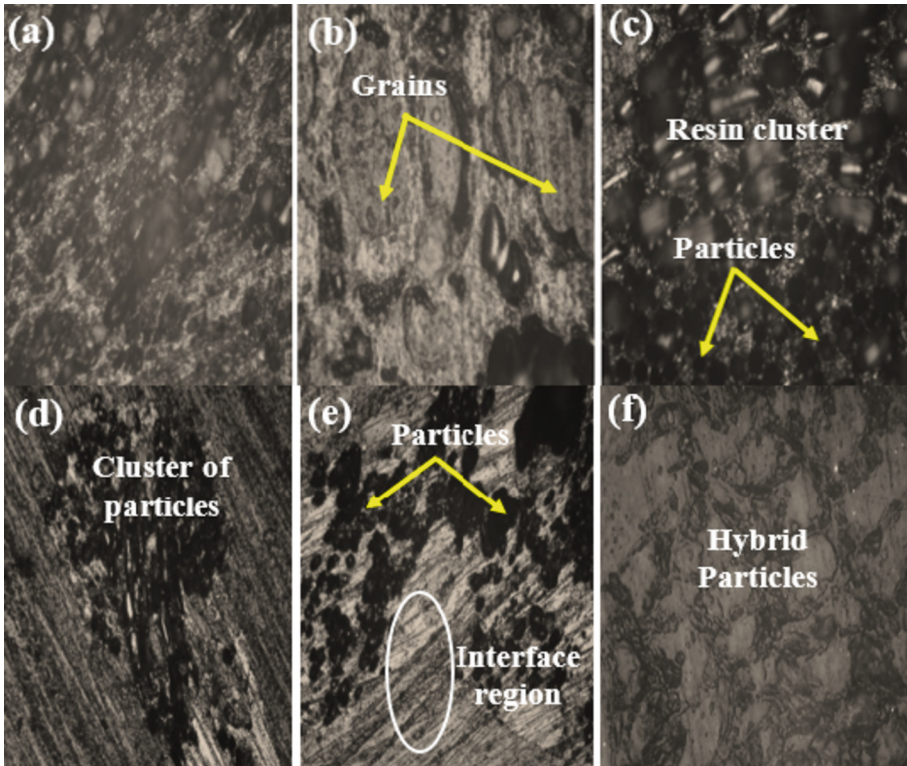


Fig. 4. (a to c) Microstructures of charcoal chips composite samples with 5 drops, 10 drops and 15 drops of hardener; (d to f) Microstructure of hybrid chips composite samples with 5 drops, 10 drops and 15 drops of hardener.

Table 1. Composite samples elemental composition

Sample	Composition (%)				
	SiO ₂	CaO	MgO	Fe ₂ O ₃	Cl
Fibre + Resin	5.404	3.025	0.591	0.286	0.309
Fibre + Metal chips + Resin	8.456	0.843	0.295	53.055	1.416
Fibre + Wood chips + Resin	4.881	0	0.342	0.337	0.447
Fibre + Granite particles + Resin	8.758	0.382	0.643	0.794	0.344
Fibre + Charcoal particles + Resin	5.124	1.357	0.600	0.167	0.307
Fibre + Hybrid chips + Resin	8.800	0.860	0.872	15.283	0.273

As seen from the Table, SiO₂ is the main composition in the entire samples ranging from 4.8 to 9 approximately. The composite samples contains high percentage of silica

which promotes hardness, stiffness and strength [11]. They also contain a fair composition percentage of magnesia which offers high thermal conductivity and excellent corrosion resistance [12], therefore neutralising corrosion vulnerability of the composite samples as a result of very high content of ferric oxide present in metal chips and hybrid reinforced composite samples. Magnesia will uphold the use of the composites in aggressive acidic environments, with calcium oxide to enhance composites melting and boiling points [13].

4 Conclusion

The microstructural and the compositional analyses of the fibre-resin and particle reinforced composite samples were successfully investigated. The surface morphology of the composite samples revealed the presence of voids, porosity and clusters of resin and particles, which could result in the decrease of the strength of the composite. The increase in the drops of hardener has reduced the number of days the samples took to cure. Only the fibre-resin reinforced composite samples produced an evenly distributed structure, and the thin fibre strands have enhanced strong mechanical bond with the resin. The charcoal particles were more obvious in the reinforced composite sample forming elliptical clusters of resin and charcoal.





References

1. Sarasini, F., Santulli, C.: Vinylester resins as a matrix material in advanced fibre-reinforced polymer (FRP) composites. *Adv. Fibre Reinf. Polym. Compos. Struct. Appl.*, 69–87 (2013)
2. Understanding fiber-reinforced plastics - studentlesson. <https://studentlesson.com/fiber-reinforced-plastics/>. Accessed 10 Nov 2021
3. Shakir, I., Hasan, K.F., Jasim, M.A.: Properties evaluation of fiber reinforced polymers and their constituent materials used in structures – a review. *Mater. Today Proc.* **43**, 1003–1008 (2021)
4. Al-shammari, M.A., Emad, S.: Experimental and numerical investigation of hyper composite plate structure under thermal and mechanical loadings. *J. Eng.* **23**(8), 56–69 (2017)
5. Younis, S.I., Oleiwi, J.K., Mohammed, R.A.: Some mechanical properties of polymer matrix composites reinforced by nano silica particles and glass fibers. *Eng. Technol. J.* **36**(12), 1283–1289 (2018)
6. Haggi, M., El Mahi, A., Jendli, Z., Akrouf, A., Haddar, M.: Static and fatigue characterization of flax fiber reinforced thermoplastic composites by acoustic emission. *Appl. Acoust.* **147**, 100–110 (2019)
7. Kumar, S., Khan, S., Kumar, R., Karloopia, J.: Fabrication and evaluation of mechanical properties of polymer matrix composite using nano fibers as a reinforcement. *Mater. Today Proc.* **46**, 1376–1383 (2021)
8. Chilali, A., Zouari, W., Assarar, M., Kebir, H., Ayad, R.: Analysis of the mechanical behaviour of flax and glass fabrics-reinforced thermoplastic and thermoset resins. *J. Reinf. Plast. Compos.* **35**(16), 1217–1232 (2016)
9. Djafari Petroudy, S.R.: Physical and mechanical properties of natural fibers. *Adv. High Strength Nat. Fibre Compos. Constr.*, 59–83 (2017)

10. Akaluzia, R.O., Edoziuno, F.O., Adediran, A.A., Odoni, B.U., Edibo, S., Olayanju, T.M.A.: Evaluation of the effect of reinforcement particle sizes on the impact and hardness properties of hardwood charcoal particulate-polyester resin composites. *Mater. Today Proc.* **38**, 570–577 (2021)
11. Properties: Silica - Silicon Dioxide (SiO₂). <https://www.azom.com/properties.aspx?ArticleID=1114>. Accessed 09 Nov 2021
12. Magnesia - Magnesium Oxide (MgO) Properties & Applications. <https://www.azom.com/article.aspx?ArticleID=54>. Accessed 09 Nov 2021
13. Calcium Oxide (CaO) - Preparation, Properties & Uses of Quicklime. <https://byjus.com/chemistry/calcium-oxide/>. Accessed 09 Nov 2021



Stability Characteristics of Water/Diesel and Biodiesel Emulsions Under the Influence of Water Dosages

Hasanain A. Abdul Wahhab¹ , Hayder A. Dhahad² , Mohammed A. Fayad³ ,
and Miqdam T. Chaichan³ 

¹ Training and Workshop Center, University of Technology-Iraq, Baghdad, Iraq
20085@uotechnology.edu.iq

² Mechanical Engineering Department, University of Technology-Iraq, Baghdad, Iraq

³ Energy and Renewable Energies Technology Center, University of Technology-Iraq, Baghdad, Iraq

Abstract. The data in this article present the effective parameters of experimental microscopic processes to investigation of the emulsifiers stability characteristics with changing the water dosage in diesel/or biodiesel fuel. As a result of the increasing demand to improve the fossil fuels properties and the application of the emulsification procedure by adding water dosages into fuel as the promising idea, it opened the way to research in identify many affecting factors these emulsions; one of the important emulsion features was stabilization period and the increasing water dosage rate in emulsion how effected on this feature was not been effectively studied. The current work interested to study the distribution of water droplets (droplet size) in the W/D (water/diesel) or W/BD (water/biodiesel) emulsions. The datasets were gained during experiments conducted with using digital microscopic image technique for five samples of W/D and W/BD emulsions 5, 10, 15, 20, and 30% (v/v) water content, Here, the experimental set-up and the major instruments used for obtaining the computed data were explained in details. The results were appeared that, the larger the amount of water content in the emulsion, the brighter milky emulsion produced. The experiments indicated that increasing the water dosage in W/D and W/BD emulsions influenced negatively on the emulsion stabilization period.

Keywords: Fuel emulsions · Emulsion stability · Digital image processing · Surfactant

1 Introduction

The main objective of using fuel emulsions (pure diesel or biodiesel with water) as fuel for a compression ignition (CI) engine is to exploit the added oxygen charge to improve the combustion process and reduce emissions [1, 2]. New researches concluded that water-in-fuel emulsions are to reduce the NO_x, CO₂, and HC emissions [2]. Many methodologies have been used to study fuel emulsions on diesel engine both inside and

outside the engine combustion chamber [3], where the problem of instability of emulsions for a long time was considered the most important problem that was researched in this field. So, the stabilization of fuel emulsions are influenced significantly by the preparing method, viscosity of fuel, water dosage in emulsion, stirring speed, and concentration of surfactants [3]. Surfactants (sometimes called emulsifiers) are considered one of the materials that are characterized by an equal ratio of polarity, compatible with water and on the other hand, non-polar or non-hydrophilic, in general, their role is a major role in weakening the surfactant of the medium in which they are dissolved. When mixed into the fuel-water mixture, the polar groups convert to water and the non-polar groups convert to the fuel thus reducing the surfactant between the two fuel/water phases [4]. Four types of surfactants materials are cationic, anionic, non-ionic and these types depend in working on the intensity of surfactant. Normally, it was high option for decreasing surfactant was to enhance a hydrophilic lipophilic balance, with other words (oil-water-lipolytic). Fuel emulsions formed when a surfactant is mixed with the two unbendable fluids water and diesel. Moreover, the combustion of surfactants without increasing emissions such as soot and free of sulfur and nitrogen must be done directly [5]. A few number of literature deals with the study of the effect of surfactant as well as the properties of W/D emulsions in relation to combustion and emissions [6]. Nadeem et al. [7] have tested the water-in-diesel emulsion prepared by adding surfactants on a four-stroke, four-cylinder engine, and concluded that there was a significant reduction in the emission of particulate matter and NO_x with the use of other types of fuel emulsion prepared by adding different surfactants. Fuel emulsions are prepared as a result of their effect on mechanical activation resulting from various mechanical devices. Therefore, the methods of mechanical mixing different by several equipment, the most important of which are: a supersonic vibrating machine, a vibrating table, a magnetic stirrer, a centrifugal type mixer ... etc. Lin and Chen [8] reported that the engine has better performance with lower CO₂ emissions by using ultrasonic vibration as fuel emulsion preparation method and the results were compared to fuel emulsion prepared by mechanical mixing, but this fuel emulsion has a negative influence with HC and NO_x emissions. Experiments conducted within one of the research studies that dealt with the effect of the speed of the mechanical homogenizer, where the number of cycles of the homogenizer was changed as a method to study the microscopic structure, showed that the speed has a direct effect on the diameter of the water droplets in the fuel [9]. The choice of emulsification technique is of equal importance, for example, the use of a mechanical agitator or ultrasound. Nowadays ultrasonic emulsifier is considered to be the best agitator due to its speed, efficacy and convenient design for effective operation. Determining the optimal procedure for preparing the emulsifier is through the optimal selection of the appropriate agitator, the speed of agitation and the rotation period, as they are the important factors for the stability of the fuel emulsion for a longer period [10–15]. Wahhab et al. [16] studied the distribution of water droplets in W/D emulsion by used the digital microscopic images processing, and the effects of water dosages and heating on the stabilization of W/D emulsion was tested [17, 18]. In this work, digital microscopy image processing technique was used to study the properties of water droplets in the W/D and W/BD emulsion, the most important of which is the water droplet diameter. Also, MATLAB code samples were developed to analyze microscopic images.

2 Materials and Methods

The experiments employed stirring emulsion homogenizer, image microscopic system, and digital image processing technique. These systems were used to collect microscopic images at various dosages and days for the W/D (water/diesel) emulsions and W/BD (water/biodiesel) emulsions, providing information on water droplets size in fuel. Image processing technique was used to collect the information's for shape, area, and diameter of the water droplets in emulsion. The Mat LAB software was used to analyze microscopic images for emulsions. Finally, the separation limits of the water/fuel emulsions were presented.

2.1 Principle of Emulsions Preparation

Components required for preparing emulsion are: Mechanical agitator (Homogenizer), diesel (and biodiesel) fuel, distilled water, burette, and pipette, as shown in Fig. 1. First step, the pipette, burette and container were thoroughly washed and cleaned dry. Second step, Diesel (or Biodiesel) was measured in the burette in required volume and poured into the homogenizer container. Third step, it calculated volume of each surfactant (span-80) were measured in the pipette and poured into the homogenizer container, same done for water. Finally, the container is placed under the mechanical agitator and the mixture is thoroughly mixed for about 10–15 min. The emulsion thus obtained is checked for stability. Homogenizer is used to thoroughly form the emulsion. It consists of a motor (1250 W, speed range 11000–30000 rpm) which is used to rotate the blades which is dipped in the mixture. There is speed control knob to optimize the speed of the motor. Water/fuel emulsions were prepared by emulsifying a distilled water into each of the two fuel (diesel and biodiesel) with adding snap-80 (2% of the final emulsion volume), at different water to fuel (W/D or W/BD) (v/v) percentages of 5%, 10%, 15%, 20%, and 30%. The amounts of each component required are illustrated in Table 1. Various trials were carried out before obtaining a stable emulsion, all samples prepared were 200 cc and kept at ambient temperature to study the emulsion stabled time, as shown in Fig. 2.

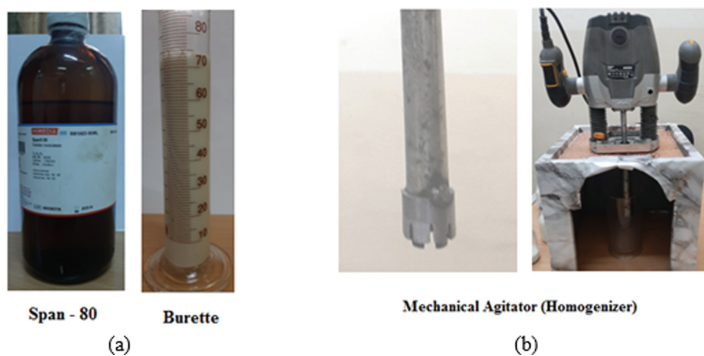


Fig. 1. Components required for preparing emulsion.

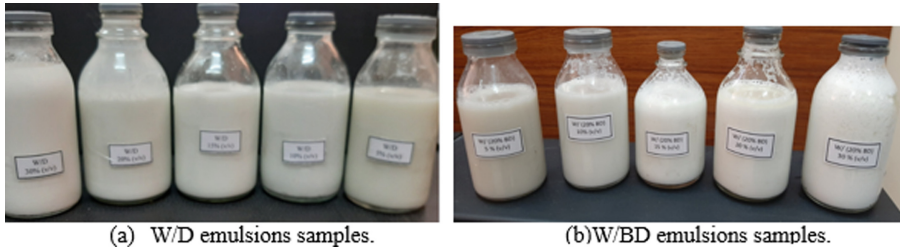


Fig. 2. Water/Fuel emulsion samples.

Table 1. Water dosages in W/D and W/BD emulsions.

W/D emulsion	W/BD (Diesel 80% + Bio diesel 20%) emulsion
93% diesel, 5% water, 2% span 80	93% BD, 5% water, 2% span 80
88% diesel, 10% water, 2% span 80	88% BD, 10% water, 2% span 80
83% diesel, 15% water, 2% span 80	83% BD, 15% water, 2% span 80
78% diesel, 20% water, 2% span 80	78% BD, 20% water, 2% span 80
68% diesel, 30% water, 2% span 80	68% BD, 30% water, 2% span 80
93% diesel, 5% water, 2% span 80	93% BD, 5% water, 2% span 80

2.2 Optical Microscope System

Figure 3 illustrates a setup for the optical microscope type Meiji Techno ML2100 during experiments. The W/D and W/BD emulsions images were showed and recorded with 400X magnification. The image acquisition system includes optical microscope filter tray ML2100, photomicrography with 35 mm digital SLR camera, camera attachment w/finder eyepieces, and integrated illuminator. The microscopic images were recorded with maximum resolution 1280 * 800 pixels.

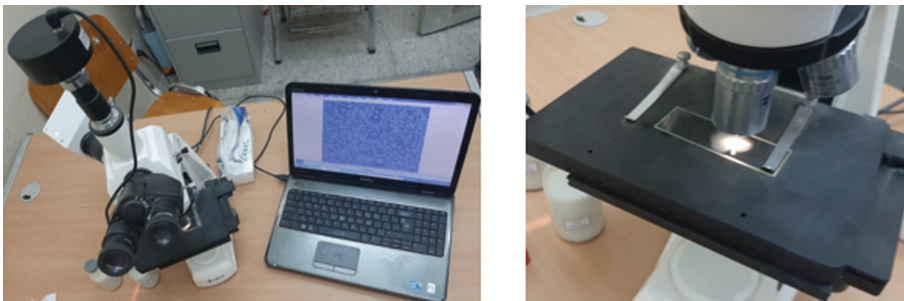


Fig. 3. Optical Microscopic System.

2.3 Digital Image Processing

The image processing techniques have been widely used in the study of microscopic processes [16]. The main purpose of the image processing technique is detection of the droplet boundaries. Particularly from the edges of the droplets which are not visibly observable, thereby making it difficult to identify the edges of the droplets by means of a simple detection technique due to a low contrast ratio along those borders. Therefore it is very necessary to apply digital image processing techniques to the raw images before they can be analyzed.

In other for the image to be process effectively, a software program was developed and was used to extract information from the microscopic images data recorded. The software program is divided into two basic stages: droplet identification and droplet verification of parameters. The working process of the algorithm for each part of the program is elaborated in this session. The MATLAB program code developed was depend on microscopic images frames for data analysis and for measuring droplet parameters i.e., diameter, area, and spatial location. Each part will be described in detail in the following paragraphs.

The algorithm considered each microscopic image as a graphics object where each element of a matrix contains three color intensities, the red, green, and blue (RGB) values. The RGB image is processed to a grey scale image with 8 bit depth using rgb 2-Gy function in MATLAB. Each pixel is represented with a numerical value from 0 (black) to 255 (white) as explained by Pratt [16], where the light spots are black and droplet contours are white in rgb 2-Gy image. As a preliminary procedure, the unwanted area from the image border was subtracted. It reduces the size of the image and the computational time. The original size of the image obtained from the microscopic camera is 1280×720 pixels and the size of the reduced area is 1013×635 pixels. After then, the program recognizes a row of all microscopic frames, when these appear the water droplets first on the microscopic lens.

Several measures were undertaken in order to determine the basic parameters of the droplet, these steps include the following:

1. Background extraction and noise reduction: Directly extracting information for the droplet from the image is a complex process due to the background noise. The noise was caused by either from particles that were stuck to the surfaces of the image or those formed from the light intensity variation. Thus, a procedure to reduce the noise level to minimal was is highly desirable. The Math Works Inc., (2016), was used to improve the droplet image quality by refining the background ordinance, using image subtraction to reduce the background noise.
2. Binary image and thresholding operation: The thresholding operation produces a binary image comparing an intensity value or threshold to the matrix pixel intensities; it replaces all pixels in the input image with luminance greater than a threshold with the value 1 (white) and replaces all other pixels with the value 0 (black). To determine occasion threshold value, many techniques have been proposed in time past by [5–7]. Generally, these techniques were based on the mean intensity value or picture intensity histogram. Figure 4 describes different image frequency intensity. For example, for a darker image (a) and a lighter image (b), which were collected during measurement of droplets size and the threshold experimentally. The thresholds were around 0.65–0.88,

which made possible to reduce light structures connected to the image. During the last step in this operation images were converted to a binary image using a threshold value of 0.76.

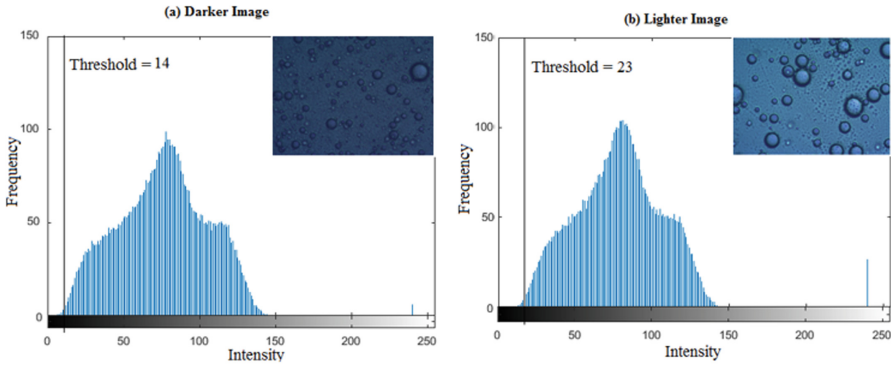


Fig. 4. Shows image intensity and frequency histogram.

3. Morphological operations on binary image: morphological operations were used to develop the quality of the binary image and thereby improving the droplet shapes. Several researchers [8–10], conducted a set of morphology image operations that depend on image based on shapes. The basic operations in morphology processing are dilation and erosion, as described by [16]. Erosion means remove some pixels on objects boundaries, while dilation adds new pixels to the boundaries of objects in binary image. In this work, erosion and dilation method was utilized. The number of pixels added or removed from the objects in an image depends on the size and shape of the structuring element used to process the binary image. Therefore, it can modify the size and the shape of the droplet; however the of combinations of these operations maintains the same size of the droplets. Speckles in the images were reduced by using an opening operation, and holes in the droplets were filled with a closing operation, which will be described below. The morphological close operation is a dilation followed by erosion, using the same structuring element for both operations. The close operation fills the holes in the droplet and smoothen the boundary of changing its size and shape. When the close operation is applied to the droplet, first it is expanded by dilation and then reduced by erosion, so the boundary is smooth and holes are filled and the shape remains the same size. The morphological open operation is erosion followed by dilation. Thus speckles on the image can be removed by using the open operation. The borders of the droplet removed by erosion can be restored by dilation, so it doesn't influence on the main droplet structure. However, the small speckles that are removed by erosion are not restored by dilation. Figure 5 shows the image processing procedures. Finally, images with the water droplets were prepared for the next step quantitative analysis such as measuring the equivalent diameter and area of the droplet.
4. Definition of the droplet parameters: one of the most important steps in droplets definition stage was the identification of calibration scale factor which records the

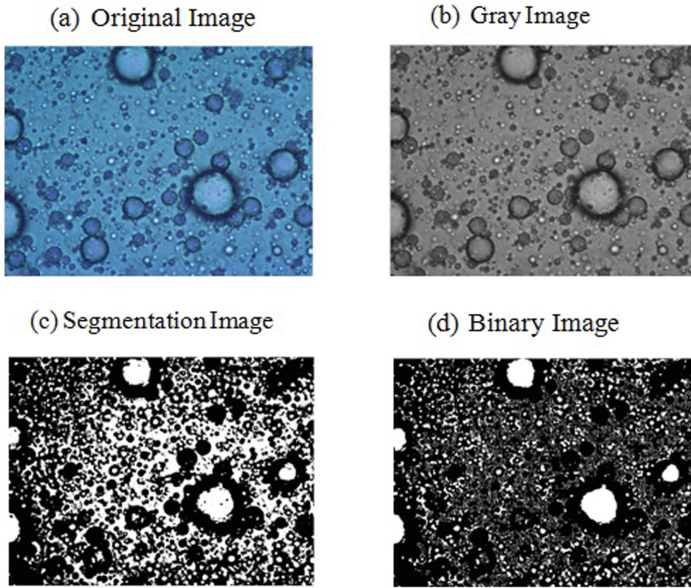


Fig. 5. Image processing procedures.

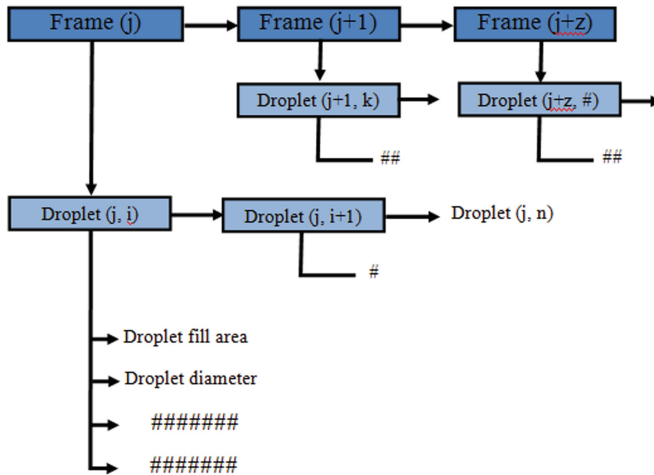


Fig. 6. A droplet structure data and geometric parameters.

calibration image. This calibration image was applied for all experiments with scale factor of 21.4 pixel/ μm . The droplet geometric parameters are as follows: droplet filled area and equivalent diameter. These parameters were measured and organized in a data structure for each droplet in an image, for a sequence of images. Figure 6 shows a droplet structure data and geometric parameters for this work, and implemented in MATLAB. A frame is a set of pixels arranged in a matrix of $(w \times h)$ elements, a

point (0, 0) representing the top left while a point (1013, 635) represented the right bottom corner bounding box in matrix. Every frame has different number of droplets, as shown in Fig. 7.

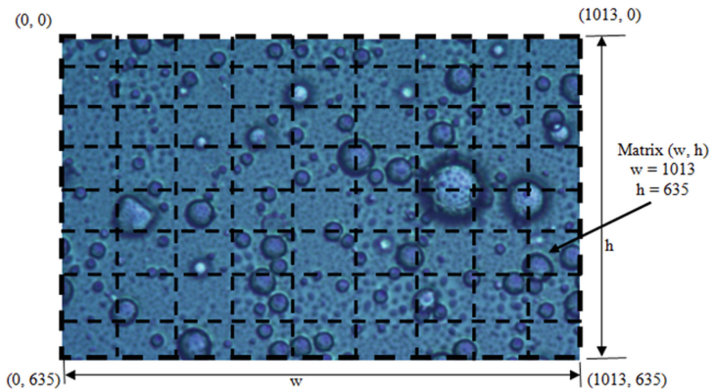


Fig. 7. The image matrix.

3 Results and Discussion

To verify if the increase in the water dosage in the emulsion affects the distribution and size of water droplets in the continuous phase (diesel or biodiesel), samples of both emulsions were analyzed with different dosages of water in the diesel emulsion (and biodiesel) with volume ratios of 5%, 10%, 15%, 20% and 30%. As shown in Fig. 8 the number and diameter of water droplets were greatly affected by the increase in the water dosage, so the volume of water droplets was increasing with the increase in the volumetric percentage of water. This result is in agreement with microscopic result of emulsion [17]. The maximum diameter of water droplets before inter separation limit for dosages: 5%, 10%, 15%, 20% and 30% were 107.3, 112.4, 117.4, 120.2 and 123.1 μm for W/D and 112.5, 123.6, 124.3, 135.4, and 137.6 μm for W/BD, respectively, as shown in Table 2. The result also appeared separation of the W/D emulsion need shorter period from W/BD emulsion. Generally, microscopic experimental tests showed an increase in the diameter of water droplets in the emulsifier as well as the accelerated degradation with the increase water dosage for emulsion when the emulsion with water was 30%. Therefore, it is clear from the above results that the properties of emulsion were changed by increasing the water dosage; density and viscosity affected the surface tension and thus reduced the stabilization period of emulsifier.

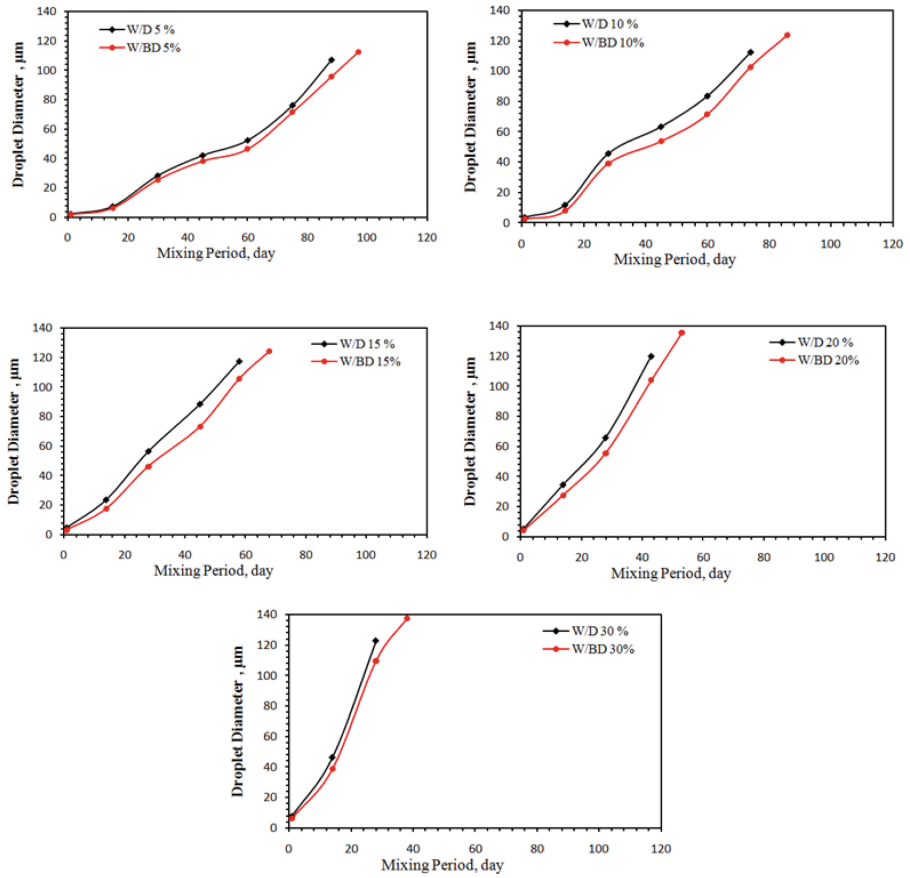
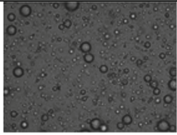
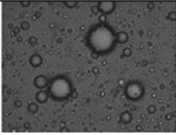
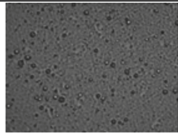
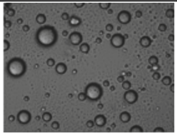
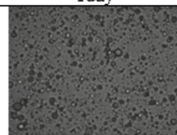
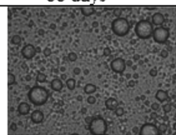
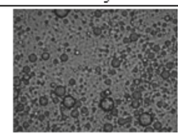
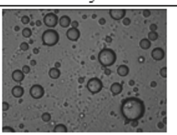
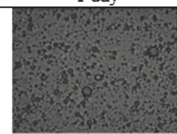
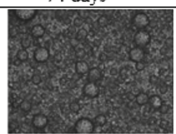
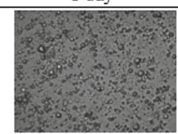
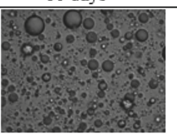
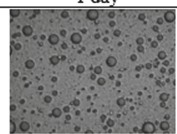
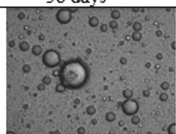
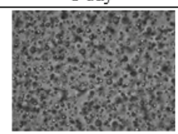
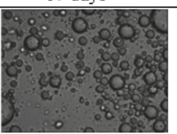
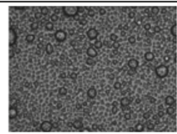
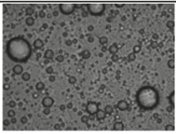
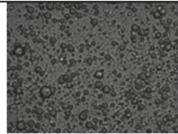
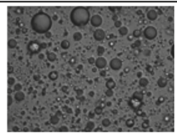


Fig. 8. Contrast of water droplet diameter with mixing period for W/D and W/BD emulsions with different water dosages.

Table 2. Microscopic images of water dosages in W/D and W/BD emulsions.

Water dosage	W/D emulsion		W/BD emulsion	
5%	 1 day	 88 days	 1 day	 97 days
10%	 1 day	 74 days	 1 day	 86 days
15%	 1 day	 58 days	 1 day	 67 days
20%	 1 day	 43 days	 1 day	 53 days
30%	 1 day	 28 days	 1 day	 38 days

4 Conclusions





The main objective of using the water-in-Diesel or Diesel-in-Water emulsions as fuel for diesel engines is to increase the oxygen charge in combustion mixture and reduce the emissions. Many affecting factors on emulsions has not been effectively identified; the distribution of water droplets in the emulsion (droplet size) with increasing water dosage of the emulsions and what can this parameter effect on stabilization period for the fuel emulsions. In the present work, the effect of emulsifier dosage (water in diesel ratio) on the stability period with using optical technique was studied. It was noted that, the larger the amount of water content in the emulsion, the brighter milky emulsion produced. The experiments indicated that increasing the water dosage in W/D and W/BD emulsions influenced negatively on the emulsion stabilization period.

References

1. Fadil, A., Mashkour, M.A., Abdul Wahhab, H.A.: Investment of blending biofuels and nanoparticles with conventional diesel fuel to improve combustion process—a review. *Adv. Mater. Sci. Eng.*, 95–107 (2023)
2. Hayder, A.D., Fayad, M.A.: Role of different antioxidants additions to renewable fuels on NOX emissions reduction and smoke number in direct injection diesel engine. *Fuel* **279**, 118384 (2020)
3. Abdul Wahhab, H.A., Al-Kayiem, H.H.: Environmental risk mitigation by biodiesel blending from *Eichhornia crassipes*: performance and emission assessment. *Sustainability* **13**(15), 8274 (2021)
4. Al-Kayiem, H.H., et al.: Performance and emissions investigation of a single cylinder diesel engine using enhanced blend biodiesel by nanoparticles. In: *AIP Conference Proceedings*. AIP Publishing LLC (2018)
5. Fu, W.B., et al.: A unified model for the micro-explosion of emulsified droplets of oil and water. *Fuel Process. Technol.* **79**(2), 107–119 (2002)
6. Fu, W.-B., et al.: A study on ignition characteristics of emulsified oil containing flammable fuel. *Fuel Process. Technol.* **80**(1), 9–21 (2003)
7. Nadeem, M., et al.: Diesel engine performance and emission evaluation using emulsified fuels stabilized by conventional and Gemini surfactants. *Fuel* **85**(14–15), 2111–2119 (2006)
8. Lin, C.-Y., Chen, L.-W.: Comparison of fuel properties and emission characteristics of two- and three-phase emulsions prepared by ultrasonically vibrating and mechanically homogenizing emulsification methods. *Fuel* **87**(10–11), 2154–2161 (2008)
9. Armas, O., et al.: Characterization of light duty diesel engine pollutant emissions using water-emulsified fuel. *Fuel* **84**(7–8), 1011–1018 (2005)
10. Hayder, A.D., Chaichan, M.T., Megaritis, T.: Performance, regulated and unregulated exhaust emission of a stationary compression ignition engine fueled by water-ULSD emulsion. *Energy* **181**, 1036–1050 (2019)
11. Ghannam, M., Selim, M.: Stability behavior of water-in-diesel fuel emulsion. *Pet. Sci. Technol.* **27**(4), 396–411 (2009)
12. Ghannam, M.T., Selim, M.Y.: Rheological properties of water-in-diesel fuel emulsions. *Int. J. Ambient Energy* **37**(1), 24–28 (2016)
13. Ghannam, M.T., et al.: Flow characteristics of xanthan solutions and their crude oil emulsions in terms of thixotropic behavior. *Pet. Sci. Technol.* **37**(11), 1279–1288 (2019)
14. Ghojel, J.I., Tran, X.-T.: Ignition characteristics of diesel– water emulsion sprays in a constant-volume vessel: effect of injection pressure and water content. *Energy Fuels* **24**(7), 3860–3866 (2010)
15. Wahhab, H.A., Mashkour, M., Madodi, S.: Investigation of water-diesel emulsion characteristics using optical technique. *J. Appl. Fluid Mech.* **13**(1), 349–355 (2020)
16. Khan, M.Y., Abdul Karim, Z.A., Aziz, A.R.A., Tan, I.M.: Experimental investigation of microexplosion occurrence in water in diesel emulsion droplets during the Leiden frost effect. *Energy Fuels* **28**, 7079–7084 (2014)
17. Yaser, H.S., Abdul Wahhab, H.A., Dhahad, H.A.: Survey to water-in-diesel emulsion characteristics as an alternative fuel for CI engine. In: Emamian, S.S., Awang, M., Razak, J.A., Masset, P.J. (eds.) *Advances in Material Science and Engineering*. LNME, pp. 81–94. Springer, Singapore (2023). https://doi.org/10.1007/978-981-19-3307-3_8
18. Yaser, H.S., Abdul Wahhab, H.A., Dhahad, H.A.: Influence of water-in-fuel (diesel and biodiesel) emulsions on the performance and emission characteristics of a single-cylinder diesel engine. In: Emamian, S.S., Awang, M., Razak, J.A., Masset, P.J. (eds.) *Advances in Material Science and Engineering*. LNME, pp. 71–79. Springer, Singapore (2023). https://doi.org/10.1007/978-981-19-3307-3_7



Prediction of a Diffusion Flame Characteristics with the Influence of Repulsive Electromagnetic Fields

Hasanain A. Abdul Wahhab¹ , Sameera S. Shijer¹ , Mohammed A. Fayad² ,
and Miqdam T. Chaichan² 

¹ Training and Workshop Center, University of Technology - Iraq, Baghdad, Iraq
20085@uotechnology.edu.iq

² Energy and Renewable Energies Technology Center, University of Technology - Iraq,
Baghdad, Iraq

Abstract. This paper describes an experimental study of influence of magnetic field on diffusion flame in the counter burner. Diffusion flames for different LPG gas flow rates propagating in counter burner of a different magnetic field intensities 1000 to 5000 gauss have been experimentally investigated. An influence of the changing fuel gas flow rate, magnetic force on the flame structure, combustion velocity and flame temperature has been determined. In the present work, the diffusion flame recording images was used to analyze the effect of changing magnetic field intensity on the flame disc diameter. Significant results were obtained in the area of counter flame. Flame disc diameter in the counter burner depend basically on the velocity of fuel and air. Flame diameters are almost the same for top and bottom flame disc and decreased with increasing the magnetic field intensity. At the fuel flow rate values ($Re = 22, 31$), the values of combustion velocity were increased with increasing magnetic intensity, and this behavior due to probably caused by effect magnetic force on oxygen zone.

Keywords: Magnetic Field · Electromagnetic induction technique · laminar diffusion flame · Combustion operations

1 Introduction

Many studies have been conducted experimentally and numerically to examine the effective controlling factors of combustion phenomenon to be utilized on combustion systems such as industrial combustion equipment; ramjets and burners [1, 2]. While diverse research has been carried out on the burners design factors to improve combustion system performance and harmful emissions from burner nozzle [3, 4], several studies interested about apply the magnetic field to enhance of combustion process [5–9]. The influence of magnetic field on propane and acetylene diffusion flames have been experimentally investigated using an electromagnetic system [10–14]. The experiments included magnetic field having various frequencies and duty ratios was established in square wave form. The maximum intensity and gradient of magnetic field were 1.3 T and 0.27 T/mm,

respectively. The results appeared that height of a flame front was reduced up to 4.5% and the brightness was enhanced up to 25% when the magnetic field was effected. Wu et al. (2016) [10] studied the influence of magnetic fields on various characteristics of laminar diffusion flames of methane on a co-annular burner. Results sure that the increasing of magnetic field, the flame height decreases while the flame temperatures increase. Further, thermal NO_x production in the flame was reduced as a result of the effect of the gradient magnetic field. In our previous tests with propane diffusion flames with slightly higher fuel flow rates, measured flame heights were about 10 mm agreeing with Roper's equations [15–17]. The review of literature showed that numerous researchers have investigated the flame structure influences from the local extinctions perspective for different fuels under influence of magnetic field. But, the effects of changing magnetic field intensity on patterns diffusion flame in complex flame burner such as counter burner haven't been widely studied. Therefore in the present work, the influence varying the magnetic field intensity on diffusion flame pattern in a counter burner was investigated. For that, counter flames for the diffusion of LPG and air has been experimented, also the present paper introduces the results of the simulation of electromagnetic induction charger.

2 Experimental Implementation

2.1 Principle of Electromagnetic Induction System

The permeability of in a magnetic burning gases differs from that of the unborn gases because of the oxygen content in the combustion region as Ferro-fluid dynamics [16, 18–20]. When the magnetic field is excited, the coils generate eddy currents which serves as an insulating obstacle in the flame front created and effects on in flame length. In the diffusion flame can detect the slight changes in the flame length outside with the fuel gas flow by measuring the amount of relative increase of the electromotive force between induction coils. It is assumed that there is no magnet sable material except for the magnetic region in the oxygen space affected by the magnetic field and no tangential components to the plane defined by either one of the induction coils in the flame region between the induction coils [21]. Thus, from the Gauss' low, the magnetic flux density becomes unique in the flame region between induction coils as well as in the combustion region. In addition, in the induction coil, the induction current is small, (in the order of 10⁻⁹ amp) and the magnetic fluid is nonconductive, thus the mutual effect of magnetic field intensity by the excitation coils and induction coils is so small. The strength of the magnetic dipole moments is defined by the magnetic susceptibility of a material. Paramagnetic materials have positive magnetic susceptibility while diamagnetic materials have a negative susceptibility. Carbon dioxide, nitrogen and most products of combustion are diamagnetic while oxygen is paramagnetic in nature [3–5]. This means that by applying an external inhomogeneous magnetic field, oxygen can be attracted towards one area while the combustion products are repelled from this area. However, at relatively low magnetic field strengths, the enhancement in combustion is accredited to the oxygen's paramagnetic characteristics since diamagnetic materials only form a weak magnetic dipole moment [10].

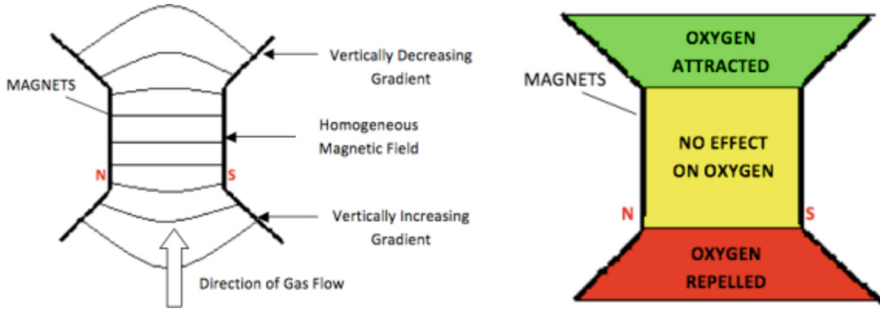


Fig. 1. Magnetic fields gradient with effect on oxygen [15].

The thermal flow of oxygen to enhance combustion features under affect repulsive magnetic fields is shown in Fig. 1 [15], one of the main effects is the direction of flow of the fuel. The fuel gas flows in a vertically upward direction, when the vertically decreasing, the oxygen flow will be forced downward opposing the direction of fuel gas flow. On the other words, the vertically increasing field will cause oxygen to flow upward along with the gas flow thus, repelling it from the reaction zone. This implies that during combustion, the oxygen concentration around the reaction zone will be increased with the use of vertically decreasing gradients thus allowing more fuel molecules to react with oxygen molecules, leading to more complete combustion.

Gases are either diamagnetic or paramagnetic in nature. Due to the magnetic susceptibility of gases, a magnetic body force can be applied to these with the use of gradient magnetic fields. The magnitude and direction of the magnetic body force follows Kelvin's equation [22, 23]:

$$F_{mag} = \frac{1}{2} \frac{X_i}{\mu_o} \nabla B^2 \quad (1)$$

Being that the order of magnitude of paramagnetic materials is significantly larger than that of diamagnetic ones, the magnetic force acting on a diffusion flame is mainly attributed to the effects on paramagnetic oxygen. For a typical diffusion flame used in this study and with magnetic field of flux density of 0 – 5000 Gauss, the magnetic forces acting on the system may vary in the range of 0–5.6 N/m³.

As it was mentioned in Sect. 1, a widely used expression to predict laminar jet flame lengths for circular burner ports was derived [20]. The expression applies to flames regardless of whether or not buoyancy is important in the reaction and is applicable for fuel jets emerging into a quiescent oxidizer or a co-flowing stream. Given that magnetic forces are similar to buoyant forces (both act on a volumetric basis) it may be assumed that the expression developed by Roper applies for laminar flames under the application of a magnetic field. Roper's expression for the flame length in a circular port is as follows:

$$L_f = 1330 \frac{\phi_f (T_\infty / T_f)}{\ln(1 + 1/S)} \quad (2)$$

where ϕ_f is the volumetric flow rate of fuel from the nozzle (m³/sec), T_∞ is the ambient oxidizer temperature (K), T_f is the mean flame temperature at the burner exit (K), and

S is the molar stoichiometric oxidizer-fuel ratio. For a generic hydrocarbon, C_xH_y , the stoichiometric ratio can be expressed as

$$S = \frac{x + y/4}{X_{O_2}} \quad (3)$$

where X_{O_2} is the mole fraction of oxygen in air.

2.2 Methodology and Experimental setup

The specifications of the main electromagnetic induction system components which include: an excitation coils, DC power supply, signal analyser, and Tesla-meter, as shown in Fig. 2. Excitation Coils (electromagnetic charger) was supplied by the DC power (0–32) voltage and (0–100) amp current as shown in Fig. 2. This charger comprised of a U-type yoke and two coils wound with 350 turns of enamel-coated copper wire with 1.5 mm diameter. The coils were linked parallel within the electrical circuit for the processing of magnetic field intensity with varying voltage. The current is of a DC power supply. To reduce the loss by eddy current in the core, the yoke was constructed with steel, the cross section area for the both of yoke poles was 32 mm (perpendicular to the flow direction: x-axis) and 80 mm (parallel to the flow direction: z-axis) to embraces the test section. A pair of the tesla meter sensors was fixed between yoke poles and test section to measure the magnetic flux signing. The excitation coils designed in this work measures variable magnetic field intensity when changing input condition of the current and voltage from 0 to 5000 gauss.

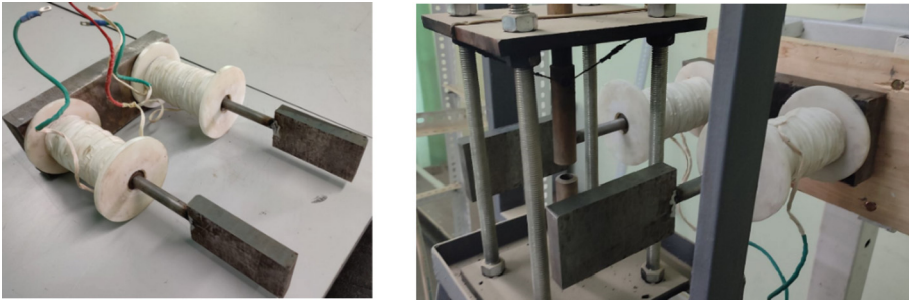


Fig. 2. Experimental electro-magnet charger.

As it is be shown from Eq. (1) the magnetic force for a gas species is depend on both the magnetic flux density and the magnetic flux gradient. A code was developed within the MATLAB environment to define the magnetic force profile on paramagnetic oxygen as a function of the perpendicular position of each of the magnetic poles. The magnetic field density profile around the cross-section of the different magnetic poles was determined with a calibration criteria of 10^{-8} . Figure 3 appear the results obtained from the numerical analysis, and to validate these results, experimental measurements for magnetic field intensity were taken in the air-gap region of the electromagnet.

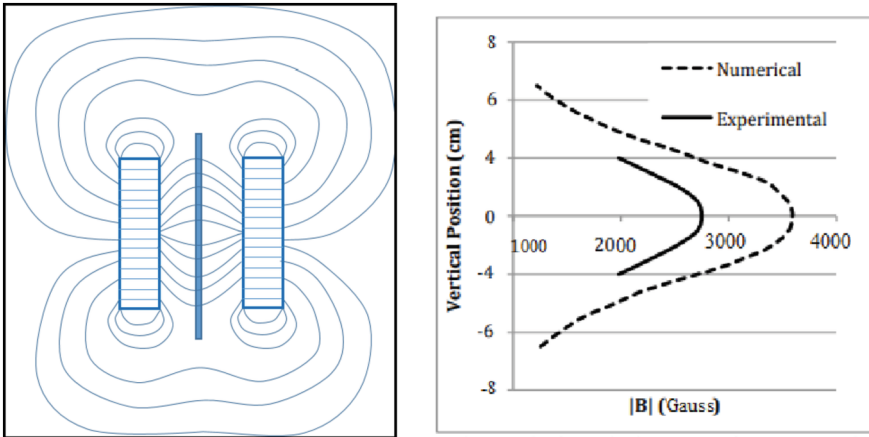


Fig. 3. Numerical results of magnetic field around circular permanent magnets and validation of numerical results by comparison to experimental measurements.

The rectangular magnets have a larger maximum force in the positive than in the negative direction. The electromagnets are third on the maximum force followed by the fixed intensity magnets, which has rather negligible forces on oxygen. For comparison purposes, the magnitude and direction of the maximum force exerted by each of the magnetic configurations is shown in Fig. 3.

3 Results and Discussion

For all cases from experiments the, the magnetic force effected on oxygen changes direction from positive to negative. To enhance counter flame characteristics, the direction of the magnetic force has to oppose the direction of the fuel flow. For example, if the burner flows in the positive vertical direction, the force on paramagnetic oxygen should be in the negative vertical direction so that oxygen is forced into the flame. It can be seen from photos in Fig. 4(a) that the increasing fuel flow rate (increase Reynolds number $Re = 22$ to 31) is decreasing flame disc oscillation. These experiments were used charger electromagnetic charger with change intensity from 1000 gauss to 5000 gauss and recorded the induction vtagages to correct the measured magnetic field values, the images of diffusion flames at different magnetic field intensity shown in Fig. 4(b).

Figure 5 shows the effect of magnetic field on the diameter of flame disc and the brightness of the flame changed as a result of the increase in the rush of oxygen towards the combustion area due to the effect of the magnetic force. When supply combustion zone with the negative gradient magnetic field, so back decreasing magnetic field, increases the supply of oxygen to the combustion region by inducing an oxygen flow to the vicinity of the flame front. This flow provides more oxygen for the combustion leading to the promotion of chemical reaction, i.e., fuel and air react faster resulting in flame disc decrease. On the other hand, the results showed that increasing the flow rate of the gaseous fuel reduces the effect of the magnetic field on the dimensions of the flame

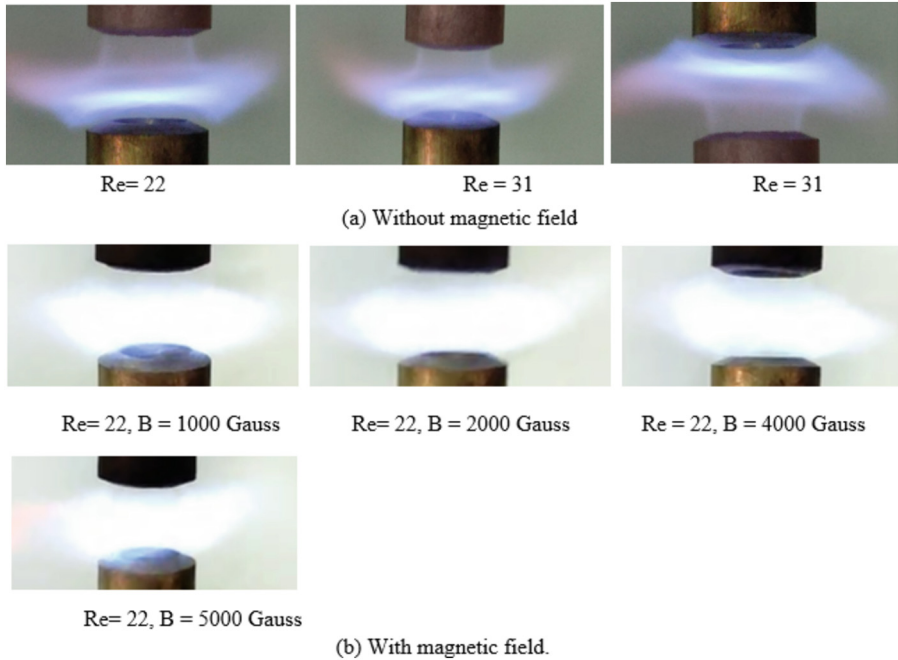


Fig. 4. Photos of (a) diffusion flames at different Reynolds numbers, and (b) diffusion flames of different magnetic field intensities.

front, and this is because the momentum force opposes the magnetic force affecting the oxygen surrounding the flame.

Figure 6 shows the effect of magnetic field on the combustion velocity and flame temperature in the combustion domain by applying magnetic field on the mid-distance between counter burner edges. For the mid-section (flame disc), the overall combustion velocity in the domain increased due to the decreasing area of the flame disc. Regarding the temperature values as a result of magnetic field applied to the flame disc of the burner, while the velocity was increased in the center of the nozzle, the temperature was remained slow affected by increasing magnetic field. The reason is that the fuel flow developed in the burner pipe before it reached the edge exit. Conversely, when magnetic field was applied to the mid-section of the burner increasingly, the maximum flame temperature was declined slightly by approximately 40° .

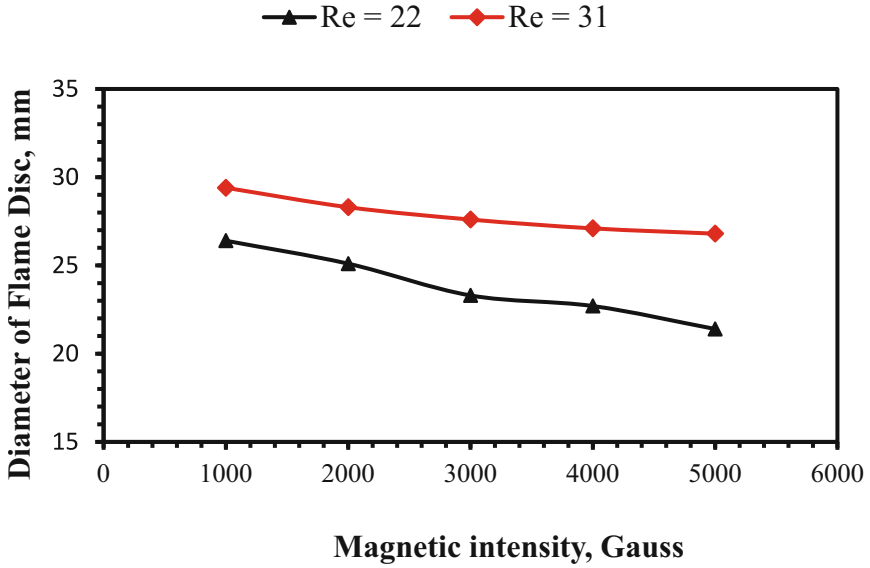


Fig. 5. Effect of magnetic field on diameter of disc flame in the counter burner.

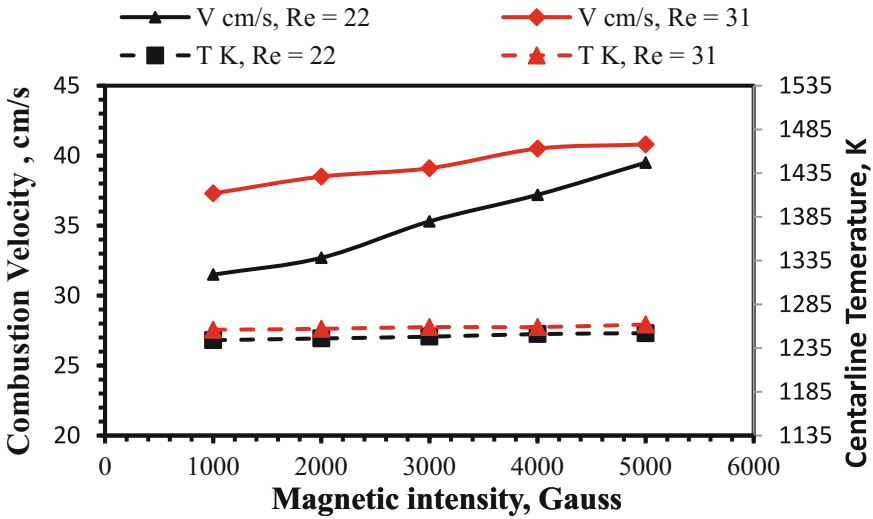


Fig. 6. Effect of magnetic field on combustion velocity and flame temperature in the counter burner.

4 Conclusions

In this work, electromagnetic induction technique applied to enhance combustion of diffusion flames in counter burner. It was shown by these experiments that the force of this type of magnets better than fixed intensity magnets, the force of previously used

experimental magnets. Experiments concluded that increasing magnetic field intensity was caused decrease flame front dimensions (flame disc diameter) and change flame brightness. The results appeared increasing in combustion velocity with applied magnetic field different intensity, while the change in the temperature of the flame is slight with the change in the intensity of the magnetic field. Future work of magnetic field effects on combustion should focus on developing magnetic configurations that can provide for even higher forces on paramagnetic oxygen.

References

1. Khaldi, F., Messadek, K., Benselama, A.M.: Isolation of gravity effects on diffusion flames by magnetic field. *Microgravity Sci. Technol.* **22**, 1–5 (2010)
2. Gilard, V., Gillon, P., Blanchard, J.N., Sarh, B.: Influence of horizontal magnetic field on a co-flow methane/air diffusion flame. *Combust. Sci. Technol.* **180**, 1920–1935 (2018)
3. Gillon, P., Blanchard, J.N., Gilard, V.: Magnetic field influence on co-flow laminar diffusion flames. *Russ. J. Phys. Chem. B* **4**, 279–285 (2010)
4. Sarh, B., Gillon, P., Gilard, V., Bodele, E.: Lengths of lifted laminar flames under vertical magnetic field gradient. *Combust. Sci. Technol.* **186**, 1422–1433 (2014)
5. Abdul-Wahhab, H.A., et al.: Survey of invest fuel magnetization in developing internal combustion engine characteristics. *Renew. Sustain. Energy Rev.* **79**, 1392–1399 (2017)
6. Abdul Wahhab, H., et al.: Mathematical modeling of the flow of diesel-CNG fuel mixture in a pipe under the influence of a magnetic field. *J. Appl. Fluid Mech.* **10**(1), 389–396 (2017)
7. Wahhab, H.A.A., et al.: Prediction of the phase distribution of diesel/CNG bubbly flow in a horizontal pipe under the influence of a magnetic field. *J. Mech. Sci. Technol.* **31**(11), 5299–5309 (2017)
8. Wahhab, H.A.A., et al.: Magneto-hydrodynamics of bubbly flow in horizontal pipe: new criteria through numerical simulation. In: *AIP Conference Proceedings*. AIP Publishing LLC (2018)
9. Mola, A.H., Abdul Wahhab, H.A., Naji, Z.H.: Effects of nozzle diameter and number of carbon atoms in fuel on flame quenching in counter burner. In: Ahmad, F., Al-Kayiem, H.H., King Soon, W.P. (eds.) *ICPER 2020. LNME*, pp. 123–131. Springer, Singapore (2023). https://doi.org/10.1007/978-981-19-1939-8_11
10. Wu, W., Qu, J., Zhang, K., Chen, W., Li, B.: Experimental studies of magnetic effect on methane laminar combustion characteristics. *Combust. Sci. Technol.* **188**, 472–480 (2016)
11. Abdul Wahhab, H.A., Aziz, A.R.A., El-adawy, M., et al.: Effect of rotating burner rim on flame stabilization: blow-off and flash back. *Int. J. Eng. Technol.* **7**, 230–233 (2018)
12. Abdul Wahhab, H.A.: Investigation of stability limits of a premixed counter flame. *Int. J. Autom. Mech. Eng.* **18**(1), 8540–8549 (2020)
13. Zamashchikov, V.V.: Some features of gas-flame propagation in narrow tubes. *Combust. Explos. Shock Waves* **40**(5), 545–552 (2004)
14. Maruta, K., Kataoka, T., Kim, N.I., Minaev, S., Fursenko, R.: Characteristics of combustion in narrow channel with a temperature gradient. *Proc. Combust. Inst.* **30**, 2429–2436 (2005)
15. Agarwal, S., Kumar, V., Shakher, C.: Temperature measurement of wick stabilized micro diffusion flame under the influence of magnetic field using digital holographic interferometry. *Opt. Lasers Eng.* **102**, 161–169 (2018)
16. Agarwal, S., Kumar, M., Shakher, C.: Experimental investigation of the effect of magnetic field on temperature and temperature profile of diffusion flame using circular grating Talbot interferometer. *Opt. Lasers Eng.* **68**, 214–221 (2015)

17. Mohammad, H., Jasim, H., Sadeq, J., Salim, A., Abas, A.: Effects of magnetic field on fuel consumption and exhaust emissions in two-stroke engine. *Energy Proc.* **18**, 327–338 (2012)
18. Chaware, K.: Review on effect of fuel magnetism by varying intensity on performance and emission of single cylinder four stroke diesel engine. *Int. J. Eng. Res. Gen. Sci.* **3**, 1174–1178 (2015)
19. Agarwal, S., Shakher, C.: Effect of magnetic field on temperature profile and flame flow characteristics of micro flame using Talbot interferometer. *Optik* **168**, 817–826 (2018)
20. Pandey, P.K., Kumar, M., Kumar, V., Shakher, C.: Measurement of temperature and temperature profile of wick stabilized micro diffusion flame under the effect of magnetic field using digital speckle pattern interferometry. *Opt. Eng.* **56**, 014106 (2017)
21. Zhen, H., Wang, Z., Liu, X., Wei, Z., Huang, Z., Leung, C.: An experimental study on the effect of DC electric field on impinging flame. *Fuel* **274**, 117846 (2020)
22. Khaldi, F., Noudem, J., Gillon, P.: On the similarity between gravity and magneto-gravity convection within a non-electroconducting fluid in a differentially heated rectangular cavity. *Int. J. Heat Mass Transf.* **48**, 1350–1360 (2005)
23. Khaldi, F.: Controlling gravity impact on diffusion flames by magnetic field. *J. Heat Transfer* **134**, 061201 (2012)



Design and Fabrication of a Livestock's Fodder Crusher

Sam Shaanika^(✉), Mutiu Erinosh, and Ester Angula

Department of Mechanical and Metallurgical Engineering, University of Namibia, P.O.
Box 3624, Ongwediva, Namibia
sshaanika@unam.na, sshaanika2018@gmail.com

Abstract. Crop residues are materials left in an agricultural field after crop harvest and are a major source of livestock feed. Due to their hard and slippery nature, livestock only feed on half, leaving the rest dispersed and wasted. This project is focused on the design and fabrication of a livestock fodder crusher to crush crop residues into livestock fodder. The crushing has improved the crop residue quality and the design consists of major components such as cutting and crushing blades, bearings, shaft and crushing chamber. The project was carried out by fabricating a manually powered fodder crusher in the welding workshop at Jose Eduardo dos Santos campus (University of Namibia) to test and evaluate the design feasibility. The fabricated manually powered fodder crusher has shown dependability and is beneficial to all rural dwellers as it does not require solar or electric powering methods.

Keywords: Crop residues · livestock · fodder · fodder crusher · manually powered

1 Introduction

Fodder or animal feed is an agricultural foodstuff used specifically to feed domestic livestock such as goats, cattle, sheep, horse and donkeys. They are food harvested and stored specifically for domestic animal consumption and it is a step up from forage that livestock graze while in the ground. The first fodder cutter called the straw chopper was invented by Hochfield in the mid 1700's and used a lever [1]. With progression in years and advance in technology, farmers demanded an easier and more efficient way to do their work and the hacksel machine was developed which consisted of a flywheel and sharp blades attached to the wheel's spoke, where fodder is pushed into a trough and chopped into pieces. With increasing cropping areas, reduction on grazing land and growing demand for livestock feeds, it is important to ensure the effective use of resource including crop residues [2]. The problem encountered is that Mahangu, maize and sorghum stovers are roughages that is always available after the harvest as livestock feeds. Due to the hard and slippery nature of the roughages, animals find it difficult to feed on. Crushers are one of the major size reduction equipment that are used in mechanical, metallurgical and other similar industries, with various size and capacity ranging from 0.1 ton/hr. to 50 ton/hr.

[3]. These crushers are classified based on the way they apply force, mechanism used to crush and the degree to which they can distort the crushed materials. Impact crushers involves the use of impact to crush materials and their commonly major components are shaft, rotor, hammers, discharge mechanism and casing [3]. There is also a cone crushers which is a compressive type of crushing machines that distort materials by squeezing or compressing the feed materials between a moving and a stationary piece of steel [4]. Similarly, there exist a jaw crusher which consists of a fixed and moving jaw and it uses reciprocating movement of the movable jaw that compresses and crush materials between itself and the fixed jaw as the material enters the zone between the jaws [5]. Egbe and Olugboji [6] designed, fabricated and tested a double roller crusher and reported that the machine had a capacity of 1.43 tonnes/hr with theoretical efficiency of crushing limestone of 60%. The authors reported that crushing takes place when applied external forces are greater than the cohesion among the molecules of the particles [6]. Jibrin et al. [7] developed a 10 kW diesel engine powered crop residue crushing machine and discovered that attaching a flywheel to the hammer mill shaft lowers the speed of the diesel engine [7]. Gupta [3] designed and analysed a horizontal shaft impact crusher and pointed out that the crushing effect depends on the kinetic energy of the hammer, interchange of energy between hammer and particles and loss of energy due to impact [3]. Manaye et al. [8] redesigned and fabricated a hammer milling machine for pasta making due to the inability of existing hammer mills to meet the demand to eliminate waste during operation. The fabricated machine incorporated a proper air circulation system that does not destroy the flour produced by overheating [8]. Mushiri and Mbohwa [9] improved the efficiency of a gold ore crushing system and reported that slacks in conveyor belts caused the failure and the transport feeding materials at reduced speed and also the worn rollers damage the belts and result in material spillage.

The main objective of this project is to design and manufacture a livestock's fodder crusher and select the best material and design concept as well as testing the performance of the fabricated crusher.

2 Design Methodology

In the design process as shown in Fig. 1, the recognition of need and problem were identified on which conceptualisations that best suit the problem of interest were based. The selected concept was then modelled, sized and simulated using SolidWorks software. The design calculations were performed on which decision making were based and a prototype was fabrication to test and evaluate the design.

Three different concepts were adopted in the design and this reflects the idea behind the design. The first concept is a manually powered fodder crusher. It has a handle fixed on one end of the shaft in which the operator can hold onto to rotate the shaft with cutting and crushing blades. The rotational motion induces a centrifugal force to cut and crush the crop residues. It is easy to operate and low in production cost. The second concept is a solar powered fodder crusher that constitute of a solar panel, battery, inverter and an induction motor. The solar panel charges the battery while as the inverter converts direct current to alternating current in order to power the induction motor. The induction motor shaft is coupled to the machine shaft with cutting and crushing blades to transmit

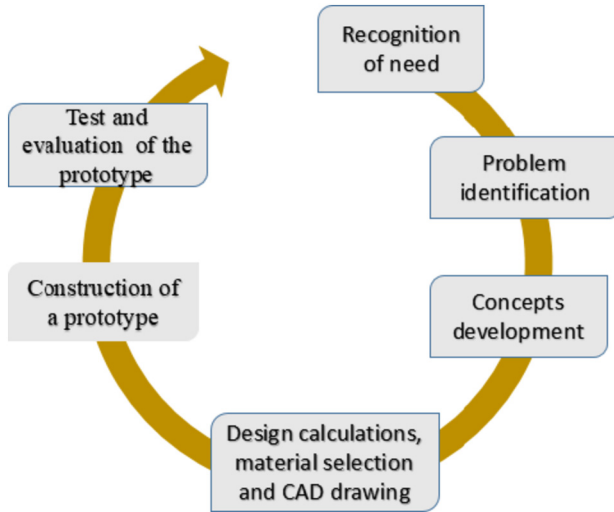


Fig. 1. Design process.

the rotational motion for crushing. The third concept is an electric powered fodder crusher that consists of an induction motor and shaft with blades. The induction motor will receive alternating current from the power source which activates electromagnetic induction from the rotating magnetic field of the stator winding thereby creating flux in the rotor and causing the shaft to rotate. The first concept was considered because on average a man can exert 60 rpm and a force of 64 N, which is enough to cause an impact to shear and crush the crop residues.

2.1 Conceptual Design

The cutting and crushing blades are rigidly attached to the shaft with a handle connected on one of its end and they all move together. As the operator turns the handle rotating the shaft with its blades, by the force of repeated impactful hit and strike, the impact with the walls of the crushing chamber, the sieve and each other, the stovers are crushed and turned into fodder. To enable effective crushing of the crop residues, a cutting and crushing mechanism are adopted as shown in Fig. 2. The cutting and crushing blades are rigidly attached to the shaft with a handle connected on one of its end and they all move together. As the operator turns the handle rotating the shaft with its blades, by the force of repeated impactful hit and strike, the impact crushed and turned the crop residues into fodder.

2.2 Design Calculations and Simulation

The design calculations are based on an average diameter of 15 mm of a crop residue stover obtained as an average of a combination of 10 stovers of Mahangu, maize and sorghum. In the design of the rotary cutter, the following assumptions were made: the

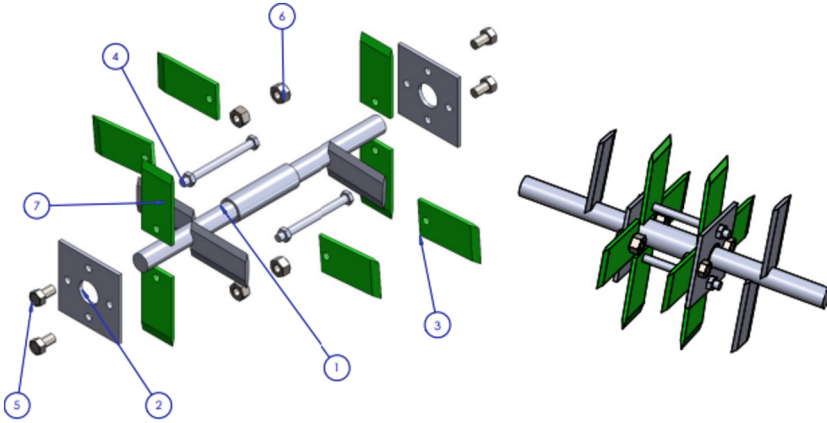


Fig. 2. Cutting and crushing mechanism.

maximum shear force of a crop residue stover is 21.7 N/mm^2 , allowance for the design shear cutter is 25%, maximum revolution a man can exert is 60 rpm and the force exerted by a man is 64 N [10]. Equation (1) expresses the cutting or crushing force needed [7].

$$F_{\text{hammer/cutter}} = S_{\text{cutter}} \times A_{\text{stover}} \quad (1)$$

where:

$F_{\text{hammer/cutter}}$ = Cutting or crushing force,

S_{cutter} = Maximum shear force of stover,

A_{stover} = Cross-sectional area of a stover [7].

The shaft was designed in accordance with the American Society of Mechanical Engineers codes for design of shafts and the following assumptions were made: Maximum allowable shear stress of mild steel is 42 MPa, shear modulus of the mild steel material is $79.3 \times 10^9 \text{ N/m}^2$, the density of mild steel is 7.85 g/cm^3 , the fatigue factor due to bending is 2, and the fatigue factor due to torsion 1.5.

The shaft will be subjected to twisting moment and Eq. (2) illustrates the diameter of the shaft [8].

$$D^3 = \frac{16}{\pi \sigma_s} \sqrt{(K_b M)^2 + (TK_t)^2} \quad (2)$$

where:

M = maximum bending moment,

K_b = fatigue factor due to bending,

T = torsional moment,

K_t = fatigue factor due to torsion,

D = shaft diameter,

σ_s = maximum allowable shear stress.

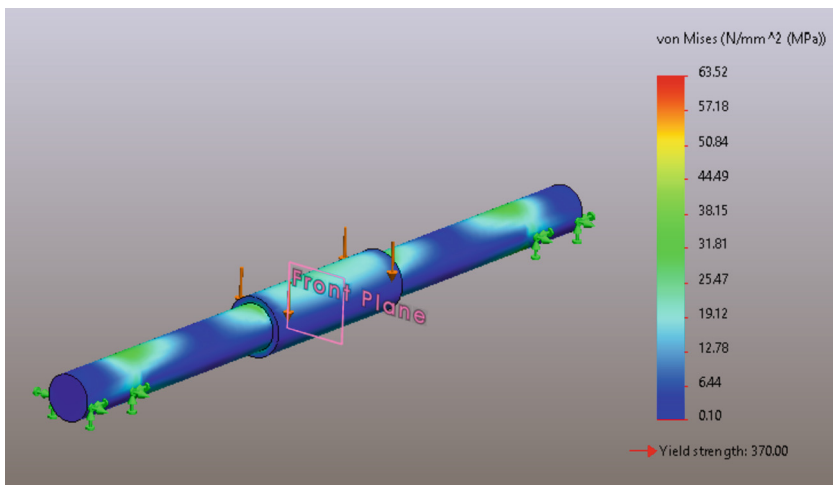
Table 1 depicts the results of the calculations for the design.

Finite Elemental Analysis of the shaft was simulated in SolidWorks software to analysis how it will respond to loading, and it yielded a safety factor of 5.8, which is

Table 1. Design calculations results.

Parameters	Symbol/Unit	Value
Average diameter of crop residue stover	D (mm)	15
Cross sectional area of a crop residue stover	A (mm ²)	176.71
Blades cutting/crushing force	F _{hammer/cutter} (N)	4 793.26
Angular velocity of cutting shaft	ω (rad/s)	6.283
Mass of a cutting/hammer blade	M (kg)	0.19625
Force required to cut a stover	F _{cutting/crashing} (N)	0.8716
Power required for cutting a stover	P _{cutting} (W)	0.616
Centrifugal force of the blades	F _{blades} (N)	9.587
Power required to be delivered to the blades	P _{blades} (W)	6.777
Torsional moment	T (N.m)	22.4 N.m
Maximum bending moment on shaft	M _b (N.m)	0.024 N.m
Shaft diameter	D _s (mm)	22.3 \approx 25

greater than 1 showing that the design is safe. The force exerted was 2000 N, and Von mises stress of 63.52 MPa and yield stress of 370 MPa were obtained as shown in Fig. 3.

**Fig. 3.** Finite Element Analysis of the shaft.

A prototype was manufactured the campus welding workshop reflecting the real working fodder crusher rather than the CAD drawing. The prototyping helped to match its intended final performance, enabled engineering judgement and its testing reduces the risk that the design may not perform as intended before the production design. The

fabrication of the fodder crusher started with the making of the frame. All other structural components of the machine sits on the frame and it carries the machine total load and stresses. In order to complete the prototype, the hopper was sized and fabricated as in the detailed design and it is made from 1.6 mm thickness mild steel flat sheets due to its high impact and tensile strength to withstand impact. The assembling of all components by welding or bolt and nuts yielded a prototype as shown in Fig. 4, and the test and the performance evaluation of the fabricated fodder crusher were successfully done.



Fig. 4. Crushed Mahangu crop residues.

3 Conclusion

The design has shown to be very dependable and can deliver, as it is design for with crushing in an enclosed chamber to eliminated dust pollution, manually powered with no operational cost involved, affordable and beneficial to all rural dwellers. The design has met its requirements to crush crop residues, beneficial to rural inhabitants and its light weight weighing about 35 kg allowing it to be portable.

References

1. Origins of the Feed Cutter: Inventors on Both Sides of the Atlantic Develop Devices - Farm Collector!Dedicated to the Preservation of Vintage Farm Equipment. <https://www.farmcollector.com/equipment/implements/origins-of-the-feed-cutter-inventors-on-both-sides-of-the-atlantic-develop-devices/>. Accessed 19 Apr 2022
2. Parthasarathy Rao, P., Hall, A.J.: Importance of crop residues in crop-livestock systems in India and farmers' perceptions of fodder quality in coarse cereals. *Field Crops Res.* **84**(1–2), 189–198 (2003)
3. Gupta, D.: Design and analysis of a horizontal shaft impact crusher **3**(1), 45 (2014)
4. Cone Crushers|McLanahan. <https://www.mclanahan.com/products/cone-crushers>. Accessed 26 Nov 2022
5. Jaw Crusher Working Principle. <https://www.911metallurgist.com/blog/jaw-crusher-working-principle>. Accessed 26 Nov 2022
6. Egbe, E.A.P., Olugboji, O.A.: Design, fabrication and testing of a double roll crusher. *Int. J. Eng. Trends Technol.* **35**(11), 511–515 (2016)
7. Jibrin, M.U., Amony, M.C., Akonyi, N.S., Oyeleran, O.A.: Design and development of a crop residue crushing machine. *Int. J. Eng. Invent.* **2**(8), 28–34 (2013)
8. Manaye, W., Hailu, B., Ashokkumar, T.: Redesign and fabrication of hammer milling machine for making pasta **12**(03), 202–218 (2019)
9. Mushiri, T., Mbohwa, C.: Design of a crushing system that improves the crushing efficiency of gold ore at a local mine: case of Zimbabwe, pp. 707–715 (2015)
10. Makange, N., Parmar, R.: Design and fabrication of an animal feed mixing machine, no. June (2016)



Design of a Solar PV Water Pumping System for Small-Scale Farming Along the Calueque-Oshakati Canal in Namibia

Sam Shaanika^(✉), Mutiu Erinosh, and Ester Angula

Department of Mechanical and Metallurgical Engineering, University of Namibia, P.O. Box 3624, Ongwediva, Namibia
sshaanika@unam.na, sshaanika2018@gmail.com

Abstract. Small-scale farmers along the canal usually use the diesel engine for the water pumping system which is associated with environmental concerns as a result of the gasses emission into the atmosphere and oil spillages. However, the diesel water pumping system is not economical because of the required extensive maintenance and constant fuel supply, and this has led to an increase in the system's overall operational costs. In this current study, a design of a solar water pumping system for the small-scale farm along the Calueque-Oshakati canal was conducted out based on the daily water requirements of 15 m^3 per hectare per day. The total dynamic head (TDH) was used to calculate an appropriate water pumping power that can meet the water requirement in the shortest possible time. A Crystalline Silicon [AC-270P/156-60S], 270 WP solar panel was been selected based on cost and efficiency for this design. Using a 5-year economic analysis period, it was determined that a solar water pumping system will be more cost-effective as compared to a diesel water pumping system. Thus, replacing the diesel water pumping system with a solar water pumping system for the small-scale farm along the Calueque Oshakati canal is the solution with economic and functional benefits.

Keywords: cost · energy · solar panel · pumping system · irrigation

1 Introduction

Based on literature, approximately 70% of the Namibian population depends on agricultural activities for reliable food supply. Most of the agriculture is rain-fed cultivation, which produces low-quality crops because of unreliable rainfalls and drought occurrences [1]. The major key problem in agricultural food production is the water scarcity as Namibia's geographical position contributes greatly to the dry conditions in the country. Currently, small-scale irrigation farming is been practiced along the Calueque-Oshakati Canal using a diesel fueled water pumps. These diesel pumps have high operational costs and are environmentally unfriendly [2].

In the literature search by some authors, it has been found that the use of photovoltaics for irrigation is an important agricultural operation. Using photovoltaics save a lot of energy that is consumed by the electric pumps used for water pumping. Solar

powered water pumping for irrigation can also be incorporated in an Automated manner hereby to ensure that water is used efficiently. Solar water pumping systems are highly recommended because they are environmentally friendly and have low maintenance and operating costs [3–8]. Solar photovoltaic (PV) water pumping has been recognized as suitable for grid-isolated rural locations in poor countries with high levels of solar radiation. Solar PV water pumping systems can provide water for irrigation without the need for any kind of fuel or the extensive maintenance as required by diesel pumps. They are easy to install and operate, highly reliable, durable and modular, which enables future expansion [9, 10].

In a design study done in New Mexico, it was found that, as compared to other energy sources for water pumping, solar based pump systems are often the best choice as they can function effectively and economically. Solar water pumps are portable and are thus more appealing to the producers. Solar water pumps are the attractive, long-term and cost-effective solution for water pumping as compared to other possible methods, for instance, the use of diesel pumps for water pumping [8]. Therefore, the design of a solar water pumping system for irrigation purposes for the small-scale farm along Calueque-Oshakati Canal was conducted. For the design of solar powered water pumping systems for irrigation purposes, the factors that need to be considered are the daily water requirements, the water source depth as well as the irrigation times.

2 Design Methodology

The design was done based on the water requirement of $15 \text{ m}^3/\text{day}$ data. Using the daily water requirements and the canal data, a suitable pump power was calculated, and the solar panel sizing was done for the lowest sun radiation day, in order to ensure that the solar system will be able to effectively power the water pump and operate effectively throughout the year. The storage tank sizing and structure analysis for the tank support was also design and analysed.

Using the solar resource data (PVGIS), the appropriate panel tilt angle had also been determined to ensure optimum operation of the solar PV system.

2.1 Weather Data of the Area Using PVGIS

Table 1 shows the estimation of solar energy output of the area around the Calueque-Oshakati canal.

Where, E_m is the average monthly electricity production from the given system [kWh]. H_m is the average monthly sum of global irradiation per square meter received by the modules of the given system [kWh/m²], and SD_m is the standard deviation of the monthly electricity production due to year-to-year variation [kWh]. It was found out that all the small-scale farmers along Calueque-Oshakati canal are using diesel water pumping systems for irrigations purposes. Figures 1 show the current water pumping system used by the farmers at the canal.

In order to ensure that the design components are easily accessible, a locally available 270 WP crystalline (AC-270P/156-60S) solar panel was selected. A crystalline panel was chosen because it is more cost effective and efficient as compared to the other panels.

Table 1. Monthly PV energy and solar irradiation.

Month	Em	Hm	SDm
January	151	202	12.9
February	121	161	11.4
March	105	141	4.99
April	71.3	99.8	1.66
May	42.7	66.7	0.476
June	28.9	49	0.368
July	35.6	57.6	0.342
August	61.6	89.9	0.595
September	99.1	136	1.35
October	139	188	4.31
November	151	202	8.21
December	163	217	9.02



Fig. 1. Diesel water pump used by the small-scale farmers.

To also ensure that there is water available, even if there is no sunshine or in the case for expansion purposes, a storage tank was proposed and the capacity should be able to hold water for minimum of 1 day. The tank is 15 m³ large in volume with a structural support of 3 m high. The support structure analysis was done using solid work software in order to ensure that the material used are strong enough to support the load of the tank and the water inside the tank. An economic analysis was also performed to determine whether it would be economical to replace the diesel water pumps with solar water pumps. This aspect of the project is very important as it will be used to convince the farmer to go

for the proposed solution, which is the implementation of solar water pumping systems [11].

3 Results and Discussions

For the purpose of determining the actual power requirement of the water pump, the inefficiencies due to loss of power in the cables and the controls during transmission and converting electricity to mechanical movements of the pump need to be considered [12]. Figure 2 shows the diagrammatic representation of the solar power water pumping system that was considered for this study.

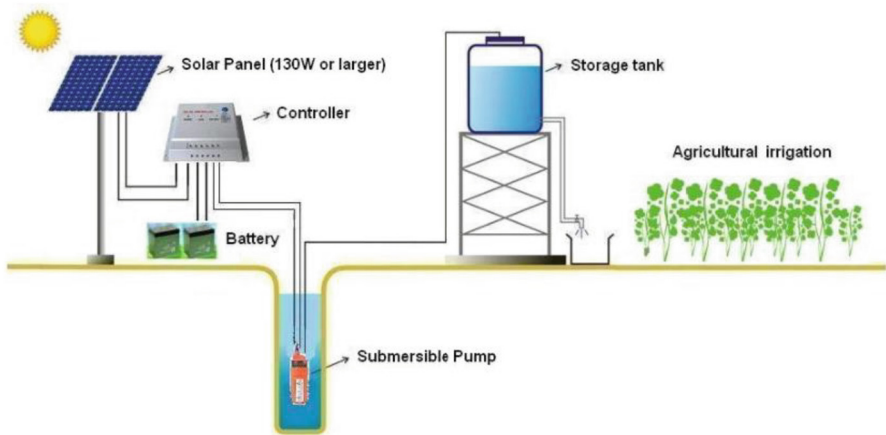


Fig. 2. Solar Powered water pumping system for irrigation [12]

At the desired operating conditions, the pump will be operating at an efficiency of 45.9%. The Pump current Demand PCD required for the pump power is given by Eq. (1):

$$P_{CD} = \frac{R_P}{E} \quad (1)$$

The required pump energy is given as (2):

$$P_E = P_P \times T \quad (2)$$

where: R_p is the Rated power, E is the Efficiency, P_E is the pump energy, and P_p is the Pump power.

Tables 2 and 3 show the solar panel selection and the solar PV system sizing.

3.1 Determining the Module Full Load Rated Energy (kWh)

Designing the solar system for the month (precisely June) where the worst solar radiation in Namibia occurs during the winter season, the total rated energy output from the panel can be obtained by using the following Eq. (3).

$$M_{FLRE} = M_{RP} \times H \quad (3)$$

Table 2. Electrical Performance of the Solar module.

Power output (<i>W</i>)	P_{max}	270
Voltage at P_{max} (<i>V</i>)	V_{mpp}	31.12
Current at P_{max} (<i>A</i>)	I_{mpp}	8.71
Open Circuit Voltage (<i>V</i>)	V_{oc}	38.21
Short Circuit Current (<i>A</i>)	I_{sc}	9.25
Module Efficiency (%)	η	16.6

Table 3. Temperature coefficients.

Voltage U_{oc}	%/K	-0.30
Current I_{sc}	%/K	0.04
Output P_{mpp}	%/K	-0.42

Solar modules have a de-rate factor of 0.8, therefore to account for the lost power, the panel required output energy is given by Eq. (4):

$$M_{OE} = M_{REO} \times 1.2 \quad (4)$$

Where: MFLRE is the Module full load rated energy, MRP is the Module rated power, H is the time (Hours), MOE is the Module Output Energy, and MREO is Modules Rated Energy Output.

3.2 Designed Solar PV System Output Quantities

In order to sufficiently power the pump, two (2) modules were connected in series in one string such that the system output quantities is be given by:

System Voltage out = 62.24 V DC, System Current out = 8.71 A and System Power out = 542.11 W.

Total system energy (TSE) is calculated using Eq. (5):

$$T_{SE} = P_O \times H \quad (5)$$

Where: P_o is the power output. For 3 h, the power output of 542.11 W generated the total system energy of 1.6263 kWh.

3.3 Solar Panel Optimum Tilt Angle

For the selected solar PV modules to produce maximum power on the 21st June (winter season) and throughout the year in the Southern Hemisphere (Tropic of Capricorn), the desired tilt angle is determined as using Eqs. (6) and (7) [10]:

$$Tilt = 90^\circ - \beta N \quad (6)$$

$$\beta N = 90^\circ + L + \delta \quad (7)$$

Where: βN – altitude angle, L – site latitude angle, and δ – solar declination angle.

In the case for expansion purposes and days where there is no sunshine, a storage tank is to be included, the capacity should be able to hold water for minimum 1 day. The storage tank capacity can be determined using Eq. (8).

$$STC = D_{WR} \times \text{days of storage} \quad (8)$$

where: STC is Storage Tank Capacity and D_{WR} is the Daily Water Requirement

The economic analysis for both diesel and solar water pumping system was also done in term of costing for the purpose of determining whether it would be economical to implement for a period of five years. Figure 3 shows the results obtained from the economic analysis for the water pumping systems.

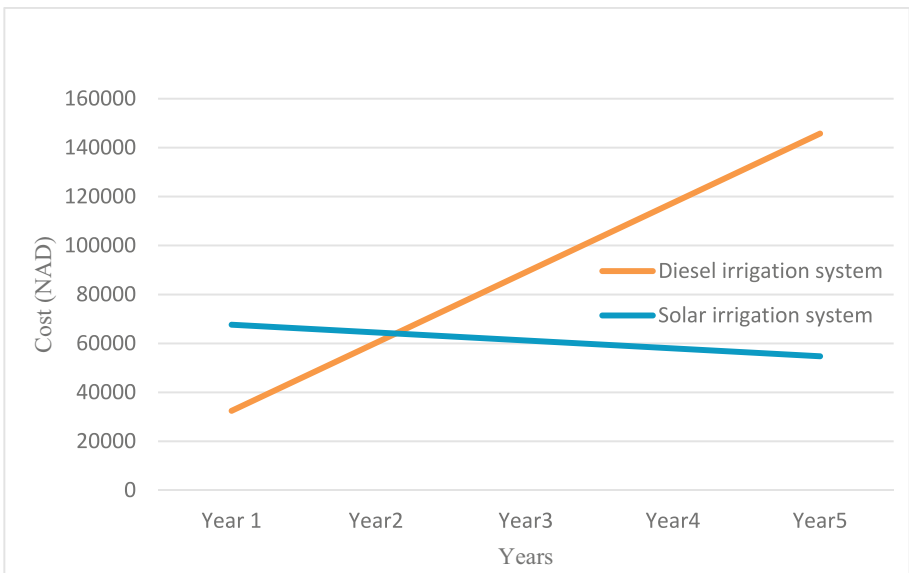


Fig. 3. Cost comparison between diesel and solar water pumping.

From the economic analysis, it can be deduced that using solar water pumping is far more economical as compared to the diesel water pumping systems. Diesel water pumping systems are more expensive due to the additional fuel that is used in these systems, yet associated with the disadvantages of scarcity and environmental unfriendliness. And comparing the operational cost of both systems for a period of 5-years, it has proven that diesel water pumping systems have higher operational cost due to the fuel and expensive maintenance cost. After a 5-year period to operate a diesel water pumping system it would cost approximately N\$ 145754 as compared the solar water pumping system with a total operating cost of approximately N\$ 67638.

4 Conclusion


The solar water pumping system requires less maintenance as compared to the diesel system and thus has less operational costs. Upon the performance of the economic analysis of the solar-powered water pumping system and economic comparison to the current existing diesel water pumping systems, it had been found that the solar water pumping system is more cost effective. The diesel water pumping system will be costing more than the solar water pumping system within 5 years of operation. The saved cost by the farmers can be used for maintenance of the canal and other operational upgrading by Namwater in Namibia.

References

1. Fiebiger, M., et al.: The Small-Scale Irrigation Farming Sector in the Communal Areas of Northern Namibia – An Assessment of Constraints and Potential, December 2010
2. Chilcott, R.P.: Health Protection Agency Compendium of Chemical Hazards: HPA Compendium of Chemical Hazards Diesel
3. S. E. E. Profile: Solar powered water pumping systems, no. January 2005, pp. 3–8 (2017)
4. Capstone Final Report: School of Science and Engineering Capstone Final Report Pumping Water Using Solar Energy for Irrigation, pp. 1–34 (2016)
5. Polak, P., Nanes, B., Adhikari, D.: A low cost drip irrigation system for small farmers in developing countries a low cost drip irrigation system for small farmers in developing countries, February 2019. <https://doi.org/10.1111/j.1752-1688.1997.tb04088.x>
6. Solar water pumps: technical, systems , and business model approaches to
7. Wandre, S.: Solar photovoltaic water pumping system for irrigation: a review, February 2016. <https://doi.org/10.5897/AJAR2015.9879>
8. Solar Water Sources: Designing Solar Water Pumping Systems for Livestock, pp. 1–12
9. Narale, E.P.D., Rathore, N.S., Kothari, S.: Study of Solar PV Water Pumping System for Irrigation of Horticulture Crops 2(12), 54–60 (2013)
10. Masters, G.M.: Renewable and Efficient Electric Power Systems
11. Treephak, K., Thongpron, J., Somsak, D., Saelao, J., Patcharaprakiti, N.: An economic evaluation comparison of solar water pumping system with engine pumping system for rice cultivation. *Jpn. J. Appl. Phys.* **54**(8S1) (2015)
12. Ravi, R.: Designing and developing solar energy operated water pump for small scale irrigation. *Int. J. Chem. Sci.* (2019)



Effect of Cobalt Oxide Nanoparticles Additives to Water Hyacinth-Diesel Mixture Biofuel on the Performance and Emissions of Single CI Engine

Raed A. Jessam¹ , Elena Magaril² , and Hasanain A. Abdul Wahhab³  

¹ Electromechanical Engineering Department, University of Technology - Iraq, Baghdad, Iraq

² Department of Environmental Economics, Ural Federal University, Yekaterinburg, Russia

³ Training and Workshop Center, University of Technology - Iraq, Baghdad, Iraq
20085@uotechnology.edu.iq

Abstract. Using diesel and biodiesel blends as fuel has been a recent field of study, especially with nanoparticle additives. Adding cobalt oxide nanoparticles (Co₃O₄) to biodiesel was verified to reduce emissions. At the same time, engine performance was not given great attention to evaluating the effect of blending nanoparticles with the diesel and biodiesel mixture on the performance characteristics of the diesel engine. Then performance and emission tests were carried out using different fuel samples in a single-cylinder diesel engine. The brake thermal efficiency for the cobalt oxide nanoparticles (50 ppm, 100 ppm) and biodiesel blends was higher than that of biofuel (D80B20) blends. It was increased by 2.5% and 4.05%, respectively, compared to the blend (D80B20). The rate of carbon monoxide emissions for the two biodiesel and cobalt oxide blends was lower than that of the biodiesel blend (D80B20), and the best reduction was for the blend (D80B20N50). It was 4.3% as compared with the biodiesel blend (D80B20). Also, the nitrogen oxide emissions for all the blends with nanoparticles were lower than that of the blend D80B20 due to shortened ignition delay and less fuel added during the combustion, which led to a reduction in nitrogen oxide emissions.

Keywords: Biofuel · Engine Performance · Emissions · Fuel Technology · Nano additive

1 Introduction

Compression ignition (CI) engines producing emissions and unburnt hydrocarbons have long been regarded as the main source of air pollution, particularly in densely populated cities. Therefore, it brought the researchers' attention as it is a dangerous source of pollution. There have been numerous types of research in reducing these emissions since diesel engines came to main use [1, 2]. Recent years have witnessed a growing awareness of solving problems related to the environment and providing clean energy sources. Many researchers have investigated the possibility of using alternative fuels

as a substitute to fossil fuels. Among the most important area of research was biofuel, which is a hydrocarbon prepared from living organisms such as plants and animals that we humans can use as an alternative fuel [2–4]. This definition of biofuels includes a general description. At the same time, in practice, it is considered a hydrocarbon fuel prepared from organic matter within a short period, compared to fossil fuels that require many years to form, as well as other types of fuels that do not depend on hydrocarbons [5]. Bio sources in their solid form have been used since the old time when humans used fire. Coke produced from plants was the first source of biofuel invested in people for heating and cooking. Researchers have discovered several ways of utilizing biofuel with new fuel technologies for improved production fields such as electricity. In the past decades, with the discovery of fossil fuels, the production and use of biofuels suffered a severe impact, as fossil fuels gained many advantages and were most popular, especially in developed countries [6]. Recently, liquid biofuels have been used as fuel for internal combustion engines, especially after the increasing demand for the use of clean energy as a source to reduce emissions. At the same time, the global demand for biofuels is increasing for many reasons.

Firstly, the conditions to combat climate change constrain the search for low-carbon alternative fuel sources [6–8]. Especially with the increasing global warming due to traffic, which represents one of the largest sources of carbon emissions, the search for ways to reduce the use of fossil fuels with renewable alternatives, such as biofuels, is an effective way to reduce these emissions [1, 8–10].

Secondly, with the expected global population growth from 8 to 10.5 billion by 2050, along with the growth of investments in the economic sector, especially in emerging economies which is reflected in a significant increase in energy consumption [11]. For governments to respond to this growing demand, we need to use natural resources more efficiently and increase the use of renewable energy, such as biofuels [12].

Thirdly, the increasing demand for energy challenges the security of resources worldwide, so biofuels are a source for enhancing energy security and protection by reducing the world's dependence on traditional fuel sources. Where biofuels are a resource equally invested globally [13–18], it also plays a key role in developing performance characteristics such as fuel development technologies. The increasing demand to improve the diesel engine's performance leads to opening the way for better investment in biofuel sources through the use of additives such as nanomaterial's.

In recent studies, the effect of Nano additives at different concentrations was tested with diesel and biodiesel (0 to 50%) to determine diesel engine performance in terms of specific brake fuel consumption, brake power, and thermal efficiency under different conditions [15–22]. Engine emissions are mainly classified into two different categories. The first is produced due to high combustion chamber temperature, such as nitrogen oxides, and the second is caused by incomplete combustion of fuels and low combustion temperature, such as hydrocarbon and carbon dioxide [19, 20]. On the other hand, incomplete combustion of diesel or fuel results in hydrocarbon production. Soot is caused by the incomplete combustion of hydrocarbon fuels and is observed in dark exhaust tailings. Generally, by comparing the performance results of a diesel engine

with a gasoline engine, it could be noted that the diesel engine releases a very low concentration of hydrocarbon, nitrogen oxides, and carbon oxides. But with the help of fuel modifications by Nano additives, these emissions were further reduced.

Maybuurov et al. [23, 24] noted that the limited possibilities for improving the quality of engine fuels by refining methods necessitate Nano additives, the combination of which in small amounts ensures an environmental and operational characteristic could be achieved to the desired level. Meanwhile, Magaril et al. [21] demonstrated that using the Nano additive, with its quick impact and relatively low cost, could be the best solution to mitigate air pollution by light hydrocarbons. They recommended further studies on the characterization of IC engine fuels enhanced by Nano additives [25–27].

This work aims to assess the influence of blending cobalt oxide nanoparticles with diesel–biodiesel, which is extracted from water hyacinth, blends on the performance characteristics of a diesel engine and the exhaust emissions. The analyses have been performed by evaluating the brake thermal efficiency, HC and NO_x emissions, and brake-specific fuel consumption at various engine loads.

2 Experimental Setup

2.1 Preparation of Test Samples Blends

In the current experiments, biofuel ethanol was produced in several steps: In the first step, leaves, petioles, and roots were separated from the water hyacinth plant, and the leaves and petioles were washed manually with tap water. In the second step, a plant specimen was dried in an oven, and the dried material was ground to powder; they were pre-treated with 1.0% NaOH for two hours. In the third step, 10 kg of water hyacinth with 6.0 wt% of sulphuric acid catalysts and a methanol-to-oil ratio of 5:1 were processed in a hydrodynamic cavitation reactor at 65 °C using circulating glycerin for 45 min. A 50 L capacity was used to produce water hyacinth oil biodiesel. Two samples have been prepared for the current investigations. D80B20 was extracted from 20% water hyacinth biofuel with 80% neat diesel based on volume and D70B30. The specifications of the three blends are shown in Table 1.

The physical and chemical properties of all studied fuel samples (D80B20N50, D80B20N100) were measured according to ASTM standards, and the results are presented in Table 1. The nanoparticle blends were prepared separately through biodiesel blend D80B20 with Co₃O₄ nanoparticles at 50 and 100 ppm of mass fraction dosage. The nanoparticles were weighed to a quantity of 50 ppm and distributed in all biodiesel blends by an ultrasonicator. The ultrasonic processor used is a model JP-4820 with a power of 60 W and a frequency of 40 kHz for 30 min to generate the nanoparticles-mixed biodiesel fuel (D80B20+50 ppm). Experiments were repeated with a similar procedure to add Nano mass at 100 ppm. These samples were then used to collect the data required for the experimental diesel engine to study its performance and emission characteristics.

Table 1. All properties of test samples used in experiments.

Fuel Type	D	D80B20	D70B30	D80B20N50	B80B20N100
Density, kg/m ³	823	832.5	833.9	831.2	831.9
Viscosity, cSt	2.1	3.12	4.69	3.18	3.19
Cetane No	52.6	52.2	52	49.4	49.8
Calorific value, kcal/kg	10288.6	10260	10256.5	10267.5	10269.7
Cloud point, °C	<−21	−21.6	−22	−21	−21
Flashpoint, °C	62	–	–	–	–

2.2 Engine Specifications and Apparatus

The experiments have been carried out using a four-stroke CI engine (single cylinder) with a set of measurement devices and a gas analyzer, as shown in Fig. 1. The CI engine works on the principle of direct and natural fuel injection. It has design features with a cylinder bore of 70 mm, a stroke of 55 mm, and a compression ratio of 17:1. The engine specification has been elucidated in Table 2. Several experimental features were collected; output power (engine load), air mass flow rate, fuel volume flow rate, and engine speed. An orifice system was used to measure the amount of air flowing into the engine by installing it in the air box. The pressure difference was recorded using a manometer. While the engine speed was recorded using a digital tachometer. The fuel consumed was measured using a fixed size with a stopwatch. BEA 460 Bosch gas analyzer was used to record exhaust gasses (emissions). New software supplied by Bosch is used as the data acquisition system and operation control. All tests were performed for constant engine speed at different engine loads. For each functional test, 3–5 min have waited until the engine has stabilized under steady conditions.

Table 2. The specifications of the test engine.

Model of engine	Loben-RB170F
Type of engine	Single cylinder, 4-stroke
Bore	70 mm
Stroke	55 mm
Displacement	0.221 L
Compression ratio	17:1
Engine speed	3000–3600 rpm
Cooling system	Air-cooled system
Injection of fuel	Direct injection



Fig. 1. S Diesel engine setup.

2.3 Uncertainty Analysis

Uncertainty analysis in the tests is crucial to provide a high confidence level in all results. It obtains by determining the repeatability and increasing interest in the results. All tests were repeated thrice. The variants of the predicted values of performance factors and exhaust emissions were used to calculate the uncertainty using the percent relative standard error, Φ , as shown in Eq. 1 [1]:

$$\Phi \% = \left(\frac{S}{Y} \right) \times 100, \quad (1)$$

S is the standard error and Y is the mean of the collected data. The standard error is calculated using Eq. 2:

$$S = \frac{\alpha}{\sqrt{k}} \quad (2)$$

where α is the standard deviation, and k is the repeatable readings of performance, combustion characteristics, and emission parameters. Overall experimental uncertainty, α_n , was calculated using Eq. 3:

$$\alpha_n = \sqrt{\alpha_1^2 + \alpha_2^2 + \dots + \alpha_i^2} \quad (3)$$

where α_n is the total uncertainty, and α_1 , α_2 , and α_i are the uncertainties of the individual parameters. The accuracies and uncertainties of the measured parameters are given in Table 3.

Table 3. Uncertainties of the measured parameters.

Parameter	Max. value	Accuracy	Uncertainty
Power (kW)	2.1	± 0.08 kW	± 0.76
Speed (rpm)	3000	± 1 rpm	± 1.85
BSFC (g/kW.h)	512	± 1.91 g/kW.h	± 0.97
CO (Vol %)	23.7%	± 0.03 Vol %	± 1.76
HC (ppm)	57	± 2 ppm	± 1.89
NOx (ppm)	1110	± 2 ppm	± 3.45

3 Results and Discussion

Figure 2 reveals the variation of the brake thermal efficiency (η_b) with the engine load for all tested blends (D, D80B20, D70B30, D80B20N50 and D80B20N100). It is observed that brake thermal efficiency of all fuel blends increases with the increase in load up to load near to the full load. In contrast, neat diesel (D) increases with the increase in load up to 90% of the full loading condition. It then starts decreasing, due to the presence of oxygen in biodiesel that improves the combustion process and increases the heat release rate. So, for this reason, with the D80B20 blend, the brake thermal efficiency was increased by 3.29% at full load. These results agree with the inferences of research work [6]. Also, Fig. 2 manifests the variation of the brake thermal efficiency (η_b) with the load for the Co_3O_4 nanoparticle blends (D80B20N50, D80B20N100). It is observed that the η_b for the nanoparticles and biodiesel blends were higher than that of (D80B20) blends at all load conditions. It was increased by about 2.5% and 4.05%, respectively, compared to the D80B20 blend.

Figure 3 shows the variation of the brake-specific fuel consumption (bsfc) with the engine load for neat diesel and the biodiesel blends D, D80B20, and D70B30, which determines the mass of fuel consumed per unit power output. It was revealed that for all fuel tests, bsfc decreased as engine load increased, improving the combustion process. For all conditions, biodiesel blends showed more fuel consumption than diesel because of the lower heating value and higher density of the blends. This result agrees with the conclusions of the research work [6], then the bsfc changed to decrease at a load near the full load. For the biodiesel blend, D80B20, the brake-specific fuel consumption increased at 11.45% at low loads and decreased at a load near the full load compared to pure diesel. It decreased by about 12.88% at full load because of the efficient burning of biodiesel blend at higher loading conditions. Figure 3 shows the variation of the brake-specific fuel consumptions (bsfc) with the engine load for the Co_3O_4 blends, D80B20N50, and D80B20N100, the bsfc for the biodiesel blends (D80B20N50, D80B20N100) was higher than that of D80B20 in all load conditions and the increase was about 3.15%, 7.04%, respectively.

If the consequences of adding biodiesel to elegant diesel will change the chemical composition of the mixture, then adding Co_3O_4 nanoparticles to the biodiesel/diesel blend will have a more impact on the fuel structure and produce a new type of fuel with

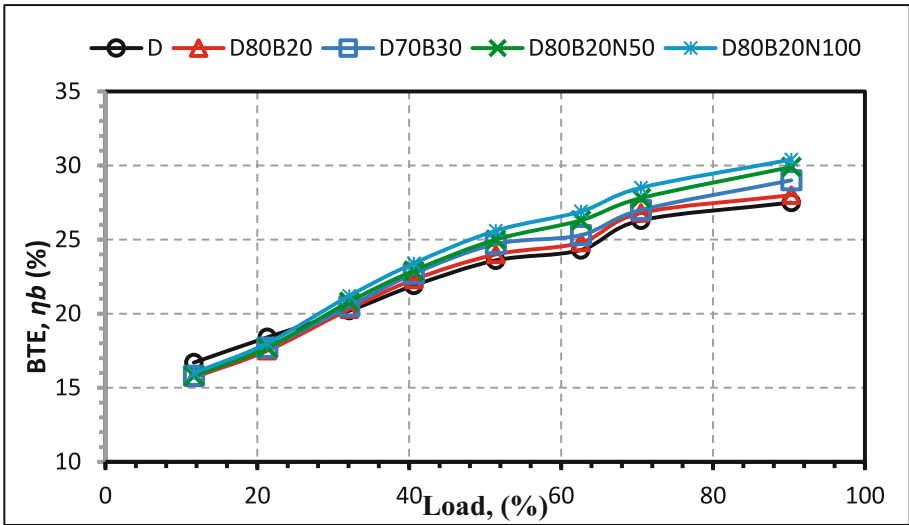


Fig. 2. Variation of brake thermal efficiency with engine load at different fuel blends.

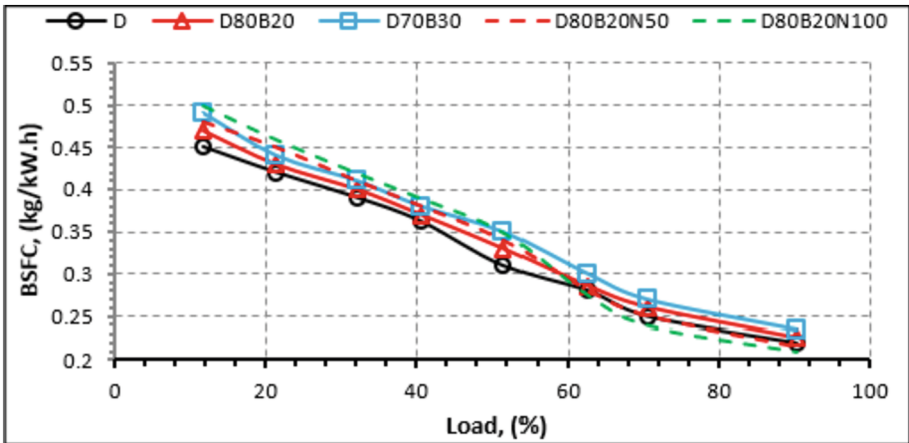


Fig. 3. Variation of brake-specific fuel consumption (BSFC) with engine load at different fuel blends.

improved combustion processes. So, exhaust gases are changing in terms of emission. The resulting CO, HC, and NO_x have been measured to specify and evaluate the emissions percentage. All parameters have been evaluated at different loading conditions of the test engine, varying from a 10% load to a 90% near full load. Figure 4 displays the CO emission of diesel fuel (D), a mixture of diesel and biodiesel B20D80, D70B30, D80B20N50, and D80B20N100 at various engine loads. Results show that the CO emissions increase with the engine load because CO emissions are extremely dependent on the air/fuel ratio. In addition, the results revealed that CO emission is reduced in D80B20

and D70B30 fuel, while the CO emission decreased for D80B20N50 and D80B20N100 in all loading conditions. This effect is evident during near full loading conditions but is not so vital at low loads because of their low values. The rate of CO emissions for the two biodiesel and Co_3O_4 blends were lower than that of the biodiesel blend (D80B20) at all load conditions, and the best reduction was for the blend D80B20N50 and was about 4.3% as compared with the biodiesel blend D80B20. This is due to higher thermal conductivity for Co_3O_4 nanoparticles and higher surface area for catalytic activity [15].

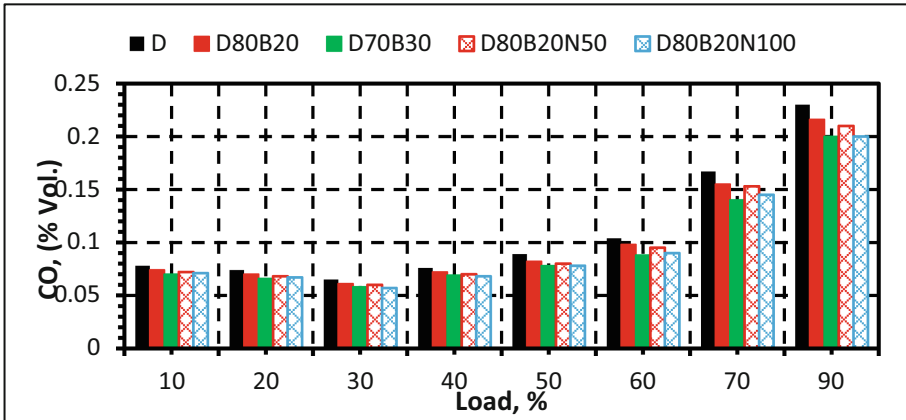


Fig. 4. The variant of CO emission for tested fuel blend samples at various engine loads.

The presence of unburned hydrocarbons in exhaust gases is one of the most important parameters for studying emission characteristics. The changing of unburnt hydrocarbons with the engine load for all tested fuels samples, D, D80B20, D70B30, D80B20N50, and D80B20N100 was given in Fig. 5. The HC emissions level for the pure diesel fuel and the biodiesel blend (D80B20) are 58 ppm and 54.22 ppm at a load near to the full load respectively, the lowering of about 7.9% is due to the higher oxygen concentration in the air-fuel mixture which can help enhance the unburnt oxidation hydrocarbon. HC emissions decrease with increasing biodiesel percentage in the blend [15]. Also, Fig. 5 indicates the change of unburned hydrocarbons (HC) with the engine load for the nanoparticle blends (D80B20N50, D80B20N100). The HC emissions increased at all load conditions for the biodiesel and Co_3O_4 blends (D80B20N50, D80B20N100). This increase was for the blend D80B20N50 and was at a rate of 3.8%. This change is due to the increased flame propagation velocity and the higher post-flame oxidation level due to the higher Cetane number in the biodiesel mixture, which ensures more quality combustion [15].

The NOx emission is related to the oxidation of nitrogen at high temperatures. The variation of the NO emissions with the engine load for all tested fuels, D, D80B20, D70B30, D80B20N50, and D80B20N100 was given in Fig. 6. For the biodiesel blend, D80B20, as compared with neat diesel fuel, the NO emission increased by about 8.9% at full load conditions. High combustion temperatures breaks the strong triple bond of nitrogen molecules, disassociates into their atomic states and participate in a series of

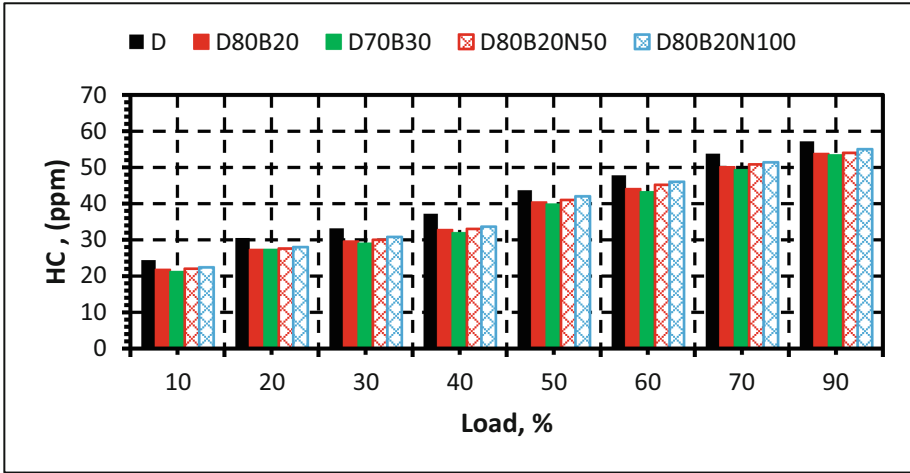


Fig. 5. The variant of HC emission for tested fuel blend samples at various engine loads.

reactions with oxygen and generates thermal NO_x [16, 20]. Also, for cases of blends with Co₃O₄ nanoparticles, the NO_x emissions were lower than that of the blend D80B20. This NO_x reduction is due to shortened ignition delay and less fuel during combustion [16]. At the full load, the NO_x lower values for the blends D80B20N50 and D80B20N100 were 7.34% and 9.87% as compared with D80B20, respectively.

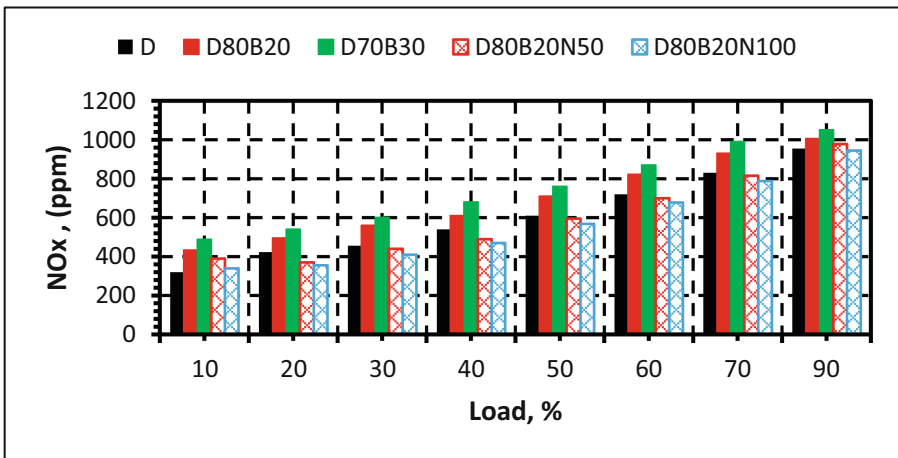


Fig. 6. The variant of NO_x emission for tested fuel blend samples at various engine loads.

4 Conclusions

The present work aims to investigate the using diesel and biodiesel (from water hyacinth) blends as a fuel has been a recent field of study, especially with nanoparticle additives. Biodiesel and Co_3O_4 nanoparticles blend formulations are reported to reduce the emissions of NO_x , CO, and particulate matter (HC) emissions without compensating the engine's performance interests to assess the influence of blending Co_3O_4 nanoparticles with diesel–biodiesel blends on performance characteristics of a diesel engine and the exhaust emissions. The physicochemical properties of all the considered fuel samples are measured according to the ASTM standards. The following conclusions are drawn based on the obtained results:

- The brake thermal efficiency for the Co_3O_4 nanoparticles (50 ppm, 100 ppm) and biodiesel blends was higher than that of biofuel (D80B20) blends at all load conditions. It was increased by about 2.5% and 4.05%, respectively, compared to the blend (D80B20).
- The rate of CO emissions for the two biodiesel and Co_3O_4 blends were lower than that of the biodiesel blend (D80B20) at all load conditions, and the best reduction was for the blend D80B20N50 and was about 4.3% as compared with the biodiesel blend D80B20.
- The NO_x emissions for all the blends with nanoparticles were lower than that of the blend D80B20 due to shortened ignition delay and less fuel was added during the combustion.
- At the full load, the NO_x lower values for the blends D80B20N50 and D80B20N100 were 7.34% and 9.87% as compared with D80B20, respectively.

Further investigations are recommended using different biofuel types and amounts of surfactant added to the diesel fuel and blends.

References

1. Abdul Wahhab, H.A., Al-Kayiem, H.H.: Environmental risk mitigation by biodiesel blending from *Eichhornia crassipes*: performance and emission assessment. *Sustainability* **13**, 8274 (2021)
2. Vellaiyan, S., Amirthagadeswaran, K.: The role of water-in-diesel emulsion and its additives on diesel engine performance and emission levels: a retrospective review. *Alex. Eng. J.* **55**(3), 2463–2472 (2016)
3. Abdul Wahhab, H.A., Mashkour, M., Madodi, S.: Investigation of water-diesel emulsion characteristics using optical technique. *J. Appl. Fluid Mech.* **13**(1), 349–355 (2020)
4. Premalatha, R.P., Parameswari, E., Davamani, V., Malarvizhi, P., Avudainayagam, S.: Biosorption of chromium (III) from aqueous solution by water hyacinth biomass. *Madras Agric. J.* **106**, 12–21 (2019)
5. Rahman, A.K.M.L., Al Mamun, R., Ahmed, N., Sarkar, A., Sarkar, A.M.: Removal of toxic Congo red dye using water hyacinth petiole, an efficient and selective adsorbent. *J. Chem. Soc. Pak.* **41**, 825–833 (2019)
6. Canazart, D.A., da Costa Nunes, A.R., Sanches, M., Conte, H.: Phytoremediation agro industrial wastewater of using macrophyte *Eichhornia crassipes*. *Braz. J. Surg. Clin. Res. BJSCR* **17**, 87–91 (2017)

7. Gogoi, P., Adhikari, P., Maji, T.K.: Bioremediation of arsenic from water with citric acid cross-linked water hyacinth (*E. crassipes*) root powder. *Environ. Monit. Assess.* **189** (2017)
8. Nash, D.A.H., et al.: Phytoremediation of nutrients and organic carbon from sago mill effluent using water hyacinth (*Eichhornia crassipes*). *J. Eng. Technol. Sci.* **51**, 573–584 (2019)
9. Sayago, U.F.C.: Design of a sustainable development process between phytoremediation and production of bioethanol with *Eichhornia crassipes*. *Environ. Monit. Assess.* **191** (2019)
10. De Vasconcelos, G.A., et al.: Effect of water hyacinth (*Eichhornia crassipes*) hay inclusion in the diets of sheep. *Trop. Anim. Health Prod.* **48**, 539–544 (2016)
11. Mahmood, S., Khan, N., Iqbal, K.J., Ashraf, M., Khaliq, A.: Evaluation of water hyacinth (*Eichhornia crassipes*) supplemented diets on the growth, digestibility and histology of grass carp (*Ctenopharyngodon idella*) fingerlings. *J. Appl. Anim. Res.* **46**, 24–28 (2018)
12. Saratale, R.G., et al.: Utilization of noxious weed water hyacinth biomass as a potential feedstock for biopolymers production: a novel approach. *Polymers* **12**, 1704 (2020)
13. Sundari, M.T., Ramesh, A.: Isolation and characterization of cellulose nanofibers from the aquatic weed water hyacinth–*Eichhornia crassipes*. *Carbohydr. Polym.* **87**, 1701–1705 (2012)
14. Setyaningsih, L., et al.: Cellulose extracted from water hyacinth and the application in hydrogel. *IOP Conf. Ser. Mater. Sci. Eng.* **673** (2019)
15. Al-Kayiem, H.H., Wahhab, H.A.A., Magaril, E., Aziz, A.R.A.: Performance and emissions investigation of a single cylinder diesel engine using enhanced blend biodiesel by nanoparticles. *AIP Conf. Proc.* **2035**(1) (2018)
16. Seela, C.R., Ravi Sankar, B.: Investigations on CI engine with nano-sized zinc oxide added Mahua Methyl Ester blends. *Int. J. Ambient Energy* **41**(2), 146–151 (2020)
17. Ghafoori, M., et al.: Effect of nanoparticles on the performance and emission of a diesel engine using biodiesel-diesel blend. *Int. J. Autom. Mech. Eng.* **12** (2015)
18. Hawi, M., et al.: Experimental investigation on performance of a compression ignition engine fueled with waste cooking oil biodiesel–diesel blend enhanced with iron-doped cerium oxide nanoparticles. *Energies* **12**(5), 798 (2019)
19. Radhakrishnan, S., et al.: Effect of nanoparticle on emission and performance characteristics of a diesel engine fueled with cashew nut shell biodiesel. *Energy Sources Part A: Recovery Util. Environ. Effects* **40**(20), 2485–2493 (2018)
20. Perumal, V., Ilankumaran, M.: The influence of copper oxide nano particle added pongamia methyl ester biodiesel on the performance, combustion and emission of a diesel engine. *Fuel* **232**, 791–802 (2018)
21. Magaril, E., Magaril, R., Al-Kayiem, H.H., Skvortsova, E., Anisimov, I., Rada, E.C.: Investigation on the possibility of increasing the environmental safety and fuel efficiency of vehicles by means of gasoline nano-additive. *Sustainability* **11**, 2165 (2019)
22. Arockiasamy, P., Anand, R.B.: Performance, combustion and emission characteristics of a DI diesel engine fuelled with nanoparticle blended jatropha biodiesel. *Periodica Polytechnica Mech. Eng.* **59**(2), 88–93 (2015)
23. Mayburov, I., Leontyeva, Y.: Transport tax in Russia as a promising tool for the reduction of airborne emissions and the development of the road network. *WIT Trans. Ecol. Environ.* **198**, 391–401 (2015)
24. Mayburov, I., Leontyeva, Y.: Fiscal instruments for regulating the sustainable development of urban transport systems in Russia. *IOP Conf. Ser. Earth Environ. Sci.* **72**, 012016 (2017)
25. Fadil, A., Mashkour, M.A., Abdul Wahhab, H.A.: Investment of blending biofuels and nanoparticles with conventional diesel fuel to improve combustion process—A review. *Adv. Mater. Sci. Eng.* 95–107 (2023)
26. Yaser, H.S., Abdul Wahhab, H.A., Dhahad, H.A.: Survey to water-in-diesel emulsion characteristics as an alternative fuel for CI engine. In: Emamian, S.S., Awang, M., Razak, J.A., Masset, P.J. (eds.) *Advances in Material Science and Engineering*, pp. 81–94. LNME, Springer, Singapore (2023). https://doi.org/10.1007/978-981-19-3307-3_8

27. Yaser, H.S., Abdul Wahhab, H.A., Dhahad, H.A.: Influence of water-in-fuel (diesel and biodiesel) emulsions on the performance and emission characteristics of a single-cylinder diesel engine. In: Emamian, S.S., Awang, M., Razak, J.A., Masset, P.J. (eds.) *Advances in Material Science and Engineering. LNME*, pp. 71–79. Springer, Singapore (2023). https://doi.org/10.1007/978-981-19-3307-3_7



Design and Fabrication of a Solar-Powered Lawn Mower

Muti Erinoshol¹(✉), Ester Angula¹, Sam Shaanika¹, and Oluwagbenga Johnson^{1,2}

¹ Department of Mechanical and Metallurgical Engineering, University of Namibia,
P.O. Box 3624, Ongwediva, Namibia
mutiuerinosho1@gmail.com

² Department of Chemical Engineering, University of South Africa, Pretoria, South Africa

Abstract. This paper presents the design and fabrication of a solar-powered lawn mower for operational convenience. It was made with a solar panel of 40 W capacity, which charges the battery of the mower. The solar panel is connected in series to an improvised charge controller that serves to prevent complete discharge or overcharge of the battery. The lawn mower has its cutting blade attached to an 80 W, 12 V DC induction motor, driven by 12 V, 45 AH lead accumulator connected in series. The DC battery (lead accumulators) is recharged using solar energy harnessed by the solar panel. Detailed design of the solar components was made and the test performance gave an effective field capacity of 1.68 m²/min which demonstrated the ease of use as well as neat mowing of the grasses. The blade height was fixed at a height of 20 mm which is used as the desired height of the cut. It was deduced that the battery which was charged for approximately 2 h is capable of mowing the grasses for 3 h or more and 99.9% efficiency was achieved with the operation.

Keywords: Lawn Mower Prototype · Solar Power · Induction Motor · Battery · Power

1 Introduction

Scythe is the first tool ever used to cut grass to a more desirable length. It is a simplistic design that contains a long wooden handle with a curved blade attached perpendicularly to its end [1]. In 1830, Edwin Beard Bidding invented the first actual motor, and the idea of a cylindrical mower machine with several blades was discovered, and this innovation opened the door for numerous advancements in a lawn cutting [1]. The design of mowers comes in different sizes depending on cost and preference [2]. The mower could be detrimental to human if not properly handled. It can cause injuries to the operator or any person close to the mower because the blades of a powered push lawn mower spin at very high speeds and can propel rocks or other objects on the ground at a high rate of speed [3]. This is very effective as it utilizes one or more revolving blades to cut a grass surface to an even height [4]. Depending on the lawn mower settings, the height could be levelled equally [5]. However, different mowers have been made that use a version of

blades made of a lightweight aluminum for cutting grasses [6]. And in order to ensure the safety of the operator, the blade should sit within a casing called a deck, which keeps the grass and other objects from flying in all directions when smashed [7]. A lawn mower with an internal spur gear system, which transfers torque to the mower spiral mechanism, was fabricated and tested. The cutting mechanism was made of a flat blade rigidly fixed to the mower frame. The advantage of the mower is that it did not emit carbon monoxide into the environment and the noise level is drastically reduced [8]. A solar powered lawn mower based on the general principle of mowing was developed. It comprises of direct current (D.C) motor, a rechargeable battery, solar panel, a stainless steel blade and control switch. The battery was recharged through the solar charging controller and its performance was evaluated on different types of grasses. The mower was found to have an efficiency of 93% and a field capacity of 1.11×10^{-4} ha/hr respectively [9]. Ismail *et al.*, introduced a new development of grass cutter, named as Smart Solar Grass Cutter, by using solar irradiance as a primary energy source with the presence of a solar panel. This grass cutter prototype was developed to reduce air pollutant and improve the current design specifically the blade position based on the previous studies [10]. Sivagurunathan *et al.*, designed and fabricated a hand-held operated machine for grass cutting by using locally available materials. The lawn mower was powered by a 12 V/1.35 A rechargeable battery which drives the DC motor up to a rotational speed of 19,300 RPM. As a result, the generated torque was transferred to the cutting head mechanism for efficient grass cutting [11]. A solar grass cutter with panels mounted to receive solar radiation with high intensity was fabricated. The mower consists of photovoltaic, dc converter, motor, controller, linear blades, and battery. The mower was a low cost and light weight system [12]. Ahmad *et al.*, designed and fabricated a two wheeler operated sickle bar mower which is used for cutting grass and shrubs. Data was collected related to the project, so that it can be helpful for taking correct decision while performing design calculation and cad modeling. When two-wheeler move forward then mower wheel rotates the shaft, gear, cam arrangement and cam convert rotary motion into reciprocating motion and finally cutting force obtained on blade edges [13].

The main objective of this project is to design and fabricate a low cost solar-powered lawn mower.

2 Design Concepts

Three different concepts were proposed in this design. In the first concept, a 12 V battery powered the lawn mower, the controller and an induction motor of 10 V. The battery is charged using electricity, once full, it can be used. The controller is used to control the voltage supply to the induction motor, therefore controlling its speed. In addition, the mower's battery needs to be charged regularly, thus it may not be suitable for use in rural areas where there is no electricity.

In the second concept, the lawn mower consists of a solar panel, an inverter and an induction motor. In this design concept the linear controller (inverter) is in-between the solar panel and the motor. The solar panel is 30 W powering a 12 V induction motor. This design is simple and has medium weight as compared to the other concepts. Due to cloud cover, there may be variations in the power generated by the solar panel, it may give so low that the motor will have speed variations or might eventually not work at all.

In the third concept, the solar powered lawn mower involves the application of solar power to charge the battery for using it to power the DC motor which in turn rotates the blades of the mower. The solar panel is 40 W powering a 12 V DC motor as shown in Fig. 1.

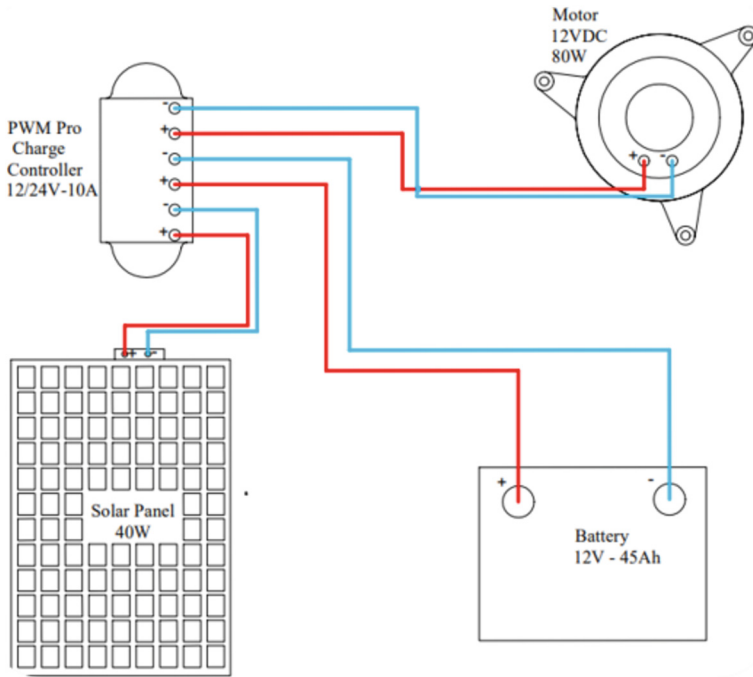


Fig. 1. Circuit diagram of design

The solar panel harnesses the solar energy. The energy generated is stored in the battery in order to make it readily available for usage. An inverter regulates the power going into the battery bank from the solar array. It ensures the battery is not overcharged during the day and that the power does not run back to the solar panel overnight and drain the batteries. The blade is attached directly to the shaft of the motor with bolts and nuts that can be adjusted manually. A stainless steel is used in the construction of the cutting blade because of its strength and weight, which can transmit same speed as that of DC motor or a little less cause of friction. The link mechanism allows the driving handle to be adjustable within the angles of 60 to 20° to fit the users in case there is a need to push the mower onwards or to match the operator's height level. The third concept was selected based on estimated operational time and performance efficiency.

2.1 Principle of Operation and 3D Model

The prototype consists of a motor, where blades are attached. Once the motor starts to rotate and the blades cut whatever is in their surroundings. The user can either decide

to adjust the handle to a preferable height. The mower can now be pushed manually to cut the grass. A Switch is located near the battery to allow the battery to be charged and in case there is, need to switch off, when there is no sunlight or battery is fully charged. The solar panel is attached to a pivot that can allow maneuvering to face the sun for maximum power generation.

Table 1 shows the motor specification at load and no load.

Table 1. Motor specifications

At No load (Motor ratings)	At load (Measured values)
12 VDC	11.5 V
80 W	6.37 A
6.67 A	
3600 rpm	

By using the measured values at the load, the power input can be determined using Eq. (1);

$$P_{in} = VI \quad (1)$$

Since the speed (N) is known to be 3600 rpm, the torque (τ) produced and the angular velocity (ω) can be deduced using Eqs. (2) and (3) for the generation of the output power (P_{out}) as shown in Eq. (4).

$$\tau = \frac{60P_{in}}{2\pi N} \quad (2)$$

$$\omega = \frac{2\pi N}{60} \quad (3)$$

$$P_{out} = \omega\tau \quad (4)$$

To calculate the efficiency of the lawn mower, Eq. 5 is used and 99.9% efficiency was achieved;

$$E = \frac{P_{out}}{P_{in}} \times 100 \quad (5)$$

The Chassis as shown in Fig. 2 is the main structure or frame where the total body is situated.

All the components such as the induction motor, charger controller, solar panel, link mechanism, wheels, battery, blades and all other apparatus are set up on the chassis. It is made of square tubes of mild steel and it carries the total load and stress. The square tubes are first measured according to size as given in the engineering drawing, once measured the universal grinder is used to cut them at a 45° angle. Welding was done



Fig. 2. Chassis

to join the square tubes together. To attach the wheels on the chassis, machining with the lathe machine was done on a 32 mm diameter mild steel circular bar to a diameter of 25 mm to obtain a loose fit for the wheels. The shaft is then milled using the milling machine and a drill machine to drill a through hole in which a pin can be attached to make sure the wheels are locked in place.

The blade is the component that completes the whole design because of its main function, which is to cut the grass as shown in Fig. 3.



Fig. 3. The blades

The blades are made of stainless steel since it has strong and highly non-corrosive as other metals. During manufacturing it was very difficult to drill the metal steel. The blades are attached to the shaft by means of a bolt and nut. This makes them to be removable once there is need for sharpening or replacement.

The solar is attached on the chassis and is allowed to rotated to face the sun. The motor is fixed between two square which are attached to the chassis. There was a need to elongate the shaft of the motor thus machining was done to a 32 mm mild steel circular bar which was machine to a size of 8 mm. Figure 4 shows the conceptual drawing of the lawn mower using the Solidworks software.



Fig. 4. CAD drawing

3 Prototype Testing

The prototype was tested on campus premises. To be safe from flying rocks, there are shield that prevent them from flying out directly to the user. Before the cutting operation, the height of the grass to be cut is measured and an area is chosen together with time. To calculate the effective field capacity of the mower, the area covered was divided with the time taken. Results are recorded and tabulated as shown in Table 2.

To cut a plot of land with lawn mower, it will take approximately 6.75 h, depending on the type of grass and the height of the grass.

Figure 5 shows the operation of the lawnmower clearing a particular region on campus field.

During the prototype testing on the lawn mower, the motor blades were filled up with grasses and the motor overheated. This is caused by the shields that are design underneath the prototype that collect grass around the blade making it to create slip due to an increase in load. Slip is the difference between the asynchronous and synchronous speed of a motor. This has now caused the rotor induced voltage to increases due to increase in slip, and causing the current to increase because of ohm's law and it exceeds the motor current ratings thus heating up and causing motor failure.

Table 2. Testing of prototype and recording

Sample Plot	Height of grass cut (mm)	Area covered (m ²)	Time Taken (mins)	Effective Field Capacity (m ² /min)
Wild grass – Plot 1	105	16	9.50	1.68
Naivasha star grass-Plot 2	200	8	6.25	1.28
Naivasha star grass- Plot 3	250	2.7	3	0.9

**Fig. 5.** Lawnmower in operation

The design has met the design requirements, through testing the design can effectively cut the grass while operating on solar and battery power and it is light weight (mower weighs 40 kg) with an average weight of 41–46 kg for standard lawn mowers.

4 Conclusion

The following conclusion can be deduced in this design:

- The design has shown to be very reliable and can deliver as it was designed for and cutting was successfully made on grasses.
- No pollutants are emitted to the atmosphere making it environmentally safe to use.
- There is no operational cost and fuel consumption.
- The introduction of sensors on the lawn mower to detect walls and stones that may damage the blades is recommended.




References

1. Shukitis, A.: Scholar Commons History of Lawn Mowers. http://scholarcommons.usf.edu/honors_ethttp://scholarcommons.usf.edu/honors_et/82. Accessed 27 July 2020

2. Power Lawn Mowers|Ohioline. <https://ohioline.osu.edu/factsheet/aex-79030>. Accessed 28 July 2020
3. The Serious Dangers of Lawn Mowers|Ross Feller Casey, LLP. <https://www.rossfeller Casey.com/news/the-serious-dangers-of-lawn-mowers/>. Accessed 28 July 2020
4. Lawn Mower Mark: What is a lawn mower? Types of lawn mowers. <http://www.lawnmowermark.com/lawn-mower/what-is-a-lawn-mower-101/>. Accessed 10 June 2020
5. Wikipedia: Lawn Mower. https://en.wikipedia.org/wiki/Lawn_mower. Accessed 10 June 2020
6. SFGATE: How a Gas Rotary Lawn Mower Engine Works|Home Guides|SF Gate. <https://homeguides.sfgate.com/gas-rotary-lawn-mower-engine-works-96717.html>. Accessed 10 June 2020
7. Howstuffworks: How Lawn Mowers Work|HowStuffWorks. <https://home.howstuffworks.com/lawn-mower.htm>. Accessed 10 June 2020
8. Anand, S.H., Elangovan, N., Mathunsingh, E., Sabrish, P.: Design & analysis of lawn mower. *Int. J. Adv. Res. Trends Eng. Technol.* **4**(19), 2–5 (2017)
9. Tanimola, O.A., Diabana, P.D., Bankole, Y.O.: Design and development of a solar powered lawn mower. *Int. J. Sci. Eng. Res.* **5**(6), 215–220 (2014)
10. Ismail, F.B., Al-Muhsen, N.F.O., Fuzi, F.A., Zukipli, A.: Design and development of smart solar grass cutter. *Int. J. Eng. Adv. Technol.* **9**(2), 4137–4141 (2019)
11. Sivagurunathan, R., Sivagurunathan, L., Hao, J.C.J.: Design and fabrication of low cost portable lawn mower. *Sch. J. Eng. Technol.* **5**(10), 584–591 (2017)
12. Pandey, S., Munj, J., Panchal, K., Paralkar, R., Kumar, A.: Fabrication of automatic solar lawn mower. *Int. J. Innov. Res. Sci. Eng. Technol.* **7**(4), 3729–3736 (2018)
13. Musheeruddin, S.M., Ahmad, K.I.: Design and fabrication of two wheeler operated sickle bar. *Int. Res. J. Eng. Technol.* **5**(10), 530–534 (2018)



Prediction of Surge/Swab Pressure in the Oil & Gas Industry: Effect of Process Parameters and Significance of Modeling

Mohammad Yusuf^{1,2} , Syahrir Ridha^{1,2}  , Shwetank Krishna³,
and Umar Nabil Sabo^{1,2}

- ¹ Department of Petroleum Engineering, Universiti Teknologi PETRONAS, 32610 Bandar Seri Iskandar, Perak, Malaysia
syahrir.ridha@utp.edu.my
- ² Institute of Hydrocarbon Recovery, Universiti Teknologi PETRONAS, 32610 Bandar Seri Iskandar, Perak, Malaysia
- ³ Chair Drilling and Completion Engineering, Montanuniversität Leoben, Franz Josef-Straße 18, 8700 Leoben, Austria

Abstract. Demand for Energy globally has been on the rise by approximately 8% between 2004 and 2019. Also, conventional energy sources are unable to meet this demand for the period under review. Therefore, the oil and gas energy industry is continuously making efforts to produce from unconventional energy sources such as oil and gas reservoirs, gas hydrates, and deep-water and geothermal energy through drilling operations. The surge/swab pressure is experienced while drilling processes in different circumstances such as, (i) during placing the casing in the well for borehole's wall stabilization (ii) during maintenance operations the run-in or pulling out the drill-string, bit removal or dismantling; (iii) the staggering motion caused by the sea waves during deep-water drilling in via floating rigs. However, predicting the surge/swab pressure with different pipe tripping speeds, fluid rheology, and well geometry is significant to dodge unexpected drilling outcomes. This review highlights the parameters on which the surge/swab pressure depends. Further, the importance of modelling in surge/swab pressure prediction along with the existing models has been explained. This study summarizes the improved understanding of the effect of rheological and geometrical parameters on surge/swab pressures. Finally, limitations and outlook have been suggested at the end to enhance the hydrocarbon recovery process and minimize the NPT during tripping.

Keywords: Drilling · Surge/Swab pressure · Tripping · Rheology · Hydrocarbon Recovery

1 Introduction

The energy demand of the world is rising due to the rise in global populations and the corresponding standard of living [1]. This rising demand is posing huge setbacks to energy industries which are mainly non-renewable energy sectors, i.e., oil and gas industries

[2]. Coal, oil, and natural gas are the major Non-renewable energy sources that make up for overall energy demand [3]. It is on record that the total global energy supply sources such as coal, oil, natural gas, nuclear, and renewable energy sources contribute about 27%, 33.1%, 24.3%, 4.3%, and 11.3%, respectively [4]. The world's energy industry constantly discovers and drills several sources of energy such as deepwater oil & gas reservoirs, geothermal, gas hydrates, etc. to meet global energy demands [5]. Moreover, petroleum drilling operations in hard-to-reach and unconventional sources of oil and gas are likely to encounter dangerous incidents of well control problems in boreholes like fluid loss, differential sticking, fluid influx, etc., which alter the efficiency of operations and economic viability among others [6]. Several good control problems are encountered due to uneven surge/swab pressure difference caused by longitudinal movement of casing and drill-string in the wellbore, which is mainly a result of pseudoplastic behavior and yield stress of drilling mud and geometrical constraints in the wellbore [7]. The drilling industry is a technology-dependent and expensive venture. Therefore, any operational cost optimization can result in saving millions of dollars. Tripping operations in drilling engineering account for a substantial amount of non-productive time (NPT) about 15–29% of total drilling time. Hence, automating the surge/swab pressure prediction under varying rheological and geometrical characteristics enables the reduction of NPT and undesirable well stability and control issues [8]. Limited studies are conducted on the prediction of pressure imbalances generated during tripping operations. However, existing models had not used the mud clinging effect for the development of the predictive model. Additionally, available models do not predict precisely in the borehole with a low diameter ratio and an automatic predictive model for forecasting surge/swab pressure is not available in the existing literature.

2 Literature Review

2.1 Parameters Affecting Surge/Swab Pressure

Pressure differential in annulus which is also referred to as surge/swab tends to create pressure in pipe tripping operations for drill-string maintenance, and casing setting etc.,. Frequencies of these pressure differential may perhaps depend on parameters of drilling design and fundamental variables of drilling fluid rheology [9]. A comprehensive survey of literature in this section to determine the effects of the variables on surge/swab pressure during petroleum drilling operations was conducted.

Rheological Parameters: It is noted that theoretical investigations revealed an increase in surge pressure gradient for high-density fluid in the laminar flow regime as compared with low-density fluid in laminar flow [10]. But then, low-density fluids performed better than fluids with high density. During drilling operations, high fluid viscosity is directly proportional to fluid consistency, but the behaviour index flows improperly and as such, to allow the drilling fluid to flow conveniently low tripping speed is important [11].

Fluid Consistency and Behavior Index: Since fluid behaviour index, n , and consistency index, K , have significant impacts on the flow of fluids with pipe tripping speed alteration, then n indicates the shear thinning characteristic of Non-Newtonian fluid, whereas as the cohesive force acting on individual particles of fluid which impedes fluid

flow can be defined as k [12]. Meuric et al. [13] conducted a significant study of axial velocity profiles in the concentric annulus that impacts the parameters during drilling operations and this study observed little distortion on the profile of fluid flow. However, the study was pretty much in contrast with normal rheological characteristics of drilling fluid. Studies by Gokedmir et al. [14], Houwen and Geehan [15] investigated pressure effects on K and n , and this study shows flow behaviour index not dependent on changes in pressure, which additionally recognized effects of fluid-shear as dependent property on flow behavior index. It was noticed that the fluid consistency index tripled atmospheric pressure because of the effects it possesses on cohesive forces in the fluid. This in turn shows that few investigations and findings [16] were conducted to determine the effects of surge/swab pressure parameters. Therefore, these studies show that surge/swab pressure is directly proportional to the value of K and n , but largely dependent on simulation-based data which is in contrast with real-life situations.

Yield Stress: Reports by Zamora and Growcock [17], also show that yield stress has both functional implications and real-world implications which is also a material property. Nguyen and Boger [18], and Hartnett and Hu [68], also share a similar idea. But in contrast, Barnes and Walters [19], considered yield stress to be an abstract phenomenon that is unrealistic. Mud yield stress stands as a rheological parameter mainly used to calculate hole cleaning, ECD, barite sag, surge/swab pressure, etc. During estimation difficulties are encountered while calculating mud yield tension using normal laboratory and field viscometers, several preferred alternatives in traditional scales and regression-analysis approaches are used [20]. Additionally, AZO Materials showed a lack of standardized techniques for determining yield tension, therefore many industries use a range of approaches. Viktorovitsj [21] also recognized these approaches, which are; ascending stress sweep tests, oscillatory flow tests, sustainable flow tests, superposition of steady stress and flow curve review.

Gel Strength: Drilling fluid's ability to swing drill cuttings in course of circulation is identified by its gel pressure. As soon as fluid movement is halted, 24 h of drilling with a substitute mud with a characteristic low gel strength can result in problems such as solids formation in the downhole and/or cuttings settling [22]. Muds with low gel strength properties significantly contribute to downhole cuttings accumulation and barite sagging. It is not said that mud of no gel strength is preferred even though high gel strength results in, structure fracturing, pressure losses and a solids management challenge. The intensity of gel required in horizontal wells surpasses that of vertical wells owing to effects of eccentricity in wellbore annular [23]. Even though gel strength is an essential mud property, the selection is most times challenging between high gel mud strength and mud having low gel strength. Therefore, a huge gap in an experimental study which clearly understands the effects of gel strength on surge/swab pressure is noticed.

2.2 Drilling Design Parameters

Wellbore Diameter Ratio: The high fluid loss transpires into problems such as the formation of a thick filter-like cake which eventually decrease the hole diameter. Alternatively, these drilling mud particles can also be resized to accommodate and produce

filter cake inside the formation in the wall of the borehole and decrease the thickness of the cake exposed with upgraded mud-dense equipment. Likewise, it is possible to decrease annulus by drill collars, bailing of bit, tool joints or even stabilizers while conducting drilling operations. Annular clearance is decreased in this technique which eventually results in the buildup of pressure that must be monitored. Possibilities to curtail this can be through several techniques such as hydration, abrasion, dehydration, and lubrication of equipment affected [24]. A huge hole gives mud even bigger pathway during tripping operations for Piston-cylinder drive working perpendicular to structure being decreased in addition travels further to reduce formation fracture [25].

Wellbore Eccentricity: The investigations and analytical studies on eccentricity effects for surge pressure gradient were conducted by several researchers [26]. Lukawski et al. [27] came up with the theoretical model for the prediction of surge/swab pressure gradient in the eccentric annulus for PL fluid. Updates are put forward in Hussain & Rasool et al. [28], study on Chukwu & Yang model by carrying out numerical analysis using simulation for YPL fluid in the eccentric annulus to properly show downhole pressure differential. A theoretical model was established in this simulation study [27], based on surge pressure ratio, and the model is certified with experimental data collected and by CFD (Computational Fluid Dynamics) models.

Pipe Tripping Speed: Safe speed (usually 30 s) should be considered during tripping in/out of the selection to increase or reduce the stand length [29]. Pump pressure should not be increased unless circulation is established, most importantly if a bit appears with the low rotary speed at the bottom. It is therefore important retaining the low gel strength characteristic of mud. Drilling fluid with high gel strength needs increased pump pressure for the return of rotary operation which may alter borehole pressure significantly more than the pressure of formation fracture. Low pipe operating speed may eventually result in the generation of increased non-productive time (NPT), and consequently, economic viability for drilling operations is hindered.

2.3 Existing Theoretical and Experimental Study on Surge/Swab Pressure

Steady-State Model: Pressure differential in the wellbore due to the axial tubular movement was studied in drilling operations. Cannon [30], moved to conduct a pioneer revision on the effects of swab pressure.

Cardwell [31] made a remarkable investigation on problems during pipe tripping operations while major issues were put in mind at initial periods of testing for causes of blowouts in regular pressure wells. During these operations, an abnormal downhole pressure differential is not much known. Figure 1 describes the plot style created as soon as the pressure gauge is released to the bottom of the cased hole and clear of the drill string. Plots from the graph show recorded pressure the moment the pipe is lowered into the hole as well as upon entry at the bottom spikes at almost the same magnitude as pressure losses. Based on experimental observation Cardwell also reported results. Also, Hughes Tool Company brought a manual with more detail titled Rotary Drilling Hydraulics [32]. Previous methods have similar effects for each stand on pipe rates of both 10 s and 30 s for a 4.4-inch OD drilling pipe in an 8.5-inch hole, simply as the only values available for experimental proof.

Musaed [33] Expressed a different equation showing drilling fluid velocities in annulus during RIH and POOH drill-string. Going by these findings, were on several scenarios of drill-string conditions as partially open or partially closed-ended and fully open. These equations established for velocity and pressure drop, turbulent flow, annular fluid in laminar flow and improved Reynolds number are presented in (Eqs. 1–4), respectively using flow properties and hydraulic diameter of drilling fluids determined by high precision viscometers, creation of lower critical velocity was noticed.

$$V_a = \frac{1.08 PV + 1.08 \sqrt{PV^2 + 12.3D^2YP}}{\partial D} \quad (1)$$

$$P = \frac{L.YP}{225 D} + \frac{PV.L.V}{1,500 D^2} \quad (2)$$

$$P = \frac{f.L.V^2}{25.6 D} \quad (3)$$

$$R_p = \frac{2965 D.V}{PV} \quad (4)$$

Burkhardt [34] made an addition to available studies conducted by Cardwell [31]. The physics-based theoretical investigation was conducted in this study and proof shows surge pressure as dependent upon flow regime (laminar or turbulent), rheological property, pipe tripping speed and wellbore geometry, Also, in this research, a parametric study is presented to understand the effects of surge pressure gradient on several parameters for open and closed-ended pipes.

Mathematically, the pipe tripping speed relationship with annular fluid velocity during tripping operations is represented as Eq. (5).

$$V_f = -k_c V_p \quad (5)$$

where, V_f and V_p are the annular fluid velocity and pipe tripping speed, respectively. k_c is the clinging constant which is related to the diameter ratio and can be determined using Fig. 1(b).

To predict surge pressure gradient for YPL fluid in the eccentric annulus for steady-state conditions, Hussain and Shariff [35] developed an alternative numerical model. The major finding was in increasing eccentricity, that pressure gradient as a result of inner pipe axial displacement reduced. Moreover, the surge pressure was shown to be inversely proportional to the blockage height because results proved that annuli having partial blockage of cuttings can produce lower surge pressure even without blockage than the other.

A study carried out to estimate surge and swab pressures for steady-state flow in annuli being exposed to the atmosphere and upper ends of drill pipes was recommended by Wolski et al. [36]. They believe that incompressible fluid drive is being formed completely, laminar, and one-dimensional. Furthermore, all validations were claimed by implying that pressure losses are comparatively insignificant because of nozzle flow, geometric fluctuations, and intermittent motion for Bingham Plastic fluid (BPL). Investigators expressed shear stress and shear rate equations providing dimensionless gradient

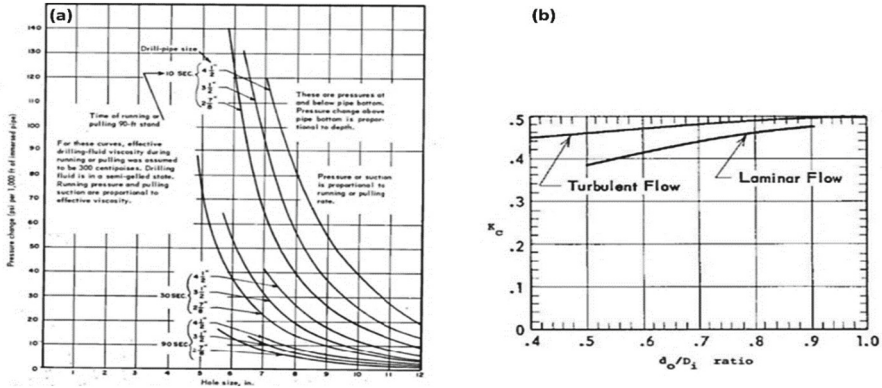


Fig. 1. (a) Effects of various pipe/casing RIH and POOH [31], (b) Graphical plot for determining clinging constantly [34]

equations of strain. In assessment, the model was proved to be in contrast with methods suggested by Fontenot and Clark [37]. Current and previous model analysis and findings showed the difference in results of pressure drop to be in the error range between 0–10%.

According to existing literature surveys of models, previous models such as Cannon [30], Cardwell [31], and Musaed [33] majorly deliberated on annular clearance and generated stresses by pipe movement on drilling fluid and pipe tripping speed. In model development, Burkhardt [34] and Schuh [38] came up with additional findings on the initially found models, bearing in mind rheological properties. Further improvements and simplifications on these models by Fontenot [37] were done to a large extent through the development of an automated computer program and resulted in the incorporation of field measurements. Although, Burkhardt, Schuh and Fontenot’s models were estimated solutions for calculating surge/swab pressure for PL and BP fluid models in concentric annulus failed to properly prove the behaviors of fluid flow of many used drilling fluids in these fields. Crespo et al. [39], and Etehadhi et al. [9] gave an exact numerical-based or dimensionless solution considering slot flow geometry for YPL fluid in the concentric annulus.

Unsteady-State Model: Lubinski et al. [40] conducted pioneer research in developing an unsteady-state model to predict surge/swab pressure differential. Lin and Hsu [41] obtained an alternative model (i.e. numerical) to define the distribution of transient fluid velocity in the concentric annulus for PL fluid under the Couette fluid flow phenomenon. Various inconsistencies were noticed in this study by MacSporran [42] concerning the expression of the annular fluid velocity profile. In another study, Lin and Hsu [43] corrected their investigations.

A representation by Lal [44] in the transient surge/swab model is a computer-inbuilt software package for PL fluid for both eccentric and concentric annuli. Furthermore, the significance of variables and parameters are presented in the investigation. Unsteady-state model development and validation with the previously Burkhardt [34] model was conducted to further test the efficiency of the model.

Mitchell [45] also offered a model for predicting surge pressure based on the transient condition of PL fluid in the laminar flow phenomenon. The transient model that was developed further validates the field data given in Burkhardt [34] (Fig. 2) and Fontenet and Clark [37]. The outcome obtained shows transient model developed at optimum during surge which is in good agreement with field data measurements in comparison to the steady-state model. Although, identification of downhole pressure differential for static condition (steady state) conditions was not achieved in Mitchell’s work.

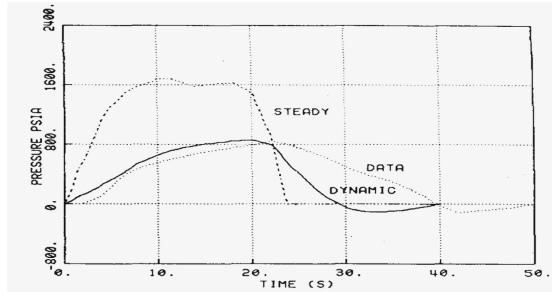


Fig. 2. Dynamic model predicted data, field data and Burkhardt steady-state model comparison [34].

A dynamic model was developed by Wang and Chukwu [46] for the prediction of surge and swab pressure for PL fluid in the concentric and eccentric annulus. A couple of curve sets were generated by using developed equations to represent dimensionless pressure gradients (see Table 1). The model surely can assist in determining ranges of pipe tripping speed to further optimize stability in formations.

Table 1. The calculated outcomes of surge pressure gradient [46].

Pipe tripping speed, <i>fts</i> ² / <i>l</i>	Surge pressure gradient, <i>psif</i> / <i>l</i>	Wang and Chukwu [46] Steady-state method, <i>psif</i> / <i>l</i>
0	2.383 (0.0165)	2.401 (0.0168)
1	3.972 (0.0276)	
2	5.958 (0.0414)	
3	8.341 (0.0579)	
4	11.122 (0.0772)	
5	14.101 (0.0979)	

ODE-based model is an alternative model to CFD (computational fluid dynamics) distribution-based models. It is often more rapid with the benefit of associating with several discipline techniques with little or no difficulty. Gjerstad [47] already developed basic sets of analytical flow equations to predict and optimize downhole pressure

surges based on the dynamic condition for the Bingham plastic model (BP). Gjerstad [47] developed a flow equation that is precise in determining the gradient of frictional pressure. Validation of the model was done with the explanation of Liu and Zhu [48] for particular wellbore geometry. The General version of this equation is presented through Eq. (6), with effective velocity V_e given in Eq. (7).

$$P = P_n(V_e) + f_{po}(V_e).f_{co}(V_e) + P_{A0} \frac{Rh}{Ro} (1 - sgn(V_e).f_{co}(V_e)) \quad (6)$$

where, P_n is the pressure gradient for Newtonian fluids, dimensionless; Ro is the outer radius of the annulus, and Rh is the radial distance of the slot wall.

$$V_e = \bar{V} + V_{e0} \quad (7)$$

where V_{e0} is the dimensionless effective fluid velocity of the outer flow region; and \bar{V} is the dimensionless average fluid velocity near the slot.

2.4 Laboratory Scale Experimental Studies

Based on current literature, very few experimental investigations were achieved by Tang et al., [44] for conditions of laminar flow in eccentric annuli. Also, another achievement for concentric annuli is by Crespo and Ahmed, [39]. Model-based regression of the numerical analysis of the narrow-slot approximation method was developed and proven experimentally. Also, Erge et al., [49] investigated the theoretical impacts of movement of inner pipe through the mathematical model to determine pressure imbalance concurrently with tripping in a coaxial annulus for YPL fluid. For authentication, adopted experimental data already existed [39] and was in tremendous agreement. Several investigations [41] on models developed considering viscous drag when fluid is in motion for detection of pressure drop in the stationary pipe. He et al., [50] also developed semi-analytical and numerical models to predict surge pressure gradients in the concentric annulus, and went further to compare with an existing theoretical model and experimental data. In our recent study, Krishna et al. [51] conducted a replica experimental investigation of tripping operations during oil and gas well drilling. Results acquired shows surge/swab pressure differential decreases with increasing eccentricity (ϵ) and increase in pipe tripping speed (V_p) with increasing diameter ratio (δ). Meanwhile, the study also drafted that gel strength increases surge/swab pressure gradient by 18% approximately.

3 Conclusion

This brief review presents a state-of-the-art review of the surge/swab pressure gradient by non-Newtonian fluid. There are several studies carried out by different researchers on the factors (i.e., fluid rheology, eccentricity, diameter ratio, and the tripping speed of pipe) influencing the surge/swab pressure. The surge/swab pressure is affected by rheological parameters which are mainly fluid consistency, behavior index, yield stress, and gel strength. The surge/swab pressure gradient generally intensifies with the rising values of

rheological parameters. However, it gets reduced with a higher value of fluid behaviour index because of PL fluid annular flow profile. Gel strength has also a considerable influence on the surge pressure (i.e., approx.~18%). The diameter ratio and annular eccentricity of the wellbore drilled also extant a significant influence on the surge pressure gradient, i.e., due to the abridged annular area and velocity of the dislodged fluid in the annulus. It has also been concluded that the surge pressure gradient decreases gradually with the ascending pipe speeds. The study also summarized that various steady-state and unsteady-state models, along with a few laboratory scale studies are being done by several researchers for the surge/swab pressure gradient predictions. It is established from the literature that there is a need for further experimental data for the development of more accurate, optimized, and robust models for surge/swab pressure predictions. Furthermore, less cumbersome models with little numerical analysis are required. Hence the New Simplified models by mathematically and analytically combining momentum equations, fluid's rheological equations, mud clinging properties and frictional pressure losses equations can be developed for better data analysis and predictions.

Acknowledgements. The authors would like to thank Universiti Teknologi PETRONAS for providing funding under YUTP grant [015LC0-366] and the Ministry of Higher Education (MOHE), Malaysia for providing financial assistance under Fundamental Research Grant Scheme [FRGS (015MA0-118)] and to conduct this work.

References

1. Qureshi, F., et al.: Latest eco-friendly avenues on hydrogen production towards a circular bio-economy: currents challenges, innovative insights, and future perspectives. *Renew. Sustain. Energy Rev.* **168**(May), 112916 (2022)
2. Abdullah, A.H., et al.: A comprehensive review of nanoparticles in water-based drilling fluids on wellbore stability. *Chemosphere* **308**(P1), 136274 (2022)
3. Athar, M., et al.: Biodiesel production by single-step acid-catalysed transesterification of Jatropha oil under microwave heating with modelling and optimisation using response surface methodology. *Fuel* **322** (February) (2022)
4. Bagherian, M.A., Mehranzamir, K.: A comprehensive review on renewable energy integration for combined heat and power production. *Energy Convers. Manag.* **224**(September), 113454 (2020)
5. IEA: Net zero by 2050: a roadmap for the global energy sector. *Int. Energy Agency* **224** (2021)
6. Miyazaki, K., Ohno, T., Karasawa, H., Imaizumi, H.: Performance of polycrystalline diamond compact bit based on laboratory tests assuming geothermal well drilling. *Geothermics* **80**, 185–194 (2019)
7. Prevedel, B., Martens, S., Norden, B., Henningses, J., Freifeld, B.M.: Drilling and abandonment preparation of CO₂ storage wells - experience from the Ketzin pilot site. *Energy Proc.* **63**, 6067–6078 (2014)
8. Sengupta, S., De, S.: Couette-Poiseuille flow of a Bingham fluid through a channel overlying a porous layer. *J. Nonnewton. Fluid Mech.* **265**, 28–40 (2019)
9. Etehad, A., Altun, G.: Functional and practical analytical pressure surges model through Herschel Bulkley fluids. *J. Pet. Sci. Eng.* **171**(May), 748–759 (2018)
10. Gjerstad, K., Time, R.W., Bjørkevoll, K.S.: Simplified explicit flow equations for Bingham plastics in Couette-Poiseuille flow - for dynamic surge and swab modeling. *J. Nonnewton. Fluid Mech.* **175–176**, 55–63 (2012)

11. Calçada, L.A., Duque Neto, O.A., Magalhães, S.C., Scheid, C.M., Borges Filho, M.N., Waldmann, A.T.A.: Evaluation of suspension flow and particulate materials for control of fluid losses in drilling operation. *J. Pet. Sci. Eng.* **131**, 1–10 (2015)
12. Ofei, T.N., Irawan, S., Pao, W.: CFD method for predicting annular pressure losses and cuttings concentration in eccentric horizontal wells. *J. Pet. Eng.* **2014**, 1–16 (2014)
13. Thorsrud, A.K., Ekeli, Ø., Hilbig, N.C.C., Bergsvik, O., Zamora, M.: Application of novel downhole hydraulics software to drill safely and economically a north sea high-temperature/high-pressure exploration well. In: IADC/SPE Drilling Conference, SPE-59189-MS (2000)
14. Gokdemir, M.G., Erkekol, S., Dogan, H.A.: Investigation of High Pressure Effect on Drilling Fluid Rheology (2017)
15. Houwen, O.H., Geehan, T.: Rheology of oil-base muds. In: SPE Annual Technical Conference and Exhibition, SPE-15416-MS (1986)
16. Tang, M., Ahmed, R., Srivastav, R., He, S.: Simplified surge pressure model for yield power law fluid in eccentric annuli. *J. Pet. Sci. Eng.* **145**, 346–356 (2016)
17. Zamora, M., Growcock, F.: The top 10 myths, misconceptions and mysteries in rheology and hydraulics (AADE-10-DF-HO-40). In: AADE Fluids Conference & Exhibition (2010)
18. Nguyen, Q.D., Boger, D.V.: Measuring the flow properties of yield stress fluids. *Annu. Rev. Fluid Mech.* **24**(1), 47–88 (1992)
19. Barnes, H.A., Walters, K.: The yield stress myth? *Rheol. Acta* **24**(4), 323–326 (1985)
20. Saasen, A., Ytrehus, J.D.: Viscosity models for drilling fluids - Herschel-Bulkley parameters and their use. *Energies* **13** (20) (2020)
21. Viktorovitsj, D.: Evaluation of Rheology and Pressure Losses for Oil-Based Drilling Fluids in a Simulated Drilling Process Dias Viktorovitsj, June 2015
22. Amede, V.G., Alfazazi, U.: Optimal drilling fluid rheological considerations for avoiding stuck pipe and fluid loss under HT horizontal well condition: Gulf of Guinea as a scenario. *Pet. Coal* **59**(5), 703–709 (2017)
23. Mohamadian, N., Ghorbani, H., Wood, D., Hormozi, H.K.: Rheological and filtration characteristics of drilling fluids enhanced by nanoparticles with selected additives: an experimental study. *Adv. Geo-Energy Res.* **2**(3), 228–236 (2018)
24. Cayeux, E., Daireaux, B., Dvergsnes, E.W.: Automation of drawworks and topdrive management to minimize swab/surge and poor-downhole-condition effects. *SPE Drill. Complet* **26**(04), 557–568 (2011)
25. Srivastav, R., Enfis, M., Crespo, F., Ahmed, R., Saasen, A., Laget, M.: Surge and swab pressures in horizontal and inclined wells. In: SPE Latin America and Caribbean Petroleum Engineering Conference, SPE-152662-MS (2012)
26. Tang, M., Zhang, T., He, S., Kong, L., Li, H., Li, Q.: Modeling of laminar flow in an eccentric elliptical annulus for YPL fluid. *J. Nat. Gas Sci. Eng.* **64**, 118–132 (2019)
27. Lukawski, M.Z., et al.: Cost analysis of oil, gas, and geothermal well drilling. *J. Pet. Sci. Eng.* **118**, 1–14 (2014)
28. Rasool, G., Shafiq, A., Khan, I., Baleanu, D., Nisar, K.S., Shahzadi, G.: Entropy generation and consequences of MHD in Darcy-Forchheimer nanofluid flow bounded by non-linearly stretching surface. *Symmetry (Basel)* **12**(4), 1–23 (2020)
29. Haff, G.R.G., Ferrete, C.A.: Effects of plyometric and sprint training **23**(46), 385–394 (2015)
30. Cannon, G.E.: Changes in hydrostatic pressure due to withdrawing drill pipe from the hole. *Drill. Prod. Pract.* (1934)
31. Iyer, M.V., Norcio, L.P., Kugler, E.L., Dadyburjor, D.B.: Kinetic modeling for methane reforming with carbon dioxide over a mixed-metal carbide catalyst. *Ind. Eng. Chem. Res.* **42**(12), 2712–2721 (2003)
32. PERF-95-Hydraulics-in-Rotary-Drilling.-Hughes-Co-1958.pdf

33. Al-Awad, M.N.J.: Prediction of critical pipe running speed during tripping in drilling operations 131–149 (1998)
34. Burkhardt, J.A.: Wellbore pressure surges produced by pipe movement. *J. Pet. Technol.* **13**(06), 595–605 (1961)
35. Hussain, Q.E., Sharif, M.A.R.: Viscoplastic fluid flow in irregular eccentric annuli due to axial motion of the inner pipe. *Can. J. Chem. Eng.* **75**(6), 1038–1045 (1997)
36. Wolski, A., Junqueira, S.L.M., Negrão, C.O.R.: A steady-state approach for evaluation of surge and swab pressures in flows with free surface boundary conditions. *J. Pet. Sci. Eng.* **122**, 208–215 (2014)
37. Fontenot, J.E., Clark, R.K.: An improved method for calculating swab and surge pressures and circulating pressures in a drilling well. *Soc. Pet. Eng. J.* **14**(05), 451–462 (1974)
38. Schuh, F.J.: Computer makes surge-pressure calculations useful. *Oil Gas J.* **31**, 96 (1964)
39. Crespo, F., Ahmed, R., Enfis, M., Saasen, A., Amani, M.: Surge-and-swab pressure predictions for yield-power-law drilling fluids. *SPE Drill. Complet* **27**(04), 574–585 (2012)
40. Lubinski, A., Hsu, F.H., Nolte, K.G.: Transient pressure surges due to pipe movement in an oil well. *Oil Gas Sci. Technol. L Inst. Fr. Du Pet.* **32**, 307–348 (1977)
41. Lin, S., Hsu, C.-C.: Generalized Couette flow of a non-Newtonian fluid in annuli. *Ind. Eng. Chem. Fundam.* **19**, 421–424 (1980)
42. MacSporran, W.C.: Generalized Couette flow of a non-Newtonian fluid in annuli. *Comments. Ind. Eng. Chem. Fundam.* **21**(1), 98 (1982)
43. Lin, S.H., Hsu, C.C.: Generalized Couette flow of a non-Newtonian fluid in annuli. Reply to comments. *Ind. Eng. Chem. Fundam.* **21**(1), 98–99 (1982)
44. Lal, M.: Surge and swab modeling for dynamic pressures and safe trip velocities. In: *IADC/SPE Drilling Conference*, SPE-11412-MS (1983)
45. Mitchell, R.F.: Dynamic surge/swab pressure predictions. *SPE Drill. Eng.* **3**(03), 325–333 (1988)
46. Wang, Y., Chukwu, G.A.: Unsteady axial laminar Couette flow of power-law fluids in a concentric annulus. *Ind. Eng. Chem. Res.* **35**(6), 2039–2047 (1996)
47. Gjerstad, K., Time, R.W.: Simplified explicit flow equations for Herschel-Bulkley fluids in Couette-Poiseuille flow—For real-time surge and swab modeling in drilling. *SPE J.* **20**(03), 610–627 (2015)
48. Liu, Y.-Q., Zhu, K.-Q.: Axial Couette-Poiseuille flow of Bingham fluids through concentric annuli. *J. Nonnewton. Fluid Mech.* **165**(21), 1494–1504 (2010)
49. Erge, O., Akin, S., Gucuyener, I.H.: Accurate modeling of surge and swab pressures of yield power law fluids in concentric annuli. In: *SPE/IADC Middle East Drilling Technology Conference Exhibition*, D031S014R003 (2018)
50. He, S., Srivastav, R., Tang, M., Ahmed, R.: A new simplified surge and swab pressure model for yield-power-law drilling fluids. *J. Nat. Gas Sci. Eng.* **28**, 184–192 (2016)
51. Krishna, S., Ridha, S., Campbell, S., Ilyas, S.U., Dzulkarnain, I., Abdurrahman, M.: Experimental evaluation of surge/swab pressure in varying annular eccentricities using non-Newtonian fluid under Couette-Poiseuille flow for drilling applications. *J. Pet. Sci. Eng.* **206**, 108982 (2021)



Study the Behaviour of Chest Freezer Working with R134a and R600a Under Pull Down and Loading States

Louay Abd Al-Azez Mahdi¹(✉), Mohammed A. Fayad¹,
Muna Kheder Jassim Al-Naamee², Miqdam Tariq Chaichan¹,
Hasanain A. Abdul Wahhab¹, and Hayder Mohsin Ali³

- ¹ Energy and Renewable Energies Technology Center, University of Technology, Baghdad, Iraq
{louay.a.mahdi, mohammed.a.fayad, miqdam.t.chaichan,
20085}@uotechnology.edu.iq
- ² Petroleum Technology Department, University of Technology, Baghdad, Iraq
150007@uotechnology.edu.iq
- ³ Mechanical Engineering Department, University of Technology, Baghdad, Iraq
20331@uotechnology.edu.iq

Abstract. In the present work, the transient state which includes the pull-down and loading period is tested for the chest freezer. The experimental work has been conducted by using a freezer of 150 L volume capacity working with R-134a and R-600a by two different compressors. The freezer is equipped with measuring devices to reading the pressure, temperature, refrigerant mass flow rate, and power consumption. The tests were done at the standard ambient temperature of 32°C. The results show the time for pull down and loading period for R-600a is short than that for R-134a and the power is also lower for R-600a. The improvement can be done by using the refrigerant R-600a (which is environmentally friendly) improving the performance of the system by reducing the power consumption and the operation time required to reach a steady state.

Keywords: Chest freezer · pull down · transient · cooling capacity · Power consumption

1 Introduction

Refrigeration operates a wide application in the domestic and commercial sectors for food reservation. One of these applications is the chest freezer. The using of the chest freezer throughout the year will be costly due to the power consumption. The thermal analysis is important in order to improving the system and reducing the power consumption around the year by suitable select the proper refrigerant.

Berger et al. [1] done a simulation for domestic cooling cycle by one dimension model for heat exchangers using numerical method. The refrigerant working with R600a. The experimental test compared with the model and good agreement yield. Borges et al. [2] measure the energy consumption for refrigerator top mount free frost by simple quasi- steady method. Cai et al. [3] carried out one-dimension dynamic model for food stuff cabinet store. Chen et al. [4] described the way to reduce the energy consumption

for small refrigerator system by simulation model and experimental tests with take attention to the effect of the dynamic characteristics. Gardenghi et al. [5] two thermal model were used to simulating domestic refrigerator working with R-134a. The first model depends on first law of thermodynamic and the second was capacitive model. Grald et al. [6] used the moving boundary approach to study the heat exchangers of the heat pump. Hermes et al. [7, 8] transient study for refrigerator 440 l capacity top-mount by Simulation model. Janssen et al. [9] experimentally test upright freezer for pull down and strat up with analysis to investigate the accuracy of the dynamic model applied. Li et al. [10] used moving boundary lumped method to represent the five models of condenser and two models for evaporator, the heat exchangers were part of vapor compression refrigeration system. The shut down and start up state was the target of the study. Martinez et al. [11] modelling dynamic performance of refrigerator by quasi steady approach. The model compared with test data in order to exam validation. Melo et al. [12] dynamic state of domestic refrigerator was study experimentally and theoretically. Pettit et al. [13, 21] one dimensional mathematical model for two phase heat transfer in condenser and evaporator depend on moving boundary approach. Rajendran et al. [14] study the behaviour of vapor compression system experimentally and analyzed the data with computer program. Rasmussen et al. [15, 16] used the lumped quality, moving boundary, and finite control volume approach to study the transient state of the vapor compression system of refrigerator. Sanama et al. [17] using finite volume method to modelling the transient for vapor compression refrigeration system and experimental test to valid the model. The results shown agreement between the model and the test data. Tagliafico et al. [18] study the transient of chest freezer by dynamic model depend on three different equations of first order. The model was simple, reliable, and agree with the experimental tests. Tulapurkar et al. [19] applied the lump model to study the transient of refrigerator in order to represent the pull down and on/off cycle of the test. Turgut et al. [20] modelling the dynamic behaviour of vapor compression refrigeration cycle working with R-134a and R-1234yf by using the finite difference method. Yuan et al. [22, 23] analyzed freezer 400 L capacity for dynamic state using conservation equations to made computer program. The validation was good for the model with the test.

The point of view for this search is to find experimentally the best refrigerant can be used for operating the chest freezer during the transient period (pull down and loading material) R-134a or R-600a where the regulations of the UN decided to phase out the refrigerant R-134a while R-600a is natural refrigerant and friend to environment.

2 Experimental Implementation

2.1 Test Apparatus

The experimental test has been done use chest freezer of 150 L internal volume (see Fig. 1). The capillary tube welded outside the suction line of the compressor. The condenser is a wire on tube condenser with equivalent length of 10.5 m and diameter of 6.35 mm, the fins with diameter of 1.2 mm. The first compressor working with R-134a is a Konor brand GQR60AA model and the second for R-600a is DONGER brand GD59N model. The evaporator was copper tube with diameter 7.937 mm is warp around the

evaporator box of the internal compartment and the circuit has equivalent length of 15 m (see Fig. 2). The type of the refrigerants is choosing which closed to AHRI-700 standard.

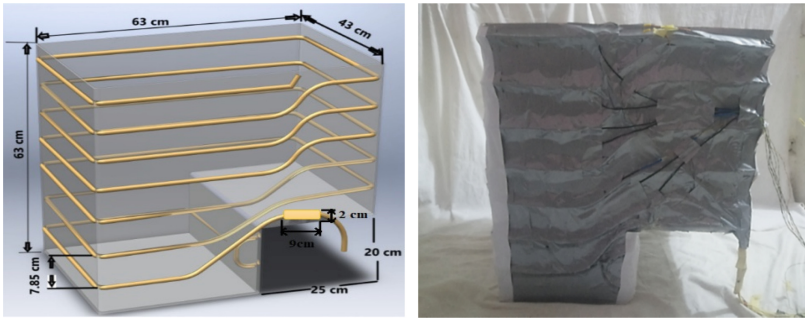


Fig. 1. The chest freezer and measuring devices.



Fig. 2. The evaporator tube loop and the insulation cover.

2.2 Measurement System

Type T thermocouples were used to measure the temperatures, with accuracy of $\pm 1^\circ\text{C}$. 13 thermocouples attached to the tubes wall of wire on tube condenser at the middle of the legs, and 7 thermocouples for the evaporator at each loop of tubes. Pressures were measured at the low sides (evaporator inlet/outlet) and high sides (condenser inlet/outlet) of the system, by four transducer types. The accuracy of the transducer was $\pm 0.5\%$, as declared by the manufacturer. Electrical power was measured by a power analyzer with an estimated accuracy for the system of the power $\pm 3\%$, the current $\pm 2\%$, and the voltage $\pm 1.2\%$. The tests were done inside a climatic room built according to specifications of ASHRAE committee 8.99.

3 The Results and Discussion

The test proceeded done by operate the chest freezer till reach the set temperature this period calls the pull-down state, after that loading the chest freezer with three water bottles of two liters size and the loading state be start, keep watching the operation of the

freezer until the evaporator box temperature return back to the temperature set at the end of the pull-down state. The temperature and the power during the test were measured and recorded and the results as following:

Figure 3 and 4 show the condenser and evaporator surface temperature at: first for pull down running without load, and second with loading three bottles of water put in it and the test run till reach the box space temperature set of the chest freezer.

The average condenser surface temperature for R-134a was around 60 °C and 52°C for R-600a at the loading states, and the box evaporator temperature was -20°C for R-134a and -25°C for R-600a. The time for pull down state is 180 min for R-134a and 120 min for R-600a, while the time cover the loading state (adding three water bottles of two liters size) for R-134a is 1260 min and 1150 for R-600a, that is mean the power consumption for this period of R-600a is lower than R-134a and the cost of the power consumption is lower for R-600a.

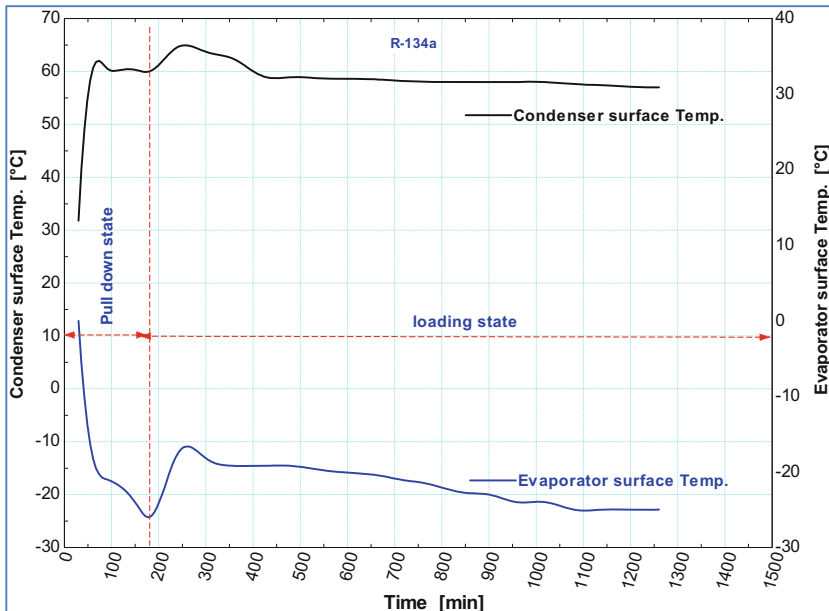


Fig. 3. The condenser and evaporator temperature for (R-134a) with time for pull down and loading states.

Figure 5 and Fig. 6 show the power consumption and the refrigerant mass flow rate for pull down and loading periods test. The R-134a average power consumption is 140W and 84 W for R-600a respectively. The behaviour of the power with the time show increase at the beginning and drop when the test working at pull down state for both refrigerant, and then increase with loading state began and drop slightly with time, the same can say for the refrigerant mass flow rate, but the average value of the power for loading period is 150 W higher with R-134a than that for R-600a which is average value 90 W.

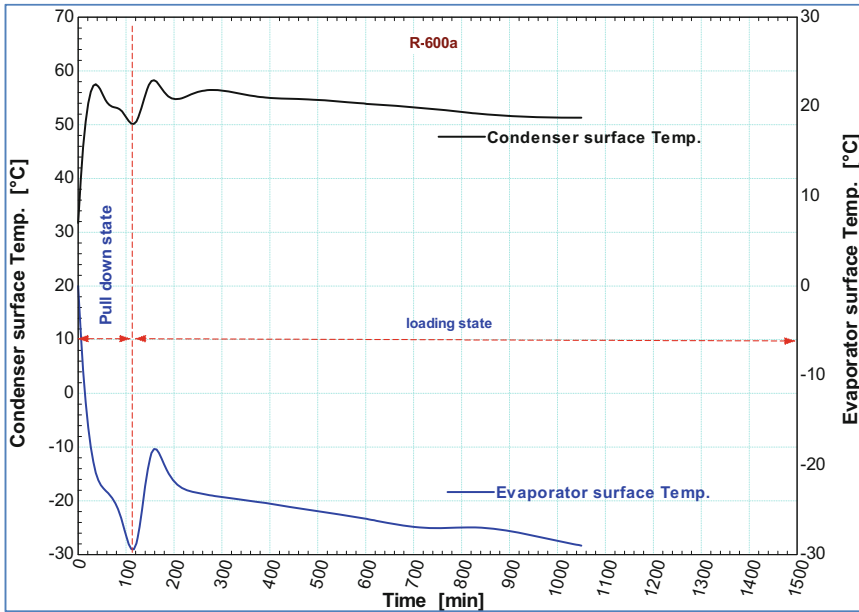


Fig. 4. The condenser and evaporator temperature for (R-600a) with time for pull down and loading states.

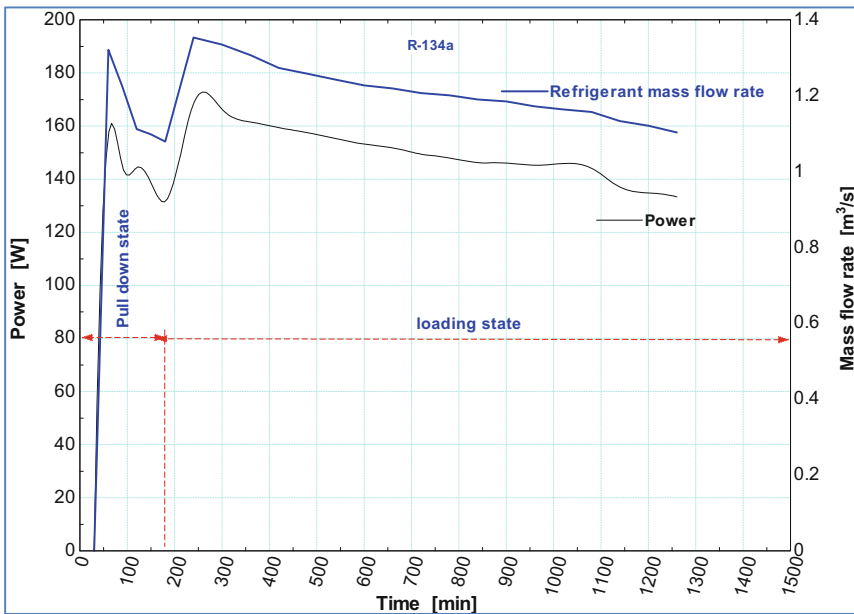


Fig. 5. The power consumption and mass flow rate for R-134a with time for pull down and loading states.

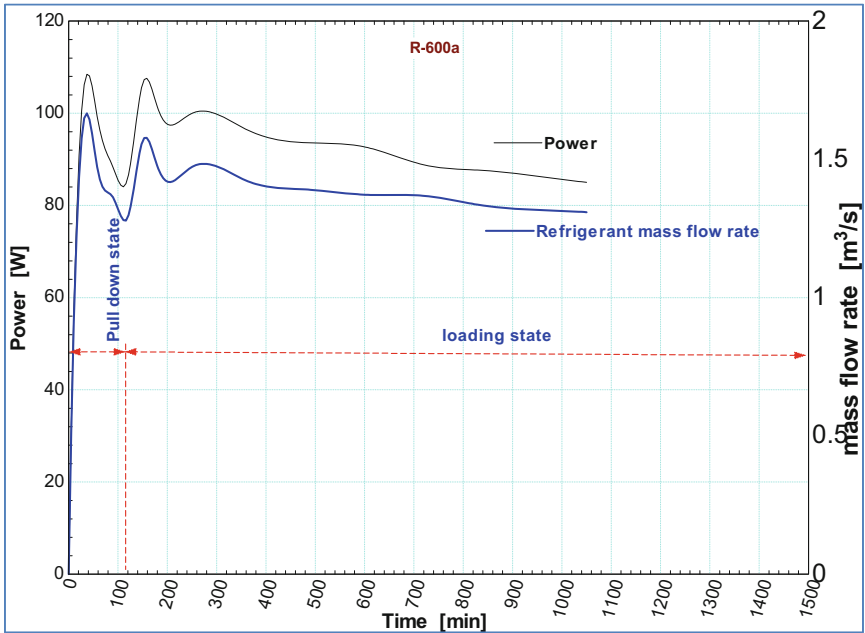


Fig. 6. The power consumption and mass flow rate for R-600a with time for for pull down and loading states.

Figure 7 and 8 comparing the freezer box temperature and water temperature when the chest freezer working with R-134a and R-600a and the time for pull down and loading periods. From the figure, the value of freezer box temperature for both refrigerants, the freezer box temperature with R-134a refrigerant is -20°C higher than the freezer box temperature -25°C for R-600a refrigerant. The time required to complete the pull-down state for R-600a refrigerant lower than the time required for R-134a. The figure shows also the change in the water phase from water to ice.

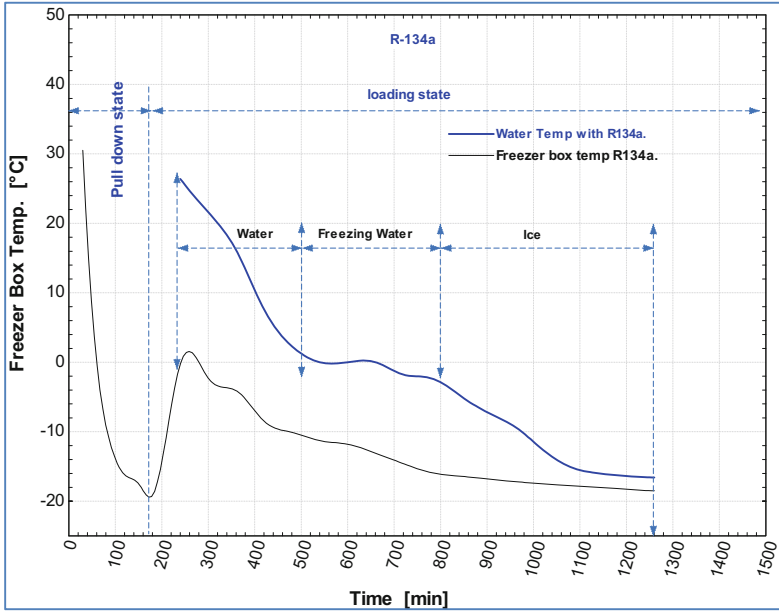


Fig. 7. Comparison of freezer box temperature and water temperature for R-134a with time for pull down and loading states.

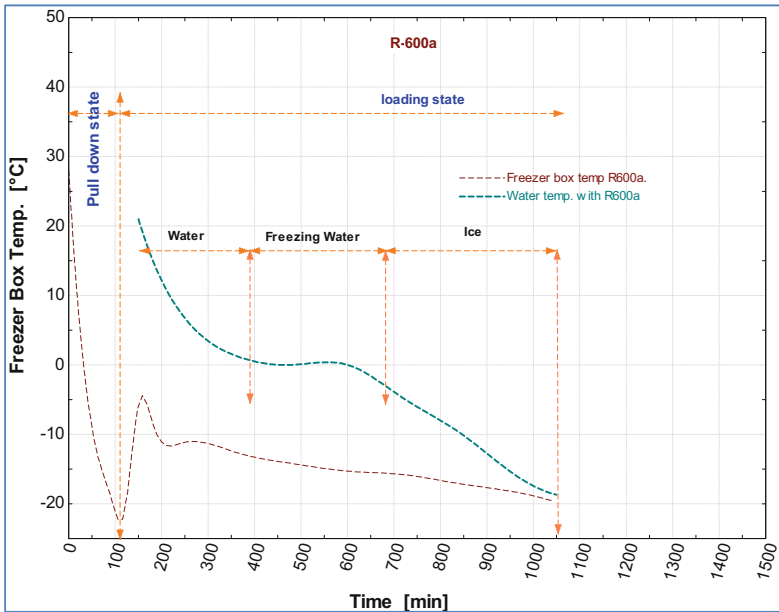


Fig. 8. Comparison of freezer box temperature and water temperature for R-600a with time for pull down and loading states.

4 Conclusions

In this work, the experimental tests were done for the chest freezer working with R-134a and R-600a to discover the case of the lower power consumption done for pulldown and loading periods. That is the target of the search. The main points extract from the work are:

- The power consumption by the system working with R-600a is lower than that for R-134a for the pull down and loading periods.
- The time required to cover the pull down for R-600a is 100 min which is shorter than that for R-134a which is 180 min.
- The power consumption for loading state by R-600a is half than that for R-134a, and the time also.
- The refrigerant R-600a is more efficient than R-134a.
- The using of R-600a for chest freezer can improving the work of the chest freezer for the required temperature inside and the power consumption that touch the target of the research.

References

1. Berger, E., Posch, S., Heimele, M., Almbauer, R., Eichinger, M., Stupnik, A.: Transient 1D heat exchanger model for the simulation of domestic cooling cycles working with R600a. *Sci. Technol. Built Environ.* **21**(7), 1010–1017 (2015)
2. Borges, B.N., Hermes, C.J.L., Gonçalves, J.M., Melo, C.: Transient simulation of household refrigerators: A semi-empirical quasi-steady approach. *Appl. Energy* **88**(3), 748–754 (2011)
3. Cai, J., Risum, J., Thybo, C.: Dynamic Heat Transfer Model of Refrigerated Foodstuff, pp. 1–8. Retrieved from (2006)
4. Chen, Z.J., Lin, W.H.: Dynamic simulation and optimal matching of a small-scale refrigeration system. *Int. J. Refrig.* **14**(6), 329–335 (1991)
5. Gardenghi, Á.R., Lacerda, J.F., Tibiriçá, C.B., Cabezas-Gómez, L.: Numerical and experimental study of the transient behavior of a domestic vapor compression refrigeration system – influence of refrigerant charge and ambient temperature. *Appl. Therm. Eng.* **190**, 116728 (2021)
6. Grald, E.W., MacArthur, J.W.: A moving-boundary formulation for modeling time-dependent two-phase flows. *Int. J. Heat Fluid Flow* **13**(3), 266–272 (1992)
7. Hermes, C.J.L., Melo, C.: A first-principles simulation model for the start-up and cycling transients of household refrigerators. *Int. J. Refrig.* **31**(8), 1341–1357 (2008)
8. Hermes, C.J.L., Melo, C.: Assessment of the energy performance of household refrigerators via dynamic simulation. *Appl. Therm. Eng.* **29**(5–6), 1153–1165 (2009)
9. Janssen, M.J.P., Kuijpers, L.J.M., Witt De, J.A.: Theoretical and experimental investigation of a dynamic model for small refrigerating systems. In: *International Compressor Engineering, Refrigeration and Air Conditioning, and High-Performance Buildings Conferences*, pp. 1–10 (1988)
10. Li, B., Alleyne, A.G.: A dynamic model of a vapor compression cycle with shut-down and start-up operations. *Int. J. Refrig.* **33**(3), 538–552 (2010)
11. Martínez-Ballester, S., Leon-Moya, B., Vesson, M., González-Maciá, J., Corberán, J.M.: Dynamic performance simulation of a household refrigerator with a quasi-steady approach. In: *International Refrigeration and Air Conditioning Conference*. Paper 1256 (2012)

12. Melo, C., Da Silva Ferreira, R.T., Pereira, R.H., Negrao, C.O.R.: Dynamic behaviour of a vapor compression refrigerator: a theoretical and experimental analysis. In: Proceedings of the International Refrigeration and Air Conditioning Conference, pp. 141–149 (1988)
13. Pettit, N.B.O.L., Willatzen, M.: A general dynamic simulation model for evaporators and condensers in refrigeration. Part II : Simul. Control Evaporator **21**(5), 404–414 (1998)
14. Rajendran, N., Pate, M.B.: A computer model of the startup transients in a vapor-compression refrigeration system. In: Commissions IIF-IIR, pp. 201–211 (1986)
15. Rasmussen, B.P.: Dynamic modeling for vapor compression systems-part I: literature review. HVAC R Res. **18**(5), 934–955 (2012)
16. Rasmussen, B.P., Shenoy, B.: Dynamic modeling for vapor compression systems-part II: simulation tutorial. HVAC R Res. **18**(5), 956–973 (2012)
17. Sanama, C., Xia, X.: Transient state modelling and experimental investigation of the thermal behavior of a vapor compression system. Math. Probl. Eng. **2021**, 9941451 (2021)
18. Tagliafico, L.A., Scarpa, F., Tagliafico, G.: A compact dynamic model for household vapor compression refrigerated systems. Appl. Therm. Eng. **35**(1), 1–8 (2012)
19. Tulapurkar, C., Khandelwal, R., Centre, T.: Transient lumped parameter modeling for vapour compression cycle based refrigerator. In: International Refrigeration and Air Conditioning Conference (2010)
20. Turgut, M. S., Çoban, M.T.: Dynamic performance comparison of R134a and R1234yf refrigerants for a vapor compression refrigeration cycle. Hittite J. Sci. Eng. **5**, 9–14 (2018)
21. Willatzen, M., Pettit, N., Ploug-Sørensen: A general dynamic simulation model for evaporators and condensers in refrigeration. part I: moving-boundary formulation of two-phase flows with heat exchange. Int. J. Refrig. **21**(5), 398–403 (1998)
22. Yuan, X., ONeal, D.L.: Development of a transient simulation model of a freezer. part I: model development. In: Proceedings of the 1994 International Refrigeration Engineering Conference at Purdue, pp. 213–219 (1994)
23. Yuan, X., ONeal, D.L.: Development of a transient simulation model of a freezer. part II: comparison of experimental data with model. In: Proceedings of the 1994 International Refrigeration Engineering Conference at Purdue, pp. 219–224 (1994)



Effects of Arc Welding Current on the Mechanical Properties of Aluminium Plate Weldments

Muti Erinosho^(✉), Ester Angula, and Sam Shaanika

Department of Mechanical and Metallurgical Engineering, University of Namibia,
P.O. Box 3624, Ongwediva, Namibia
mutiuerinosho1@gmail.com

Abstract. This study presents the effect of arc welding current on the mechanical properties and microstructure of the welded aluminium plates. The welded samples were prepared for tensile test, microstructural analysis, microhardness and XRF analysis. The tensile test results recorded a maximum UTS value of 88.333 MPa in sample E welded at a current of 90 A while sample A welded at a current of 50 A exhibited the lowest UTS of 33.70 MPa. Sample E produced a fine structure with fine dendrites. The tertiary dendrite grains showed a good sign of high strength when compared to the primary and coarse dendrite grains that were formed in sample A, welded at 50 A. The hardness values were presented and decreased as the welding current was increased from sample B to sample D and later increased in sample E, which could be as a result of the cooling rate at high heat input.

Keywords: Aluminium · Microhardness · Tensile strength · Microstructural analysis · XRF

1 Introduction

Aluminium is one of the most abundant metals in nature, and its alloys are widely used in the industry due to their mechanical properties and corrosion resistance. It is a difficult metal to weld due to the oxide layer that should be removed from its surface before welding [1]. There is high demand of aluminium in the industry, which has necessitated the high efficiency, and quality of aluminium alloy for aerospace parts [2]. The increase in the applications of aluminium alloys in all the sectors of the industry is a driving force for the development and efficiency of joining the metal without much adverse effect on their mechanical properties [3]. Most engineers focused on the performance and life span of materials and ensure that they do not fail in service [4]. One of the problems encountered by Aluminium alloy is porosity. This is well known defect that can cause cosmetic problems and reduce the ductility and degrading the mechanical properties [5]. The limitation of fatigue life is determined by the size of pores generated most especially in its cast form [6]. Previous studies have shown that inclusions, like oxide films, assist in the nucleation of the pores and thus have a significant influence on the prior porosity formed [7]. TIG welding was done on Aluminium 6082 substrate

by Kumar et al. [8], and AA5356 filler wire with a diameter of 2.4 mm was used as the filler wire. Taguchi orthogonal array L9 (Minitab 19) was used to evaluate the amount of runoff and to analyse the specimens. It was reported that, the tensile strength of the welded joint increased by 43.87%, with an increase in welding current due to the heat generated at the weld interface. In addition, the tensile strength of the welded joint was increased by approximately 3%, and decreased by 0.94% in hardness value when the travel speed was increased [8].

The main aim of this study is to investigate the effects arc welding current on the welded Aluminium plates through the microstructural analysis, mechanical properties and XRF analysis. The tensile testing will justify the quality of the weld through the ultimate tensile strength (UTS), as well as the maximum tension load.

2 Experimental Procedure

An aluminium sheet of 1250 mm × 2250 mm, 3 mm thick, was cut into four plates of the same dimensions, 625 mm × 150 mm each. These plates were welded together using electric arc welding machine. The weldment length is 120 mm, which was maintained, and the interval between each weld was approximately 130 mm. Before welding operation, the surfaces of the plates were neatly cleaned, and rough edges were scraped, to achieve a good alignment.

The chemical composition of the Aluminium that makes up the sheet is shown in Table 1.

Table 1. Chemical Composition of Aluminium sheet

Elements	Al	Si	Fe	Mg
% wt. Composition	98.456	0.526	0.847	0.128

The main focus of this work is based on the quality of the weld created when the two plates are welded together using five different currents 50 A, 60 A, 70 A, 80 A and 90 A. This was achieved using the THERMADYNE DC inverter 160 welding machine. The alumoid 12SI electrode with a diameter of 2.5 mm was used as the electrode. The four work pieces of dimension 150 mm × 625 mm × 3 mm in two pairs were each clamped and tagged at the two ends along the length 625 mm, with a common interval of approximately 130 mm between each weld. The welding speed was maintained at 52.3 m/s on average. Figures 1 show the joined Aluminium plates at varying currents.

Welding was done in one pass using the arc-welding machine using a self-shielding 2.5 mm thick electrode. The welding current was varied during the welding operation while maintaining the voltage at 10 V.

Table 2 shows the welding parameters used, displaying the weld beads based on their varying currents.

After welding, the samples were cut for tensile test and other characterizations such as microstructure, microhardness and XRF analysis. Tensile test was conducted on the

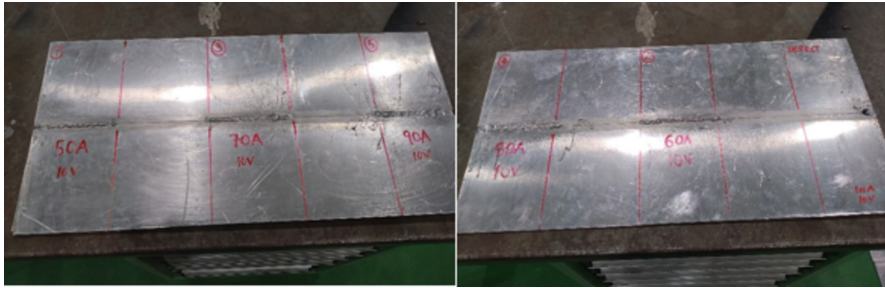


Fig. 1. Welded Aluminium plates at varying current

Table 2. Welding parameters

Parameters	Values				
Welding Current (A)	50	60	70	80	90
Welding Voltage (V)	10	10	10	10	10
Gas flow rate (l/min)	45	45	45	45	45
Welding speed (mm/min)	2.28	2.29	2.30	2.30	2.32

dog-bone shaped specimens using the Zwick/Roell Z150 tensile testing machine at the Engineering Laboratory, University of Namibia. The tensile test is the most extended method for the mechanical characterization of materials. The basic parameters determined in this test are the elastic modulus, yield stress, tensile strength and elongation according to the ASTM E8/E8M-15a standards. Ten (10) samples were tested, two (2) under every welding current for repeatability. Some samples were cut for metallographic preparation and mounted in polyfast. The mounting method uses pressure and heat to encapsulate the samples. The mounted samples were ground and polished for microstructural analysis. Keller's reagent was prepared for the etchant with 190 ml of H₂O, 5 ml of HNO₃, 10 ml of HCl, and 2 ml of HF. The microstructural examination was conducted using an optical microscope at low and high magnification. The microhardness test was conducted on Zwick/Roell ZHU250top machine. A total number of 15 indents were done on each sample using a load of 1 kgf since this is the minimum load that can be applied. X-ray Fluorescence (XRF) spectroscopy analysis was done on the welded samples for the compositional analysis using the Titan XRF analyser.

3 Results and Discussion

In this section, the results of the tests conducted are discussed and presented. The different weldment were characterized and analysed through XRF, tensile testing, microstructural, and microhardness evaluations. Aluminium is a challenging metal to weld, especially with an arc welding process. Aluminium requires using specific equipment and special techniques to achieve a high-quality weld. Unlike carbon steel, aluminium does not

change colour before it reaches the melting point. The flux from an aluminium electrode creates a mess after it cools. The welding currents were varied from 50 A to 90 A respectively. There was no undercut on sample A welded at a current of 50 A but start to be obvious from sample B welded at 60 A due to more heat input initiated as the current is increased. At sample E welded at current of 90 A, the alumoid electrode created a hole through the plates and excessive penetration, which justifies high heat input. The microstructural analyses were done on the welded samples from sample A welded at a current of 50 A to sample E welded at current of 90 A. Figures 2 (a) to (e) depict the microstructure of the entire welded samples welded at current of 50 A to 90 A.

The grain sizes have been observed to increase as the welding current and the heat input increases. Dendrites were detected in the entire samples, transient from coarse grains to fine dendrite grains as the current was increased, and the dendritic arms were found disappearing thereby causing more grains to migrate and form new structure (recrystallize). The grain sizes of sample D increased drastically. This could occur as a result of the increase in the heat input as the welding current was increased. A big porosity was observed in sample E welded at a current of 90 A and colonies of new grains are formed inside the bigger grains in the entire sample E. The formation of weld structures starts from the dendrite phase nucleation and growth processes in a melted weld pool metal, where in primary dendrites were formed at the lowest welding current. These primary dendrites are concentrated, with little and tight spaces in between them as seen in Fig. 2 (a). They are small in sizes and as the welding current increases, another pattern of dendrites was formed, which is the secondary dendrites. These are mid-sized dendrites, with fine grains of average sizes. The larger dendrite grains occurred at the highest welding current of 90 A, with fine shapes of the grains.

The Vicker's hardness value of the deposit appeared to be in a good range when compared to the parent material. Figure 3 shows the plot of the hardness values against the sample's welding currents.

The average hardness value of sample A welded at 50 A is HV 101.9 and increases to HV 106 in sample B welded at 60 A and later decreased in sample C and further decreased in sample D. Among the entire welded samples, sample B exhibits the highest average microhardness value of HV 101.9 while sample D displays the lowest average microhardness value of HV 92. From this indication, it shows that within the secondary dendrites colony, the hardness values decrease as the welding current increases. Although there is a sharp rise in the hardness value of sample E and this could be as a result of the high heat input and the cooling rate exhibited at a welding current of 90 A.

This behavior has also created room for defect formation in the sample.

The tensile strength of the welded samples was tested on the tensile testing machine. A total number of 10 samples, 2 per welding current were prepared for the tensile test.

Figure 4 shows the entire tensile test specimens after fracturing.

It was observed that in samples D and E welded at current of 80 A and 90 A respectively, the fracturing did not occur at the weld and which shows that the two samples had good weld quality. Figure 5 shows the graph of standard force versus extension for om sample E welded at 90 A.

Among the entire tensile specimens, sample E fractured at the maximum tensile load of approximately 2385 N on average. The trend is such that the first sample welded at 50

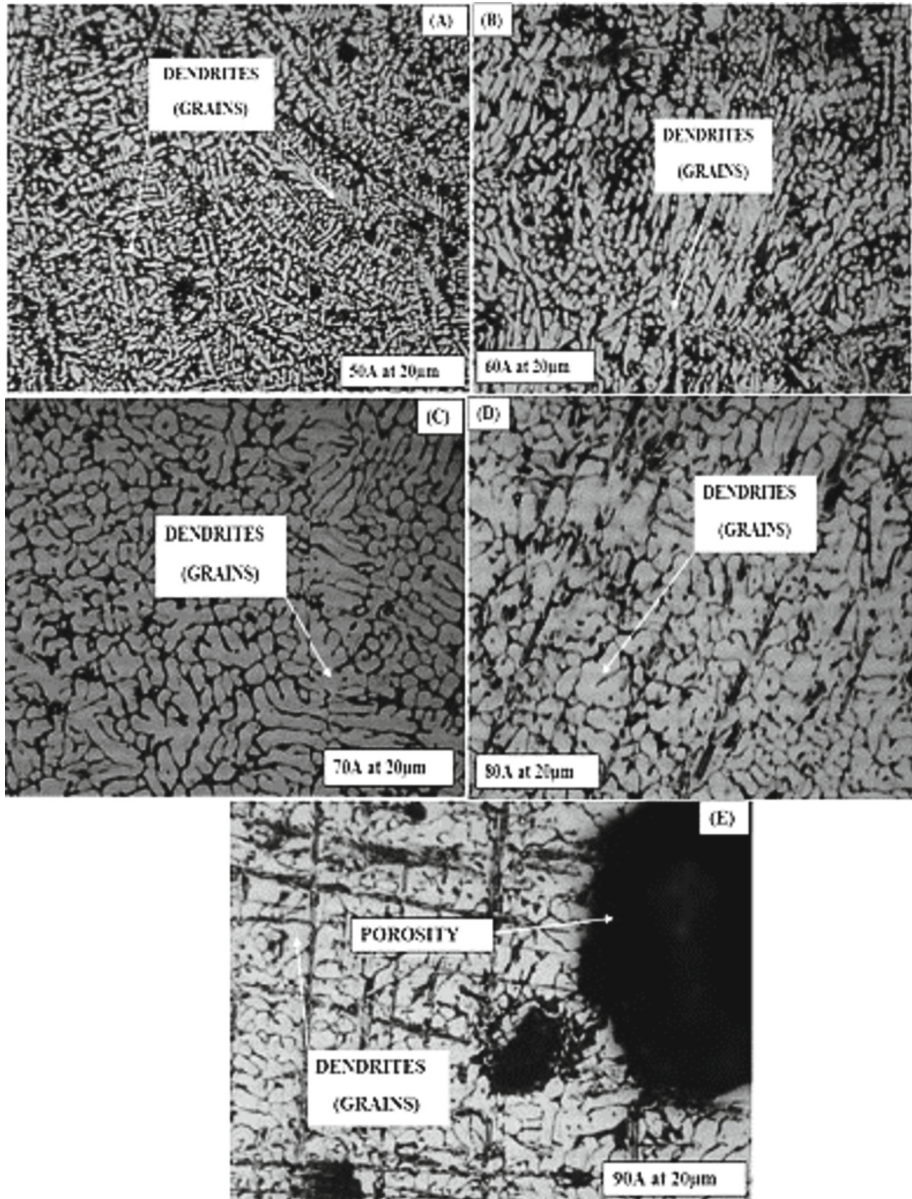


Fig. 2. Microstructures of welded Aluminium at varying currents (A) 50A, (B) 60A, (C) 70A, (D) 80A and (E) 90A

A fractured at the lowest tensile load of 910 N. A huge difference was observed between the welded sample B and sample C with an interval of 664 N.

From these results, it can be concluded that the weld joint obtained at sample A welded at 50 A is more ductile than the welded sample C and sample D. However, the

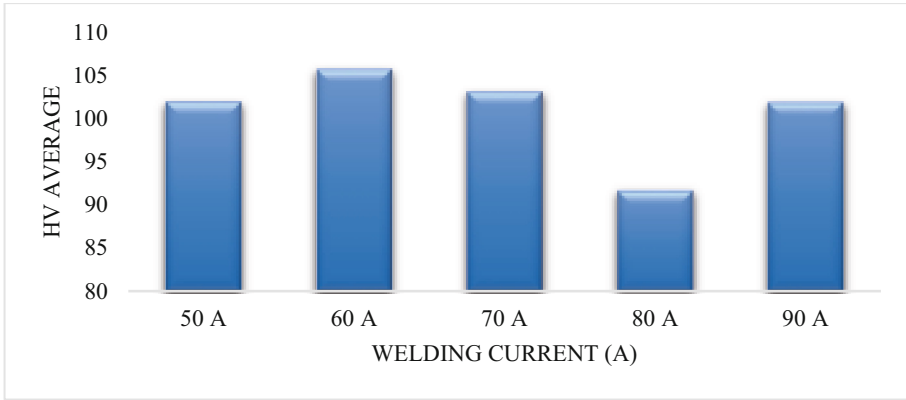


Fig. 3. Average hardness values against the welding current

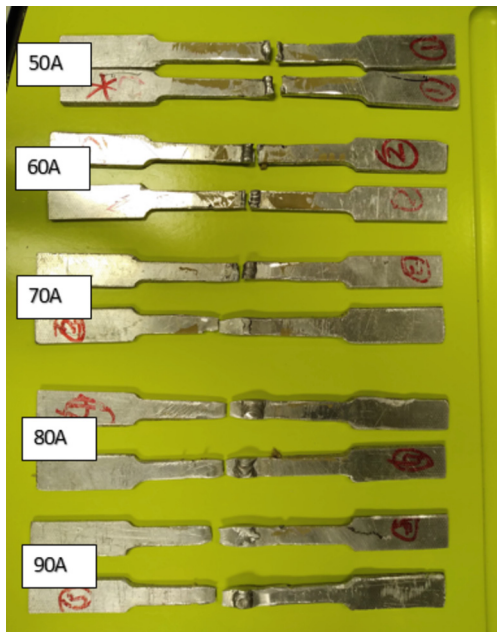


Fig. 4. Tensile test specimens after fracturing

sample E welded at 90 A is stronger and least ductile among the five samples. There was a significant rise in standard force observed from sample C welded at 70 A to sample E welded at the maximum current of 90 A. Both samples D and E, welded at 80 A and 90 A, respectively, revealed a maximum standard force at maximum yield point of approximately 2315 N. For these samples, the elongation is slightly higher compared to the samples A and B. It could also be concluded that the effect of heat input favours the strength of the joint and slightly reduce ductility.

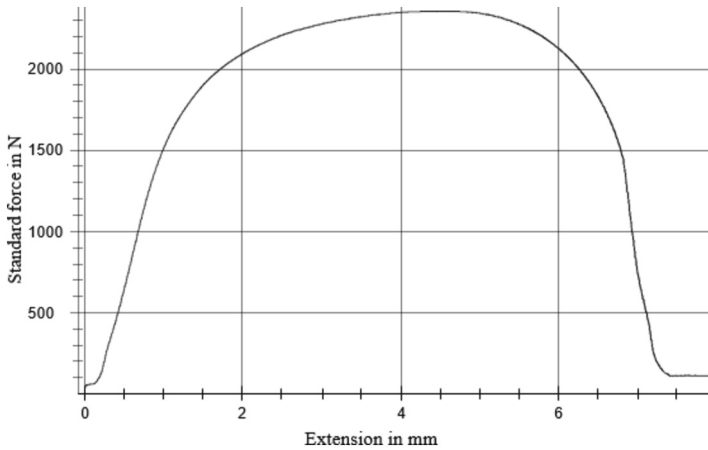


Fig. 5. Graph of Standard force vs. Extension for sample E.

Figure 6 depicts the graph of UTS against the welding current used.

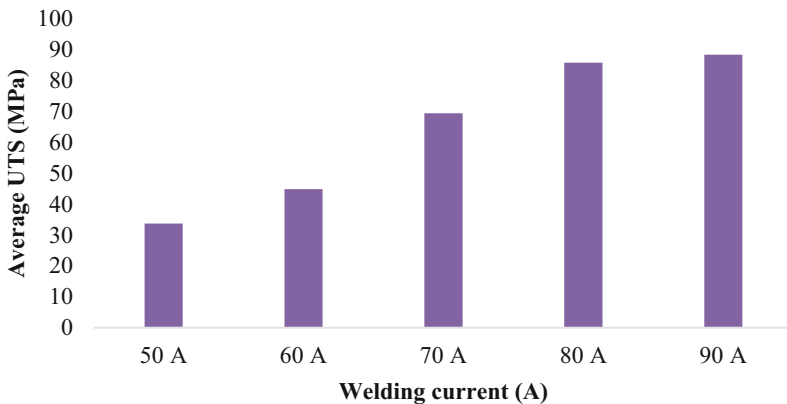


Fig. 6. Average UTS value against the welding currents

From the graph in Fig. 6, it could be observed that there was a regular increase in the UTS value from sample A welded at the current of 50 A to sample E welded at the current of 90 A. Sample E gives the highest average UTS value of 88.3 MPa while sample A gives the lowest average UTS value of 33.7 MPa. There is a decrease in the elastic modulus from the welding current of 90 A in sample E to sample A. In general, the modulus of elasticity is inversely proportional to the average UTS values of the samples. In the XRF analysis that was carried out on the entire samples, the dominant elements are Aluminium (Al), Silicon (Si), Iron (Fe), Magnesium (Mg), Copper (Cu), Titanium (Ti) and Cobalt (Co). The percentage weight (wt.%) of Al was observed to have increased from sample A welded at 50 A to sample C welded at 70 A. The wt.% of Mg ranges between 0.114% and 0.410%. Cu content decreases from sample A welded

at 50 A to sample D welded at 80 A. A sudden increase in Cu content was observed in sample E welded at 90 A. The highest value of wt.% of Si occurred in sample A with 11.089% whereas the lowest amount occurred in sample E that was welded at 90 A with 0.526%. This Si content has an impact on the tensile strength of the samples.

4 Conclusion

The weldment characterization of Aluminium was investigated in this study and the following conclusions were drawn:

- The grain refinement showed better strength and ductility, hence gives a boost to the mechanical state of the Aluminium weldment and its performance.
- It was observed that the UTS values of the entire welded samples increased with increase in the welding current. Sample E presented the highest average UTS value of 88.3 MPa while sample A gave the lowest average UTS value of 33.7 MPa.
- The microstructures showed that a small increase in welding current could cause effective grain refinement in obtaining a good weld. The smallest grain sizes were achieved in sample A welded at 50 A.
- The hardness and tensile strength were increased in the samples welded with increasing current and heat input. The hardness value has doubled, while the strength increase is by approximately 50%.
- The presence of porosity in sample E welded at a current of 90 A is as a result of the melt pool created by the heat input and as well as the thickness of the plate.

References

1. Nunez, P., Jones, S.: Cradle to gate: life cycle impact of primary aluminium production. *Int. J. Life Cycle Assess.* **21**(11), 1594–1604 (2016)
2. Wang, Y., et al.: Refining microstructure of medium-thick AA2219 aluminium alloy welded joint by ultrasonic frequency doublepulsed arc. *J. Mater. Res. Technol.* **23**, 3048–3061 (2023). <https://doi.org/10.1016/j.jmrt.2023.01.174>
3. De Schrynmakers, P.: Life cycle thinking in the aluminium industry. *Int. J. Life Cycle Assess.* **14**(1), 2–5 (2009). <https://doi.org/10.1007/s11367-009-0072-x>
4. Hensel, M.U., Hensel, D.S., Menges, A.: Material performance. *Archit. Des.* **78**(2), 34–41 (2008)
5. Mohamed, A.M.A., Samuel, A.M., Samuel, F.H., Doty, H.W.: Influence of additives on the microstructure and tensile properties of near-eutectic Al–10.8%Si cast alloy. *Mater. Des.* **30**(10), 3943–3957(2009)
6. Zhu, X., Yi, J., Jones, J., Allison, J.: A probabilistic model of fatigue strength controlled by porosity population in a 319Type cast aluminum alloy: part I. model development. *Metall. Trans. A-Phys. Metall. Mater. Sci.* **38**, 1111–1122 (2007)
7. Yao, L., Cockcroft, S., Maijer, D., Zhu, J., Reilly, C.: Study of microporosity formation under different pouring conditions in A356 aluminum alloy castings BT - light metals 2011. S. J. Lindsay, Ed. Cham: Springer International Publishing, pp. 783–789 (2016)
8. Kumar, G.S., Ramesh, M., Dinesh, S., Paramasivam, P., Parthipan, N.: Investigation of the TIG Welding Process for Joining AA6082 Alloy Using Grey Relational Analysis. In: *Advances in Materials Science and Engineering*, vol. 2022, Article ID 5670172, p. 8. <https://doi.org/10.1155/2022/5670172>



Design of a Passive Dust Suppression System for the Coal Staithes

Ester Angula^(✉), Mutiu Erinosh, Sam Shaanika, and Erasmus Shaanika

Department of Mechanical and Metallurgical Engineering, University of Namibia,
P.O. Box 3624, Ongwediva, Namibia
eangula@unam.na

Abstract. The coal dust at the power plant poses a risk to the health of workers at the plant, and nearby occupants, necessitating a solution to suppress its generation. This was successfully achieved with this design. The problem, as well as possible solutions were extensively researched, and the obtained information were used to develop potential concepts. Different concepts were considered and analysed based upon the design requirement. Of all concepts developed, a fog/mist suppression system best fit the design requirements, providing efficient and cost-effective dust suppression, without compromising the environment or integrity of the coal in the staith. To determine the required pipe diameters to supply water to each nozzle at sufficient pressure and flow rate, fluid flow analysis was performed using PIPENET. Based on the behaviour of the spray, the nozzle was determined to produce satisfactory conditions for the purpose of the design. Although evidence from literature reviewed and analyses performed on the system give valid reason to justify the viability of the design, it would still benefit from more extensive testing to better optimize it. Further testing could be achieved through more vigorous simulation using more computing than was presently available at the time, or the fabrication of a prototype.

Keywords: Coal · Dust suppression · Staith

1 Introduction

Evidence from studies has shown that exposure to coal dust can potentially lead to negative health effects such as emphysema, pneumoconiosis, and increased cancer risk [1–3]. The risk of exposure to these dust particles is significantly higher for people who may live or work near places where coal is handled. The rising coal dust also lowers visibility, as it obscures the vision of any working within its vicinity. Another issue associated with coal dust is its tendency to ignite and explode [4, 5]. All these are problems experienced at the local considered Power Station coal staith. The considered power station is a coal-fired thermal, and is situated in northern area of Windhoek. To minimize the risk of exposure to the dust particles, and create a safer environment for the workers and others nearby, measures must be taken to suppress the amount of dust generated. Therefore, the primary objective of the study was to design a dust suppression system for coal staith at a local power plant. The requirements for the

design were to ensure effectively capture airborne coal dust particles, the system must be semi-automated, cost-effective as possible, and environmentally friendly.

2 Materials and Methods

Based on the literature reviewed, few concepts were considered viable for the suppression of dust in the coal staith at considered Power Station. Each of the concepts was evaluated based upon the design requirement to determine the most optimal among them. The following were the four concepts considered [7]:

- Plain Water Suppression
- Water Spray with Chemical additives
- Water with surfactant foam
- Fog/mist suppression

Upon evaluation of the four concepts selected, a concept evaluation matrix was developed to determine which was the most optimal design based on the design requirements. The concept evaluation matrix found the fog/mist dust suppression system to be the most optimal design concept as it best fit the requirements initially set out for the design. As the nature of droplets in the fog/mist suppression system is important to not only its effectiveness but also the integrity of the coal, the selection of equipment for the spray generation was important, with the following being evaluated to determine their suitability [7]:

- Sprinklers
- Rain guns
- Water spray nozzles
- Fog cannons

Based on the evaluation matrix for the selection of spray equipment, water spray nozzles were found to be most suitable for the purpose of the design. The chosen concept was further refined to give specifications for all the necessary components. The detailed design process entailed the following:

- Development of pipe plans and schematic diagrams
- Selection of spray nozzles
- Sizing and selection of pipes
- Sizing and selection of pumps

3 Design Parameters

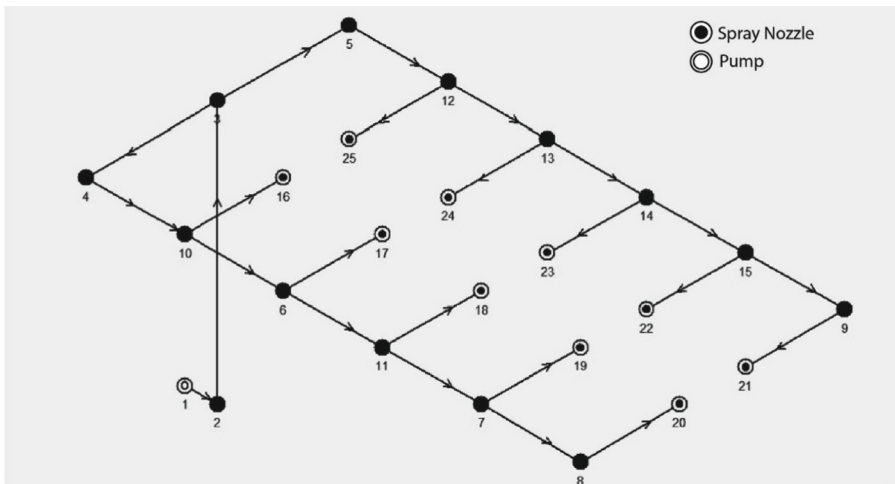
The design parameters for the coal staith are shown in Table 1.

Table 1. Design Parameters

Parameter	Value
Staith length	333.6 m
Staith width	13.52 m
Staith height	14.63 m
Number of coal transfer points	5
Distance between transfer points	55.6
Radius of dust diffusion from transfer points [6]	1.5 m
Mean dust particle diameter [6]	50 m

3.1 Pipe Plan and Schematic Diagram

The dimensions of the coal staith and the positions of the coal transfer points along the length of the staith, were determine using structural engineering drawing of the coal staith. Furthermore, with this information, the path and positioning of the pipe network supplying the spray nozzles were determined. Figures 1, 2 and 3 show the simplified schematic diagram, a plan view, and an elevation view of the pipe network, respectively.

**Fig. 1.** Pipe schematic diagram

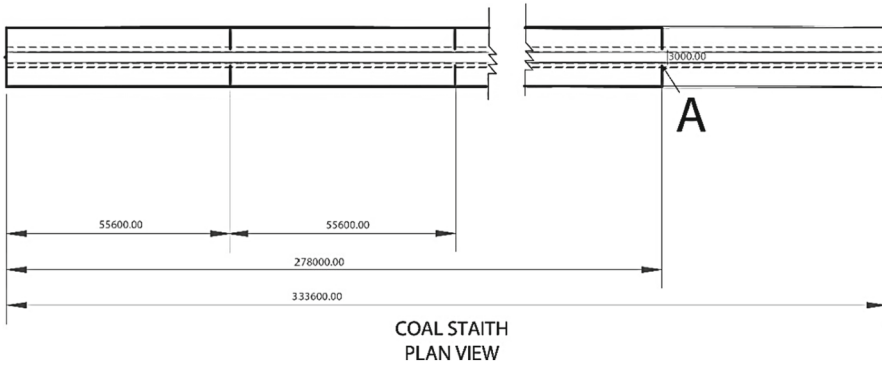


Fig. 2. Pipe Network Plan View

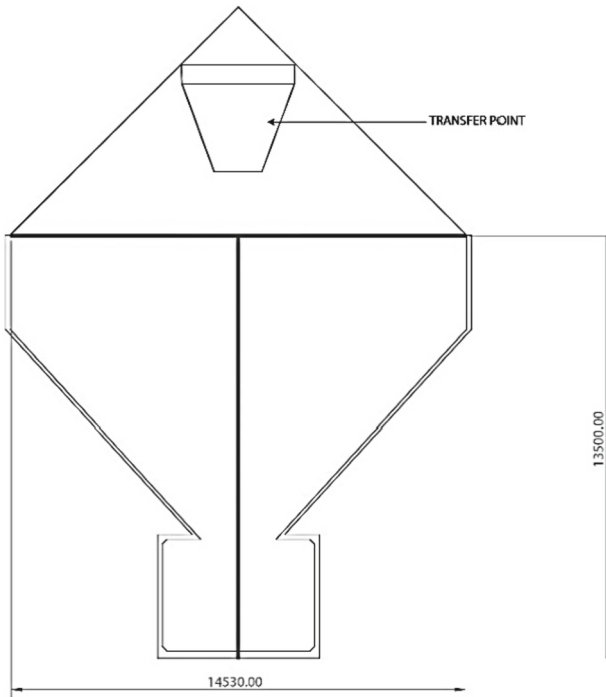


Fig. 3. Pipe Network Elevation

3.2 Spray Nozzle Selection

When selecting an appropriate spray nozzle, the following were taken into consideration:

- Droplet size
- Spray coverage

The spray coverage of the nozzle was to be large enough to cover the entire dust diffusion distance from the transfer point, and the droplets produced were to have a volumetric mean diameter near 50 μm . No evidence was found of standards for spray nozzles, therefore the selection of nozzles was guided by literature concerning the topic and information provided by the manufacturers of the selected nozzles. To determine spray coverage, the following equation acquired from Spray Systems Co was used [8]:

$$TSC = 2L \tan\left(\frac{TSA}{2}\right) \quad (1)$$

As this value of spray coverage was only theoretical, testing was to be done by simulation to determine its validity. The operating parameters of the selected nozzles are presented in Table 2.

Table 2. Selected nozzles' operating parameters

Name	Spraying Systems Co Type N Hydraulic Atomizing nozzle
Orifice diameter	1.9 mm [19]
Flow rate	245 l/hr [19]
Pressure	80 bar [19]
Theoretical Spray angle (TSA)	90°
Distance from transfer point	1.5 m
Theoretical Spray coverage	3 m

3.3 Pipe Sizing and Selection

The sizing of the pipes for the water supply of the spray nozzles was done with accordance to the SANS 4427 standard for Polyethylene pipes & fittings for water supply. To determine the required pipe diameters to supply water to each nozzle at sufficient pressure and flow rate, fluid flow analysis was performed using PIPENET, taking into consideration all friction losses, and local losses in the pipe network. After performing the fluid flow analysis, it was found that DN20 PN12.5 High Density Polyethylene (HDPE) piping throughout the entire network is sufficient to supply all nozzles with the required pressure and flow rate to produce the desired spray conditions.

3.4 Pump Sizing and Selection

Figure 4 shows the pump curve of the selected pumps at the specified operating point.

Through the use of the PIPENET application, it was found that a pump supplying 2450 l/hr at 84.51 bar/830 m of total dynamic head would be needed to sufficiently supply the spray nozzles. However, it proved difficult to find a pump to satisfy the given operating conditions. To combat this, a serial pump installation was considered. Three EDUR 409A142L pumps were selected for this purpose, each operating at a flow rate of 2.45 m³/hr and 276.48 m of dynamic head.

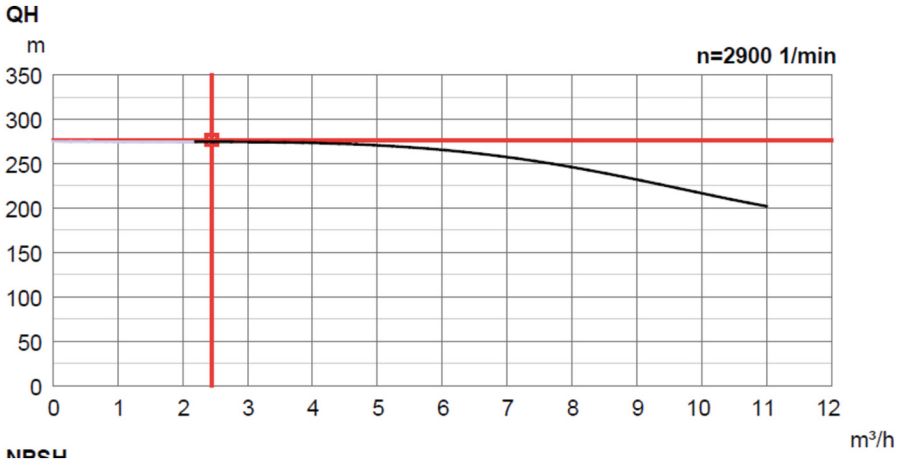


Fig. 4. EDUR 409A142L pump curve

3.5 Semi-Automation

To achieve semi-automation in the system, the pumps are only run when the conveyor belt is in motion. A rotation sensor will be installed on the belt to detect when the belt is in motion. The EDUR pumps controlled by sensors and will be operated by signals from rotation sensor.

4 Results and Discussion

Based on data provided by the manufacturer, a theoretical spray angle of 90° could be achieved with the selected nozzle. The validity of this was tested by simulation using ANSYS FLUENT. A nozzle of 1.9 mm orifice diameter sprayed water at the 80 bar into a cubic element of air, and the spray pattern was observed, as shown in Figs. 5 and 6.

Based on the behaviour of the spray, the nozzle was determined to produce satisfactory conditions for the purpose of the design. Figures 5 and 6 indicate that the spray covers a significantly large area, justifying the selection of the nozzle and the distance from the transfer point.

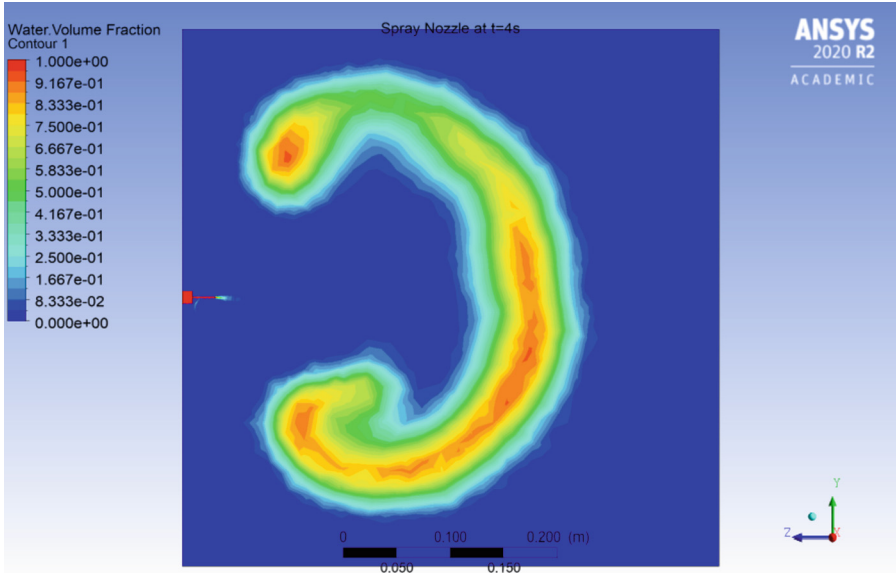


Fig. 5. Volume fraction of spray water in air at $x = 0$ m from the nozzle

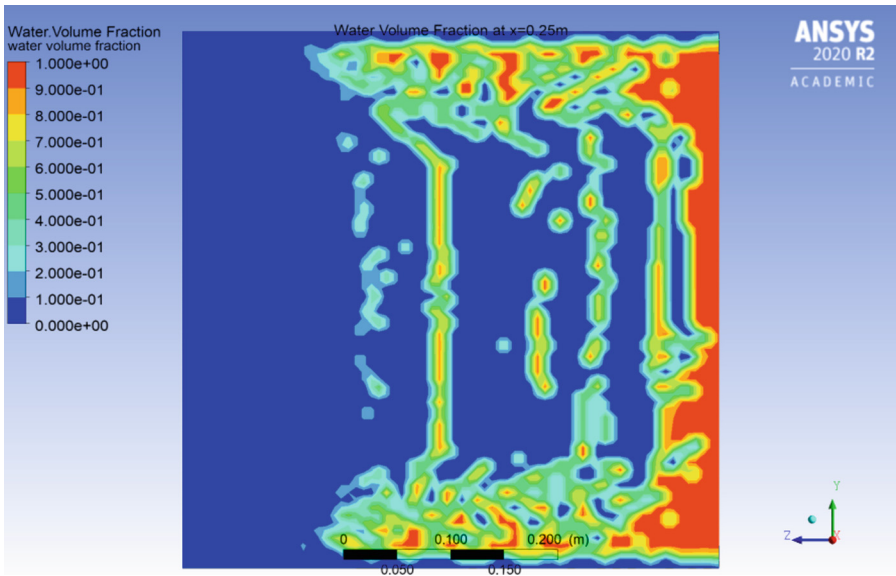


Fig. 6. Volume fraction of spray water in air at $x = 0.25$ m from the nozzle

5 Conclusion

The coal dust at the plant poses a risk to the health of workers at the plant, and nearby occupants, necessitating a solution to suppress its generation. This was successfully achieved with this design. The problem, as well as possible solutions were extensively researched, and the obtained information were used to develop potential concepts. Of all concepts developed, a fog/mist suppression system best fit the design requirements, providing efficient and cost-effective dust suppression, without compromising the environment or integrity of the coal in the staith. Although evidence from literature reviewed and analyses performed on the system give valid reason to justify the viability of the design, it would still benefit from more extensive testing to better optimize it. Further testing could be achieved through more vigorous simulation using more computing than was presently available at the time, or the fabrication of a prototype.

References

1. Ishtiaq, M., Jehan, N., Khan, S.A., Muhammad, S., Saddique, U., Iftikhar, B.: Potential harmful elements in coal dust and human health risk assessment near the mining areas in Cherat, Pakistan. *Environ. Sci. Pollut. Res.* **25**(15), 14666–14673 (2018)
2. Cohen, R.A.C., Patel, A., Green, F.H.Y.: Lung disease caused by exposure to coal mine and silica dust. *Semin. Respir. Crit. Care Med.* **29**(6), 651–661 (2008)
3. Kuempel, E.D., Wheeler, M.W., Smith, R.J., Vallyathan, V., Green, F.H.Y.: Contributions of dust exposure and cigarette smoking to emphysema severity in coal miners in the United States. *Am. J. Respir. Crit. Care Med.* **180**(3), 257–264 (2009)
4. Cashdollar, K.L.: Overview of dust explosibility characteristics. *J. Loss Prev. Process Ind.* **13**, 183–199 (2000)
5. Cashdollar, K.L.: Coal dust explosibility. *J. Loss Prev. Process Ind.* **9**(1), 65–76 (1996)
6. Gao, G., Shen, J., Liang, Q.: Study of dust diffusion at transfer point of belt conveyor based on Study of dust diffusion at transfer point of belt conveyor based on FLUENT. In: *Journal of Physics: Conference Series*, vol. 1064, The 2nd International Conference on Fluid Mechanics and Industrial Applications 12–14 July 2018, Guilin, China (2018)
7. Blyth, D.: A Practical Guide to Dust Suppression. <https://www.sealpump.com/wp-content/uploads/2016/03/Kolour-GoWeb-Dust-Suppression-Booklet-whole-1.pdf>
8. Spraying Systems Middle East FZE, Water Misting Nozzles & Systems. <https://www.spray-nozzles.co.za/wp-content/uploads/2019/02/CannonJet.pdf>



Design and Fabrication of a Hand Operated Sweeping Machine

Muti Erinosho^(✉), Ester Angula, and Sam Shaanika

Department of Mechanical and Metallurgical Engineering,
University of Namibia, P.O. Box 3624, Ongwediva, Namibia
mutiuerinosho1@gmail.com

Abstract. The aim of cleaning is to keep our surroundings sanitised and avoid spreading dirt and contaminants to others and ourselves. In developing countries like Namibia, land pollution primarily results from different industrial activities such as construction, manufacturing, repairing etc. These materials are generally removed or swept by humans employed to do the job or by municipality trucks. The traditional method of sweeping has been evaluated and observed to be detrimental to human health. In order to address this issue of promoting cleanliness in the country and substitute the traditional method of cleaning with a modern mechanised method, this project presents the design and fabrication of a hand-operated sweeping machine that is eco-friendly and more cost-effective. The machine used a chain and sprocket mechanism and operated on a simple principle of centrifugal motion of cylindrical brush throwing dust particles from the ground surface onto a collector. The design model was modelled using Solidworks software and analysed. Relevant assumptions were made and mathematical formulas were applied to perform calculations on the bending moment, stresses and chain length. A physical prototype was fabricated and tested. The product was observed to cause no form of pollution or danger to the environment.

Keywords: Design · 3D model · Design concepts · Chain length · Prototype fabrication

1 Introduction

Please A sweeper or cleaner may refer to either a person's occupation, or machine that cleans streets and facilities. In the history of sweeping, street sweepers have been employed in cities since sanitation and waste removal become a priority [1]. A street-sweeping person would use a broom and shovel to clean off litter, animal waste and filth that is accumulated on ground. Later water hoses were used to wash the streets. Machines were created in the 19th century to do the job more efficiently [2]. Today, modern street sweepers are mounted on truck bodies and can vacuum debris that accumulates in streets and alongside the roads. Street sweeping either manual or mechanical has been a normal operation for most municipalities for hundreds of years. The earliest sweepers were manual efforts using a broom, shovel with either push or horse-drawn carts. Street

sweeping materials consisted of trash, dirt and vegetation. The first motorized sweeper was developed in the early 20th century [3]. The mechanical broom sweeper remains today by far the most common piece of equipment in the majority of countries to keep facilities and public places clean of gross pollutants. In present days, street sweeping materials have changed, with gross pollutants including more plastics and paper products than would have been present even 50 years ago along with discarded items associated with cars and trucks using the roadway [4]. The accumulated dirt on the ground can be collected using various techniques. Bisen et al., designed and developed a dust cleaning machine for cleaning of dust beside the road divider [5]. The principle of working of this machine is such that the motor is mounted on arm which is fixed at right side of frame and motor is operated by battery through which scrubber brush rotates and provides sweeping action. Dust is then sucked by cyclone vacuum dust collector and collected into the tank and the cyclone dust collection efficiency was calculated to be 66.69% [5]. A pedal operated sweeper for cleaning the roads and facilities was developed by Manikandan et al. [6]. In this work, the target users of the machine and form of energy required to drive the machine were presented. The machine is applicable in airport, industrial road, highways, parking, and railways platform. The energy required to drive the machine is the same as of the normal bicycle, which means that there is no need to power the device with electricity or any other forms of energy. Chain and sprockets were used to transmit the rotary motion resulting from the rear wheel onto the brush [6]. Siddanna et al., introduced a street sweeping machine which is a combination of electrical and mechanical devices. The primary objective of this work was to develop a street sweeper, which is simple and cost effective. Power source is to provide rotary motions for brushes. This system consists of DC motor, shaft and battery. The motor rotates from the power of battery. The motor is connected to shaft to which the brushes are attached. The use of the developed street sweeper resulted in a reduction of cleaning cost and drudgery involved in cleaning was completely eliminated [7]. Ashim et al., introduced a mechanically operated road sweeper that can be used in the side area of roads where dust has been piled up in maximal amount. In their design, a prototype was designed using Solidworks software and detailed mathematical calculations and the analysis for design specification of each and every part of the machine components was performed [8]. The design and fabrication of multipurpose eco-friendly cleaning machine by Praveen et al., was reviewed. The primary objective of this project was to use easily available materials with low cost and that has good mechanical properties, can be easily fabricated and easy to use and control [9]. A smart street cleaning machine for cleaning the roads, colleges, hospitals, auditoriums, malls and workshops was developed. The principle of working of the machine is such that when a pedal of cycle is started to rotate, cycle will be moving in forward direction due to the rear axle that will also be moving along with cycle. Due to this axle rotation, wheels will also rotate [10]. All the literatures under this section were critically reviewed and there was a substantial lack of evidence that the particular design with its unique features has been done. Most of the projects did not consider the constraint of weight and therefore there was difficulties in pushing those machines due to heavy weight. In addition, some mechanical sweepers introduced by various designers did not instigate the idea of reducing human effort with respect to the machines they have introduced. Namibia is a developing country and the

most common method of cleaning is still traditional method. However, this cleaning method is associated with multiples of shortcomings such as low cleaning efficiency, high labour cost, very slow and cause health hazards to individuals who does the job. Hence, this project focused on designing and fabricating a hand operated sweeping machine that is fast, cheap and more efficient.

2 Design Process and Selection

The design was selected and fabricate in the department of mechanical and metallurgical engineering at the University of Namibia, JEDS Campus based on the availability of materials. Since cleaning has become a fundamental aspect of sanitation and disease prevention such as respiratory diseases, it is of utmost important to explore and innovate new techniques of cleaning which are more reliable and efficient. The problem was investigated through emphasizing and by defining user's requirements. The most common problem associated with traditional method of cleaning, especially in developing countries like Namibia, is labour ergonomics and cost. The analysis of the mechanisms that are used in the prototype of the push on sweeper were studied. Sweeping technologies used in the world and Namibia were designed and certain information was deduced from them. Using software, the model's critical parts that are subjected to forces of high magnitude has been analysed and simulated in order to evaluate the factor of safety. The prototype of hand operated sweeping machine was fabricated using preferred local available materials, modern process and appropriate tools. The fabricated prototype was then tested to observe if its performance has met the functional requirements as desired or not. The observed data during testing were noted and rectifications were carried out to optimize the overall performance of the hand operated sweeper.

2.1 Design Concepts

Two design concepts were ideated in this design work and the best and affordable one is selected for the fabrication.

Design Concept 1

The first design concept exhibits the solar powered hand operated sweeping machine, which uses solar energy as source of energy required to charge the battery that powers the induction motor. The conventional photovoltaic cell absorbs the light energy from the sun and charge the 12 V battery. The battery stores the electrical energy and power the 25 Watts induction motor through a 240 V DC-AC inverter when cleaning is required. A spindle shaft of the motor is mounted on the pulley drive that rotates together with the motor. A smaller pulley is mounted on the shaft onto which the cylindrical tube brush is mounted. A flat belt is used to transmit power from the spindle shaft to the shaft were the sweeping brush is mounted. The pulley drive ratio is 3. As the brush rotates at a controlled speed, it experiences a clockwise torque and centrifugal force, in the same direction as torque, that drag the debris in the collector in front the brush.

The advantages of this concept are high sweeping efficiency, can be made from locally available materials and reduces human effort.

Design Concept 2

The second design concept displays the hand operated sweeping machine that requires no use of electrical or any other form of conventional energy source, but uses man power instead. The mechanism and working principle of the machine work on a simple principle mechanism of chain and sprockets. Two radial wheels each of 200 mm diameter and mass of 1.7 kg are mounted on the rear shaft of 25 mm diameter that is aligned by two pillow block bearings. The two pillow block bearings are permanently welded and resting on the frame of the machine. The cylindrical tube brush is mounted on the front shaft of 20 mm diameter. Two sprockets, (larger sprocket and smaller sprocket), having a ratio of 2, are incorporated in the system to transmit the power through the chain drive. As the operator pushes the machine forward, the rear shaft rotates together with the wheels. The fixed bigger sprocket on the rear shaft also rotates with these components and this rotary motion is transmitted to the front shaft by means of the chain drive. The advantages of this concept are easy to fabricate, low maintenance cost, light weight, reduces human effort, and no mechanical vibrations. Hence, the design concept 2 was selected due to these advantages.

3 Design Modelling

Figure 1 shows the CAD assembly of a hand operated sweeping machine, modelled using Solidworks software. The complete assembly consists of the base frame, handle, a collector, sprockets, chain drive, shaft, wheels and brush.

The base frame is one of the major components on which the various components such as shafts, bearings, brushes, collector and other components are mounted. It carries the load exerted on it due to various components and load of the garbage collected during sweeping operation. The configuration for the frame was selected such that it provides the load handling and easiness. Mild steel square tubes were used for the construction of the frame. The handle acts as the component for transmitting the manual power from hand of the operator to the frame to push the machine. The handle is made up of long mild steel square tubes, round tube and two plates, for support. The motion in horizontal plane is constrained by its rectangular configuration structure and attachment of the structure with the inclined support constraints the vertical motion the handle. The collector is used to collect the dirt dragged by the brush. The holding plate at its back is provided to stabilize it in horizontal plane, by placing it into the pin. The two handles are provided to provide the easy handling of collector and dumping of the collected debris. The collector also has an inclined sheet plate in front of it, with a clearance of 1 mm which allows the debris and sand to be easily accumulated in the collector. The two sprockets having different diameters and a ratio of 2, have been used to transmit the power acting as a spur gear varying speeds and torque. The sprocket selected in this design are made of Mild Steel and are similar to the ones of the bicycle. The chain drive is used to transmit the power from the rear shaft to the front shaft. Figure 2 illustrates the 3D model of a chain drive used in this design.



Fig. 1. CAD assembly of a hand operated sweeping machine.

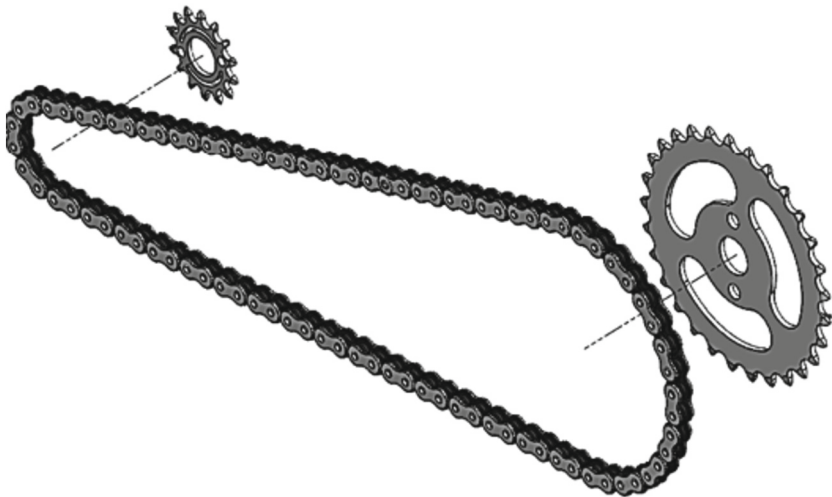


Fig. 2. Chain drive

The chain drive transfers the rotary motion in the same direction as that of the driven shaft. The mild steel bush chain was selected in this design, due to its light weight, low

cost and low slip factor. It consists of various chain components such as internal and external components. It is meshed with the sprockets into the groove between successive teeth. The two shafts carry the radial load resulting from external and internal loading, and transmit the rotational motion. Due to its strength and affordability, mild steel was also selected for the shaft material and various calculations has been done to determine the proper application of the two shafts. The brush used in the prototype fabrication was improvised due to unavailability of appropriate brush. The normal brooms were bought from local markets and a brush was constructed from those two. The brush is mounted onto the shaft using bolts and nuts that rigidly hold it in place. The core function of the brush is to sweep and pick up the garbage from the ground surface into the collector. The bristles are twisted together to provide a round shape that allows efficient sweeping. The wheels creates the rotational motion at torque to the machine due to friction between the ground and the friction of the material of the wheels when pushing the machine in the forward direction. The wheels also transfer the load subjected on the frame into the ground, absorbing vibrations and providing dynamic equilibrium of loads of the machine.

The cost analysis is an important economical aspect that has to be considered during design process. This allows the designer to evaluate and select the best alternative in terms of prices of required materials. Table 1 shows the cost analysis of the entire design project.

Table 1. Cost Analysis

Material		Description	Quantity	Cost (N\$)
Square tube	Mild Steel	5000 mm	4	206.25
Flat Bar	Mild Steel	(450 × 50 × 5) mm	1	171.50
Sprockets	Mild Steel	t = 3 mm (D = 15 mm, d = 7 mm)	2	99.99
Bush Chain	Mild Steel	L = 1340 mm	1	124.99
Flat sheet	Mild Steel	700 mm × 410 mm × 3 mm	1	260.00
Round bar	Mild Steel	D = 25 mm & d = 20 mm	2	120.00
Round tube	Mild Steel	D = 25 mm, L = 550 mm	1	25.00
Bearings	Stainless Steel	2(UCP0025) & 2(UCP0020)	4	704.78
Brush	Polypropylene bristles	280 mm × 170 mm	2	201.05
Wheels	Polypropylene	D = 200 mm & d = 75mm	4	435.2
Bolts and Nuts	Mild Steel	MM06	6	79.99
∑ Total				2428.75

4 Design Calculations and Analysis

For the shaft calculation, using the rear wheel specification Table, the speed of the rear shaft is obtained from the following relations.

The circumferential length (perimeter), $[C_L]$, of the rear wheel is given by Eq. (1):

$$C_L = \pi \times d \quad (1)$$

where, $[d]$ is the diameter of the rear wheel

The average time taken by the operator to travel a distance of 5000 mm was 12.5 s and time taken to complete one revolution of the wheel as 2.3 s. The speed of the front shaft is evaluated using the speed ratio between the sprockets. The speed ratio of the sprockets, $[S_r]$, is given by Eq. (2):

$$S_r = \frac{D}{d} \quad (2)$$

where, $[D]$ is the diameter of the larger sprocket and $[d]$ is the diameter of the smaller sprocket. To compute for the torque, the moment of inertia $[I]$, was evaluate, for both shafts, which is given by Eq. (3).

$$I = \frac{1}{2} (Mr^2) \quad (3)$$

where, $[M]$ is the mass of the shaft and $[r]$ is the radius of the shaft.

Since the torque can be evaluated using the angular velocity of the shaft, the power transmitted by the rear shaft can be computed from the relation in Eq. (4):

$$P = \frac{2\pi NT}{60} \quad (4)$$

The length of the chain $[L]$ in Eq. (5) is equal to the product of the number of chain links $[K]$ and the pitch of the chain $[p]$.

Mathematically;

$$L = K \times p \quad (5)$$

The number of chain links is given by the following relation:

$$K = \frac{T_1 + T_2}{2} + \frac{2x}{p} + \left(\frac{T_1 - T_2}{2\pi} \right)^2 \frac{p}{x} \quad (6)$$

where, $[T_1]$ and $[T_2]$ are the number of teeth on the larger sprocket and smaller sprocket respectively and $[x]$ is the centre-to-centre distance between the sprockets. Hence, the total chain length is 1185.45 mm.

To accomplish the manufacturing of the prototype, several tools and equipment have been used. Figure 3 shows the final prototype of the sweeper.

These tools include the auxiliary tools such as, measuring tools, cutting tools, marking tools and CNCs machines such as lathe machine and drilling machine. The prototype was tested on the University premises. Testing was done on a 100 m² littered plot, after fabrication in order to observe the sweeping efficiency of the machine. The problems encountered during sweeping are that some materials were too big to be dragged into the collector by the brush. Also, plastic materials tend to roll over and stuck between the chain and smaller sprocket, which caused the machine to be difficult to push.



Fig. 3. Prototype of the sweeping machine

5 Conclusion

- This design project was a success, since the prototype was successfully designed and fabricated.
- The time taken to sweep an area of 100 m², was 6 min, which is 2 times less than time taken by manual cleaning.
- The total length of the chain between the small and the large sprocket was calculated to be 1185.45 mm.
- The final product is light weight (31.2 kg) and cause negligible fatigue during sweeping and the evaluated cost was approximately N\$ 2500.

References

1. Day, C.E.: Street-cleaning problems and practices. In: Twenty-Eighth Annual Road School, pp. 171–177
2. History of Sweeping group. <https://baboregroup.wixsite.com/group/history-of-sweeping>. Accessed 23 Nov 2021
3. Pal, V., Mall, V.R., Prakash, M., Agrawal, S., Singh, V., Dharmendra, D.: Design and fabrication of brooming machine. *Int. J. Civil Mech. Energy Sci.* **5**(3), 7–11 (2019)
4. Aderinmoye, A.K., Adekunle, A.A.: Design and construction of a street sweeping machine. *Int. J. Eng. Appl. Sci. Technol.* **5**(2), 626–630 (2020)
5. Bisen, R., Ukey, A., Manohare, M., Bharti, Y., Burande, K., Bobde, S.R.: Design and development of dust cleaning machine for cleaning of dust beside the road divider. *Int. Res. J. Eng. Technol.* **7**(5), 1055–1059 (2020)

6. Sivasubramanian, S., Manikandan, M., Sabariraj, V., Vishal, S.: Design and fabrication of pedal operated hack saw. *Int. J. Eng. Res. Technol.* **6**(4), 1–4 (2018)
7. Madhu, P., Chalawadi, S.S., Srikantha N., Pinjar, R.D., Shridhara, M.: Development and Fabrication of Street Sweeping Machine. Project Reference No: 41S_BE_1941, pp. 1–3
8. Khanal, A., Bhandari, B.B., Chaudhary, P., Ghimire, A., Pandeya, D.P.: Design, Fabrication and Testing of Mechanically Operated Road Sweeper. Tribhuvan University Institute of Engineering, pp. 1–18 (2018)
9. Praveen, H., Harish Gowda, G.R., Ramageri, A.G., Kallammanavar, A., Kulkarni, P.P., Kallihal, G.B.: Design and fabrication of multipurpose eco- friendly cleaning machine. *Int. J. Res. Appl. Sci. Eng. Technol.* **6**(5), 2333–2337 (2018)
10. Meshram, S.J., Mehta, G.D.: Design and development of tricycle operated street cleaning machine. *J. Inf. Knowl. Res. Mech. Eng.* **4**(1), 702–706 (2016)



Study on Silica Content of Peat Soil and Concrete Reinforced Aluminium AA7075 Chips by Cold Compaction Method: Hardness and Physical Properties

Nurul Farahin Mohd Joharudin¹, Noradila Abdul Latif^{1,2}(✉),
Mohammad Sukri Mustapa^{1,2}, Muhd Rizuan Rusli¹, Kamarul-Azhar Kamarudin¹,
Wahyu Mulyo Utomo³, Ahmed Sahib Mahdi⁴, and Mohammed Hussein Rady⁵

- ¹ Faculty of Mechanical and Manufacturing Engineering, Universiti Tun Hussein Onn Malaysia, 86400 Parit Raja, Batu Pahat, Johor, Malaysia
farahin.joharudin@gmail.com
- ² Mechanical Failure Prevention and Reliability (MPROVE), Universiti Tun Hussein Onn Malaysia, 86400 Parit Raja, Batu Pahat, Johor, Malaysia
- ³ Faculty of Electrical and Electronic Engineering, Universiti Tun Hussein Onn Malaysia, 86400 Parit Raja, Batu Pahat, Johor, Malaysia
- ⁴ Mechanical Department, Southern Technical University, Basra, Iraq
- ⁵ Mechanical Engineering Department, University of Wasit, Kut, Iraq

Abstract. New combination of metal matrix-based composite can be used in the engineering industry due to its lightweight, high impact strength, and high fatigue life. The use of silica content in various engineering applications gives significant environmental and economic benefits. The hardness and physical properties by using reinforcements of peat soil and concrete reinforced aluminium AA7075 chips were investigated. The silica content of peat soil and concrete particles has been characterized by conducting x-ray fluorescence and field emission scanning electron microscopy with energy dispersive x-ray spectroscopy. The results show the constituent element in the peat soil and concrete was silicon dioxide which are 36.31 wt.% and 46.62 wt.%, respectively. The result of peat soil shows that the hardness was increased up to 7.5 wt.% of peat soil with 80.09 Hv 0.1 and then decreased with increasing in mass composition. The trends hardness for concrete reinforced chips shows that the hardness increased when the composition of concrete increase with the highest value at 12.5 wt.% with 71.34 Hv 0.1. The study of metal matrix-based composite from peat soil and concrete shows beneficial improving the properties of these composites, which were dependent to the composition of reinforcement, hence potentially used in engineering field.

Keywords: AA7075 chips · Concrete · Peat soil · Hardness · Cold compaction

1 Introduction

Any substance that contains two or more different materials is referred to as a composite material. Organic, metal, or ceramic can all be used as the base material. A composite material is a mixture of two or more materials with good mechanical properties compared to those of individual components [1]. Better physical characteristics, low weight, high strength, high fatigue strength, and high surface smoothness and appearance are the significant features of composite materials [1–3]. When compared to conventional materials, the novel material may be employed to achieve the goals of good strength, lower weight, and corrosion resistance. Concrete reinforcement, epoxy reinforced with graphite or carbon fibres, and other materials are examples of composite systems. Composite materials are a specific type of material that may be utilised for structural elements as well as applications in the automotive and aerospace industries. Aluminium with silicon carbide reinforcement replaced the present parts that were manufactured using aluminium oxide reinforcement in aluminium metal matrix-based composites to enhance the properties [4, 5].

Metal matrix composite materials made of aluminium are useful in aerospace and engineering. Hybrid metal matrix composite is a term used to describe a mixture of at least three metal alloys or reinforcing materials of two types that have been atomically bonded together in various forms [6]. A study was conducted on the various aluminium metal matrix composite gears that are often used in the power transmission systems of automobiles and other types of machinery to transmit power. Aluminium metal matrix material composites were preferred primarily because of their excellent mechanical characteristics and light weight, making them ideal for producing lightweight automotive components. Materials used in this study project were Al 6061-T6, Al 6106-T6, Al 7050-T7451, and Al 7075-T651 [6, 7].

Metal matrix-based composites are being used more commonly in engineering. This was mostly caused by the lightweight and good strength of composite materials. In this study, aluminium-silicon carbide-boron carbide (Al-SiC-B₄C) based metal matrix composite was produced using mechanically alloyed ball milling and powder metallurgical approaches [8]. There are two methods for determining the dynamic behaviour of carbon fibre reinforced polymer leaf springs [9, 10]. For this, an impact test was used. Three distinct composite springs were examined, with a steel spring serving as the basic application. Stir casting, powder metallurgy, and centrifugal casting are the most common methods used to create composite materials made of aluminium [11]. A connecting rod for automobiles is made of a metal that's been reinforced with aluminium oxide. Wing panels for aeroplanes is made from aluminium that has been strengthened with silicon carbide whiskers. For rocket and helicopter manufacture, graphite fibres are employed in the aluminium matrix [12]. For the structures of satellites and spacecraft, graphite fibres are employed in the magnesium matrix [12]. The most of conventional auto parts, such piston stems, brake drums, and connecting rods, have been replaced with composite materials based on metal matrix [13]. The investigation focused on the metal matrix-based composite advanced materials, which were employed in applications for the auto and aircraft industries because of their good mechanical characteristics, low weight, and creep resistance [13]. The majority of engineering and structural applications may employ composite materials because of their thermal and mechanical qualities, ease of

development, and low cost [14, 15]. The analysis of data from previous and current years indicates that metal matrix composites have a significant potential for the development of automotive components.

The light material is designed to replace outdated, conventional steel automotive components. The design, production, and development of automotive components may be expedited using metal matrix composite. The uses of natural materials or waste is one innovation for reducing production costs in aluminium composite manufacture. Previously, the employment of industrial and agricultural waste such as fly ash, rice husk ash, and bagasse ash had been widely developed [16–18]. In previous finding, sea sand was used as a concrete aggregate [19, 20]. However, because sea sand contains chemical components like aluminium oxide, silicon dioxide, and titanium dioxide, high-tech materials like composites might be made from this material. The world can transition into a new lightweight and very durable material due to recent research in this area. This knowledge assists researchers' studies into novel metal matrix composite materials used to produce automotive components and offers a way for the globe to move toward a healthy and green environment. This study aims to compare the hardness and physical properties of peat soil and concrete particles reinforced metal matrix of aluminium AA7075 chips.

2 Experimental Material and Procedure

2.1 Materials

Metal matrix used in this study was an aluminium AA7075 recycling chips with weight percentages in chemical composition of aluminium = 87.18 wt.%, zinc = 9.49 wt.%, copper = 2.59 wt.%, silicon = 0.31 wt.%, chromium = 0.28 wt.% and others = 0.15 wt.% [18]. The as-received block of aluminium AA7075 was turned into chip produced by the computer numerical control of high-speed milling machine model Mazak Nexus 410A-II CNC Mill, with parameter setup of feed rate at 1100 mm/min, depth cut of 1 mm and cutting of velocity at 345 m/min. The chips were then cleaned using ultrasonic bath apparatus model FRITSCHE ultrasonic cleaner Labarett 17, for 1 h by using acetone solution (CH_3COCH_3) to remove substances such as oil and grease that attached to the chips during milling process. To remove the remaining acetone from the chip, the drying process was carried out for 1 h at 75 °C using drying oven [21, 22].

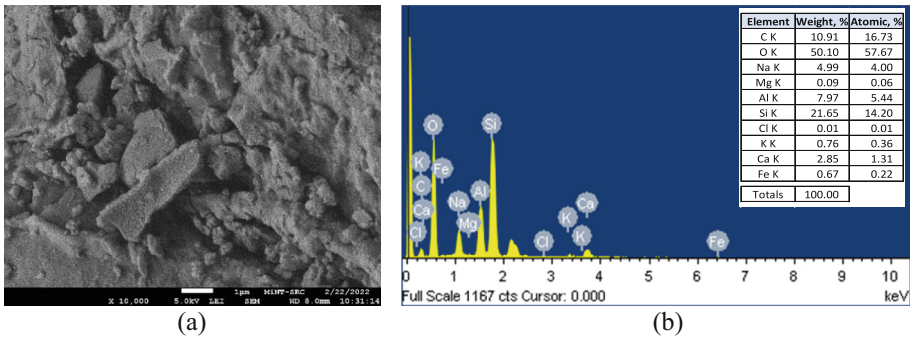
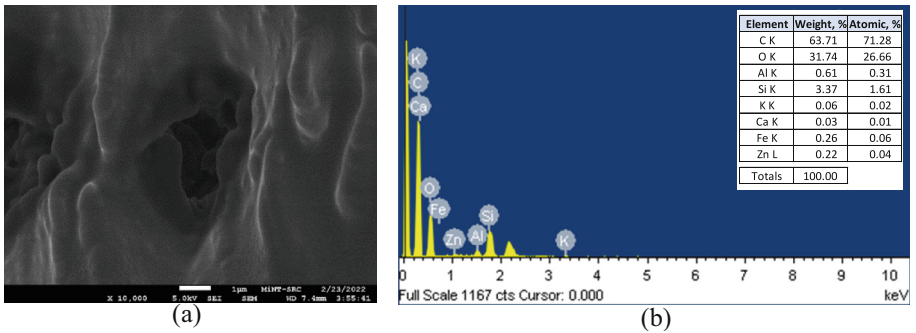
The reinforcement materials used in this study i.e., peat soil and concrete particles. These reinforcement materials have been used because of its main composition is silicon dioxide (SiO_2) known as silica. The characterization of chemical composition was conducted by using x-ray fluorescence (XRF) analysis for peat soil and concrete particles, Table 1 and Table 2, respectively. The reinforcement materials also have been characterized by using field emission scanning electron microscopy with energy dispersive x-ray spectroscopy (FESEM-EDX) to provides topographical and the elemental composition of materials for peat soil and concrete particles, Fig. 1 and Fig. 2, respectively. In the preparation of reinforcement materials, a ball mill was used to obtain smaller particle size using a high impact mill with a porcelain jar for 10 min. The particle size of 63 μm was then separated using a vibrator type apparatus model FRITSCHE-analysette 3, during 30 min at amplitude of 1.

Table 1. Chemical composition of peat soil material in weight percentage (wt.%).

SiO ₂	CaO	Fe ₂ O ₃	Al ₂ O ₃	SO ₃	P ₂ O ₅	Cl	TiO ₂	K ₂ O	CuO	ZnO	Others
36.39	22.01	16.02	8.37	8.16	2.75	2.12	1.52	1.04	0.65	0.28	0.68

Table 2. Chemical composition of concrete in weight percentage (wt.%).

SiO ₂	CaO	Al ₂ O ₃	Fe ₂ O ₃	K ₂ O	SO ₃	MgO	P ₂ O ₅	TiO ₂	Cl	Others
46.62	33.43	7.98	6.60	2.03	1.48	0.55	0.44	0.34	0.18	0.34

**Fig. 1.** Topographical and the elemental composition of peat soil; (a) FESEM, (b) EDX.**Fig. 2.** Topographical and the elemental composition of concrete; (a) FESEM, (b) EDX.

2.2 Preparation of Samples

The samples preparation of metal matrix based-composites by using powder metallurgy method. The composition of metal matrix based-composite mixing is prepared, Table 3. The mixed materials were then are poured into the mould to produce samples using the uniaxial hydraulic press machine model Carver model 3851-0, with setting parameters

of compaction at load of 9 tons with the holding time of 20 min. The samples were then sintered by using tube furnace under controlled parameter. The zinc stearate burned out after 30 min at 300 °C, and the sintering process began within 60 min at 552 °C [22].

Table 3. The composition of recycling aluminium AA7075 chips with reinforcement particles.

Reinforcement particles	Composition of metal matrix based-composite
None	100 wt.% of AA7075 chips
Peat soil (PS)	97.5 wt.% of AA7075 chips + 2.5 wt.% of PS 95.0 wt.% of AA7075 chips + 5.0 wt.% of PS 92.5 wt.% of AA7075 chips + 7.5 wt.% of PS 90.0 wt.% of AA7075 chips + 10.0 wt.% of PS 87.5 wt.% of AA7075 chips + 12.5 wt.% of PS
Concrete (C)	97.5 wt.% of AA7075 chips + 2.5 wt.% of C 95.0 wt.% of AA7075 chips + 5.0 wt.% of C 92.5 wt.% of AA7075 chips + 7.5 wt.% of C 90.0 wt.% of AA7075 chips + 10.0 wt.% of C 87.5 wt.% of AA7075 chips + 12.5 wt.% of C

2.3 Analysis of Samples

The Vickers method was used for the hardness test, which was followed by the standard ASTM E-384. The Vickers hardness test machine equipped with a diamond indenter, with eight indenters used to determine the average. The physical test consists of measuring the density (g/cm^3), porosity (%), and water absorption (%) of metal matrix based-composites using the Archimedes Principle was conducted by using an electronic balance from Mettler Toledo Germany. The analysis was conducted in accordance with ASTM B328 for density and ASTM B962–17 for porosity.

3 Results and Discussion

3.1 Hardness

The comparison of hardness between peat soil and concrete particles reinforced aluminium AA7075 chips, Fig. 3. The hardness of fully aluminium AA7075 chips used in this study is 53.49 Hv 0.1. The addition of peat soil particles as reinforcement has showing the increasing of the hardness. At the composition of 2.5 wt.% of peat soil, the hardness is 67.59 Hv 0.1 which is higher than hardness of unreinforced sample. The hardness of peat soil is enhanced up to 7.5 wt.% of peat soil with 80.09 Hv 0.1 and subsequently decreases with increasing mass composition. The addition of concrete as reinforcement also has showing the increasing of the hardness when the addition of 2.5 wt.% of concrete is 55.63 Hv 0.1. The hardness trends for concrete particles reinforced aluminium AA7075 chips revealed that the hardness increased as the concrete

composition increased, with the highest value at 12.5 wt.% and 71.34 Hv 0.1. Previous study reported that range of hardness of rice husk ash reinforced aluminium chips was 55.33 to 63.02 Hv [18]. Meanwhile, other researchers found that the addition of silica sand as reinforcement of aluminium matrix increased the hardness of metal matrix composites up to 15 wt.% at 25 HB [23]. In summary, it revealed that the better hardness significantly for silica reinforced aluminium matrix. Hence, silica reinforcements essential to improve the behaviour of metal matrix composite compared to the unreinforced aluminium matrix composite.

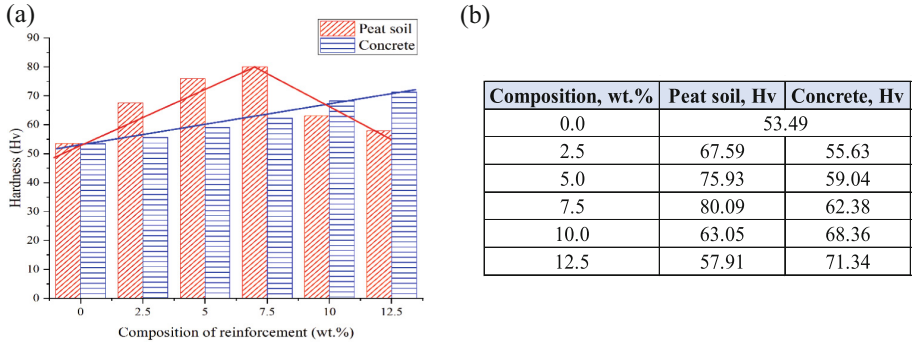


Fig. 3. The comparison hardness between peat soil and concrete particles reinforced aluminium AA7075 chips; (a) Graph of hardness, (b) Table data of hardness.

3.2 Physical Properties

The density of peat soil and concrete particles reinforced aluminium AA7075 chips, Fig. 4(a). The range of density for fully aluminium chips and reinforced aluminium composites was 2.34 g/cm^3 to 2.46 g/cm^3 , which is density independently to the composition of reinforcements. The graph of porosity and water absorption of peat soil and concrete particles reinforced aluminium AA7075 chips shows the same trends as higher the density, lower the porosity and water absorption, Fig. 4(b) and Fig. 4(c), respectively. Porosity and water absorption were dependence to the hardness for peat soil and concrete particles reinforced aluminium AA7075 chips, respectively. Silica content in reinforcement is influence to the porosity and water absorption prop. The physical properties of aluminium reinforced silica sand were observed to decrease as the weight fraction of silica increased for density whereas porosity was higher, respectively [24]. The improvement in physical properties can be directly correlated to the development of better material.

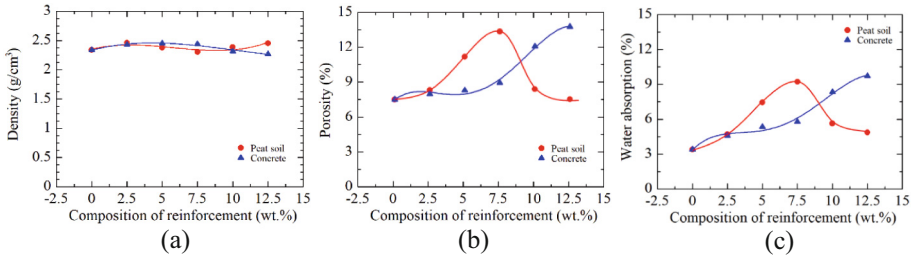


Fig. 4. The graph of physical properties of peat soil and concrete reinforced aluminium AA7075 chip; (a) Density, (b) Porosity, (c) Water absorption.

4 Conclusions

To conclude this study, peat soil and concrete was a potentially used as reinforcement agent for aluminium AA7075 chips. The source of silica from peat soil and concrete particles can be used to replace conventional silica sources. Industrial waste such as aluminium AA7075 chips also can be recycled into metal matrix composite that can be used in manufacturing of lightweight products in engineering fields. The addition of peat soil and concrete as a reinforcement for the metal matrix composite produced an increasing on the hardness of the material compare to fully aluminium AA7075 chips. The hardness of aluminium AA7075 chips was improved to 80.09 Hv 0.1 by adding 7.5 wt.% of peat soil reinforcement. Similar results produced when the concrete is used as reinforcement to the aluminium AA7075 chips. The hardness of metal matrix composite was influenced to the composition while it was dependently to the density at increasing composition. Subsequently, the hardness was dependent to the porosity and water absorption for both peat soil and concrete particles reinforced aluminium AA7075 chips.

Acknowledgement. This research was supported by the Universiti Tun Hussein Onn Malaysia through the TIER 1 Grant Scheme, grant No. Q147. We also want to thank the Universiti Tun Hussein Onn Malaysia for sponsoring this work under research grant K067.

References




1. Ngo, T. (ed.): Composite and Nanocomposite Materials - From Knowledge to Industrial Applications. IntechOpen (2020)
2. Singh, H., Brar, G.S., Kumar, H., Aggarwal, V.: A review on metal matrix composite for automobile applications. *Mater. Today: Proc.* **43**, 320–325 (2021)
3. Che Berhanuddin, N.I., Mohd Rozlan, S.A., Zaman, I., Mustapa, M.S., Abdullah, M.E., Bahrudin, I.A.: Effect of thermal expansion and sonication on mechanical properties and adhesive toughness measurement of polymer/graphene composite. *Mater. Sci. Forum* **889**, 14–18 (2017)
4. Chandio, A.D., Ansari, M.B., Hussain, S., Siddiqui, M.A.: Silicon carbide effect as reinforcement on aluminium metal matrix composite. *J.-Chem. Soc. Pak.* **41**, 650–654 (2019)

5. Alaneme, K.K., Adetomilola, V.F., Nthabiseng, B.M.: Development of aluminium-based composites reinforced with steel and graphite particles: structural, mechanical and wear characterization. *J. Market. Res.* **8**(1), 670–682 (2019)
6. Senthilkumar, T.S., Venkatesh, S.A., Kumar, R., Kumar, S.S.: Evaluation of mechanical properties of Al-6082 based hybrid metal matrix composite. *J. Chem. Pharm. Res.* **8**, 58–64 (2016)
7. Prawoto, Y., Ikeda, M., Manville, S.K., Nishikawa, A.: Design and failure modes of automotive suspension springs. *Eng. Fail. Anal.* **15**(8), 1155–1174 (2008)
8. Bodukuria, A.K., Eswaraiab, K., Rajendra, K., Sampatha, V.: Fabrications of Al- SiC-B4C metal matrix composite by powder metallurgy and evaluating mechanical properties. *Perspect. Sci.* **30**, 266–274 (2017)
9. Mouleeswaran, S., Vijayaragan, S.: Analytical and experimental studies on fatigue life prediction of steel and composite leaf spring for light passenger vehicles using life data analysis. *Mater. Sci.* **13**, 141–146 (2007)
10. Subramanian, C., Senthilvelan, S.: Effect of reinforced fiber length on the joint performance of thermoplastic leaf spring. *Mater. Des.* **31**(8), 3733–3741 (2010)
11. Verma, R.K., Parganiha, D., Chopkar, M.: A review on fabrication and characteristics of functionally graded aluminum matrix composites fabricated by centrifugal casting method. *SN Appl. Sci.* **3**, 227 (2021)
12. Nturanabo, F., Masu, L., Kirabira, J.B.: Novel applications of aluminium metal matrix composites. In: *Aluminium Alloys and Composites*. IntechOpen (2019)
13. Singla, M., Dwivedi, D.D., Singh, L., Chawla, V.: Development of aluminum-based silicon carbide particulate metal matrix composite. *J. Miner. Mater. Character. Eng.* **8**, 455–467 (2009)
14. Layth, M., Ansari, M.N.M., Pua, G., Jawaid, M., Islam, M.S.: A review on natural fiber reinforced polymer composite and its applications. *Int. J. Polymer Sci.* **2015**, 24394 (2015)
15. Abdul Latif, N., Mohd Joharudin, N.F., Ismail, F.H., Mustapa, M.S.: Effect of strain rates on tensile properties of kenaf fiber and rice husk silica reinforced polypropylene composites. *Int. J. Integr. Eng.* **11**(5), 174–179 (2019)
16. Bharathi, V., Ramachandra, M., Srinivas, S.: Influence of Fly Ash content in Aluminium matrix composite produced by stir-squeeze casting on the scratching abrasion resistance, hardness and density levels. *Mater. Today: Proc.* **4**(8), 7397–7405 (2017)
17. Sounthararajan, V.M.: Dynamic modulus of elasticity of sugar cane bagasse ash in fiber reinforced concrete by using ultrasonic pulse velocity. *Int. J. Civil Eng. Technol.* **9**, 166–175 (2018)
18. Mohd Joharudin, N.F., et al.: Effect of amorphous silica by rice husk ash on physical properties and microstructures of recycled aluminium chip AA7075. *Materialwissenschaft Werkstofftech.* **50**(3), 283–288 (2019)
19. Xiao, J., Qiang, C., Nanni, A., Zhang, K.: Use of sea-sand and seawater in concrete construction: current status and future opportunities. *Constr. Build. Mater.* **155**, 1101–1111 (2017)
20. Zhang, Q., Xiao, J., Liao, Q., Duan, Z.: Structural behavior of seawater sea-sand concrete shear wall reinforced with GFRP bars. *Eng. Struct.* **189**(3), 458–470 (2019)
21. Joharudin, N.F.M., Latif, N.A., Mustapa, M.S., Badarulzaman, N.A.: Effects of untreated and treated rice husk ash on physical properties of recycled aluminium chip AA7075. *Int. J. Integr. Eng.* **12**(1), 132–137 (2020)
22. Latif, N.A., et al.: Crystalline rice husk silica reinforced AA7075 aluminium chips by cold compaction method. *Materialwissenschaft Werkstofftech.* **52**(10), 1121–1128 (2021)
23. Khamsuk, S., Joosawat, A., Panomtong, N., Wongtimnoi, K.: Enhancement of mechanical properties of porous aluminum by silica sand particles. *IOP Conf. Series: Mater. Sci. Eng.* **244**, 012024 (2017)

24. Daniel-Mkpume, C.C., Okonkwo, E.G., Aigbodion, V.S., Offor, P.O., Nnakwo, K.C.: Silica sand modified aluminium composite: an empirical study of the physical, mechanical and morphological properties. *Mater. Res. Exp.* **6**, 076539 (2019)



Numerical Modeling of an Open-Flow PV/T Cooling Collector

Amged Al Ezzi¹ , Hasanain A. Abdul Wahhab² , and Raed A. Jessam¹ 

¹ Electromechanical Engineering Department, University of Technology- Iraq, Baghdad, Iraq

² Training and Workshop Center, University of Technology- Iraq, Baghdad, Iraq
20085@uotechnology.edu.iq

Abstract. This paper presents computational simulation results of an open-flow flat plate water cooling collector attached to the rear side of a PV panel to extract the excessive heat from the PV panel. The numerical analysis was carried out using ANSYS FLUENT 17.0 by solving 3D conservative equations of mass, momentum and energy and utilizing the $k-\epsilon$ turbulent model and near-wall treatment for standard wall functions. The open-flow cooling collector included a matrix of 120 cube bulges with dimensions $15 \times 15 \times 15$ mm arranged in 8 rows and 15 columns. The bulges were fixed on the bottom of the upper surface of the cooling collector. Four values of water flow rates of 1.5, 2.0, 2.5, and 3.5 l/min were tested. The numerical simulation showed that increased cooling water flow rates lead to a decrease in the thermal energy release rate through a decrease in the temperature difference. The results show that the water temperature difference between the outlet and inlet decreases with increasing water flow rates by 7.8%, 11.7% and 14.9% when changing the flow rates from 1.5 to 2.0, 2.5, and 3.5 l/min, respectively. The highest temperature difference is at the lowest flow rate.

Keywords: PV/T collector · Open-Flow Collector · Solar Collector Simulation

1 Introduction

In 1973, the scientist Bo'ër proposed the first hybrid antenna to collect solar energy [1, 2] and the idea was originally created to assemble photovoltaic cells and thermal systems. These systems themselves depend, to a great extent, on solar energy. For this reason, experiments and studies were accomplished in the past, and till now, the process has been continued [3, 4]. The hybrid solar collector has many advantages, including its being lightweight compared to other collectors like electrical and thermal units, low cost, and aesthetically better than other systems. It repurposes high heat, which usually decreases the efficiency of a system. Subsequently, it is more efficient, takes less space, does not emit harmful gases, and does not make any noise and thus can be used in urban areas [5, 6]. Othman et al. [7] theoretical and practical investigations of the influence of the fins on the solar hybrid air collector were conducted to quantify the thermal and electrical efficiency. Use air as a heat transfer fluid for solar cells and boost electrical efficiency. It was determined that a cooling medium such as fins is required. Lowering

the operating temperature helps to get a decent level. The fins are crucial for developing absorbent elements to accomplish the PV/T hybrid's high-power thermal and electrical efficiency [8–11]. Rahou et al. [12] designed and tested solar roofing systems to enhance electricity efficiency and supply on-site hot water applications are covered. The systems are composed of an ordered succession of amorphous solar cells with an oscillating flux linked by glass wool from the bottom of the photovoltaic panel.

With a combined efficiency of 70.53% to 81.5%, the PV/T collector is fitted for a portable solar tracker that can be de, for example, mass flow rate and signed to expose to the greatest amount of radiation with changing variables such as mass flow rate and solar radiation [13–15]. Mohd et al. [16] studied solar radiation performance in electrical and thermal energy and several experiments using photovoltaic panels and a photovoltaic /thermoelectric collector. The experiment was conducted on a PV/T complex with mass flow rates ranging from 0.012 kg/s to 0.0255 kg/s. Water flows into the PV/T collector via convection by absorbing stainless steel aids in heat transmission. With rising radiation, production rises. The effectiveness of PVT changes with radiation intensity. An energy plus stress study was performed. The overall power output was compared to the power output of the PV panel without absorption. For 700 W/m^2 , the electrical power grew by 22.48%, whereas for 900 W/m^2 , it climbed by 20.87% [17, 18].

A new cooling method by a backside water tank is investigated experimentally and numerically by Reda et al. [20], Al-Kayiem, et al. [21], and Reda et al. [22]. They circulated the cooling water between the water tank and an underground ground-buried heat exchanger. They claimed that their approach solved two problems in PV technology. First, they managed to reduce the PV surface temperature during the hot daytime and warm the PV module at night to eliminate the condensate formation. Eliminating the condensate eradicates the formation of a mud layer on the PV surface.

Hybrid solar PV/T generates electricity and heats air and water. All previous research studies propose a new PV cooling have demonstrated that researchers are eager to find a way to harness solar energy. In this paper, a new design of PV/T cooling collector has been studied. The objective is to investigate the system performance at various water flow rates. The computationally simulated transient thermal behavior of the PV/T cooling collector system was accomplished using ANSYS fluent 17.0.

2 CFD Simulation of Open-flow Cooling Collector

For engineering applications, CFD simulation techniques are a powerful tool for modeling thermo fluid problems and analyzing their physical phenomena at various design and operational parameters. The radiation model pre-processing tool in the commercial CFD software ANSYS 17.0 FLUENT was used in the current simulation. (Provides a solar load model for calculating radiation effects from sun rays entering a computational domain) SolidWorks ver. 2017, are used to model and simulate the open-flow flat solar collector. A new model under different conditions was suggested. Several steps have been followed to complete the successful simulation, as depicted in Fig. 1.

The standard $k-\varepsilon$ model has been used to analyze the new cooling system in two important ways: the realizable $k-\varepsilon$ model contains an alternative formulation for the turbulent viscosity, and a modified transport equation for the dissipation rate, ε , has been

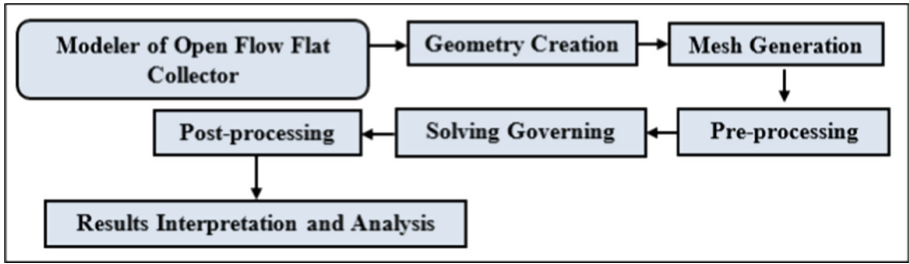


Fig. 1. Simulation steps in ANSYS 17.0.

derived from an exact equation for the transport of the mean-square vorticity fluctuation. The turbulence kinetic energy, k , and its rate of dissipation, ε , are obtained from the following transport equations:

$$\frac{\partial}{\partial t}(\rho E) + \frac{\partial}{\partial x_i}[u_i(\rho E + p)] = \frac{\partial}{\partial x_j} \left(k_{eff} \frac{\partial T}{\partial x_j} + u_i(\tau_{ij})_{eff} \right) + S_h \tag{1}$$

$$(\tau_{ij})_{eff} = \mu_{eff} \left(\frac{\partial u_j}{\partial x_i} + \frac{\partial u_i}{\partial x_j} \right) - \frac{2}{3} \mu_{eff} \frac{\partial u_k}{\partial x_k} \delta_{ij} \tag{2}$$

where E is the total energy, k_{eff} is the effective thermal conductivity, and $(\tau_{ij})_{eff}$ is the deviatoric stress tensor.

$$k_{eff} = k + \frac{cp\mu_t}{Pr_t} \tag{3}$$

where k , in this case, is thermal conductivity. The default value of the turbulent Prandtl number is 0.85. And in the case k- ε model, the effective thermal conductivity is

$$k_{eff} = \alpha c_p \mu_{eff} \tag{4}$$

The coefficient, α is calculated from $\alpha_o = 1/Pr$

A computational fluid dynamics (CFD) model is developed to simulate and investigate the heat transfer from the PV panels to the cooling system for various shapes and parameters, such as inlet water temperatures and water flow rates. Preparing a computational domain is the first step in CFD simulation. The computational model of the new cooling system is a 3D open-flow PV cooling model created in Solidworks software. The computational model is shown in Fig. 2. This cooling system is designed with 120 cubic bulges. The dimensions of the cooling chamber are 600 mm width \times 1100 mm length \times 30 mm thickness. The water inlet and outlet pipe’s diameters are 13 mm. Cubic bulges, made of Aluminum, have 15 \times 15 \times 15 mm, as shown in Fig. 3.

The governing equations are solved in numerical computational cells. Unstructured meshing is used to mesh the collector domain with tetrahedral elements. Because of the complex geometry, unstructured tetrahedral meshing was chosen. A mesh-independent solution is recommended to remove the influence of mesh size. When the grid size does not affect the solution, the optimal grid size is chosen. The 3D meshed geometrical open-flow cooling collector model is shown in Fig. 4. The fine meshing scheme produced

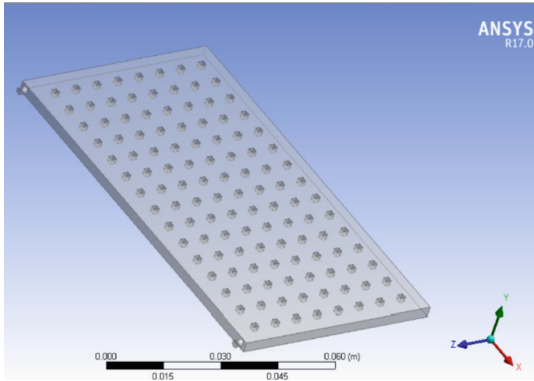


Fig. 2. Computational domain prepared of open flow cooling collector.

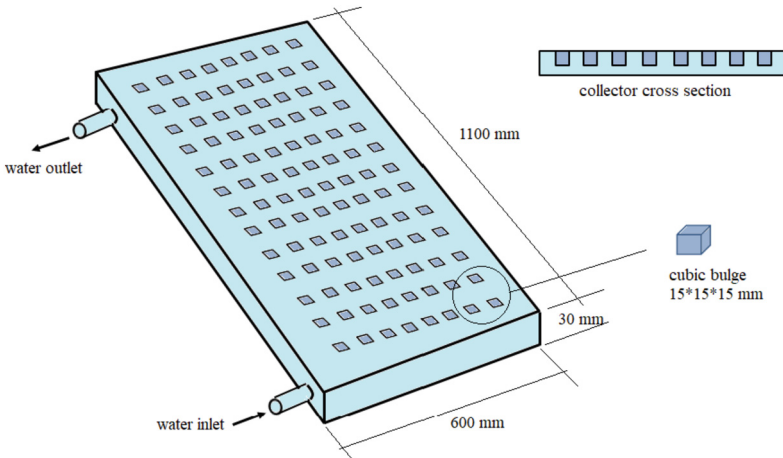


Fig. 3. Cooling collector geometry with internal bulge details.

the most accurate and comparable results for heat transfer inside the cooling collector, velocity, and temperature distribution behavior under the influence of a bulge shape. As a result, the fine mesh was chosen for the simulations and result interpretation. The computational model had 96914 nodes and 564314 fine mesh elements.

The model is used to calculate the PV/T system's values. Input parameters, which are temperature and water mass rate. Table II shows the numerical parameters chosen at the cooling collector inlet and outlet. The numerical simulation was then performed for the same real conditions. The FPC numerical simulation was successfully completed, and the results were compared to experimental measurements in the literature. Using significant values of the same parameters, the effects of increasing temperature, water flow rate, and bugles shape on cooling collector performance were investigated further. The simulation variables are configured in Table 1. These parameters and variables were fed into the CFD simulation as inputs, and the output parameters were related

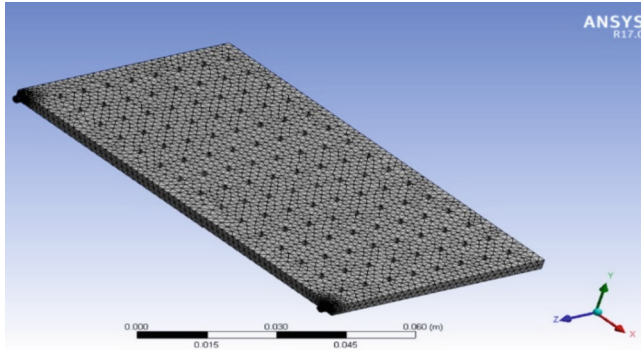


Fig. 4. Meshing criteria of the cooling system model.

to temperature distribution, pressure distribution, velocity gradation of tangential and vertical components, and so on.

Table 1. Simulation parameters.

Temperatures	Water flow rates	Initial-reference values
As measured in the experiment, within ranges of Tw.in = 303–314 K Tamb = 303–308 K NOTE: Input from experimental data	1.5 l/min 2.0 l/min 2.5 l/min 3.5 l/min	Water Density = 1000 kg/m ³ Water Viscosity = 1.0016 kg/m.s Solar irradiance = 29 to 1112 W/m ² , as measured in the experimental investigation Gravitational acceleration = – 9.81 m/s ²

3 Results and Discussion

Figure 5 shows the contours of temperature distribution of the proposed model of the open flow cooling collector for different flow rates 1.5, 2.0, 2.5, and 3.5 l/min at noon. Case (a) for the water flow rate was 1.5 l/min at noon, while the cases (b) to (d) for water flow rate were 2, 2.5, and 3.5 l/min at 12:00 pm, respectively. It can be seen that with the increased water flow rate, the upper cover temperature decreases at the same solar radiation conditions. In the mid position of the open flow cooling collector, the upper cover temperatures are found for different water flow rates of 1.5, 2.0, 2.5, and 3.5 l/min are 326.6 K, 321.4 K, 318.5 K and 313.4 K, respectively. The total reduction percentage for the upper surface temperature of the cooling system for different water flow rates 1.5, 2.0, 2.5, and 3.5 l/min were 6.4, 9.8, and 11.08%, respectively, at 12:00 pm. This decrease in the upper collector surface temperature is due to the cooling capacity the high temperature of the water. This result is close to the experiments of Said A. [19], where the cooling reduction ratio was 3% between the cooled collectors at a flow rate of 1.5 l/min.

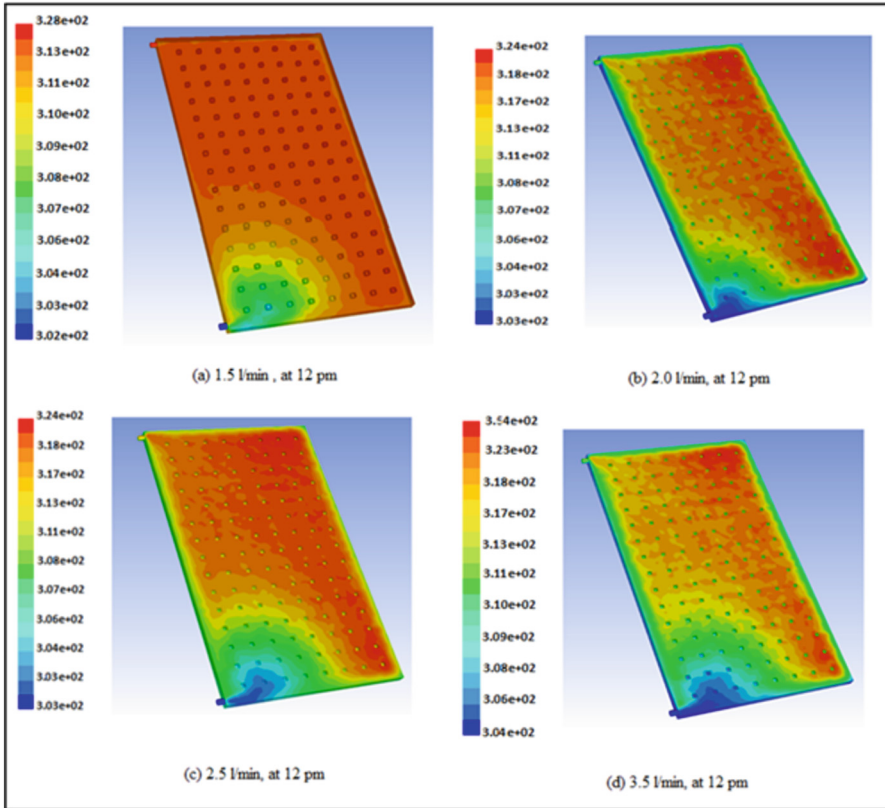


Fig. 5. Contours of temperature distribution for the new cooling system, for different water flow rates at 12:00 pm.; (a) 1.5 l/min, (b) 2.0 l/min, (c) 2.5 l/min, and (d) 3.5 l/min.

Figure 6 represents the relationship of water temperature difference between inlet and outlet of the cooling collector (ΔT) with daily time at different water flow rates. The net addition water heat has been chosen as the comparison parameter at basic value at water flow rate 1.5 l/min. In detail, the curves show a good agreement with increasing time, also the increase of inlet water flow rate reduces ΔT during a daily time. It can be notice from the numerical results when cooling with water and releasing different flow rates that the higher the flow rate, the lower the temperature difference, while the highest difference is at the lowest flow rate. Theoretical results showed that the difference in inlet and outlet temperatures decreases with increasing water flow rates, with the decreasing percentages being 7.8%, 11.7% and 14.9% when changing the flow rates to 2.0, 2.5, and 3.5 l/min, respectively.

Figure 7 represents the relationship between the average upper surface temperatures of the new cooling collector with the daily time. It can be noticed that the higher the flow rate, the lower the collector temperature due to cooling, and there is an improvement in the system parameters such as efficiency and energy gained. The results show that the average temperature of the upper surface of the cooling collector decreases with the

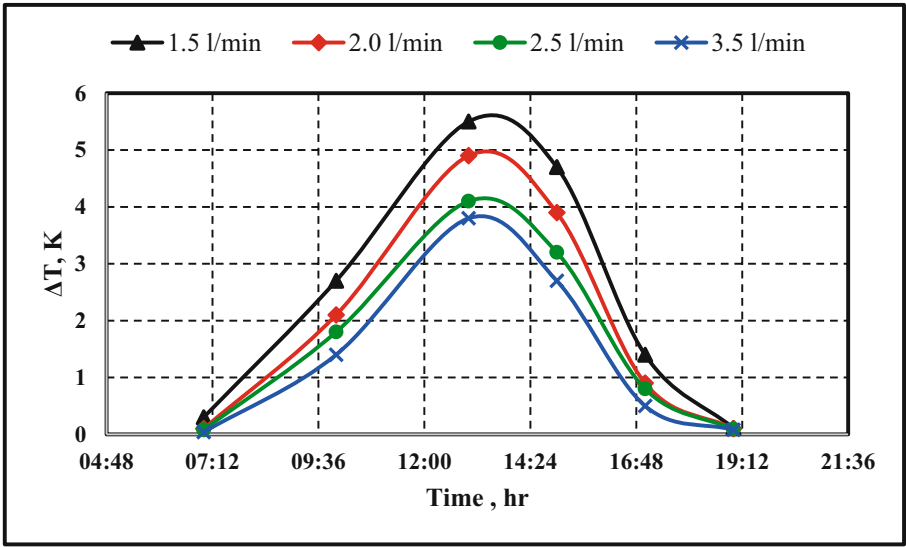


Fig. 6. Simulated transient behavior of the water temperature difference between the inlet and outlet for the cooling system at different water flow rates.

increase in water rates where the decreasing rates were 3.2%, 4.8%, and 5.9% when changing the flow rates to 2, 2.5, and 3.5 l/min, respectively.

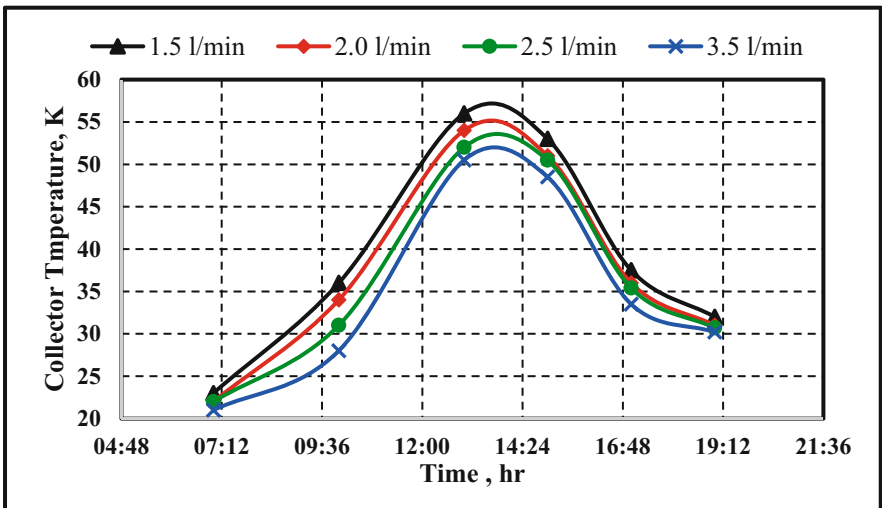


Fig. 7. Simulated average temperature of upper surface the cooling collector at different water flow rates.

4 Conclusions

This work describes a numerical analysis to study the influence of water flow rates through an open flow cooling collector with a new design for PV/T cooling. The temperature distribution for different water flow rates with 120 cubic bulges fixed on the bottom of the upper cover of the cooling collector have been studied. The following conclusions are drawn:

- The numerical results showed that the difference in inlet and outlet temperatures decreases with increasing water flow rates, by 7.8%, 11.7% and 14.9% when changing the flow rates to 2.0, 2.5, and 3.5 l/min, respectively.
- The average temperature of the upper surface of the cooling collector decreases with the increase in water rates by 3.2%, 4.8%, and 5.9% when changing the flow rates to 2, 2.5, and 3.5 l/min, respectively.

References

1. Al-Maliki, W.A.K., Al-Hasnawi, A.G.T., Wahhab, H.A.A., Alobaid, F., Epple, B.A.: Comparison study on the improved operation strategy for a parabolic trough solar power plant in Spain. *Appl. Sci.* **119**, 576 (2021)
2. Wahhab, H.A.A., Al-Maliki, W.A.K.: Application of a solar chimney power plant to electrical generation in covered agricultural fields. *IOP Conf. Ser. Mater. Sci. Eng.* **671**, 012137 (2020)
3. Al-Maliki, W.A.K., et al.: A comparison study on the improved operation strategy for a parabolic trough solar power plant in Spain. *Appl. Sci.* **11**(20), 9576 (2021)
4. Al-Maliki, W.A.K., et al.: Advances in process modelling and simulation of parabolic trough power plants: a review. *Energies* **15**(15), 5512 (2022)
5. Kazem, H.A., Chaichan, M.T., Yousif, J.H.: Evaluation of oscillatory flow photovoltaic/thermal system in Oman. *Int. J. Comput. Appl. Sci.* **1**, 429–436 (2019)
6. Alrahman, C.A.: Master Level Thesis European Solar Engineering School No. 200, August 2015 Evaluation of a PVT Air Collector Master, 215 (2016)
7. Othman, M.Y., et al.: Performance studies on a finned double-pass photovoltaic-thermal (PV/T) solar collector. *Desalination* **209**(1–3), 43–49 (2007)
8. Joshi, A.S., et al.: Performance evaluation of a hybrid photovoltaic thermal (PV/T) (glass-to-glass) system. *Int. J. Therm. Sci.* **48**(1), 154–164 (2009)
9. Jin, G.L., et al.: Evaluation of single-pass photovoltaic-thermal air collector with rectangle tunnel absorber. *Am. J. Appl. Sci.* **7**(2), 277 (2010)
10. Sarhaddi, F., et al.: An improved thermal and electrical model for a solar photovoltaic thermal (PV/T) air collector. *Appl. Energy* **87**(7), 2328–2339 (2010)
11. Ismaeel, A.A., Wahhab, H.A.A., Naji, Z.H.: Performance evaluation of updraft air tower power plant integrated with double skin solar air heater (2021)
12. Rahou, M., et al.: Performance study of a photovoltaic thermal system with an oscillatory flow design. *J. Solar Energy Eng.* **136**(1), 011012 (2014)
13. Michae, L., Joe, J., Selvarasan, I.: Experimental investigation of a copper sheet-laminated solar photovoltaic thermal water collector. *Energy Effi.* **10**(1), 117–128 (2017)
14. Al-Shamani, A.N., et al.: Experimental studies of rectangular tube absorber photovoltaic thermal collector with various types of nanofluids under the tropical climate conditions. *Energy Conv. Manag.* **124**, 528–542 (2016)

15. Hussein, H.A., Numan, A.H., Ruaa, A.A.R.: Improving the hybrid photovoltaic/thermal system performance using water-cooling technique and Zn-H₂O nanofluid. *Int. J. Photoenergy* **2017**, 1–14 (2017)
16. Razali, N.F.M., et al.: Experiment study of water based photovoltaic-thermal (PV/T) collector. *Int. J. Electr. Comput. Eng.* **9**(1), 118 (2019)
17. Kazem, H.A.: Evaluation and analysis of water-based photovoltaic/thermal (PV/T) system. *Case Stud. Thermal Eng.* **13**, 100401 (2019)
18. Abdullah, A.L., et al.: Technology progress on photovoltaic thermal (PVT) systems with flat-plate water collector designs: a review. *J. Adv. Res. Fluid Mech. Thermal Sci.* **59**(1), 107–141 (2019)
19. Abdul-Ganiyu, S., et al.: Study effect of flow rate on flat-plate water-based photovoltaic-thermal (PVT) system performance by analytical technique. *J. Clean. Prod.* **321**, 128985 (2021)
20. Reda, M.N., Spinnler, M., Al-Kayiem, H.H., Sattelmayer, T.: Assessment of condensation and thermal control in a photovoltaic panel by PV/T and ground heat exchanger. *Solar Energy* **221**, 502–511 (2021)
21. Al-Kayiem, H.H., Reda, M.N.: Analysis of solar photovoltaic panel integrated with ground heat exchanger for thermal management. *Int. J. Energy Prod. Manag.* **6**(1), 17–31 (2021)
22. Reda, M.N., Spinnler, M., Al-Kayiem, H.H., Sattelmayer, T.: Analysis of ground thermal control systems for solar photovoltaic performance enhancement. *WIT Trans. Ecol. Environ.* **246**, 41–50 (2020)



Impact Strength of Bio-Fibrous Concrete

Rowena Richard¹, Samatar Hassan¹, Deshvinder Kaur¹, Badraan Abdalla¹,
Saeed Cheema¹, Sook Kee², Hok Chai Yam², Abideen Ganiyu³, Fadilat Ayeronfe⁴,
and Muyideen Abdulkareem¹ (✉)

¹ Department of Civil and Environmental Engineering, Faculty of Engineering, Technology and Built Environment, UCSI University, Kuala Lumpur, Malaysia

muyikareem@gmail.com

² Department of Biotechnology, Faculty of Applied Sciences, UCSI University, 56000 Cheras, Kuala Lumpur, Malaysia

³ Department of Civil Engineering, Military Technological College, Muscat, Oman

⁴ Faculty of Engineering Technology, Universiti Tun Hussein Onn Malaysia, Johor, Malaysia

Abstract. Concrete is one of the most widely used materials in the world. Concrete is utilized in the construction of buildings, bridges and roads owing to their advantageous properties. However, occurrence of cracks in concrete poses a great hazard to the durability of concrete that could result in decrease of the service life of the structures. Researches have come up with numerous solutions to overcome this problem which include using bacteria to self-heal concrete and using Fibre-Reinforced Concrete (FRC). In this study, bacteria of genus *bacillus* which is *bacillus subtilis* was used to examine the effects of bacteria in concrete. Kenaf fibre which is a type of natural fibre was added into the concrete mix at 1%, 2% and 3% quantity to evaluate the strength of concrete. Concrete mix of water-cement ratio 0.45, 0.50, 0.60 were designed and casted in cylindrical shaped moulds. The testing of the concrete samples was carried out at 56th day with the aid of the impact testing machine to analyze the impact resistance of the samples. Results obtained from this investigation show that the concrete samples with the lowest water-cement ratio have the highest impact strength while samples with the highest water-cement ratio have the weakest impact strength. The presence of kenaf fibre in the concrete helped the concrete to gather more strength to achieved their ultimate rack resistance.

Keywords: Bio-fibrous concrete · Kenaf fibre · Impact strength · Bacillus subtilis · Water-cement ratio

1 Introduction

Structures everywhere in the world have one common and essential material that is used to maintain their integrity which is concrete. Concrete is broadly used owing to their durability, strength, flexibility and reflectivity. In general, concrete is typically made up of aggregates such as gravel, stones, sand and also includes adhesive that is combination of cement and water [1].

Regardless of their versatility, concrete pose some flaws in their properties [2]. Concrete cracking is one of the major problems faced by concrete. Cracking in concrete is sometimes inevitable especially in the case where the cracks occur even before the concrete is being loaded in the interfacial transition zone (ITZ) because of its natural property [3]. There are many factors that contribute to the occurrence of cracks in concrete. These factors include the type and amount of cement being used, curing conditions of the concrete and sizes of aggregates used during casting of concrete [4].

Over the years, researchers have conjured up several approaches to overcome the issue in concrete fragmentation. One of the approaches is by using fibre-reinforced concrete (FRC). FRC is a combination of cement, mortar or concrete and intermittent, distinct, uniformly distributed appropriate fibres. Fibres are generally produced using various materials including glass, polypropylene and steel that progressively expand to several applications particularly in the fabrication of FRC. Besides its ability to increase the strength of concrete, fibres' primary function is to bond matrix cracks that form while concrete is loaded and thus, providing several post-cracking ductility [5]. When a concrete matrix is enhanced with fibres, the endurance strength of the material towards cracking that resulted from external loads, thermal gradients or shrinkage can be increased [6].

Introduction of admixtures in concrete with natural or synthetic chemicals or additives during concrete mixing help in increasing properties of either fresh or hardened concrete in terms of workability, initial and final strength and stability [7]. Mineral admixtures in concrete have been a common practice in the industry for a long time now. There are several mineral admixtures that can be added to enhance the quality of concrete such as metakaolin, Fly Ash, Palm Oil Fuel Ash, GGBS, Silica Fume and Rice Husk Ash. Mineral admixtures work by manipulating the hardened properties of concrete [8].

Besides that, researchers have conducted countless experimental studies and laboratory explorations in the past decades with the aim of generating innovative strategies to subsidize cementitious materials with self-healing properties [9]. Three different approaches consisting of autogenous healing, bacterial production of $CaCO_3$ and encapsulation of polymeric material have been successfully accomplished for self-healing in concrete thus far. The durability of concrete has proven to increase as well as the occurrences of crack formation of concrete are reduced with the help of self-healing bacteria based on researches that have been carried out [10]. The demand of application of biological repair procedure in employing microorganisms that are able to produce mineral is highly sought after due to its nature of being harmless, pollution free, sustainable and natural [9].

The aim of this study to determine the impact resistant of bio-fibrous concrete with *bacillus subtilis* microorganisms and kenaf fibre. Bio-concrete samples of three (3) different water-cement ratio (0.45, 0.50 and 0.60) and three (3) different Kenaf fibre contents (1%, 2% and 3%) were prepared. The bio-concrete samples were casted in cylindrical moulds of 154 mm diameter and 64 mm thickness and tested after 56 days. Control samples consisting of zero fibre and zero microorganisms were also prepared as a benchmark for this study.

2 Experimental Materials and Method

2.1 Aggregates and Cement

The materials used in this study were all procured from local supplier in Kuala Lumpur, Malaysia. All the materials used in this experiment were securely stored in the laboratory under room temperature. Ordinary Portland cement conforming to MS EN 197-1:2007 was used. For coarse aggregates and fine aggregates, crushed granites with a size of 20 mm and sand were used respectively. To regulate the effect of self-healing in concrete, the maximum size of coarse aggregate was limited.

2.2 Microorganisms

Bacillus subtilis bacteria was used in this study. *Bacillus Subtilis* is a typical bacterium of soil with the ability to generate calcite precipitates on appropriate medium accompanied with source of calcium. This bacterium is categorized as a gram-positive bacterium with rod-like shapes. The bacteria work by producing calcium carbonate or limestone to fill the occurrence of cracks. The limestone that is produced by the bacteria will harden and thus filling in the cracks. The bacteria were used in two ways in this study. First is as surface pre-treatment of the Kenaf fibre to reduce the water absorption ability of the fibre and second is as an additive in the concrete mix. A measurement of 50 ml of the bacteria was used as additive as well as surface pre-treatment.

2.3 Kenaf Fibre

Fibre used in this investigation is Kenaf fibre which is a type of natural fibre. The usage of Kenaf fibre in this experiment is to investigate the strength and ductility of concrete when incorporated with this fibre. The volume of kenaf fibres in this experiment were divided into three proportions which were 1% (124g), 2% (248g) and 3% (373g). The fibres were saturated with *bacillus subtilis* bacteria before being added in the concrete mix. The preparation of the Kenaf fibres prior to being added into the concrete mix involved separating the fibres by hand and cutting them into small strands of 5cm to ensure they are properly combined together in the concrete mix. The Kenaf fibres were soaked overnight with bacteria of 50 ml before the casting of concrete. The Kenaf fibre used in this experiment was purchased from the National Kenaf and Tobacco Board (LKTN) in Kelantan, Malaysia.

2.4 Mix Proportion and Test Specimens

Control samples and 48 concrete mixtures were prepared and studied to investigate the properties of bio-fibrous concrete. Cylindrical moulds of 154 mm diameter and 64 mm thickness were used to cast the concrete samples. Mix ratio of 1:2:4 was applied in this study. The mixing of the concrete mixtures was done using a concrete mixer. Cement, coarse aggregates and fine aggregates were mixed together in the concrete to ensure all the materials bond well with each other. Water infused with 50 ml *bacillus subtilis* bacteria was then gradually poured into the concrete mixer with the rest of the materials. Afterwards the Kenaf fibres that were soaked overnight with bacteria were added into the mix. The concrete samples were cured in a water tank for 56 days before testing.

2.5 Impact Test

The impact resistance of the samples was tested using a testing equipment in accordance with ACI 544. The test was conducted by plunging a 4.5 kg drop hammer from 457 mm height onto a steel ball of 63 mm that is placed on surface of the samples. For each sample, two reading were recorded to determine the impact strength. First reading was the number of blows required for the samples to yield the first noticeable crack to determine the primary crack resistance. Second reading was the number of blows for the samples to reach failure to determine the final crack resistance.

3 Results

3.1 Effect of W/C on Impact Strength

The impact strengths of the concrete samples were recorded and analysed after 56 days. The result of control samples with zero fibre and zero bacteria is shown in Fig. 1 and bio-concrete with *bacillus subtilis* bacteria is shown in Fig. 2. From Fig. 1, w/c ratio of 0.45 showed promising result with the highest number of blows at 226 and 236 for initial crack and failure respectively. For each sample, blow counts of 10 blows or less were plunged onto the samples for the samples to reach their ultimate failure from their first cracks. From Fig. 2, at 0.45 w/c ratio the sample showed good resistance to impact with the sample showing its first visible crack at 217 blow count and failure at 251 blows. However, sample with 0.60 w/c ratio showed significantly low strength. At just 56 blow counts, the sample experienced its first visible crack and an additional 12 blow counts from its initial crack to reach failure at 68 blow counts. The sample showed weak resistance to impact due to amount of water present in the sample. As observed in Figs. 1 and 2, the strength of the concrete samples decreases as the w/c ratio increases. The addition of *bacillus subtilis* bacteria in the bio-concrete only improved slightly at 0.45 w/c ratio at their ultimate strength (failure) as compared to the control sample.

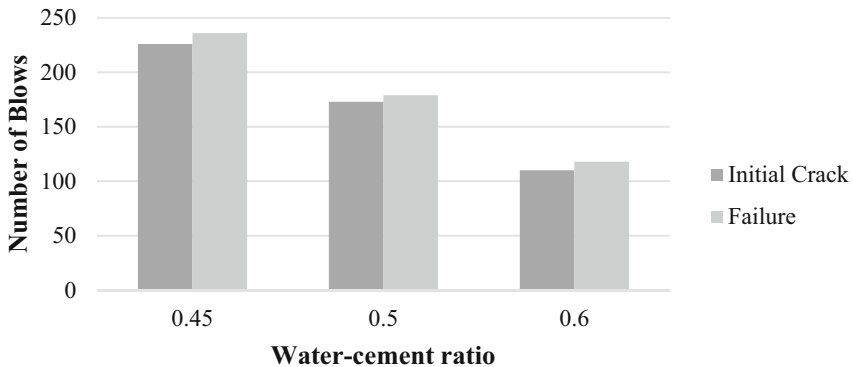


Fig. 1. Control samples with different w/c ratios

3.2 Effect of Kenaf Fibre on Impact Strength

Bio-fibrous concrete comprised of *bacillus subtilis* bacteria with 1%, 2% and 3% Kenaf fibre were tested after 56 days. The impact strength results of the concrete samples are shown in Figs. 3, 4 and 5. From Fig. 3, the impact strength of each sample decreases as the water-cement ratio increases. For bio-concrete with 2% Kenaf fibre, 0.45 w/c ratio showed weak impact endurance at just 28 blows at initial crack and 41 blows at failure as observed from Fig. 4. The 0.50 w/c ratio showed a more promising result even though it contained a higher water content in its sample. For bio-concrete with 3% Kenaf fibre, sample with 0.50 w/c ratio once again showed the highest blow counts at the first crack and failure at 38 and 78 respectively amongst all samples as observed in Fig. 5.

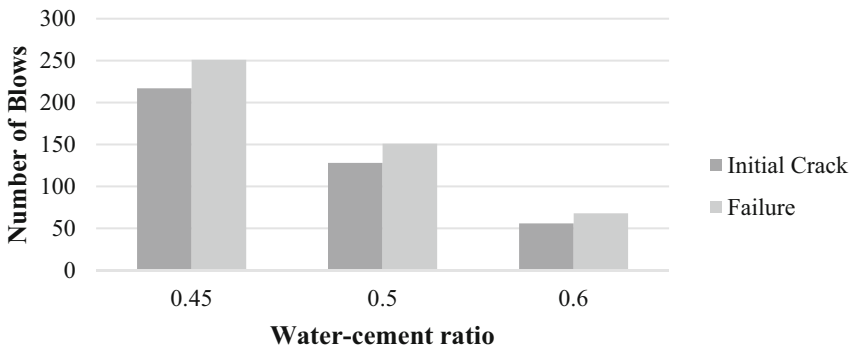


Fig. 2. Bio-concrete with different w/c ratios

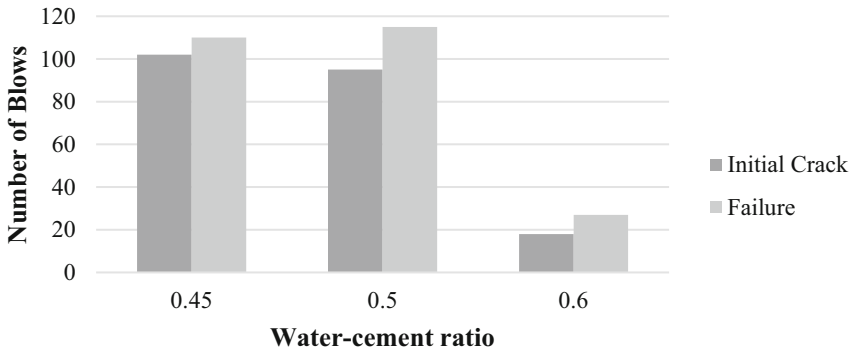


Fig. 3. Bio-concrete with 1% Kenaf fibre

The addition of Kenaf fibre have varying effects on concrete depending on the amount of fibre that was incorporated inside. At 1% Kenaf fibre, the impact strength of the concrete decreases as the water-cement ratio increases. This can be seen from Fig. 3 where 0.45 w/c ratio demonstrated the highest strength at 102 and 110 blow counts for the initial crack and failure respectively while 0.60 w/c ratio demonstrated very low impact strength at only 18 and 27 blows counts for initial crack and failure respectively.

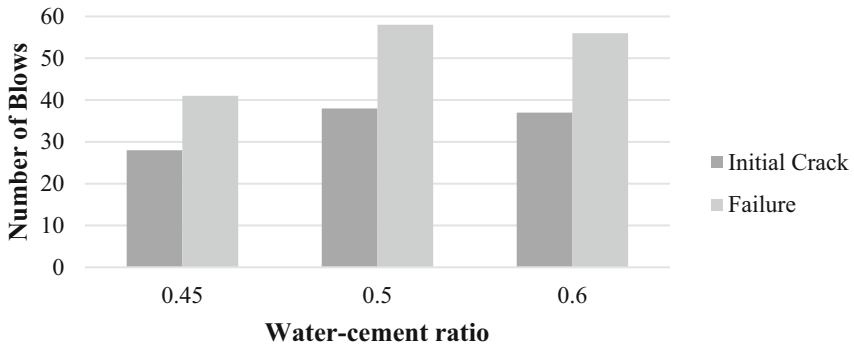


Fig. 4. Bio-concrete with 2% Kenaf fibre

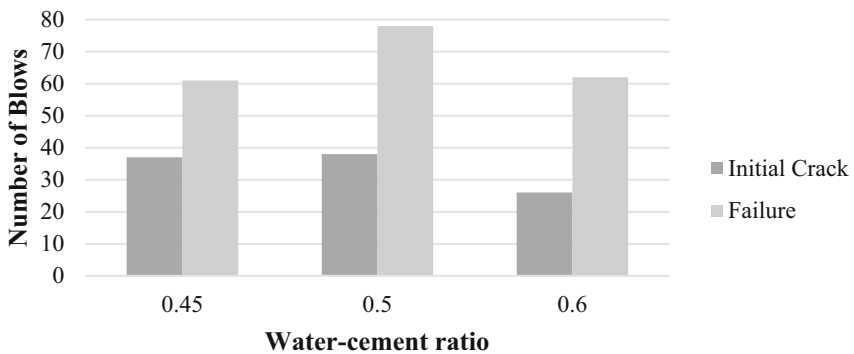


Fig. 5. Bio-concrete with 3% Kenaf fibre

The concrete showed weak resistance to impact due to amount of water present in the sample. From Figs. 4 and 5, the impact strength initially increased at 0.50 w/c ratio before decreasing slightly at 0.60 w/c ratio. The effects of Kenaf fibre in the concrete samples helped the concrete to withstand the impact loading the samples were subjected to during the testing. The fibre helped the samples to sustain their strength under the impact loading from their initial crack until they reach their ultimate strength. One observation can be taken from Fig. 5 with w/c ratio of 0.50 and 3% fibre content. The sample encountered its first initial crack at 38 blow counts but managed to sustain the impact loading for more than 35 blow counts before finally reaching its failure at 78 number of blows. The ability of the sample to sustain such impact is owing to the fibre incorporated inside the sample that helped the sample to hold together longer because the fibre acts as a bonding material inside the concrete.

4 Conclusions

Investigation of impact resistance of bio-fibrous concrete with *bacillus subtilis* and microorganisms was carried out in this study. Kenaf fibre of different volume (1%, 2% and 3%) were incorporated into the concrete mix of 0.45, 0.50 and 0.60 w/c ratio.

Control samples and 48 cylindrical concrete samples were prepared and casted in this investigation. The results show that the impact strength of concrete decreased as the amount of fibre content increased. Nonetheless, the Kenaf fibre incorporated inside the concrete helped give the concrete extra strength to endure the impact loading subjected to it.

Acknowledgement. The authors would like to thank the UCSI University for their financial support through the Research Excellence and Innovation Grant (REIG-FETBE-2021/002).

References

1. Jin, L., Yu, W., Li, D., Du, X.: Numerical and theoretical investigation on the size effect of concrete compressive strength considering the maximum aggregate size. *Int. J. Mech. Sci.* **192**, 106130 (2021)
2. Olukotun, N., Sam, A.R.M., Lim, N.H.A.S., Abdulkareem, M., Mallum, I., Adebisi, O.: Mechanical Properties of Tin Slag Mortar. *Recycling* **6**(2), 42 (2021)
3. Golewski, G.L.: Evaluation of morphology and size of cracks of the Interfacial Transition Zone (ITZ) in concrete containing fly ash (FA). *J. Hazard. Mater.* **357**, 298–304 (2018)
4. Zhan, P.-M., He, Z.-H.: Application of shrinkage reducing admixture in concrete: a review. *Constr. Build. Mater.* **201**, 676–690 (2019)
5. Mindess, S.: *Developments in the Formulation and Reinforcement of Concrete*. Woodhead Publishing, Sawston (2019)
6. Micelli, F., Renni, A., Kandalaf, A.G., Moro, S.: Fiber-reinforced concrete and ultrahigh-performance fiber-reinforced concrete materials. In: *New Materials in Civil Engineering*, pp. 273–314. Elsevier (2020)
7. Okashah, A.M., Abdulkareem, M., Ali, A.Z., Ayeronfe, F., Majid, M.Z.: Application of automobile used engine oils and silica fume to improve concrete properties for eco-friendly construction. *Environ. Clim. Technol.* **24**(1), 123–142 (2020)
8. Dey, S., Kumar, V., Goud, K., Basha, S.: State of art review on self compacting concrete using mineral admixtures. *J. Build. Pathol. Rehabil.* **6**(1), 1–23 (2021)
9. Luo, J., et al.: Interactions of fungi with concrete: Significant importance for bio-based self-healing concrete. *Constr. Build. Mater.* **164**, 275–285 (2018)
10. Wang, J., Ersan, Y.C., Boon, N., De Belie, N.: Application of microorganisms in concrete: a promising sustainable strategy to improve concrete durability. *Appl. Microbiol. Biotechnol.* **100**(7), 2993–3007 (2016)



Dynamic Analysis of Floating Offshore Wind Turbine Subjected to Combined Deepwater Environmental Loads

Ahmad Mahamad Al-Yacouby^(✉), Mohamad Azri bin Kamarulbahrin, and M. S. Liew

Civil and Environmental Engineering Department, Universiti Teknologi PETRONAS,
32610 Seri Iskandar, Perak, Malaysia

ahmad.alyacouby@utp.edu.my, aalyacouby@gmail.com

Abstract. The use of wind energy is rapidly growing worldwide as wind energy systems are emerging as a promising technology for utilizing offshore wind resources for large scale generation of electricity. However, developing optimum floating wind turbine for Deepwater application is a challenging task. Thus, in this study, the dynamic analysis of floating offshore wind turbine subjected to combined Deepwater environmental loads is investigated experimentally. A spar type floating wind turbine was modeled, and a parametric study was performed to determine the critical parameters influencing the dynamic response of the platform. The outcome of the study shows that the dynamic response of the structures is affected by the wave, wind, current properties, and water depth.

Keywords: Dynamic Analysis · Floating Offshore Wind Turbine · Deepwater · Combined Environmental Loads

1 Introduction

Onshore wind energy is currently near the development limit in some countries due to visual and noise impact constraints that make it increasingly difficult to find appropriate sites for future growth [1, 2]. Offshore wind energy developments have greatly reduced visual impacts, less turbulence, and lower noise constraints allowing higher turbine rotor speeds and larger turbines [2]. Moreover, offshore wind energy possesses a number of properties enabling significant cost reduction such as higher full-load hours per year, longer lifetimes and higher electricity production. Offshore wind power plants can produce up to 50% more electricity than their onshore cousins, due to higher and steadier wind speeds [2]. A worldwide wind atlas based on data from about 8000 locations [5] where wind speeds were calculated at 80 m illustrates the potential of global offshore wind resources. Constructions of offshore wind turbine plants is feasible as large offshore turbines can be transported by barges or ships. Land-based wind farm capacity is limited in scale while offshore farms with more than 100 MW capacities are possible [2]. Moving offshore is said to be driving the wind energy technology development [3]. According to International Energy Outlook (2008), the primary energy consumption in

Malaysia from the year 1998 to 2006 has been increasing from 1.7 to 2.6 quadrillion Btu. Realizing the increase in primary energy consumption, this non-renewable energy is gradually depleting and contributes to pollutions such as the emission of greenhouse gases [6]. Renewable Energy Act 2011 was finally established in 2011 in support of government directions towards greener and more sustainable energy. Though wind energy was not part of the RE Act 2011 schedule, the potential for wind energy utilization is found to be feasible from early studies. Based on the monthly summary of marine meteorological observations published by the Malaysian Meteorological Service (MMS), Chiang et al. (2003) analysed the potential of offshore wind energy resource at 16 locations in Malaysia. It is estimated that the annual offshore wind speed for Malaysian waters is approximately 1.2 to 4.1 m/s, with higher values being 3.3 to 4.1 m/s in eastern Peninsular Malaysia [7].

Therefore, Malaysian Government direction towards greener and more sustainable energy was clearly expressed with the enactment of the Renewable Energy Act 2011. The policy was introduced in support with the CO₂ Emission Reduction, offshore companies currently started their own renewable energy team to study and the aim of this study is to evaluate the dynamic motion response of the Floating Offshore Wind Turbine, specifically for Spar type, using the 3D Model Simulation Software, Orcina OrcaFlex. The response parameters in OrcaFlex will be as per Table 1. The environmental criteria will be based on Sabah Deep Water of Malaysian Waters.

Table 1. Response Parameters and Orcaflex Output Variables

Response Parameters	OrcaFlex Output Variables
Vertical Acceleration	GZ acceleration
Roll Motion	Rotation 1
Pitch Motion	Rotation 2
Angular Motion	Rotation 1 + Rotation 2

Parametric study is also to be conducted along the way using the same Metocean Criteria Basis to determine on the important parameter's relationship with the dynamic motion response for the floating wind turbine (Spar type). Subsequent paragraphs, however, are indented.

2 Theoretical Background

2.1 Wave Spectrum

Aligned with the research project goal to determine the dynamic motion response of the structure based on the real offshore field, only irregular wave spectrum will be considered as part of the analysis instead of the regular wave. The JONSWAP wave frequency spectrum has been selected for the analysis because of its extensive measurements by the Hassemann et al. (1973) in the Joint North Sea Wave Project off the coast of the German

island of Sylt where it is formulated from the modification of Pierson-Moskowitzs (PM) spectrum for a developing sea state in a fetch limited situation. JONSWAP spectrum could be expressed as:

$$S_J(f) = \alpha g^2 \left((2\pi)^{-4} \right) f^{-5} \exp \left[- \left(\frac{5}{4} \right) \left(\frac{f}{f_m} \right)^{-4} \right] \gamma^{\exp \left[\frac{(f-f_m)^2}{2\sigma^2 f_m^2} \right]} \quad (1)$$

Where:

$S_J(f)$ = wave spectral density (m/Hz)

g = acceleration due to gravity

γ = gamma : peak enhancement factor, for $\gamma = 1$,

α = alpha : Philips parameter / equilibrium range constant

f = frequency (Hz)

f_m = peak frequency (Hz)

σ = sigma, enhancement width parameter (a & b)

3 Methodology

3.1 Model Properties

The research project was carried out based on the default model which was developed and made available by Orcina OrcaFlex – “K01 Floating Wind Turbine”. This basis of the model was developed by the National Renewable Energy Laboratory (NREL). The summary for the structure and its system are illustrated in Tables 2, 3 and Figs. 1, 2 [8].

Table 2. Wind Turbine Data Overview

Property	Value(s)
Rating	5-MW
Blade Quantity	3
Control System(s)	Variable Speed, Variable Blade Pitch
Drivetrain	High Speed, Multiple-Stage Gearbox
Rotor Diameter	126 m
Hub Diameter	3 m
Cut-in, Rated, Cut-out Wind Speed	3 m/s, 11.4 m/s, 25 m/s
Main Shaft Tilt	5°
Rotor Mass	110.00 te
Nacelle Mass	240.00 te
Tower Mass	347.46 te

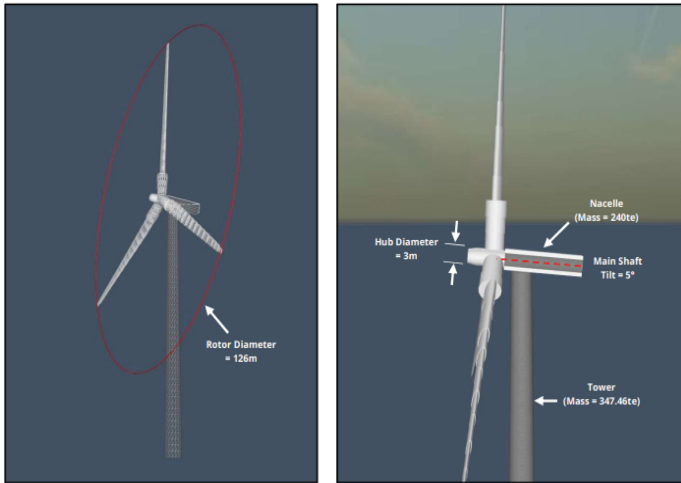


Fig. 1. Wind Turbine System

Table 3. Blade Structural Properties

Property	Value(s)
Blade Material	Glass fibre
Blade Length (Root to Tip)	61.5 m
Overall Blade Mass	17.740 te
Radial CM (relative to Blade Root)	20.475 m
Blade Pre-cone Angle	2.5°

RAOs are computed in tandem with the generation of a hydrodynamic database, which is a model of the effects of water pressure upon the ship's hull under a wide variety of flow conditions. Together, the RAOs and hydrodynamic database provide (in as much as this is possible within modelling and engineering constraints) certain assurances about the behaviour of a proposed ship design. They also allow the designer to dimension the ship or structure so it will hold up to the most extreme sea states it will likely be subjected to (based on sea state statistics). As in previous phases of the OC3 project, Phase IV uses the turbine specifications of the National Renewable Energy Laboratory (NREL) offshore 5-MW baseline wind turbine [11], which is a representative utility-scale, multi-megawatt turbine that has also been adopted as the reference model for the integrated European UpWind research program. Numerous floating platform concepts are possible for offshore wind turbines, including sparbuoys, tension leg platforms (TLPs), barges, and hybrid concepts thereof. At the request of the OC3 participants, the spar-buoy concept called "Hywind," developed by Statoil of Norway [11],

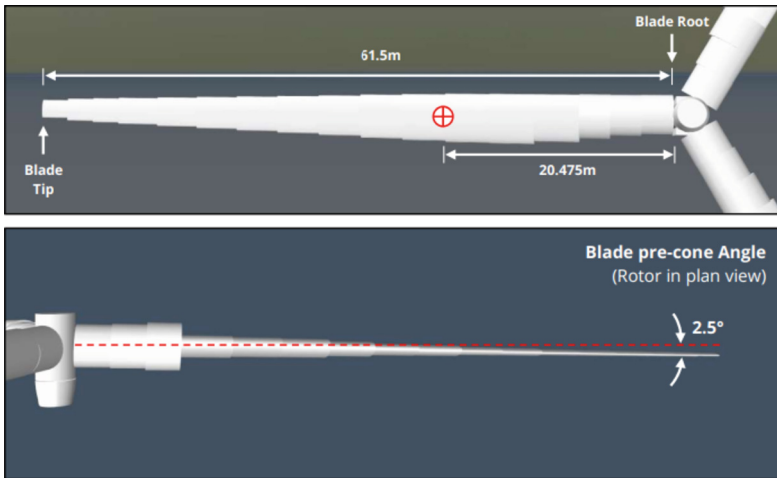


Fig. 2. Blade Properties

In Phase IV, the rotor nacelle assembly of this 5-MW turbine which includes the aerodynamic and structural properties, remains the same, but the support structure (tower and substructure) and control system properties have been changed. 11 was chosen for the modelling activities of Phase IV. This concept was chosen for its simplicity in design, suitability to model, and propinquity to commercialization. Finn Gunnar Nielsen and Tor David Hanson of Statoil were contacted, and they graciously supplied detailed platform and mooring system data to assist in the development of this model. The data provided was intended for the conceptual version of the Hywind platform developed to support a 5-MW wind turbine, as analyzed by Nielsen, Hanson, and Skaare [13] and Larsen and Hanson [14]. The originally supplied data has been condensed and sanitized by Jason Jonkman of NREL at the request of Statoil. This to ensure that it is suitable for public dissemination. Jason Jonkman also slightly made changes to the original data so that the platform design is appropriate for supporting the NREL 5-MW baseline turbine, which has properties that are slightly different than the turbine properties used by Statoil in their development of the system. In conclusion, the finalized version by Jason Jonkman is now referred to as the “OC3-Hywind” system and are to make sure that model is not the similar version of the Statoil’s original Hywind concept [11]. The properties of the developed model are presented in Table 4. For additional materials related to the dynamic analysis of floating offshore wind turbines, the readers can refer to [4, 9, 10, 12, 15–19].

Table 4. Floating Platform Structural Properties

Property	Value
Depth to Platform Base Below SWL (Total Draft)	120 m
Elevation to Platform Top (Tower Base) Above SWL	10 m
Depth to Top of Taper Below SWL	4 m
Depth to Bottom of Taper Below SWL	12 m
Platform Diameter Above Taper	6.5 m
Platform Diameter Below Taper	9.4 m
Platform Mass, Including Ballast	7,466,330 kg
CM Location Below SWL Along Platform Centerline	89.9155 m
Platform Roll Inertia about CM	4,229,230,000 kg · m ²
Platform Pitch Inertia about CM	4,229,230,000 kg · m ²
Platform Yaw Inertia about Platform Centerline	164,230,000 kg · m ²

4 Results and Discussions

4.1 SET 1: Extreme Condition Return Period (RP)

The extreme conditions were taken based on the Extreme Value for the specific Return Period (RP). Looking at the table below, it is clear showing that as the Return Period is getting much more extreme, the parameters directional omni value is showing a higher magnitude and are directly related.

4.2 Data Collection

Referring to Table 5, the three (3) test runs was set up with the parameters obtained from the Metocean Criteria. These three test runs are the 3 load cases which is “100 × 100 × 100”, “50 × 50 × 50” and “10 × 10 × 10”. These numbers actually representing the Extreme Value of Return Period (in years, i.e., 100-Years × 100-Years × 1000-Years) for the mentioned years respectively and a combination of the value for the parameters with the extreme Return Period for Wave, Wind and Currents. Based on these set of inputs, the simulations and analysis were run, and the result extracted are GZa which represent the vertical acceleration, Roll and Pitch Max Rotation in terms of degree and the maximum angular motion resulted from the parameters set (Table 6).

The overall process flow of the research project is presented in Fig. 3.

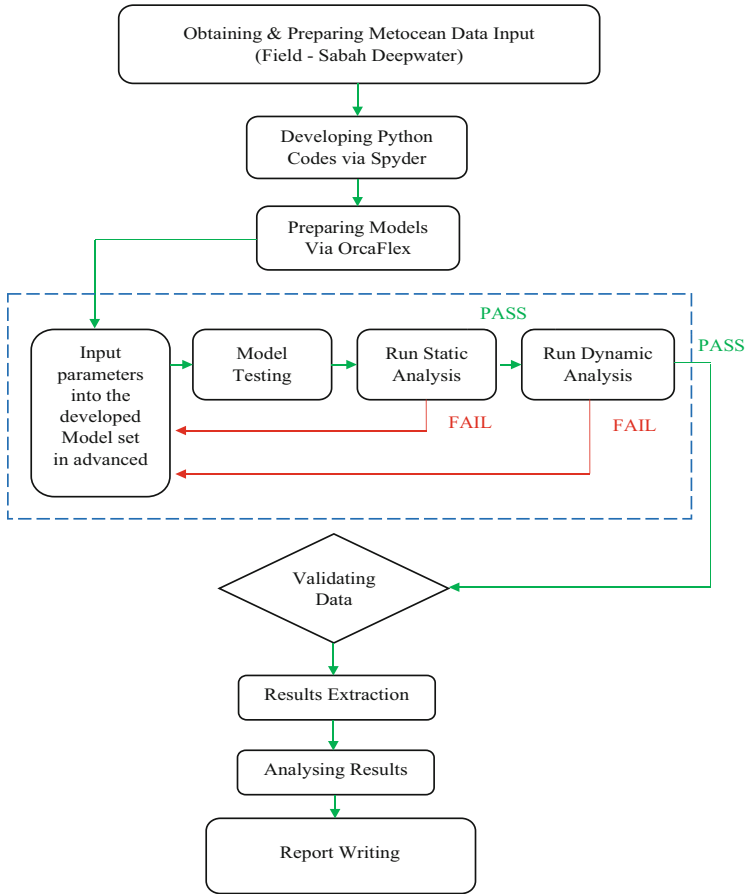


Fig. 3. Process Flow Chart for Research Project

Table 5. Return Period and its Wave Parameters Value

	1-year RP	10-year RP	50-year RP	100-year RP
Parameters	OMNI			
Hs (m)	3.7	4.9	5.7	5.9
Tz (s)	6.5	7.5	8.1	8.3
Tp (s)	9.1	10.6	11.4	11.6
Hmax(m)	7.2	9.4	10.4	10.8
Tass (s)	8.5	9.8	10.5	10.8

Table 6. SET 1 Results

Test Run 1									
		Dir	Hs	Tp	Active_Current	GZa, m/s ²	Max_Rotation1 (Roll), deg	Max_Rotation2 (Pitch), deg	Max_Angular_Motion, deg
100x 100 x 100	0	180	5.9	11.6	Surf_100Y_N	1.03	0.53	-26.08	26.09
	1	135	4.9	9.7	Surf_100Y_NE	0.8	-18.91	-18.72	26.61
	2	90	2.6	5.1	Surf_100Y_E	0.54	-21.12	-0.08	21.12
	3	45	2.9	5.6	Surf_100Y_SE	0.5	-14.52	15.39	21.16
	4	0	3.8	7.4	Surf_100Y_S	0.85	1.09	26.05	26.07
	5	315	4.2	8.1	Surf_100Y_SW	0.87	20.84	20.12	28.97
	6	270	4.5	8.7	Surf_100Y_W	0.92	29.33	0.63	29.34
	7	225	5.2	10.2	Surf_100Y_NW	0.63	18.11	-14.27	23.06
Test Run 5									
		Dir	Hs	Tp	Active_Current	GZa, m/s ²	Max_Rotation1 (Roll), deg	Max_Rotation2 (Pitch), deg	Max_Angular_Motion, deg
50 x 50 x 50	0	180	5.7	11.4	Surf_50Y_N	0.99	0.49	-25.26	25.26
	1	135	4.7	9.4	Surf_50Y_NE	0.81	-18.3	-18.15	25.77
	2	90	2.5	5	Surf_50Y_E	0.51	-20.41	-0.08	20.41
	3	45	2.7	5.5	Surf_50Y_SE	0.45	-14.02	14.87	20.44
	4	0	3.6	7.3	Surf_50Y_S	0.66	0.94	25.26	25.28
	5	315	4	7.9	Surf_50Y_SW	0.79	19.95	19.32	27.77
	6	270	4.2	8.5	Surf_50Y_W	0.85	28.32	0.59	28.33
	7	225	4.9	9.9	Surf_50Y_NW	0.46	17.28	-8.75	19.37
Test Run 9									
		Dir	Hs	Tp	Active_Current	GZa, m/s ²	Max_Rotation1 (Roll), deg	Max_Rotation2 (Pitch), deg	Max_Angular_Motion, deg
10 x 10 x 10	0	180	4.9	10.6	Surf_10Y_N	0.84	0.42	-23.5	23.5
	1	135	4.1	8.8	Surf_10Y_NE	0.68	-17.04	-16.92	24.01
	2	90	2.1	4.6	Surf_10Y_E	0.35	-18.65	-0.05	18.65
	3	45	2.4	5.1	Surf_10Y_SE	0.37	-12.87	13.76	18.84
	4	0	3.1	6.8	Surf_10Y_S	0.7	0.79	23.61	23.62
	5	315	3.4	7.4	Surf_10Y_SW	0.57	18.25	17.85	25.53
	6	270	3.7	8	Surf_10Y_W	0.63	26.22	0.49	26.22
	7	225	4.3	9.2	Surf_10Y_NW	0.52	15.75	-12.82	20.31

4.3 Data Analysis

Based on the extracted results for GZa, the highest GZa value occurs for the case “100-Year \times 100-Year \times 100-Year” with the result of 1.03 m/s^2 . This value was as a result of with the highest value for Wave Height, Hs and Wave Period, Tp (Figs. 4, 5 and Tables 7, 8).

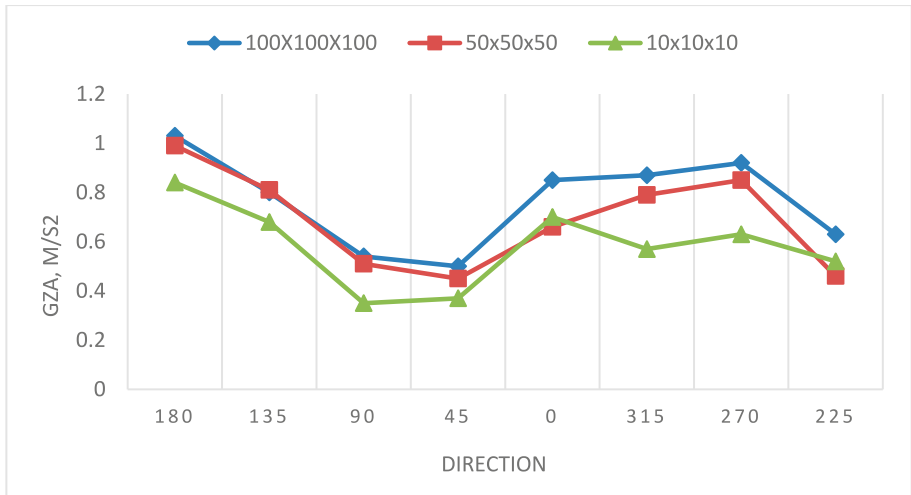


Fig. 4. SET 1: GZa

Table 7. SET 1: GZa Highest Load Case

GZa	Dir	Hs	Tp	Active_Current	GZa, m/s^2	
100x100x100	0	180	5.9	11.6	Surf_100Y_N	1.03
50x50x50	0	180	5.7	11.4	Surf_50Y_N	0.99
10x10x10	0	180	4.9	10.6	Surf_10Y_N	0.84

For Roll, the highest recorded was at 29.33° and this is for the “100-Year \times 100-Year \times 100-Year” with Wave Height, Hs, of 4.5 m and Wave Period, Tp, of 8.7 s. The highest parameters value still gives the highest motion response for Roll. The lowest Roll motion resulted from Hs and Tp of 3.7 m and 8 s respectively and the load case is for “10-Year \times 10-Year \times 10-Year”.

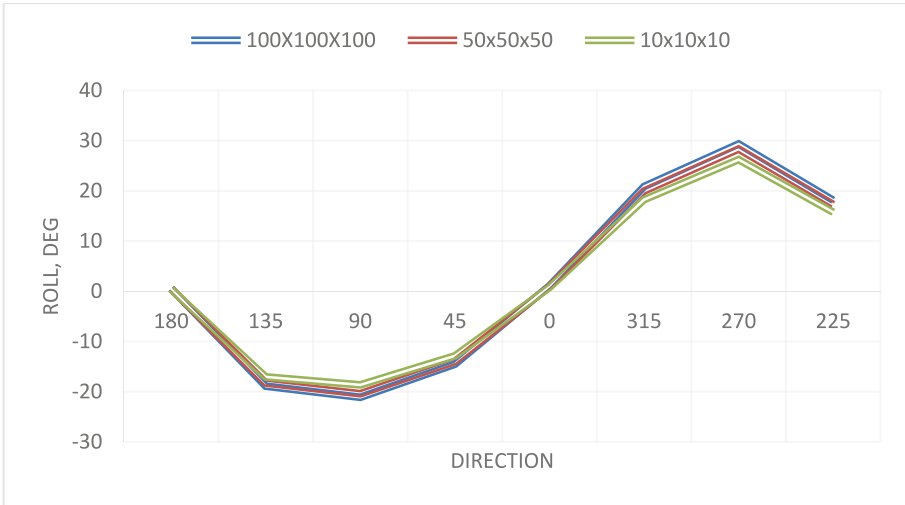


Fig. 5. SET 1: Maximum Roll

Table 8. SET 1: Roll Highest Load Case

Roll	Dir	Hs	Tp	Active_Current	Max_Rotation1 (Roll), deg.	
100x100x100	6	270	4.5	8.7	Surf_100Y_W	29.33
50x50x50	6	270	4.2	8.5	Surf_50Y_W	28.33
10x10x10	6	270	3.7	8	Surf_10Y_W	26.22

For Pitch, the maximum recorded motion is at 26.05° and the load case which give this result is for “100-Year × 100-Year × 100-Year” as well. The parameters for Wave Height, Hs, and Wave Period, Tp, is the highest at Load Case “100-Year × 100-Year × 100-Year” (Figs. 6, 7 and Tables 9, 10).

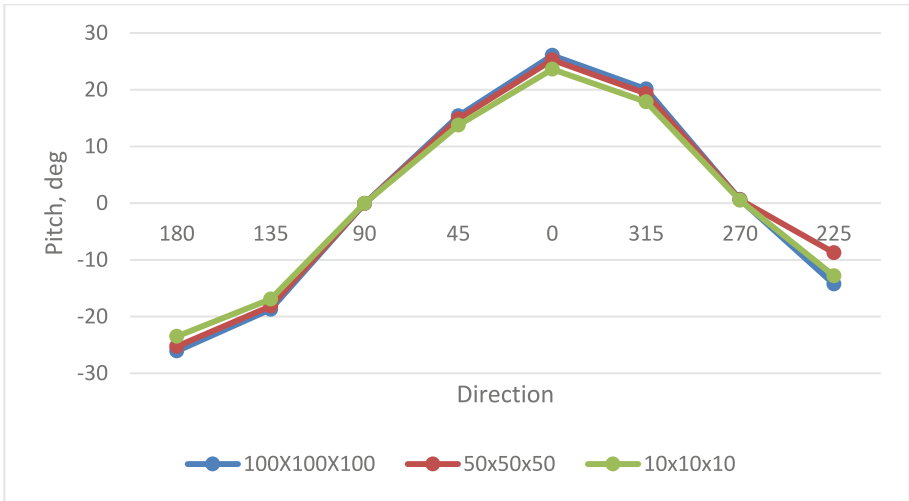


Fig. 6. SET 1: Maximum Pitch

Table 9. SET 1: Pitch Highest Load Case

Pitch	Dir	Hs	Tp	Active_Current	Max_Rotation1 (Roll), deg.	
100x100x100	4	0	3.8	7.4	Surf_100Y_S	26.05
50x50x50	4	0	3.6	7.3	Surf_50Y_S	25.26
10x10x10	4	0	3.1	6.8	Surf_10Y_S	23.61

Lastly for Set 1, for the Angular Motion, the highest recorded motion was resulted from the load case of the “100-Year × 100-Year × 100-Year” with Wave Height, Hs, of 4.5 m and Wave Period, Tp, of 8.7 s. The result for the motion recorded at 29.34°. The lowest is still for Load Case of “10-Year × 10-Year × 10-Year” which having the lowest parameters values for Hs and Tp.

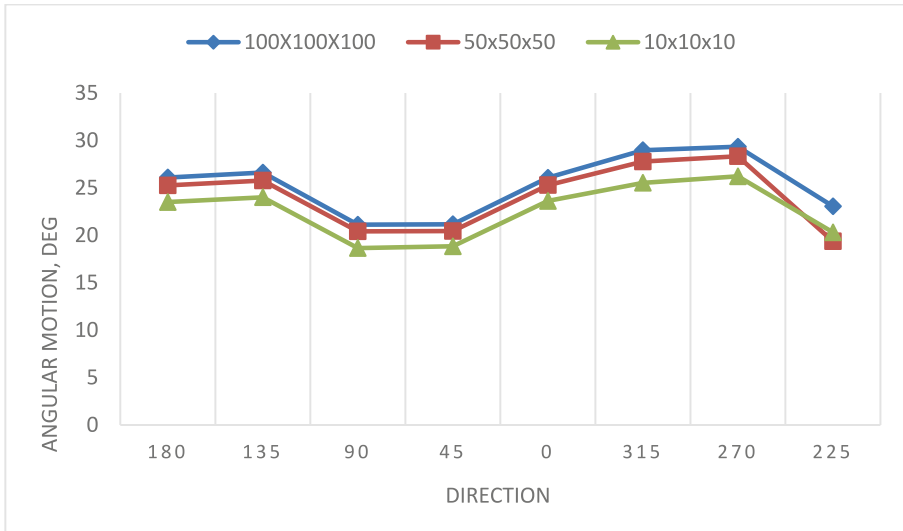


Fig. 7. SET 1: Max Angular Rotation

Table 10. SET 1: Angular Motion Highest Load Case

Angular Motion	Dir	Hs	Tp	Active_Current	Max_Angular_Motion, deg.	
100x100x100	6	270	4.5	8.7	Surf_100Y_W	29.34
50x50x50	6	270	4.2	8.5	Surf_50Y_W	28.33
10x10x10	6	270	3.7	8	Surf_10Y_W	26.22

5 Conclusions

In conclusions, based on the results and discussions made in the previous chapter, it is clear that the parameters of the metocean do play role for the dynamic motion of the Floating Offshore Wind Turbine- Spar Type (S-FOWT). The greater the parameters values such as Hs, Tp, Wind Speed will eventually result in greater magnitude for the dynamic motion response. As for the water depth, though as discussed, though the parameters used were not proper as the metocean basis is meant for 1000 m water depth, the water depth do affect the motion but with the same response trendline. Since the study focus on the Wind Turbine, wind effects were studied and results showing that as the magnitude of the wind increases, the dynamic motion response resulted in the same manner. This is clear as higher wind velocity would result in higher wind load impacting the structure thus giving a greater motion response.

- For the governing components of the dynamic motion response, as the oil and gas industry is focusing more on the wave-current governances as the focus was always on the hull motion, this does not be the case for wind turbine as the wind factor is required to be studied as well as the wind factors will eventually affects the motion

response in the roll and pitch while the wave-current factors have major impact on the Vertical Acceleration (GZ acceleration).

- These factors and results have to be analyzed in depth to make sure that overall structure of the floating offshore wind turbine is always within the design limit and the greater concern when it comes to the dynamic motion response is that the overall structure does not coincide or greater than the wind-wave-current natural frequency to avoid the resonance effects which might be disastrous to the overall system.

Acknowledgments. The authors would like to acknowledge the continued support by Universiti Teknologi PETRONAS (UTP) and the financial support provided by Yayasan UTP, grant number 015LC0-95 & 015LC0-313.

References

1. Alam, S.S., Omar, N.A., Ahmad, M.S.B., Siddiquei, H.R., Nor, S.M.: Renewable energy in Malaysia: strategies and development. *Environ. Manag. Sustain. Dev.* **2**(1), 51 (2013)
2. Albani, A., Ibrahim, M.Z.: Investigation on wind energy potential at Sabah State of Malaysia (2011)
3. Azmi & Associates. Wind Energy Landscape in Malaysia (2020)
4. Muzathik, A.M., Wan Nik, W.B., Ibrahim, M.Z.: Wind Engineering (2009)
5. Lip-Wah, H., Ibrahim, S., Kasmin, S., Omar, C.M.C., Abdullah, A.M.: Review of offshore wind energy assessment and siting methodologies for offshore wind energy planning in Malaysia. *Am. Int. J. Contemp. Res.* **2**(12), 72–85 (2012)
6. Aldhshan, S.R.S., et al.: Energy consumption and spatial assessment of renewable energy penetration and building energy efficiency in Malaysia: a review. *Sustainability* **13**(16), 9244 (2021)
7. Hashim, F.E., Peyre, O.S.C.A.R., Lapok, S.J., Yaakob, O.M.A.R., Din, A.H.M.: Offshore wind energy resource assessment in Malaysia with satellite altimetry. *J. Sustainabil. Sci. Manag.* **15**(6), 111–124 (2020)
8. Orcina Orcaflex Report. Orcina Project 1405, Wind Turbine Validation Report (2018)
9. Mekhilef, S., Safari, A., Chandrasegaran, D.: Feasibility study of off-shore wind farms in Malaysia. *Energy Educ. Sci. Technol. Part A: Energy Sci. Res.* **29**(1), 519–530 (2012)
10. Chakrabati, K.: Handbook of Offshore Engineering, vol. 1 (2005)
11. Jonkman, J., Musial, W.: Offshore Code Comparison Collaboration (OC3) for IEA Task 23 Offshore Wind Technology and Deployment (2010)
12. Jeon, M., Lee, S., Kim, T., Lee, S.: Wake influence on dynamic load characteristics of offshore floating wind turbines. *Aiaa J.* **54**(11), 3535–3545 (2016)
13. Skaare, B., Hanson, T.D., Nielsen, F.G.: Importance of control strategies on fatigue life of floating wind turbines (2007)
14. Nielsen, F.G., Hanson, T.D., Skaare, B.: Integrated dynamic analysis of floating offshore wind turbines (2006)
15. Moan, T.Z., et al.: Recent Developments of the Design and Analysis of Floating Wind Turbines. ISCOT: Developments In Fixed & Floating Offshore Structures. The Royal Institution of Naval Architects, Busan, Korea (2012)
16. Ren, Y., Venugopal, V., Shi, W.: Dynamic analysis of a multi-column TLP floating offshore wind turbine with tendon failure scenarios. *Ocean Eng.* **245**, 110472 (2022)

17. Ding, H., Han, Y., Zhang, P., Le, C., Liu, J.: Dynamic analysis of a new type of floating platform for offshore wind turbine. In: ISOPE International Ocean and Polar Engineering Conference, pp. ISOPE-I. ISOPE (2016)
18. Subbulakshmi, A., Verma, M.: Transient response reduction of floating offshore wind turbine subjected to sudden mooring line failure. *Ocean Eng.* **271**, 113702 (2023)
19. Huang, W., Li, B. and Chen, X., 2023. A new quasi-dynamic method for the prediction of tendon tension of TLP platform. *Ocean Eng.* **270**, 113590 (2023)



Continuum Modelling of Carbon Nanotube Composites: A Review

N. Omar¹(✉), Z. A. Rasid¹, and M. Z. Hassan²

¹ Malaysia-Japan International Institute of Technology, Universiti Teknologi Malaysia, Jalan Sultan Yahya Petra, 54100 Kuala Lumpur, Malaysia
o.rihan286@gmail.com

² Razak Faculty of Technology and Informatics, Universiti Teknologi Malaysia, Jalan Sultan Yahya Petra, 54100 Kuala Lumpur, Malaysia

Abstract. Carbon nanotubes (CNTs) have been proven to show exceptional mechanical properties such as longitudinal elastic modulus of up to 1TPa and elastic strain of around 5%. Possessing these excellent properties, while having a fibre-like structure, CNTs have considerable potential to act as fillers in highly strong and light CNT composite (CNTC) materials. However, from experiments conducted, the biggest challenge before these nanocomposites can become a reality is that they do not show the expected excellent properties. This has led to extensive research into determining the effective properties of the CNTC using the preferred method of fully or semi-continuum modelling through the application of the finite element method (FEM). In this paper a review on aspects of the continuum representation of CNTCs is conducted. It covers the development, analysis and results of partial or full continuum modelling conducted in the last decades. A close-to-reality model must consider at least 5 CNT characteristics: length, interphase, waviness, orientation and agglomeration that cover 4 scales from nanoscale through micro- and meso- to macro-scale. The earlier nanocomposite continuum representatives mostly consisted of a CNT fibre surrounded by a matrix that could only catch the CNT characteristics at nano- and micro-scales and thus provided nanocomposite properties that were close to the rule of mixture (ROM) values but very far from experimental values. However, the recent representations manage to reach macro-scale level while representing important CNT characteristics such that the results were found to be close to the experimental results.

Keywords: Carbon nanotube · Nanocomposites · Multiscale modelling

1 Introduction

Carbon Nanotubes are known to possess many tremendously good mechanical, electrical and thermal properties [1, 2]. This is a result of their near-perfect seamless cylindrical microstructure, shaped naturally from a graphene sheet. With these advantages, CNTs have been proposed for use as nanofillers for polymer composites [3, 4] to form the so called CNT nanocomposites (CNTC).

In characterization studies of CNTC, its properties have been predicted using experimental [5], analytical [6] and modelling approaches [7]. While the experimental approach is expensive and time consuming, the molecular mechanics/molecular dynamics (MM/MD) approach [8, 9], requires huge computational time. Furthermore, the hard analytical method is limited to simpler geometry [10].

As such, the FEM based modelling approach that represents the CNT-matrix system as continuums has been the popular method as it is simpler, cheaper while giving greater insights to the CNT-matrix interactions.

In this paper, a review is conducted on the modelling of CNT nanocomposites using full and semi-continuum approaches that covers the representative volume elements (RVEs) both with and without the CNT-matrix interphase. In short, the review covers the journey of the continuum modelling in providing a close-to-reality model that gives results that agree closely with experimental results. The continuum modelling is explained starting by representing a lone CNT fibre encompassed by a matrix and then moving to models that exhibit the nanocomposites at the meso- and macro-scales. The processes of developing each representation are detailed out and the effectiveness of each model is discussed and compared. Finally, the conclusions are given along with recommendations for prospective future works.

2 The Continuum Modelling Approach

The challenge in conducting continuum modelling of a CNTC comes from the huge scale difference between the nano material and the matrix as all the characteristics of the CNT need to be considered. Failing to do so will cause the model to give solutions close to results due to the rule of mixture (ROM) but very far from the experimental findings.

Figure 1 shows how CNTs are typically positioned in a matrix, moving from nano-scale to micro-, meso- and macro-scales. While the length, waviness and defects of the CNTs can be considered at the nano- and micro-scales, the random orientation and agglomeration of the CNT can only be seen at the larger meso- and macro-scales [11]. As such, a full-scale model covering from nano- until the macro-scale is required to offer a close-to-real representation of the nanocomposite.

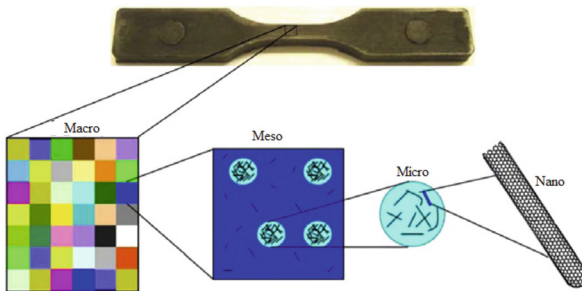


Fig. 1. From macro- to nano-scale in representing a CNT composite [11]

In the FEM continuum modelling approach, all or part of the constituents of the CNT composites are represented as equivalent continua. As an example, a CNT has been represented in FEM as a space-frame structure with each of its bonds is treated as an equivalent hollow cylinder, a solid cylinder, or simply an equivalent fibre (EF) [12]. The issue here is to get the right properties of the equivalent continuum to represent the real CNT structure.

2.1 The Representative Volume Element

The CNT composite in the FEM continuum modelling approach is represented as a unit cell or better known as the RVE, which basically consists of a matrix and a CNT.

With reference to Fig. 2, the characteristics of a CNT composite with repeated similar cells that give the global periodicity can be represented as a RVE with careful application of boundary and interface conditions.

The simplest RVE model assumes a perfect bonding or perfect load transfer between CNT and matrix where each phase is assumed to form a continuum. In this complete continuum representation, a long or short CNT fibre surrounded by a matrix is represented as a solid RVE at the nano-scale. The RVE is given appropriate boundary conditions and loaded such that the deformation obtained through the FEM can be applied in derived formulae to determine the CNTC's effective properties. While this representation does not consider the CNT-matrix interphase, it can still consider CNT characteristics such as CNT length, waviness and defects.

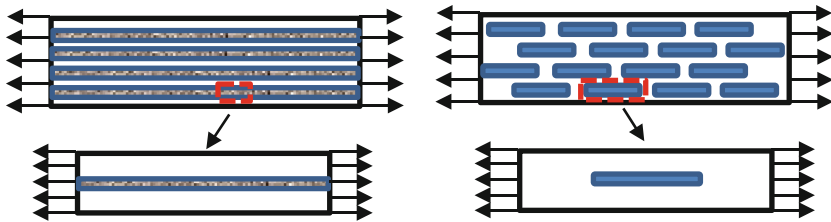


Fig. 2. Representing a unit cell as the whole CNT composite [11]

A strong CNT-matrix interface has been shown by CNTC along with an effective load transfer between the two constituents as indicated by experiments [13]. As such, more realistic models that consider the CNT-matrix scale difference i.e., an interphase is added to the RVE in order to cater for the CNT-matrix non-bonded relations. This so-called multiscale RVE model is a three-phase representation being made of matrix, CNT and their interphase. While considering the interphase improves the model, it can remain limited to considering CNT characteristics at the nano- and micro-scales as it considers only a single CNT fibre. Here, the macroscopic behaviours of the CNT composites are predicted assuming the well-dispersed and uniform distributions of the CNTs that result in the global periodicity of the nanostructures [14].

Referring to Table 1(b)–(d), depending on the phases whether they are in atomic (A) or continuum (C) forms, here the multiscale representative can be categorized into

3 types according to the order of arrangement of the CNT, interphase and matrix: the A-A-C [15], A-C-C [16] and C-C-C models [17]. As an example, in the A-A-C model, the CNTs are represented at the atomic level such that carbon atoms and the inter-atomic covalent bonds are modelled as FEM nodes and beam elements respectively. The CNT-matrix van der Waals (vdW) interactions between the matrix and CNT which is weak and non-bonded may be represented as a truss element while the matrix is taken as a solid continuum.

3 Modelling the Two-Phase CNT Composite

Referring to Table 1(a), For simplicity, modelling CNT composites began by representing a single CNT fibre that was surrounded by a matrix with the CNT-matrix bonding assumed to be perfect. This approach is expected to give results that is comparable to those from ROM because of their similar assumptions.

3.1 Predicting the Effective Properties

Using this approach, Liu and Chen [18] applied a quarter-scale continuum model to represent the CNT and the matrix. Here, a square RVE consisting of a matrix and a short SWCNT, both represented as continuum elements with assumed dimensions of the CNT continuum and stiffness ratio of $E_{cnt}/E_m = 10$, was analyzed using FEM to determine the RVE's load transfer capability.

The results from both FEM and boundary element (BEM) methods corresponded well. Furthering this study, investigations were conducted to predict the four transversely isotropic effective properties (longitudinal modulus, E_z , transverse modulus $E_x = E_y$, ν_{xy} and Poisson's ratio, $\nu_{zx} = \nu_{yz}$ of long and short CNT composites using a cylindrical RVE [19], square RVE [20] and hexagonal RVE [21] while applying three loading cases of axial stretch, lateral uniform load and torsional load. In all cases, derivations were made to determine formulae for the effective properties.

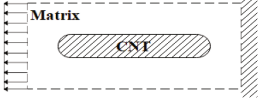
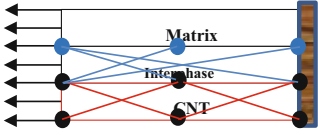
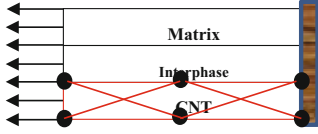
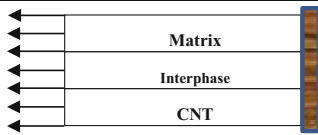
Comparing the results of the three RVEs, the hexagonal RVE was found to give results close to those of the cylindrical. The use of cylindrical RVE has been preferred by researchers [22] since CNTs with various radius can be easily modelled especially in a form of concentric cylinder [23]. The results of the effective properties showed the substantial contribution provided by the CNT to the nanocomposites.

3.2 The Effect of CNT Characteristics

Several researchers studied the influences of factors on the CNTC properties: CNT waviness [24], pinhole defects [25] and CNT orientation [26]. With the global periodicity assumption, the fibre-matrix bonding was assumed to be perfect and formulae for the effective property were derived.

The Effect of CNT Waviness. In reality, due to the vdW interactions along with electrostatic forces, CNTs are typically curled, agglomerated and aggregated [27]. Through a micromechanical modelling [24] and continuum modelling of the two-phase CNTC

Table 1. The categories of nanocomposite continuum models.

Types	Model	Descriptions
(a) No interphase		Both CNT and matrix are continuum elements
(b) A-A-C model		CNT and interphase are represented at the atomic scale while matrix is taken as solid continuum.
(c) A-C-C model		CNT in atomic scale but the interphase and matrix are in solid continua.
(d) C-C-C model		All constituents are modelled as continua

[28], the increase in the CNT waviness ratio ($w = a/L$) has significantly decreased the E_z and the ultimate strength of the CNT composite. The influence of CNT waviness was even more significant when completely randomly oriented CNTs with different waviness were applied [28]. In the analytical work of Stein and Wardle [29], a simulation framework that was capable of analysing 105 CNTs with realistic morphologies and waviness ratio, w , it was shown that the waviness was responsible for the huge over-prediction of the CNT composite elastic modulus and as such results from experiment [30] can be reproduced.

The Effect of CNT Defects. Several defects in the CNT atomic network may be developed during the growth and purification of CNT, the irradiation process with energetic particles [31] and the functionalization process [32]. A process of adding a small organic group to the nanotube sidewall [33] may be conducted to upgrade the vdW interactions into the matrix–CNT covalent bonds [34]. In this process however, the strong chemical bonding and the formation of SP3 hybridised sites may cause defects such as the pinhole defect. A research was conducted on the influence of pinhole defects on the effective properties of the CNTC by applying a continuum representation for both the CNT and the matrix [25]. A single long and short CNT were modelled as a hollow cylindrical continuum with added pinholes and waviness. Two types of pinholes with diameter 0.4 nm and 0.8 nm were placed on the CNT in z -direction at equal gaps. It was discovered that even a waviness or a pinhole defect has immensely modified the overall properties of the CNT composites. A square RVE representing a perfectly bonded CNT-matrix interphase was used [35] to study the effect of CNT fibre breakages on the redistribution of stress at

the broken CNT location. The RVE was given a strain and a nonlinear behaviour of the CNT was incorporated into the analysis. It was determined that the ineffective length of the defective CNT was 28% for the CNT/Epoxy composite and only 3% CNT/Titanium composite.

The Effect of CNT Direction. The fully continuum two-phase model was used to determine the influence of the orientation of a single CNT on the axial and lateral modulus [26]. It was found that the higher the angle of inclination of the CNT angle the lower the effective axial and lateral modulus. The orientation effect was, however, reduced if the waviness factor was included. In a work by Moghaddam et al. [36], the consequence of the high CNT inclination angle that decreased the properties was insignificant as the angle reaches 60° , 30° and 15° for the axial modulus, Poisson's ratio and the transverse elastic modulus, respectively. The role of limiting certain effects of a CNT at a certain CNT angle of orientation was also discovered by Huang and Rodrigue [37] where at a 30° angle of orientation and volume fractions (VF s) greater than 0.74%, the stresses (tensile and shear) can no longer be influenced.

4 The Continuum Approach in Multiscale Modelling with interphase

In multiscale continuum modelling, CNT composites are represented in a form of RVE comprising the CNT, the matrix and the CNT-matrix interphase. Here, the models are given names based on the phases of the RVE's constituents, as given in Table 1. The major contribution of this modelling is the use of the vdW forces within the interaction between the CNT and matrix. However, only composites with one CNT fibre contained by the interphase and matrix are considered, thus exposing the weakness of this modelling that may consider the nanoscale level only.

4.1 The A-A-C model

The benefit of the A-A-C model is the CNT lattice structure is kept even though the model of the matrix is simplified to a continuum [38]. Several researchers have investigated the A-A-C model of the CNTC that vary mainly in terms of their modelling of the interphase between CNT and matrix. The effects of several CNT characteristics and the non-linearity assumption of the model were also considered.

Modelling Truss Rods as the Interphase. Li and Chou [39] used the multiscale modelling approach to determine the CNT-matrix load transfer within a nanocomposite loaded with a compressive load before the buckling behaviour of this nanocomposite was studied. Using a cylindrical RVE, both continuous and short CNT fibres were considered. Applying FEM, the CNTs were represented as nodes (carbon atoms) connected by beam elements (covalent bonds) whereas the epoxy matrix was represented as a continuum. The CNT-matrix interphase that was characterized by vdW interactions was represented as truss rods that connected the carbon atoms and the inner surface nodes of the matrix continuum, as shown in Fig. 3. The properties of the rods, representing the

vdW low level CNT-matrix interactions were determined based on the “6–12” potential of Lennard-Jones. The longitudinal modulus was determined to match well with the ROM’s result.

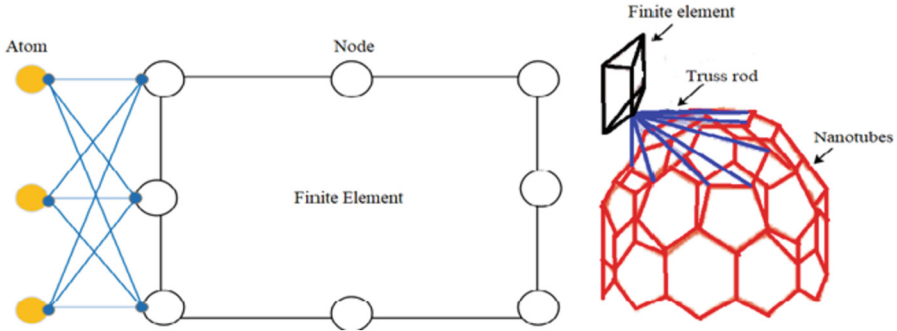


Fig. 3. The A-C-C model: (a) the lateral surface and (b) the end cap region of the nanotube [39]

Modelling Beams as the Interphase. Joshi et al. [40] used the A-A-C multiscale model to examine the effect of CNT chirality on the stiffness of the CNTCs. In contrast to [39], the interfacial region was characterized discretely by beam elements that connected the atoms of the nanotubes radially with the corresponding nodes at the inner cylindrical surface of the matrix. Various parametric studies were conducted including the effect stiffness, tensile strength and chirality of the CNT on the mechanical behaviour of the CNTCs. The results for the elastic and shear moduli were found to agree closely with those of the ROM. The same A-A-C model was applied to investigate the influences of chiral angle, vacancy defect locations and number of vacancy defects on the elastic properties and strength of the nanocomposites subjected to axial loading [41]. As the CNT was modelled in atomic form, the modification of the CNT atomic structure was done by omitting 1 atom and 3 bonds for a single vacancy representation. It was found that the nanocomposite strength increased as the chiral angle increased while the maximum stress of the nanocomposites decreased as the location of the vacancy defect was moved away from the fixed point of the RVE. Furthermore, it was found that even a single vacancy can highly influence the Young’s modulus of the CNT composites.

Modelling Spring Elements as the Interphase. Applying the A-A-C multiscale modelling Method, Shokrieh and Rafiee [42] used ANSYS software to simulate a cylindrical RVE that predicted the effective elastic properties of a CNTC. Referring to Fig. 4, a SWCNT was represented at the atomic level where carbon atoms were treated as nodes and the strong bonds between them were represented by Timoshenko beam elements. The interphase region was modelled using the Combin39 non-linear spring elements of ANSYS software to represent vdW interactions. The non-linear characteristic behaviour of the spring elements was according to the Lennard-Jones “6–12” [43]. Three load cases were given to the RVE in a process to determine the longitudinal, shear and transverse moduli. It was found that the RVE exhibited highly non-linear behaviour under tensile load. The longitudinal elastic modulus was shown to recover if the length of the CNT

was between 100nm and 10 μ m. The results show that the CNT and the interphase can be considered as having comparable properties to a long fibre as the results followed the trend in Odegard et al. [44].

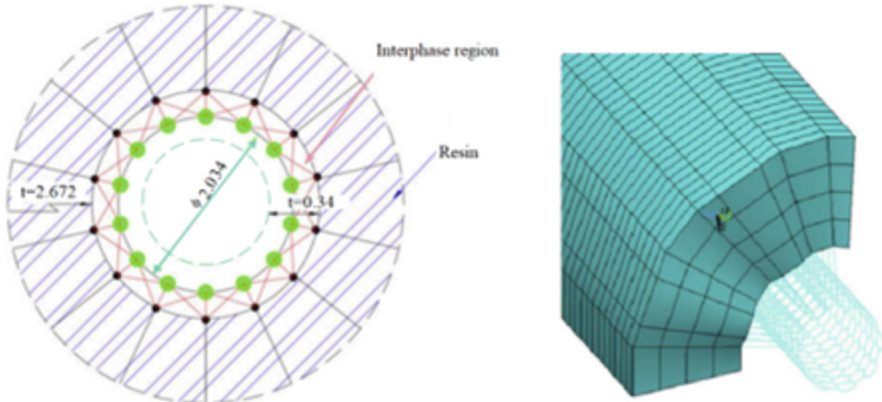


Fig. 4. (a) The schematic view of the CNT composite, (b) the cut section of the real FEM model [42]

Modelling Joint Elements or Links as the Interphase. A new method of representing the interfacial region was to treat it as a heterogeneous region that was constructed in a discrete manner by bringing together joint elements of varying stiffness [45]. While the CNT was represented at the atomic level using spring-based elements to represent the covalent bonds, the matrix was treated as an isotropic continuum. With this multiscale model, studies were conducted on the various stress-transfer characteristics of the CNTC in the RVE. When the interfacial region was tested with different values of stiffness, the normalized stiffness of the CNTC provided the meaningful influence of the interfacial stiffness on the elastic characteristics of the CNTC. The study also found that the transfer of stress was influenced by the atomic microstructure, VF of CNT and the E of the interphase region.

4.2 The A-C-C Model

An RVE such as shown in Fig. 5 was used to examine the influence of interphase thickness (t_{if}) and stiffness on the transfer of stress and the E_{eff} of CNT composites [16]. The SWCNT was represented based on an atomic molecular structural mechanical approach in which the covalent bond was treated as a Timoshenko beam. Being a continuum, the interface and matrix were modelled using brick elements while it was assumed that CNT-matrix stress transfer occurred fully. The 3-phase RVE was validated using past experimental results and the results from a CNT composite model without the interphase. It was found that both results using the fully continuum approach were in close agreement. However, the results for the 3-phase model with interphase were found

to give higher values than the experimental values for the SWCNT-polymer composite due to the presence of stress concentration regions as a consequence to the weak boundary layer in the interphase region.

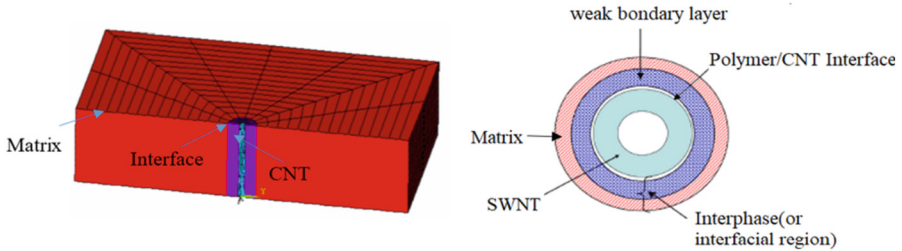


Fig. 5. (a) The RVE of the A-C-C model (b) The cross-section of the RVE [72]

4.3 The C-C-C Model

Several researchers have considered continuum modelling for all three phases of the CNT composites. The difference between these models was on how the properties and thickness for the interphase continuum were assumed or determined. As stressed by Zuberi and Esat [22], both mechanical properties and thickness of the interphase have not been reported yet, experimentally. As such, the difference in the results on the significance of the interphase on the CNTC's effective properties is expected.

Interphase Property as a Ratio-to-Matrix Property. Wan et al. [17] applied a full three-phase continuum model to conduct a numerical study on the effect of CNT dimension and the CNT-matrix interphase on effective moduli of the CNT composite. The CNT and the matrix were treated as a continuum while the interphase was a homogeneous continuum of the same width as the CNT and assumed to have hard stiffness ($E_{int} = 10 E_{matrix}$) or soft stiffness ($E_{int} = 0.3 E_{matrix}$). It was found that the effect of CNT length was significant in ensuring the occurrence of full load transfer and that the critical length of the CNT for this study was 271nm. The effect of the interface was found to be only slightly so for the effective properties. Similar effect was found by Ayatollahi et al. [46] that used an equivalent cylindrical beam element to represent CNT such that the nonlinear properties of the SWCNT was described using the beam elements. Golestanian and Shojaie [47] assumed the E of the interphase as 3.2 GPa and 100 GPa where the Young's modulus of the matrix was given values between 3.2 GPa and 100 GPa. The study revealed that for the interphase models, the effect of the interphase on the E_{eff} was significant only for low-modulus polymers. Zuberi and Esat [22] researched the influences of CNT diameters and chirality on the E_z and Poisson's ratio of CNTCs by applying a RVE with the C-C-C model. The E of the interphase was assumed to be 20GPa while the interphase thickness was 3 times the CNT thickness. The armchair RVEs gave the highest values of the E_z and ν followed by the chiral and zig-zag RVEs.

Gradient Functions of the Interphase Properties. In a study by Perez and Aviles [48], a cylindrical RVE consisting of CNT, matrix and an interphase was applied to determine

the influence of the interphase on the effective properties. All three phases were modelled as continuum with transversely isotropic material properties. Specifically, the interphase parameters considered were thickness and varying E across the interphase's thickness. The study showed that the CNT-to-matrix modulus ratio and thickness have significant effects on the properties of the CNTCs.

Molecular Dynamic Approach to Determine the Interphase Properties. A study by Guru et al. [49] combined the MD and FEM approaches to investigate the CNTC's constituent properties. The CNT was modelled as a space frame structure and the E of the covalent bond was calculated based on the modified Morse potential [50]. The MD method was used to predict the E of the matrix functionalized with a DETA curing agent. The modulus and thickness of the interphase were 18 GPa and 0.3 nm respectively, estimated through the MD method. Nonetheless, in the C-C-C modelling study using ANSYS software, the modulus and thickness of the interphase were simply varied. It was found that the effect of the E of the interphase on the E_z of the CNTC was substantial.

The Interphase Cohesive Law of Interphase Properties. Focusing on the effect of the CNT-matrix interfacial shear strength (ISS) on the ultimate strength of a CNT composite, Mohammadpour and Awang [51] conducted tensile tests using ANSYS on a multiscale cylindrical RVE with an interphase layer. The CNT-matrix non-bonded interaction that was based on the interphase cohesive law was characterized by the vdW force such that if the shear stress is above the ISS, the interface has failed at that specific element. The material nonlinearity of matrix was modelled using the multilinear isotropic hardening material model. The results in Fig. 6 shows that strong ISS gave good upgrading in the elastic behaviour of the CNTCs.

The Effect of Functionalization and Defects of CNTs. Rafiee and Pourazizi [38] conducted studies at micro level on the influence of functionalized CNT on the E of the CNT composites. Two types of interphase regions were used and compared. In the first type, the A-A-C model of CNT with C-C covalent bonds and the CNT-matrix vdW interactions were applied. The results was the functionalization reduced the E of the RVE. The contribution of the functionalization in improving the mechanical properties of the CNT composites will occur at the mesoscale. The combined improving and decreasing effects of the functionalization of CNT on the effective properties of nanocomposites were studied by Esbati and Irani [52] The studies considered six RVEs having parameters such as the non-linear behaviour of the CNT, nonlinear vdW interactions, nonlinear covalent bonds, structural defects and fractures in the matrix. The RVEs may also differ in length, chiral indices and interphase regions. In each case, a cylindrical RVE was used, applying the nonlinear FEM in ANSYS software. As in the study by Rafiee and Pourazizi [38], two types of interphases were considered. The study found that the RVEs containing functionalized CNTs provided a better representation of the mechanical properties compared to the RVEs with normal CNTs.

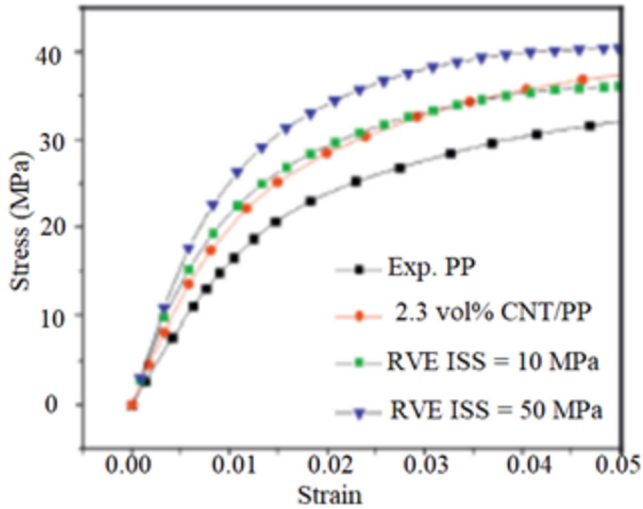


Fig. 6. The tensile test of CNT composites [51]

5 The Mesoscale Modelling of CNT Composites

The models previously discussed considered only one CNT fibre surrounded by a matrix. CNT characteristics such as length, chirality, orientation and defects were considered, all at nano- to micro-scales. To provide modelling closer to the real CNT composite at the macroscale, a representation of the nanocomposite should consider other characteristics of the CNT such as random orientation and agglomerations that can be seen at the mesoscale, as described in Fig. 2. It is known that CNT dispersion problems within the matrix have resulted in a random distribution of CNT and, due to high CNT length-to-diameter ratios and relatively strong intermolecular vdW interactions, there is a tendency for CNT to form bundles that later aggregate into agglomerates. To model a CNT composite with better accuracy, CNT-composite representations should consider CNT characteristics at all nano-, micro-, meso- and macro-scales. This is a big modelling problem as it involves a huge scale difference between nano- and macro-scales. Some of the meso- and macro-scale modelling described below can be referred in the diagrams in Table 2.

5.1 The Effect of CNT Randomness

In modelling the macroscopic properties of CNTCs, Afroos et al. [53] established the effect of short CNT fibre randomness on the elastic characteristics of the nanocomposites. CNT fibres were estimated as effective cylindrical fibres, represented by a 3D truss element applied in the MSC-Marc FEM software.

The RVE is divided into several hexagonal elements and randomness was considered to increase as the number of nodes was increased. Up to 15 RVEs representing 0%, 2.5%, 5% and 10.48% of CNT were used. The study found that the increase in randomness

of the CNT fibres will decrease the axial modulus and the ultimate strength of the CNT nanocomposite.

Improving this study while continuing to use the parallel CNT fibres that experienced perfect bonding with matrix, Makvandi and Öchsner [54] considered CNT fibre positions that were overlapping one another and also CNT fibres that were joined at nodes to become long fibres. The results indicated that the E of the CNTC was significantly influenced by the CNT positions whether they are completely separated, overlapped, or sharing the same nodes.

Tserpes and Chanteli [55] estimated the linear characteristics of the CNT composite at micro/mesoscales utilizing their earlier work on homogenizing the elastic properties at the nanoscale. A composite of a polystyrene matrix with randomly-aligned CNTs was modelled with specimen dimensions reaching macroscale level. The dimensions of the CNTs and how they were distributed were obtained from experimental observations [56]. Assuming uniform dispersion, all elements of the CNT composites were treated as RVE and a pseudorandom function was used to match specific orientations and elements. The tensile modulus predicted for the polystyrene matrix reinforced with randomly aligned CNT was found to agree excellently with the experimental data. Furthermore, CNT orientation has a substantial effect on the elastic stiffness where the tensile modulus diminished for angles of orientation greater than 45° .

5.2 The Effect of CNT Agglomerations

A cylindrical RVE containing CNTs, matrix and their interphase was modelled to represent the CNT composite, giving the effective fibre (EF) characteristics of the CNT composite at nanoscale [57]. Using Cauchy–Born rule, the Lennard–Jones was associated with the Park–Paulino–Roesler potential to represent the CNT–epoxy interphase. In the so-called two-scale approach, the EFs were then dispersed into the matrix randomly to numerically create another micro-scale, EF–matrix RVE using the Python script in the ABACUS. Effective properties of this RVE at the micro-scale were determined with and without considering the effect of agglomerations. The agglomerations were created by clustering half of the CNT RVE into 1, 2 and 4 colonies. The numerical and experimental results were discovered to match the experimental results after considering the agglomeration effects at microscale.

In a study by Chanteli and Tserpes [58], a cubic RVE with CNT agglomerates surrounded by matrix was modelled using ANSYS software. Scanning electron microscopy (SEM) images were applied to provide the parameters for the agglomerates. The average diameter of the CNT was found to be 29 nm while the mean length was 210 nm. The study found the opposite effect of agglomeration and waviness where the increase of CNT agglomeration decreased the elastic properties while the increase of waviness increased the linear properties.

Bhuiyan et al. [59] integrated experimental and FEA to study the influence of four CNT characteristics: random dissemination, bundle formation, waviness and orientation with respect to the loading. In the FEA studies, 3D RVEs were applied consisting of multiple equivalent solid CNTs [60], polypropylene and the interphase. The C–C–C model was used. Random coordinates were given for the centre of mass of the CNT while the CNT orientations were modelled based on an angle θ with respect to the

direction of longitudinal loading (x) and an angle ϕ with respect to a defined ($x-z$) plane. The thickness and stiffness of the interphase were determined from the experiment conducted using atomic force microscopy (AFM) which gave the average values of the interphase thickness and modulus as 20 nm and 0.7 GPa respectively. Further, the AFM was applied to describe the tensile modulus, the size of the CNT agglomerates and the CNT distribution used in the FEA. The diameters of agglomerates comprising 3, 7 and 19 CNT were determined as 40, 65 and 100 nm respectively while Young's modulus values were 35, 30 and 12 GPa respectively. The FEA showed that the effective aspect ratio of the CNT was $L/D = 65$. Two leading factors working against the great potential of the CNT nanocomposites (see Fig. 7) were found to be CNT agglomeration and waviness. The FEA results from applying the experimentally-obtained data were found to agree excellently with experimental results.

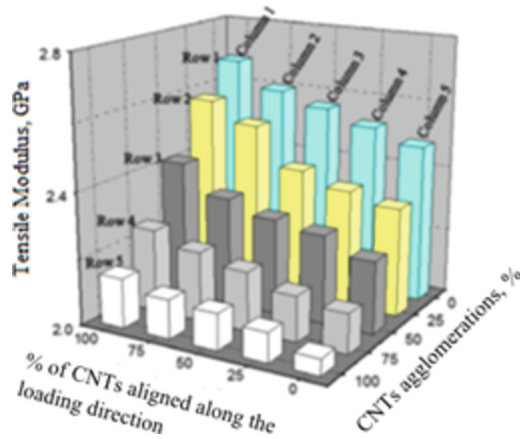


Fig. 7. The effect of CNT alignment and agglomeration on the tensile modulus of CNT composite [60]

5.3 The Stochastic Modelling of CNT Composites

In novel research by Shokrieh and Rafiee [11], a hierarchical, multi-scale, modelling technique called N3M was established to study the effective characteristics of CNTCs. Referring to Fig. 8, the approach used a stochastic modelling procedure with a different RVE applied each at the nano-, micro-, meso- and macro-scales where random parameters of length and interphase (nano), orientation, agglomeration, curvature (meso) and dispersion of CNT (macro) were considered.

At nanoscale, a composite consisting of a CNT fibre, the matrix and their interphase was modelled to give an EF. EFs with different lengths were distributed randomly within a matrix to become another RVE at microscale. At macroscale, the bulk CNT composite was divided into several blocks using a regular tessellation technique where each block was an RVE at mesoscale that consisted of several spherical agglomerated CNTs and fully-dispersed CNTs. The properties of each block at mesoscale were calculated using

an improved micromechanical model and the overall properties at macroscale were calculated using an averaging method. The results of the elastic stiffness and Poisson's ratio were determined and agreed excellently with past experimental results. Improvements were made to the N3M model [11] by Rafiee and Firouzbakht [61] who now used an irregular tessellation technique that considered the local position of each aggregate of CNT. The irregular tessellation was used to divide the RVE at mesoscale into heterogeneous polygons based on an irregular pattern provided by the Bayes classification algorithm combined with the Voronoi approach. The new method gave results that agree well with the findings of the N3M model and the experimental observations.

In a different approach without considering CNT-matrix interphase, the hierarchical multiscale modelling of CNT composites was used to study the influence of weight fraction of the CNTs and ISS based on sensitivity analysis on the damping characteristics of the CNTCs. Savvas et al. [62] used the space frame structure to model the CNTs that was later converted to EBE, the equivalent beam element (EBE) of the CNT. Applying the FEM, this EBE at nano-scale was used as the basic micro-scale building block for the construction of full length CNTs covering several EBEs embedded in the polymer. While the EBEs were assumed to behave linearly, the polymer, modelled as continuum was equipped with viscoelastic behavior applying the Maxwell–Wiechert material model. Without considering the interphase region, a nonlinear bond-slip friction-type model was used to represent the interfacial load transfer mechanism between the CNT and the matrix. While the straight CNTs can be considered easily, the average properties of wavy CNTs were determined using stochastic Monte Carlo simulation. The study showed the importance of a successful functionalization process that gives an increased ISS to achieve optimum damping characteristics. Furthermore, to improve damping properties of the CNTCs, it is crucial that CNTs are made to be straight. The results here were quite close to those of [63].

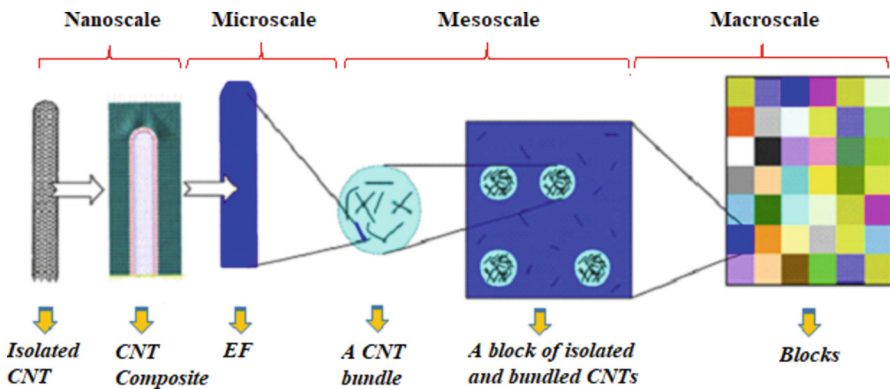


Fig. 8. Steps in hierarchical multi-scale modelling [11]

5.4 The Multiscale Modelling with Fuzzy CNT-Matrix

The difficulties to get the expected properties even after great deals of studies conducted on modelling of the CNT composites due to the agglomeration of CNTs, among others in the manufacturing process of the CNTs have led to attempt to grow CNTs directly on the fibre surface [64], a procedure that was found to be advantageous [65].

In the study by Kundalwal and Ray [64], the implementation of the radially grown CNT on carbon fibre surfaces or better known as fuzzy fibre [66] that can be assumed as transversely isotropic was proven to significantly improve the transverse effective properties of the fuzzy fiber-reinforced composite (FFRC). Applying the micromechanics model, two methods of cell approach and FEM were used to determine the effective properties of the nano composites.

A study [67] was conducted to toughen the interfacial fiber-matrix region with carbon nanostructures (CNS) while considering the effect of the orientation of the CNS. A multiscale micromechanical model consisted of the simplified unit cell (SUC) and Eshelby methods were used in finding the effective elastic modulus properties of FFRC [68]. For accurate property prediction with respect to experimental values, the study revealed that CNT should be characterised as wavy, randomly distributed, behaving in transversely isotropic manner and having interphase region with the matrix. The study found that the improvement of longitudinal modulus can be neglected while the transverse modulus was found to improve significantly.

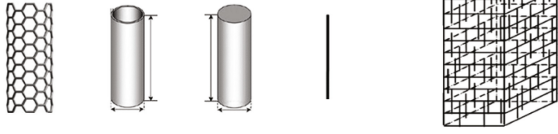
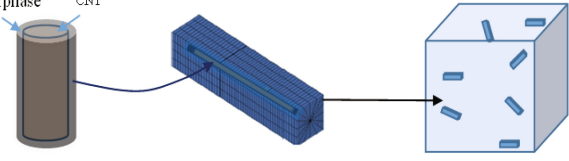

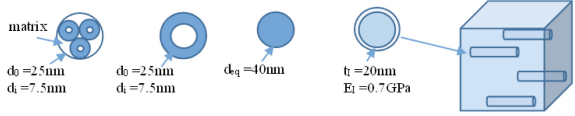
In a study by Rafiee and Ghorbanhosseini [69], Young's modulus of unidirectional FFRP having radially aligned CNTs on the surface of the core fiber was theoretically predicted following their previous work of bottom-up modelling CNT composites [11] that covers the four nano-, micro-, meso- and macro-scale. While the Young's modulus of the FFRP was determined using the deterministic modelling, the Monte-Carlo simulation technique for stochastic modelling was employed as the effects of CNT curvature and VF were considered as random variables. The results showed a very closed agreement with the experimental findings from Kulkarni et al. [70].

6 Concluding Remarks and Future Perspectives

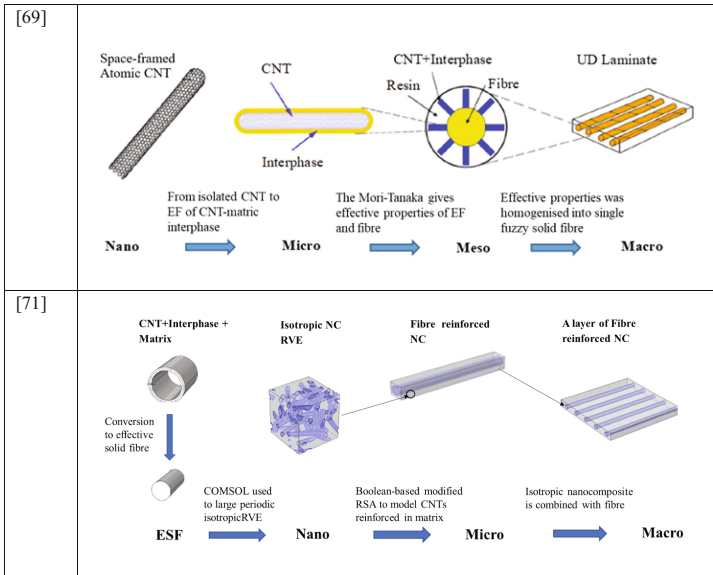
It had been expected that CNTs would improve mechanical properties of CNTCs but experimental researches have shown that CNT provided improvements that are much lower than those predicted by the ROM. This paper reviews the progress of FEM-applied continuum representation of CNTCs over the last two decades as the most suitable method of analysis in predicting close-to-reality values of effective properties of CNT nanocomposites. The journey of this continuum modelling has gone through several stages:

1. It started with the 2-phase continuum representation with an assumption of perfect bonding between the phases. Hence, the results are similar to the results of the ROM, as expected. Here, the linkage between the nanoscale and the upper scales in the form of an interphase was neglected.

Table 2. CNT composite modelling: from nana to macro

Ref	Modelling of Marco-scale CNT composites
[53]	<p>Space-framed Atomic CNT An equivalent hollow CNT An equivalent solid CNT A CNT FEM truss element CNT composite</p>  <p><i>Representing a space-framed CNT as a truss element</i></p> <p><i>Randomized CNTs into matrix for tensile test</i></p> <p>Nano → Nano → Macro</p>
[55]	<p>CNT with interphase RVE of a MWCNT composite CNT composite</p>  <p><i>Forming an RVE with a CNT with interphase</i></p> <p><i>Dispersing RVE randomly into matrix for tensile test</i></p> <p>Nano → Micro → Macro</p>
[57]	<p>Equivalent Fibre CNT composite</p>  <p><i>Homogenization of randomly oriented and agglomerated (clustered) CNTs for tensile test</i></p> <p>Nano → Macro</p>
[60]	<p>CNT agglomerates (CA) Equi. hollow CA Equi. solid CNT (ESC) ESC with interphase (ESCI) CNT composite</p>  <p><i>Representing agglomerated CNTs as ESCI applying data from AFM</i></p> <p><i>Dispersing randomly oriented ESCI into matrix for tensile test</i></p> <p>Nano → Nano → Macro</p>

(continued)

Table 2. (continued)

- The journey then progressed to considering the CNT-matrix interphase where CNT, matrix and their interphase have been treated in atomic or continuum forms. The nanocomposites have been classified in this paper as the A-A-C, A-C-C and C-C-C models, referring to the atomic (A) or continuum (C) representation of the phases. As in the first stage model, these models merely consisted of a CNT fibre surrounded by matrix and with the assumption of the CNT dispersion being globally symmetrical; the considered RVE can only capture the CNT characteristics as composite fillers at the nano- and micro-scales. As such, even with tackling the scale difference between CNT and matrix in considering the interphase, these representations considered CNT characteristics of length, waviness, orientation and defects only whilst ignoring the important characteristics of CNT randomness and agglomeration which give results close to those of the ROM.
- Several researchers have modelled mesoscale nanocomposites that can capture the randomness and agglomeration of the CNT. By applying the concept of EFs, one method is simply taking an RVE with a greater number of randomized EFs so that the size of the RVE now reached mesoscale. In hierarchical modelling, an RVE has been used at each of the nano-, micro-, meso- and macro-scales where the EF representation of the previous scale can be applied in a random fashion in the next higher scale. The hierarchical representation was proven to give results close to the experimental values.

With mesoscale modelling providing some success, the accurate continuum modelling for CNT nanotubes is closed to giving the full elastic constitutive relations of the CNT nanocomposite. Further, deeper understanding on the main culprit in the reduction

of properties may lead to simpler modelling at nano- or micro-scale that may also provide results that are close to experimental results. For example, the analytical work of Stein and Wardle [41] that used the better representation of waviness to give the elastic properties that were close to experimental values should be emulated in continuum modelling. With these modelling successes, the main task is to improve the CNT characteristics that lead to the failure of the CNTC. The manufacturing process of the CNT composite needs to be improved such that the scattering of CNT within the matrix will be straighter, more uniform and less agglomerated.

References

1. Thirugnanasambantham, K., et al.: Strengthening mechanisms of aluminium (Al) carbon nano tube (CNT) composites: a comprehensive review–Part I. *Mater. Today: Proc.* **60**, 1468–1473 (2021)
2. Gargeya, B.S.K., et al.: Study of debonding phenomena at interface and its implication on mechanical behaviour of epoxy-CNT nano-composite using molecular dynamics simulation. *Mater. Today: Proc.* **21**, 1111–1115 (2020)
3. Sobhani, E., et al.: Agglomerated impact of CNT vs. GNP nanofillers on hybridization of polymer matrix for vibration of coupled hemispherical-conical-conical shells. *Aeros. Sci. Technol.* **120**, 107257 (2022)
4. Mohamad Senusi, N.A., et al.: Effect of CNT/CNC hybrid nanofiller on PVA/CNT/CNC nanocomposite. *Mater. Today: Proc.* **66**, 3087–3091 (2022)
5. Selvaraj, R., Ramamoorthy, M., Arumugam, A.B.: Experimental and numerical studies on dynamic performance of the rotating composite sandwich panel with CNT reinforced MR elastomer core. *Compos. Struct.* **277**, 114560 (2021)
6. Hu, Z., et al.: New symplectic analytic solutions for buckling of CNT reinforced composite rectangular plates. *Compos. Struct.* **303**, 116361 (2023)
7. Quinteros, L., García-Macías, E., Martínez-Pañeda, E.: Micromechanics-based phase field fracture modelling of CNT composites. *Compos. B Eng.* **236**, 109788 (2022)
8. Wang, J.F., et al.: Molecular dynamics-based multiscale nonlinear vibrations of PMMA/CNT composite plates. *Mech. Syst. Signal Process.* **153**, 107530 (2021)
9. Gogoi, R., Sethi, S.K., Manik, G.: Surface functionalization and CNT coating induced improved interfacial interactions of carbon fiber with polypropylene matrix: a molecular dynamics study. *Appl. Surf. Sci.* **539**, 148162 (2021)
10. Nguyen, P.D., et al.: Buckling response of laminated FG-CNT reinforced composite plates: analytical and finite element approach. *Aerosp. Sci. Technol.* **121**, 107368 (2022)
11. Shokrieh, M.M., Rafiee, R.: Stochastic multi-scale modeling of CNT/polymer composites. *Comput. Mater. Sci.* **50**(2), 437–446 (2010)
12. Yengejeh, S.I., Kazemi, S.A., Öchsner, A.: Carbon nanotubes as reinforcement in composites: a review of the analytical, numerical and experimental approaches. *Comput. Mater. Sci.* **136**, 85–101 (2017)
13. Qian, D., et al.: Load transfer and deformation mechanisms in carbon nanotube-polystyrene composites. *Appl. Phys. Lett.* **76**(20), 2868–2870 (2000)
14. Sheikhejad, O., et al.: Molecular dynamic simulation of carbon nanotube reinforced nanocomposites: the effect of interface interaction on mechanical properties. *MOJ Poly. Sci.* **2**(1), 6–10 (2018)
15. Li, C., Chou, T.-W.: Multiscale modeling of carbon nanotube reinforced polymer composites. *J. Nanosci. Nanotechnol.* **3**(5), 423–430 (2003)

16. Banerjee, D., Nguyen, T., Chuang, T.-J.: Mechanical properties of single-walled carbon nanotube reinforced polymer composites with varied interphase's modulus and thickness: a finite element analysis study. *Comput. Mater. Sci.* **114**, 209–218 (2016)
17. Wan, H., Delale, F., Shen, L.: Effect of CNT length and CNT-matrix interphase in carbon nanotube (CNT) reinforced composites. *Mech. Res. Commun.* **32**(5), 481–489 (2005)
18. Liu, Y., Chen, X.: Continuum models of carbon nanotube-based composites using the boundary element method. *Electron. J. Bound. Elements* **1**(2), 316–335 (2003)
19. Liu, Y., Chen, X.: Evaluations of the effective material properties of carbon nanotube-based composites using a nanoscale representative volume element. *Mech. Mater.* **35**(1–2), 69–81 (2003)
20. Chen, X., Liu, Y.: Square representative volume elements for evaluating the effective material properties of carbon nanotube-based composites. *Comput. Mater. Sci.* **29**(1), 1–11 (2004)
21. Le, M.-T., Huang, S.-C.: Modeling and estimating the effective elastic properties of carbon nanotube reinforced composites by finite element method. *工程科技與教育學刊* **11**(2), 145–158 (2014)
22. Zuberi, M.J.S., Esat, V.: Investigating the mechanical properties of single walled carbon nanotube reinforced epoxy composite through finite element modelling. *Compos. B Eng.* **71**, 1–9 (2015)
23. Wang, J., Liew, K.: On the study of elastic properties of CNT-reinforced composites based on element-free MLS method with nanoscale cylindrical representative volume element. *Compos. Struct.* **124**, 1–9 (2015)
24. Fisher, F., Bradshaw, R., Brinson, L.: Fiber waviness in nanotube-reinforced polymer composites—I: modulus predictions using effective nanotube properties. *Compos. Sci. Technol.* **63**(11), 1689–1703 (2003)
25. Joshi, U.A., Sharma, S.C., Harsha, S.P.: Analysis of elastic properties of carbon nanotube reinforced nanocomposites with pinhole defects. *Comput. Mater. Sci.* **50**(11), 3245–3256 (2011)
26. Joshi, U.A., Sharma, S.C., Harsha, S.P.: Effect of carbon nanotube orientation on the mechanical properties of nanocomposites. *Compos. B Eng.* **43**(4), 2063–2071 (2012)
27. Alian, A., Meguid, S.: Molecular dynamics simulations of the effect of waviness and agglomeration of CNTs on interface strength of thermoset nanocomposites. *Phys. Chem. Chem. Phys.* **19**(6), 4426–4434 (2017)
28. Paunekar, S., Kumar, S.: Effect of CNT waviness on the effective mechanical properties of long and short CNT reinforced composites. *Comput. Mater. Sci.* **95**, 21–28 (2014)
29. Stein, I.Y., Wardle, B.L.: Influence of waviness on the elastic properties of aligned carbon nanotube polymer matrix nanocomposites. In: 57th AIAA/ASCE/AHS/ASC Structures, Structural Dynamics, and Materials Conference (2016)
30. Handlin, D., et al.: Three-dimensional elastic constitutive relations of aligned carbon nanotube architectures. *J. Appl. Phys.* **114**(22), 224310 (2013)
31. Sammalkorpi, M., et al.: Mechanical properties of carbon nanotubes with vacancies and related defects. *Phys. Rev. B* **70**(24), 245416 (2004)
32. Yengejeh, S.I., et al.: Simulations of graphene sheets based on the finite element method and density functional theory: comparison of the geometry modeling under the influence of defects. *J. Nano Res.* **47**, 128–135 (2017)
33. Hu, H., et al.: Sidewall functionalization of single-walled carbon nanotubes by addition of dichlorocarbene. *J. Am. Chem. Soc.* **125**(48), 14893–14900 (2003)
34. Li, Y., Seidel, G.: Multiscale modeling of the interface effects in CNT-epoxy nanocomposites. *Comput. Mater. Sci.* **153**, 363–381 (2018)
35. Kirtania, S., Chakraborty, D.: Multi-scale modeling of carbon nanotube reinforced composites with a fiber break. *Mater. Des.* **35**, 498–504 (2012)

36. Moghaddam, F., Ghavanloo, E., Fazelzadeh, S.: Effect of carbon nanotube geometries on mechanical properties of nanocomposite via nanoscale representative volume element. *J. Solid Mech.* **8**(3), 568–577 (2016)
37. Huang, J., Rodrigue, D.: The effect of carbon nanotube orientation and content on the mechanical properties of polypropylene based composites. *Mater. Des.* **55**, 653–663 (2014)
38. Rafiee, R., Pourazizi, R.: Influence of CNT functionalization on the interphase region between CNT and polymer. *Comput. Mater. Sci.* **96**, 573–578 (2015)
39. Li, C., Chou, T.-W.: A structural mechanics approach for the analysis of carbon nanotubes. *Int. J. Solids Struct.* **40**(10), 2487–2499 (2003)
40. Joshi, U.A., Sharma, S.C., Harsha, S.P.: A multiscale approach for estimating the chirality effects in carbon nanotube reinforced composites. *Physica E* **45**, 28–35 (2012)
41. Joshi, U.A., Sharma, S.C., Harsha, S.P.: Characterizing the strength and elasticity deviation in defective CNT reinforced composites. *Compos. Commun.* **2**, 9–14 (2016)
42. Shokrieh, M.M., Rafiee, R.: Prediction of mechanical properties of an embedded carbon nanotube in polymer matrix based on developing an equivalent long fiber. *Mech. Res. Commun.* **37**(2), 235–240 (2010)
43. Battezzati, L., Pisani, C., Ricca, F.: Equilibrium conformation and surface motion of hydrocarbon molecules physisorbed on graphite. *J. Chem. Soc. Faraday Trans. 2: Molec. Chem. Phys.* **71**, 1629–1639 (1975)
44. Odegard, G., et al.: Constitutive modeling of nanotube-reinforced polymer composites. *Compos. Sci. Technol.* **63**(11), 1671–1687 (2003)
45. Spanos, K., Georgantzinos, S., Anifantis, N.: Investigation of stress transfer in carbon nanotube reinforced composites using a multi-scale finite element approach. *Compos. B Eng.* **63**, 85–93 (2014)
46. Ayatollahi, M., Shadlou, S., Shokrieh, M.: Multiscale modeling for mechanical properties of carbon nanotube reinforced nanocomposites subjected to different types of loading. *Compos. Struct.* **93**(9), 2250–2259 (2011)
47. Golestanian, H., Shojaie, M.: Numerical characterization of CNT-based polymer composites considering interface effects. *Comput. Mater. Sci.* **50**(2), 731–736 (2010)
48. Hernández-Pérez, A., Avilés, F.: Modeling the influence of interphase on the elastic properties of carbon nanotube composites. *Comput. Mater. Sci.* **47**(4), 926–933 (2010)
49. Guru, K., et al.: Effect of interface on the elastic modulus of CNT nanocomposites. *J. Nanomech. Micromech.* **6**(3), 04016004 (2016)
50. Tserpes, K., et al.: Multi-scale modeling of tensile behavior of carbon nanotube-reinforced composites. *Theore. Appl. Fract. Mech.* **49**(1), 51–60 (2008)
51. Mohammadpour, E., Awang, M.: Nonlinear Multi-Scale finite element method to predict tensile behavior of carbon Nanotube-Reinforced polymer composites. *J. Nano Res.* **26**, 169–176 (2014)
52. Esbati, A.H., Irani, S.: Mechanical properties and fracture analysis of functionalized carbon nanotube embedded by polymer matrix. *Aerosp. Sci. Technol.* **55**, 120–130 (2016)
53. Afrooz, I.E., Öchsner, A., Rahmandoust, M.: Effects of the carbon nanotube distribution on the macroscopic stiffness of composite materials. *Comput. Mater. Sci.* **51**(1), 422–429 (2012)
54. Makvandi, R., Öchsner, A.: A refined analysis of the influence of the carbon nanotube distribution on the macroscopic stiffness of composites. *Comput. Mater. Sci.* **77**, 189–193 (2013)
55. Tserpes, K.I., Chanteli, A.: Parametric numerical evaluation of the effective elastic properties of carbon nanotube-reinforced polymers. *Compos. Struct.* **99**, 366–374 (2013)
56. Thostenson, E.T., Chou, T.-W.: On the elastic properties of carbon nanotube-based composites: modelling and characterization. *J. Phys. D Appl. Phys.* **36**(5), 573 (2003)
57. Javadinejad, M., et al.: Using the equivalent fiber approach in two-scale modeling of the elastic behavior of carbon nanotube/epoxy nanocomposite. *Nanomaterials* **8**(9), 696 (2018)

58. Chanteli, A., Tserpes, K.I.: Finite element modeling of carbon nanotube agglomerates in polymers. *Compos. Struct.* **132**, 1141–1148 (2015)
59. Bhuiyan, M.A., et al.: Defining the lower and upper limit of the effective modulus of CNT/polypropylene composites through integration of modeling and experiments. *Compos. Struct.* **95**, 80–87 (2013)
60. Bhuiyan, M.A., et al.: Understanding the effect of CNT characteristics on the tensile modulus of CNT reinforced polypropylene using finite element analysis. *Comput. Mater. Sci.* **79**, 368–376 (2013)
61. Rafiee, R., Firouzbakht, V.: Predicting Young's modulus of aggregated carbon nanotube reinforced polymer. *Mech. Adv. Compos. Struct.* **1**(1), 9–16 (2014)
62. Savvas, D., Papadopoulos, V., Papadrakakis, M.: The effect of interfacial shear strength on damping behavior of carbon nanotube reinforced composites. *Int. J. Solids Struct.* **49**(26), 3823–3837 (2012)
63. Spitas, V., Spitas, C., Michelis, P.: Modeling of the elastic damping response of a carbon nanotube–polymer nanocomposite in the stress-strain domain using an elastic energy release approach based on stick-slip. *Mech. Adv. Mater. Struct.* **20**(10), 791–800 (2013)
64. Kundalwal, S., Ray, M.: Effective properties of a novel continuous fuzzy-fiber reinforced composite using the method of cells and the finite element method. *Eur. J. Mech.-A/Solids* **36**, 191–203 (2012)
65. Yamamoto, N., et al.: High-yield growth and morphology control of aligned carbon nanotubes on ceramic fibers for multifunctional enhancement of structural composites. *Carbon* **47**(3), 551–560 (2009)
66. Mathur, R., Chatterjee, S., Singh, B.: Growth of carbon nanotubes on carbon fibre substrates to produce hybrid/phenolic composites with improved mechanical properties. *Compos. Sci. Technol.* **68**(7–8), 1608–1615 (2008)
67. Kundalwal, S., Kumar, S.: Multiscale modeling of stress transfer in continuous microscale fiber reinforced composites with nano-engineered interphase. *Mech. Mater.* **102**, 117–131 (2016)
68. Hassanzadeh-Aghdam, M.K., Ansari, R., Darvizeh, A.: Micromechanical analysis of carbon nanotube-coated fiber-reinforced hybrid composites. *Int. J. Eng. Sci.* **130**, 215–229 (2018)
69. Rafiee, R., Ghorbanhosseini, A.: Predicting mechanical properties of fuzzy fiber reinforced composites: radially grown carbon nanotubes on the carbon fiber. *Int. J. Mech. Mater. Des.* **14**(1), 37–50 (2018)
70. Kulkarni, M., et al.: Elastic response of a carbon nanotube fiber reinforced polymeric composite: a numerical and experimental study. *Compos. B Eng.* **41**(5), 414–421 (2010)
71. Srivastava, A., Kumar, D.: Mechanical characterization and postbuckling behavior of carbon nanotube–carbon fiber reinforced nanocomposite laminate. *Proc. Inst. Mech. Eng. C J. Mech. Eng. Sci.* **232**(1), 106–123 (2018)



Investigation of Interfacial Behavior of SN100C and SN97C Solders with HASL Surface Finish Using Microwave Energy

N. H. Noor Izza, M. A. Rabiatul Adawiyah, and O. Saliza Azlina^(✉)

Faculty of Mechanical and Manufacturing Engineering, Universiti Tun Hussein Onn Malaysia,
86400 Parit Raja, Batu Pahat, Johor, Malaysia
salizaz@uthm.edu.my

Abstract. The growth of intermetallic compounds (IMCs) of HASL/SN97C (Sn-3.0Ag-0.5Cu) and HASL/SN100C (Sn-0.7Cu-0.05Ni-0.007Ge) during reflow soldering and isothermal ageing was investigated. Scanning electron microscopy (SEM) was used for the characterisation examination of the materials, with assistance from dispersive X-ray analysis. New layer IMC of Cu_3Sn formed between Cu_6Sn_5 and the HASL substrate after exposure to the ageing process, while Ag_3Sn nano-sized was also formed on the intermetallic surface of HASL/SN97C. After ageing, the intermetallic layer's average thickness increased. The IMC produced at the HASL/SN100C interface after reflow and ageing process had an average thickness of 6.54 μm and 8.50 μm , respectively. While the thickness of the IMC created after reflowing and ageing is 7.41 μm and 8.53 μm correspondingly for HASL/SN97C. Based on the observation, after the ageing procedure, the IMC thickness for both HASL/SN100C and HASL/SN97C increases. The results found that both SN97C/HASL and SN100C/HASL had contact angles of 26.64° and 35.76°, respectively. The spreading area in SN97C/HASL (976.68 μm^2) was significantly larger than that in SN100C/HASL (233.26 μm^2) due to the lower contact angle.

Keywords: Lead-free solder · HASL · Microwave energy · Reflow · Ageing

1 Introduction

Printed circuit boards (PCBs) are the insulations board with the desired thickness and stiffness that are typically utilized in a variety of electronic devices. In essence, surface finishes are applied to PCB to produce the necessary properties such as solder joint reliability, the copper pads' corrosion resistance and the provision of crucial connections between the devices [1–4]. Furthermore, Yoon and Jung [5] stated that criteria including solderability, solder joint quality, cost, ease of application, and material compatibility are taken into consideration when choosing a surface finish and the statement also agreed by Ramli *et al.* [6]. The purpose of PCB surface finishes is to preserve the exposed copper circuit while also providing a solderable surface during component soldering to the boards [7]. There are currently few surface finishes utilised in the semiconductor sector

[8–11]. One of the most surface finishes widely used is hot air solder levelling (HASL). HASL serves as a barrier to prevent the underlying copper from oxidizing and offers protection against corrosions induced by environmental and humidity-related pollutants [6]. A pre-cleaning cycle, preheating, flux coating, solder coating, levelling with hot air knives, cooling, and a post-cleaning phase make up the crucial HASL process [6, 12].

As a result, the HASL protective finish affects the quality of the soldered components due to interfacial intermetallic compounds (IMCs) formed by the interaction of liquid solder and the protective finish on the PCB. Good solderability can give advantages to the formation of high-quality solder joints. According to Gain and Zhang [13], solderability consists of two underlying properties which are spreadability and wettability. Spreadability serves the purpose of allowing solder to fill the gap (open surface). Wettability refers to how easily molten solder spreads across a surface that has been connected. Wettability is defined as the thermodynamics of the interface between the solder and substrate material, which can measure the rate and level of the wetting process during soldering [14, 15]. The wetting quality is determined using contact angle as stated by Wang *et al.* [16]. The study made by Li [17] indicated that poor solderability could lead to a weak solder joint, which would shorten the product's service life. This is one of the major issues facing the semiconductor industry because it may affect the solderability of solder joints.

Additionally, the solder starts to moisten the substrate when IMC starts to develop. According to the work by Dusek *et al.* [18], a good metallurgical bond was established via a solder joint with a thin IMC layer. However, these researchers also mentioned that an excessive IMC layer at the solder/substrate may decrease the mechanical properties of the solder because IMC is brittle. It is important to understand solderability and IMC formation because they work in tandem to ensure that solder joints are properly bonded. Therefore, SN100C/HASL was used to conduct additional research and was compared to SN97C/HASL in terms of IMC behavior and solderability of the solder joint.

2 Materials and Method

The material under investigation was a PCB surface finish (HASL) with dimensions of $20 \times 20 \times 1$ mm and a diameter of $1000 \mu\text{m}$ pads surface (Fig. 1). The solder paste made of SN100C (Sn-0.7Cu-0.06Ni-0.005Ge) and SN97C (Sn-3.0Ag-0.5Cu) was applied on the HASL pads board to make the electrical connections. A thin layer of no-clean flux was put on the board before the solder paste was placed. For reflow process, the samples were placed in the crucible alumina boat with contained iron powder and the crucible was heated to 200°C in a microwave for 80 s. The sample was subsequently cooled to room temperature. After being reflowed, the samples were aged for 1000 h at 150°C in an ordinary oven.

The cross-section examination was selected for metallographic characterization. The samples were mounted in epoxy resin before being subjected to metallographic techniques. The scanning electron microscope (SEM) was used to examine the characterizations of IMC formations and wettability angle, and energy dispersive x-ray (EDX) was used to identify the element of IMC composition.

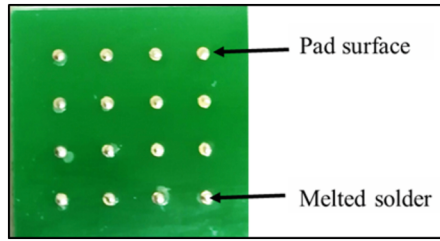


Fig. 1. Sample of solder/HASL joint.

3 Results and Discussion

The cross-sectioned images of SN100C/HASL and SN97C/HASL are displayed in Fig. 2. Meanwhile, in Fig. 3, the full image of the solder joints for both SN100C/HASL and SN97C/HASL is presented. For a cross-sectional process, back-scattered electron (BSE-SEM) was used to produce clear images of the IMC structure and layer at the interface.

3.1 Intermetallic Compound Formation

The reflow of a solder joint typically involves the three stages of spreading, base metal dissolving, and intermetallic compound formation. The HASL substrate was exposed to the molten solder during the reflow process, whereupon they reacted to form bonds. Then, as a result of a chemical interaction between solders/HASL, IMC layers were created at the solders interfaces. According to Fig. 2, the IMC of Cu_6Sn_5 was formed after reflowed for both SN100C/HASL (Fig. 2(a)) and SN97C/HASL (Fig. 2(c)) as revealed by EDX spectrum analysis. The average composition of the Cu_6Sn_5 was 33.68 wt.% Cu and 66.32 wt.% Sn. The morphology of Cu_6Sn_5 IMC existing as a scalloped shape was observed at the interface. Similar reported by previous researchers [6, 19].

Besides Cu_6Sn_5 , a thin layer of Cu_3Sn was seen at the interface (Figs. 2(b) and 2(d)) due to the reduction of the Cu atoms on the Cu_6Sn_5 /solder. Cu_3Sn precipitated at the Cu_6Sn_5 /HASL interface after a set incubation period, then Cu_6Sn_5 precipitated first at the solder/HASL interface during the ageing process. As a result, Cu_3Sn formed and grew faster over ageing time, which was composed of 71.85wt.% Cu and 28.15wt.% Sn. Consequently, no Cu_3Sn was found following the reflow process. Regarding the grain and size morphologies, it was found that the shape of the grains led to faceted, and size became larger with prolonged age duration.

The total IMC thicknesses for SN100C/HASL and SN97C/HASL as reflowed and aged solder junctions are shown in Table 1. The average thickness of the IMC layers following a certain ageing period was then calculated by averaging the five observable zones, and thicknesses. Based on Table 1, the IMC thickness for both solder joints grows with ageing time. Yang and Kim [20] and had acknowledged that the growth of IMC thickness was controlled by diffusion. It implies that, in accordance with linear kinetic theory, the reaction rate determined the growth rate. As a comparison, the IMC thickness of SN100C/HASL was thinner than that of the SN97C/HASL solder joint. However, the IMC thickness in SN100C/HASL was not significantly different from

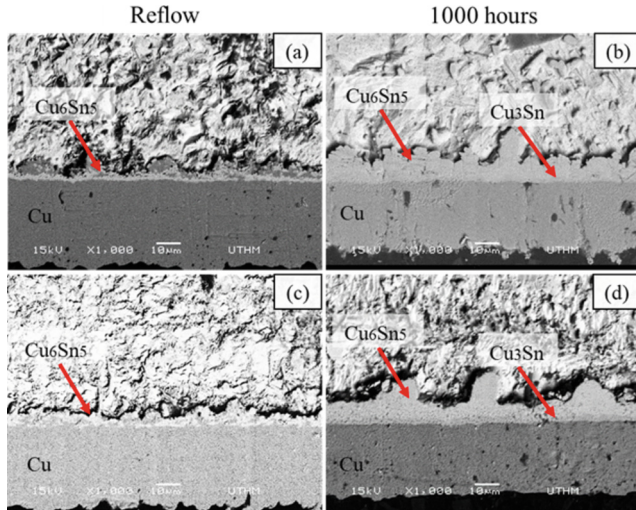


Fig. 2. SEM micrographs of cross-sectional after reflowed and aged solder joints for HASL finish (a, b) SN100C (c, d) SN97C

those that formed in SN97C/HASL. It was recorded that the difference between the two layers was approximately $0.87 \mu\text{m}$ (as reflowed) and $0.03 \mu\text{m}$ (aged).

Additionally, the addition of Ni and Ge to the SN100C solder alloy may help partially explain the changes in IMC thickness between the two solder joints. The slight inclusion of Ni substantially slows the formation of Cu_6Sn_5 IMC and stops it from growing larger and coarser as solidification progresses. Meanwhile, it was thought that Ge addition could slow the formation of the IMC layer by preventing Sn and Cu inter-diffusion in the solid state and also increasing the stability of Cu_6Sn_5 . Similar findings have been reported by previous studies [6, 21]. From the findings, it was believed that the solder joint of SN100C/HASL can withstand interfacial IMC cracks.

Table 1. Total IMC thickness of solder joints

Solder joint	Reflow	1000 h
SN100C/HASL	$6.54 \mu\text{m}$	$8.50 \mu\text{m}$
SN97C/HASL	$7.41 \mu\text{m}$	$8.53 \mu\text{m}$

3.2 Solderability Analysis

Wettability of SN100C/HASL and SN97C/HASL solder joints has been observed in this research (Fig. 3). The results found that SN97C/HASL and SN100C/HASL had contact angles of 26.64° and 35.76° , respectively. The spreading area in SN97C/HASL ($976.68 \mu\text{m}$) was significantly larger than that in SN100C/HASL ($233.26 \mu\text{m}$) due

to the lower contact angle. From the observation, both solder joints' wetting qualities were deemed to be 'good' due to a contact angle value of less than 40° . Despite this, SN97C/HASL solder joint was regarded as having 'very good' wetting quality because the contact angle value was less than 30° , as mentioned by Jung and Jung [15]. According to Ramli *et al.* [6], a small addition of Ge in Sn-Cu-Ni solder alloy can control drossing of the molten solder because it acts as an antioxidant. These researchers also thought that Ge would be able to reduce the surface tension of molten solder. Besides, the enlargement images revealed the presence of Cu_6Sn_5 and Ag_3Sn in the bulk solder (Fig. 3(a)), but no IMC was observed there, as can be seen in Fig. 3(b). Therefore, the findings clearly indicate that the Ge addition to SN100C/HASL improves its solderability.

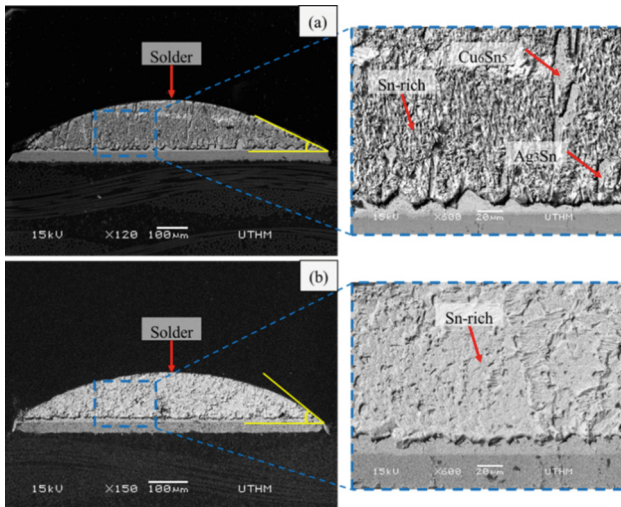


Fig. 3. SEM images of cross-section view with contact angle: (a) SN97C/HASL and (b) SN100C/HASL.

4 Conclusion

The goal of the current work was to examine the interfacial behavior of SN100C/HASL and SN97C/HASL on the IMC layer and solderability. The results of this investigation increased our comprehension of IMC formation and growth as well as solderability of the solder joint. The main conclusions obtained are as follows:

1. A layer of Cu_6Sn_5 initially formed at the interface between solder/HASL and appeared as a scalloped shape after reflowed. New layer IMC of Cu_3Sn formed /between Cu_6Sn_5 and the HASL substrate after exposure to the ageing process. The IMC thickness and grain size morphology thickened and changed to a faceted shape with ageing duration.

2. SN100C/HASL has a thinner IMC layer, but larger contact angle and smaller spreading area with good solderability due to the small addition of Ni and Ge. While

SN97C/HASL has a thicker IMC layer, but smaller contact angle and larger spreading area to generate a very good solderability.

3. The general conclusion is that as IMC thickness decreases, solderability increases and the reliability of solder joints improved. Therefore, the type of solder alloy used had an impact on the IMC growth at the interface and solderability solder joint.

Acknowledgements. This research was supported by Ministry of Higher Education Malaysia (MOHE) through Fundamental Research Grant Scheme (FRGS/1/2019/TK03/UTHM/02/6), and facilities provided by faculty of Mechanical and Manufacturing Engineering, Universiti Tun Hussein Onn Malaysia. Special thank you to Nihon Superior (M) Sdn. Bhd as a research collaborator.

References

1. Berni, R., Catelani, M., Fiesoli, C., Scarano, V.L.: A Comparison of alloy-surface finish combinations considering different component package types and their impact on soldering reliability. *IEEE Trans. Reliab.* **65**(1), 272–281 (2016). <https://doi.org/10.1109/TR.2015.2455973>
2. Berni, R., Catelani, M., Fiesoli, C., Scarano, V.L.: A soldering reliability study: a comparison among alloy-surface finish combinations considering different component packaging. *Stat. Appl.* **33**(1), 43–63 (2021). <https://doi.org/10.26398/IJAS.0033-002>
3. Milad, G.: Surface finishes in a lead-free world. *Circuit World* **34**(4), 4–7 (2008). <https://doi.org/10.1108/03056120810918051>
4. Chaillot, A., Venet, N., Hokka, J., Defense, A., Space, T.A., Defense, A.: ENEPIG Finish : An Alternative Solution For Space printed Circuit Boards. *Proc. Microelectron. Packag. Conf.*, pp. 1–6 (2013)
5. Yoon, J.W., Jung, S.B.: Effect of surface finish on interfacial reactions of Cu/Sn-Ag-Cu/Cu(ENIG) sandwich solder joints. *J. Alloys Compd.* **448**(1–2), 177–184 (2008). <https://doi.org/10.1016/j.jallcom.2006.10.052>
6. Ramli, M.I.I., Mohd Salleh, M.A.A., Mohd Sobri, F.A., Narayanan, P., Sweatman, K., Nogita, K.: Relationship between free solder thickness to the solderability of Sn–0.7Cu–0.05Ni solder coating during soldering. *J. Mater. Sci. Mater. Electron.* **30**(4), 3669–3677 (2019). <https://doi.org/10.1007/s10854-018-00647-5>
7. Baciur, M., et al.: Effects of PCB substrate surface finish, flux, and phosphorus content on ionic contamination. *J. Mater. Eng. Perform.* **24**(2), 754–758 (2015). <https://doi.org/10.1007/s11665-014-1357-1>
8. Kim, J., Jung, S.B., Yoon, J.W.: Effects of a phosphorous-containing Pd layer in a thin-ENEPIG surface finish on the interfacial reactions and mechanical strength of a Sn–58Bi solder joint. *J. Alloys Compd.* **820**, 153396 (1)–153396 (9) (2020). <https://doi.org/10.1016/j.jallcom.2019.153396>
9. Yi, P., Xiao, K., Ding, K., Dong, C., Li, X.: Surface failure mechanism of PCB-ENIG in typical outdoor atmospheric environments. *Mater. Res. Bull.* **91**, 179–188 (2017). <https://doi.org/10.1016/j.materresbull.2017.03.017>
10. Sung, Y.G., Myung, W.R., Jeong, H., Ko, M.K., Moon, J., Jung, S.B.: Mechanical reliability of the epoxy Sn-58wt.%Bi solder joints with different surface finishes under thermal shock. *J. Electron. Mater.* **47**(7), 4165–4169 (2018). <https://doi.org/10.1007/s11664-018-6224-7>
11. Li Fang, J., Chan, D.K.: The advantages of mildly alkaline immersion silver as a final finish for solderability. *Circuit World* **33**(2), 43–51 (2007). <https://doi.org/10.1108/03056120710750940>

12. Yang, Y.: Failure analysis for bad wetting on HASL PCB. In: 18th Int. Conf. Electron. Packag. Technol. ICEPT 2017, pp. 126–129 (2017). <https://doi.org/10.1109/ICEPT.2017.8046421>
13. Gain, A.K., Zhang, L.: Interfacial microstructure, wettability and material properties of nickel (Ni) nanoparticle doped tin–bismuth–silver (Sn–Bi–Ag) solder on copper (Cu) substrate. *J. Mater. Sci. Mater. Electron.* **27**(4), 3982–3994 (2016). <https://doi.org/10.1007/s10854-015-4252-0>
14. Sun, L., Zhang, L.: A review: the wettability and oxidation resistance of Sn-Zn-x lead-free solder joints. In: *Int. Conf. Power Electron. and Energy Eng. (PEEE 2015)*, 2015, pp. 188–190 (2015). <https://doi.org/10.2991/peee-15.2015.50>
15. Jung, D.H., Jung, J.P.: Review of the wettability of solder with a wetting balance test for recent advanced microelectronic packaging. *Crit. Rev. Solid State Mater. Sci.* **44**(4), 324–343 (2019). <https://doi.org/10.1080/10408436.2018.1490249>
16. Wang, W., Choubey, A., Azarian, M.H., Pecht, M.: An assessment of immersion silver surface finish for lead-free electronics. *J. Electron. Mater.* **38**(6), 815–827 (2009). <https://doi.org/10.1007/s11664-009-0761-z>
17. Li, W.: Failure Analysis on Bad Wetting of ENIG Surface Finish Pads. In: *Proc. Int. Conf. Electron. Packag. Technol. (ICEPT)*, pp. 538–541 (2015)
18. Dušek, K., et al.: Influence of flux and related factors on intermetallic layer growth within sac305 solder joints. *Materials (Basel)* **14**(24) (2021). <https://doi.org/10.3390/ma14247909>
19. Rabiatal Adawiyah, M.A., Saliza Azlina, O.: Comparative study on the isothermal aging of bare Cu and ENImAg surface finish for Sn-Ag-Cu solder joints. *J. Alloys Compd.* **740**, 958–966 (2018). <https://doi.org/10.1016/j.jallcom.2018.01.054>
20. Yang, M., Li, M., Kim, J.: Texture evolution and its effects on growth of intermetallic compounds formed at eutectic Sn37Pb/Cu interface during solid-state aging. *Intermetallics* **31**, 177–185 (2012). <https://doi.org/10.1016/j.intermet.2012.07.004>
21. Mohd Salleh, M.A.A., McDonald, S.D., Gourlay, C.M., Belyakov, S.A., Yasuda, H., Nogita, K.: Effect of Ni on the formation and growth of primary Cu₆Sn₅ intermetallics in Sn-0.7 wt.%Cu solder pastes on Cu substrates during the soldering process. *J. Electron. Mater.* **45**(1), 154–163 (2016). <https://doi.org/10.1007/s11664-015-4121-x>



Potential Utilization of Acetylene as an Alternative Fuel in Petrol Engine

O. L. Rominiyi¹, O. M. Ikumapayi¹(✉), T. S. Ogedengbe², M. A. Akintunde³,
E. P. Nsien¹, and S. A. Afolalu¹

¹ Department of Mechanical and Mechatronics Engineering, Afe Babalola University, Ado Ekiti, Nigeria

ikumapayi.omolayo@abuad.edu.ng

² Department of Mechanical Engineering, Nile University of Nigeria, Abuja, Nigeria

³ Department of Mechanical Engineering, Federal University of Technology, Akure, Nigeria

Abstract. Acetylene is not particularly hazardous, but when produced from calcium carbide, it can have dangerous impurities including phosphine and arsine residues, giving it a unique garlic-like odor. It, like most light hydrocarbons, is extremely combustible. It can then be synthesized from eggshells, instead of leaving Egg Shells as waste causing environmental pollution. It can be used as a substitute fuel for a petrol engine, thereby converting waste to wealth. By using acetylene gas as fuel in a petrol engine, there is less emission as compared to other conventional fuels. The production of acetylene carried out from the bio waste eggshells and snail shells will be synthesized, it is usually produced by the mixture of calcium carbide and water. The main objectives of this project are to produce the alternative fuel from eggshells and snail shells, determine the physicochemical properties of the fuel produced from the bio waste, evaluate the combustion characteristics of the acetylene produced from bio waste, and utilize the acetylene produced from bio waste to run a petrol engine.

Keywords: Acetylene · Biowaste · Environment · Alternative fuel · Petrol

1 Introduction

Acetylene (C₂H₂) is a synthesis gas that is created when water and calcium carbide react. The reaction can be conducted continuously and without the use of complicated machinery or apparatus [1]. Street merchants and mine workers have both used acetylene produced in this way, and others for lighting. Such illumination sources are commonly referred to as “carbide lamps” or “carbide light” [2]. In the nineteenth century, it was used to light dwellings and mining tunnels with “acetylene lamps” [2]. It produces a very high flame (over 5400°F or 3000 °C) and a pungent garlic odor when combined with oxygen [3]. It has no color, is unstable, very combustible, and emits a flame that reaches temperatures of more than 5400°F (3000 °C) [4]. With a molecular weight of 26 with 2 carbon atoms, and that of CO₂ is 44 with 1 carbon 66 atoms. When acetylene undergoes complete combustion it gives 2 mol of CO₂. This demonstrates that when acetylene is burned, 3.38 lb of CO₂ are produced (2 × 4426), demonstrating that CO₂ emissions are quite low compared to those of Sox and NO_x, which are extremely minimal [5].

However, the usage of acetylene as a motor or lighting fuel in the industry has been almost non-existent. In modern times, the use of acetylene as a fuel has primarily been restricted to welding-related applications or acetylene torches for welding. Acetylene is utilized in most of these applications in the form of a solution, such as acetylene dissolved in acetone [6]. With the revolution of industries delivering autonomous vehicles and enabling livestock owners from the need to use animals. However, this has created a challenge of our natural climate change due to the quantity of CO₂ discharged into the atmosphere by the engines combustible gasoline making it seem that transportation by car wouldn't be a sustainable and realistic way to live [6]. Thus Shelke [7] investigated the workings of acetylene on SI engines with little changes to its original, thereby making it suitable for use on an economic and environmental level by lowering the operating costs and minimizing its pollution emission. Making it more efficient and environmentally friendly as a sustainable alternative fuel option. Rising fuel costs and pressure to decrease the environmental consequences of non-renewable fuel burning are the major drivers for customers to investigate alternative fuels. GHG-emitting industries are under more pressure to decrease their environmental effect [8].

Moreover, the best way to assure that more cars are fueled by carbon-neutral sources is not by dismantling a distribution system that includes a massive network of gas stations and refineries. The natural replacement for gasoline is the biofuel fuel made from biomass, such as crops, and it may be utilized in current combustion engines without modification. Recently, scientists at Oak Ridge National Laboratory created genetically modified switchgrass to produce a plant with a higher energy density and a more straight-forward conversion process [9]. Most biofuels, including ethanol, are created by releasing sugars from the starches in agricultural products like corn or sugarcane. The process of enzyme digestion, which disassembles polymeric macromolecules into their component parts, does this. The fermentation of the sugars is followed by distillation and drying, a labor- and energy-intensive process [7]. The Oak Ridge scientists were able to lessen the amount of lignin, a chemical substance found in plant cell walls, by encoding a piece of RNA that would prevent three-quarters of lignin formation and inserting it into the DNA of the switch grass. Reduced production of lignin, which is primarily responsible for maintaining cell integrity, makes it simpler to lock carbohydrates inside plants. As a result, the rate of biomass conversion to fuel increases significantly, up to 40% [8].

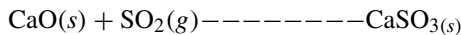
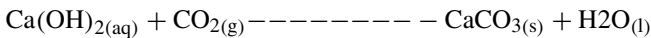
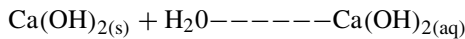
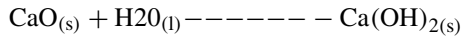
Wulff et al. [10] investigated the behavior of diesel at various power levels and speeds by using acetylene as the primary fuel and diesel as the secondary fuel in a dual fuel mode at various power outputs and speeds, achieving positive results such as lower NO_x, HC, and CO emissions when compared to base diesel fuel. Lakshamanan et al. [11] used the timed manifold injection technique to investigate the performance and emissions characteristics of an acetylene-fueled engine at various flow rates. The optimal condition in manifold injection technique was 10o ATDC with injection time of 90o crank angle, resulting in a minor gain in brake thermal efficiency for all gas flow rates, according to the research. NO_x emissions reduced when flow rates increased, however smoke levels increased slightly. There was also a decrease in HC, CO, and CO₂ emissions. Is it, however, conceivable to replace fossil fuels in transportation with biomass? A potential shift in biodiversity is one of the risks linked with biomass conversion, as a larger part of the land would be required to produce the right plants [12]. Converting

land for biofuel production, according to the Millennium Ecosystem Assessment, would result in a tremendous release of greenhouse gases. A hectare of prairie land converted to biofuels might release up to 300 tonnes of CO₂, and if a forest is destroyed to create a place for biofuels, the amount rises to 1,000 tonnes [11].

1.1 Sequence of Production

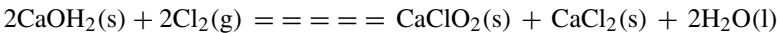
Lime (CaO) is a white solid with a high level of basicity. Slaked lime, which is the chemical composition calcium hydroxide, is formed when lime reacts rapidly with water. During this process, a significant amount of heat energy is released [13].

Limewater is an alkaline solution made from calcium hydroxide that is weakly soluble in water. The production of calcium carbonate occurs when carbon dioxide gas is transported through or over limewater [14].

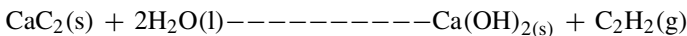
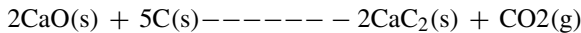


Large amounts of gaseous product are produced by coal and gas-fired power plants, some of which is sulfur dioxide. Slaked lime and lime are both used to lower sulfur emissions [14].

Calcium hypochlorite, a popular form of ‘swimming pool’ chlorine, is created when slaked lime combines with chlorine gas [15, 16].



When calcium oxide is burned with coke, a kind of carbon, it becomes calcium carbide. When calcium carbide is mixed with water, acetylene is produced. This fuel powers the oxy-acetylene gas torch, which is used to cut and weld metals [17–19].



2 Materials and Methods

2.1 Calcium Carbonate

This is a chemical compound with the formula CaCO₃ which is gotten from Egg Shells and Snail Shells which are Organic materials used as a form of bio-waste for the production of Acetylene. The Calcium carbonate was produced after it had gone through stages of washing, drying and grinding. The manufacturing procedure is eco-friendly. The procedure produces (CaCO₃) egg and snail shell as a byproduct as presented in Fig. 1.

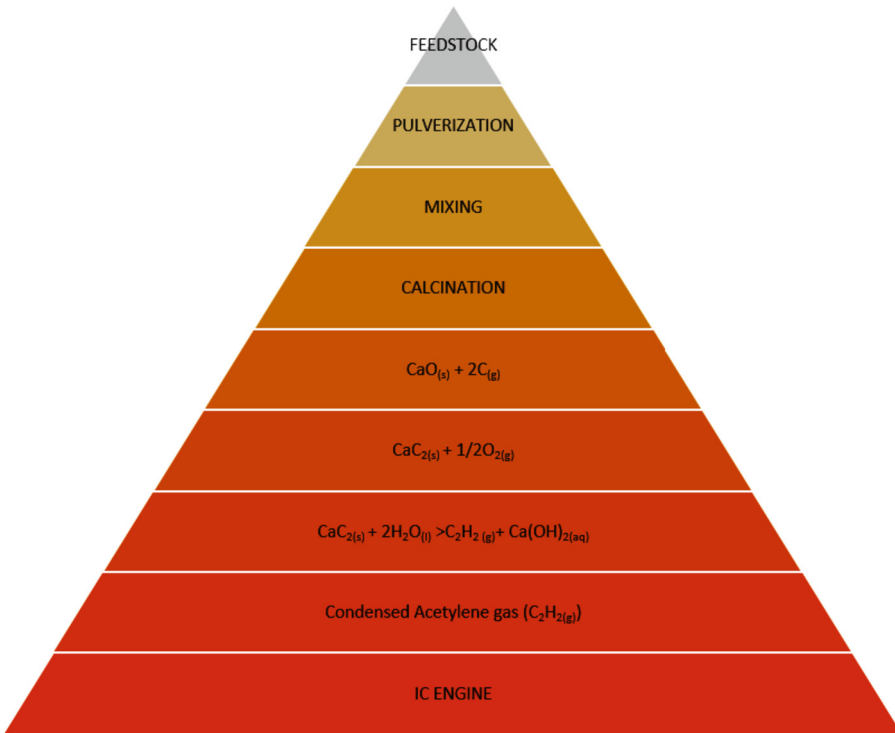
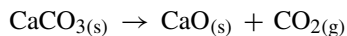


Fig. 1. Flow-chart for the production of CaCO_3 from Biowaste

2.2 Calcium Oxide

The Calcium oxide was produced from the thermal decomposition of the Calcium Carbonate (CaCO_3). This is accomplished by heating the material to above $825\text{ }^\circ\text{C}$ ($1,517\text{ }^\circ\text{F}$), a process called calcination or lime-burning for the purpose of liberating a molecule of carbon dioxide (CO_2), leaving quicklime in the element.



2.3 Acetylene Production

The calcium oxide produced from the egg shells will be then taken and placed in a Soxhlet Apparatus within a conical flask of about 30g, passed through an acidified solution of CuSO_4 for the purification and water dropping with Graphite which acts as the carbon in the solution, it is then heated. Using the condenser the Acetylene gas produced will then be taken to liquid whereby it will then be compressed into a cylinder.



This process will then repeated with different ratios of calcium oxide from egg shell and snail shell respectively. It will then be mixed in ration proportion of 70:30 for both egg and snail shell (CaCO_3).

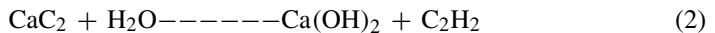
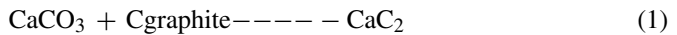
2.4 Internal Combustion (IC) Engine

After the acetylene was produced a flame test was conducted, it was used to run a fuel generator of 2.5kva using a dual fuel carburetor for the acetylene gas intake with the mixture of fuel to increase the mechanical efficiency of the engine.

3 Results and Discussions

3.1 Production Reaction

Calcium carbonate and graphite interact in nature to form calcium carbide rocks. These reactions (i) and (ii) are now taking place. Natural water and calcium carbide should be combined to produce acetylene. Acetylene gas can therefore be produced by anyone who has a gas collecting container and storage apparatus. This equation is all that is needed to create acetylene in welding shops' acetylene gas generators.



Acetylene gas has a higher calorific value than gasoline and is sufficiently flammable. Acetylene has a molecular weight of 26 and two carbon atoms, while CO_2 has a molecular weight of 44 and one carbon 66 atom (C_2H_2 gas density = 0.068 lb/ft³) (usually the material and safety data sheet will include this detail of information). Perform the conversion equations below to obtain an emission factor for acetylene, taking into account that each mole of acetylene creates two moles of CO_2 when totally burned (i.e., each pound of acetylene produces 3.38 lb of CO_2 ($2 \times 44/26$)):

The outcome of this computation shows that the amount of CO_2 emitted is quite low and that other pollutants, such as NO_x and SO_x , are incredibly little in comparison to CO_2 .

3.2 Characterization of the Acetylene Gas

After the Acetylene extraction, the physicochemical properties of the acetylene were determined according to American Society for Testing and Method (ASTM) standard procedures. The properties include density, acid value, saponification value, pH, kinematic viscosity and specific gravity (See Fig. 2 and Table 1).

i. Density

The density was determined at room temperature and at 40 °C. The empty density bottle (pycnometer) was measured and noted as w_1 .

Additionally, the bottle was thoroughly cleaned and drained before each Acetylene was added. The weight of the bottle was then noted as W_3 . Equation below was used to determine the oil's density;

$$R.D = \frac{W_O}{W_w} = \frac{w_3 - w_1}{w_2 - w_1}$$

$$\rho_{oil} = R.D \times 1g/cm^3$$

ii. Kinematic viscosity

Transesterification reaction, reduces the viscosity in both edible and non-edible oils. Before and after the creation of biodiesel from *Gmelina arborea* seed oil, the viscosity was measured according to ASTM D445 procedure. The programmable rheometer was used in carrying out this analysis. The rheometer comprises of a spindle, stainless cup and a rotor. The oil was preheated to 60 °C and was poured into the stainless cup of the DV-III –ultra –programmable rheometer (Brookfield: model III U).

The rotor and spindle was immersed into the cup and the rheometer was set to a speed of 100 rpm. The dynamic viscosity was immediately recorded when the temperature dropped to 40 °C, room temperature and 15 °C. The kinematic viscosity was determined.

$$\mu = \frac{\mu_D}{\rho_{oilat40^{\circ}C}}$$

iii. Determination of the PH value

The concentration of hydrogen ions in a solution, expressed in mol/dm³, is indicated by the pH of the solution. It determines the acidity or alkalinity of a solution. In this study, the pH reading was determined using the Oakion ion-700 pH meter. The probe of the pH meter was placed inside the beaker after the condensed gas had been poured into a 50 ml container. Thereafter, the pH value was determined when the reading remained stable.

iv. Pour point

To allow the formation of paraffin wax crystals, the specimen is refrigerated. Then the test-tube is withdrawn and turned after every 3 °C to check for surface movement. The test-tube is maintained horizontally for 5 s if the specimen does not flow when tilted. If flow does not occur, the temperature is increased by 3 °C this is to get the final measurement with flow, and the result is the pour point temperature.

v. Flash point

To ensure that the top of the meniscus would be at the filling line, the beaker was filled at a temperature that was convenient and no higher than 56 °C. The light test flame would be turned on and set to a range of 3.2 to 4.8 mm. The sample was heated to a temperature change of 14–170°C/m. The heat source was reduced to a rate of 5–6 °C per minute when the sample was around 56 °C below the predicted flash. The test flame was used when the temperature hit each successive 2 °C mark, starting at least 28 °C below the flash threshold. The test flame was held over the center of the cup in one direction, at a right angle to the diameter and no higher than 3 mm over the upper edge of the cup. When the subsequent flame was used, it was passed in the reverse direction. The test flame crossed the cup in about one second. The flash point is the temperature at which an instantaneous flash occurs when flame is applied.

vi. Calorific Value

A bomb calorimeter was used to determine the calorific value (1108 OXYGEN BOMB). The following are comprehensive guidelines for setting up the sample and charging the 1108 oxygen bomb.

vii. Calorimeter Operation

The following steps should be followed to test a sample and standardize the 1341 simple calorimeter:

viii. Cetane numbers

The Cooperative Fuel Research (CFR) Committee established a method for measuring cetane quantities in the 1930s, which was later standardized as ASTM D613. The fuel is run in a single cylinder CFR Cetane Engine with a constantly variable compression ratio. The cetane number scale is defined by two basic reference fuels (hydrocarbons):

- i. The cetane number of 100 is allocated to n-hexadecane (also known as cetane, n-C₁₆H₃₄), which has excellent ignition quality;
- ii. The cetane number of zero is assigned to 1-methylnaphthalene, which has poor ignition quality.

ix. Moisture content

For Egg shells:

Weight of samples = 17.58g

Weight of dry sample = 17.44g

$$\frac{\text{weight of sample} - \text{weight of dry sample}}{\text{weight of sample}} \times 100$$

$$\frac{17.58 - 17.44}{17.58} \times 100 = 0.796$$

For Snail Shells:

Weight of sample = 10.15g

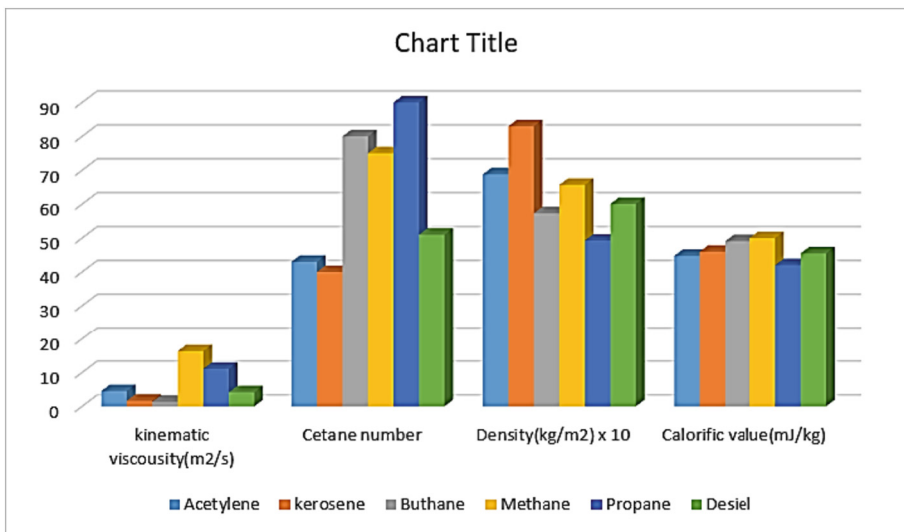
Weight of dry sample = 9.98g

$$\frac{\text{weight of sample} - \text{weight of dry sample}}{\text{weight of sample}} \times 100$$

$$\frac{10.15 - 9.98}{10.15} \times 100 = 1.675$$

Table 1. Analysis comparison of Acetylene with the following factions of crude feed.

Test	Acetylene	Kerosene	Butane	Methane	Propane	Diesel
Calorific value (mJ/kg)	44.752	46	49.1	50	42	45.5
Kinematic viscosity(m ² /s)	4.5×10^{-4}	1.64×10^{-6}	1.31×10^{-6}	16.33×10^{-6}	11.1×10^{-6}	4.16×10^{-6}
Density (kg/m ²)	688	830	573	657	493	601
Cetane no	43	40	80	75	90	51

**Fig. 2.** Physicochemical properties of gases under investigation

4 Conclusion

In future, fossil fuels will soon run out and already, we have a sharp shortage of fuel as prices rise yearly. It is also known that acetylene is found to be cheap and abundantly made of calcium carbonate. It is also seen that the production of acetylene from bio-waste eggshell and snail shell is possible, thereby making its usage readily available for production.

Acetylene also has an advantage due to its exhaust emission, which has already been seen as an added advantage for future use. Fuels in general produces CO₂, CO, NO_x during combustion and some hydrocarbon unburnt. As a gas, acetylene enables a more uniform mixture with the air, which also results in better mixing of the fuel for combustion, which is subsequently used as a power source in both urban and rural locations. It is also a useful fuel for all SI and CI engine vehicles for future purposes.

Acknowledgements. The authors wish to acknowledge the financial support offered by the Founder of Afe Babalola University (ABUAD) Ado Ekiti.

References

1. Brusca, S., Lanzafame, R., Marino Cugno Garrano, A., Messina, M.: On the possibility to run an internal combustion engine on acetylene and alcohol. *Energy Procedia* **45**, 889–898 (2014)<https://doi.org/10.1016/j.egypro.2014.01.094>
2. Hanna, R.: Optimising for Alternative Fuels, Optimising Alternative (2021)
3. Meda, V.S.: Optimization of Induction Length and Flow Rates of Acetylene in Diesel Engine, MS Thesis, National Institute of Technology, Orissa, India (2011)
4. Kumar, S., Kumar, A., Gandhi, S., Mahla, S.: Performance Study of Acetylene-Aspirated Diesel Engine with Different Flow Rates, August 2016
5. Sudheesh, K., Mallikarjuna, J.M.: Development of an exhaust gas recirculation strategy for an acetylene-fueled homogeneous charge compression ignition engine. *Proc. Inst. Mech. Eng. Part D J. Automob. Eng.* **224**(7), 941–952 (2010)<https://doi.org/10.1243/09544070JAUTO1364>
6. Lavingiya, D., Choksi, J., Bhalani, M., Kondhiya, G., Bambhania, H.: Performance analysis of single cylinder four stroke SI engine using dual fuel : acetylene and ethanol blend. **2**, 732–736 (2017)
7. Shelke, S.: Water Engine by Using Acetylene GAS. May (2019). <https://doi.org/10.32628/IJSRSET>
8. Mamilla, V.R.: Experimental Investigations on Fabrication of S. I Engine using LPG and Acetylene as Alternate Fuel, August (2019)
9. Sharma, P.K., Kuinkel, H., Shrestha, P., Poudel, S.: Use of acetylene as an alternative fuel in IC engine. *Mechanica Confab* **1**(March), 19–22 (2012)
10. Wulff, J., Hulett, W., Sunggyu, L.: Internal combustion system using acetylene fuel. United States Patent No 6076487
11. Lakshmanan, T., Nagarajan, G.: Performance and emission of acetylene-aspirated diesel engine. *Jordan J. Mech. Indust. Eng.* **3**(2), 125–130 (2009)
12. SOCIETY, A. C. (1998). Discovery of the Commercial Processes for Making Calcium Carbide and Acetylene. National Historic Chemical Landmarks, 1–8. <http://portal.acs.org/portal/PublicWebSite/education/whatischemistry/landmarks/calciumcarbideacetylene/index.htm>
13. Ashok, V.M.S., Khan, N.I.: Experimental investigation on use of welding gas (Acetylene) on SI Engine. In: Proceedings of AER Conference, IIT (2006)
14. Ganeshan, V.: *Internal Combustion Engine*, 3rd edn. McGraw Hill Book Company, Singapore (2007)
15. Manyik, R.M., Dietz, C.M., Sargent, H.B., Thribolet, R.O., Schaffer, R.P.: *Acetylene, Properties and Manufacturing from Calcium Carbide*, 2000. Online. <http://onlinelibrary.wiley.com/doi/10.1002/0471238961.0103052013011425.a01/abstract>. Accessed 28 Apr 2017
16. Krammart, P., Tangtermsirikul, S.: Properties of cement made by partially replacing cement raw materials with municipal solid waste ashes and calcium carbide waste. *Constr. Build. Mater.* **18**, 579–583 (2004)
17. Ghazal, O.H.: Combustion analysis of hydrogen-diesel dual fuel engine with water injection technique. *Case Stud. Ther. Eng.* **13**(100380), 1–10 (2019)
18. Özel, S., Vural, E., Binici, M.: Taguchi method for investigation of the effect of TBC coatings on NiCr bond-coated diesel engine on exhaust gas emissions. *Int. Adv. Res. Eng.* **04**(01), 014–020 (2020)
19. Barrios, C.C., Saez, A.D., Hormigo, D.: Influence of hydrogen addition on combustion characteristics and particle number and size distribution emissions of a TDI diesel engine. *Fuel* **199**(2017), p.162–168 (2017)



Development of a Filter-Based Fruit Preservation System via Refrigerating System

Ojo P. Bodunde^{1,2}, Omolayo M. Ikumapayi^{2(✉)}, Rasaq A. Kazeem³,
Adebayo T. Ogundipe⁴, Jesutoni R. Oluwafemi⁵, Oritsetsolayemi O. Awani²,
and Vincent A. Balogun⁶

¹ Department of Mechanical and Automation Engineering,
The Chinese University of Hong Kong, Shatin 999077, New Territories, Hong Kong
² Department of Mechanical and Mechatronics Engineering, Afe Babalola University,
Ado-Ekiti 360001, Nigeria

ikumapayi.omolayo@abuad.edu.ng

³ Department of Mechanical Engineering, University of Ibadan, Ibadan 200005, Nigeria

⁴ Directorate of Information Communication Technology,

Afe Babalola University, Ado Ekiti 360101, Nigeria

⁵ Department of Aeronautical and Astronautical Engineering, Afe Babalola University,
Ado-Ekiti 360001, Nigeria

⁶ Department of Mechanical Engineering, Edo State University Uzairue,
Iyamho, Edo State, Nigeria

Abstract. The development of fruits is among the most important of human developments. Fruits have been in existence even before man. A great revolution began when the early hunters discovered they could plant seeds, influence growth, and maintain plant fertility. Throughout the millennia, mankind has indeed succeeded to grow fruits, but have also developed their own specialty types with distinct tastes or engineered to grow in specific places. Fruits is not only seen as a source of food but as a source of raw materials to create other products. The preservation of these fruits is highly essential. This report entails the development of a fresh fruit preservation system. It combines the use of an ethylene filter and the vapour compression refrigeration system to keep fresh fruits from losing their value. During the project, the previous contributions to the field, made by others, were considered, and applied. The device was made to hold and preserve 13 kg worth of fruit. The ethylene filter comprises of potassium permanganate which oxidizes ethylene and keeps the fruit from spoiling. The evaluation of the system was done by comparing the conditions of the fruit under different controlled conditions. The COP of the system was found to be 0.98 and the fruits were in better condition under the refrigerated ethylene absorption condition.

Keywords: Fruit preservation · Refrigerating system · COP · ethylene filter

1 Introduction

The development of fruits is among the most important of human developments. Fruits have been in existence even before man. When early hunters found they could plant seeds, regulate growth, and preserve plant fertility, a great revolution began. Mankind

has not only succeeded in growing fruits throughout millennia but has also invented their own specialty types with flavors or engineered to grow in specific locations. Fruits is not only seen as a source of food but as a source of raw materials to create other products [1].

Food, by its very nature, starts to spoil as soon as it is harvested. Ancient man had to control nature to exist. In cold climates, he froze meat in ice, while in hot climates, he sun-dried meats [2]. He was no longer required to devour the harvest right away but could save part for later use. Each civilization conserved their local food sources utilizing the same basic food preservation processes, such as drying, freezing, and fermenting [2, 3].

When fresh fruits are plucked, they are at their peak quality; their quality can only be maintained or degraded when they are handled and kept. Refrigeration of perishable food goods (in this case, fresh fruits) is an application area of thermodynamics and heat transport [4]. Refrigeration slows down the biological and chemical processes in foods, as well as the deterioration and loss of quality that occurs as a result. Temperature has a considerable influence on the rate of growth of microbes in meals [5]. Cooling can extend the life of fresh fruits by several days, and temperature management can change the ambient conditions to more favorable levels. The basic goal of refrigeration is to produce and maintain a temperature that is lower than the ambient temperature [5, 6]. Man discovered in prehistory that his game would survive through times when food was scarce unless it was preserved in snow or in the coolness of a cave for use during the times of scarcity. The first stage in the development of cooling foods was to add chemicals to water, such as potassium nitrate or sodium nitrate, to cause the temperature to drop. This method of cooling wine was first reported in 1550, as were the terms to refrigerate [7, 8]. Refrigeration has evolved over time, and it is thought to have been invented in 1856 by an American businessman named Alexander C. Twinning. Shortly afterwards, an Australian named James Harrison analyzed Twinning and Gorrie's refrigerators and introduced vapour compression refrigeration to the meatpacking and brewing sectors. The most extensively utilized type of cooling is vapour compression refrigeration [9, 10].

To preserve fresh fruits, this study combines vapour compression refrigeration and ethylene control mechanisms. Because fresh fruits are living things, they continue to emit heat, which adds to the refrigeration burden. Fruit storage life can be considerably increased by removing the field heat and cooling as soon as feasible after harvesting [11]. Ethylene is a colorless gas produced by plants that acts as a growth regulator. In this sense, ethylene works similarly to hormones in mammals [12]. It causes ripening throughout a plant's natural development cycle. When optimizing post-harvest storage conditions, all ethylene-producing sources should be evaluated. The development of this fresh fruit preservation system is important especially to the agricultural industry as it aims to keep fruits fresh for longer periods.

1.1 Ethylene and Ethylene Control

In extremely small concentrations, ethylene gas is a natural plant hormone that has been shown to affect plant development and enhance ripening. Ethylene is produced in a variety of ways, including naturally by Internal combustion engines, plants, natural gas

and cigarette smoke leaks are among them [13]. It is not commonly tested during the transportation chain because to the low concentration at which it is effective and the difficulties in detecting its presence, and it has frequently been linked in poor product outcomes. On fresh fruits, the presence of ethylene gas can have both negative and positive consequences. The softening of certain fruit's flesh and the beginning of ripening of stored fruit are both negative impacts. Russet spotting in lettuce, bitterness in carrots, toughening of asparagus, yellowing of squash and cucumber, blossom abscission and closure, leaf abscission and chlorosis are all instances of the ethylene influence on fruits [14]. When ethylene is administered to fruit before the natural ripening process begins, it has beneficial effects such as faster and more even fruit ripening. Ethylene can also be used to ripen citrus fruits and to get some flowers and bulbs to grow. Ripening or damaged fruit are natural sources of ethylene, but other plant tissues also create it, which can cause decay or wilting [15]. Fruits that have been cut from a growing plant are still alive and breathing. Ethylene can be found in the gaseous respiration products of fruits, the generation of ethylene by typical healthy flower and plant tissue and cut or damaged leaves and tissue. Ethylene is produced in a variety of ways, with apples being one of the most prolific producers [16]. Ethylene sensitivity is usually inversely proportional to its rate of generation. In a low carbon dioxide and low ethylene atmosphere, scald that develops after several months of storage can be prevented. When optimizing post-harvest storage conditions, all ethylene-producing sources should be considered, as ethylene exposure can cause quality loss in some fruits [17].

1.2 Ethylene Measurement

In the laboratory, ethylene can be measured using a basic gas chromatograph equipped with a flame ionisation detector. Except in the bigger fruit stores that have a gas chromatograph, this is not commonly done in the business environment. Occasional testing is performed, with air samples collected and sent for examination. The issue then becomes determining how much has been lost and having faith in a sample that may have traveled hundreds of kilometers. Metal toothpaste tubes, according to one fruit exporter, are great for this purpose. Any technology other than detector tubes for measuring ethylene during maritime transportation is problematic and is not usually used [18]. The chamber is filled with molybdatepalladium reagent, and the most sensitive will show an ethylene concentration of 0.5 to 10 l/litre. The amount of ventilation required is calculated using carbon dioxide concentration as a quantifiable tracer, which is thought to be related to ethylene concentration. Portable gas chromatographs with a photoionization detector (PID), which are generally accessible but still rather expensive, may successfully quantify ethylene in the field. The device employed in this study, a Photovac 10S50, uses air as a carrier gas and can operate for several hours on internal batteries. It can detect and measure ethylene at concentrations as low as 0.01 ul/litre. Other less expensive technology that uses a PID detector and a pump is also available. Despite its sensitivity, such technology is unable to distinguish between ethylene and other hydrocarbons [19].

1.3 Ethylene Removal - Ventilation with Air

The most frequent method for removing ethylene in conventional and container transport is forced ventilation with air. Land stores typically lack a fresh air ventilation system, relying instead on frequent door openings. Ventilation has the problem of requiring ambient air to be frozen and dehumidified, using refrigeration power and hence energy. The evaporator coils must also be defrosted frequently because the ambient air contains a lot of water. Temperature regulation and distribution in a cargo are poor prior to and during a defrost cycle. The use of outside air for ventilation must be free of ethylene contamination from other sources, such as pollution from internal combustion engines [20].

2 Methodology

The system uses the refrigeration cycle to limit the respiration of fruits. The fresh fruits are washed to remove any dirt on them and kept on the trays in the cooling chamber. The thermostat regulates the temperature of the cooling chamber between 4 °C – 8 °C slowing the respiration rate, action of microorganisms and delaying deterioration. The ethylene absorption filter is placed directly on to the air circulating system, directly in the flow of air. As air passes through the filter the potassium permanganate oxidizes, scrubbing the air clean..

2.1 Design Specifications

The device was designed to cool and preserve 13 kg of fresh fruits, for evaluation. The parameters based on Ashrea 2010 handbook specifications [21]. Therefore, the working parameters are:

- i. External length = 910 mm
- ii. External breadth = 900 mm
- iii. External height = 1800 mm
- iv. Internal length = 710 mm
- v. Internal breadth = 700 mm
- vi. Internal height = 1600 mm
- vii. Cooling temperature = 6 °C
- viii. Ambient temperature = 25 °C

2.2 Material Selection

The following are the selection criteria for the development of the fresh fruit preservation system.

2.2.1 Trays Holding the Fruit

For the trays holding the fruit stainless steel mesh was selected for the following reasons:

- i. High thermal conductivity
- ii. Non corrosive
- iii. No chemical reaction with fruits

2.2.2 Casing of the Internal Cabinet

For the internal cabinet housing, the product aluminum was chosen due to the following reasons:

- i. Good thermal conductivity
- ii. Corrosion resistant
- iii. Low density

2.2.3 Casing of the external Cabinet

For the external component housing the components and the internal casing, galvanised steel was chosen for the following reasons:

- i. High strength and ductility
- ii. Corrosion resistant

2.2.4 Insulation

Heat loss from the refrigerator compartment is prevented by the refrigerator's insulation. Because of the following qualities, polyurethane was chosen as the insulating material:

- iv. High insulating strength
- v. Low thermal conductivity
- vi. Water absorption rate of 0

A thickness of 100 mm was selected.

2.2.5 Choice of Refrigerant

The most crucial component of the refrigeration system is the refrigerant. The operating and cycle of the refrigeration system are determined by the refrigerant in the system. Standard refrigerant properties must be met by the refrigerant. These qualities are designed in order to keep the surroundings stable so that the refrigeration does not harm the atmosphere or the environment while in operation. The following attributes must be present in a refrigerant [22]:

- i. ozone and environmentally friendly
- ii. low boiling temperature
- iii. vaporization pressure lower than atmospheric
- iv. high heat of vaporization
- v. non-flammable and non-explosive

R-134a had all the desired properties of the refrigerant mentioned above and thus was chosen as the refrigerant for this study.

2.3 Cooling Load Calculations

Cooling load is the amount of heat that must be removed from the refrigerator space to provide and maintain the desired temperature. The total cooling load is calculated from all the heat gained from various sources listed below [23]:

- i. Transmission load.
- ii. Air change load due to door opening.
- iii. Product load of goods reduced to storage temperature.
- iv. Heat of respiration.

3 Results and Discussions

3.1 Transmission Load

This is heat conducted into the refrigerated space through its walls, floor and ceiling. The transmission load according to Ashrae handbook (2002) [24] is determined from Eq. 1.

$$Q_{\text{transmission}} = A_o U T \quad (1)$$

where,

$Q_{\text{transmission}}$ is the transmission load. (W)

A_o is the total external surface area of the refrigerated area. (m²)

T is the temperature difference between the cooling temperature and ambient temperature. (°C)

U is the thermal transmittance. (w/m²c)

$$\text{Thermal transmittance (U)} = \text{Conductivity (k)}/\text{thickness (t)} \quad (2)$$

Given that,

Conductivity of aluminium = 0.14 w/mk

Thickness of aluminium (t) = 0.3 m

Using Eq. 2, we can deduce that:

$$\text{Thermal transmittance (U)} = 0.14/0.3 = 0.47\text{W}/\text{m}^2\text{c}$$

$$\begin{aligned} \text{Area (A}_o\text{)} &= [(1.8 \text{ m} \times 0.91 \text{ m}) \times 2] + [(1.8 \times 0.9) \times 2] \\ &+ [(0.91 \times 0.9) \times 2] = 8.16 \text{ m}^2 \end{aligned}$$

$$T = 25^\circ\text{C} - 6^\circ\text{C} = 19^\circ\text{C}$$

Using Eq. 3.1, the transmission load is given as:

$$Q_{\text{transmission}} = 8.16 \times 0.47 \times 19 = 72.9 \text{ W}$$

3.2 Air Infiltration Load

This is the heat gain due to the surrounding warm air entering the refrigerated space through the cracks and the opening of the door. This occurs when the warm air from outside enters the refrigerated space to replace the denser cold air inside.

Assumptions:

- i. Under worst conditions, the amount of air infiltration is estimated to be 0.2 air changes per hour.
- ii. The entire infiltration air is cooled to 6 °C before it leaves.

Noting that the infiltration of ambient air will cause the air in the cold storage room to be changed 0.75 times every hour, the mass flow rate at which air enters the room was calculated from Eq. 3.

$$m_{air} = (V_{room}/V_{air})(ACH) \quad (3)$$

where,

V_{room} is the volume of the room

V_{air} is the specific volume of the dry air in the room

ACH is the air change per hour

Using Eq. 3 the mass flow rate at which air enters the room is:

$$m_{air} = (1.6 \times 0.6 \times 0.7)/0.78)(0.75) = 0.65/\text{hour}$$

The sensible infiltration load of the refrigerated space can be determined from Eq. 4.

$$Q_{infiltration, \text{ sensible}} = m_{air} (h_{ambient} - h_{room}) \quad (4)$$

where,

h is the enthalpy of air

m_{air} is the mass flow rate of air

using Eq. 4, the sensible infiltration load was calculated as:

$$Q_{infiltration, \text{ sensible}} = 0.65(25.153 - 6.036) = 12.43\text{W}$$

The latent infiltration load of the refrigerated space can be determined from Eq. 5.

$$Q_{infiltration, \text{ latent}} = (\omega_{ambient} - \omega_{room})m_{air}h_{fg} \quad (5)$$

where,

ω is the humidity ratio of air

h_{fg} is the heat of vaporization of water

Using Eq. 3.5 the latent infiltration load is deduced as:

$$Q_{infiltration, \text{ latent}} = (0.019826 - 0.005832)0.65 \times 40.65 = 0.37\text{W}$$

NB: the values of specific volume, enthalpy and the humidity ratio are determined from the psychrometric chart

The total infiltration load can be calculated using Eq. 3.6.

$$\text{Total infiltration load}(Q_{infiltration}) = Q_{infiltration, \text{ sensible}} + Q_{infiltration, \text{ latent}} \quad (6)$$

From Eq. 6 the infiltration load was deduced as:

$$Q_{infiltration} = 12.43 + 0.37 = 12.8\text{W}$$

3.3 Product Load

This is the amount of weight that must be removed from the refrigerator's contents in order to lower their temperature. Equation 7 determines that the heat removed from the products accounts for the majority of the refrigeration load.

$$Q = mc(T1 - T2)/t \quad (7)$$

where;

Q is the product load. (W)

M is the mass of the product. (kg)

C is the specific heat. (j/kg.k)

T1 and T2 is the mass average temperatures of the products before and after cooling

t is the cooling time

The product weight and specific heat for the four products are given in Table 1.

Table 1. Table showing Mass and Specific Heat of Products

Product	Mass (kg)	Specific heat (j/kg.k)
Mangoes	4	3.74
Tomatoes	3	3.98
Oranges	3	3.77
Bananas	3	3.35
	13	14.84
TOTAL		

Using Eq. 8 the product load of each product was determined as shown below:

$$Q_{\text{product}} = Q_{\text{mangoes}} + Q_{\text{tomatoes}} + Q_{\text{oranges}} + Q_{\text{bananas}} \quad (8)$$

$$Q_{\text{mangoes}} = 4 \times 3.74 \times (25 - 6) = 284.24W$$

$$Q_{\text{tomatoes}} = 3 \times 3.98 \times (25 - 6) = 226.86W$$

$$Q_{\text{oranges}} = 3 \times 3.77 \times (25 - 6) = 214.89W$$

$$Q_{\text{bananas}} = 3 \times 3.35 \times (25 - 6) = 190.95W$$

$$\text{Total product load } (Q_{\text{product}}) = 284.24 + 226.86 + 214.89 + 190.95 = 916.94W$$

3.4 Heat of Respiration

Fresh fruits are living items that continue to breathe at varied rates for days, if not weeks, after they have been harvested. During respiration, a sugar such as glucose reacts with oxygen to form CO₂ and H₂O. This reaction mechanism releases heat from respiration, which contributes to the refrigeration burden when cooling fruits.

$$Q_{\text{respiration}} = \sum m_i q_{\text{respiration}} \tag{9}$$

where,

Q_{respiration} is the refrigeration load due to respiration. (W)

m is the mass of the product. (kg)

q_{respiration} is the heat of respiration for the fruits stored in the refrigerated space.

(w/kg)

the heat of respiration for the following fruits are given in Table 2.

Table 2. Table showing the heat of respiration of the products

Product	Heat of respiration (w/kg)
Mango	0.7
Tomato	0.3
Orange	0.6
Banana	0.3

$$Q_{\text{respiration}} = (4 \times 0.7) + (3 \times 0.3) + (3 \times 0.6) + (3 \times 0.3) = 6.4W$$

3.5 Safety Factor

To account for probable inconsistencies between design specifications and actual operation, the predicted load is increased by 10%.

$$\text{Total cooling load (Q}_{\text{total}}) = Q_{\text{transmission}} + Q_{\text{infiltration}} + Q_{\text{respiration}} + Q_{\text{product}} + \text{safety factor} \tag{10}$$

$$Q_{\text{subtotal}} = 72.9 + 12.8 + 6.4 + 916.94 = 1009.04W$$

$$\text{Safety factor of 10\%} = 100.904$$

$$Q_{\text{total}} = 1009.04 + 100.904 = 1109.94W$$

$$\text{COP} = Q_k/W \quad (11)$$

where,

Q_k is the refrigerating effect = 1109.94 W

W is the compressor power = 559.27 W

Using Eq. 11 the COP was deduced as:

$$\text{COP} = 1109.94/559.27 = 0.98$$

3.6 Performance Evaluation of the Developed Fresh Fruit Preservation System

Tests were carried out in order to evaluate the functionality of the device. The results determine the efficiency and effectiveness of the developed device.

3.6.1 Load Test of the Fresh Fruit Preservation System

The load test of the fresh fruit preservation system was subjected to the following:

i. Coefficient of performance of the system

The COP, which is computed as the ratio between refrigerating capacity and electrical power provided to the compressor, is used to determine the overall performance of the refrigeration system. Compressor power (W , kW), refrigerating effect (Q , kW), and coefficient of performance are representative performance characteristics in the refrigeration system (COP).

ii. Physiological weight loss of fruits

The weight discrepancies between fruits preserved in ambient and colder conditions. Equation 12 was used to calculate the percentage weight reduction [25].

$$\text{Percentage weight loss} = \frac{\text{original weight} - \text{new weight}}{\text{original weight}} \times 100 \quad (12)$$

iii. Colour change and firmness

Changes in the color of the fruits were observed in both the colder and ambient conditions, as well as physical weight reduction. The observed color variations were based on the physical appearance of the fruits. It was noticed that the tactile texture was noticeable. There was also a change in firmness after storing the fruits in cooler and ambient conditions.

3.7 Physiological Weight Loss of Fruits

The refrigeration system was loaded with 13 kg of fresh fruit goods, both with and without the ethylene filter, with the same amount stored at room temperature. Throughout the experiment, the temperature of both the system and the ambient environment was measured, and the physiological weight loss was assessed. Table 3 shows the results of physiological weight loss of the products and percentage of weight loss during the experiment. The graph showing percentage weight loss of products across five days is shown in Fig. 1.

Table 3. Physiological weight loss of the products

Product	Weight loss of product in refrigerator (without ethylene filter) (g)	Day 1	
		Weight loss of product in refrigerator (with ethylene filter) (g)	Weight loss of product in ambient conditions (g)
Mangoes	1.9	1.3	10.67
Tomato	1.7	1	9.3
Orange	2	1.4	14.7
Banana	3	0.5	13.45
		Day 2	
Mangoes	3.2	1.5	14.5
Tomato	3	1.5	13.95
Orange	3.7	1.4	16.5
Banana	3.9	1	16.3
		Day 3	
Mangoes	4	1.7	20.8
Tomato	4.2	2.2	18.6
Orange	3.9	1.5	13.65
Banana	4	1.2	20.4
		Day 4	
Mangoes	4.7	2	17.25
Tomato	5	2.7	15.5
Orange	4.3	1.9	12.4
Banana	4.5	1.9	18.6
		Day 5	
Mangoes	5.2	2.5	15
Tomato	5.7	3.15	12.4
Orange	5	2	13
Banana	4.9	1.5	16.7

3.8 Percentage Weight Loss

Using Eq. 12 the percentage weight loss was found for the products for everyday and is shown in Table 4.

The graph of percentage weight loss of the products per day under different conditions is shown in Figs. 2, 3 and 4.

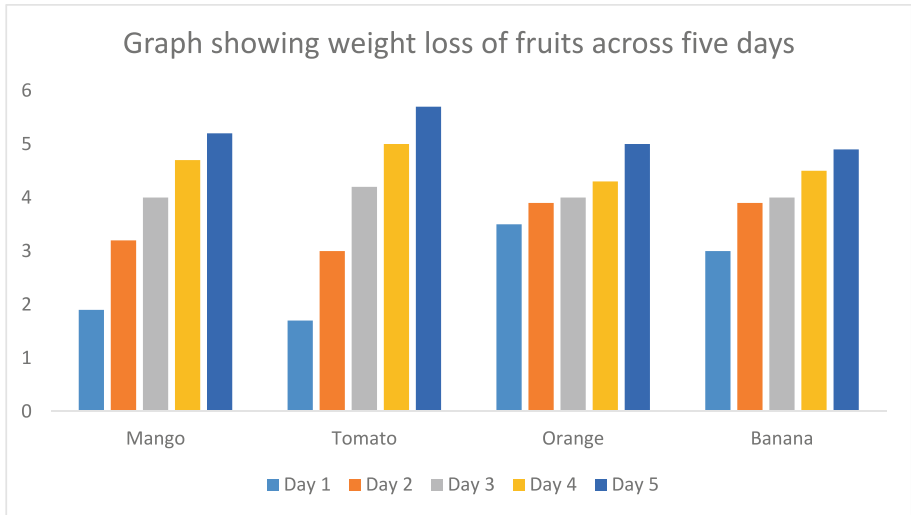


Fig. 1. Graph showing weight loss of fruits across five days

Table 4. Percentage weight loss of the products

Product	Percentage weight loss of product in refrigerator %	Day 1	Percentage weight loss of product in ambient temperature %
		Percentage weight loss of product in refrigerator (with ethylene filter) %	
Mangoes	0.48	0.33	2.67
Tomato	0.57	0.3	3.1
Oranges	0.67	0.47	4.9
Banana	1	0.17	4.48
		Day 2	
Mangoes	0.8	0.38	4.83
Tomato	1	0.5	4.65
Oranges	1.2	0.46	5.5
Banana	1.3	0.3	5.43
		Day 3	
Mangoes	1.2	0.43	5.2
Tomato	1.4	0.73	6.2
Oranges	1.3	0.5	4.55
Banana	1.3	0.4	6.8

(continued)

Table 4. (continued)

Product	Percentage weight loss of product in refrigerator %	Day 1	Percentage weight loss of product in ambient temperature %
		Percentage weight loss of product in refrigerator (with ethylene filter) %	
		Day 4	
Mangoes	1.17	0.5	4.3
Tomato	1.67	0.9	5.16
Oranges	1.43	0.63	4.13
Banana	1.5	0.5	6.2
		Day 5	
Mangoes	1.3	0.63	3.75
Tomato	1.9	1.05	4.13
Oranges	1.67	0.67	4.3
Banana	1.63	0.5	5.57

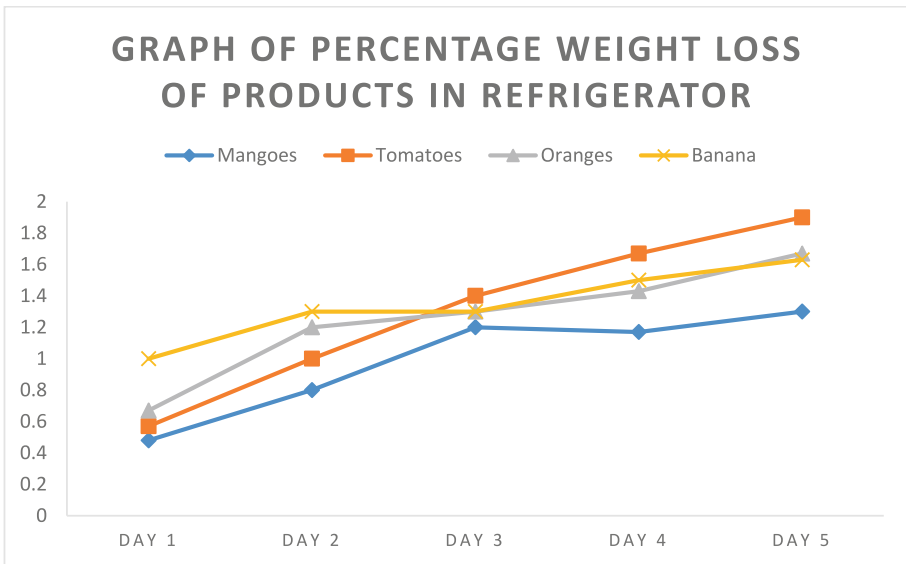


Fig. 2. Graph of percentage weight loss of products in refrigerator

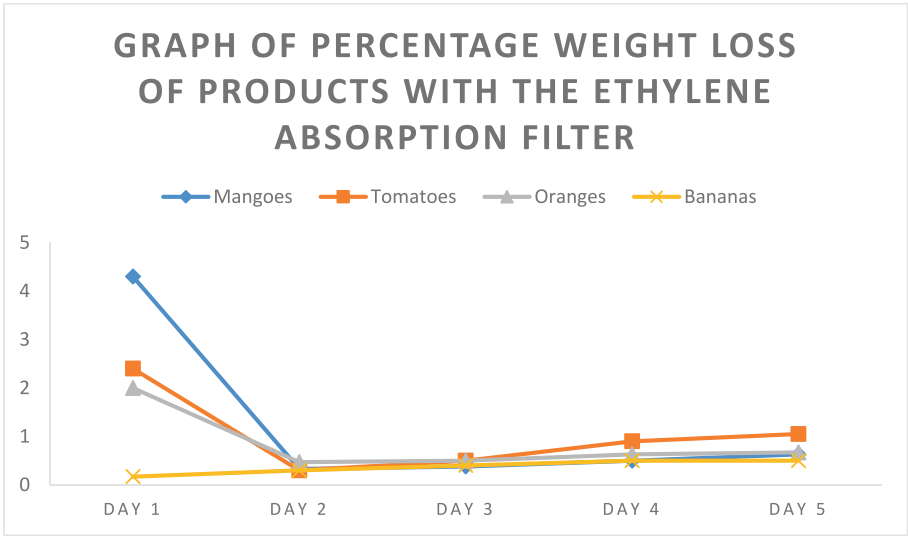


Fig. 3. Graph of percentage weight loss of products with the ethylene absorption filter

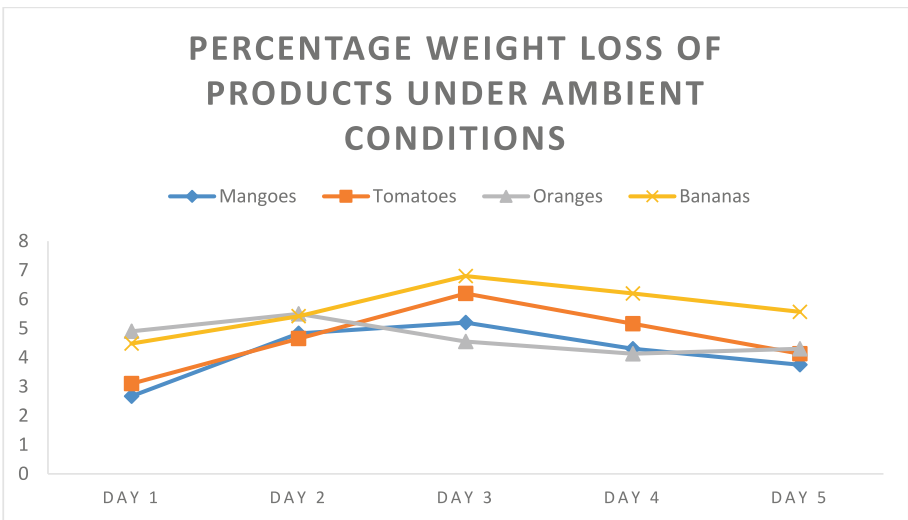


Fig. 4. Graph of percentage weight loss of products under ambient conditions

4 Conclusion

After comparing the percentage weight loss, the refrigeration system with the ethylene absorption filter combined with the refrigeration system performed better than all other conditions.

Acknowledgements. The authors wish to acknowledge the financial support offered by Afe Babalola University Ado Ekiti, Nigeria for the payment of article publication charges (APC).

References

1. Afolalu, S.A., Ikumapayi, O.M., Adeoye, A.O.M., Bello, K.A., Ogundipe, A.T., Banjoko, M.O.: Performance assessment of varying nanoparticles in a base mineral oil for domestic refrigeration system. *Mater. Today Proc.* **62**, 3350–3354 (2022). <https://doi.org/10.1016/j.matpr.2022.04.246>
2. Ajuka, L.O., Ikumapayi, O.M., Akinlabi, E.T.: Entropy generation of graphene nanoplatelets in micro and mini channels: nanofluid flow in automotive cooling applications. *Int. J. Heat Technol.* **40**(4), 917–926 (2022). <https://doi.org/10.18280/ijht.400408>
3. Sunmonu, M.O., Falua, K.J., David, A.O.: Development of a low-cost refrigerator for fruits and vegetables storage. *Int. J. Basic Appl. Sci.* **02**(03), 85–93 (2014)
4. Ajuka, L.O., Odufa, M.K., Oyewola, M.O., et al.: Modeling of viscosity of composite of $\text{TiO}_2\text{-Al}_2\text{O}_3$ and ethylene glycol nanofluid by artificial neural network: experimental correlation. *Int. J. Interact. Des. Manuf.* (2022). <https://doi.org/10.1007/s12008-022-00906-0>
5. Afolalu, S.A., Ikumapayi, O.M., Okwilagwe, O., Yusuf, O.O., Oloyede, O.R.: Performance evaluation of varying nanoparticles derived from aloe vera plant for domestic refrigeration system. *RASAYAN J. Chem.* **15**(03), 1812–1815 (2022). <https://doi.org/10.31788/RJC.2022.1536807>
6. Cengel, Y.A.: *Introduction to Thermodynamics and Heat Transfer*. McGraw Hill Higher Education, New York (2007)
7. Blanpied, G.D.: A study of the relationship between fruit internal ethylene concentration at harvest and post-storage fruit quality of cv empire apples. *J. Hortic. Sci.* **61**(4), 465–470 (2015). <https://doi.org/10.1080/14620316.1986.11515727>
8. Diley, C.L.: *New technology on measuring the effect of ethylene of fruits in controlled atmosphere* (1985)
9. Dover, C.J.: *Effects of maturity at harvest on control of ethylene levels in store* (1985)
10. Fennema, O.R.: *Food chemistry*, Third edition (1997)
11. Fitz, J.: *Preservation of fruit and vegetables*, Agromisa foundation (2003)
12. Lawton, A.R.: *Measurement of ethylene Gas prior to and during transport*, international institute of refrigeration (1991)
13. Nagalakshmi, K., et al.: The design and performance analysis of refrigeration system using R12 and R134a refrigerants (2014)
14. Oyedepo, A., Oyedepo, S.O., Oyebanji, J.A.: *Design and development of vapor absorption refrigeration system for rural dwellers* (2012)
15. Pruthi, J. S. (1999). *Quick freezing preservation of foods, principles, practises, R&D needs*
16. *Vapor compression refrigeration* (2014). Retrieved 01 June 2017, From m.wikipedia.org:en.m.wikipedia.org/wiki/special:history/vapour-compression_refrigeration
17. Zakari, M.D.: Design and construction of an evaporative cooling system for the storage of fresh tomato, *ARPN J. Eng. Appl. Sci.* (2016)
18. Afolalu, S.A., Ikumapayi, O.M., Ogundipe, A.T., Yusuf, O.O., Oloyede, O.R.: Development of nanolubricant using aloe vera plant to enhance the thermal performance of a domestic refrigeration system. *Int. J. Heat Technol.* **39**(6), 1904–1908 (2021). <https://doi.org/10.18280/ijht.390626>
19. Derens, E., Laguerre, O., Palagos, B.: Analysis of effecting factors on domestic refrigerator temperature in use. *Bull. de l'Academie Nationale de Med.* **185**, 311–322 (2001)

20. Kao, J.Y., Kelly, G.E.: Factors affecting the energy consumption of two refrigerator-freezers. *ASHRAE Trans.* **102**, 1–11 (1996)
21. ASHREA Refrigeration Handbook. Refrigeration (2010)
22. ASHREA Refrigeration Handbook. Refrigeration load, Chapter 8 (1998)
23. Lagendijk, E., Assere, A., Derens, E., Carpentier, B.: Domestic refrigeration practices with emphasis on hygiene: analysis of a survey and consumer recommendations. *J. Food Prot.* **71**, 1898–1904 (2008)
24. ASHREA Refrigeration Handbook. Refrigeration load, Chapter 12 (2002)
25. Terpstra, M.J., Steenbekkers, L.P.A., De Maertelaere, N.C.M., Nijhuis, S.: Food storage and disposal: consumer practices and knowledge. *Br. Food J.* **107**, 526–533 (2005)



Agro-Based Nano Coolant for Car Engines: Synthesis and Evaluation

Sunday A. Afolalu^{1,4}, Omolayo M. Ikumapayi^{1,5(✉)}, Temitayo S. Ogedengbe²,
Abayomi Adegbenjo³, Tien-Chien Jen⁴, Adebayo T. Ogundipe⁶,
and Bernard A. Adaramola¹

¹ Department of Mechanical and Mechatronics Engineering, Afe Babalola University,
Ado Ekiti 360101, Nigeria

ikumapayi.omolayo@abuad.edu.ng

² Department of Mechanical Engineering, Nile University of Nigeria, Abuja 900001, Nigeria

³ Department of Automobile Technology Education, Federal College of Education (Technical),
Lagos 100001, Akoka, Nigeria

⁴ Department of Mechanical Engineering Science, University of Johannesburg,
Johannesburg 2092, South Africa

⁵ Department of Mechanical and Industrial Engineering Technology,
University of Johannesburg, Johannesburg 2092, South Africa

⁶ Directorate of Information Communication Technology, Afe Babalola University,
Ado Ekiti 360101, Nigeria

Abstract. Coolants play essential roles in automobile engines as they serve the dual purpose of cooling and lubrication. The choice of coolants in engines is therefore very essential as they could influence the life of the engine. The widely acceptable coolants for automobile engines are basically ethylene glycol and water. However, with recent advancement in technology as well as a call for a reduction in pollution, there has been a consideration for better coolants and as such a development of an agro-based nano coolant for automobile engine became necessary. In this study, a nano coolant was developed using nanoparticles from Rice Husk Ash (RHA) which was sonicated at different concentrations of between 0.001 g/L – 0.0035 g/L volume fractions and dissolved in distilled water. Nanoparticle size was characterized using a Scanning Electron Microscope (SEM) analysis and thermo physical properties of the nanofluid were determined. The performance of the developed nanofluid was evaluated using the pour point, flash point and viscosity tests of the nanofluids applied on a developed cooling rig. The “Water + Ethylene Glycol + Nanofluid (0.001% Concentration)” mixture performed best, having the highest heat transfer rates at as well as the highest viscosity value of 65.0 ± 1.20 at 100 °C, pour point value of -22°C and flash point value of 92.90°C , which surpasses the corresponding values of the control samples.

Keywords: Agrowaste · Coolants · Nanoparticle · Nanofluid · Rice Husk

1 Introduction

The automobile engine is an example of an internal combustion engine. By combustion, the fuel's chemical energy is transformed into heat energy, and the engine converts some of this heat energy into mechanical energy [1]. The cooling system is a mechanism put in place in the automobile engine to help aid the heat transfer process. It comprises passages inside the engine blockheads, a water pump, a thermostat, a radiator, a pressure cap and interlinking hoses. The cooling system has a significant impact on vehicle performance. Radiators are commonly known as heat exchangers, which are devices that take thermal energy from one medium (i.e. liquid or gas) and pass it to another medium (i.e. liquid or gas) for the purposes of cooling and heating. It is estimated that around 35 and 30% of the input energy in a water-cooled engine is wasted in the coolant exhaust gases, respectively. The production of brake power consumes about 20–25% of the overall heat generated (useful work). The cooling system is intended to remove 30–35% of the total heat generated. Friction loses the remaining heat, which is transported away by the exhaust [2, 3].

Agro-industrial waste once was seen as neither a cost nor a profit as commonly used for the creation of compost or feed [4, 5]. This paradigm is changing, thanks to the development of many novel technologies for repurposing agro-industrial waste and adding value to it. As a result, at the current state of the art, recovering added-value materials from a trash can improve the food production chain's overall economic and environmental sustainability [6]. Agricultural waste management has recently emerged as a source of concern for policymakers concerned with sustainable agriculture and long-term growth. Agricultural waste has traditionally been dumped into the environment, either with or without treatment. To avoid pollution of air, water, and land resources, as well as the transfer of dangerous compounds, wastes must be viewed as potential resources rather than as undesirable and unwanted [7–9]. Rice husk (RH) is an agricultural waste. The rice grain's hard outside protection shell accounts for 20–25% of its weight [10]. During rice milling, the husk is removed. Rice husk is made up of the following ingredients: cellulose (50%), lignin (25–30%), silica (15–20%), and moisture (10–15%). It accounts for about 20% of the total weight of rice. The bulk density of rice husk is modest, ranging from 90 to 150 kg/m³ [11, 12]. Rice husk ash (RHA) and 13 to 16 MJ kg⁻¹ of heat energy are produced when rice husk is burned [12]. RHA is produced by the combustion of rice hulls and is a possible source of amorphous reactive silica. The ash is an excellent heat insulator. During the burning of rice husk, the majority of the evaporable components are lost slowly, and the silicates are the main leftovers. The features of the ash are determined by (1) the rice husk content, (2) the burning temperature, and (3) the burning period. Rice husk ash (RHA) is an agricultural waste byproduct that waste managers have a significant issue in disposing of. Parboiling plant RHA is a severe environmental danger, and it is urgently required to reduce it [13]. Researchers have attempted the development of nanofluids for various applications. Ezzat & Hasan, [14] examined the thermal conductivity increase of alumina water nanofluid at varied volume concentrations of 0.13%, 0.24%, 1%, and 1.7% with suitable sonication. They calculated a thermal conductivity improvement of 0.3–4.5% for nanofluids with particle concentrations of 0.13–1.7 vol%. (Kim et al., 2012) created a thermal conductivity enhancement of nanofluids using spherical and fibrous Al₂O₃ nanoparticles (5.5 vol

percent) and ethylene glycol as the base fluid in the temperature range of 20–80 °C. They discovered that as the temperature was raised, Fibrous alumina nanofluids' heat conduction rose from 15.5% to 25.8%. They also discovered that fibrous nanofluids had a better thermal conductivity enhancement than spherical nanofluids. Saleemi et al., [15] created an Al₂O₃ nanofluid based on Antifreeze N (ANF)-water mixture (50–50% by weight). ANF is a common antifreeze coolant made up of E.G., and other corrosion-inhibiting materials. The study found that nanofluids containing Al₂O₃ particles with sizes of 20 nm, 40 nm, 150 nm, and 250 nm increased thermal conductivity by 2.3%, 6%, 11.2%, and 6.1%, respectively. This study therefore focuses on the development of a nano-coolant for automobile engines.

2 Materials and Methods

2.1 Materials

The materials and reagents used to prepare the Silica nanoparticles were Rice Husk Ash, Sodium hydroxide (NaOH) pellets [AR Grade: 97% purity], Sulfuric acid H₂SO₄, Deionized water, Magnetic stirrer, Litmus paper. The R.H. used for this experiment, and was sourced from a local farm. First, it was washed in water to remove impurities, like sand, and then dried in the sun for 8 h, then burned in the muffle oven into the ashes at 500 °C for 8 h (Fig. 1d).

2.2 Equipment

The equipment used for the study includes Muffle Furnace (Capacity: 2000 °C), Magnetic Stirrer (Stuart US 152 heat-stir), Centrifuge (JZ Centrifuge Model 0406-2), Ultrasonic Bath, Digital Electronic Weighing Balance, Beaker (1000 ml, J-Sil Borosilicate), Centrifuge Tubes (10 ml), Spatula (stainless steel).

2.3 Experimental Procedure: Nanoparticle Preparation

The preparation of nanoparticles from Rice Husk Ash (RHA) required the initial ashing (Fig. 1a) of the rice husk after which silica nanoparticles were synthesized from the RHA by three main procedures which includes reaction process, centrifugation process and calcination process.

2.3.1 Reaction Process

20 g RHA was measured using a computerized electronic weighing balance that was calibrated and combined with a mixture of 80 g of NaOH pellets and 1000 ml of deionized water to form an aqueous solution. The mixture was then stirred in a beaker using Stuart US 152 heat-stir magnetic stirrer/hot plate for a duration of 4 h at 100 °C to give a black solution of sodium silicate. (Fig. 1b). To precipitate the silica, the solution was stirred and allowed to cool to room temperature before being titrated with 450 ml of 10% H₂SO₄ until it was neutralized to a pH of 7. After that, it was left to age for 48 h to further precipitate the silica gel.

2.3.2 Centrifugation Process

Using a centrifuge, the nanoparticles formed in the solution were removed from the solution. The separation was done on the principle of the centrifugal force driving the particles to the bottom of the centrifuge tube and the fluids floating above the particles. The solution produced at the end of the reaction procedure was placed into 10ml centrifuge tubes and rotated for 15 min in a J.Z. Centrifuge Model (Fig. 1c) at 4000 rpm. With the nanofluid above them, the nanoparticles were deposited at the bottom of the centrifuge tubes, and the fluid above was poured out and kept in a container while the NPs were left inside the centrifuge tubes. This procedure was continued till the mixture was thoroughly centrifuged.

2.3.3 Calcination Process

Following the centrifuging process, the NPs were taken out from the centrifuge tubes and calcined in crucibles. The NPs went through calcination for 6 h in a muffle furnace at extremely high temperatures. After that, as shown in Fig. 1d, a white powdery substance was collected. To remove any clumps, using a pestle, the powder was crushed in a mortar.

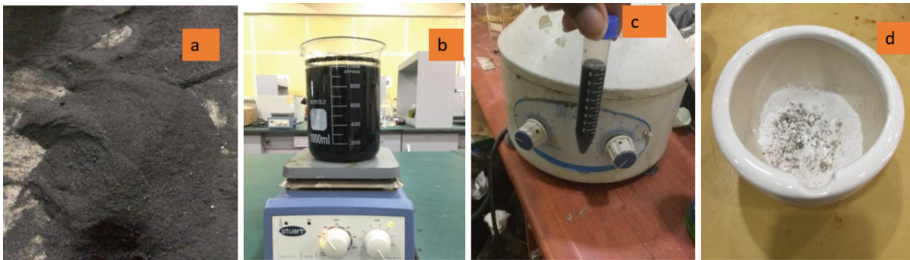


Fig. 1. Nanoparticles Preparational Steps (a) Smooth RHA powder (b) Heating and magnetic stirring of the solution (c) Centrifuge tube containing solution to be centrifuged (d) Silica nanoparticles after calcinations.

2.3.4 Silica Nanofluid Preparation

Three varying concentrations of the nanoparticles listed in Table 1 were weighed out. A broad range of silica nanofluid concentrations were created by varying the masses of the Silica NPs added to 7.5 L of deionized water and 1.5 L of ethylene glycol.

To ensure that the fluid was homogeneous, the samples were stirred continuously in an Ultrasonic bath (Fig. 2a) at durations of 1 h at a time.

Table 1. Nanofluid volume fractions showing various concentrations

Sample	Volume fraction (In 9000ml)	Volume fraction (g/L)
A	31.6 g	0.0035 g/L
B	22.1 g	0.0025 g/L
C	9.4 g	0.001 g/L

2.4 Characterization of RHA and SiO₂ Nanoparticles

Using the JEOL-JSM 7600F Scanning Electron Microscope/EDS (Fig. 2b) the rice husk ash and the generated nanoparticle powder were characterized to explore the microstructure, to check the components, and to discover the phases.



Fig. 2. Equipment for Nanofluid preparation (a) Ultrasonic Bath. (b) JEOL-JSM 7600F Scanning Electron Microscope.

2.5 Cooling Fluid Preparation

Five different cooling fluids with varying compositional mix were prepared for the study. This includes water, ethylene glycol, water + ethylene glycol + nanofluid (0.0035% Concentration), water + ethylene glycol + nanofluid (0.0025% Concentration), water + ethylene glycol + nanofluid (0.001% Concentration).

(a) Water

12 L of water was prepared and used for the first cooling process. It was poured into the reservoir tank and circulated through the system.

(b) Ethylene Glycol

7.5 L of ethylene glycol was prepared and used for the second cooling process. It was poured into the reservoir tank and circulated through the system.

(c) Water + Ethylene Glycol + Nanofluid (0.0035% Concentration)

The “water + ethylene glycol + nanofluid” cooling fluid mixture was mixed in a ratio of 31.6g of nanofluid(Silica) which was mixed with one and a half (1.5) litres of ethylene glycol and seven and a half (7.5) litres of water to form the cooling fluid mixture.

(d) Water + Ethylene Glycol + Nanofluid (0.0025% Concentration)

The “water + ethylene glycol + nanofluid” cooling fluid mixture was mixed in a ratio of 22.1g of nanofluid(Silica) which was mixed with one and a half (1.5) litres of ethylene glycol and seven and a half (7.5) litres of water to form the cooling fluid mixture.

(e) Water + Ethylene Glycol + Nanofluid (0.001% Concentration)

The “water + ethylene glycol + nanofluid” cooling fluid mixture was mixed in a ratio of 9.4g of nanofluid (Silica) which was mixed with one and a half (1.5) litres of ethylene glycol and seven and a half (7.5) litres of water to form the cooling fluid mixture.

2.6 Construction of an Experimental Rig

The construction and welding of the framework of the experimental rig were started using mild steel to construct the framework. The framework dimensions were Length – 61.2 cm, Breadth – 107 cm, Height – 91 cm. The construction and welding of the reservoir tank using the galvanized steel. Galvanized steel was used to avoid rust and corrosion since the tank will contain various fluids at various times. The reservoir tank had the following dimensions Length – 46.5 cm, Breadth – 34.5 cm, Height – 25.5 cm. The tank was designed to have a drainage outlet at the bottom middle of the tank. The design caused the tank to slope downwards towards the drainage outlet at the bottom middle part of the tank. This was done to avoid crevice corrosion occurring inside the tank. Two bars of galvanized steel were welded to the surface inside that tank at specific points to serves as bases on which the boiling rings would be clipped inside the tank. The tank has four different outlets, two large outlets and two small outlets. The two small outlets were created by cutting through the top edges of the tank at both the left and right parts, this was to enable the outlet wires of the two boiling rings to be passed out easily. Two metallic pipes were attached to the two large outlets which served as inlet passages for the fluid to flow out of the tank into the pump. A cover with a handle was also constructed for the reservoir tank. We also used galvanized steel for the cover and then attached the cover to the tank using

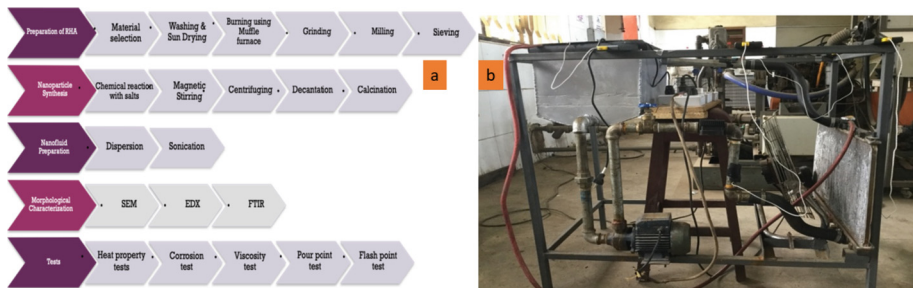


Fig. 3. Experimental (a) Process Flow (b) Rig

two hinges. The cover had the following dimensions Length – 48.3 cm, Breadth – 35.1 cm. The experimental process flow and rig is shown in Fig. 3a & b.

3 Results and Discussions

3.1 Spectroscopic Testing

The developed silica nanoparticles were subjected to an Electro Dispersive X-ray spectroscopy (EDS) examination, and the resulting graph is seen in Fig. 4. This study showed that the chemical composition of silica was found in the created flow graph in Fig. 4. The significant elements of the NP are 44.5% of Silica and 22% of Oxygen and we can see the presence of major phases of SiO₂ in the graph. Rice husk contains various other elements, such as Carbon, Sulphur, Potassium, Sodium, Magnesium, and Iron, because the husk was not leached before the burning, and while the heating was sufficient to completely remove other trace elements and inorganic impurities, rice husk still contains these additional elements.

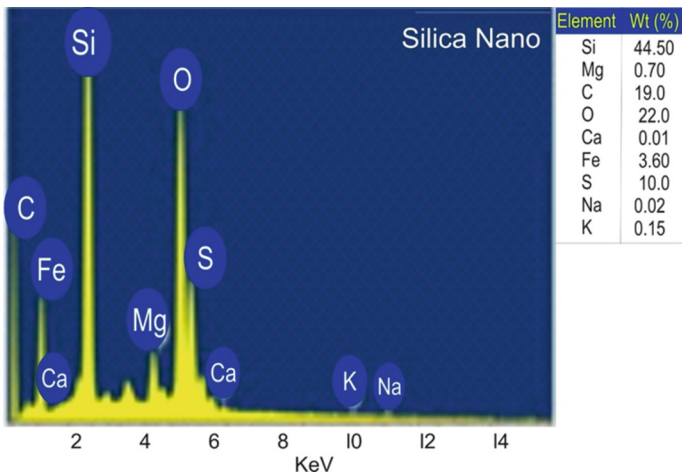


Fig. 4. EDS Micrograph of developed silica nanoparticles.

3.2 Microstructural Testing

The powdered silica nanoparticles that have been developed were examined with a JOEL-JSM 7600F scanning electron microscope and the picture shown in Fig. 5 is the image that was created. Digimizer™ was used to conduct picture analysis. Digimizer™ image analysis software was also used to evaluate the SEM micrographs. To take the SEM image, we set these requirements: Using a voltage of 20 kV and a working distance of 15mm, the device is magnified to 12000X for a clearer image. At the maximum magnification of 10000X, round and circular nanoparticles can be spotted in the SEM

images of the resultant solution. On additional examination, smaller particles measuring from 10 to 28 nm in diameter could be found, having a mean particle size of 18.585 nm. The produced powder is silica nanoparticles (Fig. 5).

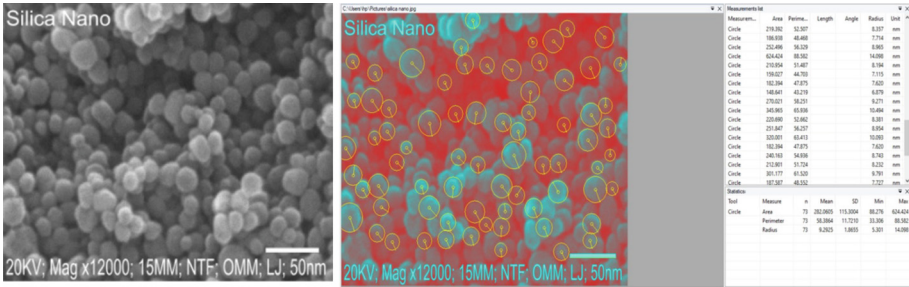


Fig. 5. SEM micrographs of the developed Silica nanoparticles and SEM analysis of the silica nanoparticles produced.

Figure 6 shows heat transfer rates of the different coolants, the graph shows that water, ethylene glycol and nanofluid (0.001% nanofluid concentration) mixture coolant has the highest heat transfer rate. The water and ethylene glycol coolants had the lowest heat transfer rates. The water, ethylene glycol and nanofluid (0.0035% nanofluid concentration) mixture transferred heat second best and showed good promise for use in radiators.

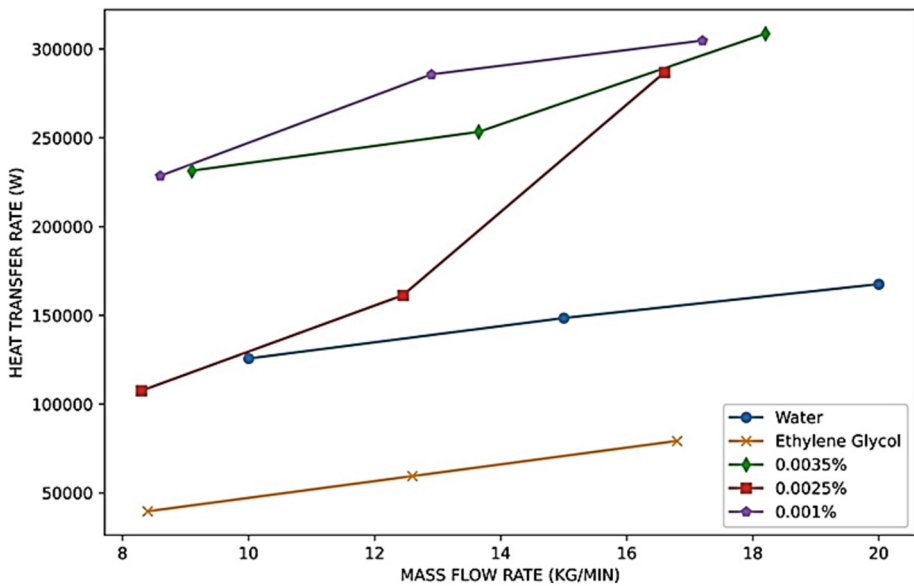


Fig. 6. Graph of heat transfer rate of the different coolants.

3.3 Pour Point

The pour point of a liquid is the temperature at which it loses its flow qualities. It is the coldest temperature at which a liquid can still be poured. Figure 7 represents the pour point values for each nano coolant fluid sample (3–5) and the control samples (1 & 2). It demonstrates that sample 1 which is one of the control samples has the highest pour point value of $-20\text{ }^{\circ}\text{C}$ that the nano coolant fluid samples can go to lower temperatures than the control sample 1 without losing their flow qualities.

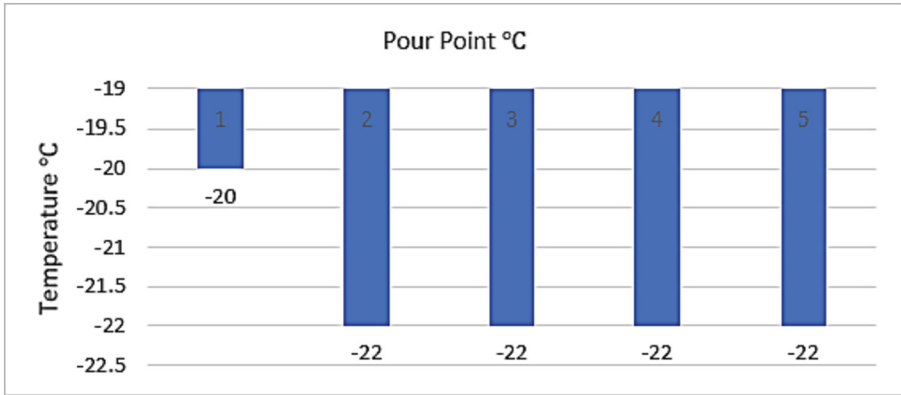


Fig. 7. Pour point value for each sample.

3.4 Flash Point

A process for determining whether a sampling mixture of vapour and air is combustible is known as flash point testing. It can also be used to identify the temperature at which a sample becomes flammable. The flashpoint of a substance is the lowest temperature at which its vapors ignite from an ignition source. Figure 8 represents the pour point values for each nano coolant fluid sample (3–5) and the control samples (1 & 2). It demonstrates that samples 3 & 5 have the highest flash points of $92.9\text{ }^{\circ}\text{C}$, which means they can withstand the highest temperatures during heat transfer without igniting, as compared to control sample 1 which has a flashpoint of $55.84\text{ }^{\circ}\text{C}$. Control sample 2 & sample 4 also have flash point values higher than that of control sample 1.

Figure 8 represents the pour point values for each nano coolant fluid sample (3–5) and the control samples (1 & 2). It demonstrates that samples 3 & 5 have the highest flash points of $92.9\text{ }^{\circ}\text{C}$, which means they can withstand the highest temperatures during heat transfer without igniting, as compared to control sample 1 which has a flashpoint of $55.84\text{ }^{\circ}\text{C}$. Control sample 2 & sample 4 also have flash point values higher than that of control sample 1.

3.5 Viscosity Test

The viscosity of a fluid is a property that indicates how resistant it is to deformation at a specified rate. The viscosity of liquids reduces significantly as the temperature rises.

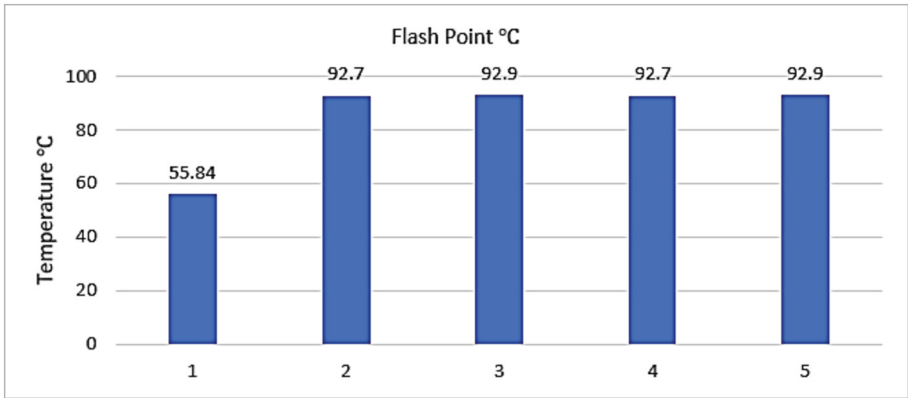


Fig. 8. Flash point value for each sample.

The data presented in Table 2 represents the viscosity values for each nano coolant fluid sample (3–5) and the control samples (1 & 2). It demonstrates that sample 5 have the highest viscosity of 65.0 ± 1.20 at $100\text{ }^{\circ}\text{C}$, and the control sample 1 having the lowest viscosity value of 40.6 ± 1.60 at $100\text{ }^{\circ}\text{C}$. All the nano coolant fluid samples have higher viscosity than the control samples.

Table 2. Viscosity values.

S/No	Sample	Viscosity Value @100 °C
1	Water	40.6 ± 1.60
2	Ethylene Glycol	62.0 ± 1.70
3	Nanofluid (0.0035%)	64.0 ± 1.30
4	Nanofluid (0.005%)	64.0 ± 1.30
5	Nanofluid (0.001%)	65.0 ± 1.20

Conclusion

In this study, five (5) cooling fluids were developed from synthesized nano-materials for the purpose of the use in automobile radiators. The effectiveness of the nanofluids was accessed using the pour point, flash point and viscosity tests. The major conclusions from the experiment are as summarized below:

- The chemical synthesis technique was used to effectively manufacture silica nanoparticle powder from Rice Husk Ash (RHA). The sizes of the Silica particles produced ranged from 10 to 28 nm, with an average diameter of 18.585 nm, well within the nanometric range.
- The constituents of the synthesized nanoparticle powder are as follows 44.5% Silica, 22% Oxygen, 19% Carbon and 10% Sulphur.

- The “Water + Ethylene Glycol + Nanofluid (0.001% Concentration)” mixture produced the maximum overall heat transfer rate which thereby goes to prove that the “Water + Ethylene Glycol + Nanofluid (0.001% Concentration)” is the best among the five cooling fluids used for this experiment.
- This “Water + Ethylene Glycol + Nanofluid (0.001% Concentration)” cooling fluid with the highest rate of heat transfer will improve the car performance thereby resulting in less consumption of fuel and therefore making it more economically efficient.

Acknowledgements. The authors wish to acknowledge the financial support offered by the Founder of Afe Babalola University (ABUAD) Ado Ekiti.

References

1. Aubrecht, G.J.: Conservation of energy, overview. In: Encyclopedia of Energy, pp. 673–686 (2004)
2. Senthilraja, S., Vijayakumar, K., Gangadevi, R. (n.d.): A comparative study on thermal conductivity of Al₂O₃/WATER, CuO/WATER AND Al₂O₃-CuO/WATER NANOFLUIDS. Digest J. Nanomaterials Biostruct. **10**(4), 1449–1458
3. Prudhvi, G., Vinay, G., Suresh Babu, G.: Cooling Systems in Automobiles & Cars. In International Journal of Engineering and Advanced Technology (IJEAT) (Issue 2) (2013)
4. Nazzaro, F., Fratianni, F., de Martino, L., Coppola, R., de Feo, V.: Effect of essential oils on pathogenic bacteria. Pharmaceuticals **6**(12), 1451 (2013)
5. Rawat, M.K., Jain, A., Singh, S.: Studies on binary lipid matrix based solid lipid nanoparticles of repaglinide: In vitro and in vivo evaluation. J. Pharm. Sci. **100**(6), 2366–2378 (2011)
6. Udugama, B., et al.: Diagnosing COVID-19: the disease and tools for detection. ACS Nano **14**(4), 3822–3835 (2020)
7. Obi, F.O., Ugwuishiwu, B.O., Nwakaire, J.N.: Agricultural waste concept, generation, utilization and management. Niger. J. Technol. **35**(4), 957–964 (2016)
8. Agarwal, R., Verma, K., Agrawal, N.K., Duchaniya, R.K., Singh, R.: Research paper. Appl. Thermal Eng. **C**(102), 1024–1036 (2016)
9. Agricultural waste concept, generation, utilization and management | Nigerian Journal of Technology. (n.d.). Retrieved May 5, 2021, 22:220
10. H., Jang, G.-W., Verniquet, A., Broeze, J., Schaer, B., Batista, A.P., Sebok, A.: A research challenge vision regarding management of agricultural waste in a circular bio-based economy. Critical Rev. Environ. Sci. Technol. **48**(6), 614–654 (2018)
11. Chand, N., Fahim, M.: Natural fibers and their composites. Tribology of Natural Fiber Polymer Composites, 1–59 (2021)
12. Singh, B.: Rice husk ash. Waste and Supplementary Cementitious Materials in Concrete: Characterization, Properties and Applications, pp. 417–460 (2018)
13. Hossain, S.K.S., Pyare, R., Roy, P.K.: Synthesis of in-situ mullite foam using waste rice husk ash derived sol by slip-casting route. Ceram. Int. **46**(8), 10871–10878 (2020)
14. Amin, M., Abdelsalam, B.A.: Efficiency of rice husk ash and fly ash as reactivity materials in sustainable concrete. Sustainable Environ. Res. **29**(1), 1–10 (2019)
15. Ezzat, A.W., Hasan, I.M.: Investigation of alumina nano fluid thermal conductivity. Int. J. Comput. Appl. Comput. Appl. **102**(11), 975–8887 (2014)
16. Saleemi, M., Vanapalli, S., Nikkam, N., Toprak, M.S., Muhammed, M.: Classical behavior of Alumina (Al₂O₃) nanofluids in Antifrogen N with experimental evidence. J. Nanomater. **2015**(112), 122 (2015)



Developing a Finite Element Model for Analysing Dissimilar Friction Stir Welding (FSW) of Al/Mg Alloys

Bahman Meyghani^{1,2}, S. Emamian³, and Mokhtar Awang⁴(✉)

¹ BKL B.V., Collse Heide 1, 5674 VM, Nuenen, The Netherlands

² Department of Mechanical Engineering, Faculty of Engineering Technology and Built Environment, UCSI University, Taman Connaught, 56000 Kuala Lumpur, Malaysia

³ Faculty of Engineering Technology, Chair of Production Technology, University of Twente, Drienerlolaan 5, 7522 NB Enschede, The Netherlands

⁴ Mechanical Engineering Department, Universiti Teknologi Petronas, 32610 Seri Iskandar, Perak, Malaysia

mokhtar_awang@utp.edu.my

Abstract. Joining of dissimilar materials have been one of the most significant challenges for many industries like aerospace, automotive, shipping and shipbuilding. Since the invention of friction stir welding (FSW), it assists the joining of different similar and dissimilar materials like aluminium, magnesium, titanium, steel, copper etc. From one side aluminium has a very wide application in different industries because of its high strength and high resistance of the corrosion. On the other hand, magnesium alloys have moderate strength and creep resistance. Therefore, joining of aluminium and magnesium attracts enormous research interests. However, investigating the temperature distribution and the mixing of the material inside the welding zone becomes as a significant challenge for researchers. Additionally, a specific friction law is required, because of the complicated friction behaviour between the tool and materials. In this research, Norton friction law is used to develop a finite element model. Then, the model is employed to investigate the thermal and mechanical behaviour, and the possibility of the void formation during FSW. The results of the study showed that, the temperature has an asymmetrical distribution in a range of 350–412 °C. The highest temperature is predicted to be around 412 °C at the aluminum side. This issue happens because the thermal diffusivity of AZ31 alloy is lower than AA 6061, therefore the peak temperature on the magnesium side is observed to be lower. Finally, the results have been compared with the numerical and experimental results of the literature in order to verify and validate the model.

Keywords: Dissimilar Materials · Aerospace · Automotive · Shipping · Shipbuilding · Friction Stir Welding (FSW) · Aluminium · Magnesium · Temperature Distribution · Material Mixing · Friction Model · Norton Friction Law · Finite Element Model. Thermal and Mechanical Behaviour · Void Formation

1 Introduction

Energy-saving and environmental protection standards are continuously improving; thus the urgent need for manufacturing structures and potential application of Aluminium/Magnesium (Al/Mg) hybrid structures in automobile, aerospace and aeroplane industries is increasing [1–6]. Moreover, aluminium and magnesium alloys are mainly applied in areas where weight saving is considered as an outstanding economic benefit [7]. Therefore, the possibilities in applications are countless with a successful combination of aluminium and magnesium in structures. Recently, the immense potential of Al and Mg alloys hybrid structures is the driving force behind the research carried out for welding of these dissimilar materials [8, 9]. To illustrate the issue, with increasing demand on the production of lightweight structures, dissimilar metal joining of aluminium and magnesium alloys has garnered immense attention. This is particularly true in industries where materials with lightweight properties with enhancing performance and the added values of the cost efficiency are needed.

The conventional methods utilised for the welding of Al and Mg are fusion welding like laser beam welding, gas tungsten arc welding and electron beam welding that leads to the frequent creation of several shortcomings like liquation induced cracking and porosity occurred during solidification. In addition to that, weld integrity is greatly affected by the formation of different kinds of intermetallic compounds (IMC) inside the welding area. Therefore, the aim to find a defect-free joint of different alloys has given rise to investigate and enhance of many alternative welding products. Here, it needs to be mentioned that, diffusion bonding, resistance spot welding, ultrasonic welding, linear friction welding and friction stir welding (FSW) are amongst the solid-state welding techniques established for such purposes. FSW is considered as one of the most feasible methods for joining of dissimilar materials, because its temperature is always lower than the alloys melting point. This allows the avoidance of defects that will be formed during the material solidification through conventional welding methods.

Complete understanding of the heat production, the heat transfer, the plastic deformation and the material flow during dissimilar FSW is crucial to enhance the welding parameters and achieve high-quality joints of Al/Mg alloys. Such underlying mechanisms of dissimilar FSW of aluminium and magnesium alloys are hard to be revealed just by experimentations. On the other hand, experimental investigations are costly and time-consuming. Over the past decades, many researchers [10–12] have focused on modelling of FSW. However, still there are some difficulties and challenges in simulating of FSW process due to its complexity, especially for dissimilar materials. Available studies for welding of Al/Mg using FSW is limited especially for AA 6061-T6, AA2024-T3 and AZ 31, ZE41A [13]. While both AA6061-T6 and AA2024-T3 are common, high strength Al alloys that are employed in many industries (due to their weight to strength ratio and a good resistance to the corrosion [14]). On the other hand, AZ 31 and ZE41A are Mg-Zn-RE alloys that have high creep resistance and moderate strength [15]. Besides, with the addition of the rare earth elements, it also possesses other advantages like purifying alloy melt, improved castability, refined microstructure and improved the mechanical and the anti-oxidation properties. These advantages caused to use the aforementioned materials as common alloys employed in military industries (for their high corrosive resistance properties) as well as in aircraft mechanisms [16]. Furthermore, due to the

different crystal structure and physical properties of each material, the characteristics of the temperature and the plastic deformation are also different in Al and Mg sides [14]. So far, some researchers [12, 17–19] performed different models founded on finite element analysis (FEA) and experimentations tests for different dissimilar magnesium alloys AZ 31B and aluminium alloys 7075. In their models, FSW partitioning method was used to assign the material properties of each part of the plate presuming the Eulerian formulation among different dissimilar sheets. In addition, the material properties including the model shape and the frequencies have been obtained. In the model, a simple friction model for the contact condition is used. Therefore, the results of the model were limited. A literature [20] claimed that modelling the large plastic deformation, material mixing in the welding zone, the temperature and the flow behaviours are some significant issues for joining aluminium to magnesium. The arbitrary Lagrangian-Eulerian (ALE) method is proposed to solve the mesh distortion problem [21]. Although, the ALE allows the simulation of the temperature, the rate dependency and the material hardening, however in the ALE technique the formation of void in FSW cannot be simulated [22]. Pure Lagrangian method also cannot handle the mesh distortion problem happening during the simulation (due to the large plastic deformation). To illustrate the issue, in the Lagrangian approach the element should be totally completed with the material, thus during the use of Lagrangian method in the case of FSW, the lack material deposition behind the tool and the defect formation cannot be simulated [23]. Therefore, in FE modelling of FSW, Lagrangian formulation is not able to overcome multi-materials or void formation simulation. Consequently, for a Lagrangian model, the domain needs to be completely filled with a particular material for satisfying the model continuity [24]. Some literature also were used smoothed particle hydrodynamics (SPH) technique for solving the mesh distortion problem caused by the plastic deformation [25], however the detailed definition of the boundary conditions in this method is difficult. This condition leads to the overprediction of the loads and the temperature [26]. Conversely, the Eulerian formulation is established on the volume-of-fluid technique. Thus, in this technique the material flows across the mesh by calculating the Eulerian Volume Fraction (EVF) inside each element. Therefore, voids formation and multi-material problems can be solved using Eulerian technique that this issue can be considered as a benefit over Lagrangian and ALE [27, 28]. It should be noted that using Eulerian can be employed in computational fluid dynamics (CFD) model, however these models are not able to simulate the material hardening, because they can only consider rigid-viscoplastic material behaviour [29]. Moreover, CFD models ignore the materials elasticity [30]. Computational solid mechanics (CSM) is a numerically based method in order to solve problems of engineering and mathematical models, thus numerical modelling is proposed as a powerful tool to get deep insight into the thermomechanical behaviour of dissimilar FSW of Al/Mg alloys. It is reported in the literature [31, 32] that, the accuracy of CFD techniques are less than the CSM methods. To illustrate, in CFD methods, finite volume methods (FVMs) is using for solving the governing equations, in which “finite volume” refers to a small volume area around each node. On the other hand, in CSM methods, finite element methods (FEMs) use for solving the governing equations in which each area (element) contains specific numbers of nodes. Therefore, in FEMs the field variable values calculate at each node leading to have more accurate results compared to FVMs.

Another problem is the implementation of an accurate friction model in a computational solid mechanic model [33]. To explain, frictional User-defined subroutines like VFRIC, VFRIC COEF, VUITERACTION etc. cannot be employed in Eulerian based CSMs models. Consequently, there is a need to modify a complicated friction law for developing an Eulerian based three-dimensional finite element model to investigate the thermomechanical behaviour and also the possibility of the void formation during FSW for joining aluminium to magnesium.

In this paper, the Norton friction law is developed by calculating the friction coefficient, slip rate and whereby the shear stress at each time increment. The calculated values are then applied to an Eulerian based computational solid mechanics finite element model to investigate the temperature evolution, the plastic deformation, the material flow, the strain/strain rate and the formation of the void etc. in FSW of dissimilar Al/Mg alloys. After that, in order to confirm the validity of the developed model, the results are compared with experiments and the numerical results of the literature. To sum up, the results of this study can help to investigate the dissimilar FSW more in detail and can increase the application of the process in different industries.

2 Methodology

The methodology of this paper is separated into two parts, the first part describes the detail information about the modified version of the Norton friction law and the second part explains the finite element model information [34].

2.1 Friction Model

In full sliding, Coulomb friction model can be used for calculating the shear stress [34],

$$\tau = \mu P \quad (1)$$

where τ is the shear stress, μ is the friction coefficient, and P is the pressure.

In the sticking condition, the Norton-Hoff viscoplastic model is used. In this model, the values of the shear stress are dependent on the contact pressure, the geometry of the contact area and also the difference between the relative velocity of the in contact surfaces [35–37].

$$\tau = -P \times g(\Delta v_g) \times \frac{\Delta v_g}{|\Delta v_g|} \quad (2)$$

where τ is the shear stress, $g(\Delta v_g)$ is the function of the relative velocity, and ΔV_g is the critical value of the relative rotating velocity.

The description for the relative velocity when $\Delta s_2 \Delta \delta_2 \geq 0$, can be explained as below,

$$\begin{cases} \Delta s_1 = \Delta \delta_1 \\ \Delta s_2 = \Delta \delta_2 \end{cases} \quad (3)$$

where δ is the relative sliding motion and s is the nonrecoverable sliding motion.

Moreover, the rotational velocity of the tool can be found as below,

$$\omega = \frac{\Delta\theta}{\Delta t} \tag{4}$$

where θ is the distance in polar coordinate and t is the time.

Furthermore, the acceleration can be calculated as below,

$$A = \frac{\Delta\omega}{\Delta t} \tag{5}$$

It needs to be mention that, as the simulation runs v_0 values (initial velocity or spin rate) should be updated, because for each increment its values are different.

Mathematical Model Boundary Conditions

In this part, the boundary conditions for calculating the relationship between the relative velocity and the friction coefficient is explained.

As can be seen in Fig. 1, four different conditions are assumed for the model including constant friction coefficient, high-speed behaviour ($SRATEM > RCRIT$), medium speed behaviour ($RCRIT > SRATEM > RTRANS$) and low-speed behaviour ($RTRANS > SRATEM$).

Where CTRANS is constant-coefficient transition slip rate, CFRIC is constant-coefficient value, RTRANS is low-medium transition slip rate, RCRIT is medium-high

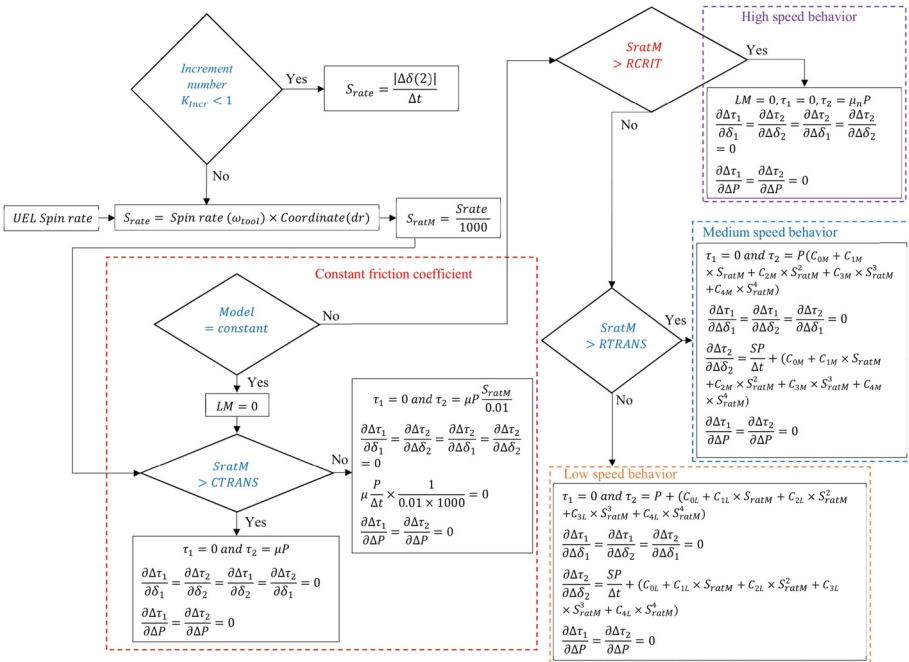


Fig. 1. The flow chart of the implementation for the contact condition

transition slip rate, HFRIC is high-speed friction coefficient, KINC is increment number, APRESS is applied pressure and SRATEM or SratM is spin rate (velocity of the flow) in meters.

As can be seen in Fig. 2, the shear stress in the r direction (τ_1) in the direction of θ is equal to zero,

$$\tau_1 = \tau_\theta = 0 \tag{6}$$

$$\tau_2 = \tau_r \neq 0 \tag{7}$$

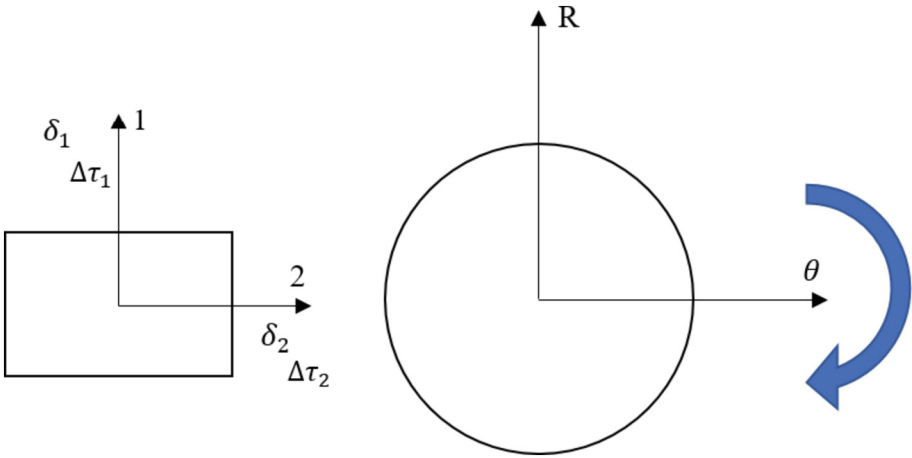


Fig. 2. The definitions for the polar coordinate

For more explanation, it should describe that, the contact between the surfaces is defined as LM. At the sliding situation LM is 0, sticking situation LM is 1; and in the open contact situation LM is 2. Furthermore, C_M and C_L are the fitting curve constants at different conditions.

2.2 Numerical Model Description

An Eulerian based finite element model in ABAQUS® environment is presented to calculate the temperature, the material movements and the void formation. Table 1 shows the descriptions of the dimensions for the tool and the workpiece [38].

The meshing of components is based on the geometry, which this issue needs to be done in the initial usage of finite element modelling. Changes of the mesh density happening because of the applied loading or boundary conditions. Hence, a high-quality mesh is necessary to represent the distributions inside the HAZ as the gradient of the temperature is experienced close to the welding nugget zone during the welding. The use of a coarse mesh may lead to a decrease in the computation time. Thus, the optimum mesh density needs to be used to maintain the accuracy of the results. In the case

Table 1. The dimensions for the tool and the workpieces

Parameter	Dimension
Shoulder diameter	12 mm
Pin length	3.8 mm
Plunge depth	3.8 mm
Dimension for each plate	100 mm × 50 mm × 4 mm

of FSW, a uniform mesh will be considered to be sufficient for the analysis on the workpiece. In addition, a symmetric model should be chosen to decrease the number of degrees of freedom, thereby decreasing the overall computation time [35, 39, 40]. The Eulerian technique in which the material and the mesh are independent of each other is used for the simulation. This issue allows the material boundary condition that should be defined accurately. Hence, no mesh distortion problem will be presented. This method is mainly applied in fluid mechanics for the observation of particles that passes successively through a spatial point. In addition, it determines the properties of the particle in terms of the spatial coordinates. To clarify the point, in this method the mesh is fixed, and the materials are allowed to flow through it. However, this does not show the deformations and the free surfaces which required additional algorithms. With that being said, the Eulerian representation is more accurate for the description of the flow and the temperature for the simulation of FSW as it avoids mesh distortions near the tool. Thus, the Eulerian representation is commonly used for the tool design, analysing the material blend as well as the force applied to the tool. Therefore, it can be concluded that the Eulerian formulation can be employed to find the temperature and the material flow field. Due to the explanation regarding the appropriation of the Eulerian technique in the welding of dissimilar materials in this work, the model is developed by using the Eulerian technique. As shown in Fig. 3, in this technique a workpiece plate (a) and a reference frame (b) should be defined.

Plasticity Modelling and Material Description

Two significant elements that need to be considered in the plasticity modelling are the temperature and the strain rate. A proposal given by Johnson and Cook [41] utilises Johnson-Cook material law to solve the problem of the large plastic deformation which causes the distortion of the mesh in an elastic-plastic situation. This law describes the von Mises equivalent flow stress as a function of the temperature and the strain rate. Moreover, the hardening needs to be defined as an isotropic hardening. This law is an empirical law allowing easy calibration via the isolation of the various effects. It is also used to assist the fitting of the parameters and prevent the potential coupling of effects such as the influence of the temperature on the strain rate hardening. Therefore, Johnson-Cook material law will be used for material modelling in this research. The Johnson-Cook material law descriptions is shown in Table 2.

$$\sigma_y = [A + B(\varepsilon_P)^n] \left[1 + C \left[\frac{\dot{\varepsilon}_P}{\dot{\varepsilon}_0} \right] \right] \left[1 - \left[\frac{T_{FSW} - T_{room}}{T_{melt} - T_{room}} \right]^m \right] \quad (8)$$

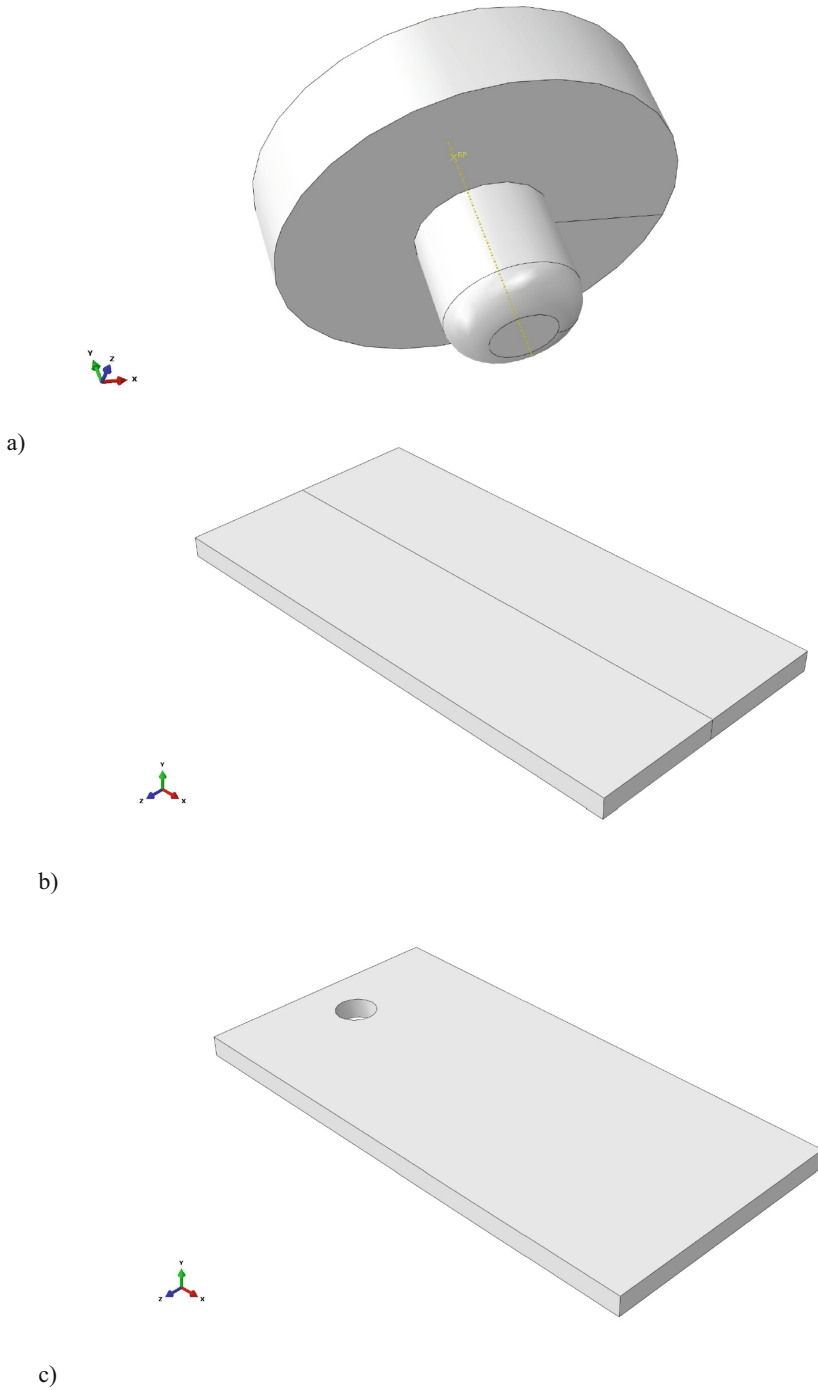


Fig. 3. a) Tool and b) Workpiece c) the reference of the model.

Table 2. The properties of the Johnson-Cook material law

Parameter	Explanation
ε_P	The effective plastic strain
$\dot{\varepsilon}_P$	The effective plastic strain rate
$\dot{\varepsilon}_0$	Normalizing strain rate
T_{room}	Room temperature
T_{melt}	Material melting temperature
A	Yield stress
B	Strain factor
n	Strain exponent
C	Strain rate factor
m	Temperature exponent

It needs to be mentioned that, when the value of the m is equal to 1, the thermal softening rate should be presumed as an unsatisfactory condition. When $m > 1$ (infinite) or if $m < 1$, the thermal softening rate should be assumed as an unphysical condition, because the reference temperature is unlikely exceptional [42]. The temperature-dependent material properties for the magnesium (AZ31) and the aluminium are listed in Table 3, Table 4, Table 5, Table 6 and Table 7.

Table 3. Material properties AZ31 (temperature dependent)

Temperature (° C)	Elasticity modulus (E)	Poisson's ratio [ν]	Thermal expansion coefficient
20	40.2	0.330	$7.7 \cdot 10^{-6}$
150	35.35	0.334	$2.64 \cdot 10^{-6}$
300	1.1	0.336	$2.7 \cdot 10^{-6}$
400	0.82	0.337	$2.7 \cdot 10^{-6}$
550	0.7	0.337	$2.95 \cdot 10^{-6}$

Table 4. Thermal properties AZ31(temperature dependent)

Temperature [T] (° C)	Thermal conductivity [k] (W/m ° C)
20	96.4
100	101
200	105
250	107

(continued)

Table 4. (continued)

Temperature [T] (° C)	Thermal conductivity [k] (W/m ° C)
300	109
400	113
420	114
440	115
460	116

Table 5. Thermal properties AZ31 (temperature dependent)

Temperature (° C)	Specific heat [C] (J/kg ° C)
20	1050
100	1130
200	1170
300	1210
350	1260
400	1300
450	1340
470	1340
500	1360

Table 6. AA 6061-T6 mechanical properties (temperature dependent)

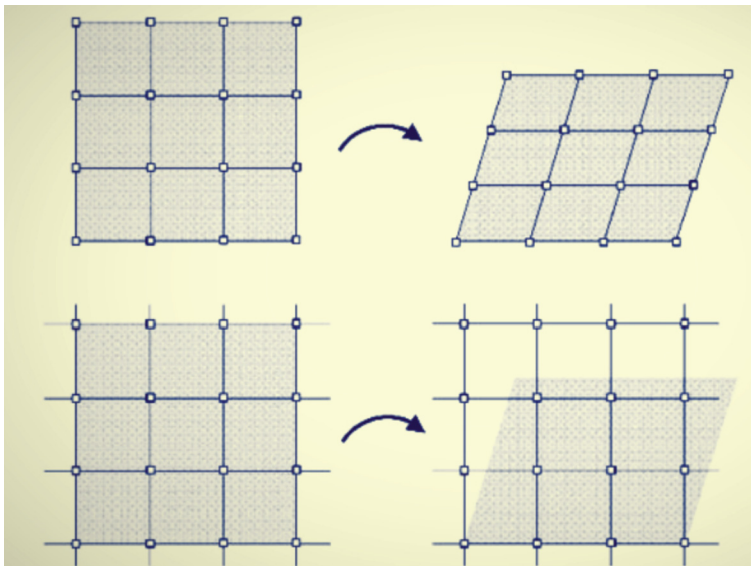
Temperature (° C)	Elasticity modulus (E)	Poisson's ratio [ν]	Thermal Expansion Coefficient	Specific Heat (J/Kg °C)
37.8	69.7	0.3	2.345×10^{-5}	95
93.3	66.2	0.3	2.461×10^{-5}	978
148.9	62.7	0.3	2.567×10^{-5}	1004
204.4	59.2	0.3	2.669×10^{-5}	1028
260	53.49	0.3	2.756×10^{-5}	1052
315.6	47.78	0.3	2.853×10^{-5}	1078
371.1	39.75	0.3	2.957×10^{-5}	1104
426.7	31.72	0.3	3.071×10^{-5}	1133

Table 7. AA6061-T6 Mechanical properties (temperature dependent)

Temperature (°C)	Thermal Conductivity (W/mK)
148.9	162
204.4	177
260	184
315.16	192
371.1	201
426.7	207
148.9	217
204.4	223

Mechanical Boundary Conditions

As a clamp, the plates have been fixed in all directions [43] and the tool position to the surface is perpendicular. It should be mention that FSW has four steps, plunging in which the tool penetrates slowly inside the plates. In the dwelling step the friction between the plates produces the heat. During the travelling the tool moves across the welding seam and join the sheets together. In the last stage the tool plunges out from the welding. The

**Fig. 4.** The initial and the final stages of Lagrangian (top) and Eulerian (down) approaches

welding rotational speed of 800 rpm and three sets for the transverse speed are applied in the simulation.

Mesh

As can be seen in Fig. 4, there is a reference frame and the grids remain motionless after moving the material across the mesh. As mentioned earlier, by using this method the mesh will not face the problem of the distortion; thus the large plastic deformation problems will be solved. Moreover, during the use of the Eulerian method for solving large plastic deformation problem, the computational costs of the simulation are less than the Lagrangian techniques. To illustrate, since the transportation of the material from one cell into another one is not available in the Eulerian technique the computational costs of this method is less than the Lagrangian method. Therefore, in this paper the Eulerian method is employed. The tool mesh is shown in Fig. 5 and the assembled model is shown in Fig. 6.

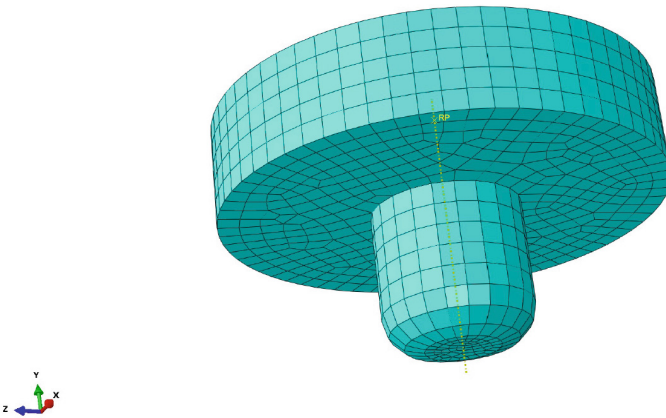


Fig. 5. The schematic view of the mesh of the tool

3 Results and Discussion

The comparison between the temperature results in the literature [44–47] (experiments and numerical model) at the welding cross-section can be observed in Fig. 7. Based on the values provided by past studies, we have plotted the computed thermal behaviour and the peak temperature. As can be seen, the computed peak temperature is observed to be higher than the measured values by the literature [47]. The results also showed that, the magnesium side has lower peak temperature. This issue causes because the ratio of thermal conductivity to the specific heat capacity of AZ31 is smaller than AA 6061 alloy, hence, the AZ31 alloy thermal diffusivity is lower than AA 6061. Thus, an asymmetrical temperature distribution in which the trend of the temperature is shifted to the aluminium side is achieved in this study.

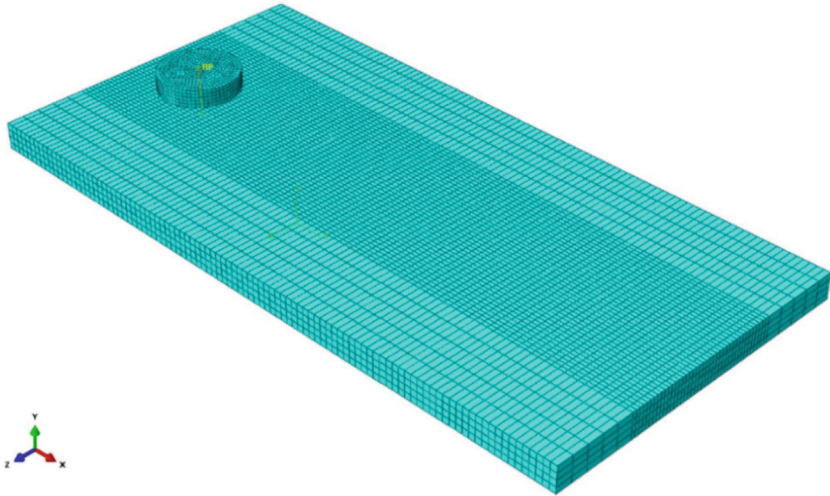


Fig. 6. The workpiece and the mesh detail in the assembled model

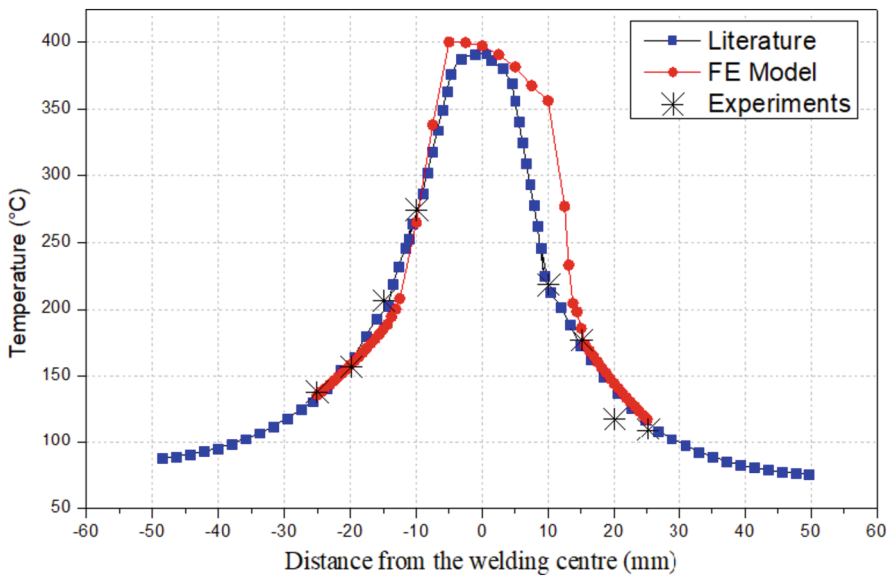


Fig. 7. The cross-section of the welding and the comparison with the literature, the left side is the aluminium side and the right side is the magnesium side [44–47]

Table 8 also indicates the values of the temperature, which is achieved in the literature for different welding sides (Al and Mg). It can be summarized that, the temperature of the welding for the dissimilar joining of AZ31 and AA 6061-T6 ranges from

430–500 °C. Table 8 also confirms that the temperature in the aluminium side is always more, as compared to the magnesium side. This occurs because aluminium material has a lower melting temperature (580 °C) compared to magnesium which will be melted at 605–630 °C.

Table 8. The reported temperature at the literature [47]

Material	Transverse speed (mm/min)	Temperature in the advancing side (°C)	Temperature in the retreating side (°C)	Average temperature (°C)
AA 6061	40	500.3	481.0	490.7
	80	490.3	474.8	482.6
	120	479.3	450.0	464.7
AZ31	40	455.3	439.0	447.2
	80	442.5	427.1	435.8
	120	438.3	418.5	428.4

The contour plot of the temperature distribution at each side of the welding can be seen in Fig. 8 and Fig. 9. As mentioned earlier, the peak temperature at the aluminium side is around 412 °C, while the temperature of almost 380 °C is achieved at the magnesium side. It can be reported that, friction and plastic deformation have contributed in the generation of the heat [47–49]. This issue also indicates that, the susceptibility of the liquation in the magnesium side is more than the aluminium side. To illustrate the issue, each material deformability is different due to the different crystal structure. Aluminium

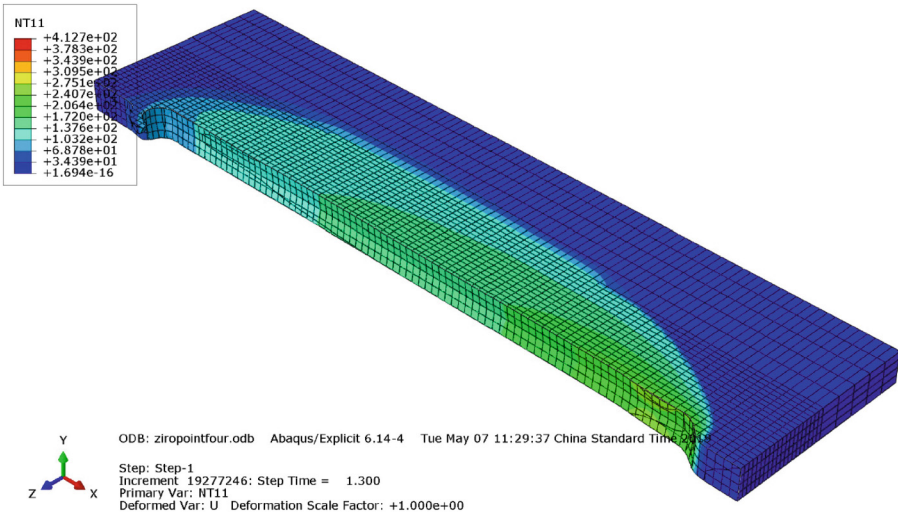


Fig. 8. The view cut section of the temperature distribution at the magnesium side

has a face-centred cubic (FCC) in which there is twelve slip system, however the structure of the magnesium has hexagonal close-packed (HCP). Due to the abovementioned description, the deformability of the aluminium is higher, whereby the generated heat by the plastic deformation at the aluminium side is higher [50]. This theory also confirms the validation of the results of this study [51].

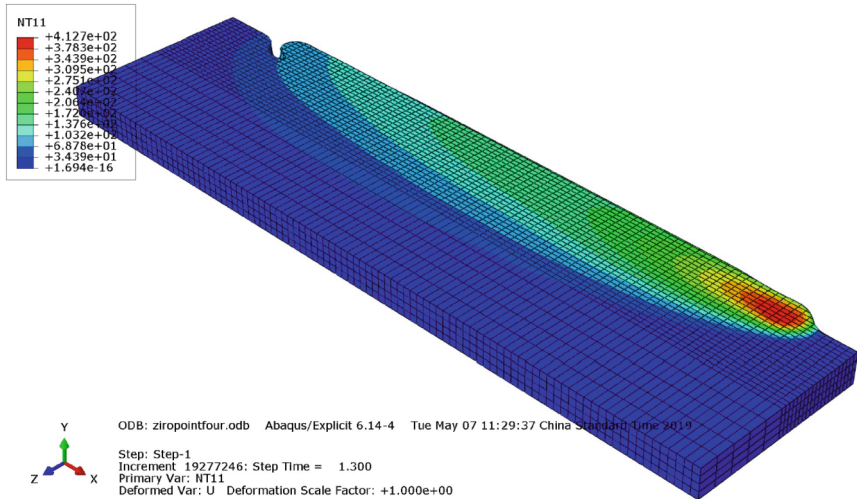


Fig. 9. The view cut section of the temperature distribution at the aluminum side

The literature [48] also reports that the dissimilar FSW has a lower temperature compared to similar FSW. In addition, from the literature reports [48], it can be claimed that the temperature range of 400 °C to 450 °C (almost the same as the values that are achieved in this study) leads to achieve a high-quality weld. Therefore, according to the good agreement between the calculated temperature values in this study and the literature, it can be predicted that the quality of the welds is acceptable.

The temperature distribution in the plates with and without the welding tool is shown in Fig. 10 and Fig. 11. As can be seen below the shoulder, the moving heat source is generated. Additionally, because of the conduction it is bounded by heat far from the welding line. By the end of the welding, the simulation predicted that the maximum temperature would reach around 412 °C, that is still lower than the melting temperature of both materials. In this light, localized heating makes it highly possible for constitutional liquation even if the predicted peak temperature is lower than the eutectic reaction temperature of the material. Besides, while the simulation approximates temperatures according to the uniform deformation field, dissimilar welding could cause localized deformation at the two alloys interfaces. This in turn will create higher localized temperatures in the literature compared to the predicted temperature values in this study.

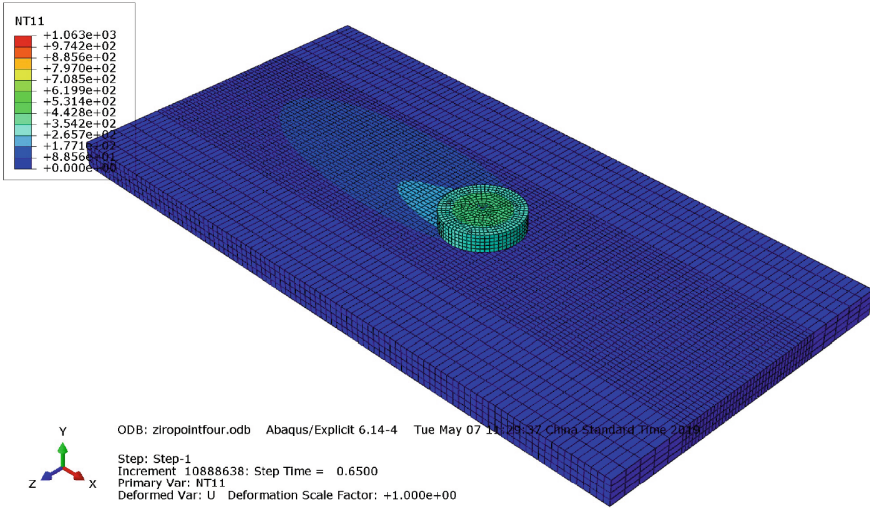


Fig. 10. The predicted values of the temperature at the tool workpiece interface

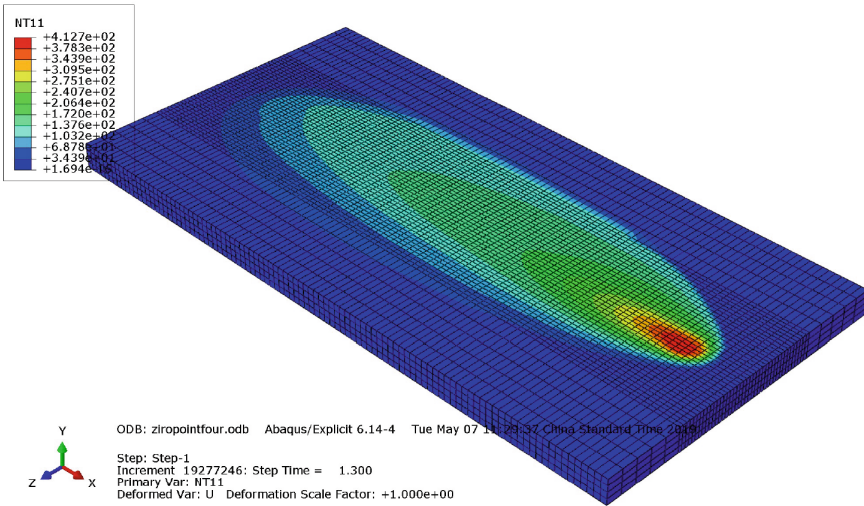
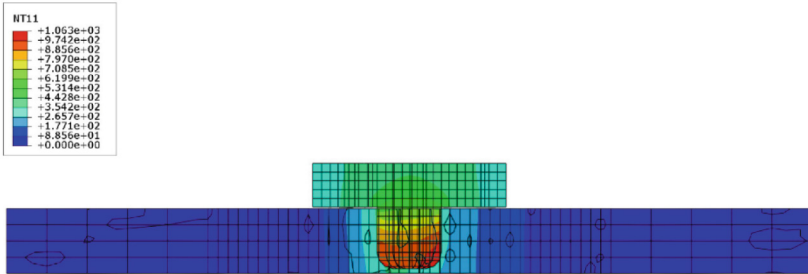


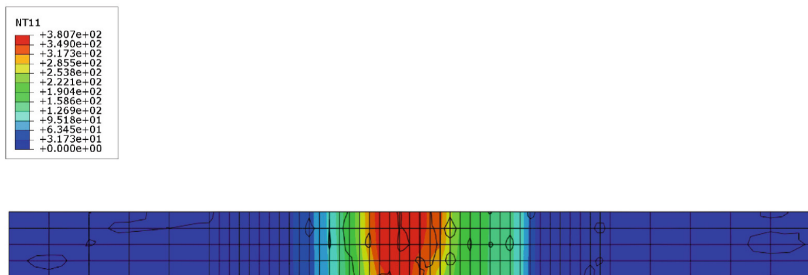
Fig. 11. Temperature distribution across the workpiece while the tool is removed

The thermal histories at the cross-section with and without the tool are shown in Fig. 12. In the Figure the tool is located at the welding central point, and the results are plotted against the peak temperature to examine the model spatial temperature prediction validity. It should be noted that in the literature these temperature values were measured by thermocouples [47, 48] and a considerable agreement between the model and the literature with an optimized error is found. This reflects that the model could accurately predict the spatial temperature distribution and the modified version of the friction law

leads to achieve high accuracy results. Additionally, a “V” form pattern for the temperature at the cross-view of the weld is showed in Fig. 12. It needs to be mentioned that, this kind of patterns have also been reported in the literature [3].



a)



b)

Fig. 12. Cross-section of the welding (a) with the tool and (b) without tool

Based on a study by Pan et al. [52] which set the thermal conductivity of Mg- 3 wt. % Al and AZ31 alloy at 80 W/mK and 84.7 W/mK, respectively at 300 K, for this present study, at 20 °C, the thermal conductivity for AZ31 alloy was set at ~ 96.4 W/m °C. Moreover, at 20 °C, the thermal conductivity data for AA 6061 alloy is set to be 162 W/mK °C, which is in line with the data recorded in the reference [52]. It is also found that similar to the previous studies [47, 53], the increase in temperature causes an increase for the conductivity data of AZ31 and AA 6061 alloys. These observations help verify the asymmetrical temperature pattern recorded during the welding. This occurrence is also caused by the fact that thermal conductivity is deemed as a direct function of density, which makes the peak temperature point closer to the AA 6061, compared to the base AZ31 alloy.

At the initial step of the welding, the heat transfer analysis is conducted by the average thermophysical properties of AA 6061 and AZ31 alloy for the stir zone. As the welding runs, it is detected that the measured temperature histories have similar trends in regard to welding cycle heating time and that the peak temperatures. On the other hand, during the cooling stage it is observed that there are some differences between the predicted values and the literature values. This issue happens because of the higher loss of the heat during the experiments that can be neglected.

The Eulerian volume fraction (EVF) for the aluminum side and the magnesium side are presented in Fig. 13 and Fig. 14, respectively. The translucence view indicates that the transverse movement of the tool across the welding seam caused the transportation of the material from the advancing side to the retreating side. As can be seen the rate of the movement of the aluminum material to the magnesium side is higher. As noted earlier, this issue occurs because the melting temperature of the aluminum is lower than the magnesium and also this material is softer compared to magnesium. Therefore, compared to the magnesium the movement of the aluminum is easier for the tool. Thus, it is predicted that the percentage of aluminum alloy inside the welding zone is higher than the magnesium. This issue is also reported in the literature. This agreement shows that the results of this study are accurate and a good correlation is achieved with the previous research [47, 54–56].

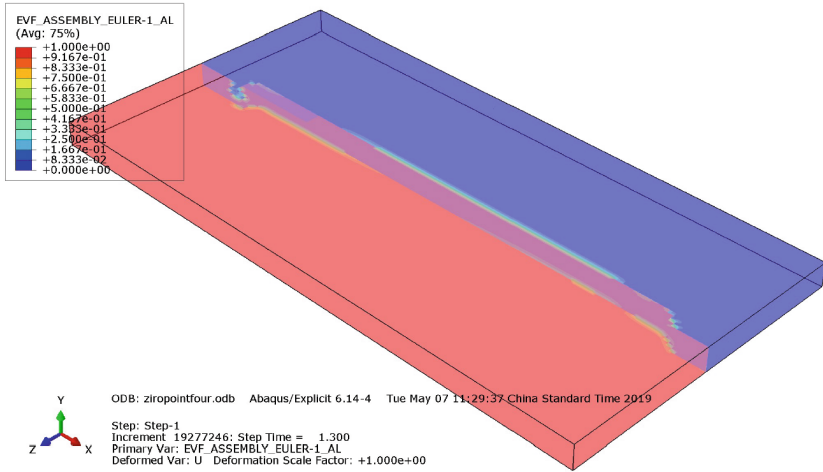


Fig. 13. The Eulerian volume fraction at the aluminum side (toggle global translucency)

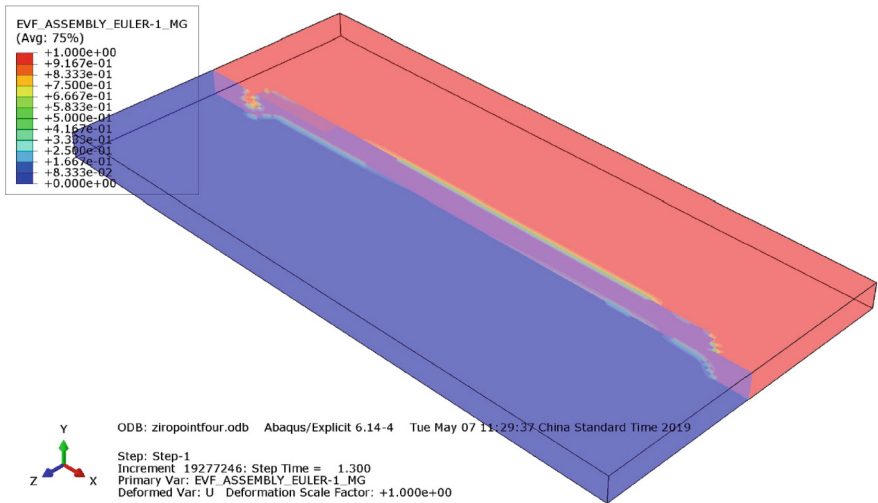


Fig. 14. The Eulerian volume fraction at the magnesium side (toggle global translucency)

Conclusions

This paper has used a developed friction model to improve finite element modelling of FSW in order to determine the temperature distribution and the Eulerian volume fraction during the dissimilar FSW of aluminium and magnesium. The significant findings of this research are listed as below,

- When the tool is located at the aluminium side of the welding, the peak temperature was reported to be higher (412 °C at the aluminium side and 380 °C at the magnesium side).
- The results of the Eulerian volume fraction indicate that the movement of the material that is located at the aluminium side is more than the material which is placed in the magnesium side, this issue happens because the aluminium material is softer.
- The prediction projected that the welding peak temperature across the welding line (412 °C) is less than the melting temperature of both alloys (550–580 °C for aluminium and 605–630 °C for magnesium).
- It was also reported that, the maximum temperature was high enough to cause liquation of eutectic transformation.
- Similar to the results of the literature at the cross-section of the welding, a “V” shape pattern was reported for the temperature.
- The simulated model showed a remarkable accuracy for the developed model by the Norton friction law, and the model is validated after comparing the results of this study with the experimental and numerical outcomes of the literature.

Acknowledgement. The authors would like to thank Professor Wallace Kaufman for his endless support.

Conflict of interest. There is no conflict of interest.

References

1. Cao, X., Jahazi, M.: Effect of tool rotational speed and probe length on lap joint quality of a friction stir welded magnesium alloy. *Mater. Des.* **32**(1), 1–11 (2011)
2. Chowdhury, S., et al.: Tensile properties of a friction stir welded magnesium alloy: effect of pin tool thread orientation and weld pitch. *Mater. Sci. Eng. A* **527**(21), 6064–6075 (2010)
3. Meyghani, B., Awang, M.: A comparison between the flat and the curved Friction Stir Welding (FSW) thermomechanical behaviour. In: *Archives of Computational Methods in Engineering*, pp. 1–14 (2019)
4. Su, H., et al.: Thermal energy generation and distribution in friction stir welding of aluminum alloys. *Energy* **77**, 720–731 (2014)
5. Chuansong, W.U., H.S., Shi, L.: Numerical simulation of heat generation, heat transfer and material flow in friction stir welding. *Acta Metall* **54**(2), 265–277 (2018)
6. Meyghani, B., Awang, M.: Introduction to Friction Stir Welding (FSW). In: *Welding Simulations Using ABAQUS*, pp. 1–3. Springer (2022)
7. Yang, C.L., Wu, C.S., Lv, X.Q.: Numerical analysis of mass transfer and material mixing in friction stir welding of aluminum/magnesium alloys. *J. Manuf. Process.* **32**, 380–394 (2018)
8. Su, H., et al.: Simultaneous measurement of tool torque, traverse force and axial force in friction stir welding. *J. Manuf. Process.* **15**(4), 495–500 (2013)
9. Su, H., Wu, C.: Determination of the traverse force in friction stir welding with different tool pin profiles. *Science and Technology of Welding and Joining*, pp. 1–9 (2018)
10. Meyghani, B.: Thermomechanical analysis of friction stir welding (FSW) on curved plates by adapting calculated temperature dependent properties. 2018, Universiti Teknologi PETRONAS
11. Meyghani, B., Awang, M.B.: Prediction of the temperature distribution during friction stir welding (Fsw) with a complex curved welding seam: application in the automotive industry. *MATEC Web Conf.* **225**, 01001 (2018)
12. Meyghani, B., Awang, M.: Arbitrary Lagrangian-Eulerian (ALE) Method. In: *Welding Simulations Using ABAQUS*, pp. 13–61. Springer (2022)
13. Kumar, S., et al.: Effect of ultrasonic vibration on welding load, macrostructure, and mechanical properties of Al/Mg alloy joints fabricated by friction stir lap welding. *Int. J. Adv. Manuf. Technol.* **100**(5–8), 1787–1799 (2019)
14. Meyghani, B., Awang, M., Emamian, S.: A mathematical formulation for calculating temperature dependent friction coefficient values: Application in friction stir welding (FSW). In: *Defect and Diffusion Forum*, pp. 73–82 (2017)
15. Kumar, S., Wu, C.: Review: Mg and its alloy—scope, future perspectives and recent advancements in welding and processing. *J. Harbin Inst. Technol. (New Ed)* **24**, 1–37 (2017)
16. Banerjee, P.C., et al.: Electrochemical investigation of the influence of laser surface melting on the microstructure and corrosion behaviour of ZE41 magnesium alloy—An EIS based study **53**(4), 1505–1514 (2011)
17. Kheireddine, A., et al.: Experimentally validated thermo-mechanically coupled FE simulations of Al/Mg friction stir welded joints. In: *ASME 2013 International Mechanical Engineering Congress and Exposition*. 2013. American Society of Mechanical Engineers Digital Collection
18. Meyghani, B., et al.: A comparison of different finite element methods in the thermal analysis of Friction Stir Welding (FSW). *Metals* **7**(10), 450 (2017)
19. Meyghani, B., Awang, M.: Post Processor and Visualization of the Results. In: *Welding Simulations Using ABAQUS*, pp. 63–67. Springer (2022)
20. Liu, L., Ren, D., Liu, F.: A review of dissimilar welding techniques for magnesium alloys to aluminum alloys. *Materials* **7**(5), 3735–3757 (2014)

21. Meyghani, B., et al.: Thermal Modelling of Friction Stir Welding (FSW) Using Calculated Young's Modulus Values. In: *The Advances in Joining Technology*, pp. 1–13. Springer (2018). https://doi.org/10.1007/978-981-10-9041-7_1
22. Meyghani, B., Wu, C.: Progress in thermomechanical analysis of friction stir welding. *Chinese J. Mech. Eng.* **33**(1), 12 (2020)
23. Miles, M., et al.: Predicting recrystallized grain size in friction stir processed 304L stainless steel. *J. Mater. Sci. Technol.* **35**(4), 491–498 (2019)
24. Sun, Z., Wu, C., Kumar, S.: Determination of heat generation by correlating the interfacial friction stress with temperature in friction stir welding. *J. Manuf. Process.* **31**, 801–811 (2018)
25. Ansari, M.A., Behnagh, R.A.: Numerical study of friction stir welding (FSW) plunging phase using smoothed particle hydrodynamics (SPH). *Modelling and Simulation in Materials Science and Engineering* (2019)
26. Meyghani, B., Awang, M., Wu, C.: Thermal analysis of friction stir welding with a complex curved welding seam. *Int. J. Eng.* **32**(10), 1480–1484 (2019)
27. Meyghani, B., Awang, M., Emamian, S.: A comparative study of finite element analysis for friction stir welding application. *ARPJ. Eng. Appl. Sci.* **11**(22), 12984–12989 (2016)
28. Su, H., et al.: Numerical modeling for the effect of pin profiles on thermal and material flow characteristics in friction stir welding. *Mater. Des.* **77**, 114–125 (2015)
29. Ansari, M.A., et al.: An efficient coupled Eulerian-Lagrangian finite element model for friction stir processing. *Int. J. Adv. Manuf. Technol.* **101**(5–8), 1495–1508 (2019)
30. Meyghani, B., Awang, M., Wu, C.: Finite element modelling of friction stir welding (FSW) on a complex curved plate. *J. Adv. Joining Process.*, 100007 (2020)
31. Meyghani, B., et al.: A comparison between temperature dependent and constant Young's modulus values in investigating the effect of the process parameters on thermal behaviour during friction stir welding: Vergleich zwischen den temperaturabhängigen und konstanten Elastizitätsmodulwerten in der Untersuchung der Prozessparameter auf die Wärmewirkung beim Rührreibschweißen. *Materialwiss. Werkstofftech.* **49**(4), 427–434 (2018)
32. Meyghani, B., Awang, M.: Thermomechanical Analysis. In: *Welding Simulations Using ABAQUS*, pp. 5–6. Springer (2022). https://doi.org/10.1007/978-94-009-1219-9_7
33. Meyghani, B., Awang, M., Emamian, S.: A mathematical formulation for calculating temperature dependent friction coefficient values: application in Friction Stir Welding (FSW). in *Defect and diffusion forum*. 2017. *Trans Tech Publ*
34. Meyghani, B., Awang, M.: *Welding Simulations Using ABAQUS: A Practical Guide for Engineers*. Springer Nature (2022). <https://doi.org/10.1007/978-981-19-1320-4>
35. Dialami, N., et al.: Enhanced friction model for Friction Stir Welding (FSW) analysis: Simulation and experimental validation. *Int. J. Mech. Sci.* **133**, 555–567 (2017)
36. Guerdoux, S., Fourment, L.: A 3D numerical simulation of different phases of friction stir welding. *Modell. Simul. Mater. Sci. Eng.* **17**(7), 075001 (2009)
37. Meyghani, B., et al.: Developing a finite element model for thermal analysis of friction stir welding by calculating temperature dependent friction coefficient. In: *2nd International Conference on Mechanical, Manufacturing and Process Plant Engineering*. Springer (2017). https://doi.org/10.1007/978-981-10-4232-4_9
38. Emamian, S., et al.: Influences of tool pin profile on the friction stir welding of AA6061. *ARPJ. Eng. Appl. Sci.* **11**(20), 12258–12261 (2016)
39. Dialami, N., et al.: Numerical simulation and visualization of material flow in friction stir welding via particle tracing. In: *Numerical Simulations of Coupled Problems in Engineering*, pp. 157–169. Springer (2014). https://doi.org/10.1007/978-3-319-06136-8_7
40. Bussetta, P., et al.: 3D numerical models using a fluid or a solid formulation of FSW processes with a non-cylindrical pin. *Adv. Modeling Simul. Eng. Sci.* **2**(1), 27 (2015)

41. Johnson, G.R., Cook, W.H.: A constitutive model and data for metals subjected to large strains, high strain rates and high temperatures. In: Proceedings of the 7th International Symposium on Ballistics. The Hague, The Netherlands (1983)
42. Wright, T.W.: The physics and mathematics of adiabatic shear bands. Cambridge University Press (2002)
43. Zhu, X., Chao, Y.: Numerical simulation of transient temperature and residual stresses in friction stir welding of 304L stainless steel. *J. Mater. Process. Technol.* **146**(2), 263–272 (2004)
44. Cole, E., et al.: Weld temperature effects during friction stir welding of dissimilar aluminum alloys 6061–t6 and 7075–t6. *Int. J. Adv. Manuf. Technol.* **71**(1–4), 643–652 (2014)
45. Zettler, R., et al.: Dissimilar Al to Mg alloy friction stir welds. *Adv. Eng. Mater.* **8**(5), 415–421 (2006)
46. Kwon, Y., Shigematsu, I., Saito, N.: Dissimilar friction stir welding between magnesium and aluminum alloys. *Mater. Lett.* **62**(23), 3827–3829 (2008)
47. Hou, Z., et al.: Residual stresses in dissimilar friction stir welding of AA2024 and AZ31: experimental and numerical study. *J. Manuf. Sci. Eng.* **140**(5), 051015 (2018)
48. Fu, B., et al.: Friction stir welding process of dissimilar metals of 6061–T6 aluminum alloy to AZ31B magnesium alloy. *J. Mater. Process. Technol.* **218**, 38–47 (2015)
49. Meyghani, B., Awang, M.: A novel tool path strategy for modelling complicated perpendicular curved movements. *Key Eng. Mater.* **796**, 164–174 (2019)
50. Firouzdor, V., Kou, S.: Al-to-Mg friction stir welding: effect of positions of Al and Mg with respect to the welding tool. *Weld. J.* **88**(11), 213–224 (2009)
51. Meyghani, B., Awang, M.: The influence of the tool tilt angle on the heat generation and the material behavior in Friction Stir Welding (FSW). *Metals* **12**(11), 1837 (2022)
52. Pan, F., et al.: Effects of friction stir welding on microstructure and mechanical properties of magnesium alloy Mg-5Al-3Sn. *Mater. Des.* **110**, 266–274 (2016)
53. Meyghani, B., Awang, M.: Developing a Finite Element Model for Thermal Analysis of Friction Stir Welding (FSW) Using Hyperworks. In: *Advances in Material Sciences and Engineering*, pp. 619–628. Springer (2020). https://doi.org/10.1007/978-981-13-8297-0_64
54. Meyghani, B., Awang, M.: Thermomechanical Simulation of FSW Using User Defined Subroutine Modeling Technique. In: *Welding Simulations Using ABAQUS*, pp. 69–122. Springer (2022)
55. Meyghani, B., Awang, M., Wu, C.: Finite element modeling of friction stir welding (FSW) on a complex curved plate. *J. Adv. Joining Process.* **1**, 100007 (2020)
56. Meyghani, B., Awang, M., Wu, C.: Thermal analysis of friction stir processing (FSP) using arbitrary Lagrangian-Eulerian (ALE) and smoothed particle hydrodynamics (SPH) meshing techniques. *Materialwiss. Werkstofftech.. Werkstofftech.* **51**(5), 550–557 (2020)



Vortex Induced Vibration of Free Span Pipeline – CFD Simulation

Ahmad Mahamad Al-Yacouby^(✉), Mohd Farid Bin Mizan, and M. S. Liew

Department of Civil and Environmental Engineering, Universiti Teknologi PETRONAS (UTP),
32610 Seri Iskandar, Perak, Malaysia

ahmad.alyacouby@utp.edu, aalyacouby@gmail.com

Abstract. VIV can cause fatigue damage to the pipeline due to excessive vibration in the long run. The effect of VIV on different pipe conditions are assessed using Three Dimensional (3D) Computational Fluid Dynamics (CFD) ANSYS software. Different geometries of pipe were modelled for different Reynolds numbers. This study presents the three-dimensional (3D) simulation result concerning the effect of pipe diameter at different pipeline span, and the effect of pipeline surface condition towards the vortex induced vibration (VIV) phenomenon on the free span subsea pipeline. In evaluating hydrodynamics forces acting on the pipe, the larger pipe diameter, longer pipe length and coarser pipe surface introduced higher hydrodynamic force on the pipe, in term of drag and lift forces. In term of the development of wake region at pipe aft, the smaller pipe diameter, shorter pipe length, and smoother pipe surface has smaller wake region size. The evaluation of different type of pipe geometries could contribute to the study of pipeline VIV suppression techniques. The study on drag reduction measure on textured pipeline as a VIV suppression device can benefits the industry whereby it can help in mitigating VIV and thus avoid pipeline failure due to fatigue from excessive cyclic loadings.

Keywords: Vortex Induced Vibration · Free Span Pipeline · CFD Simulation · Drag Forces · Inertia Forces

1 Introduction

Subsea pipeline is exposed to dynamic load due to current and wave. The uneven topography surface of the seabed resulting the pipeline undergoes the free span. The VIV phenomenon occurs on the pipeline caused by the ocean currents. The movement of the fluids around the pipe raises the vortex at the rear side of the oncoming flow, hence cause vibration on the free span pipeline structures. The effective way to reduce the impact of VIV is by adding a suppression device. Therefore, the flow characteristic and the impact of VIV on several scenarios need to be assessed and analyzed. In this study, the flow characteristic on different outer diameter of pipeline, different span length of free span pipeline and different pipeline surface condition will be conducted.

Offshore pipelines are primarily used for transporting oil and gas over long-distance point of extraction or production to the points of consumption. Deep water pipelines are

being laid on the seabed and used for offshore gas and oil transportation. Due to the unevenness of the seabed, part of a pipeline may become unsupported, which is called free span.

A free span can also be caused by rock beams, artificial support, change of seabed topology and strudel scours (Veritas, 2006). Subsea pipeline free spanning occurs when pipeline is losing contact to the seabed over an appreciable distance on a rough seabed. The free span of the subsea pipeline is considerable in certain allowable length, but need to be reduced to prevent damages to the pipeline. Pipeline free span can result in failure due to excessive yielding and fatigue. Two causes of fatigue damage to subsea pipeline free spans exist, which are waves and underwater current. Free span can occur due to unsupported weight of the pipeline section and dynamic loads from waves and currents as shown in Fig. 1.

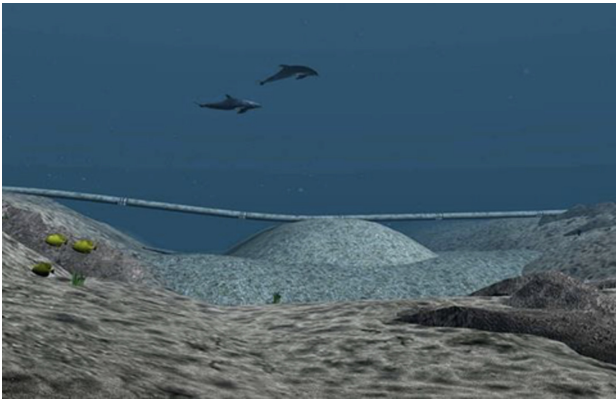


Fig. 1. Free span pipeline

Stress arising within the boundary layer, which is “a very thin layer in the neighborhood of the body” (Schlichting 1968). The bottom currents could cause significant dynamic stresses if fluid structure interaction in these free-span pipeline areas causes the pipeline to oscillate (vortex shedding). In summary, the key factor for free span pipeline includes Water Particle velocity, Pipeline Diameter (Pipe + Coating), Stiffness of the spanning pipe (diameter, wall thickness, end boundary effects), Mass (pipe + contents + coating + added mass) and Gap span between seabed and pipe.

Pipeline span analysis is an important tool used in offshore and ocean technology for structural failure due to overstress from steady state loads, fatigue failure as a result of vibrations from dynamic loads (such as Vortex Induced Vibrations, VIV) and severe damage due to third party activities (hooking from trawl gears or drop objects) (Palmer, A. & King, A., 2004; Shittu, 2012; Xing, 2011). According to Gou et al. (Guo, Song, Ghalambor, Lin, & Chacko, 2005), pipeline spanning usually occurs when the contact between the pipeline and seabed is lost over a long depression on a rough seabed.

The formation of submarine pipeline spans may have a critical influence on the safety and integrity of the pipelines (JP & Partners, 1993; Shittu, 2012). Spans can be developed during pipelay as a result of irregularity in the bedform (coupled with factors such as pipe

weight, pipe stiffness, among other), service life of the pipeline, the dynamic seabed-scouring and horizontal movements of the seafloor (Rezazadeh, Zhu, Bai, & Zhang, 2010). Deep water pipelines are highly susceptible to this effect since wave induced velocities and accelerations will decay with increasing water depth (Koushan, 2009). VIV is a major source of dynamic stresses in free span pipelines as a result of steady current. If the vortex shedding frequency which is caused by normal flow reaches to the natural frequency of pipeline, pipeline starts to vibrate and VIV occurs which may cause pipeline fatigue damage (Shabani, Taheri, & Daghighi, 2017). Ideally, assessment models should account for the vibration of span due to both waves and underwater current. However, in this research, only Vortex Induced Vortex from underwater current will be investigated due to the assumption that waves have no effect on the free span one-hundred meters or more below sea level. The sea currents are typically higher in deep-water areas than in shallower areas. For additional materials related to the topic, the reader can refer to [2–8, 13, 14, 17, 18].

2 Theoretical Background

Textured pipe has been proposed to improve the propagation buckling capacity of subsea pipelines. Due to its special geometry, textured pipe may have the potential to mitigate the vortex induced vibration (VIV) by altering the wake vortex street formation. In the Study, the effectiveness of using a full-diamond textured pipe for VIV suppression is numerically investigated in a coupled fluid-structure interaction (FSI) framework [16]. The textured pipe is cylindrical with local facets rather than a smooth wall along its longitudinal direction. With different parameters, different facet shapes can be obtained for the textured pipe. A full-diamond pattern known as the Yoshimura origami shape [15] was adopted - H.M. Nikoo et al. Figure 2 illustrates the geometric shape of the textured cylinder. The cylinder consists of a series of periodically arrayed diamond lobes, in which the solid and dashed lines represent the mountains and valleys in the folded full-diamond module, respectively. The relationship between different geometry parameters can be described as follows [15]:

$$\cos\theta = \frac{b}{l} \tan \frac{\pi}{2N} \quad (1)$$

$$\varphi = \pi - 4\alpha = \pi - \frac{2\pi}{N} \quad (2)$$

$$\tan\alpha = \frac{l}{b} \cos\theta \quad (3)$$

where:

θ = angle between folded lobes along the circumference and the horizontal plane

N = Number of folded lobes

α = the horizontal projection of the angle between the horizontal crease and the other two creases (in the same lobe)

φ = interior angle of the cross-sectional polygon

l, b = width and the distance between the vertexes of the two neighboring diamond lobes.

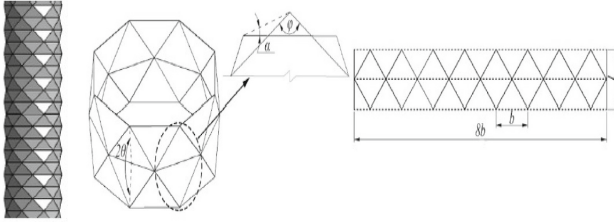


Fig. 2. Geometry details of a full-diamond (octagonal) textured pipe [3]

The study was conducted for both textured and smooth cylinder for the same diameter and mass. From the study, textured pipe has improved propagating buckling capacity compared to the smooth pipe. Due to its special geometry, this pipe is believed to be able to obviously reduce the vortex-induced vibration (VIV). The study conducted a 3D numerical simulation on the effectiveness of using a typical full-diamond (octagonal) textured cylinder for VIV control. A two-way coupled fluid-structure interaction (FSI) framework is developed by coupling the ANSYS mechanical and FLUENT solvers together. An equivalent smooth pipe is also numerically investigated. Numerical results showed that the textured cylinder can more evidently suppress VIV especially when the cylinder is vibrating under a relatively large normalized velocity. The upper oscillation regime which commonly exists in the conventional smooth cylinder is eliminated by the textured cylinder. The textured pipe can evidently reduce the hydrodynamic forces associated with the VIV phenomenon. In this study, the span length of the textured pipe towards VIV phenomenon is further investigated.

2.1 Overview of Pipeline Diameter

The frequency of vortex shedding is a function of the pipe diameter, current velocity, and Strouhal Number. If the vortex shedding frequency which also referred to as the Strouhal frequency is synchronized with the natural frequencies of the pipeline, resonance will occur, and the pipeline span will vibrate. The pipeline span is designed so that its natural frequency is sufficiently far from the vortex shedding frequency, as it could prevent pipeline failure due to vortex excited motions [1]. The vortex-shedding frequency is calculated based on the following equation (4):

$$f_s = \frac{SU_c}{D} \tag{4}$$

f_s = Vortex Shedding Frequency, S = Strouhal Number, U_c = Design Current velocity
 D = Pipe Outside Diameter

The pipeline span natural frequency is calculated based on the following Equation (5):

$$f_n = \frac{C_e}{2\pi} \sqrt{\frac{EI}{M_e L_s^4}} \tag{5}$$

F_n = Pipe span Natural Frequency

L_s = Span length

M_e = Effective Mass

C_e = End condition constant

Strouhal Number is the dimensionless frequency of the vortex shedding and is a function of the Reynolds Number. Reynolds Number, Re is calculated using below equation (6):

$$Re = \frac{U_c D}{\nu_k} \quad (6)$$

where, ν (kinematic viscosity of fluid) = $(1.2 \times 10^{-5} \text{ ft}^2 / \text{sec}$ for water at 60°F)

Different type of pipe diameter will give different vortex shedding frequency. The pipeline material properties will be based on API 5L standards. Different grade of pipe as defined in API 5L standards will yield different natural frequency of pipe.

3 Project Methodology

3.1 CFD Simulation

The motions of the cylinder and the fluid should be solved in FSI framework. The two-way FSI algorithm is developed by coupling the ANSYS Mechanical finite element (FE) solver for the solid part (cylinder) together with the FLUENT finite volume (FV) solver for the fluid part. The coupling between the two systems is achieved in ANSYS workbench. In this simulation, at each time step, the fluid motion equations are solved in the FLUENT FV solver and the estimated hydrodynamic loads are transferred to the mechanical part as inputs on the cylinder. Within the same time step, the structural dynamics equation is solved in the ANSYS Mechanical FE solver, which in turn causes deformation in the mesh grids of the fluid part. This procedure continues up to a stage where the vibrations of the cylinder reaches an almost steady state condition.

3.1.1 Computational Domain and Mesh Generation

A 3-D rectangular computational fluid domain will be developed to capture the VIV responses and the wake vortices. Figure 3 outlines the computational blocks, generated mesh grids and the corresponding boundary conditions that will be used for both the smooth and textured (rough) cylinders. In both cases (smooth and textured cylinders), the center of the elastically-mounted cylinders will be determined from the inlet and outlet boundaries. The cross-flow width of the domain, and the span length of the domain need to be determined as well. Based on previous study [9–12], the center of cylinders = 20D and 30D from the inlet and outlet boundaries (D=cylinder mean diameter), cross flow width = 40D, span length = 8D. A steady uniform flow with a freestream velocity of $u = U_\infty$ is specified at the velocity-inlet boundary ($x = 20D$) [3].

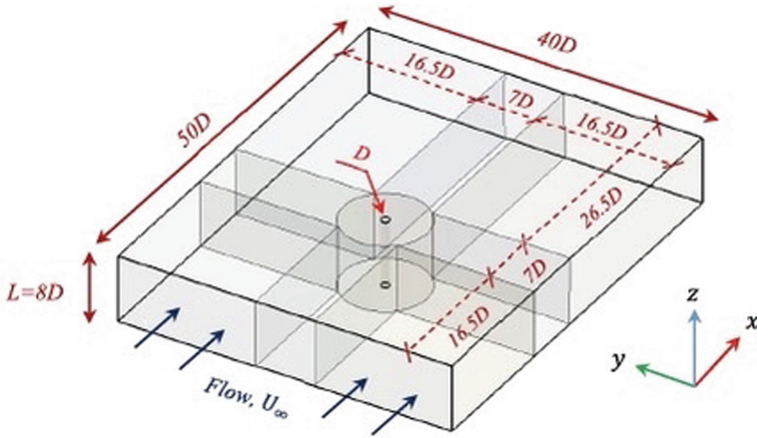


Fig. 3. Computational fluid domain adopted in Fluent Solver [3].

4 Results and Discussions

In order to simulate the effect of different pipe diameters towards VIV, three individual simulations were conducted as presented in Table1. The pipe with diamond textured pipe (known as textured pipe) was enclosed in a fluid domain which is simulated as a boxed-shaped fluid domain. The simulation for scenario A, B and C were run and the results were captured and analyzed. The captured results include Drag and lift force calculation, current velocity along the x-direction via velocity contours and vectors, and as well as cumulative force calculation acting on the pipe. The extreme conditions were taken based on the Extreme Value for the specific Return Period (RP). Generally, as the return period gets much more extreme, the parameter’s omni directional value is becoming higher.

Table 1. Different pipe diameter simulation parameters

Scenario	Diameter (m)	Thickness (m)	Span Length (m)	Surface Condition
A	0.254	0.0254	2.032	Textured
B	0.381	0.0254	2.032	Textured
C	0.508	0.0254	2.032	Textured

4.1 Effects of Pipe Diameter

Taking scenario B as an example, a thin viscous region or the boundary layer is created when a viscous fluid moves over the stationary pipe. The flow outside the viscous region is considered as inviscid. The pressure is minimum when the flow velocity is maximum. The fluid pressure is increasing in the direction of flow. At the maximum fluid pressure,

the fluid flow local velocity gradient approaches zero. At the boundary layer, the velocity of the fluid at the surface of the pipe is equal to the object velocity. Since the pipe is stationary, the fluid velocity at the pipe surface is equal to zero (no slip boundary of the fluid). Looking at the velocity contour, the fluid velocity is almost zero on the upstream side of pipe surface (green/cyan contour ~ 0 m/s). At this point, the fluid detaches from the surface. The detachment of fluid flow from the pipe surface is known as flow separation. The fluid velocity continues to increase from this boundary until it nearly reaching the fluid free stream velocity of 1.8m/s. From the velocity contours, the flow velocity is reaching to maximum 2.92 m/s. Beyond the separation point, the reverse flow occurs near the surface and the velocity gradient becomes negative. The fluid flow is deflecting away from the pipe surface. As a comparison, the smaller diameter of pipe has higher current velocity acting in the X-direction and the current velocity is reduced $\sim 30\%$ when the pipe diameter is increased by 50%.

Flow separation over the pipes induced wake behind the pipe. The low pressure behind the pipe is referred as a wake. The interaction between the forward and reversed flow in the wake region generates fluid rotation or vortex. The Reynolds number dictates the occurrence of flow separation over a body and influence the magnitude of flow separation. As for this simulation, Scenario A has Re Number: 496956.52, Scenario B has Re Number: 745434.78, Scenario C has Re Number: 993913.04 . As the current velocity is constant, the larger diameter of pipe will yield higher Reynolds number.

The presence of a wake region on the downstream side of the pipe is the cause of the drag force component on the pipe. The pressure differential between the upstream side (high pressure) and the downstream side (wake-low pressure) caused a force to be exerted in the direction of particle velocity. From the simulation result, the larger diameter of pipe has higher drag force compared to the smaller diameter of pipe. As the water particle hits the pipe surface and travel from the center of pipe to the uppermost part of the pipe, the drag force acting on the pipe was building up and gradually decreased when it reaches the uppermost side of the pipe. As the particle travel from uppermost side to the downstream side of the pipe, the force drastically increased. The maximum force is generated at the downstream side of the pipe. To compare, textured pipe with larger diameter of 0.381m has maximum drag force of 1280N compared to smaller pipe diameter of 0.254m with 553N of maximum drag force (Fig. 4). With the increment of 50% in pipe diameter, the drag force has significantly increased to more than 100%. (130% for case B, and 160% for case C). As for the lift force, the increment of pipe diameter has increased the maximum lift force which acting in the opposite direction of drag force. Max X-Velocity on different pipe diameter and Max Drag force and Lift force on different pipe diameter are presented in Fig. 5 and Fig. 6 respectively.

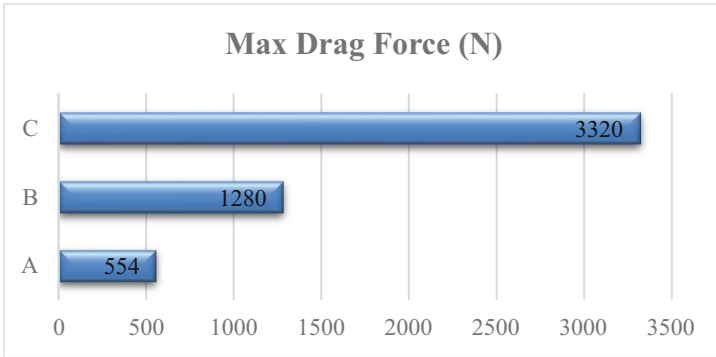


Fig. 4. Max Drag force on pipes with different diameters

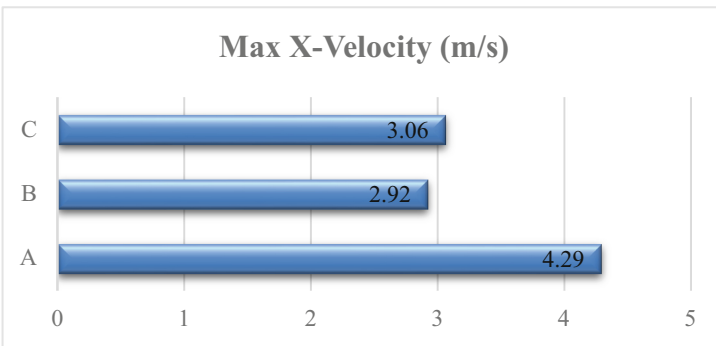


Fig. 5. Max X-Velocity on pipes with different diameters

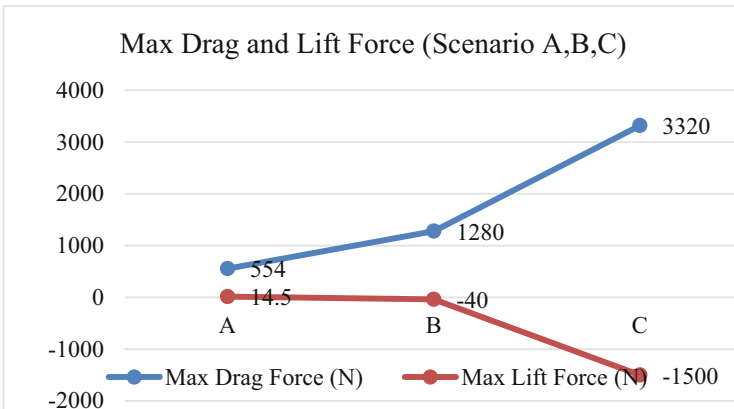


Fig. 6. Max Drag and Lift forces on pipes with different diameters

4.2 Effects of Span Length on VIV

In order to simulate the effect of different pipe span length towards VIV, three individual simulations were conducted, where each simulation has a different pipe length as shown in Table 2.

Table 2. Simulation of Different Pipe Span Length dimension

Scenario	Diameter (m)	Thickness (m)	Span Length (m)	Surface Condition
D	0.254	0.0254	2.032	Textured
E	0.254	0.0254	4.064	Textured
F	0.254	0.0254	6.096	Textured

As for the force generation, the drag force prediction from the 3 scenarios is compared in presented in Fig. From the result, one can observe that the pipe with the longest span length (Case F) has experienced the higher drag force compared to the shorter pipe span length (Case D and E). The maximum force is generated at the downstream side of the pipe. To compare, case F pipe with the longest span length has maximum drag force of 1700N compared to the shortest pipe span length (Case D) with 553N of drag force (Fig. 7). The longest span length pipe has larger surface area compared to the shorter pipe which contributes to higher drag force. Generation. To compare, the 100% increment of pipe length (2.032m to 4.064m), the drag force is significantly increased by 94.04%. The Max X-Velocity on different pipe span length and the comparison of Max Drag force and Lift force on pipe with various span lengths are presented in Figs. 8 and 9 repetitively.

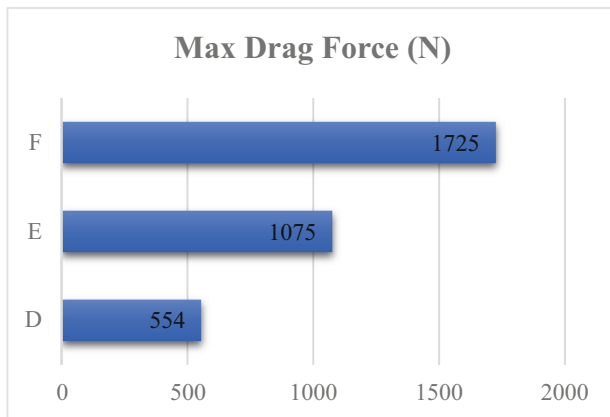


Fig. 7. Max Drag force on pipes with different span lengths

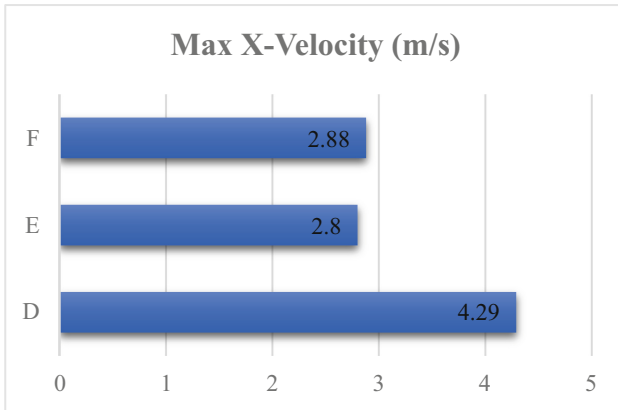


Fig. 8. Max X-Velocity on pipes with different span lengths

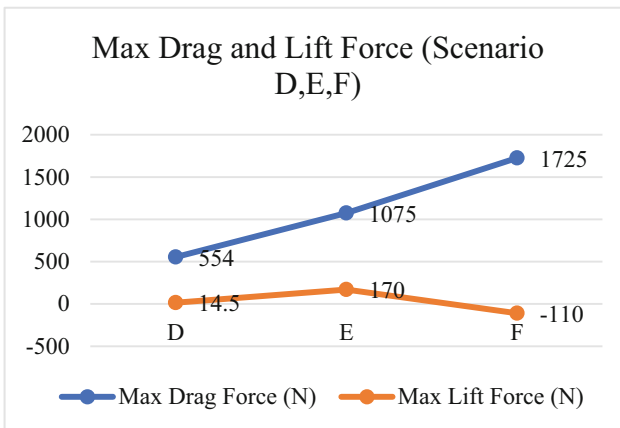


Fig. 9. Max Drag force and Lift force on pipes with different span lengths

5 Conclusions

In this research, the effect of different pipe diameter, different pipe span length and different pipe surface condition were assessed towards the vortex induced vibration (VIV) on subsea free span pipeline. A series of 3 dimensional simulations were carried out using ANSYS FLUENT software.

The 1st group of simulation is aimed to analyze the effect of different pipe diameters on VIV. The VIV effect on free span subsea pipeline were assessed by analyzing the drag force, lift force and current velocity acting on the pipes. From the simulation results, the larger diameter of pipe will introduce higher drag force on pipe surface and higher lift force acting on opposite direction of the drag force. The larger diameter of pipe will have lower fluid velocity at the downstream side (low pressure area) of the pipe.

The 2nd group of simulation is aimed to analyze the effect of different pipe span length towards VIV on free span subsea pipeline. From the simulation results, the longer length of pipe will introduce higher drag force on pipe surface and higher lift force acting on opposite direction of the drag force. The longer pipe span length will also have lower fluid velocity at the downstream side (low pressure area) of the pipe.

While for the 3rd group of simulation, the effect of different pipe surface towards VIV on free span subsea pipeline were assessed. From the simulation results, the coarser textured pipe will generate higher drag force acting on pipe surface and higher lift force acting on opposite direction of the drag force. The coarser pipe surface will also have lower fluid velocity at the downstream side (low pressure area) of the pipe and higher reverse flow at the pipe downstream side.

Acknowledgments. The authors would like to acknowledge the continued support by Universiti Teknologi PETRONAS (UTP) and the financial support provided by Yayasan UTP, grant number 015LC0 95 & 015LC0-313.

References

1. Guo, B., Song, S., Chacko, J., Ghalambor, A.: Offshore Pipelines, 51–53 (2005)
2. Schoefs, F.: Sensitivity and uncertainty studies for the modelling of marine growth effect on offshore structures loading. In: Proceedings of 21st International Conference on Offshore Mechanics and Arctic Engineering, pp. 1–7 (2002)
3. Nikoo, H.M, Bi, K., Hao, H.: Vortex-induced vibration of a full-diamond textured cylinder at subcritical Reynolds numbers (2022)
4. Kiu, K.Y., Stappenbelt, B., Thiagarajan, K.P.: Effects of uniform surface roughness on vortex-induced vibration of towed vertical cylinders. *J. Sound Vibr.* **330**(20), 4753–4763 (2011)
5. Zhou, B., Wang, Xi., Gho, W.M., Tan, S.K.: Force and flow characteristics of a circular cylinder with uniform surface roughness at subcritical Reynolds numbers. *Appl. Ocean Res.* **49**, 20–26 (2015). <https://doi.org/10.1016/j.apor.2014.06.002>
6. VIV and Wave Fatigue of Risers. In: Bai, Y., Qiang Bai, Q. (eds.) *Subsea Pipelines and Risers* (2005)
7. Matin Nikoo, H., Bi, K., Hao, H.: Three-dimensional vortex-induced vibration of a circular cylinder at subcritical Reynolds numbers with low-Re correction. *Mar. Struct.* **66**, 288–306 (2019)
8. Bourguet, R., Karniadakis, G.E., Triantafyllou, M.S.: Lock-in of the vortex-induced vibrations of a long-tensioned beam in shear flow. *J. Fluid. Struct.* **27**, 838–847 (2011)
9. Law, Y.Z., Jaiman, R.K.: Wake stabilization mechanism of low-drag suppression devices for vortex-induced vibration. *J. Fluid Struct.* **70**, 428–449 (2017)
10. Matin Nikoo, H., Bi, K., Hao, H.: Effectiveness of using pipe-in-pipe (PIP) concept to reduce vortex-induced vibrations (VIV): three-dimensional two-way FSI analysis. *Ocean Eng.* **148**, 263–276 (2018)
11. Prasanth, T., Mittal, S.: Vortex-induced vibrations of a circular cylinder at low Reynolds numbers. *J. Fluid Mech.* **594**, 463–491 (2008)
12. Zhao, M., Cheng, L., An, H., Lu, L.: Three-dimensional numerical simulation of vortex-induced vibration of an elastically mounted rigid circular cylinder in steady current. *J. Fluid Struct.* **50**, 292–311 (2014)
13. Menter, F.R.: Two-equation eddy-viscosity turbulence models for engineering applications. *AIAA J.* **32**, 1598–1605 (1994)

14. Cebeci, T.: Analysis of turbulent flows. Elsevier, Oxford (2004)
15. Yang, K., Xu, S., Shen, J., Zhou, S., Xie, Y.M.: Energy absorption of thin-walled tubes with pre-folded origami patterns: numerical simulation and experimental verification. *Thin-Walled Struct.* **103**, 33–44 (2016)
16. Wilcox, D.C.: Turbulence modeling for CFD, 3rd edn. CA: DCW Industries La Canada (2006)
17. Zahari, M.A., Dol, S.S.: Effects of different sizes of cylinder diameter on vortex-induced vibration for energy generation. *J. Appl. Sci.* **15**, 783–791 (2015)
18. Yttervik, R., Larsen, C.M., Furnes, G.K.: Fatigue from vortex-induced vibrations of free span pipelines using statistics of current speed and direction. In: Proceedings of the ASME 2003 22nd International Conference on Offshore Mechanics and Arctic Engineering. Volume 2: Safety and Reliability; Pipeline Technology. Cancun, Mexico. June 8–13, pp. 687–698. ASME (2003)



Material Flow and Temperatures Prediction in Friction Stir Extrusion Process Using Smoothed Particle Hydrodynamics

Venkata Somi Reddy Janga, Mokhtar Awang^(✉), and Eric J. Lee

Department of Mechanical Engineering, Universiti Teknologi PETRONAS,
32610 Seri Iskandar, Malaysia
mokhtar_awang@utp.edu.my

Abstract. An innovative solid-state processing method called friction stir extrusion (FSE) has the potential to save a significant amount of processing time and energy by plastically deforming metal flakes, or billets into parts. A few numerical models are developed to understand the complex physics of the FSE process and most of the FSE research is now experimental studies. The models developed so far are based on grid-based methods. In this study, a mesh-free simulation framework for the FSE process using a lagrangian formulation - smoothed particle hydrodynamics (SPH) is used. A 3-D thermomechanical, SPH-based model was modelled to simulate the extrusion of AA6061 wires by the FSE process. The numerical model is developed based on the previous experimental study of FSE. The results of temperature distribution, material flow, and plastic strains during the FSE process are presented. The smooth extrusion of the material started after the material reached a temperature of 660 K. The maximum temperature of the process reached 83.6% of the melting temperature of AA6061-T6. The material flow patterns predicted by the model are consistent with the material flow studies of the FSE process of earlier studies.

Keywords: Smoothed Particle Hydrodynamics (SPH) · Friction Stir Extrusion (FSE) · Thermo-mechanical Model · Simulation · Meshless method · Solid-state Processes · Material Flow

1 Introduction

A solid-phase manufacturing process, friction stir extrusion (FSE) invented and patented by The Welding Institute [1]. Figure 1 displays a schematic representation of the FSE. The die first compresses the precursor material in the process chamber by applying a downward vertical force. Then, as the vertical force is increased, the die turns. The temperature will rise as a result of heat being produced by friction between the die and the billet material. When the temperature is high enough, the precursor material consequently softens and deforms. The softened/plasticized precursor material is extruded out of the extrusion hole at the centre of the die to create a solid wire under continuing compression and frictional heating. FSE produces a product with significantly greater ductility than

a conventional extrusion technique as it enhances the microstructure [2]. FSE is a direct way of recycling metals, which saves a significant amount of material, labour, and energy as compared to conventional recycling techniques [3]. These features of the FSE process have boosted its progress in recent years, and it has evidenced great potential in industries like the automotive, aerospace, advanced manufacturing, and recycling of metal waste.

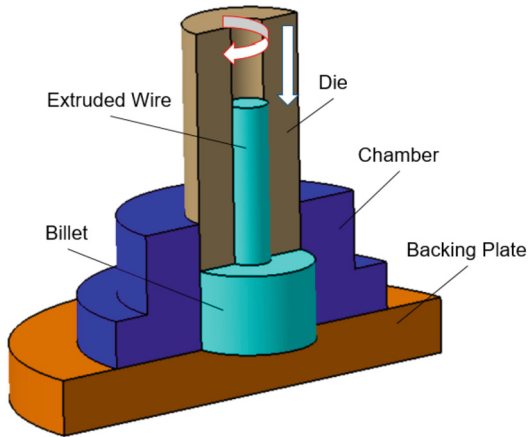


Fig. 1. Schematic representation of friction stir extrusion (FSE) process.

A few experimental studies on the friction extrusion method were published earlier. Tang and Reynolds [4] performed several tests using chips made of an aluminium alloy at various die rotation speeds. Li et al. [5] presented experimental research on material flow during friction extrusion of aluminium alloys. Zhang et al. [6] used analytical, computational, and experimental methods to investigate the material flow phenomenon in the FSE process. There are only a few numerical models for FSE that are published because of the related computational difficulties. To predict the temperatures, microstructure, and microhardness Behnagh et al. [7] developed a 2-D numerical model based on coupled Eulerian-Lagrangian (CEL) formulation. Baffari et al. [8] developed a 3-D numerical model using the updated lagrangian formulation in the DEFORM-3D software to simulate the FSE process of AZ31 material. Their model could accurately predict the strain, microstructure, and temperatures. For the FSE of AA6061 wires, Zhang et al. [9] presented material flow patterns using a 3-D model developed in Fluent (ANSYS). Karwa [10] developed a model in FORGENxT® for the FSE process, and detailed analyses of the simulation results were done to examine all aspects of the FSE procedure. The numerical models stated above on the FSE process were based on grid-based techniques. SPH, a Lagrangian particle method, unlike grid-based methods, was initially developed for astrophysics simulations [11, 12]. SPH can handle severe deformations, which sometimes could not be handled in grid-based approaches. It is difficult for grid-based numerical methods to accurately describe material contacts and boundaries during the simulation, but the particle representation in SPH makes this easy. Furthermore, the tracking of field variables dynamically is made possible by SPH's Lagrangian nature.

It is challenging, and expensive to experimentally investigate the thermo-mechanical characteristics (temperatures, strain, and material flow) during the FSE process involving high-temperature gradients and extensive deformations. Therefore, numerical simulation is required to understand the physics and material flow behaviour during FSE. From the literature, the SPH formulation proved ideal for processes involving large deformations and temperatures. In this paper, a 3-D thermo-mechanical was developed to simulate the FSE process using the SPH formulation available in Altair-Radioss. The temperatures and detailed material flow behavior during the FSE process are presented.

2 Methodology

The SPH Lagrangian formulation available in Altair-Radioss is used to model the FSE process. The experimental study from the earlier work is replicated by numerical simulations [9]. Therefore, the material, tool set dimensions, and the FSE process parameters are all taken from the earlier study.

2.1 Geometry

The billet, die, and chamber constitutes the geometries employed in the numerical model of the FSE process. Figure 2 displays the detailed dimensions of the geometries used in the model. The geometries were first modelled and assembled in CATIAv5, and then imported to Altair-Radioss. In the experiment, the backing anvil and chamber are tightly held together. As a result, the chamber geometry used in the model contains the backing anvil included. For the material, however, a cylindrical geometry (billet) was used to represent the material in powdered form. Also, the height of the billet is decreased to reduce the computational time.

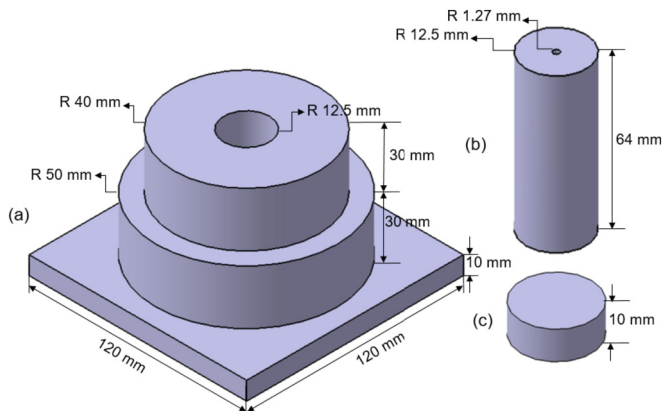


Fig. 2. Geometries of FSE process numerical model (a) chamber; (b) die; (c) billet.

2.2 Material and Material Model

Very high strain rates and temperature gradients are present throughout the FSE process. It is important to choose a constitutive law that can represent the flow stress interaction with strain rate, temperature, and strain rate. The following equation, which expresses the Johnson-Cook material law, is frequently used in the numerical modelling of related solid-state processes. [13, 14].

$$\sigma_y = \left[A + B \left[\varepsilon^{pl} \right]^n \right] \cdot \left[1 + C \ln \left(\frac{\dot{\varepsilon}^{pl}}{\dot{\varepsilon}^0} \right) \right] \cdot \left[1 - \left[\frac{T - T_r}{T_m - T_r} \right]^m \right], \quad (1)$$

where the equivalent plastic strain is ε^{pl} , the plastic strain rate is $\dot{\varepsilon}^{pl}$, the material flow stress is σ_y , and $\dot{\varepsilon}^0$ denotes the reference plastic strain rate. The material constants m —coefficient of thermal softening, n —coefficient of strain hardening, A —quasi-static yield strength, B —strain hardening constant, and C —strengthening coefficient—are derivatives at the reference strain rate. The billet is made of AA6061-T6 material. The material properties, coefficients, and constants for the Johnson-Cook material law were taken from the earlier study [15]. For the die and chamber, H13 steel and O1 steel (assumed to be isotropic) are applied respectively, similar to the earlier study [9].

2.3 Mesh, Contact, and Boundary Conditions

Due to the large contrast between the diameter of the extrusion hole and the die's outer diameter, which is a ratio of 1:10, the model used in the simulation uses a hexahedron solid mesh on the rotating die (4134 elements). Tetra mesh is used to model the chamber (20165 elements) because of its shape and dimensions, which produce a compact mesh that is suitable for containing SPH particles. The SPH particles are distributed in a simple cubic net shape to maximize the building of the net shape and allow for precise layer-by-layer material flow tracking of the particles. The letter c stands for the distance from one particle to its nearest neighbour, which is 1.31 mm. The equation below uses the aluminium alloy's (AA 6061) density (2700 kg/m^3) to calculate each particle's mass.

$$m_p = c^3 \rho \quad (2)$$

where m_p defines a particle's mass and ρ defines material density, c stands for the pitch distance between the particles.

The developed numerical model uses the node-to-surface (TYPE 7) contact algorithm in Altair Radioss. This contact is described as a multi-purpose contact interface that allows for the incorporation of heat from friction into the contact between the main surface and secondary nodes. This contact makes use of the penalty method, a technique that reduces computation time during simulations by having secondary nodes and major segments. The SPH particles are secondary nodes and the main segments are die and chamber surfaces that are in or going to be in contact with the SPH particles. As the temperature rises, incipient melting can cause tool slippage. As a result, it is advised to choose a friction coefficient that varies with temperature [16]. The simulation makes use of Coulomb's friction law and the temperature-dependent friction coefficient. A coefficient of 11 N/mm/s/K was used to define the heat transfer between the contact interfaces

of the die, chamber (tools), and workpiece [13, 14]. The thermal expansion coefficient varies with temperature, according to a study by Meyghani et al. [17]. The thermal expansion coefficient dependent on temperature findings was taken into consideration when developing the simulation model for FSE.

In this study, it is assumed that the initial temperature at which the simulation takes place is 298K, an ideal room temperature. Convective heat loss through the model is not taken into consideration to reduce the computational time. The focus of the research study is on the material flow and temperatures in the billet, therefore friction between the die and the extrusion chamber is also ignored. The total time of the simulation is 23 s. The chamber is constrained in all directions, and the die is restricted to rotate about its axis and move in the vertical direction.

3 Results and Discussion

Figure 3 shows the nodal temperature plots from the numerical for the extruded SPH particles (4 particles) to represent the trend of temperatures in the billet. The temperature trends of the simulation are similar to the experimental temperature trends but lower than the temperatures from the prior study [9]. This could be due to the coarser meshing of the toolset which simplifications are made to reduce computational time. The temperatures are maintained at around the room temperature until around 4.5 s, and thereafter a sudden rise is observed. Up to 4.5 s, the die compresses the material and the sudden rise of the temperature is when the rotating die face comes in contact with the particles. The sudden temperature rise is up to 470 K from room temperature. Thereafter, a gradual rise in the temperature is observed until the end of the process. The highest temperatures obtained from the numerical model are around 700 K, which is at the end of the process. The softening and movement of the material are directly impacted by the temperatures during the FSE process. Figure 4 displays the temperature contours for the numerical model at various times during the process. The temperature distribution is symmetrical around

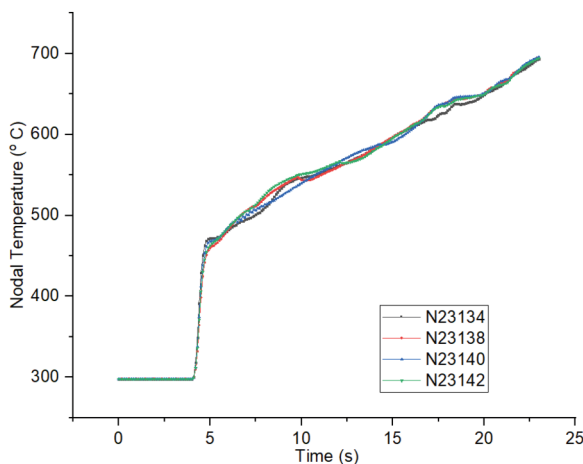


Fig. 3. Temperature plot from the FSE numerical model measured at extruded particles.

the die central axis. The extrusion of wire from the billet was initially started at a time around 16 s, with and temperature of 610 K. Enhanced extrusion of material is observed when then temperatures crossed 660 K, i.e. after 18 s. This temperature is 77% ($0.77T_m$) of the melting temperature of the material AA6061. The maximum temperature in the numerical model is 715 K, which is 83.6% of the melting temperature T_m .

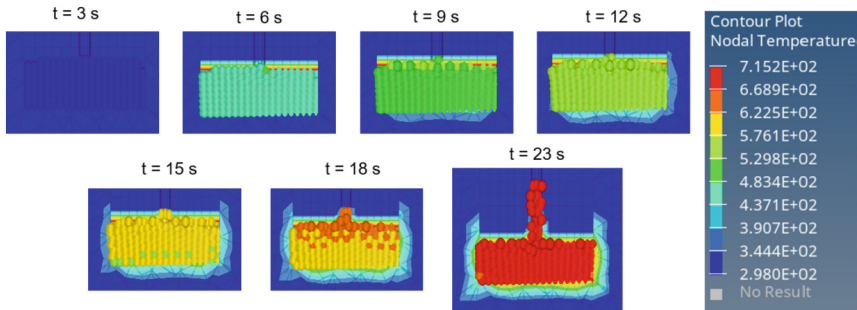


Fig. 4. Temperature distribution during the FSE process.

The material flow patterns during the FSE process are shown in Fig. 5. According to Li et al., the behaviour of the FSE material flow varies with the distance from the die's central axis [18]. Simple shear extrusion occurs when the material is at the dead centre of the die, and spiral deformation occurs when the material is $1/3$ and $2/3$ of the die's radius. As seen in Fig. 5, the red-highlighted SPH particle's movement at the centre in the vertical direction is shear extrusion. The billet's centre material was extruded through the hole in the die with a minimum lateral deformation as they are not subject to the rotating die's shear force. A significant amount of deformation along a spiral path is observed around the surrounding particles. The particles (material) at $1/3$ and $2/3$ of the die's radius were forced to spin with the die due to the strong shear force produced by friction between the billet and the die. As the die plunged further, the material near the extrusion hole is extruded initially. The material, which is further away continued to spin until they were extruded.

Figure 6 shows images of the plastic strain and billet deformation at various times as predicted by the simulation. No computational problems were identified because SPH is meshless, even though the billet material underwent significant plastic deformation. The rotating die slowly compresses on the billet with advancing speed in the vertical direction, as seen in Fig. 6. The billet's top surface is heated and deformed by extrusion (compressive) and shear forces. First, the top billet face experienced plastic strain. As the time increased, the temperature of the billet increased and more particles in the high shear zone plasticized, as shown in Fig. 6. The material is plasticized before being extruded to produce a wire, see the front view at 23 s. The extruded wire from the simulation has a total length of 14.5 mm and a processing duration of 23 s.

The pattern of material flow and the behaviour of the deformation is further illustrated by the displacement of the particles. According to Li et al. [18], severe deformation and complex patterns are seen at a $2/3$ radius of the die. As illustrated in Fig. 7, the developed numerical model shows the pattern of deformation and material flow over

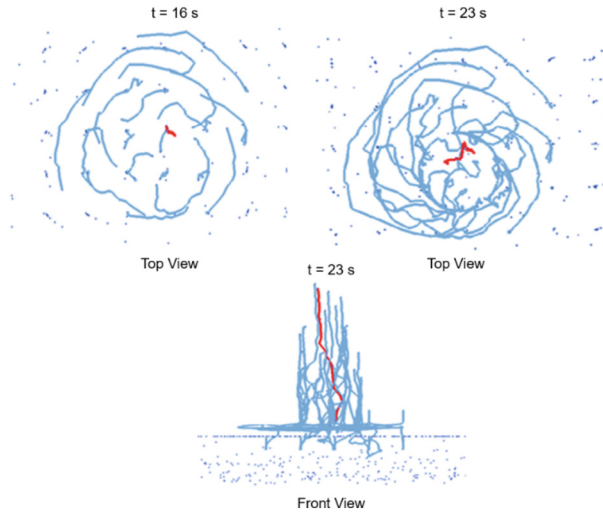


Fig. 5. Tracing of particles to represent material flow during the FSE process.

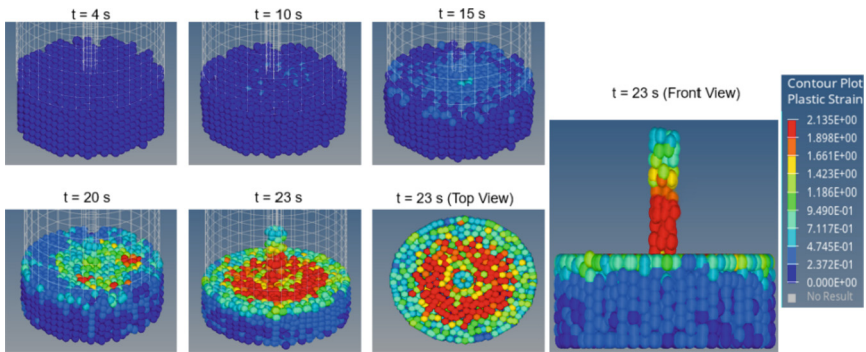


Fig. 6. Plastic strains at different times during the FSE process.

a range of times, allowing the material flow to be further analysed. From $t = 7$ s to $t = 10$ s, it is possible to observe uniform behaviour in the material flow behaviour. Due to the die's rotation, the uniform deformation can be seen to have a spiral pattern. At $t = 11$ s, complex deformation of the material is seen to begin; particles begin to experience maximum centrifugal force, and the directions of their displaced particle paths started to coincide. The zoomed view at 12 s in Fig. 7 depicts the particle paths crossing, indicating an interflow between the particles. At $t = 23$ s where the particle displacement is observed to be tangential to the die's rotation. The particle's trajectory is unaffected by the centrifugal force exerted on it because the chamber wall produces an equal and opposite reaction force on the particle known as a centripetal force, which creates a dead zone. The movement of the die in the plunging direction and the normal force acting cancel each other out, forcing the particle to remain stagnant. This allows for only one degree of freedom for movement, which is a rotational movement along

the die's rotational direction. This behaviour is consistent with Zhang et al. [9]. They concluded that the dead zone occurs between the shoulder of the die and the chamber wall based on their observation of a similar flow pattern. The material is trapped at the corner of the die shoulder as a result of the phenomena of material flow seen at 12 s, where material flows depict a convection flow. A dead zone is created when the particles at the die shoulders are forced against the chamber wall by the surrounding particle kinetic energy.

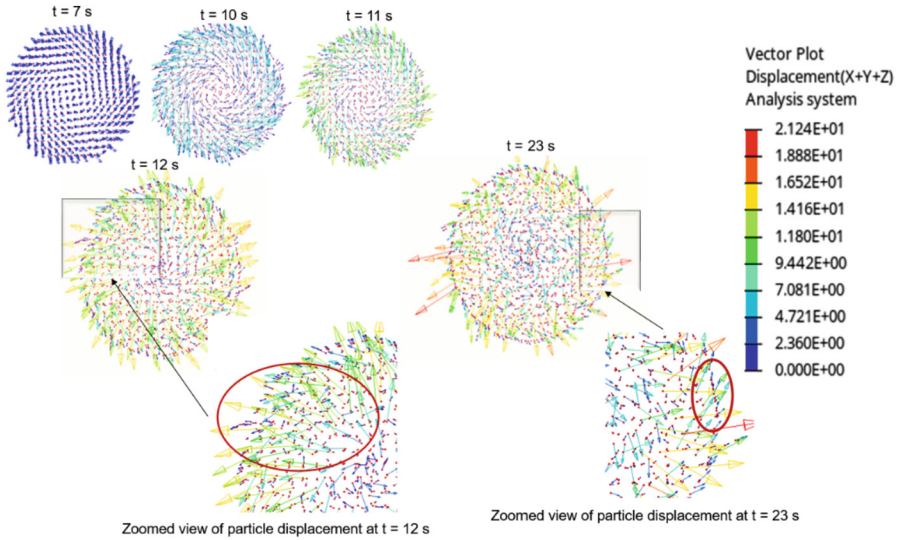


Fig. 7. Displacement vectors at different times during the FSE process.

4 Conclusions

The simulation of the FSE process is performed using SPH lagrangian formulation in Altair Radioss. The model can predict temperatures, plastic strains, and material flow patterns during the process. The results of temperatures, plastic strains, and detailed material flow analysis are presented in this study. Although the temperatures obtained from the numerical model show similar trends, the temperatures are lower compared to the experimental temperatures from the earlier study. The model could withstand severe plastic deformations due to meshless SPH formulation. The material flow patterns and plastic strains predicted by the models are consistent with the earlier studies of the FSE process. Additional studies without simplifications are needed to explore in more detail how well the model predicts the temperatures, especially in the toolset during the FSE process. Also, the process duration should be increased for a deeper understanding of the temperature and material flow behaviour. In that regard, denser SPH, finer toolset meshing, incorporating the convection to the surroundings, and longer run time simulation should be incorporated in future models.

Acknowledgment. Authors are thankful for the financial aid from the Universiti Teknologi PETRONAS.

References

1. Thomas, W.M., Nicholas, E.D., Jones, S.B.: Forming metallic composite materials by urging base materials together under shear. <https://patents.google.com/patent/US5262123A/en> (1993)
2. Whalen, S., Overman, N., Joshi, V., Varga, T., Graff, D., Lavender, C.: Magnesium alloy ZK60 tubing made by Shear Assisted Processing and Extrusion (ShAPE). *Mater. Sci. Eng., A* **755**, 278–288 (2019). <https://doi.org/10.1016/j.msea.2019.04.013>
3. Gronostajski, J., Matuszak, A.: The recycling of metals by plastic deformation: an example of recycling of aluminium and its alloys chips. *J. Mater. Process. Technol.* **92–93**, 35–41 (1999). [https://doi.org/10.1016/S0924-0136\(99\)00166-1](https://doi.org/10.1016/S0924-0136(99)00166-1)
4. Tang, W., Reynolds, A.P.: Production of wire via friction extrusion of aluminum alloy machining chips. *J. Mater. Process. Technol.* **210**, 2231–2237 (2010). <https://doi.org/10.1016/j.jmatprotec.2010.08.010>
5. Li, X., Tang, W., Reynolds, A.P., Tayon, W.A., Brice, C.A.: Strain and texture in friction extrusion of aluminum wire. *J. Mater. Process. Technol.* **229**, 191–198 (2016). <https://doi.org/10.1016/j.jmatprotec.2015.09.012>
6. Zhang, H., Zhao, X., Deng, X., Sutton, M., Reynolds, A., McNeill, S.: Investigation of material flow during friction extrusion process. *Int. J. Mech. Sci.* **85**, 130–141 (2014)
7. Behnagh, R.A., Shen, N., Ansari, M.A., Narvan, M., Besharati Givi, M.K., Ding, H.: Experimental analysis and microstructure modeling of friction stir extrusion of magnesium chips. *J. Manuf. Sci. Eng.* **138** (2015). <https://doi.org/10.1115/1.4031281>
8. Baffari, D., Buffa, G., Fratini, L.: A numerical model for Wire integrity prediction in Friction Stir Extrusion of magnesium alloys. *J. Mater. Process. Technol.* **247**, 1 (2017). <https://doi.org/10.1016/j.jmatprotec.2017.04.007>
9. Zhang, H., Li, X., Deng, X., Reynolds, A.P., Sutton, M.A.: Numerical simulation of friction extrusion process. *J. Mater. Process. Technol.* **253**, 17–26 (2018). <https://doi.org/10.1016/j.jmatprotec.2017.10.053>
10. Karwa, C.: *Finite Element Modelling and Analysis of the Friction Stir Extrusion Process*. Ohio State University, Columbus (2019)
11. Gingold, R.A., Monaghan, J.J.: Smoothed particle hydrodynamics: theory and application to non-spherical stars. *Mon. Not. R. Astron. Soc.* **181**, 375–389 (1977). <https://doi.org/10.1093/mnras/181.3.375>
12. Lucy, L.B.: A numerical approach to the testing of the fission hypothesis. *Astron. J.* **82**, 1013–1024 (1977). <https://doi.org/10.1086/112164>
13. Janga, V.S.R., Awang, M., Yamin, M.F., Suhuddin, U.F.H., Klusemann, B., dos Santos, J.F.: Experimental and numerical analysis of refill friction stir spot welding of thin AA7075-T6 sheets. *Materials* **14**, 7485 (2021). <https://doi.org/10.3390/ma14237485>
14. Janga, V.S.R., Awang, M.: Influence of plunge depth on temperatures and material flow behavior in refill friction stir spot welding of thin AA7075-T6 sheets: a numerical study. *Metals* **12**, 927 (2022). <https://doi.org/10.3390/met12060927>
15. Akram, S., Jaffery, S.H.I., Khan, M., Fahad, M., Mubashar, A., Ali, L.: Numerical and experimental investigation of Johnson-Cook material models for aluminum (Al 6061–T6) alloy using orthogonal machining approach. *Adv. Mech. Eng.* **10**, 1687814018797794 (2018). <https://doi.org/10.1177/1687814018797794>

16. Awang, M.: Simulation of Friction Stir Spot Welding. Study of Friction Phenomena. West Virginia University Libraries, FSSW Process (2007)
17. Meyghani, B., Awang, M.B., Momeni, M., Rynkovskaya, M.: Development of a finite element model for thermal analysis of friction stir welding (FSW). IOP Conf. Ser.: Mater. Sci. Eng. **495**, 012101 (2019). <https://doi.org/10.1088/1757-899X/495/1/012101>
18. Li, X., Tang, W., Reynolds, A.P.: Visualization of material flow in friction extrusion. In: ICAA13: 13th International Conference on Aluminum Alloys, pp. 1659–1664. John Wiley & Sons, Ltd (2012). <https://doi.org/10.1002/9781118495292.ch248>



Comparative Study of an Evacuated Tube with a Copper Heat Tube and a New Receiver for Air Heating by a Parabolic Trough Collector

Ayad K. Khliief^(✉), Akram H. Abed, and Arshad A. Al Jalil

University of Technology, Baghdad, Iraq
50113@uotechnology.edu.iq

Abstract. The investigation of the performance traits of two types of thermal receivers used in parabolic sunray air heaters is the primary goal of this work. At the focal length of a parabolic trough, one evacuated tube receiver, with a copper heat tube placed in it (case 1), and one with a pyramidal square receiver and fins (case 2), was used to compare the effectiveness of sunray air heaters. The temperatures at the heat exchangers' output and the efficiency of the receiver are used to evaluate the collector. It has been noted that the case 1 heat exchanger outperforms the case 2 heat exchanger in terms of system performance. When case 1 and case 2 are used, the maximum output temperatures of the air at 0.015 kg/s are 53 °C and 47 °C, respectively, at 950 W/m². In the case of heat exchanger 1, the efficiency of the solar air heater ranges from 11% to 12%, while the increase is from 8.9% to 9.6% for the heat exchanger of case 2.

Keywords: Sunray air heater · receiver with several arranged tetragonal pyramidal elements · parabolic trough collector

1 Introduction

Due to dependence on conventional fuels and the limited supply of energy supplies, the world will have to deal with this issue in the future. Renewable energy sources are cyclical in nature and never run out. Solar energy is the most popular and modern form of permanent power and has been used to no end in a variety of industries [1]. A different type of solar collector is created in solar thermal technology to gather solar radiations and convert them to heat [2]. Solar energy has an endless supply and is fully pollution-free. The easiest and most effective approach to utilize solar energy is to convert it into thermal energy for heating purposes. Flat plate and evacuated tube (ET) collectors are frequently used for low- and moderate-temperature heating, while concentrated collectors are utilized when a high temperature is needed to heat the air. The employment of accumulators is influenced by a variety of criteria, including their high efficiency, low manufacturing costs, low operating and installation costs, and other relevant practical considerations for the given application [3]. The solar powered air heater is manufactured by combining an evacuated tube with a parabolic sump. The preparation and design

of sunray air heating collectors has been the subject of many experiments and research studies in recent years. According to studies [4, 5], hot air output from an evacuated tube collector with a parabolic sump can be advantageous for many applications requiring a range of temperatures. Singh et al. [6] Experiment using helical inserts in an evacuated tube collector (ETC) sunray air heater for low mass rates revealed a 6.4% increase in thermal efficiency. An experimental test of a brand-new multi-surface trough solar concentrator was done by Zheng et al. [7]. They put to the test three receivers packed with a thin black wire mesh and with various airflow channel geometries. The air flow rate was the variable parameter. The test revealed that at a particular air flow rate, daily average efficiency can reach roughly 0.6. The highest temperature ever recorded was 140 °C. Jamal-abad et al. [8] Investigation of heat transfer in a tubular sunray air heater filled with a porous medium. The results showed that as the shape parameter of the porous media increases, the heat removal factor of the collector increases. Wang et al. [5] studied a system comprised of ten connected compound parabolic concentrators with a U-shaped copper tube heat exchanger inside through simulation and experimental investigations. The air temperature at the exit reached over 200 °C on a sunny day with an air volume flow rate of 6.8 to 7.1 m³/h. The tested system had an efficiency of up to 0.5.

According to the literature, there is an apparent scarcity of parabolic trough air heating structures in an actual climatic and ecological context. The present research aims to enrich the field of research in parabolic trough air heating systems. The following points are implemented to accomplish the chief objective.

- Experimental analysis of an evacuated tube receiver with a copper heat tube inserted into it at different operating conditions (case 1).
- Experimental investigation for the novel receiver consisting of several arranged tetragonal pyramidal elements (case 2) and compares them with case 1.

2 Experimental Setup

Considering the economic aspect while meeting the research needs, the design shown in Fig. 1 is relied upon. The parabolic trough collector system includes a trough with an aperture area (1.2 × 2) with a focal length of 0.53, oriented from north to south. The heat transfer fluid (HTF) is placed in a trough to gradually obtain heat as it travels through the receiver. The reflector, receiver, and supporting structure make up the parabolic trough solar collector (PTSC). The parabolic reflector, which was developed specifically for concentrating solar energy applications and has a high reflectivity (80%), will help focus sunlight onto a receiver at the center of the trough.

2.1 Modification Made in the Evacuated Tube Receiver (case 1)

In this study, a modified evacuated tube from a conventional solar water heater (open on one end) was used as a receiver tube in the parabolic trough, as shown in Fig. 1. The specifications for the evacuated tube are listed in Table 1. Two borosilicate glass tubes with exceptional chemical and heat resistance make up this tube. The outer surface of the inner diameter is covered with a sputtered solar selective layer. The inner and outer tubes of the solar heat pipe are joined by a bond. The annular region between the outer

and inner tubes is vacuumed in order to stop heat losses. The evacuated receiver tube has two holes to allow for a separate admission and outflow of the fluid from the tube. For this, a T-type valve system has been developed. Through a valve, the fluid enters perpendicular to the axis of the evacuated tube and exits parallel to the tube. Figure 2 displays the modified evacuated tube that was utilized in the testing. The air coming out of the tube can be collected, at a later period of time.

Table 1. Technical data for the evacuated tube

Evacuated tube receiver	Material of glass	Borosilicate Glass 3.3
	Coating type	ALN/AIN-SS/Cu (aluminium nitride, AIN-SS, copper)
	Absorptance, α	≥ 0.94
	Emission ratio, ε	≤ 0.06
	Solar transmission rate, τ	$\geq 92\%$
	Inner & outer diameter of glazing (mm)	43, 59 mm
	Length of tube, L_g (mm)	1830 mm

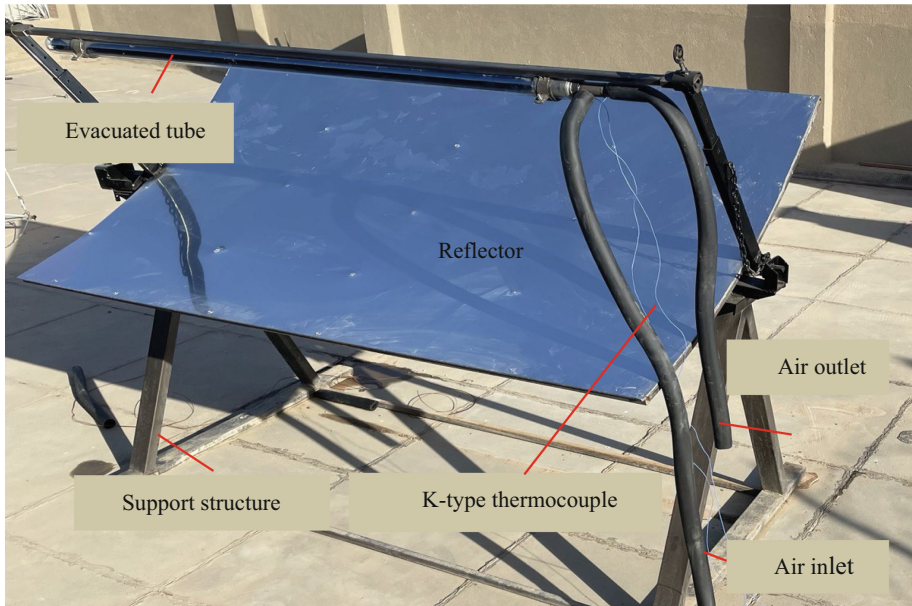


Fig. 1. Concentrating solar collector with the evacuated tube receiver.

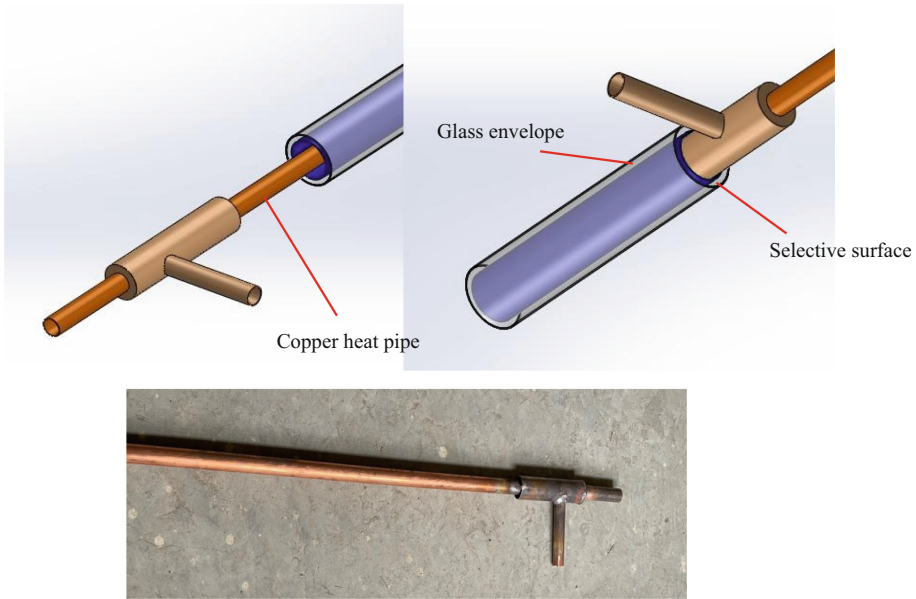


Fig. 2. Modified evacuated tube for parabolic trough collector.

2.2 Straight Hierarchical Square Receiver Design (Case 2)

The new receiver is modular and the developable is a result of its division into separate elements. With the new design, heat acquisition is intended to be increased, especially through the use of geometry that promotes solar radiation absorption. The new receiver is made up of several hierarchical square elements arranged that have been positioned so that their vertices face a parabolic trough. Concentrated sun energy reflected on the heating surface is absorbed by the working fluid in the channels behind the heating surfaces. To improve heat transfer between the working fluid and the heating plate, rectangular fins are provided at the back of the heating plate. As seen in Fig. 3, they are formed of thin, flat metal sheets that are horizontally positioned, allowing heat to be efficiently transported from the front surface of the receiver through the fin body and released into the working fluid. By selecting the proper materials based on the intensity of the heat, the efficiency of the fins can be increased. To stop heat loss, insulation is provided for the back side of the receiver. The measuring instruments and measurement accuracy parameters are listed in Table 2.

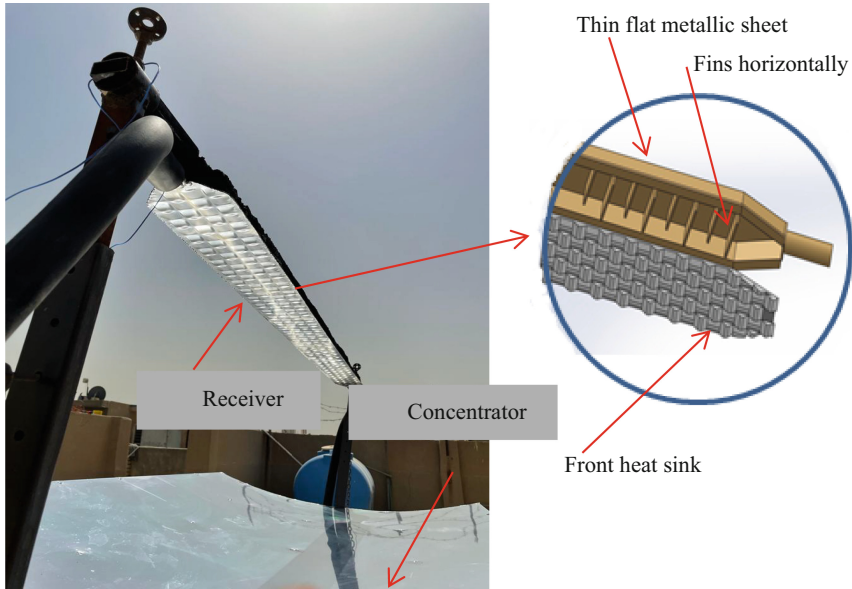


Fig. 3. Concentrating solar collector with the receiver as an air heater

Table 2. Measuring tools and specifications.

Device	Measuring parameters	Range	Accuracy
Pyranometer	Global Radiation	0–2000 W/m ²	±5%
K-type thermocouple	Temperature	0–200 °C	±0.2%
Anemometer	Air velocity	0.4–30 m/s	±(2% + 2 m/s)

3 Thermal Performance Analysis of PTAC

Formulations for assessing the energy performance of PTAC are presented in this section. The performance of PTAC is assessed in quasi-stable conditions in accordance with ASTM E905–87, Standard Test Method for Determination of Thermal Performance of Tracked Concentrated Solar Collectors (CSP). The useful heat transfer rate (Q_u) transferred to the process air in the absorption tube is calculated as [9];

$$Q_u = \dot{m} * (C_{p.T_{out}} * T_{out} - C_{p.T_{in}} * T_{in}) \quad (1)$$

where C_p stands for air-specific heat and \dot{m} stands for air mass flow rate. These quantities may be modeled as continued curves as a function of temperature.

$$C_p(T) = 1050 - 0.365T + 0.85 \times 10^{-3}T^2 - 0.39 \times 10^{-6}T^3 \quad (2)$$

The overall thermal efficiency of a PTAC is determined as follows [9]:

$$\eta = \frac{Q_u}{Q_s} = \frac{\int_{\tau_1}^{\tau_2} \dot{m} * (C_{p.T_{out}} * T_{out} - C_{p.T_{in}} * T_{in}) d\tau}{\int_{T_1}^{T_2} A_{ap} \cdot DNI d\tau} \quad (3)$$

$$Q_s = A_{ap} \cdot DNI \quad (4)$$

4 Experimental Results and Discussion

The experiments were performed at the Science and Technology Research Center of the University of Technology in Baghdad, Iraq (33.3152°N, 44.3661°E) from 10:00 AM to 13:00 PM in October. This section evaluates the results of external tests. As a result, the system performance parameters for Case 1 and Case 2 with varying radiation intensities were compared using the inlet air flow rate of 0.015 kg/s.

Case 1 and Case 2 were used to evaluate the thermal performance of the system at moderate temperatures and on different days. Solar radiation and outside air temperature are the two data points of the system during the day. Similar settings were used to test Cases 1 and 2, as these variables may vary from day to day owing to varying weather conditions, which might alter the performance of the experimental setup. Figure 4 shows the variation in solar radiation and ambient air temperature over time. With the passage of time, the intensity of solar radiation rises, and the similar tendency can be seen in the ambient air temperature. With time, the amount of radiation absorbed by the ground rises, raising the ambient air temperature. The intensity of solar radiation increases and peaks at 951 W/m² and 954 W/m² for Case 1 and Case 2, around 12:30 and 13:00 PM respectively. At the same times, the highest ambient air temperatures for Case 1 and Case 2 were 31 °C and 31.1 °C, respectively. Low flow air is sequentially administered to each of the heat exchangers in the absorber tube in order to measure the temperature difference reached. The outlet temperature values of the case 1 and 2 heat exchangers are measured for three hours in the same experimental procedure.

The variation of the temperature difference and thermal efficiency of the heat exchangers case 1 and 2 at different solar radiations is shown in Figs. 5 and 6. It is noted from Fig. 5 that the receiver in Case 1 has a peak difference in temperature of 18 °C, whereas the receiver in Case 2 has a peak difference in temperature of 15 °C. The temperature difference of Case 1 is consistently slightly higher than the receiver of Case 2 as shown in Fig. 5. For lower solar radiation levels in the first hour, the rate of increase in temperature difference is 12% higher for Case 1 than for Case 2 but at peak hours in the afternoon the average percentage increase is only 13%.

Figure 6 shows the trend in the effect of different levels of solar radiation on thermal efficiency. With the case 1 heat exchanger, the efficiency of the solar air heater ranges from 11% to 12%, approximately remaining constant. With an increase from 8.9% to 9.6% in efficiency variance, the case 2 heat exchanger follows the same trend. This tendency can be explained by the fact that the effectiveness of a solar air heater is exactly proportional to the temperature differential between the outlet and inlet air. Figure 6 also shows that the difference in the maximum efficiencies of the air heater with the heat

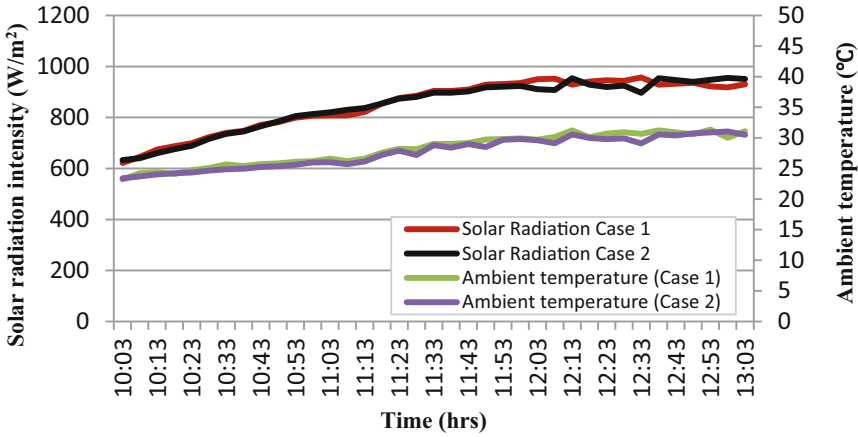


Fig. 4. Variation of solar Intensity, ambient temperature with Time using Case 1 and Case 2

exchanger of case 1 and case 2 is 21.6% when the solar radiation is 633 W/m^2 while the difference becomes minimum at 953 W/m^2 , which is 17.9%.

The results of tests utilizing heat exchangers for case 1 and case 2 under varying solar irradiation are displayed in Fig. 7 and are compared to the parabolic collector outlet temperatures discovered from the trials. The findings indicate that the temperature of the outside air rises as radiation intensity rises. For instance, we discover that under the same solar radiation conditions (950 W/m^2), case 1’s output temperature of the receiver is $53 \text{ }^\circ\text{C}$, while case 2’s outlet temperature is $47 \text{ }^\circ\text{C}$. The output temperature is brought closer to instance 1 (case 1), where the difference is only $6 \text{ }^\circ\text{C}$.

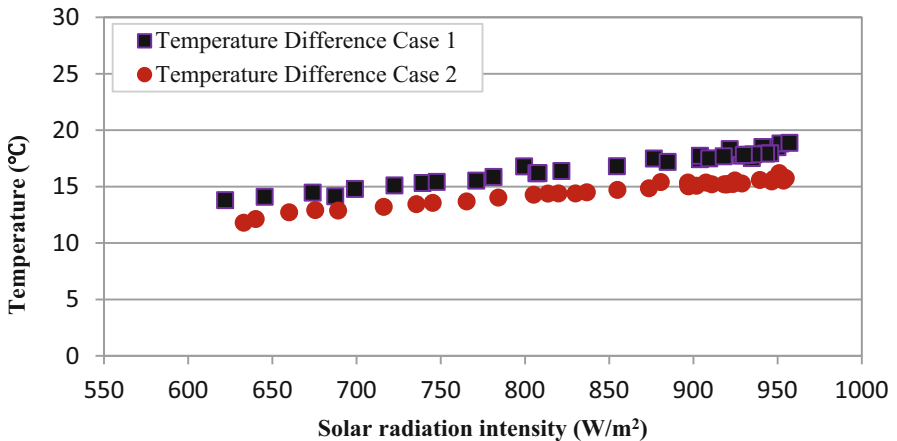


Fig. 5. Variation of temperature difference with solar intensity Case 1 and Case 2

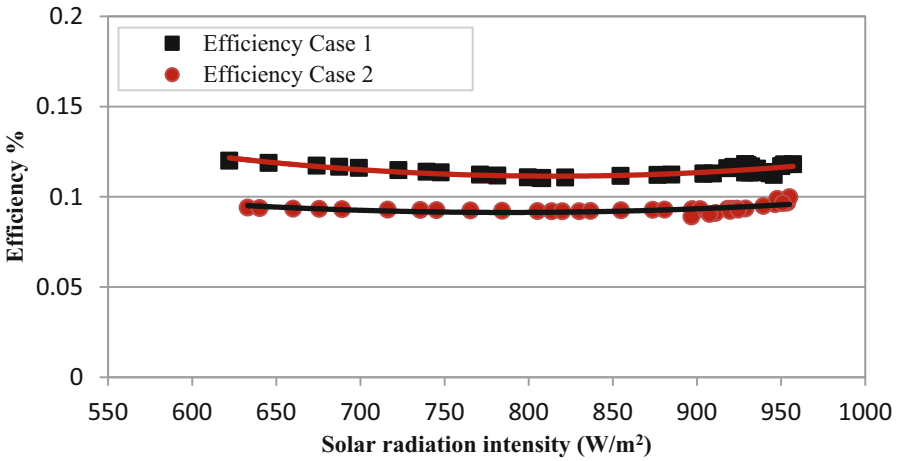


Fig. 6. Variation of efficiency with solar intensity Case 1 and Case 2

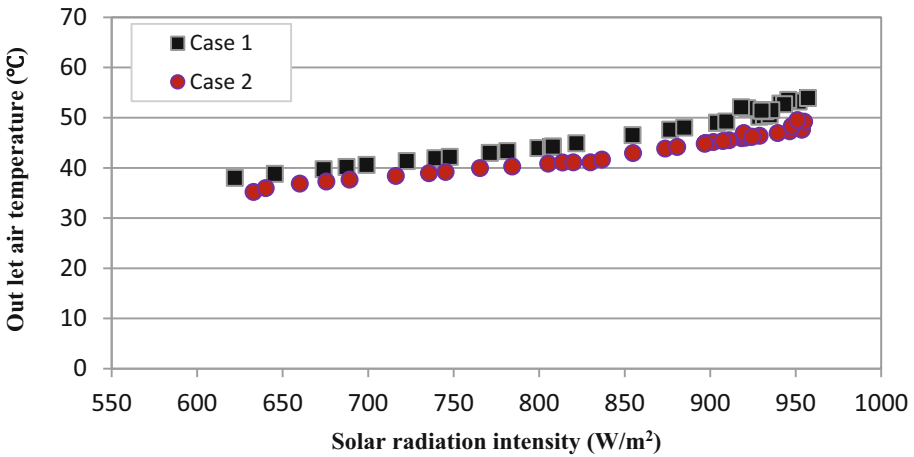


Fig. 7. Variation of temperature with solar intensity Case 1 and Case 2

5 Conclusions

When two different types of receivers are utilized (cases 1 and 2), the equivalent collector is used as a research tool to assess the thermal efficiency of an air heater. To calculate the thermal efficiency and air temperature differential, the solar collector’s performance was tested at various solar radiation levels. When case 1 and case 2 are used, the maximum output temperatures of the air at 0.015 kg/s are 53 °C and 47 °C, respectively, at 950 W/m². The air temperature difference in case 1 is constantly slightly higher than the receiver of case 2. The receiver in case 1 has a temperature difference of 18 °C, while case 2 has a temperature difference of 15 °C at a solar radiation intensity of 950 W/m².

In the case of heat exchanger 1, the efficiency of the solar air heater ranges from 11% to 12%, while the increase is from 8.9% to 9.6% for the heat exchanger of case 2.

References

1. Farjana, S.H., Huda, N., Mahmud, M.P., Saidur, R.: Solar process heat in industrial systems—a global review. *Renew. Sustain. Energy Rev.* **82**, 2270–2286 (2018)
2. Morrison, G.L., Budihardjo, I., Behnia, M.: Water-in-glass evacuated tube solar water heaters. *Sol. Energy* **76**(1–3), 135–140 (2004)
3. Gupta, M.K., Kaushik, S.C.: Performance evaluation of solar air heater for various artificial roughness geometries based on energy, effective and exergy efficiencies. *Renew. Energy* **34**(3), 465–476 (2009)
4. Jebasingh, V.K., Herbert, G.J.: A review of solar parabolic trough collector. *Renew. Sustain. Energy Rev.* **54**, 1085–1091 (2016)
5. Wang, P.Y., Guan, H.Y., Liu, Z.H., Wang, G.S., Zhao, F., Xiao, H.S.: High temperature collecting performance of a new all-glass evacuated tubular solar air heater with U-shaped tube heat exchanger. *Energy Convers. Manag.* **77**, 315–323 (2014)
6. Singh, I., Vardhan, S.: Experimental investigation of an evacuated tube collector solar air heater with helical inserts. *Renew. Energy* **163**, 1963–1972 (2021)
7. Zheng, H., Tao, T., Ma, M., Kang, H., Su, Y.: Experimental test of a novel multi-surface trough solar concentrator for air heating. *Energy Convers. Manag.* **63**, 123–129 (2012)
8. Jamal-Abad, M.T., Saedodin, S., Aminy, M.: Heat transfer in concentrated solar air-heaters filled with a porous medium with radiation effects: a perturbation solution. *Renew. Energy* **91**, 147–154 (2016)
9. Zhao, Z., Bai, F., Zhang, X., Wang, Z.: Experimental study of pin finned receiver tubes for a parabolic trough solar air collector. *Sol. Energy* **207**, 91–102 (2020)



Characterization of Diamond-Like Carbon on WC and H13 Tool Steel to Improve the Wear Resistance of FSW Tool

S. Emamian¹(✉), M. Awang², and Bahman Meyghani³

¹ Faculty of Engineering Technology, Department of Mechanics of Solids, Surfaces and Systems, University of Twente, P.O. Box 217, 7500 AE Enschede, the Netherlands

s.s.emamian@utwente.nl

² Department of Mechanical Engineering, Faculty of Engineering, Universiti Teknologi PETRONAS, Seri Iskandar, Malaysia

³ Department of Mechanical Engineering, Faculty of Engineering Technology and Built Environment, UCSI University, Taman Connaught, 56000 Kuala Lumpur, Malaysia

Abstract. As the demand to weld high-strength materials through a friction stir welding (FSW) technique increases, the need for a better non-consumable rotating tool also increases as it has to be able to endure high frictional and thermal deformation, while the work-piece undergoes intense plastic deformation at high temperatures. The main sources of heat generation during the FSW method consist of the friction force between the tool and workpiece as well as the plastic deformation. H13 tool steel and tungsten carbide were assigned as base materials for the FSW tool. Diamond-like carbon was chosen for coating the FSW tool. Analysis of the coated surface showed the presence of DLC was observed to grow uniformly on the surface.

Keywords: DLC · Wear resistance · FSW · Characterization

1 Introduction

Recently, FSW has been proven as an alternative joining technique for high-melting materials such as steel, titanium, and so on. The process does not require the use of filler metals but could yield better joint strengths with reduced distortion and residual stresses. Among the key benefits of FSW in the aspect of metallurgical are less distortion, excellent metallurgical properties in the joint area, good microstructure, and absence of cracking. In addition, other advantages of the FSW technique include zero requirements of shielding gas and surface cleaning, as well as eliminating the secondary grinding process and reducing the consumable materials for environmental benefits. However, one of the critical factors in a successful FSW technique is the selection process of tool materials for different workpiece materials.

FSW tool design is one of the most important factors to consider when designing an FSW joining process. The tool provides several functions, including generating heat, intermixing the materials, creating forging pressure, and containing material within the

joint, thereby preventing surface weld flash and formation of defects such as wormholes, sheet-thinning, or hooking defects. Additionally, tool geometry must often facilitate a stable force or torque control scheme and be compatible with a range of plunge depths. Moreover, pin shape has also contributed to a significant impact on the flow of material. The voids during FSW could be omitted with a proper pin profile design. The choice of a particular tool design is based on a number of factors, such as the joint configuration, the thickness of the material, and the nature of the application, among others [1].

The FSW tool life is the duration of welding that took place until the tool is no longer usable. It was found that the most common factor affecting tool life is tool wear. The rotation and translation of the tool through the workpiece have resulted in its wear. The FSW tool may also deform plastically due to a reduction in yield strength at elevated temperatures in an environment of high loads. Therefore, the tools used for welding high-strength materials such as steels are often liquid-cooled [2, 3].

However, detailed studies on tool wear in FSW are still lacking, with diffusion and abrasion being the expected wear mechanisms. Wear-through abrasion is particularly significant and is a main problem in this research field. It has been reported that the wear rates decreased considerably after the initial wear and the smoothed (or self-optimized) tools, could continue producing good quality welds, similar to those shown in Fig. 1 [4-6].

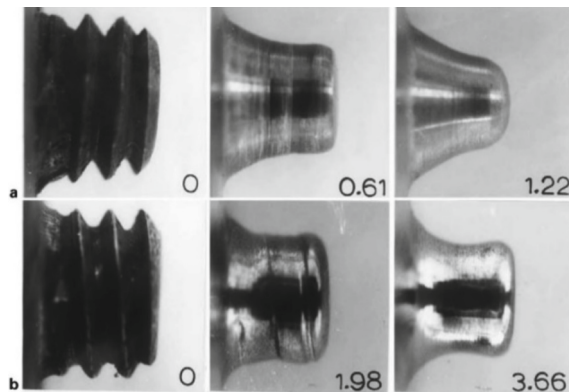


Fig. 1. Evolution of tool shape due to wear in FSW of Al 6061 + 20% Al₂O₃ metal matrix composite with oil-hardened steel tool at 1000 rpm and travel speeds of (a) 3 mm/s and (b) 9 mm/s: distances travelled by tool in meters are indicated [4].

1.1 FSW Tool Materials for MMCs

In some cases, special techniques have been used to reduce tool wear. For example, in lap joints of dissimilar materials, the tool is placed on a softer material, and contact between the tool and the harder material is avoided to reduce the tool's wear. Welding of dissimilar metals in butt joint configuration by offsetting the tool towards the softer alloy side needs to be more thoroughly tested. Some of the other strategies to reduce the

tool wear include welding at lower welding speeds, preheating the workpiece to reduce its mechanical resistance, preheating the tool above the ductile to a brittle transition temperature, and using sufficient inert gas cover [7–10]. The other method to increase the strength of the FSW tool is through coating the material in producing higher tool life for joining the hard materials.

A non-consumable rotating tool of friction stir welding is one of the most critical components in ensuring a proper solid-state joining of the workpiece. Material selection for the tool is an important criterion that determines the type of workpiece material that could be welded, the life expectancy of the tool, and the overall user experience [11]. This is because the tool has to be able to retain its dimensional stability and design features when approaching the workpiece's solidus temperature through the process of thermos-mechanical deformation [12]. Some of the important characteristics that have to be considered for tool material selection are the material strength at ambient and elevated temperature, stability at elevated temperature, wear resistance, tool reactivity, fracture toughness, coefficient of thermal expansion, machinability, uniformity in density and microstructure, as well as the material availability [11, 12].

The rapid development of the FSW process in joining the aluminum alloys and its successful implementation into commercial applications has motivated its application to other non-ferrous materials (Mg, Cu, Ti, as well as their composites), steel, and even thermoplastics. However, a potential obstacle to the commercial success of FSW on high-temperature materials such as titanium and steel is in the identification and/or development of suitable tool materials and the advantages over current welding methods [13]. More recent studies have shown that this process was successful in producing sound joints of Al + Al₂O₃ and Al + SiC whiskers of MMCs, in which fusion welding has not been able to produce similar joint qualities for these materials [14]. In this section, the related research of the FSW technique on Al matrix composites and its respective tool materials dated from 2001 are reviewed and presented.

Prado et al. [15] have used carbon steel for the FSW tool in order to develop a joint of AA 6061 + 20% Al₂O₃. It was found that the maximum wear rate was 0.67%/cm, but was reduced after 1000 rpm. It was approximately 0.42%/cm at 1500 rpm and 0.56%/cm at 2000 rpm. In another study, Prado et al. [4] considered the self-optimization tool during FSW of AA6061 + 20% Al₂O₃. The self-optimized tool shape changed to some extent with increasing weld speed at a constant tool rotation speed of 1000 rpm. These observations suggested that shape-related solid-state flow control is an essential feature of FSW and especially in assuring limited tool wear and optimum, long tool life. Even in the case of very hard MMCs, FSW can afford essentially little or no tool consumption when the tool shape is optimized. Tool optimization occurs for smooth tool shapes with no threads or screw features, especially in the FSW process on MMC materials.

In the following year, Fernandez and Murr [5] conducted characterization testing on the tool wear for the FSW of AA 359 + 20% SiC. They found that by decreasing the rotation speed and increasing the welding speed, the tool wear could be reduced. It is notable that their results were similar to the Prado et al. [4] with regards to the self-optimization tool of the weld after a specified weld length. In a new study, Liu et al. [16] have utilized WC-Co as tool material in order to analyze the wear characteristics during the FSW of AC4A + 30% SiC. Their results as in Fig. 2, clearly indicated that different

locations of pin exhibited different wear profiles. The maximum pin wear occurred at the third of the pin length near the pin root. Meanwhile, reducing the welding speed would also increase the possibility of wear during the FSW.

There was another research by Marzoli et al. [17], which performed FSW on AA6061 + 20% Al₂O₃. The tool was made of an ultra-hard material, which was able to withstand the strong abrasion of the alumina particles. It was apparent that the alloy could also be welded with processing parameters that were comparable to those used for its unreinforced counterpart.

One of the most common types of tool material is hot-worked tool steel. This is due to the fact that the hot-worked tool steel is easy to machine, as well as being at a low cost. AISI H13 which is a chromium-molybdenum hot-worked, air-hardened steel is a common tool material for FSW due to its characteristics of tremendous wear, fatigue, and thermal resistance, as well as possesses excellent strength at elevated temperature when coupled with a workpiece of aluminum alloys [11, 12, 18]. Based on ASTM A681, the hardness value for hot-worked tool steel ranges from 28 to 53 HRC, depending on the tempered temperature [19]. AISI H13 was found to be able to weld copper of thickness up to 3 mm, but tool degradation was observed at the thickness of 10 mm. It also undergoes a high tool wear rate when applied on a workpiece of high metal strength. In this research, we would utilize this tool material together with tungsten carbide for the coating and hence to improve its strength and the tool life for the FSW process on the MMC workpiece.

Emamian et al. [20] focused on the improvement of FSW tool life in joining the aluminum matrix composites, through surface enhancement. H13 tool steel and tungsten carbide, as a base material, were used for the FSW tool, and graphene, carbon nanotubes, and diamond-like carbon were chosen for coating the FSW tool. The result of wear measurement indicates that the wear resistance of the diamond-like carbon (DLC)-coated tungsten carbide was higher than the others. The tool life of the coated tungsten

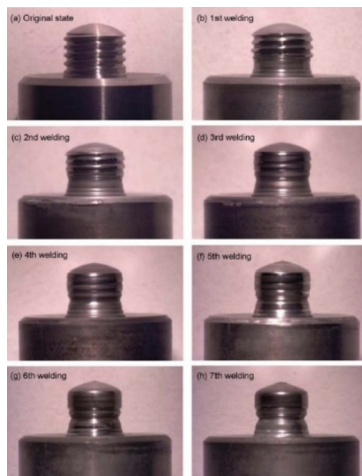


Fig. 2. Appearance of the threaded tool after each FSW experiment [16].

carbide (WC)-DLC was prolonged to approximately 41%. In addition, it is predicted that the FSW tool can be effective for up to 1200 mm of the weld joint.

1.2 FSW Tool Wear

Wear is related to interactions between surfaces and specifically, the removal and deformation of material on a surface as a result of the mechanical action of the opposite surface. In materials science, wear is defined as erosion or sideways displacement of material from its “derivative” or original position on a solid surface performed by the action of another surface. Wear prevention must be considered in the planning and design phases, in which several solutions are readily available to reduce its occurrence. These include the use of lubricants, choice of contact condition, the manner of operation of the mechanical system, and increasing the strength of materials that are in contact with each other.

The design of a particular tool should satisfy many essential requirements. The geometry of the tool is very important as the mixing of the material would affect the quality of the weld. High stresses with high temperatures as well as abrasive wear are depending on the tool materials. The development tool design and technology have evolved relatively in point of geometry, material, and coating over the past two decades. Robinowicz [21] was among the first to develop an understanding of wear processes, indicating that the wear phenomena could be well-predicted. Abrasive wear, dynamic effects, and high temperature play important roles in the tool during welding. Hence, good wear resistance, desired toughness, and high-temperature strength are suitable properties for tool materials [11]. Production of a quality FSW requires the proper material selection of the tool for the desired application.

Wear resistance, toughness, thermal expansion, and machinability are the main characteristics that should be investigated to select the tool material [11]. There are several tool materials available to use depending on the type of workpiece. Table 1 summarizes the tool materials with their distinctive characteristics [22].

It has been mentioned earlier that the fusion welding of Al-MMCs may lead to harmful reaction during melting phase. In comparison with the fusion welded joint, the FSW of Al-MMC's produced a homogeneous microstructure with a uniform hardness profile [23].

Prado et al. [15] examined the different rotation speeds with constant traverse speed on Al-MMC. They found that the maximum tool wear was at 1000 rpm, and wear rate was 0.64%/cm. But, after the threshold of 1000 rpm rotational speed, the wear rate has declined at 0.42%/cm for 1500 rpm and 0.56%/cm for 2000 rpm, accordingly. In their other research, Prado et al. [4] investigated the different of traverse speeds on Al-MMC using hardened steel right hand screws. Similarly, it was found that at relatively high welding speeds and after an initial wear period, tool wear essentially ceased. On the other hand, Fernandez and Murr [5] have used threaded steel tool pin for FSW on Al 359 + 20% SiC, to examine the effect of high rotation speeds and low traverse speed of the welding process. By increasing the traverse speed and reduction of rotation, tool wears has considerably declined. Their research was an extended work of Shindo et al. [6], whereby the effects of pin tool rotation speed were included on the shape optimization

and reduced wear phenomenon. In addition, the effects of traverse speed on the optimized pin tool rotation speed were also determined.

Bhat et al. [24] have examined H-13 steel for the FSW tool coated with B4C on Al6092 + 17.5%SiC. It was observed that the coating was worn away after only a few centimeters. Besides, Liu et al. [16] used WC-CO threated hard alloy for the FSW tool on welding of Al-MMC joint with 30% SiC at 2000 rpm rotation speed with three different traverse speeds. An appreciable tool wear was observed, in which the shoulder size and pin length were changed slightly. Furthermore, the radial wear of the pin was observed very differently at several locations of the pin. The maximum wear was finally produced at a location of about one-third pin length from the pin root. Explicitly, the welding speed provided a decisive effect on radial wear rate of the pin. The lower the welding speed, the higher the wear rate, and the maximum wear rate would be produced at the initial welding stage.

Table 1. Some materials that are useful for tools with their characteristics

No	Materials	Characteristics
1	Hot work steel	<ul style="list-style-type: none"> – Most commonly used material – Easy machinability – Thermal fatigue resistance – Wear resistance – Especially for aluminum and copper
2	Nickle and cobalt alloys	<ul style="list-style-type: none"> – High strength – Excellent ductility – Hardness stability – Creep resistance – These alloys derive their strength from precipitates, so the operational temperature must be kept below the precipitation temperature (typically 600–800 °C)
3	Refractory metals (W, Mo)	<ul style="list-style-type: none"> – High temperature strength – Strongest alloys between 1000–1500 °C – Expensive – Difficult machining – Brittle due to powder processing
4	Tungsten base alloys	<ul style="list-style-type: none"> – good strength – high operational temperature
5	Composites (WC, WC-CO, TiC)	<ul style="list-style-type: none"> – Superior wear resistance – reasonable fracture toughness
6	Steels with PCBN coating	<ul style="list-style-type: none"> – high operational temperature – excellent wear resistance – low fracture toughness – expensive tool

Prater et al. [25] have presented the work that involved investigation on the effects of FSW parameters on tool wear of metal matrix composites (Al 359/SiC/20P). The Taguchi's method was utilized to evaluate the rate of influence of rotation and traverse speeds, as well as the length of weld joint on the wear characteristics in FSW of the MMCs. Prater [26] in her extended work has found that the abrasion wear in FSW of MMCs was based on three observations. First is an asymptotic behavior of the wear rate over long distances as documented in Prado et al. [4]. Secondly, circumferential grooving is evident on worn tool surfaces and lastly is strong dependence of wear on the particle size of reinforcement. When hardness ratio is less than 1, the hardness of the reinforcement is exceeding the hardness of the tool ($H_r > H_t$). Therefore, by increasing the hardness ratio (by reducing the hardness of reinforcement or increasing the tool hardness), the amount of wear on tool will be decreased. For that, Prater et al. [27] has further evaluated the wear resistance of various tool materials for FSW of MMCs, including O1 steel, Micrograin WC, Sub-Micrograin WC, and WC coated with diamond. The tested workpieces consisted of Al359 with 20%SiC and Al359 containing 30%SiC. It was found that the use of harder materials in the FSW of MMCs would prolong the tool life. The diamond coatings were found at highly effective at combating wear insofar as tool fracture can be prevented. The diamond coated tool has lasted up until 28 inches (71 cm) welded length without any fracture. In addition, Prater et al. [28] developed a dimensionless parameters that can be used to evaluate the amount of volumetric wear in FSW tool for MMCs.

Inevitably, wear increases with the percentage of reinforcement, but the degree of the increase is somehow nonlinear. For cemented carbide tools (WC-Co), tools with micrograins exhibit better wear performance than those of the submicro-grain structures, potentially because smaller particles are more easily stripped away from the tool surface by abrasive action. Whereas, coarser grains appear to impede abrasive wear during FSW. Moreover, it was highlighted that the effective wear mitigation in FSW of MMCs is critical to enable their use in larger structures (consisting of several welded components) or higher volume applications.

Prater [29] has summarized from the previous studies performed by her team on the FSW on MMCs as per following. It was found that the properties of MMCs reflect their status as prime materials for use in aerospace structures, but weldability is the primary barrier to their inclusion in aerospace structures. Despite its impact on joining metal composites and other high-strength alloys, little is known about tool wear in FSW. Thus, a diamond-coated on WC tool is highly recommended for the use in welding the MMCs materials. The characteristics that should be considered in choosing the tool material for FSW include, no harmful effect to the base metal, resistance to wear, possesses low thermal coefficient of thermal expansion, good thermal fatigue strength when undergoing repeated thermal cycle, high strength at ambient and elevated temperature, high fracture toughness, dimensional stability and creep resistant, as well as be able to prevent damage during plunging and dwelling [30].

1.3 Coating Materials for the Enhancement of the FSW Tool Life

Thorough studies have been conducted with regards to the life span of the tool. Various factors contribute to the damage of the FSW tool such as geometry of the tool, welding

parameters and FSW tool materials. The use a correct geometry tool and proper welding parameters could prolong the FSW tool life. In addition to the factors mentioned, the material of the tools and methods in improving the strength prove to be as important. The most usable method to improve the quality of the tool surface is through coating on the hard materials that diffuses on the substrate materials. The allotropes of carbon including graphene, carbon nanotubes and diamond-like-carbon are well-known for their unique properties such as hardness. Furthermore, carbon bonds readily with other atoms including other carbon atoms, and is capable of forming a covalent bonds. Emamian et al. [31] highlights the characterization of the carbon-based coatings in regard to selected coating parameters through Field emission scanning electron microscope, energy dispersive spectroscopy, Raman Spectra, and X-Ray photo electron spectroscopy techniques. The analysis shows presence of graphite like structures whereas Carbon Nanotubes (CNT) was observed to be grown uniformly on the surface.

1.4 Diamond-Like-Carbon (DLC)

Carbon is one of the most amazing elements among all others. It exists in more than 90% of all known chemical substances and has the largest number of allotropes. Diamond-like-carbon (DLC) exhibits outstanding mechanical and tribological properties and therefore, the coating using this material could be utilized in a wide range of engineering applications to control friction and wear. Figure 3 shows a ternary diagram that indicates specific domains of different carbon-based coatings with respect to their sp^2 and sp^3 type bonding characteristics and hydrogen contents [32].

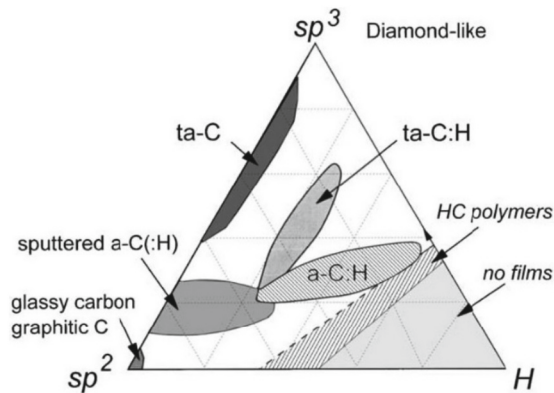


Fig. 3. Ternary phase diagram bonding in amorphous carbon-hydrogen alloys [32].

The carbon sp^3 is a perfect symmetry of diamond which has properties such as high hardness and low wear rate in various tribological conditions [33, 34]. On the other hand, sp^2 as a graphite structure with a weak van der Waals bonding has a low hardness and high wear rate in a frictional conditions [35, 36]. In addition, amorphous carbons consist of carbon atoms with mixture of both sp^3 and sp^2 coordinated bonds [37]. The left axis of the above figure shows amorphous carbon (a-C), which is hydrogen free.

The sp^2 of this section is a glassy carbon, but is not the DLC. However, a-C of higher sp^3 content is the DLC, created with sputtering. At higher level of sp^3 , a specific type of amorphous carbon is observed, known as tetrahedral amorphous carbon (ta-C) which is made from ion or plasma beams. The bottom right of the diagram in Fig. 3 comprises of large amount of hydrogen, indicating only the gas molecules [38].

Historically, the earliest attempts to produce DLC films back to 1953 when Heinz Schmellenmeier reported a black carbon film derived from C_2H_2 gas in glow-discharge plasma. The films produced high hardness and hence, were very resistance to the scratching of other hard objects. Later, Eisenberg and Chabot in the early 1970s have produced such films using an ion beam deposition system [39]. Their films were very hard and hence resistant to scratching and also possessed a high dielectric constant, high index of refraction, excellent optical transparency, and high resistance to corrosion in strongly acidic solutions. As the DLC films are typically amorphous and dense, they are less prone to pin-hole defects. For that reason, DLC provides the only choice of material for coating that can offer both high hardness and low friction under dry sliding conditions [38]. There are different methods of deposition of ta-C, which is listed in the Table 2.

Table 2. Types of ta-C DLC coatings with historical overview [37]

Year	Coating Type
1976	Direct Cathodic Vacuum Arc Evaporation (DCVAE)
1978	Filtered Cathodic Vacuum Arc Evaporation (FCVAE)
1988	Pulsed Arc (P-Arc)
1991	Laser Arc (L-Arc)
1994	High Current Arc (HC-Arc)
2002	Modulated Pules Arc (MP-Arc)

There are some researchers that have conducted studies which focused on the coating using DLC on various materials. For instance, Lessiak and Haubner [40] coated DLC on the hard metals using CVD as intermediate layers. The diamond was synthesized by the hot-filament chemical vapor deposition (HF-CVD). In other research, Fan Ye et al. [41] used microwave plasma enhanced chemical vapor deposition in order to deposit DLC on WC-Co substrate. The above studies have utilized interlayer coating processes in order to improve the adhesion of the coated layers. As mentioned earlier, tool wear is a key issue for the FSW of aluminum matrix composites (AMCs), especially when the volume fraction of reinforcing particulates is relatively high. Thus, the DLC-coated tool may provide the solution in preventing or reducing the wear rate during the FSW.

Due to the harmful reactions between reinforcing hard particles and liquid aluminum, a fusion welding of aluminum metal matrix composites (Al-MMC's) poses several difficulties. Since FSW is a solid process, this technique provides a good option for joining Al-MMC's. In comparison to the fusion welded joint, FSW on Al-MMC's produces a homogeneous microstructure with a uniform hardness profile. Critical issue in FSW of MMCs is short duration of tool life. The most common factor that is affecting on tool

life is wear phenomenon. There are reinforcing particles such as Silicon Carbide (SiC) in MMCs that are hard enough to easily worn out the tool materials. Therefore, tool life is a critical and become one of the main problems in FSW of MMCs.

One of the most important issues in improving the surface quality is through coating a hard material on the FSW tool. Choosing the suitable coating material and its process parameters always have been a challenge for the researchers. Therefore, in order to improve the FSW tool life, coating of the hard material on the FSW tool surface and investigation of its quality is required.

It was found that some of the literatures focused on FSW tool materials to prevent the wear. On the other hand, several studies had only used a limited range of the coating materials. Therefore, a comprehensive comparison between the coating methods and coating materials was apparently absent. Due to the above-mentioned problems, the improvement of the tool life in the literature was not very encouraging. For instance, the maximum tool life obtained by Prater et al. [27] for tungsten carbide coated with diamond was only 28 inches (71cm). Thus, researchers are still looking for the approved methods in significantly improving the tool life. This research will intend to develop an improved FSW tool and to investigate the effect of surface enhancement on quality of the tool and subsequently its tool life.

2 Experimental Procedures

Diamond, the sp^3 -bonded allotrope of carbon, has long held a special place in the hearts and minds of both of scientists and the public at large. To the scientist, diamond is impressive because of its wide range of extreme properties. As shown in Table 3, by most measures, the diamond is ‘the biggest and the best’; it is the hardest known material, has the lowest coefficient of thermal expansion, is chemically inert and wear resistant, offers low friction, possesses high thermal conductivity, offers electrically insulating and optically transparent from the ultraviolet (UV) to the far infrared (IR).

Table 3. Properties of diamond [42]

Property	Diamond
Hardness	10 (Mohs scale)
Thermal Conductivity	$20 \text{ W cm}^{-1} \text{ K}^{-1}$
Thermal Expansion	$1.1 \times 10^{-6} \text{ K}^{-1}$
Melting Point	4000 °C

As mentioned, the DLC is the only material or coating that can provide both high hardness and low friction under dry sliding conditions. Since their initial discovery in the early 1950s, DLC films have emerged as one of the most valuable engineering materials for many industrial applications, including microelectronics, optics, manufacturing, transportation, and biomedical fields. By the way, due to its similar properties near to

the diamond especially for the hardness, it offers is a good option for the improvement in strength of the materials.

There are many developments in the DLC coating technologies, including magnetron sputtering, plasma enhanced chemical vapor deposition, pulsed-laser deposition and cathodic. These technologies provide the kinds of flexibility that a specialist needs in designing and developing multifunctional DLC coatings having a multilayered or nanostructured/nanocomposite architecture with excellent hardness, friction, toughness, and corrosion resistance.

The raw tungsten carbide and H13 tool steel were manufactured by Microcarbide Sdn Bhd. Then, the cubes were sent to Singapore to be coated by Oerlikon Balzers Company. The tool and cubes were coated using physical vapor deposition (PVD) process. In the PVD process, the tungsten carbide was evaporated by bombardment with ions via sputtering process. At the same time, a reactive gas (a gas containing carbon) was added to form a compound with the metal vapor which was deposited on the tool and cube as a thin, highly adherent coating. By rotating the part at a constant speed for about several axes, a uniform coating thickness was successfully obtained.

3 Results and Discussions

DLC is a class of amorphous carbon material that displays some of the typical properties of diamond. The primary desirable qualities are hardness and wear resistance. Therefore, this material provides one of the options of this research to enhance the surface of the FSW tool and hence its lifespan. Some characterization and mechanical tests have been performed to evaluate the quality of the coating on H13 tool steel and tungsten carbide.

3.1 Microstructure Analysis

Field Emission Scanning Electron Microscope (FESEM) with energy dispersive spectroscopy (EDS) was employed to determine any abnormalities or surface defects (i.e. cracks) that would be present at the material interface.

Images of the interface were recorded at several magnifications (minimum of 100x). EDS was then used to determine the type of element present along the cross section of the coated sections for friction stir welding tool. The percentage of elements were recorded and tabulated.

Field emission scanning electron microscopy (FESEM) machine of Carl Zeiss SUPRA 55VP machine was used to measure the thickness of the coating and to evaluate the chemical properties of the cross section. FESEM would indicate the elemental and topographical information at magnifications of 10× to 300,000×, and has unlimited depth of field. The principle of FESEM involves high energy of electron collides with the atoms of the material to produce the signals that is useful for the substrate's surface topography and properties [43].

This method is better than scanning electron microscope (SEM) as it provides larger magnification than SEM. Prior to the testing of FESEM, the samples were prepare accordingly. The coated tungsten carbide was grinded and polished at one side of the coating. The grinding process started with the roughest grade of the sandpaper and

ended with the smoothest sand paper. Diamond paste was used to polish the side of the cube. The same preparation process has been done for those of the H13 steel specimens. Diamond-like-carbon has been used to coat on top of the H13 tool steel and tungsten carbide. In this section, analysis on both tool materials are discussed.

Figure 4 reveals that the thickness of the DLC on top surface of the H13 tool steel was around $10.09\ \mu\text{m}$. Three spots were selected to evaluate the elements composition; spot a was selected on the coating section, spot b was at the interface between the coating and substrate, and spot c was selected on the substrate and far from the coating section. From the ESD, it was found that the amount of carbon on the sport a was more than those of spot b and c. Moreover, the amount of Fe also increased from spot a to spot b.

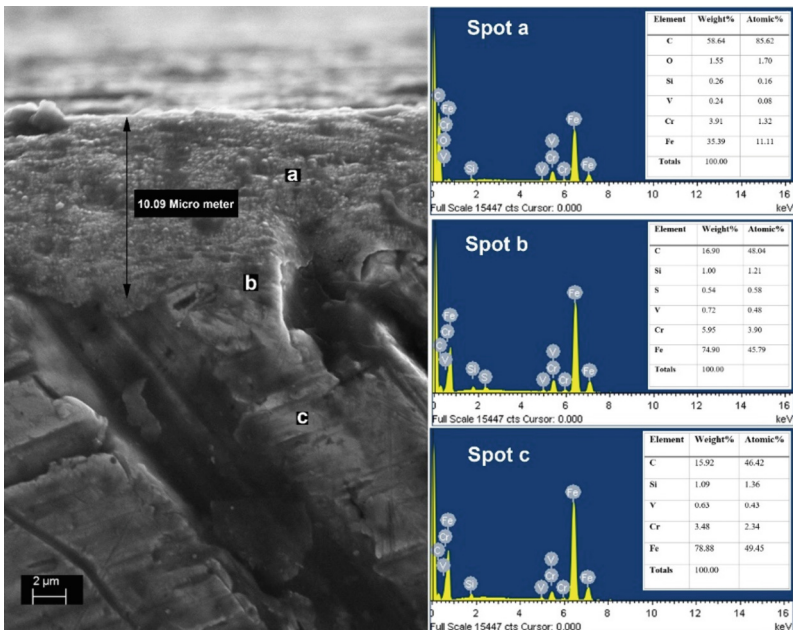


Fig. 4. Cross section of DLC coated on H13 tool steel and elements comparison of spots a, b, and c.

In addition, Fig. 5 indicates mapping images to evaluate the amount of the coated carbon on top of the H13 tool steel. It can be seen that the carbon was successfully coated on the top surface of the substrate. By the way, iron and chromium was also found to be distributed homogeneously as the H13 tool steel was composed of these elements. In conclusion, from the FESEM images and EDS as well as those mapping images, it could be concluded that the DLC was effectively coated on the H13 tool steel.

Diamond-like-carbon was also deposited on top of the tungsten carbide. Figure 6 shows the thickness of the DLC coated on tungsten carbide and elements comparison at different spots.

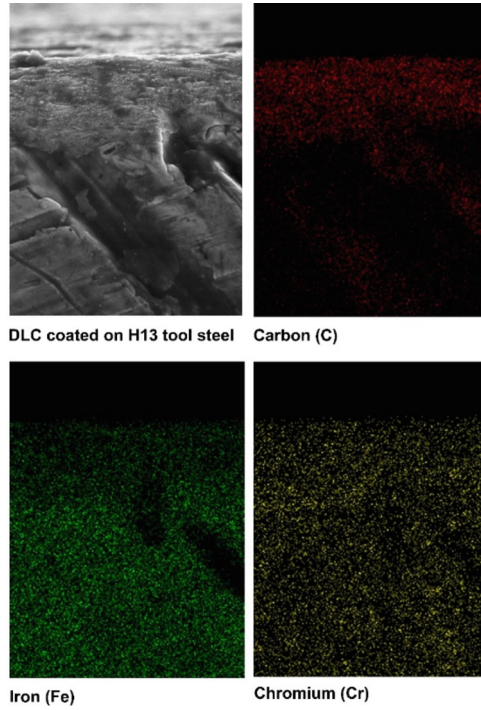


Fig. 5. Mapping of DLC coating on the H13 tool steel

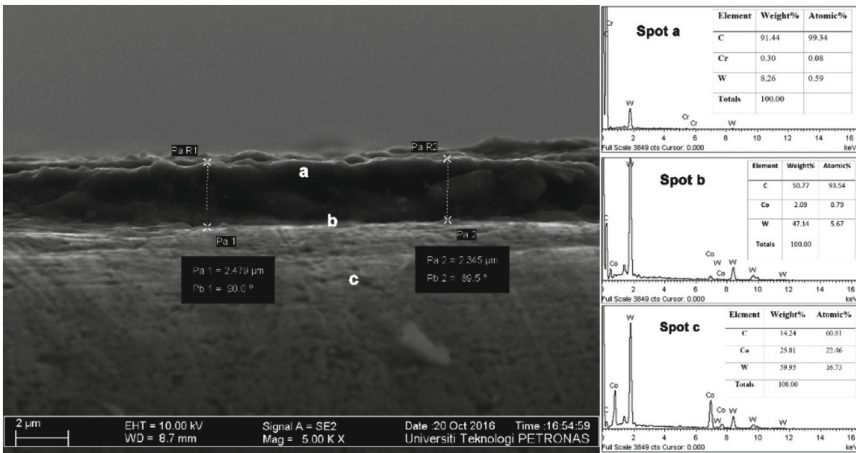


Fig. 6. Cross section of DLC coated on tungsten carbide and elements comparison of spots a, b, and c

Thickness of the coated DLC was measured at around $2.4\ \mu\text{m}$. As shown in Fig. 7, spot a consisted of maximum amount of carbon, which proved the appropriate layer of coating.

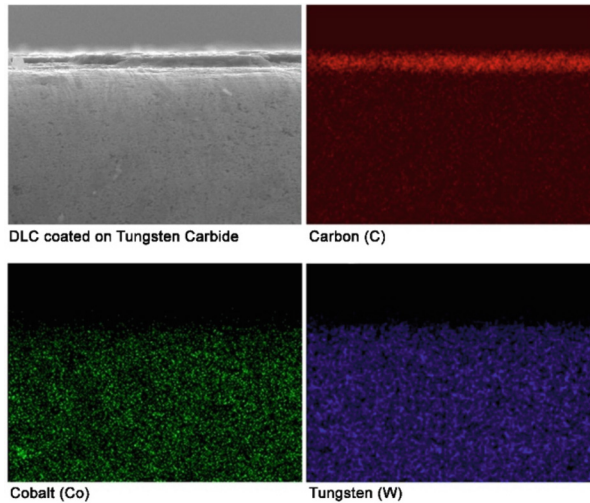


Fig. 7. Mapping of DLC coating on Tungsten

3.2 Raman Spectroscopy

Raman spectroscopy was conducted with a spectral resolution of $4\ \text{cm}^{-1}$, using an argon ion laser with a wavelength of $514.5\ \text{nm}$. Data collection of the Raman spectra was carried out with the use of a high throughput holographic imaging spectrograph. Moreover, the experiment was conducted at standards room temperature and pressure. Raman spectroscopy offers an analysis of inelastic light scattering and, when applied to molecules, would provide an insight into their chemical structure [44].

Based on the Raman spectrum obtained by Raman spectroscopy, three prominent peaks could determine the presence of carbon. These peaks are the D peak, G peak, and 2D peak. The D peak signifies that the synthesized carbon contains disorders and defects. It has been reported that these conditions might occur due to surface dislocations, corrugation, and possibly the interaction of carbon with the substrate itself [45]. The presence of disorder in sp^2 -hybridized carbon systems results in resonance Raman spectra, and thus makes Raman spectroscopy one of the most sensitive techniques to characterize disorder in sp^2 carbon materials. Meanwhile, the G peak is due to the in-plane vibration of sp^2 carbon atoms. G-band arises from the stretching of the C-C bond in graphitic materials, and is common to all sp^2 carbon systems. Finally, the 2D peak is due to the stacking order of carbon sheets [46]. 2D-band is a second-order two-phonon process and exhibits a strong frequency dependence on the excitation laser energy.

Raman spectroscopy has also been performed on DLC coated samples. Figure 8 shows the results for Raman. The intensities of the two characteristic G and D bands

were 1550cm^{-1} and 1350cm^{-1} , respectively, which are typical for diamond-like-carbon. The quality of the result could be compared with [47–49].

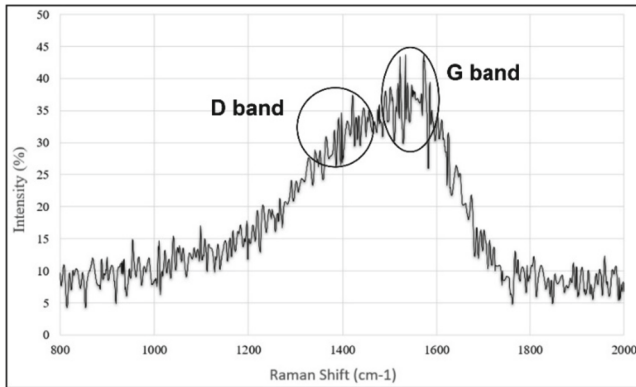


Fig. 8. Raman spectrum measured for the DLC

4 Conclusion

It is obvious that the use of FSW in joining metal matrix composites would cause removal of the aluminum carbide, which is considered as welding defect in the conventional methods. Moreover, in such welding process, hazardous fumes would also be removed. Increasing the surface strength with the DLC coating on tungsten carbide through physical vapor deposition could reduce pollution of coating and increase the tool life.

Physical vapor deposition has been used in order to coat DLC on H13 and tungsten carbide substrates. In order to evaluate the characteristics and quality of the coated materials, several materials characterizations were performed.

The characterization results of the DLC coating on H13 tool steel and tungsten carbide proved that the DLC could be coated properly on substrates. Microstructural analysis has verified that carbon has been successfully diffused on top of the substrates.

References

1. Gibson, B., Lammlein, D., Prater, T., Longhurst, W., Cox, C., Ballun, M., et al.: Friction stir welding: process, automation, and control. *J. Manuf. Process.* **16**, 56–73 (2014)
2. Cam, G.: Friction stir welded structural materials: beyond Al-alloys. *Int. Mater. Rev.* **56**, 1–48 (2011)
3. Rai, R., De, A., Bhadeshia, H., DebRoy, T.: Review: friction stir welding tools. *Sci. Technol. Weld. Joining* **16**, 325–342 (2011)
4. Prado, R., Murr, L., Soto, K., McClure, J.: Self-optimization in tool wear for friction-stir welding of Al 6061+ 20% Al₂O₃ MMC. *Mater. Sci. Eng., A* **349**, 156–165 (2003)

5. Fernandez, G., Murr, L.: Characterization of tool wear and weld optimization in the friction-stir welding of cast aluminum 359 + 20% SiC metal-matrix composite. *Mater. Charact.* **52**, 65–75 (2004)
6. Shindo, D., Rivera, A., Murr, L.: Shape optimization for tool wear in the friction-stir welding of cast Al359-20% SiC MMC. *J. Mater. Sci.* **37**, 4999–5005 (2002)
7. Lee, C.Y., Choi, D.H., Yeon, Y.M., Jung, S.B.: Dissimilar friction stir spot welding of low carbon steel and Al–Mg alloy by formation of IMCs. *Sci. Technol. Weld. Joining* **14**, 216–220 (2009)
8. Dressler, U., Biallas, G., Mercado, U.A.: Friction stir welding of titanium alloy TiAl6V4 to aluminium alloy AA2024-T3. *Mater. Sci. Eng., A* **526**, 113–117 (2009)
9. Miles, M.P., Feng, Z., Kohkonen, K., Weickum, B., Steel, R., Lev, L.: Spot joining of AA 5754 and high strength steel sheets by consumable bit. *Sci. Technol. Weld. Joining* **15**, 325–330 (2010)
10. Chen, Y., Nakata, K.: Microstructural characterization and mechanical properties in friction stir welding of aluminum and titanium dissimilar alloys. *Mater. Des.* **30**, 469–474 (2009)
11. Meilinger, A., Torok, I.: The importance of friction stir welding tool. *Prod. Processes Syst.* **6**, 25–34 (2013)
12. Fuller, C. B.: Friction stir tooling: tool materials and designs. In: *Friction Stir Welding and Processing*, pp. 7–36 (2007)
13. Mishra, R.S., Ma, Z.Y.: Friction stir welding and processing. *Mater. Sci. Eng. R: Rep.* **50**, 1–78 (2005)
14. Storjohann, D., Barabash, O., David, S., Sklad, P., Bloom, E., Babu, S.: Fusion and friction stir welding of aluminum-metal-matrix composites. *Metall. and Mater. Trans. A* **36**, 3237–3247 (2005)
15. Prado, R.A., Murr, L.E., Shindo, D.J., Soto, K.F.: Tool wear in the friction-stir welding of aluminum alloy 6061+20% Al₂O₃: a preliminary study. *Scripta Materialia* **45**, 75–80 (2001)
16. Liu, H.J., Feng, J.C., Fujii, H., Nogi, K.: Wear characteristics of a WC–Co tool in friction stir welding of AC4A+30 vol%SiCp composite. *Int. J. Mach. Tools Manuf.* **45**, 1635–1639 (2005)
17. Marzoli, L.M., Strombeck, A.V., Dos Santos, J.F., Gambaro, C., Volpone, L.M.: Friction stir welding of an AA6061/Al₂O₃/20p reinforced alloy. *Compos. Sci. Technol.* **66**, 363–371 (2006)
18. Zhang, Y.N., Cao, X., Larose, S., Wanjara, P.: Review of tools for friction stir welding and processing. *Can. Metallur. Q.* **51**, 250–261 (2012)
19. ASM Specialty Handbook - Carbon and Alloy Steels: ASM International (1996)
20. Emamian, S.S., Awang, M., Yusof, F., et al.: Improving the friction stir welding tool life for joining the metal matrix composites. *Int. J. Adv. Manuf. Technol.* **106**, 3217–3227 (2020). <https://doi.org/10.1007/s00170-019-04837-1>
21. Rabinowicz, E.: *Friction and Wear of Materials*. Wiley, New York (1965)
22. Mishra, R.S., Mahoney, M.W.: *Friction Stir Welding and Processing*: ASM International (2007)
23. Storjohann, D., Babu, S., David, S., Sklad, P.: *Friction stir welding of aluminum metal matrix composites* (2005)
24. Bhat, B.N., Carter, R.W., Ding, R.J., Lawless, K.G., Nunes Jr, A. C., Russell, C.K., et al.: Friction stir welding development at NASA-marshall space flight center, pp. 117–128 (2001)
25. Prater, T., Strauss, A., Cook, G., Machemehl, C., Sutton, P., Cox, C.: Statistical modeling and prediction of wear in friction stir welding of a metal matrix composite (Al 350/SiC/20p). *J. Manuf. Technol. Res.* **2**, 45–58 (2010)
26. Prater, T.J.: Predictive process modeling of tool wear in friction stir welding of metal matrix composites (Order No. 3576880). Available from ProQuest Dissertations & Theses Global. (1467745615) (2012). <https://search.proquest.com/docview/1467745615?accountid=47520>

27. Prater, T., Strauss, A., Cook, G., Gibson, B., Cox, C.: A comparative evaluation of the wear resistance of various tool materials in friction stir welding of metal matrix composites. *J. Mater. Eng. Perform.* **22**, 1807–1813 (2013)
28. Prater, T., Cox, C., Gibson, B., Strauss, A.M., Cook, G.E.: Dimensional analysis and a potential classification algorithm for prediction of wear in friction stir welding of metal matrix composites. *Proc. Inst. Mech. Engineers Part C: J. Mech. Eng. Sci.* **226**, 2759–2769 (2012)
29. Prater, T.: Friction stir welding of metal matrix composites for use in aerospace structures. *Acta Astronaut.* **93**, 366–373 (2014)
30. Chiteka, K.: Friction stir welding/processing tool materials and selection. *Int. J. Eng. Res. Technol. (IJERT)* **2**, 8–18 (2011)
31. Emamian, S., et al.: Comparison of carbon-based nanomaterials characteristics on H13 tool steel: Vergleich der Eigenschaften Kohlenstoff-basierter Nanomaterialien auf H13 Werkzeugstahl. *Materialwiss. Werkstofftech.* **48**(3–4), 198–204 (2017)
32. Robertson, J.: Diamond-like amorphous carbon. *Mater. Sci. Eng. R: Rep.* **37**, 129–281 (2002)
33. Artini, C., Muolo, M.L., Passerone, A.: Diamond–metal interfaces in cutting tools: a review. *J. Mater. Sci.* **47**, 3252–3264 (2012)
34. Field, J.E.: *The Properties of Natural and Synthetic Diamond*. Academic Press, Cambridge (1992)
35. Sengupta, R., Bhattacharya, M., Bandyopadhyay, S., Bhowmick, A.K.: A review on the mechanical and electrical properties of graphite and modified graphite reinforced polymer composites. *Progress in Polymer Science* **36**, 638–670 (2011)
36. Pierson, H.O.: *Handbook of Carbon, Graphite, Diamonds and Fullerenes: Processing, Properties and Applications*. William Andrew, Amsterdam (2012)
37. Vetter, J.: 60 years of DLC coatings: historical highlights and technical review of cathodic arc processes to synthesize various DLC types, and their evolution for industrial applications. *Surf. Coat. Technol.* **257**, 213–240 (2014)
38. Donnet, C., Erdemir, A. (eds.): *Tribology of Diamond-Like Carbon Films*. Springer US, Boston (2008). <https://doi.org/10.1007/978-0-387-49891-1>
39. Aisenberg, S., Chabot, R.: Ion-beam deposition of thin films of diamondlike carbon. *J. Appl. Phys.* **42**, 2953–2958 (1971)
40. Lessiak, M., Haubner, R.: Diamond coatings on hardmetal substrates with CVD coatings as intermediate layers. *Surf. Coat. Technol.* **230**, 119–123 (2013)
41. Ye, F., Li, Y., Sun, X., Yang, Q., Kim, C.-Y., Odeshi, A.G.: CVD diamond coating on WC-Co substrate with Al-based interlayer. *Surf. Coat. Technol.* **308**, 121–127 (2016)
42. Kohn, E., Ebert, W.: Electronic devices on CVD diamond. In: Dischler, B., Wild, C. (eds.) *Low-Pressure Synthetic Diamond*, pp. 331–359. Springer, Heidelberg (1998). https://doi.org/10.1007/978-3-642-71992-9_17
43. Hoe, F.J., Aizawa, T., Yukawa, S.: Synthesis and characterization of doped and undoped nano-columnar DLC coating. *Jurnal Teknologi (Sci. Eng.)* **62**, 17–24 (2013)
44. Le Ru, E.C., Etchegoin, P.G.: A quick overview of surface-enhanced Raman spectroscopy. In: *Principles of Surface-Enhanced Raman Spectroscopy*, pp. 1–27. Elsevier (2009). <https://doi.org/10.1016/B978-0-444-52779-0.00007-6>
45. Ni, Z., Wang, Y., Yu, T., Shen, Z.: Raman spectroscopy and imaging of graphene. *Nano Res.* **1**, 273–291 (2008)
46. John, R., Ashokreddy, A., Vijayan, C., Pradeep, T.: Single- and few-layer graphene growth on stainless steel substrates by direct thermal chemical vapor deposition. *Nanotechnology* **22**, 165–701 (2011)
47. Deng, X., Kousaka, H., Tokoroyama, T., Umehara, N.: Tribological behavior of tetrahedral amorphous carbon (ta-C) coatings at elevated temperatures. *Tribol. Int.* **75**, 98–103 (2014)

48. Zhang, D., Shen, B., Sun, F.: Study on tribological behavior and cutting performance of CVD diamond and DLC films on Co-cemented tungsten carbide substrates. *Appl. Surf. Sci.* **256**, 2479–2489 (2010)
49. Rincón, C., Zambrano, G., Carvajal, A., Prieto, P., Galindo, H., Martínez, E., et al.: Tungsten carbide/diamond-like carbon multilayer coatings on steel for tribological applications. *Surf. Coat. Technol.* **148**, 277–283 (2001)



Optimization of Superhydrophobic Surface Preparation Using One-Step Immersion and Control Variate Method

Shuai Zhang², Yong Chai Tan¹(✉), Hui Xin Che¹, Vin Cent Tai¹, Yaw Yoong Sia¹, Shamini Janasekaran⁴, and Walisijiang Tayier³

¹ Centre for Modelling and Simulation, Faculty of Engineering, Built Environment and IT, SEGi University, 47810 Petaling Jaya, Malaysia
tanyongchai@segi.edu.my

² School of Mechanical and Electrical Engineering, Zhoukou Normal University, Chuanhui District, Jinshi Rd, Zhoukou 466001, Henan, China

³ Department of Mechanical Engineering, Faculty of Engineering, Built Environment and IT, SEGi University, 47810 Petaling Jaya, Malaysia

⁴ Centre for Advanced Materials and Intelligent Manufacturing, Faculty of Engineering, Built Environment and IT, SEGi University, 47810 Petaling Jaya, Malaysia

Abstract. This paper focuses on the influence of immersion time, concentration, and temperature on the formation process of copper stearate on the surface of copper sheet. One-step immersion and control variate method was adopted in this research to produce superhydrophobic surface on copper sheet. In the proposed method, pre-treated pure copper samples were immersed in stearic acid-ethanol solution with different concentrations (1, 2 and 3 g/l) for different durations (0.5, 1, 1.5, 2, 2.5, and 3 h) at different temperatures (20, 30, 40, 50, 60 and 70 °C). A total of 108 superhydrophobic surfaces were prepared and investigated using this control variate method. The superhydrophobic surfaces were characterized and analyzed using scanning electron microscope, contact angle measuring instrument and fourier transform infrared spectrometer. The preparation of copper surface for superhydrophobic effect was found to be at optimal, when stearic acid concentration at 2 g/l, immersion temperature at 60 °C and the immersion time of 90 min.

Keywords: Copper · Superhydrophobic Surface · Contact Angle · Immersion Process · Control Variate Method

1 Introduction

Surface wettability, the degree of infiltration of a body to a solid, is one of the important characteristics of solid surface. Microstructure surface of lotus leaf with hydrophobic waxy substance was first explained in 1997 to clarify super hydrophobicity phenomenon [1–8]. Superhydrophobic surface of metal has great importance in self-cleaning, oxidation resistance, drag reduction, friction reduction, anti-scaling and great prospects for industrial applications [9, 10]. Preparation of superhydrophobic self-cleaning film on metal substrate not only can achieve the modification effect, but also avoid the tendency

of scaling between metal and corrosive medium, providing a parameter basis for the preparation of large area of superhydrophobic surface [11–14]. The micro-nano layer structure and waxy substance on lotus leaf surface are the main reasons for the formation of superhydrophobic surface, which provide guidance for the construction of artificial superhydrophobic surface.

At present, many preparation methods of superhydrophobic copper surface have been reported in the literature, such as electrochemical deposition [15], vapor deposition method [16], etching method [17], template method [18], laser and plasma technology [19], mechanical processing method [20], direct immersion method [21], sol-gel [22], electrostatic spinning method [23], self-assembly method etc. [24]. The wettability of metal surface is determined by its chemical composition and microscopic geometry. Superhydrophobic surface can be constructed using two-step method: roughening a surface and modifying the surface with low energy material [25–28].

The preparation of superhydrophobic surface using two-step method, is more complicated and not practical for large scale production. A novel one-step immersion method was introduced where sheet metal (copper and zinc) were immersed in an anhydrous ethanol solution of tetradecanoic acid for 3 to 5 days to obtain the flower-like micro-nano structure superhydrophobic surfaces [29]. One-step immersion method to soak copper sheet in anhydrous ethanol solution of palmitic acid was used to obtain superhydrophobic surface; the influence of experimental concentration and immersion time on surface wettability of copper sheet were discussed [30].

The above one-step immersion method was used to prepare the superhydrophobic surface, which was relatively simple to operate and easy to produce in a large scale. However, the soaking time used to obtain the superhydrophobic surface in the experiment was relatively long, and the formation rule of this flower-like structure was not explored.

In this paper, one-step immersion method was used to prepare the superhydrophobic surface on the copper sheet. The copper sheet was immersed in 95% ethanol solution of stearic acid to obtain the superhydrophobic surface with grass-like microstructure. The influence of soaking time, soaking concentration and soaking temperature on the self-assembly process of copper stearate on the surface of copper sheet was studied, and the formation rule of grass-like structure on the surface of copper sheet was revealed. This method uses simple technology, equipment, and shorter soaking time.

2 Experiment

2.1 Sample Preparation

Copper sheet (99.95 wt %) with 10 mm length, 5 mm width, and 1 mm thickness dimensions was prepared for the experiment. The copper sheet was polished using sandpaper (400 #) to obtain micro-textured surface. Distilled water and ethanol were used to remove organic matter and oxides from the surface of the copper sheet. Pre-treated pure copper samples were immersed in stearic acid-ethanol solution with different concentrations (1, 2, and 3 g/l) for different durations (0.5, 1, 1.5, 2, 2.5, and 3 h) at different temperatures (20, 30, 40, 50, 60, and 70 °C). After a total of 108 samples were being experimented, the copper samples were taken out of the solution, washed with ethanol and distilled water, then air-dried.

2.2 Characterisation

Phenom Pro X scanning electron microscope with accelerating voltage of 5 kV was used in this experiment to characterize the microstructure and morphology of the sample surface.

Fourier transform infrared spectroscopy was conducted using a small amount of surface material scrapped from the pure copper surface and superhydrophobic copper surface. The sample for superhydrophobic copper surface was taken from the stearic acid concentration of 2 g/l, soaking temperature at 60 °C and soaking time of 90 min. Superhydrophobic copper surface sample is in sky-blue color powder form when detected by Perkin Elmer Spectrum 100. It is an attenuated total reflectance-Fourier transform infrared spectrometer and has the resolution of 0.5 cm⁻¹.

The sample was placed on the measurement platform of the OCA20 contact angle meter, and the static contact angle was measured by the lying drop method (sessile drop method) at room temperature. The measured water droplet (distilled water) amount was 5 μl, and the average value of 6 different points on the surface of the sample was taken.

3 Results and Discussion

3.1 Superhydrophobic Surface Microstructure Analysis

Images of the copper surfaces under different preparation conditions were taken using scanning electron microscope, Fig. 1. The reaction rate of copper oxide and the amount of copper stearate increased on the surface of copper sheet as the of stearic acid concentration increased from 1 to 3 g/l. Up to 70 μm in diameter of grass structure of and 35 μm long of nano-acicular structure formed in the copper surface with the increase of concentration. However, when concentration exceeded 2 g/l, the adjacent nano-needles structure overlapped with each other to form block due to excessive of nano-needles produced.

Many bud-like structures formed on the surface of the copper sheet when soaking duration, $t = 30$ min. A little copper oxide was generated and the amount of copper stearate formed on the surface was very small due to the short immersion duration. These bud-like structures were the embryonic form of nano-needle structure. Copper oxide and copper stearate increased with the soaking duration. However, when $t = 180$ min, excessive nano-needles structure was produced and overlapped with each other to form block.

With soaking temperature at 20 °C, many micron grass-like structures with diameters of about 50 μm were formed on the surface. However, no grass-like structure was observed as the temperature rose to 70 °C.

3.2 Infrared Spectrogram Analysis of Superhydrophobic Surface Materials

Fourier transform infrared spectrometer was used to capture the infrared spectrogram of the sky-blue material on the surface of the copper sheet sample after immersion, Fig. 2 (a) and the infrared spectrogram of stearic acid, Fig. 2 (b). Based on the stearic acid infrared spectrogram, there were two characteristic peaks at the high frequency region

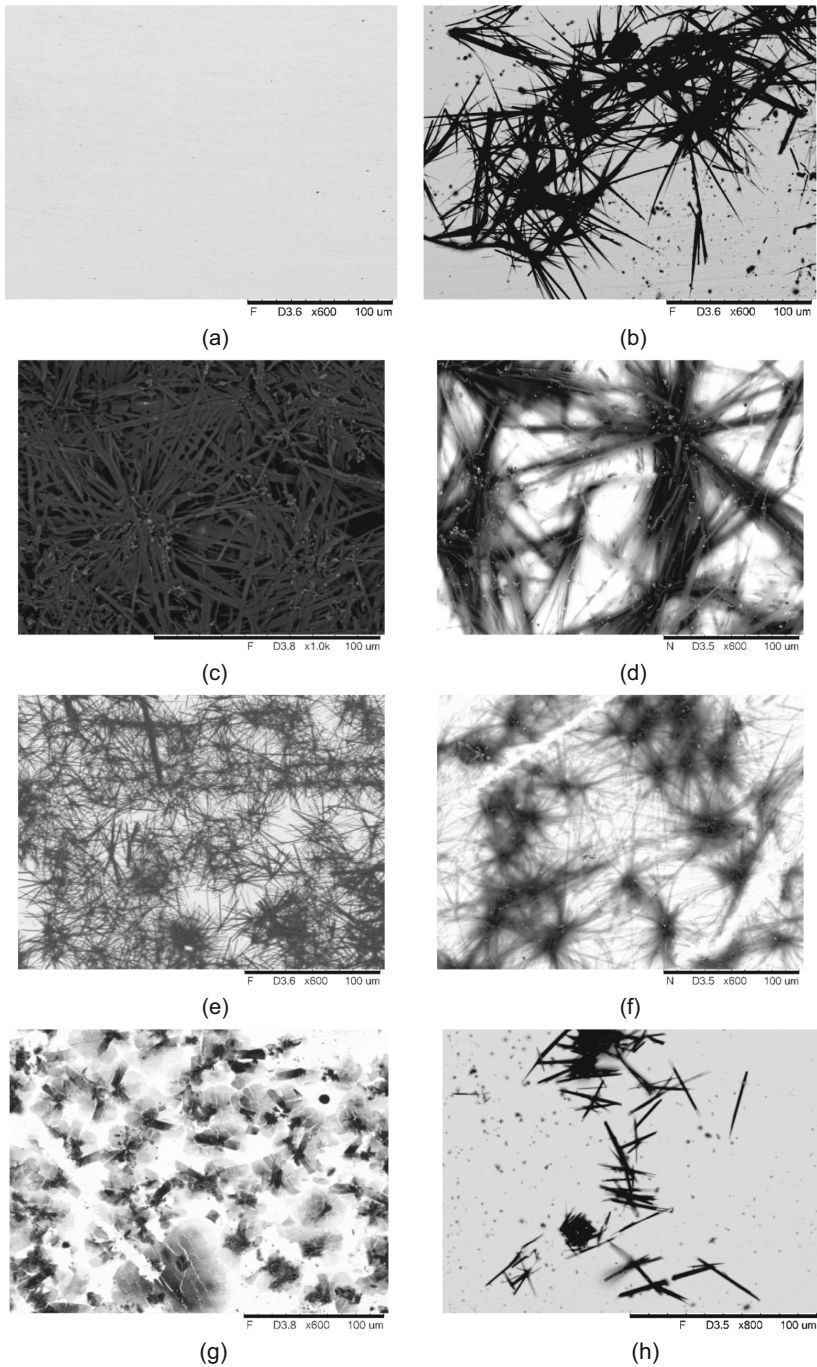


Fig. 1. Scanning Electron Microscope Images of the Copper Surfaces (a) Pure Copper; (b), (c) and (d) Immersed in 1 g /*l*, 2 g /*l*, 3 g /*l* solutions at 60 °C for 90 min, respectively; (e) and (f) Immersed in 2 g /*l* solution at 60 °C, for 30 min and 180 min, respectively; (g) and (h) Immersed in 2 g /*l* solution for 90 min, at 20 °C and 70 °C, respectively.

at 2916 cm^{-1} and 2849 cm^{-1} , caused by the symmetric and asymmetric stretching vibration of the functional group CH_2 , respectively. There was an absorption peak in the low frequency region at 1702 cm^{-1} , due to carbonyl stretch of stearic acid.

As for the sky-blue substance on the surface of the copper plate, there were two characteristic peaks in the high frequency region of Fourier transform infrared spectrum at 2915 cm^{-1} and 2849 cm^{-1} respectively, similar to stearic acid Fourier transform infrared spectrum. A characteristic peak was generated in the low frequency region at 1586 cm^{-1} , which is corresponding to the group $-\text{COO}$ peak ($-\text{COO}$ absorption peak from 1610 cm^{-1} to 1560 cm^{-1}). An asymmetric deformation vibration of $-\text{CH}_3$ was observed at 1444 cm^{-1} . The above analysis shows that the microcluster was not $\text{CH}_3(\text{CH}_2)_{16}\text{COOH}$ powder, but the stearic acid had chemical reaction on the surface of the copper sheet to form copper stearate ($\text{Cu}[\text{CH}_3(\text{CH}_2)_{16}\text{COO}]_2$) [31–33].

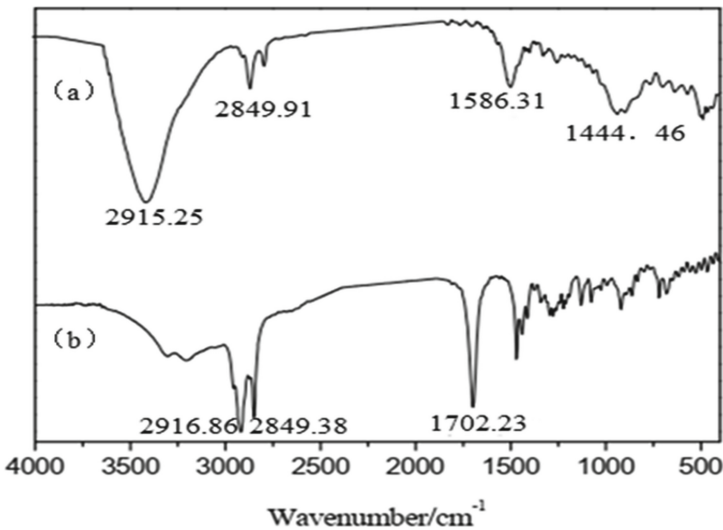


Fig. 2. Fourier Transform Infrared Spectrogram of (a) Copper Stearic; (b) Stearic Acid.

3.3 Contact Angle Measurement and Analysis

Images of the three different states of water droplets contact angle on the copper sample surface: hydrophilic, hydrophobic and superhydrophobic, Fig. 3. Superhydrophobic surfaces are contact angle with at least 150° . Majority of the surfaces achieved were hydrophobic based on the results, Fig. 4.

Contact angle of pure copper started with hydrophilic surface, however as the soaking concentration, soaking temperature and soaking duration increased, the contact angle initially increased but decreased eventually. This phenomenon can be explained by Cassie theory which state that due to large amount of air trapped between the needle cluster on the surface, the water droplets cannot penetrate, and thus convex droplets were formed on the surface of the solid, thus form the phenomenon of super hydrophobic. However,

as more and more modifier molecules adsorbed on the surface, the surface becomes flatter and the captured air between the nanoparticles is gradually expelled. Therefore, the contact angle becomes gradually decreases as the gas phase composition decreasing at the three-phase interface.

Contact angle of copper surfaces immersed in stearic acid-ethanol solution with different concentrations (1, 2 and 3 g/l) for different duration (0.5, 1, 1.5, 2, 2.5, and 3 h) and different temperatures (20, 30, 40, 50, 60 and 70 °C), Fig. 4. The preparation of copper surface for superhydrophobic effect was found to be optimal when stearic acid concentration at 2 g/l, soaking temperature at 60 °C and soaking time of 90 min.

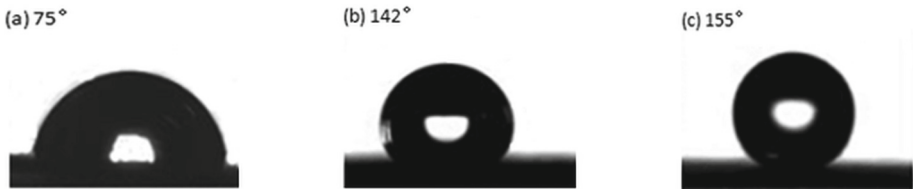


Fig. 3. Surface Water Contact Angle of Copper Plate, (a) Pure Copper; (b) Hydrophobic Copper; (c) Superhydrophobic Copper.

3.3.1 Effect of Stearic Acid Concentration on Copper Surface Structure and Wettability

The contact angle value was low when the copper immersed in low concentration of stearic acid-ethanol solution with temperature at 60 °C and immersing duration at 90 min. The contact angle achieved maximum value with concentration at 2 g/l. However, the contact angle decreased when concentration exceeded 2 g/l. With concentration of stearic acid-ethanol solution at 1 g/l, the reaction rate between stearic acid-ethanol solution and copper was slow due to the small number of stearic acid molecules and the film could not cover the entire surface of the copper sample, which then affected the formation of microstructure on the surface of copper. While when immersed in the 3 g/l concentration stearic acid-ethanol solution, it caused over production of copper stearate and nano-needle structures overlapped with each other and reduced the roughness of the surface, thus decreasing the contact angle of water droplets on the surface.

3.3.2 Effect of Immersing Time on Copper Surface Structure and Wettability

The contact angle value on the surface of the sample increased significantly with the increasing of immersing duration with temperature set at 60 °C and concentration of stearic acid-ethanol solution at 2 g/l. The contact angle reached the maximum value at 90 min immersion time and gradually decreased as the immersion time increased further. This was due the diameter of the grass structure and the length of the nano-needle structure remained unchanged, but the density of the nano-needle structure on the single micron grass-like structure increased. When the immersing time reached 180 min, the density of the nano-needle structure was too large, and the nano-needle

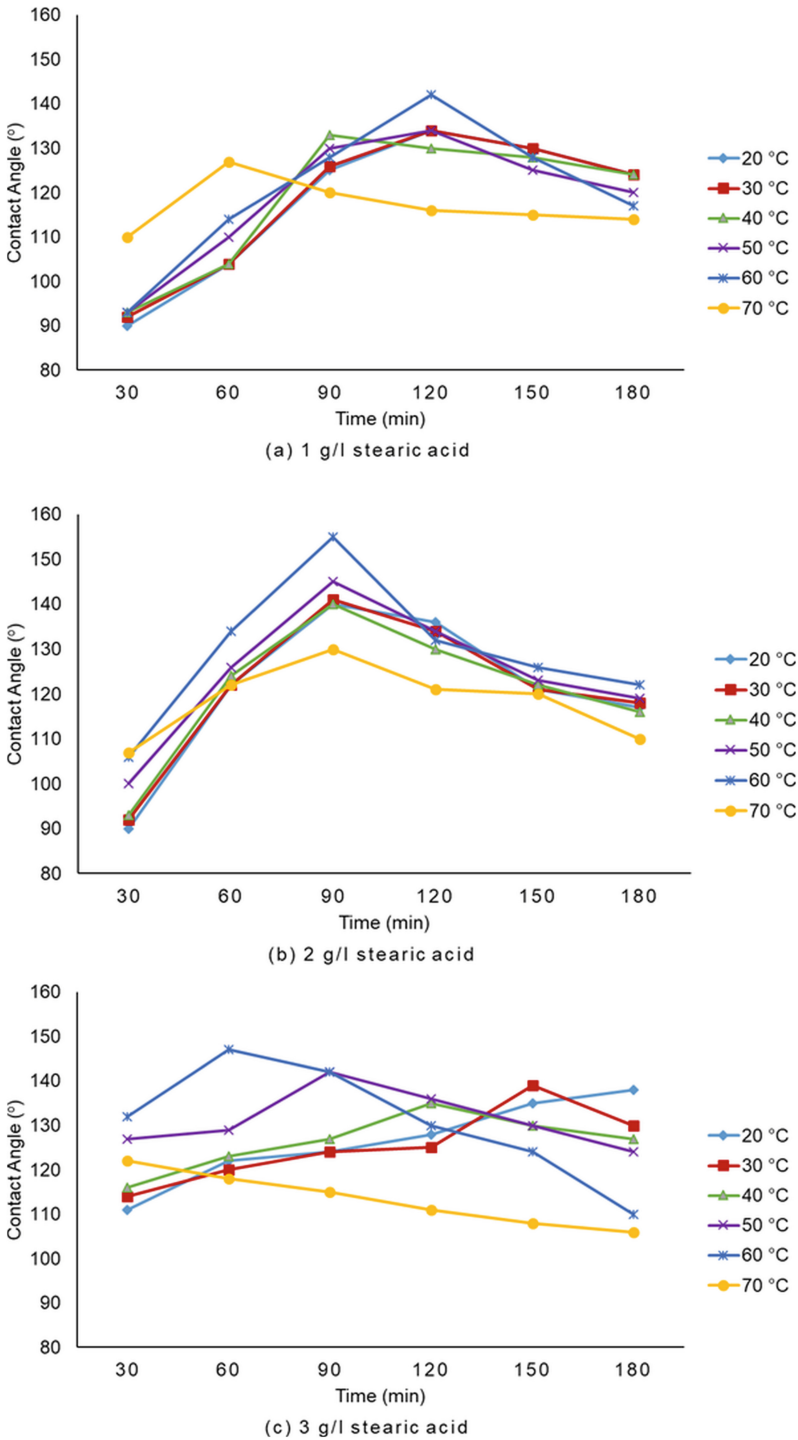


Fig. 4. Contact Angle of Prepared Copper Surface at different concentration level of Stearic Acid: (a) 1 g /ℓ; ; (b) 2 g /ℓ; ; (c) 3 g /ℓ.

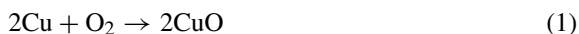
structure overlapped into block, thus reduced the roughness of the surface, and reduced the contact angle of water droplets.

3.3.3 Effect of Immersing Temperature on Copper Surface Structure and Wettability

The maximum contact angle achieved when the immersion temperature at 60 °C with concentration of stearic acid-ethanol solution at 2 g/l and immersion time of 90 min. The contact angle of sample was increasing with the increasing of immersion temperature. However, the contact angle decreased when it reached 70 °C immersion temperature. This may be due to copper stearate dissolve easily in ethanol solution at higher temperature.

3.4 Analysis on the Formation Mechanism of Copper Sheet Surface Structure

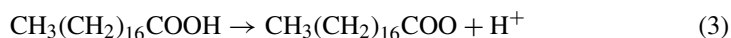
According to the surface microstructure of copper sheet and the results of infrared spectrum analysis as well as related literature, the possible mechanism of copper surface microstructure formation was due to the copper can be naturally oxidized by the dissolved oxygen in ethanol solution and this spontaneous oxidation reaction can be accelerated drastically in the ethanol solution of stearic acid [29, 34, 35]. When the copper sheet is immersed in 95% ethanol solution of stearic acid, the surface of the copper sheet reacts with the oxygen in the solution as shown in Eq. (1).



Due to the presence of stearic acid in the solution, the copper oxide generated on the surface of the copper sheet react with stearic acid, as shown in reaction Eq. (2).



Copper stearate was obtained on the surface of copper sheet, which is difficult to dissolve in ethanol and water solution. The grass-like structure of copper stearate on the surface of copper sheet was observed. Some literatures [29, 30] also reported that fatty acid salts with grass-like structure could be obtained on the surface of copper plates by soaking in anhydrous ethanol solution of fatty acids. However, soaking time could be very long (3–5 days). In this paper, stearic acid can be formed as an ion shown in Eq. (3) because the solution contained a certain amount of water (from 95% ethanol).



It was believed that under the action of these water, ions and higher temperatures, the oxidation rate on the surface of the copper sheet may be accelerated, which resulted in a shorter duration for the self-assembly of the copper sheet to form copper stearate grass-like structure.

4 Conclusions

In this paper, one-step immersion method was adopted to obtain the superhydrophobic surface by immersing the copper sheet in stearic acid and 95% ethanol solution. The superhydrophobic surface with grass-like microstructure can be obtained by self-assembly of copper stearate $\text{Cu}[\text{CH}_3(\text{CH}_2)_{16}\text{COO}]_2$ on copper sheet, with only 90 min of immersion time.

The effects of immersion time, concentration, and temperature on the surface structure of copper sheet were studied. The experimental results showed that there were many grass-like structures of copper stearate on the surface of the superhydrophobic copper sheet, and it was found that these structures changed with the immersion time, concentration, and temperature. Different surface structures under different conditions lead to different wettability of copper sheet surface. The preparation of copper sheet for superhydrophobic surface effect was found to be at optimal when stearic acid concentration at 2 g/l, soaking temperature at 60 °C and immersion time of 90 min.

5 Data Availability Statement

The data that support the findings of this study are available from the corresponding author upon reasonable request.

Acknowledgements. The project is funded by the Ministry of Higher Education Malaysia, under the Fundamental Research Grant Scheme (FRGS), Grant No. FRGS/1/2018/TK03/SEGI/02/1.

Author Contributions. Y.C. Tan, S. Zhang, W. Tayier, and H.X. Che were involved in conceptualization, investigation, writing—original draft, project management. V.C. Tai, Y.Y. Sia and S. Janasekaran were involved in investigation, writing—review and editing.

Conflict of Interest. The authors declare no financial or commercial conflict of interest.

References

1. Barthlott, W., Neinhuis, C.: *Planta* **202**, 1 (1997)
2. Akbari, R., Godeau, G., Mohammadizadeh, M.R.: *ChemPlusChem* **84**(4), 368 (2019)
3. Anbarasan, R., Palanikumar, S., Devi, A.A.: *Progress Natl. Sci.: Mater. Int.* **29**, 371 (2019)
4. Cui, W., Jiang, Y., Mielonen, K.: *Appl. Surf. Sci.* **466**, 503 (2019)
5. Feng, L., Wang, J., Shi, X.: *Appl. Phys. A* **125**, 1 (2019)
6. Gonzales, J., Kurihara, D., Maeda, T.: *Materials* **12**, 1 (2019)
7. He, J., Li, B., Wu, H.: *Surf. Eng.* **35**, 387 (2018)
8. Jiang, X., Xu, E., Wu, G.: *Chem. Eng. Sci.* **212**, 1 (2020)
9. Pan, R., Zhong, M.: *Chin. Sci. Bull.* **64**, 1268 (2019)
10. Peng, J., Zhao, X., Wang, W.: *Langmuir: the ACS J. Surf. Colloids* **35**, 8404 (2019)
11. Qin, L., Chu, Y., Zhou, X.: *ACS Appl. Mater. Interfaces* **11**, 29388 (2019)
12. Ran, M., Zheng, W., Wang, H.: *Mater. Sci. Technol.* **35**, 313 (2019)
13. Rioboo, R., Demnati, I., Amin Ali, M.: *J. Colloid Interface Sci.*, 560, 596 (2020)

14. Tsai, B.F., Chen, Y.C., Ou, S.F.: *Int. J. Appl. Ceram. Technol.* **16**, 211 (2019)
15. Xue, C.H., Wang, H.D., Ji, Z.Y.: *ACS Omega* **4**, 19756 (2019)
16. Zeng, Y., Qin, Z., Hua, Q.: *Surf. Coat. Technol.* **362**, 62 (2019)
17. Pan, L., Dong, H., Bi, P.: *Appl. Surf. Sci.* **257**, 1707 (2010)
18. Feng, L., et al.: *Angew. Chem.* **2004**, 43 (2012)
19. Xin, B., Hao, J.: *Chem. Soc. Rev.* **39**, 769 (2010)
20. Zhu, L., Feng, Y., Ye, X., Zhou, Z.: *Sens. Actuators, A* **130–131**, 595 (2006)
21. Feng, L., Li, H., Song, Y., Wang, Y.: *Appl. Surf. Sci.* **256**, 3191 (2010)
22. Li, R.X., Wang, Z., Liang, S.K.: *Appl. Mech. Mater.* **423–426**, 391 (2013)
23. Song, H.J., Shen, X.Q., Ji, H.Y., Jing, X.J.: *Appl. Phys. A* **99**, 685 (2010)
24. Crick, C.R., Parkin, I.P.: *Chem. A Eur. J.* **16**, 3568 (2010)
25. Li, J., Liu, X., Ye, Y., Zhou, H., Chen, J.: *J. Phys. Chem. C* **115**, 4726 (2011)
26. Shulga, Y.M., Melezhik, A.V., Kabachkov, E.N.: *High Energy Chem.* **53**, 47 (2019)
27. Qian, B., Shen, Z.: *Langmuir* **21**, 9007 (2005)
28. Lee, J.A., McCarthy, T.J.: *Macromolecules* **40**, 3965 (2007)
29. Wang, S., Feng, L., Jiang, L.: *Adv. Mater.* **18**, 767 (2006)
30. Wang, F.P., Yan, S.J.: *Chin. J. Appl. Chem.* **29**, 1291 (2012)
31. Wan, Y., Wang, Z., Liu, Y., Qi, C., Zhang, J.: *Tribol. Lett.* **44**, 327 (2011)
32. Zhang, Y., Zhang, L., Xiao, Z.: *Chem. Eng. J.* **369**, 1 (2019)
33. Zhang, Z., Li, Z., Hu, Y.: *Appl. Phys. A* **125**, 1 (2019)
34. Zhao, M., Li, W., Wu, Y.: *Materials* **12**, 1164 (2019)
35. Si, Y., Guo, Z.: *Nanoscale* **7**, 5922 (2015)



Replacement of Solar Dish Collectors to Provide Heat in the Power Plant: Case Study Malaysia

Chen Rui Geach¹, Kamyar Mehranzamir², Ateeb Hassan¹,
Hadi Nabipour Afrouzi¹ (✉), Elammaran Jayamani¹, and Seyed Morteza Alizadeh³

¹ Faculty of Engineering, Computing, and Science, Swinburne University of Technology
Sarawak, Kuching, Malaysia

100087812@students.swinburne.edu.my, {ahassan, HAfrouzi,
ejayamani}@swinburne.edu.my

² Department of Electrical and Electronic Engineering, University of Nottingham Malaysia,
Selangor, Malaysia

kamyar.mehranzamir@nottingham.edu.my

³ School of Electrical Engineering, Engineering Institute of Technology, Melbourne, Australia
morteza.alizadeh@eit.edu.au

Abstract. Greenhouse gases such as carbon dioxide (CO₂), methane (CH₄), and nitrous oxide (N₂O) will be produced during the combustion of fossil fuels to generate electricity. Besides, the available resource of fossil fuels such as coal and natural gas are declining. However, thermal power plants in Malaysia are still using the conventional way to produce heat in the boilers and gas turbines instead of using solar energy. Thus, this research aims to investigate the possibility of providing heat to the power plant in Malaysia by using the heat collected from solar dish collectors instead of using the combustion of fossil fuels, and the heat will be stored by using phase change material (PCM). The solar radiation at the chosen power plant, which is Sejingkat Power Plant, will be simulated by using the ASHRAE model in MATLAB. Next, the modeling of the designed solar dish collector and thermal energy storage (TES) by using phase change materials (PCM) are simulated in MATLAB as well. The simulated result shows that there is high solar radiation, and the designed solar dish collector can achieve high thermal efficiency. The TES is expected to store enough amount of energy for the time without sunlight or night time usage.

Keywords: Solar radiation · solar dish collector · TES · PCM · Sejingkat Power Plant

1 Introduction

Energy is getting important for human beings nowadays, and the energy demand is getting higher. However, the production of energy using non-renewable energy such as fossil fuels has brought negative impacts not only to the environment but also on human health. Fossil fuels had even contributed 99.5% of global greenhouse gases emission.

Moreover, the accessibility of fossil fuel reserves is also getting lesser [1]. Thus, renewable energy which can solve these problems is highly required. Among the renewable energy, solar energy can be considered the cleanest energy source. It will not release any greenhouse gases that will speed up global warming or cause any bad impacts on human health. Due to the high temperature required in the power plant, the solar dish collector is the most suitable type of solar energy collector to collect and provide heat to the boilers of the power plant rather than using the combustion of fossil fuels such as coals and natural gases. This is because it can reach a higher temperature range with its higher concentration of thermal power compared to other types of concentrating solar power (CSP) technologies [2].

2 Literature Review

2.1 Solar Radiation Model

Global solar radiation on a horizontal surface consists of direct solar radiation and diffuse solar radiation [3]. ASHRAE Clear-sky Model is a basic and simpler tool for solar radiation modeling and is widely used in engineering and other fields of study. For a clear sky, it can be assumed that direct solar radiation occupies 70% of the global solar radiation.

2.2 Solar Dish Collector

The two main components of the solar dish collector are the concentrator and the receiver. According to [4], the concentrator is mainly used to collect and concentrate solar radiation in a small area. The quality of the concentrator mainly depends on the reflectance of the concentrator. According to [5], the reflector surface will mostly have a high reflectivity which is between 70% to 95%. Besides, in order to achieve a high temperature, normally, the concentration ratio is typically higher than 2000. Moradi and Mehrpooya [6] uses concentration ratio up to 3000 in their design to obtain a high temperature. After the concentrator of the parabolic dish concentrates the solar radiation to the focal point, the receiver, which is located at the focus, will absorb the energy reflected from the concentrator [2]. The intercept factor is one of the most important factors in matching the concentrator and receiver. The larger the intercept factor, the more solar power will enter the receiver, and the lower the receiver loss [7]. Finally, Wu, et al. [8] did research, and the result shows that the efficiency will be the maximum when the tilt angle is 90° .

2.3 Phase Change Materials and Thermal Energy Storage

The phase change materials (PCM) have the advantage of storing the heat at almost the same temperature range, and the temperature difference between the process of charging and discharging is very small [9]. High-temperature PCMs are those with melting points more than 300°C and above, and inorganic salts are the primary choice for the high-temperature PCM [10]. They have a sharp transition at the melting point, high latent heat, high thermal conductivities, and high density. The type of storage for PCMs is

known as latent heat storage. For latent heat storage, latent heat refers to the heat stored during the changes in phase. The energy required to change the phase of solid to liquid is called as ‘heat of fusion’ while the energy required to change the phase of liquid to gas is called as ‘heat of vaporization’ [11].

3 Methodology

3.1 Specifications of the Selected Power Plant

Sejngkat Power Plant, which is in Kuching, Sarawak, Malaysia, is selected for this research. It is a coal-fired power plant. The location of this power plant is at 1.6376° N, 110.4638° E, with an average temperature of 26 °C or 299K annually [12]. The temperature required in this power plant is 540 °C, and it consists of two units of boilers that can generate 50 MW of electricity and another two units of boilers that can generate 55 MW of electricity [13] with a total output power of 210 MW.

3.2 Development of Solar Radiation Model

The solar radiation on a horizontal surface is predicted by using ASHRAE Clear-sky Model. The direct solar radiation reaching the earth’s surface, $G_{B,norm}$ is calculated by [3]

$$G_{B,norm} = Ae^{\frac{-K}{\sin\alpha}} \quad (1)$$

where A, apparent extraterrestrial flux, and K, optical length, can be expressed by the Eqs. (2) and (3) [3].

$$A = 1160 + 75 \sin\left[\frac{360}{365}(N - 275)\right] \quad (2)$$

$$K = 0.174 + 0.035 \sin\left[\frac{360}{365}(N - 100)\right] \quad (3)$$

The direct solar radiation on a horizontal surface, G_B can then be found by [3]

$$G_B = G_{B,norm}\sin\alpha \quad (4)$$

The diffuse solar radiation on a horizontal surface, G_D will be predicted by assuming the solar radiation reaches from all directions equally. The Equation can be expressed by [3]

$$G_D = 0.095 + 0.04\sin\left[\frac{360}{365}(N - 100)\right]G_{B,norm} \quad (5)$$

Finally, the global solar radiation, G_T on a horizontal surface can be obtained by [3]

$$G_T = G_B + G_D \quad (6)$$

The calculated result based on Eq. 1 to Eq. 6 is the solar radiation on a horizontal surface on a specific day from sunrise to sunset. So, the average solar radiation on each day is calculated and followed by the average solar radiation throughout the year.

3.3 Development of Solar Dish Collector

The solar dish collector is designed in order to obtain high thermal efficiency, and Table 1 shows the design parameters of the solar dish collector. Then, the useful and dissipated heat of the solar dish collector can be calculated based on the equations stated below. The net solar heat transferred, Q_s can be obtained by [14]

$$Q_s = G_b A_a \quad (7)$$

where G_b will be the direct solar radiation on a horizontal surface and A_a Is the aperture area of the concentrator.

Table 1. Design of solar dish collector.

Parameters	Symbol	Value
Aperture area of the collector	A_a	33.18 m ²
Non-shading factor	λ	0.99
The reflectivity of the reflector	ρ	0.94
Transmission-absorption	$\tau\alpha$	0.90
Receiver intercept factor	γ	0.99
The tilt angle of the cavity	φ_1	$\pi/2$
Cavity surface emittance	ε_c	0.9
Concentration ratio	C	3000
Aperture area of the receiver	A_r	0.0111 m ²
Diameter of the receiver	d_r	0.1187 m
Cavity length	L	0.1424 m
Area of internal cavity wall	A_w	0.0642 m ²

The amount of useful heat delivered by a solar dish collector, Q_u will be equal to the energy absorbed by the heat transfer fluid under a steady-state condition. Thus, the Equation can be expressed by [6]

$$Q_u = Q_r - Q_l \quad (8)$$

where Q_l and Q_r are the total heat loss from the receiver and the radiation falling on the receiver, respectively, which can be calculated by Eqs. (9) and (10) [15].

$$Q_r = Q_s \eta_o \quad (9)$$

$$Q_l = Q_{lk} + Q_{lc} + Q_{lr} \quad (10)$$

Q_{lk} is the conductive heat loss, Q_{lc} is the convective heat loss and Q_{lr} is the radiative heat loss from the receiver aperture. Finally, the thermal efficiency of a solar dish

collector, η_c can be written as [16]

$$\eta_c = \eta_o - \frac{Q_l}{Q_s} \quad (11)$$

3.4 Selection of Phase Change Material (PCM)

The chosen PCM that will be used in this research is 53% wt. BaCl₂ – 28% wt. KCl – 19% wt. NaCl is a type of eutectic compound. It also can be known as CL540 [17]. The properties of the CL540 are summarized in Table 2. CL540 will be chosen because its melting point of it is very similar to the desired operating temperature in this study which is 540 °C. Besides, CL540 also has high stability, and its melting point and latent heat show almost no change after being cycled 200 times [18]. Moreover, it also has a very small amount of subcooling effect [17].

Table 2. Summary of the properties of CL540

Properties	Value	Unit
Composition	53:28:19	%
Melting point	541.98	°C
Latent heat	164.96	kJ/kg
Specific heat	0.63 [s] 0.95 [l]	kJ/kg·K
Density	3011 [s] 2374 [l]	kg/m ³
Thermal conductivity	0.37 [l]	(W/mK)

3.5 Modeling of Thermal Energy Storage (TES)

The modeling of an ideal TES system, $T_{idealTES}$ is done by assuming that the temperature is constant throughout the tank. Thus, the energy brought by the inlet stream is assumed to mix with the PCM in the TES system instantly, and the heat transfer between them is at a maximum rate. The Equation of the ideal TES system with can be expressed as below [19]:

$$\frac{dE(t)}{dt} \approx \frac{E(t) - E(t - \Delta t)}{\Delta t} = \dot{m}_l(t)C_{HTF} \cdot (T_l(t) - T_{idealTES}(t - \Delta t)) - \dot{m}_u(t)C_{HTF} \cdot (T_{idealTES}(t - \Delta t) - T_u(t)) - \dot{Q}_{loss} \quad (12)$$

where the $E(t)$ is the energy stored at the current time step, $E(t - \Delta t)$ is the energy stored at the previous time step. Then, \dot{m}_l is the loading mass flow rate, C_{HTF} is the specific heat capacity of the heat transfer fluid which is molten salt (60% wt. NaNO₃ – 40% wt. KNO₃); in this research, the loading inlet temperature is denoted as T_l , $T_{idealTES}$ is the

temperature of the thermal energy storage, \dot{m}_u is the unloading mass flow rate and \dot{Q}_{loss} is the heat loss from the tank to the surrounding.

$E(t)$ itself can indicate both the stored energy and the phase change of the PCM. The PCM will be in the solid phase when the value of $E(t)$ is lower than $E_{pcm_{min}}$. Then, the PCM will be in the liquid phase when the value of $E(t)$ is higher than $E_{pcm_{max}}$. The equations of $E_{pcm_{min}}$ and $E_{pcm_{max}}$ is expressed in Eqs. (13) and (14).

$$E_{pcm_{min}} = [(1 - \phi) \cdot V \cdot \rho_w \cdot c_w \cdot T_m] + [(\phi \cdot V) \cdot \rho_{pcm} \cdot c_{pcm} \cdot T_m] \quad (13)$$

$$E_{pcm_{max}} = E_{pcm_{min}} + [(\phi \cdot V) \cdot \rho_{pcm} \cdot h_{pcm}] \quad (14)$$

From Eqs. (13) and (14), ϕ represents the volume fraction of the PCM in the TES system, V is the total volume of the storage tank, ρ_w is the water density, T_m is the melting point of the PCM, ρ_{pcm} is the PCM density and h_{pcm} is the enthalpy or the latent heat of the PCM.

4 Results and Discussion

4.1 Solar Radiation Model

Figure 1 and Fig. 2 show the simulated results for average daily and monthly solar radiation at the selected location, which is Sejingkat Power Plant, Kuching. Since only concentrating solar power (CSP) technology is being used in this research, only direct solar radiation will be taken into consideration. From Fig. 1, the minimum daily direct solar radiation is 606 W/m^2 while the maximum is 687.7 W/m^2 . The yearly average direct solar radiation throughout the year will be 651.2 W/m^2 . From Fig. 2, obviously that the average solar radiation in Kuching is almost consistent every month, which means that it is suitable to implement solar energy.

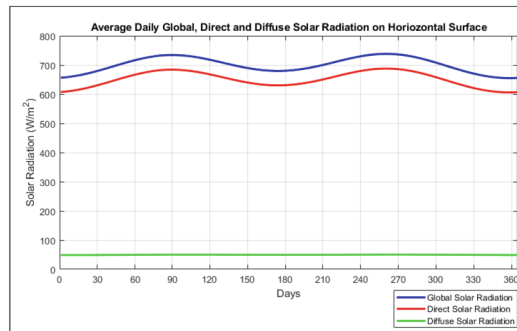


Fig. 1. Average daily solar radiation on the horizontal surface

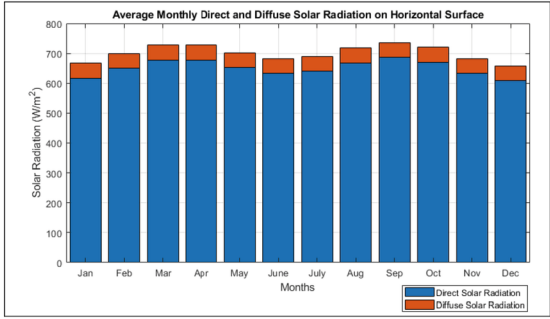


Fig. 2. Average monthly solar radiation on the horizontal surface

4.2 Solar Dish Collector

The yearly average solar radiation is being used to simulate the thermal efficiency and useful heat collected, as shown in Fig. 3 and Fig. 4. Based on Fig. 3, the efficiency of the solar dish collectors will decrease when the temperature of the wall temperature increases. This is because the amount of heat loss will increase when the temperature is high as a large amount of heat is concentrating at a point. Moreover, when the thermal efficiency of the solar dish collector decreases, the amount of energy that can be collected will reduce too (Fig. 4). When the wall temperature is at 540 °C or 813 K, the thermal efficiency and the amount of heat collected will be 81.66% and 17.65 kW, respectively.

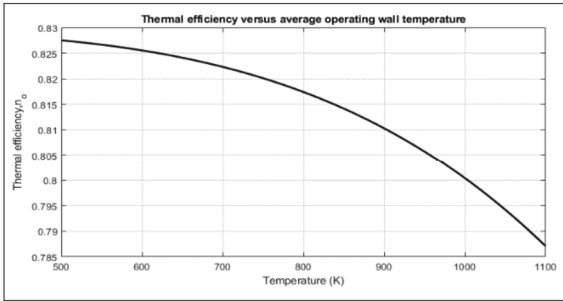


Fig. 3. Thermal efficiency versus average operating wall temperature

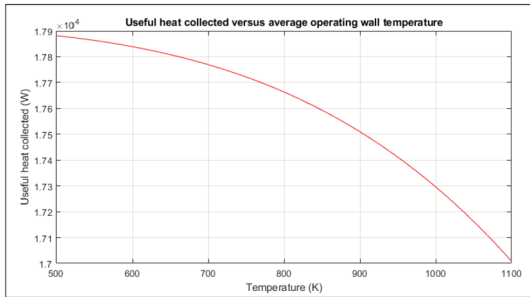


Fig. 4. Useful heat collected versus average operating wall temperature

4.3 Thermal Energy Storage with Phase Change Material

Referring to Fig. 5, the temperature change behavior of the PCM is split into three different regions. In the first region, the PCM will receive heat from the heat transfer fluid and start to increase from the initial temperature (500 °C) until it reaches the melting point (542 °C). In the second region, the phase change of the PCM starts, and it changes from solid to liquid. The temperature remains constant at (542 °C) throughout this region. Finally, in the third region, the temperature of PCM continues to increase until it reaches the set-point temperature (580 °C) and the PCM is fully melted.

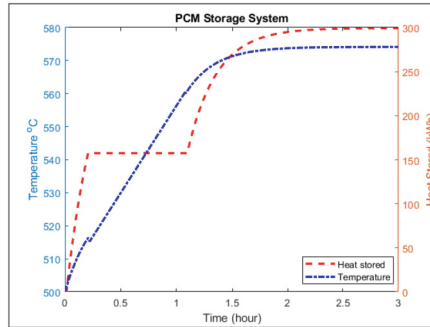


Fig. 5. Temperature and energy storage changes in PCM storage

4.4 Number of Solar Dish Collectors Needed

Since the total power needed for the power plant is 210 MW, and each solar dish collector can collect up to 17.65 kW on average, 11901 solar dish collectors are required. Besides, assuming that another 210 MW of energy will be stored in the TES, the total number of solar dish collectors needed is 23802 pieces.

5 Validation

The validation of the solar radiation model and solar dish collectors will be done with other sources and references. The solar radiation model has been validated by the research done by Tabassum, et al. [20]. They measured the solar radiation in Kuching by using a light meter, and the result shows that the average solar radiation is 636.16 W/m² which is similar to simulated results (651.2 W/m²).

For the solar dish collectors, the validation was done with Wu, et al. [16] and Moradi and Mehrpooya [6]. Based on Fig. 6, the thermal efficiency of the designed solar dish collector in this research is very similar to others.

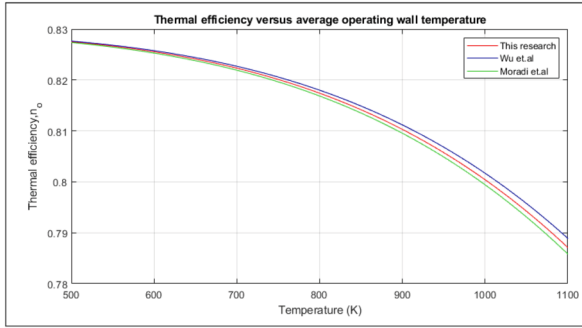


Fig. 6. Validation for thermal efficiency of solar dish collector

6 Research Limit and Future Work

The limitations faced in this research are the constraints in designing a TES system with PCM. There are a lot of parameters lacking proper data, and rough assumptions need to be made. Besides, the selection of a suitable TES from other research papers is also hard to be done as most of the current research is based on low temperatures. So, more research can be carried out on designing a proper TES system with PCM to obtain better a result.

7 Conclusion

In conclusion, this research proves that it is possible to implement solar dish collectors in Sejingkat Power Plant, Kuching, Malaysia. This is because the simulated result shows that the yearly averagely solar radiation in Kuching is up to 651.2 W/m^2 . With the high solar radiation, each of the designed solar dish collectors can collect 17.65 kW of heat, and its efficiency is up to 81.66%. A thermal energy storage system with phase change materials can also be implemented to store the heat energy. A total amount of 23802 solar dish collectors is needed to harness enough amount of solar energy for both the power plant and thermal energy storage system. However, deeper research on the design of TES needs to be carried out to obtain a result with higher accuracy.

References

1. Afrouzi, H.N., et al.: Sizing and economic analysis of stand-alone hybrid photovoltaic-wind system for rural electrification: a case study Lundu, Sarawak. *Clean. Eng. Technol.* **4**, 100191 (2021)
2. Hafez, A.Z., Soliman, A., El-Metwally, K.A., Ismail, I.M.: Design analysis factors and specifications of solar dish technologies for different systems and applications. *Renew. Sustain. Energy Rev.* **67**, 1019–1036 (2017). <https://doi.org/10.1016/j.rser.2016.09.077>
3. Khatib, T., Elmenreich, W.: *Modeling of Photovoltaic Systems Using MATLAB: Simplified Green Codes*, pp. 213–217. Wiley, New York (2016). <https://doi.org/10.1002/9781119118138.index>

4. Affandi, R., Ab Ghani, M.R., Ghan, C.K., Pheng, L.G.: The impact of the solar irradiation, collector and the receiver to the receiver losses in parabolic dish system. *Procedia-Soc. Behav. Sci.* **195**, 2382–2390 (2015). <https://doi.org/10.1016/j.sbspro.2015.06.220>
5. Günther, M., Shahbazfar, R.: Advanced CSP teaching materials: Chapter 7 solar dish technology. In: *EnerMENA*, DLR (2016)
6. Moradi, M., Mehrpooya, M.: Optimal design and economic analysis of a hybrid solid oxide fuel cell and parabolic solar dish collector, combined cooling, heating and power (CCHP) system used for a large commercial tower. *Energy* **130**, 530–543 (2017). <https://doi.org/10.1016/j.energy.2017.05.001>
7. Affandi, R., Pheng, L., Ab Ghani, M.R., Gan, C.: The effects of solar irradiance, reflecting material and intercept factor to the solar power intercepted by receiver 1kW parabolic dish. *Appl. Mech. Mat.* **785**, 581–585 (2015). <https://doi.org/10.4028/www.scientific.net/AMM.785.581>
8. Wu, S.-Y., Xiao, L., Cao, Y., Li, Y.-R.: Convection heat loss from cavity receiver in parabolic dish solar thermal power system: a review. *Sol. Energy* **84**(8), 1342–1355 (2010). <https://doi.org/10.1016/j.solener.2010.04.008>
9. Sarbu, I., Sebarchievici, C.: A comprehensive review of thermal energy storage. *Sustainability* **10**(1) (2018). <https://doi.org/10.3390/su10010191>
10. AS Fleischer 2015 Types of PCMs and their selection Eds Thermal Energy Storage Using Phase Change Materials Fundamentals and Applications SpringerBriefs in Applied Sciences and Technology SAST Springer Cham 37 47 https://doi.org/10.1007/978-3-319-20922-7_3
11. Gil, A., et al.: State of the art on high temperature thermal energy storage for power generation. Part 1—concepts, materials and modellization. *Renew. Sustain. Energy Rev.* **14**(1), 31–55 (2010). <https://doi.org/10.1016/j.rser.2009.07.035>
12. Kuching Climate (Malaysia). CLIMATE-DATA.ORG. <https://en.climate-data.org/asia/malaysia/kuching/kuching-5122/>. Accessed April 30 2021
13. Leong, H.Y., Ong, D.E.L., Sanjayan, J.G., Nazari, A.: Suitability of Sarawak And Gladstone Fly Ash to produce geopolymers: a physical, chemical, mechanical, mineralogical and microstructural analysis. *Ceram. Int.* **42**(8), 9613–9620 (2016). <https://doi.org/10.1016/j.ceramint.2016.03.046>
14. Pavlovic, S., Bellos, E., Le Roux, W.G., Stefanovic, V., Tzivanidis, C.: Experimental investigation and parametric analysis of a solar thermal dish collector with spiral absorber. *Appl. Thermal Eng.* **121**, 126–135 (2017). <https://doi.org/10.1016/j.applthermaleng.2017.04.068>
15. Ebrahimi, A., Ghorbani, B., Lohrasbi, H., Ziabasharhagh, M.: Novel integrated structure using solar parabolic dish collectors for liquid nitrogen production on offshore gas platforms (exergy and economic analysis). *Sustain. Energy Technol. Assess.* **37**, 100606 (2020). <https://doi.org/10.1016/j.seta.2019.100606>
16. Wu, S.-Y., Xiao, L., Cao, Y., Li, Y.-R.: A parabolic dish/AMTEC solar thermal power system and its performance evaluation. *Appl. Energy* **87**(2), 452–462 (2010). <https://doi.org/10.1016/j.apenergy.2009.08.041>
17. Jacob, R., Liu, M., Sun, Y., Belusko, M., Bruno, F.: Characterisation of promising phase change materials for high temperature thermal energy storage. *J. Energy Storage* **24**, 100801 (2019). <https://doi.org/10.1016/j.est.2019.100801>
18. Liu, M., et al.: Review and characterisation of high-temperature phase change material candidates between 500 C and 700 °C. *Renew. Sustain. Energy Rev.* **150**, 111528 (2021). <https://doi.org/10.1016/j.rser.2021.111528>
19. Dadak, A., Mehrpooya, M., Kasaean, A.: Design and development of an innovative integrated structure for the production and storage of energy and hydrogen utilizing renewable energy. *Sustain. Energy Technol. Assess.* **45**, 101123 (2021). <https://doi.org/10.1016/j.seta.2021.101123>
20. Tabassum, M., Kashem, S., Ahmed, J.: Feasibility study of solar power system in residential area **5**, 10–17 (2020)



Modelling the Performance Efficiency of Construction Companies in Malaysia Using Data Envelopment Analysis

Shun Jinn Lim, Weng Hoe Lam^(✉), and Weng Siew Lam

Department of Physical and Mathematical Science, Faculty of Science, Universiti Tunku Abdul Rahman, Kampar Campus, Jalan Universiti, Bandar Barat, 31900 Kampar, Perak, Malaysia
whlam@utar.edu.my

Abstract. Construction industry is a central of economic contributor across all countries world widely. As construction sector is one of the income contributions for economic expansion in Malaysia, therefore this paper aims to model and assess the performance efficiency of the construction sector companies using Data Envelopment Analysis (DEA) model. The results of this study show that 9 construction companies had been categories as efficient companies which achieve efficiency score of 1.00, i.e.: FAJAR, HOHUP, KERJAYA, MUHIBBAH, PEB, SUNCON, TSRCAP, ZECON and ZELAN. Then the potential improvement had been proposed on the inputs and outputs according to the best possible solution of DEA model so that the inefficient companies can be revamped to efficient companies.

Keywords: Construction companies · Data envelopment analysis · Linear programming model · Inputs · Outputs

1 Introduction

Construction industry is a central of economic contributor across all countries world widely. According to Twelfth Malaysia Plan, Malaysia Gross Domestic Product (GDP) aimed to achieve the average 4.5% to 5.5% within the period of 2021 to 2025 [1]. Malaysia is a developing country, and construction sector is one of the backbones of economic development. In recent year, said year 2021, Construction Industry Development (CIDB) Malaysia had launched Construction 4.0 Strategi Plan that involved in 4.0 Industry Evolution. The integration technologies with construction sector will help to robust the economic in Malaysia, such that the contribution of GDP growth as well as offering job opportunities in different areas of expertise toward high income country [2]. Bursa Malaysia was set up in year 1930 and formally named as Kuala Lumpur Exchange Malaysia (KLSE). Among in ASEAN, Bursa Malaysia one of the largest bourses, providing chances for company, government and related group to sell securities through a range of exchange-related products and services.

2 Literature Review

Bursa Malaysia play an important role in economic Malaysia as a bridge between companies, governments and other clients and holders as well as consumers to provide a variety of exchange related services and products in order to sell securities to the investing public [4]. Under equities prices, there are six markets to be chosen, i.e.: main market, ACE market, LEAP market, Structured Warrants, ETF and bond. The reason that choosing main market because the companies that listed are the companies well-establishes if compare to ACE and LEAP market.

COVID-19 outbreak gave the bad impact to the economic Malaysia include construction sector. Implementation of Moving Control Order on 11 March 2020, construction industry as a non-essential sector and all of the construction projects were force to fully close down during the period announced by government. According to [4], the construction industry has experienced a wide range of difficulties, such as unemployment, time constraints, interrupted revenue streams, deferred licences, travel bans, serious health and safety concerns, and labour and equipment shortages as well as other possible issues. All of these difficulties have had an impact on the timely completion of projects in construction sector [5–8].

The term of efficiency generally gives the meaning on efficient operation as measured by a comparison of production with cost [9]. One of the popular measurement tools to identify efficiency is Data Envelopment Analysis (DEA). The used of DEA traditionally invented by [10] for non-profit organization to compute the efficiency through the ratio of varied inputs and outputs. This benefited for the organization to understand their management performance, either in term of financial, or human resources, etc. The stabilization on the application of DEA were widely used in bank sector, education, agricultures, stock market, etc. [11–23].

Application on DEA in construction industry by [24] to evaluate the efficiency of construction sites by obtaining the result that the primary variable that correlates with the effectiveness of building sites is the quantity of incidents that occur there, which is the output of the DEA framework. A study on DEA model integrated with Distance friction minimization (DFM) method and target-oriented (TO) approach for the Regional Construction in China had been done by [25] with the findings showed that inefficient allocation and use of crucial resources is to blame for the uneven performance of regional construction productive efficiency. A research paper brought about the dominant of DEA model as benchmarking tool as well as provides for the determination of indicator target values [11]. Other relevant studies on application of DEA in construction industry can be found in [26–30]. Due to lacking of the study on the efficiency of construction sector in Malaysia, as construction sector as one of the income contributions for economic expansion in Malaysia, therefore this paper aims to examine the efficiency of the construction sector companies in year 2019 using Data Envelopment Analysis (DEA) with BCC Model.

3 Data and Methodology

Data Envelopment Analysis (DEA) was further established by [10] after first proposed by [31]. DEA is a linear programming model that under categories non-parametric method as does not require any specified sample size and assumption of study yield to be made. It is a very useful ranking method to financial study, i.e., financial ratio analysis which only require in ordinal data to perform the measurement of efficiency for the decision-making unit (DMU) that desired to investigate support by efficiency score between the range from 0 to 1. By obtaining the efficiency score equal this means that the outstanding of particular DMU. In this study, the data were extracted via the company annual report in each of the year as shown in the Bursa Malaysia. Income statement from each company in the construction sector under the categories of main market had been extracted, hence the data is considered reliable. A total of 51 companies in year 2019 are used in this study for the efficiency investigation which adopted three inputs: debt to assets ratio, dept to equity ratio and current ratio; three outputs: earnings per share, return on equity and return assets. An optimization software, namely LINGO helped to obtain the results for in this study. Deployment of BBC output maximization-oriented model which proposed by [33,34,35] in this study as shown in below:

$$h_k = \sum_{r=1}^s u_r y_{rk} + \alpha \tag{1}$$

Subject to

$$\sum_{i=1}^m v_i x_{ij} - \sum_{r=1}^s u_r y_{rj} - \alpha \geq 0; j = 1, 2, 3, \dots, n \tag{2}$$

$$\sum_{i=1}^m v_i x_{ik} = 1 \tag{3}$$

$$u_r, v_i \geq \varepsilon; r = 1, \dots, s; i = 1, \dots, m. \tag{4}$$

where

- h_k is relative efficiency of DMU_k.
- s is the number of outputs.
- u_r is the weights to be determined for output r .
- m is the number of inputs.
- v_i is the weights to be determined for input i .
- n is the number of entities.
- ε is the positive value.
- α is the free variable.

4 Empirical Results

The efficiency ranking score for each construction company in year 2019 as presented at Fig. 1. Total 9 out of 51 construction companies had been categories as efficient companies which achieve efficiency score achieve at 1, i.e.: FAJAR, HOHUP, KERJAYA, MUHIBBAH, PEB, SUNCON, TSRCAP, ZECON and ZELAN. Meanwhile the other 47 companies are grouped in inefficient companies as obtained the efficiency score less than 1.

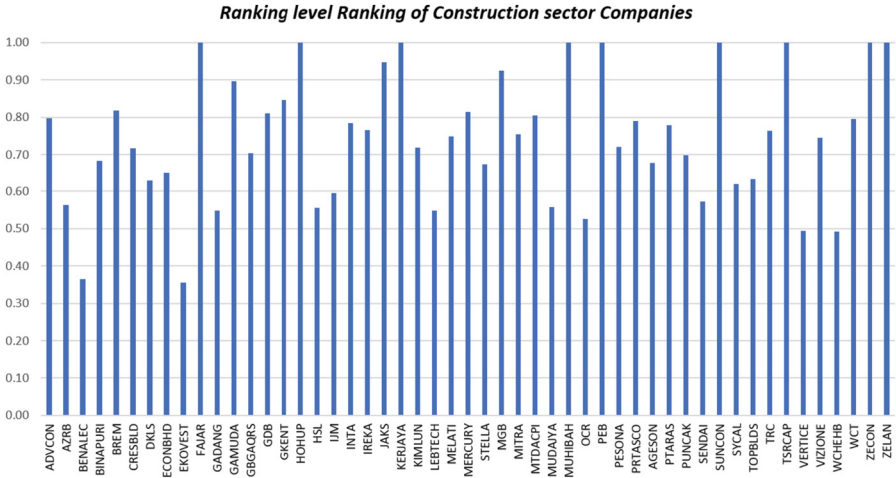


Fig. 1 Ranking level Ranking of Construction sector Companies

The current efficiency companies with the optimal coefficient are specifically employed as the reference set as the criterion measurement in order to convert those inefficient companies into efficient companies. For examples, the benchmarking of the efficient companies: MUHIBBAH, SUNCO and TSRCAP, as reference sets, with coefficients of 0.6055606, 0.2558982 and 0.1385412 based on the best solution of the DEA model, is necessary for ADVCON to obtain the efficiency score of 100%.

The potential improvement on three inputs and three outputs had been proposed according to the best possible solution of DEA model so that the inefficient companies can be revamp to efficient companies. For instance, ADVCON had been proposed to increase the company outputs and decrease the inputs (Fig. 2).

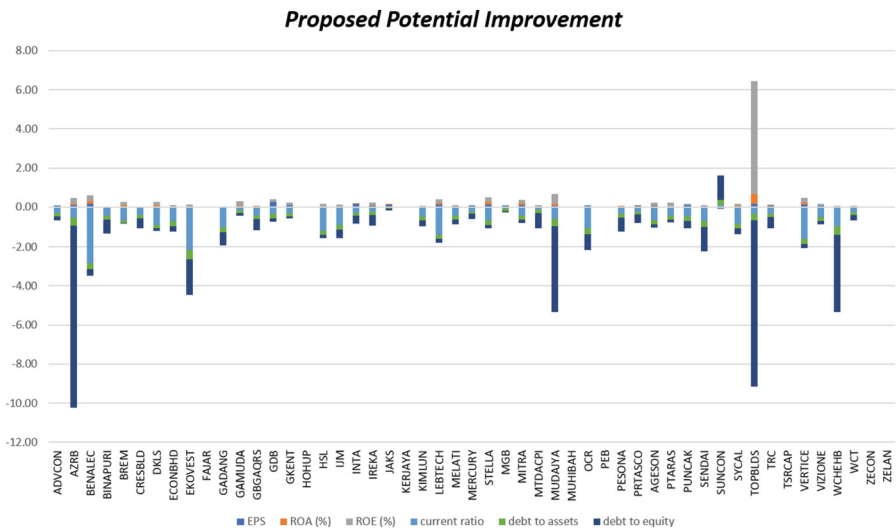


Fig. 2 Proposed Potential Improvement

5 Conclusion

DEA is a non-parametric linear programming method and it is a very useful ranking method on the financial study for decision making unit. As construction sector as one of the income contributions for economic expansion in Malaysia, the construction firms should be aware of their existing financial standing. In this study, 9 companies had been evaluated as efficient companies, which are FAJAR, HOHUP, KERJAYA, MUHIBBAH, PEB, SUNCON, TSRCAP, ZECON and ZELAN. For inefficient companies, the potential improvement on the inputs and outputs had been proposed so the companies can rearrange their resources. This study is notable since it successfully estimated the potential for improvement for construction sector businesses listed in Bursa Malaysia for the year 2019.

Acknowledgements. This study is supported by Universiti Tunku Abdul Rahman, Malaysia.

References

1. Economic Planning Unit. Rancangan Malaysia Kedua Belas (2021). <https://rmke12.epu.gov.my/bm>
2. CIDB. CIDB Malaysia (2021). <https://www.cidb.gov.my/en/construction-info/technology/ir40-construction>
3. What Is the Role of Bursa Malaysia? Ask Media Group (2020). <https://www.reference.com/business-finance/role-bursa-malaysia-14492130a213f99b>
4. Mohsen, A., et al.: Impact of the COVID-19 pandemic on construction industry in Malaysia. In: 2021 3rd International Sustainability and Resilience Conference: Climate Change, November, pp. 237–241 (2021). <https://doi.org/10.1109/IEEECONF53624.2021.9667984>
5. Biswas, A., et al.: The impact of COVID-19 in the construction sector and its remedial measures. *J. Phys. Conf. Ser.* **1797**(1) (2021). <https://doi.org/10.1088/1742-6596/1797/1/012054>
6. Zamani, S.H., Rahman, R.A., Fauzi, M.A., Yusof, L.M.: Effect of COVID-19 on building construction projects: Impact and response mechanisms. *IOP Conf. Ser. Earth Environ. Sci.* **682**(1) (2021). <https://doi.org/10.1088/1755-1315/682/1/012049>
7. Jagun, Z.T., Nyakuma, B.B., Daud, D., Samsudin, S.: Property development during the COVID-19 pandemic: challenges and outlook in Malaysia. In: *Environmental Science and Pollution Research International*, 1–10. Advance Online Publication (2022). <https://doi.org/10.1007/s11356-021-18378-2>
8. Akman, S., Zakaria, S., Kaur, A., Singh, M.: Impacts of Covid-19 outbreak on civil engineering activities in the Malaysian construction industry: a review. *Jurnal Kejuruteraan*, **33**(3), 477–485 (2021). <https://doi.org/10.17576/jkukm-2021-33>
9. Merriam-Webster (n.d.) Efficiency. In: Merriam-Webster.com dictionary. Retrieved July 15 (2022). <https://www.merriam-webster.com/dictionary/efficiency>
10. Charnes, A., Cooper, W.W., Rhodes, E.: Measuring the efficiency of decision making units. *Eur. J. Oper. Res.* **2**(6), 429–444 (1978)
11. Horváthová, J., Mokrišová, M., Vrábliková, M.: Benchmarking—a way of finding risk factors in business performance. *J. Risk Financ. Manag.* **14**(5), 221 (2021). <https://doi.org/10.3390/jrfm14050221>
12. Rajasekhar, R.: Financial Performance Evaluation of Construction Industries. *Int. J. Sci. Res. Publ.* **7**(1), 157–175 (2017)

13. Syuhaida, I., Aminah, Y.: Benchmarking the performance of Malaysia's construction industry. *Manag. Res. Pract.* **1**(1), 1–13 (2009)
14. YougbarÃ©, J.W.: Analysis of agricultural performance in burkina faso using data envelopment analysis. *Eur. J. Pure Appl. Math.* **14**(2), 366–379 (2021). <https://doi.org/10.29020/nybg.ejpam.v14i2.3888>
15. da Silva e Souza, G., Belchior Silva Moreira, T., Gomes, E.G.: Potential improvement of agricultural output for major producers based on DEA efficiency measurements. *Pesquisa Operacional* **31**(1), 79–93 (2011). <https://doi.org/10.1590/s0101-74382011000100006>
16. Fenyves, V., Tarnóczy, T., Zsidó, K.: Financial performance evaluation of agricultural enterprises with DEA method. *Procedia Econom. Finance* **32**(15), 423–431 (2015). [https://doi.org/10.1016/S2212-5671\(15\)01413-6](https://doi.org/10.1016/S2212-5671(15)01413-6)
17. Badoi, A.C.: Risk return efficiency: a data envelopment analysis on the cross section of stock returns. November, 1–43 (2016)
18. Ferus, A.: The DEA method in managing the credit risk of companies. *Ekonomika*, 109–118 (2008)
19. Hassan, N., Siew, L.W., Shen, S.Y.: Portfolio decision analysis with maximin criterion in the Malaysian stock market. *Appl. Math. Sci.* **6**(109–112), 5483–5486 (2012). <http://www.scopus.com/inward/record.url?eid=2-s2.0-84867320648&partnerID=40&md5=a02af47859f152c726546ec0dbf31a0e>
20. Jiang, H., He, Y.: Applying data envelopment analysis in measuring the efficiency of Chinese listed banks in the context of macroprudential framework. *Mathematics* **6**(10) (2018). <https://doi.org/10.3390/math6100184>
21. Onder, E., Altintas, A.T.: Financial Performance Evaluation of Turkish Construction Companies in Istanbul Stock Exchange (BIST). *Int. J. Acad. Res. Account. Finan. Manag. Sci.* **7**(3), 108–113 (2017). <https://doi.org/10.6007/ijarafms/v7-i3/3237>
22. Gökşen, Y., Doğan, O., Özkarabacak, B.: A data envelopment analysis application for measuring efficiency of university departments. *Procedia Econ. Finan.* **19**(15), 226–237 (2015). [https://doi.org/10.1016/s2212-5671\(15\)00024-6](https://doi.org/10.1016/s2212-5671(15)00024-6)
23. Visbal-Cadavid, D., Martínez-Gómez, M., Guijarro, F.: Assessing the efficiency of public universities through DEA. A case study. *Sustainability (Switzerland)* **9**(8), 1–19 (2017). <https://doi.org/10.3390/su9081416>
24. Nahangi, M., Chen, Y., McCabe, B.: Data envelopment analysis (Dea) for safety-based efficiency evaluation of construction sites (2018)
25. Luo, M., Fan, H.: A target-oriented data envelopment analysis for regional construction efficiency improvement in Mainland China, June, pp. 298–309 (2019)
26. Chiu, C., Wang, M.: An integrated DEA-based model to measuring financial performance of construction companies (2011)
27. Lam, W.S., Lam, W.H., Jaaman, S.H., Liew, K.F.: Performance evaluation of construction companies using integrated entropy–fuzzy VIKOR model. *Entropy* **23**(3):320 (2021). <https://doi.org/10.3390/e23030320>
28. Riko, H., Pramudya, P.U.: Efficiency measurement of building construction sector companies listed on Indonesia stock exchange: stochastic frontier analysis approach. *Asian J. Manage. Sci. Educ.* **9**(2), 1–15 (2020)
29. Gaurav, R.D., Abhay, M.J.: Evaluation of Indian construction companies using financial tool. *Int. J. Sci. Technol. Eng.* **1**(11), 210–216 (2015)
30. Chiu, C.Y., Wang, M.W.: An integrated DEA-based model to measuring financial performance of construction companies. *WSEAS Trans. Bus. Econ.* **8**(1), 1–15 (2011)
31. Farrell, M.J.: The measurement of productive efficiency. *J. Roy. Stat. Soc. Ser. (General)* **120**(3), 253–290 (1957)

32. Ling, O.P.K., A. A.: Data envelopment analysis for stocks selection on Bursa Malaysia. *Arch. Appl. Sci. Res.* 2(5): 11–35 (2010); Martić, M., Novaković, M. and Baggia, A. (2009).
33. Martić, M., Novaković, M., Baggia, A.: Data envelopment analysis - basic models and their utilization. *Organizacija* 42(2) (2009). <https://doi.org/10.2478/v10051-009-0001-6>



Analysis on the Performance of Technology Companies Using TOPSIS Model

Kah Fai Liew, Weng Siew Lam^(✉), and Weng Hoe Lam

Department of Physical and Mathematical Science, Faculty of Science, Universiti Tunku Abdul Rahman, Kampar Campus, Jalan Universiti, Bandar Barat, 31900 Kampar, Perak, Malaysia
lamws@utar.edu.my

Abstract. Information Technology (IT) plays a central role in the information age. IT is a combination of communication technology and computer technology. The advancement and development of IT is a great achievement for a nation that is beneficial to society, organizations and all the people over the world. IT can offer a good opportunity for companies to introduce new products and services quickly, possess the potential to reach more customers and collaborate with business partners and global suppliers. This study is conducted to determine the financial performances of the IT companies with the proposed Technique for Order of Preference by Similarity to Ideal Solution (TOPSIS) model. Moreover, the ranking of the companies is identified according to their performances. The findings demonstrate AAPL outperformed the other companies in terms of financial performance. This study highlights the significance of the assessment, comparison and ranking of the financial performances of IT companies by using the proposed TOPSIS model.

1 Introduction

Information Technology (IT) is referred to a set of equipment and techniques which are created in order to optimize information systems. In the present age implementation, development and maintenance of information systems is an essential business process in IT management. In the current era the use of new technologies and information systems, IT is quite crucial to improve the efficiency of the organization and hence, it will accelerate the pace to achieve the company's ultimate goals.

IT is very important to determine the success or failure of a knowledge management system [1]. Advanced knowledge management in IT can enhance the knowledge transfer speed as well as the organization's domain of knowledge. According to Shirazi et al. [2], IT involves various communication media and innovations that connect individuals and information systems. The development of IT companies should be greatly focused on by the government since IT has become an integral and vital part of every business plan. Therefore, the performance of the IT companies can be analyzed to order to understand the status of the companies.

Technique for Order of Preference by Similarity to Ideal Solution (TOPSIS) model compares the decision alternatives to the negative ideal solution (NIS) and positive ideal solution (PIS). TOPSIS model is a useful and effective tool in solving the multi-criteria

decision-making (MCDM) problems [3–6]. MCDM problems involve determining the best decision alternative by considering multiple decision criteria [7–23]. TOPSIS model aims to identify the alternative that has the longest separation distance from the NIS and the least distance to the PIS [24–26]. The ranking of the alternatives will be constructed according to their relative closeness to the ideal solution [27].

In this study, TOPSIS model is proposed to analyze the financial performance of the IT companies listed in Dow Jones Industrial Average (DJIA). The aim of this paper is to analyze and compare the IT companies’ financial performance with the proposed conceptual framework based on TOPSIS model. Moreover, the ranking of the companies is determined. The organization for the remainder of this paper is as follows. The data and methodology that is used in this study are enumerated in Sect. 2. Next, Sect. 3 presents the findings of this study. The last section of this paper is ended with a conclusion.

2 Data and Methodology

The data of this study consists of financial ratios such as DER, DAR, ROE, ROA, EPS and CR [28–30] for the period of 2015–2020. The decision alternatives in this study are AAPL, CSCO, IBM, MSFT and CRM. TOPSIS is a MCDM model that has been proposed to tackle various problems of decision making [31–38]. The TOPSIS model can be expressed as follows [39, 40]:

Step 1: Calculation of the weighted normalized decision matrix as follows:

$$v_{ij} = w_j \times r_{ij}, \quad j = 1, 2, 3, \dots, n; \quad i = 1, 2, 3, \dots, m \tag{1}$$

where w_j = weights of the criterion j and r_{ij} is the normalized decision matrix.

Step 2: Computation of the alternatives’ separation distance from the PIS (S^+) and NIS (S^-).

$$S_i^+ = \sqrt{\sum_{j=1}^n (v_j^+ - v_{ij})^2}, \quad i = 1, 2, 3, \dots, m \tag{2}$$

$$S_i^- = \sqrt{\sum_{j=1}^n (v_j^- - v_{ij})^2}, \quad i = 1, 2, 3, \dots, m \tag{3}$$

where $v_j^+ = \{(\max v_{ij} | i \in I), (\min v_{ij} | i \in I')\}$ and $v_j^- = \{(\min v_{ij} | i \in I), (\max v_{ij} | i \in I')\}$

Step 3: Determination of the alternatives’ relative closeness coefficient respect to the ideal solutions (s_{iw}).

$$s_{iw} = \frac{s_i^-}{(s_i^+ + s_i^-)}, \quad 0 \leq s_i \leq 1 \tag{4}$$

Step 4: The decision alternatives are ranked according to their s_{iw} . The alternative with the biggest value of s_{iw} will be the best decision company. Ranking is important to the companies for benchmarking purpose [41–43].

3 Empirical Results

Table 1 depicts the weighted normalized decision matrix.

Table 1. Weighted Normalized Decision Matrix

Company	DER	DAR	ROE (%)	ROA (%)	EPS	CR
AAPL	0.0594	0.0830	0.1012	0.1215	0.0411	0.0520
CSCO	0.0299	0.0628	0.0371	0.0593	0.0285	0.0999
IBM	0.1449	0.0962	0.1131	0.0546	0.1500	0.0473
MSFT	0.0461	0.0816	0.0580	0.0805	0.0524	0.1071
CRM	0.0151	0.0320	0.0033	0.0067	0.0054	0.0376

Figure 1 and Fig. 2 demonstrate the PIS and NIS for the financial ratios, respectively.

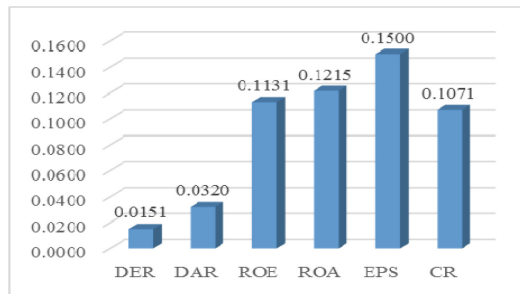


Fig. 1. PIS for the financial ratios.

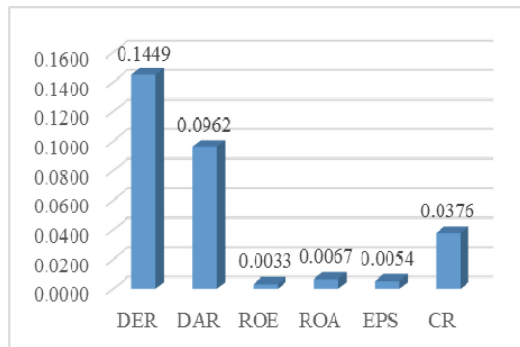


Fig. 2. NIS for the financial ratios.

As can be seen from Fig. 1 and Fig. 2, the companies may know their strengths and weaknesses in their financial ratios. Hence, the companies can maintain their strengths

and improve on their weaknesses based on the PIS and NIS. The separation distance of the companies to the PIS is presented in Fig. 3, whereas Fig. 4 shows the separation distance of the companies from the NIS.

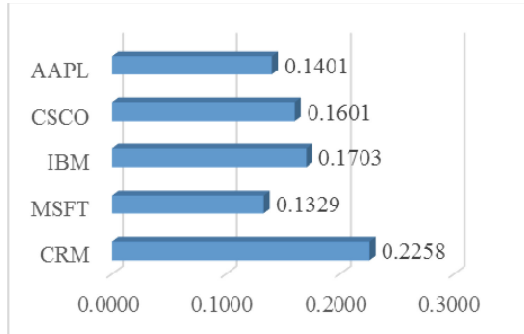


Fig. 3. Separation distance of the companies to the PIS.

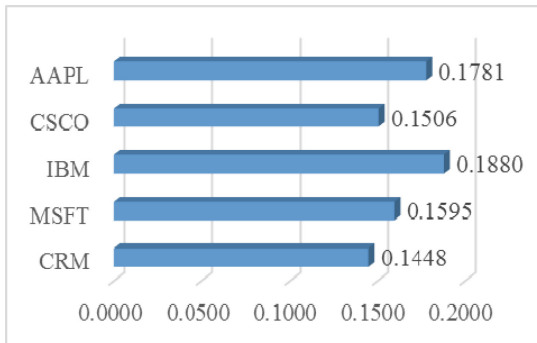


Fig. 4. Separation distance of the companies from the NIS.

According to Fig. 3, the distance from the PIS for MSFT is 0.1329, closely followed by AAPL (0.1401), CSCO (0.1601) and lastly IBM (0.1703). From here, it can be concluded that MSFT is closest to the PIS. Therefore, MSFT is identified as a well-performed company. On the other hand, the separation distance of the companies from the NIS is calculated and presented in Fig. 4. The best company will have the longest distance from the NIS, whereas the separation distance for the underperformed company will be the shortest. IBM has the longest distance of 0.1880 from the NIS, followed by AAPL (0.1781), MSFT (0.1595), CSCO (0.1506) and finally CRM (0.1448). Table 2 presents the overall performance of IT Companies.

From Table 2, AAPL achieved the highest s_{iw} (0.5594), hence AAPL obtained the first ranking. The second ranking is achieved by MSFT (0.5454), followed by IBM (0.5247), CSCO (0.4846) and finally CRM (0.3908).

Table 2. Performance of IT Companies Listed in DJIA

Company	Relative Closeness to the Ideal Solution (s_{iw})	Ranks
AAPL	0.5598	1
CSCO	0.4846	4
IBM	0.5247	3
MSFT	0.5454	2
CRM	0.3908	5

4 Conclusions

This study aims to evaluate the financial performance of IT companies with the proposed TOPSIS model. The findings of this paper indicate that the best company is AAPL with the highest s_{iw} , followed by MSFT, IBM, CSCO and CRM. Hence, AAPL achieved the first ranking in this study. The other companies can take the well-performed company such as AAPL to be a benchmark for continuous improvement in the future. For future research, the financial performance of the firms from various fields can be studied and explored with the proposed TOPSIS model.

Acknowledgments. This study is supported by Universiti Tunku Abdul Rahman, Malaysia.

References

1. Johannessen, J.A., Olaisen, J., Olsen, B.: Mismanagement of tacit knowledge: the importance of tacit knowledge, the danger of information technology, and what to do about it. *Int. J. Inf. Manag. Manag.* **21**, 3–20 (2021)
2. Ghafarian Shirazi, H.R., Qhorbani, M., Afrasyabi, R.: A study on the role and importance of information technology in the establishment of knowledge management in training and education. *Eur. Online J. Nat. Soc. Sci.* **2**, 2262–2270 (2014)
3. Lam, W.S., Lam, W.H., Liew, K.F., Chen, J.W.: An empirical study on the preference of fast food restaurants in Malaysia with AHP-TOPSIS model. *J. Eng. Appl. Sci.* **13**, 3226–3231 (2018)
4. Lam, W.S., Bakar, M.A., Lam, W.H., Liew, K.F.: Multi-criteria decision making in the selection of mobile network operators with AHP-TOPSIS model. *J. Eng. Appl. Sci.* **12**, 6382–6386 (2017)
5. Lam, W.S., Lam, W.H., Liew, K.F.: Data analysis on the performance of technology sector in Malaysia with Entropy-TOPSIS model. *Commun. Comput. Inf. Sci.* **886**, 194–203 (2018)
6. Bhattacharjee, P., Debnath, A., Chakraborty, S., Mandal, U.K.: Selection of optimal aluminum alloy using TOPSIS method under fuzzy environment. *J. Intell. Fuzzy Syst.* **32**, 871–876 (2017)
7. Lam, W.S., Liew, K.F., Lam, W.H.: Investigation on the efficiency of financial companies in Malaysia with data envelopment analysis model. *J. Phys. Conf. Ser.* **995**(1), 012021 (2018)
8. Liew, K.F., Lam, W.S., Lam, W.H.: An empirical evaluation on the efficiency of the companies in Malaysia with data envelopment analysis model. *Adv. Sci. Lett.* **23**(9), 8264–8267 (2017)

9. Lam, W.S., Chen, J.W., Lam, W.H.: Data driven decision analysis in bank financial management with goal programming model. In: Badioze Zaman, H., et al. (eds.) *IVIC 2017. LNCS*, vol. 10645, pp. 681–689. Springer, Cham (2017). https://doi.org/10.1007/978-3-319-70010-6_63
10. Lam, W.S., Lam, W.H., Jaaman, S.H., Liew, K.F.: Performance evaluation of construction companies using integrated Entropy-Fuzzy VIKOR model. *Entropy* **23**(3), 320, 1–16 (2021)
11. Lam, W.H., Lam, W.S., Liew, K.F.: Improvement on the efficiency of technology companies in Malaysia with data envelopment analysis model. In: Badioze Zaman, H., et al. (eds.) *IVIC 2017. LNCS*, vol. 10645, pp. 19–30. Springer, Cham (2017). https://doi.org/10.1007/978-3-319-70010-6_2
12. Lam, W.S., Liew, K.F., Lam, W.H.: An optimal control on the efficiency of technology companies in Malaysia with data envelopment analysis model. *J. Telecommun. Electron. Comput. Eng.* **10**(1), 107–111 (2018)
13. Lam, W.S., Chen, J.W., Lam, W.H.: An empirical study on the selection of fast food restaurants among the undergraduates with AHP model. *Am. J. Inf. Sci. Comput. Eng.* **2**(3), 15–21 (2016)
14. Lam, W.S., Lam, W.H., Liew, K.F., Bakar, M.A., Sim, J.X.: Analysis on the e-learning method in Malaysia with AHP-VIKOR model. *Int. J. Inf. Educ. Technol.* **11**(2), 52–58 (2021)
15. Lam, W.S., Leong, W.B., Lam, W.H.: Selection of mobile network operator based on multi-criteria decision making model using analytic hierarchy process. *Math. Stat. J.* **1**(1), 12–18 (2015)
16. Lam, W.S., Lam, W.H., Bakar, M., Sek, X.Y.: An empirical evaluation on the preference of mobile broadband in Malaysia with analytic hierarchy process model. *Adv. Sci. Lett.* **24**(11), 8573–8577 (2018)
17. Lam, W.S., Lee, W.K., Lam, W.H.: Multi-criteria decision making in job selection problem using analytic hierarchy process model. *Math. Stat. J.* **1**(2), 3–7 (2015)
18. Lam, W.S., Bishan, R.S., Lam, W.H.: An empirical study on the mold machine-tool selection in semiconductor industry with analytic hierarchy process model. *Adv. Sci. Lett.* **23**(9), 8286–8289 (2017)
19. Lam, W.S., Liew, K.F., Lam, W.H.: Performance evaluation of construction companies in Malaysia with entropy-VIKOR model. *Eng. J.* **25**(1), 297–305 (2021)
20. Lam, W.H., Din, M.A., Lam, W.S., Chen, J.W.: Evaluation on the performance of suppliers in Malaysia with TOPSIS model. *J. Fundam. Appl. Sci.* **10**(6S), 406–415 (2018)
21. Lam, W.H., Lam, W.S., Liew, K.F., Wong, S.C.: Data driven decision analysis on the selection of course programmes with AHP-TOPSIS model. *Int. J. Supply Chain Manag.* **7**(4), 202–208 (2018)
22. Lam, W.S., Bishan, R.S., Lam, W.H., Liew, K.F.: An empirical evaluation on the preference of supermarkets with analytic hierarchy process model. *J. Phys. Conf. Ser.* 012037 (2018)
23. Lam, W.S., Bakar, M.A., Lam, W.H., Chen, J.W., Ma, H.L.: Evaluation on the preference of coffee shops among undergraduate students with analytic hierarchy process model. *Int. J. Supply Chain Manag.* **7**(4), 209–215 (2018)
24. Hwang, C.L., Lai, Y.J., Liu, T.Y.: A new approach for multiple objective decision making. *Comput. Oper. Res.. Oper. Res.* **20**, 889–899 (1993)
25. Wang, E.: Benchmarking whole-building energy performance with multi-criteria technique for order preference by similarity to ideal solution using a selective objective-weighting approach. *Appl. Energy* **146**, 92–103 (2015)
26. Guo, S., Zhao, H.: Optimal site selection of electric vehicle charging station by using fuzzy TOPSIS based on sustainability perspective. *Appl. Energy* **158**, 390–402 (2015)
27. Chmielarz, W., Zborowski, M.: Analysis of e-banking websites' quality with the application of the TOPSIS method—a practical study. *Procedia Comput. Sci.* **126**, 1964–1976 (2018)
28. Ong, P.L., Kamil, A.A.: Data envelopment analysis for stocks selection on Bursa Malaysia. *Arch. Appl. Sci. Res.* **2**, 11–35 (2010)

29. Dalfard, V.M., Sohrabian, A., Najafabadi, A.M., Alvani, J.: Performance evaluation and prioritization of leasing companies using the super efficiency data envelopment analysis model. *Acta Polytechnica Hungarica* **9**, 183–194 (2012)
30. Rahmani, I., Barati, B., Dalfard, V.M., Shirkouhi, L.H.: Nonparametric frontier analysis models for efficiency evaluation in insurance industry: a case study of Iranian insurance market. *Neural Comput. Appl. Comput. Appl.* **24**, 1153–1161 (2014)
31. Lam, W.S., Liew, K.F., Lam, W.H.: Evaluation on the financial performance of the Malaysian banks with TOPSIS model. *Am. J. Serv. Sci. Manag.* **4**, 11–16 (2017)
32. Lam, W.S., Liew, K.F., Lam, W.H.: Investigation on the performance of construction companies in Malaysia with Entropy-TOPSIS model. *Earth Environ. Sci.* **385**, 012006 (2019)
33. Lam, W.S., Lam, W.H., Bakar, M.A., Lee, P.F.: Data driven decision analysis on the performance of electronic companies with TOPSIS model. *J. Adv. Inf. Technol.* **13**(1), 61–66 (2022)
34. Liew, K.F., Lam, W.S., Lam, W.H.: Financial network analysis on the performance of companies using integrated Entropy-DEMATEL-TOPSIS model. *Entropy* **24**(8), 1056 (2022)
35. Liew, K.F., Lam, W.S., Lam, W.H.: Financial analysis on the company performance in Malaysia with multi-criteria decision making model. *Syst. Sci. Appl. Math.* **1**, 1–7 (2016)
36. Lam, W.H., Lam, W.S., Liew, K.F.: Performance analysis on telecommunication companies in Malaysia with TOPSIS model. *Indonesian J. Electr. Eng. Comput. Sci.* **13**, 744–751 (2019)
37. Wang, Z., Hao, H., Gao, F., Zhang, Q., Zhang, J., Zhou, Y.: Multi-attribute decision making on reverse logistics based on DEA-TOPSIS: a study of the Shanghai end-of-life vehicles industry. *J. Clean. Prod.* **214**, 730–737 (2019)
38. Triantaphyllou, E., Shu, B., Sanchez, S.N.: Multi-criteria decision making: an operations research approach. *Encyclopedia Electr. Electron. Eng.* **15**, 175–186 (1998)
39. Yue, Z.: TOPSIS-based group decision-making methodology in intuitionistic fuzzy setting. *Inf. Sci.* **277**, 141–153 (2014)
40. Ou, Y., Yi, L., Zou, B., Pei, Z.: The linguistic intuitionistic fuzzy set TOPSIS method for linguistic multi-criteria decision makings. *Int. J. Comput. Intell. Syst.* **11**, 120–132 (2018)
41. Lam, W.S., Lam, W.H., Jaaman, S.H.: Portfolio optimization with a mean-absolute deviation-entropy multi-objective model. *Entropy* **23**(10), 1266 (2021)
42. Lam, W.S., Liew, K.F., Lam, W.H.: Evaluation on the efficiency of healthcare companies in Malaysia with data envelopment analysis model. *SCIREA J. Math.* **1**(1), 95–106 (2016)
43. Lee, P.F., Lam, W.S., Lam, W.H.: Evaluation and improvement of the efficiency of logistics companies with data envelopment analysis model. *Eng. J.* **25**(6), 45–54 (2021)



Diagnosis of Mycobacterium Tuberculosis via K-Means and Canny Edge Detection

Jia Wei Lim¹, Ting Rang Ling¹, Xin Hui Tsen¹, Sarah Jane Kho¹, Hui En Lee¹, Patrick Guda anak Benjamen², Mong How Ooi³, and Hong Siang Chua¹(✉)

¹ Faculty of Engineering, Computing and Science, Swinburne University of Technology Sarawak Campus, 93350 Kuching, Sarawak, Malaysia

hschua@swinburne.edu.my

² Pathology Department, Sarawak General Hospital, Jalan Hospital, 93586 Kuching, Sarawak, Malaysia

³ Department of Paediatrics, Sarawak General Hospital, Jalan Hospital, 93586 Kuching, Sarawak, Malaysia

Abstract. Tuberculosis is one of the leading causes of death with 2,000 death cases in Malaysia each year. This raises the importance of quick and accurate diagnosis of tuberculosis to ensure timely treatment. Most low-middle-income countries, including Malaysia, have been adopting sputum smear microscopy to detect tuberculosis, but such method is time consuming, labour intensive and inaccurate. Other detection methods such as mycobacterium culture and sensitivity test, and chest x-ray offer higher accuracy, but are much more expensive. Therefore, our study employed image processing technique on microscopic image of patients' sputum samples to substitute human labour for rapid and accurate tuberculosis diagnosis. K-means algorithm was used as an image segmentation technique, followed by image classification using Canny Edge Detection algorithm to obtain the bacilli count. The bacilli count per sputum sample was used as a parameter to conduct tuberculosis diagnosis by World Health Organisation standard. The proposed method combining K-means and Canny Edge Detection algorithm achieved 88.9% diagnosis accuracy. On-going work has been carried out to assess the feasibility of utilising Machine Learning Model Builder from ML.net to decide the best algorithm for acid-fast bacilli counting based on the patients' sputum samples training data.

Keywords: canny edge detection · Image processing · k-means · Mycobacterium · Tuberculosis

1 Introduction

Sputum smear microscopy test is a tuberculosis diagnosis test that is carried out on the sputum samples of the patient. Despite being theoretically the most effective diagnosis method of tuberculosis [1], it is inefficient and inaccurate due to reliance on human power which introduces human errors and limitations. Therefore, this research focuses on reducing the reliance of human power in the observation of microscope slides by

utilising computer vision and machine learning, in hopes that they could serve as a reliable and faster solution to increase the efficiency of the sputum smear microscopy test.

Meraj *et al.* [2] reviewed several attempts on diagnosing tuberculosis, which included using a General Regression Neural Network (GRNN) algorithm. The GRNN algorithm used an input pattern consisting of 21 special parameters that are classified into demographic, constitutional symptoms and radiographic findings, achieving diagnosis accuracy of 92.3% [3]. In addition, Santos *et al.* [4] utilised the Artificial Neural Network (ANN) to develop and evaluate the prediction model to diagnose Smear Negative Pulmonary Tuberculosis. The prediction model only considered physical signs and symptoms of the disease. The neural network was implemented using a multilayer feedforward method architecture with Back Propagation and achieved an accuracy of 74%. Temurtas and Tanrikulu [5] reported an attempt to diagnose tuberculosis based on 38 chosen features. The study applied GRNN and Back Propagation algorithms, achieving 93.18% and 93.04% accuracy respectively. Temurtas and Tanrikulu [5] also implemented two different Multilayer Neural Networks (MLNN) model structures which were the Levenberg-Marquardt (LM) and Back Propagation with Momentum (BPwM) for the training. The performance of the MLNN models was accessed using a three-fold cross-validation method and achieved an accuracy of 95.08%.

The work presented in this paper reports an attempt to detect mycobacterium tuberculosis from the microscopic images of the sputum smear slides through image processing by coupling K-means algorithm with the Canny Edge Detection algorithm.

2 Methodology

A. Microscope Image of Patient Sputum Sample

Figure 1 shows a microscope image of the sputum sample that was observed under a microscope with ultraviolet light. The slide was prepared by smearing the sputum sample over an area of 1.5 cm × 2 cm or 2 cm × 3 cm while ensuring the smear is sufficiently thin for light to pass through. The slides are then dried and stained. Malaysia uses the Auramine stain that would require ultraviolet (UV) light to be shone on the slides for the bacilli to glow green. After drying and staining, the slides are then observed under a microscope with UV light. A total of nine sputum samples was prepared and analysed using the proposed image processing technique in this study.

B. K-Means Clustering and Canny Edge Detection

The overall flowchart of the image processing algorithm for mycobacterium tuberculosis detection is shown in Fig. 2. The two main components of the algorithm consisted of image segmentation via K-means algorithm and image classification via Canny Edge Detection algorithm.

The K-means algorithm is a form of unsupervised learning that can be used for clustering purposes via image segmentation [6]. Unsupervised learning is a machine learning technique where the machine's goal is to discover hidden patterns within the data without the help of predetermined labels [6]. Clustering is a method that segments

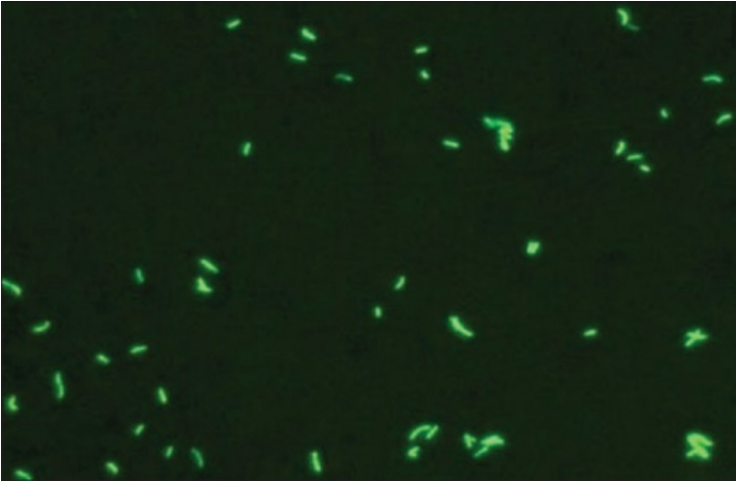


Fig. 1. Microscope image of patient sputum sample with the bacilli glowing green.

an image into a specific number of groups [7]. The members of the group are classified based on the similarity of the members in the group [7]. Figure 3 illustrates the clustering of several data points by groups. The K-means algorithm consists of two main parts, the first part is defining the centroid, k and the second part is classifying each data point based on the similarity of the data to the cluster. The second step is repeated until no points are left in the data set, whereas new centroids, k may need to be recalculated based on the clusters formed throughout the process.

The Canny Edge Detector is a multi-stage algorithm that is used to monitor the number of edges of an object in a picture while suppressing noise [9]. The Canny Edge detector works through four major steps, smoothing, edge direction and location determination, non-maximum suppression, and threshold [9]. Smoothing is done via Gaussian filters, and the edge direction is calculated with the equation for step edge below [10, 11]:

$$G_n = \frac{\delta G}{\delta n} = n \cdot \nabla G \quad (1)$$

In the step edge Eq. (1), G_n is the first derivative of G in the n direction, whereas G is the Gaussian filter [10] and is given in (2).

$$G(x, y) = e^{-\frac{x^2+y^2}{2\sigma^2}} \quad (2)$$

In (2), x, y tells the image coordinates and σ is the standard deviation of the associated probability distribution [10].

For an image g , the direction n is estimated as shown in (3).

$$n = \frac{\nabla(G * g)}{|\nabla(G * g)|} \quad (3)$$

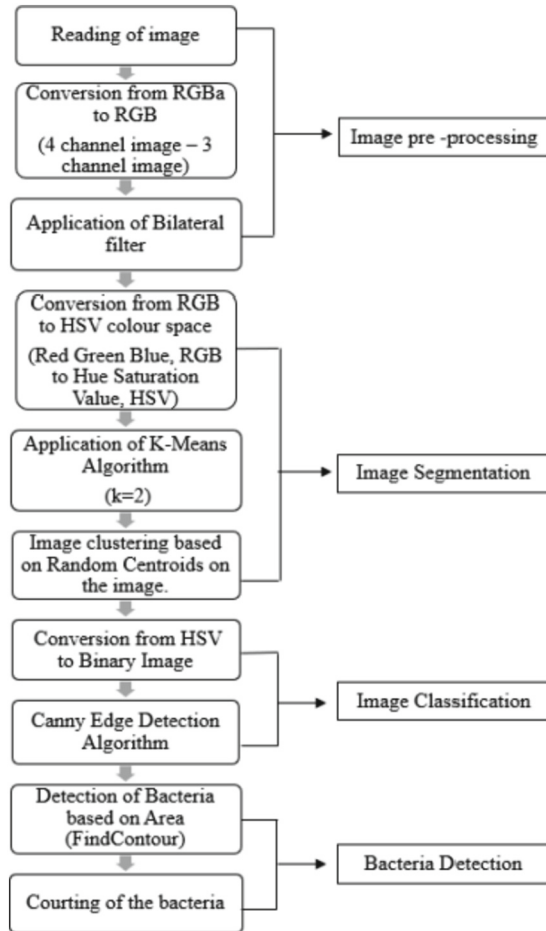


Fig. 2. Overall flow chart of TB detection algorithm.

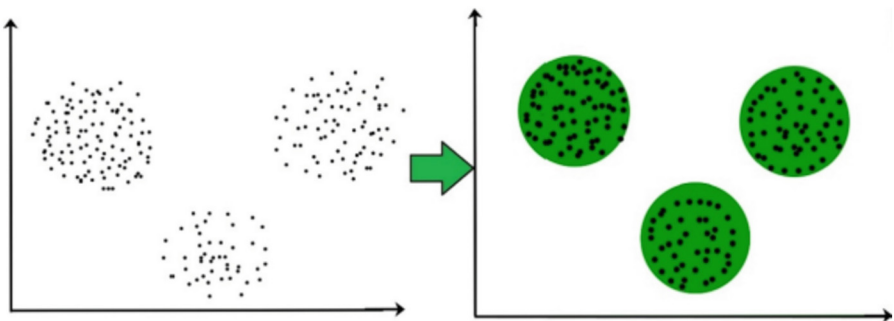


Fig. 3. Clustering of several data points into groups [8].

The edge location (4) is defined as the local maximum in the direction n of the operator G_n , convolved with the image, g [11].

$$\frac{\delta}{\delta n} G_n * g = 0 \tag{4}$$

By substituting (4) into (1), (5) is obtained as the non-maximum suppression, which is responsible for suppressing or thinning the edges of the image.

$$\begin{aligned} \frac{\delta}{\delta n} G_n * g &= 0 \\ \frac{\delta}{\delta n} \frac{\delta G}{\delta n} * g &= 0 \\ \frac{\delta^2}{\delta n^2} G * g &= 0 \end{aligned} \tag{5}$$

The K-means algorithm and the Canny Edge Detector algorithm were meant to work together in the final algorithm. The K-means algorithm clustered the bacilli found on the microscope image, followed by the edge detection using the Canny Edge Detector. The bacilli were then identified based on the area and their numbers were counted. The overall algorithm proposed in Fig. 2 was integrated into a mobile application.

C. Medical Standard Used for Tuberculosis Diagnosis

Table 1 shows the medical standard used for the classification of the diagnosis results, specified by the World Health Organisation (WHO).

Table 1. WHO standards for TB diagnosis classification.

200× Magnification	400× Magnification	Diagnosis
0 Acid-Fast Bacillus (AFB)	0 AFB	No AFB observed
1–4 AFB in one field	1–2 AFB in one field	Confirmation required
5–49 AFB in one field	3–24 AFB in one field	Scanty
3–24 AFB in one field	1–6 AFB in one field	1+
25–250 AFB in one field	7–60 AFB in one field	2+
More than 250 AFB in one field	More than 60 AFB in one field	3+

3 Results and Discussion

The mobile application integrated with the proposed image processing algorithm was tested using images obtained from the Sarawak General Hospital prior to the COVID-19 pandemic. Table 2 summarises the diagnosis result by the image processing algorithm.

Table 2. Tuberculosis diagnosis result by coupling K-means algorithm with the Canny Edge Detection algorithm.

Magnification	Image Name	Manual Count	Medical Classification (Range)	Actual Diagnosis	System Count	System Classification (Diagnosis)	Count % Error	Diagnosis Accuracy
400x Magnification	121916	359	More than 60 AFB in one field	3+	69	3+	80.78	Correct
	122232	404	More than 60 AFB in one field	3+	98	3+	75.74	Correct
	122247	425	More than 60 AFB in one field	3+	244	3+	42.59	Correct
	122308	442	More than 60 AFB in one field	3+	567	3+	28.28	Correct
	122647	0	0	No AFB detected	0	No AFB detected	0	Correct
	123231	239	More than 60 AFB in one field	3+	197	3+	17.57	Correct
	123300	220	More than 60 AFB in one field	3+	200	3+	9.09	Correct
	123305	196	More than 60 AFB in one field	3+	165	3+	15.82	Correct
	125206	0	0	No AFB detected	10	Scanty	- (divided by 0)	Wrong
					Average	30.00	88.89%	

For the case of image 125206, the counting error was 10 due to lens flair present on the captured image captured as shown in Fig. 4(a). Figure 4(a) shows that the lens flair present is highly identical to an acid-fast bacillus (AFB) in Fig. 4(b) in terms of colour and size, hence causing confusion in the system.

The average bacilli count percentage error of the proposed algorithm was 30%. While the average bacilli count percentage error was high, it should be noted that the sample size of the available images was very small. In addition, the classification of the tuberculosis diagnosis is based on the number range of AFB, hence it is not necessary for the AFB count to be exactly accurate. In terms of diagnosis classification, the proposed algorithm

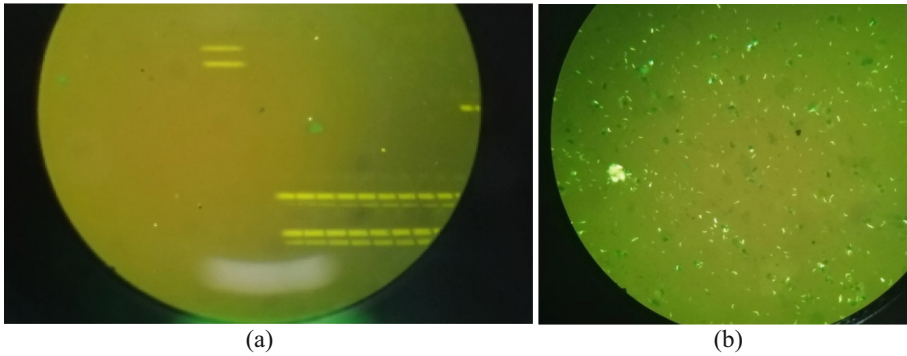


Fig. 4. Comparison between (a) lens flare and (b) AFB.

was able to classify the diagnosis correctly eight out of nine tests, which translated to a diagnosis accuracy of 88.89%.

4 Conclusion

In conclusion, the proposed image processing algorithm by coupling K-means with Canny Edge Detection algorithm achieved tuberculosis diagnosis accuracy of 88.89%. However, a larger sample size was required to better conclude on the accuracy of the system. Future work on this project includes assessing the viability of using Microsoft's Machine Learning Model Builder to decide the best algorithm for Acid-Fast Bacilli counting.

Acknowledgement. The authors would like to thank the Sarawak General Hospital for providing the samples for the purpose of this study.

References

1. Desikan, P.: Sputum Smear Microscopy in tuberculosis: Is it still relevant? *Ind. J. Med. Res.* (2013). <https://www.ncbi.nlm.nih.gov/pmc/articles/PMC3705651/>. Accessed 04 July 2022
2. Meraj, S.S., Yaakob, R., Azman, A., Mohd Rum, S.N., Ahmad Nazri, A.S.: Artificial intelligence in diagnosing tuberculosis: a review. *Int. J. Adv. Sci. Eng. Inf. Technol.* **9**(1), 81 (2019)
3. El-Solh, A.A., Hsiao, C.-B., Goodnough, S., Serghani, J., Grant, B.J.B.: Predicting active pulmonary tuberculosis using an artificial neural network. *Chest* **116**(4), 968–973 (1999)
4. Santos, A.M., Pereira, B.B., Seixas, J.M., Mello, F.C., Kritski, A.L.: Neural networks: an application for predicting smear negative pulmonary tuberculosis. In: *Advances in Statistical Methods for the Health Sciences*, pp. 275–287 (2007)
5. Er, O., Temurtas, F., Tanrikulu, A.Ç.: Tuberculosis disease diagnosis using artificial neural networks. *J. Med. Syst.* **34**(3), 299–302 (2010)
6. Qamar, U., Raza, M.S.: *Data Science Concepts and Techniques with Applications* (2020)

7. Dhanachandra, N., Manglem, K., Chanu, Y.J.: Image segmentation using K-means clustering algorithm and subtractive clustering algorithm. *Procedia Comput. Sci.* **54**, 764–771 (2015)
8. Clustering in Machine Learning. GeeksforGeeks (2022). <https://www.geeksforgeeks.org/clustering-in-machine-learning/>. Accessed 10 July 2022
9. Ansari, M.A., Kurchaniya, D., Dixit, M.: A comprehensive analysis of image edge detection techniques. *Int. J. Multim. Ubiquit. Eng.* **12**(11), 1–12 (2017)
10. Sonka, M., Hlavac, V., Boyle, R.: *Image Processing, Analysis and Machine Vision*. Chapman & Hall Computing, London (1993)
11. Bezdek, J.C., Keller, J., Krisnapuram, R., Pal, N.R.: Image processing and computer vision. In: *Fuzzy Models and Algorithms for Pattern Recognition and Image Processing*, pp. 547–678 (1999)



Geo-tracing of Coffee Beans Using Metal Oxide Semiconductor Gas Sensors Array

Ashlee Jude Anak Nyaut¹, Hui En Lee¹, Zehnder Jarroop Augustine Mercer², Sing Muk Ng³, and Hong Siang Chua¹ (✉)

¹ Faculty of Engineering, Computing and Science, Swinburne University of Technology Sarawak Campus, 93350 Kuching, Sarawak, Malaysia

hschua@swinburne.edu.my

² Malaysian Pepper Board, Lot 1115, Jalan Utama, Tanah Putih, 93916 Kuching, Sarawak, Malaysia

³ Sarawak Energy Berhad, Research and Development Department, 93050 Kuching, Sarawak, Malaysia

Abstract. The determination of food freshness and quality using human senses can be biased. Coffee is a beverage known for its popularity and increase in demand. The quality and price of coffee differ based on its geo-origins. This paper reports on the application of metal oxide semiconductor (MOS) gas sensors array in geo-tracing of coffee beans. The MOS gas sensors array, consisting of four models of sensors, was used for headspace volatile organic compound (VOC) sampling of coffee beans from Brazil, Ethiopia, Columbia and Vietnam to generate sensor responses profile corresponding to each geo-origin. Principal component analysis (PCA) was employed on the sensor responses data for dimension reduction, followed by multiclass classification to geo-trace each coffee bean sample. The methodology yielded an overall coffee beans geo-tracing accuracy up to 97.5% using classification models such as fine gaussian support vector machine (SVM), fine k-nearest neighbour (KNN), weighted KNN, boosted trees, bagged trees, subspace KNN and random under-sampling (RUS) boosted trees.

Keywords: coffee · e-nose · Gas sensor · Geo-tracing · Headspace sampling · Machine learning · Metal oxide semiconductor

1 Introduction

The importance of food analysis is significant as the masses are getting more knowledgeable and informed of the impact food has on health. In over a decade, the prices of Arabica beans have skyrocketed especially from supplying countries as Brazil and Columbia [1]. At the same time, there is a rising popularity of coffee concept stores in Malaysia with customers ranging from experienced coffee lovers to inexperienced party goers, who are just there for experience and oblivious with the quality or the origins of the beans [2].

Therefore, a reliable and trustworthy method of geo-tracing coffee beans is crucial hence this study proposed the use of MOS gas sensors for such purpose. The applications

of MOS gas sensors include determining the presence of harmful components and the level of freshness in food [3]. For instance, MOS gas sensors are used to detect the fungal growth in coffee based on their responses on headspace mycotoxins [4]. Another application of MOS gas sensors is the detection of foodborne bacterial pathogens based on analysis of static and dynamic sensor responses using a linear classifier, which yielded 90% accuracy with supervised dimensionality reduction [5]. Research work by Lee *et al.* [6–8] demonstrated the success of geo-tracing Malaysia, India and Vietnam black pepper using an array of MOS gas sensors.

The work presented in this paper reports an attempt to geo-trace coffee beans from Brazil, Ethiopia, Columbia and Vietnam using the responses of MOS gas sensors array.

2 Methodology

Each coffee bean sample used in this study was prepared as a bulk of five beans, without any sample pre-processing. Coffee bean samples from four producing countries – Brazil, Ethiopia, Columbia and Vietnam – were investigated. Ten samples were prepared for each producing country, therefore a total of 40 sets of sample data were analysed and compared.

The e-nose assembled by Lee *et al.* [6–8] (refer to Fig. 1), which comprised of four Figaro MOS gas sensors – TGS2600, TGS2602, TGS2620 and TGS2611-C00, was used for headspace sampling of the coffee bean samples.

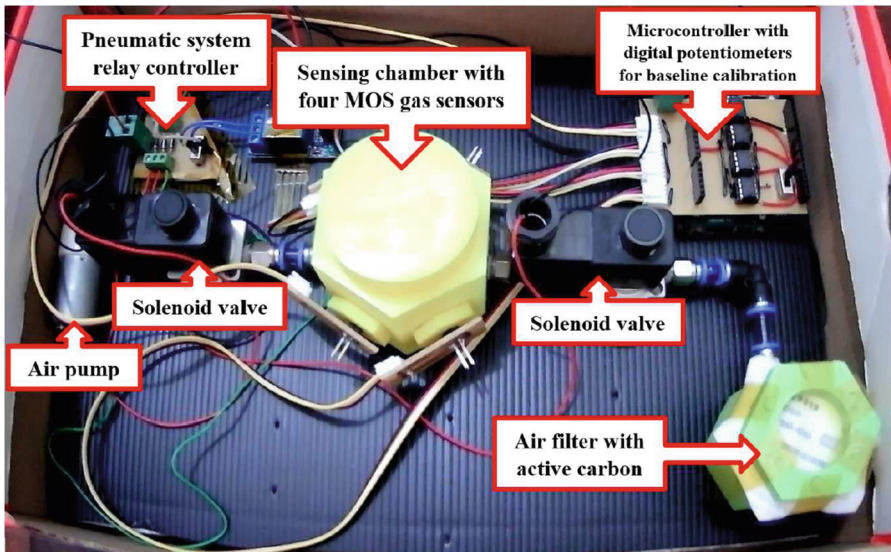


Fig. 1. E-nose assembled by Lee *et al.* in their study [8].

The sampling duration was 600 s for each sample so that the sensor responses could reach steady state. The sample data consisted of four variables, which were the steady

state sensor responses from the four MOS gas sensors used. Steady state sensor response of each gas sensor was presented as the percentage change in sensor output voltage at steady state compared to its baseline [6–8].

Principal component analysis (PCA) was employed on the four-variable sample data, generating four PCA scores – PC1, PC2, PC3 and PC4. This was followed by four-dimensional classification models training to classify the coffee bean samples by country of origin based on the PCA scores. The classification models used in this study comprised of decision trees, discriminant analysis, naïve bayes, support vector machines (SVM), k-nearest neighbour (KNN) and ensemble classifiers.

3 Results and Discussion

Figures 2, 3, and 4 show the scatter plots of coffee bean samples data after employing PCA on steady state sensor responses. The data points were coloured based on four classes – Brazil, Ethiopia, Columbia and Vietnam.

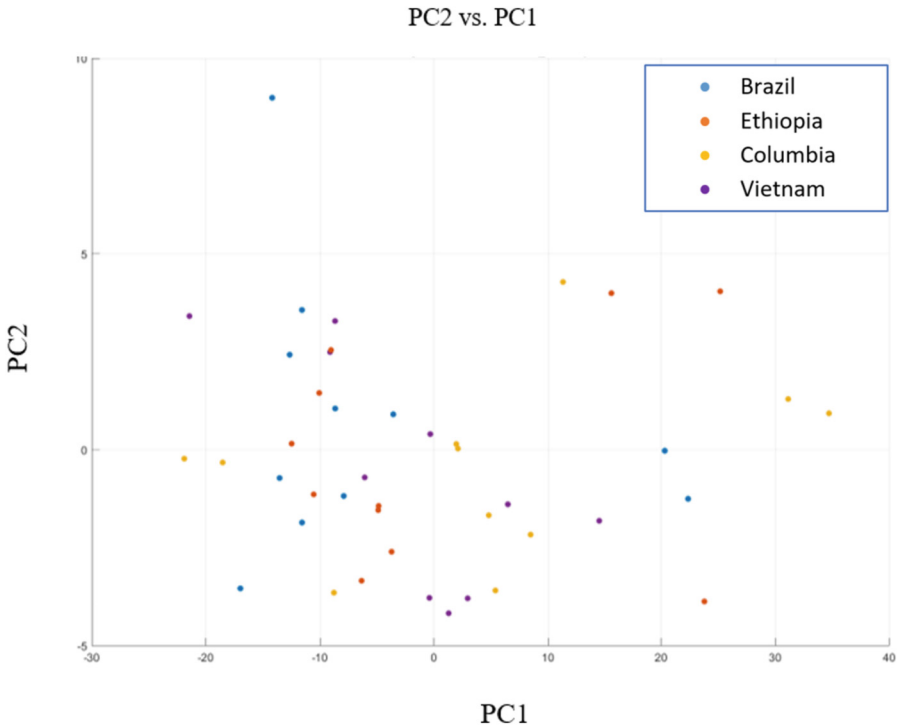


Fig. 2. PC2 vs PC1 scatter plot.

Based on manual inspection of PC2 vs PC1 scatter plot in Fig. 2, Brazil and Ethiopia sample datasets showed little interclass separation with slight interclass overlapping. On the other hand, Columbia sample data had the greatest intraclass separation, as

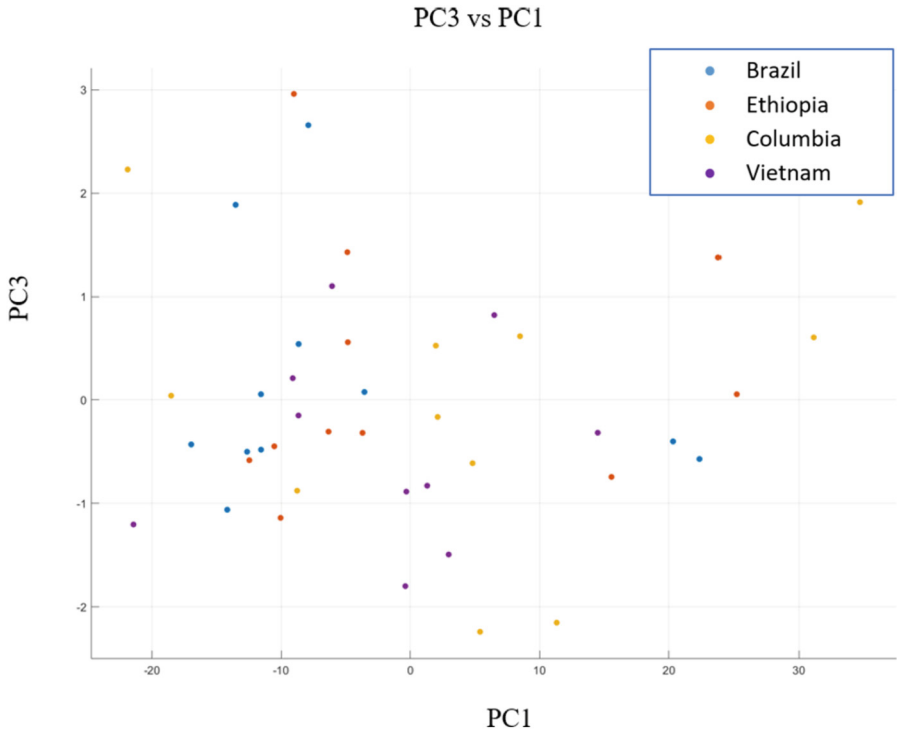


Fig. 3. PC3 vs PC1 scatter plot.

demonstrated by its widespread data points placements on the PC2 vs PC1 scatter plot. Most of Vietnam sample data overlapped with Columbia sample data. High degree of overlapping for all classes of samples suggested that coffee bean samples geo-tracing based on PC2 vs PC1 alone was not feasible.

By manually inspecting PC3 vs PC1 scatter plot in Fig. 3, Brazil and Ethiopia sample datasets showed less interclass separation compared to Fig. 2, however with less interclass overlapping, hence greater distinguishability between the two data regions of Brazil and Ethiopia samples. On the other hand, Columbia and Vietnam sample data demonstrated decline in distinguishability compared to PC2 vs PC1 scatter plot as the data points placements were more widespread, demonstrating greater intraclass separation.

PC4 vs PC1 scatter plot in Fig. 4 demonstrated similar data distribution pattern compared to PC3 vs PC1 scatter plot in Fig. 3. However, slight improvement could be observed in terms of smaller intraclass separation for each class of sample data.

By examining each PCA scatter plot from a two-dimensional perspective, overlapping of sample data between the four countries of origin showed that it was impractical to geo-trace the coffee bean samples by two-dimensional classification. In this study, PCA was followed by four-dimensional classification for better separability of sample data. Table 1 shows the geo-tracing accuracy corresponding to each country's samples

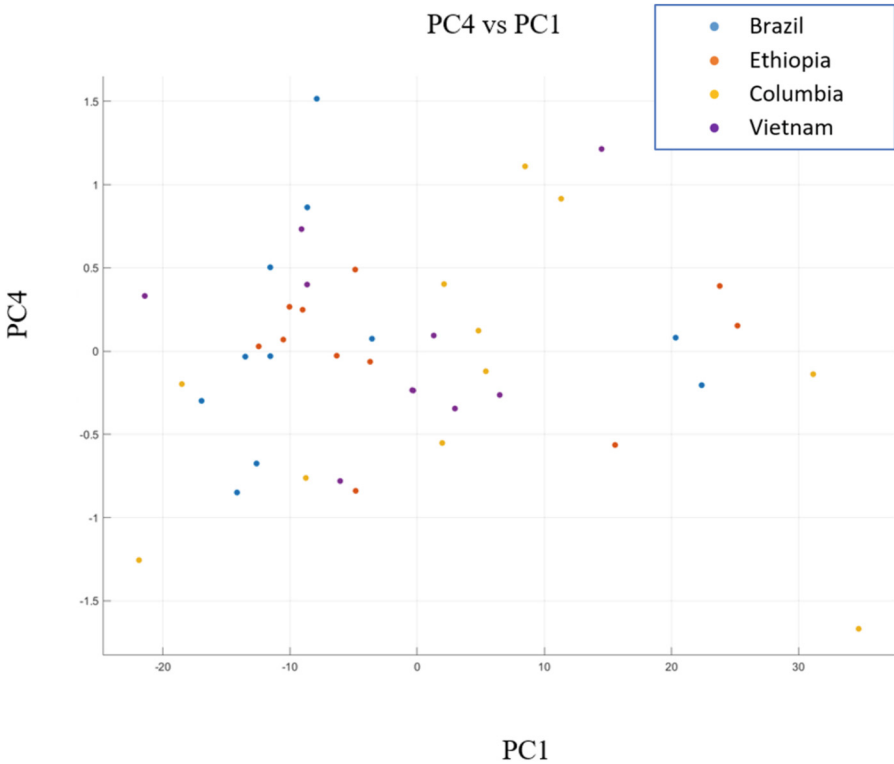


Fig. 4. PC4 vs PC1 scatter plot.

and overall geo-tracing accuracy for each of the 24 classification models trained in this study.

The country with the most distinguishable sample data is Brazil with the greatest number of classification models (9 out of 24) achieving 100% geo-tracing accuracy for Brazil samples. The country with the least distinguishable sample data is Vietnam with only the least number of classification models (3 out of 24) achieving 100% geo-tracing accuracy for Vietnam samples. From the detailed analysis of geo-tracing result, Brazilian and Columbian coffee bean samples close resemble each other in terms of sensor response. Similar resemblance behaviour was detected for coffee bean samples from Ethiopia and Vietnam. By comparing all the classification models, fine Gaussian SVM, weighted KNN, boosted trees, bagged trees, subspace KNN and random under-sampling (RUS) boosted trees achieved the highest overall geo-tracing accuracy of 97.5%, with only one misclassification case for either Ethiopian or Vietnamese coffee bean sample data.

Table 1. Coffee bean samples geo-tracing accuracy of trained classification models.

No	Classification Model	Coffee Bean Geo-Tracing Accuracy (%)				
		Brazil	Columbia	Ethiopia	Vietnam	Overall
1	Fine Tree	70	70	70	60	67.5
2	Medium Tree	70	70	70	60	67.5
3	Coarse Tree	60	90	60	30	60
4	Linear Discriminant	60	40	10	50	40
5	Quadratic Discriminant	50	50	60	60	55
6	Gaussian Naïve Bayes	40	40	40	40	40
7	Kernel Naïve Bayes	80	60	70	40	62.5
8	Linear SVM	40	30	0	0	17.5
9	Quadratic SVM	60	60	90	70	70
10	Cubic SVM	70	100	100	100	92.5
11	Fine Gaussian SVM	100	100	90	100	97.5
12	Medium Gaussian SVM	50	60	90	50	62.5
13	Coarse Gaussian SVM	60	20	30	60	42.5
14	Fine KNN	100	100	100	90	97.5
15	Medium KNN	60	10	60	10	35
16	Coarse KNN	100	0	0	0	25
17	Cosine KNN	60	40	30	10	35
18	Cubic KNN	40	0	50	10	25
19	Weighted KNN	100	100	100	90	97.5
20	Boosted Trees	100	100	90	100	97.5
21	Bagged Trees	100	100	100	90	97.5
22	Subspace Discriminant	60	40	10	50	40
23	Subspace KNN	100	100	100	90	97.5
24	RUS Boosted Trees	100	100	100	90	97.5

4 Conclusion

By using the methodology in this study, coffee bean samples from Brazil, Columbia, Ethiopia and Vietnam could be geo-traced with 97.5% accuracy. This was achieved by training Fine Gaussian SVM, Weighted KNN, Boosted Trees, Bagged Trees Subspace KNN or RUS Boosted Trees models using four-dimensional PCA scores of MOS gas sensor responses. With a more controlled sampling methodology, the stability and consistency of sensor responses could increase, leading to improvement on geo-tracing accuracy. Future work of this research could include detecting adulteration of coffee bean involving mixture of coffee beans from multiple producing countries and MOS

gas sensors temperature modulation to alter selectivity hence improve dimensionality of sensor data.

References

1. Perez, M.G., Hunter, A.: Arabica coffee prices are the highest in almost a decade. Bloomberg.com (2021)
2. Ting, H., Lau, W.M., Cheah, J.H., Yacob, Y., Memon, M.A., Lau, E.: Perceived quality and intention to revisit coffee concept shops in Malaysia: a mixed-methods approach. *Br. Food J.* **120**(5) (2018)
3. Berna, A.: Metal oxide sensors for electronic noses and their application to food analysis. *Sensors* **10**(4), 1424–8220 (2010). <https://doi.org/10.3390/s100403882>
4. Seberveglieri, V., Falasconi, M., Gobbi, E., Pulvirenti, A., Fava, P.: Early detection of fungal contamination on green coffee by a MOX sensor based electronic nose. *AIP Conf. Proc.* **1362**(1), 119–120 (2011). <https://doi.org/10.1063/1.3626328>
5. Green, G., Chan, A., Dan, H., Lin, M.: Using a metal oxide sensor (MOS)-based electronic nose for discrimination of bacteria based on individual colonies in suspension. *Sens. Actuat. B Chem.* **152**(1), 21–28 (2011)
6. Lee, H.E., Mercer, Z.J.A., Ng, S.M., Shafiei, M., Chua, H.S.: Geo-tracing of black pepper using metal oxide semiconductor (MOS) gas sensors array. *IEEE Sens. J.* **20**(14), 8039–8045 (2020). <https://doi.org/10.1109/JSEN.2020.2981602>
7. Lee, H.E., Chua, H.S., Mercer, Z.J.A., Ng, S.M., Shafiei, M.: Fraud detection of black pepper using metal oxide semiconductor gas sensors. In: 2021 IEEE Sensors, 31 Oct.–3 Nov. 2021, pp. 1–4 (2021). <https://doi.org/10.1109/SENSORS47087.2021.9639658>
8. Lee, H.E., Mercer, Z.J.A., Ng, S.M., Shafiei, M., Chua, H.S.: Metal oxide semiconductor gas sensors-based E-nose and two-stage classification: authentication of Malaysia and Vietnam black pepper samples. In: 2022 IEEE International Symposium on Olfaction and Electronic Nose (ISOEN), 29 May–1 June 2022, pp. 1–4 (2022). <https://doi.org/10.1109/ISOEN54820.2022.9789618>



A Review of Common PV Array Configuration Schemes for Maximum Output Power

Lawrence Sii Ying Ting¹(✉), Hadi Nabipour Afrouzi¹, Hong Siang Chua¹,
and Jubaer Ahmed²

¹ Faculty of, Engineering Computing and Science, Swinburne University of Technology
Sarawak, 93350 Kuching, Malaysia

lting@swinburne.edu.my

² School of Engineering and Built Environment,
Edinburgh Napier University, Edinburgh EH8 9AD, UK

Abstract. Partial shading of a PV array is a key concern in PV systems since it results in significant decrement of output power. The drop in output power is caused by non-uniform irradiances experienced by the PV array. Various PV array configuration schemes and shade dispersion techniques have been reported in the literature, such as Series-Parallel, Total Cross-Tied, Bridge-Linked, SuDoKu, Electrical Array Reconfiguration, and Dragonfly Algorithm. These schemes and techniques are popular and effective in improving maximum output power and mismatch power loss under partial shading. The advantages and drawbacks of each configuration strategy under various operating situations are discussed in this paper.

Keywords: PV array Reconfiguration · Maximum Output Power · Mismatch Power Loss · Partial Shading

1 Introduction

Global electricity demand is gradually increasing, yet there is a substantial supply-demand gap for fossil fuels. The growing demand for renewable energy is intended to alleviate the worldwide crisis of fossil fuels and ensure long-term energy security. In recent years, the energy harvested from PV (Photovoltaic) modules has continuously increased, making PV systems the most potential renewable energy generation source in grid connected power systems and off-the grid electricity systems. Photovoltaics has had the most rapid cost reductions of any energy technology, with the trend showing that greater savings are still in the pipeline. Despite these benefits, it should be noted that the efficiency of PV arrays is extremely low. Furthermore, the power output of PV modules fluctuates with irradiance and temperature. As a result, maximum efficiency cannot be ensured throughout the day. A PV module is made up of a series of cells connected in series. When a PV module is partially shaded, it receives a different level of irradiation. Shaded PV cells produce less current and must carry the same current as unshaded cells that produce more current [1]. As a result, the shaded cells act as a load, drawing

power from the unshaded cells and eventually raising the temperature inside the shaded cells, causing hot spots that destroy the PV modules [2]. Bypass diodes can be used to address the issue of hot spots. The disadvantage of using bypass diodes is that a partially shaded PV module generates less power because these diodes introduce multiple peaks on a P-V curve [3]. The maximum power point tracking (MPPT) techniques proposed by the researchers [4, 5] aim to improve power generation under partial shading conditions. These techniques required large numbers of solid-state converters embedded with algorithms, which raises the cost. To address these shortcomings, the authors [6, 7] proposed different configuration schemes to improve power generation. Series-parallel (SP), total cross-tied (TCT), bridge-linked (BL), SuDoKu, Electrical Array Reconfiguration (EAR), and Dragonfly Algorithm (DA) are the current existing configuration methods. Examples of static configuration methods are SP, TCT, BL, and SudoKu. In cross-tie configurations such as TCT and BL, there are alternate current paths for current to flow because ties are connected in between PV modules' strings. SuDoKu is a shade dispersion technique used to equalized the row current to improve the performance of TCT configuration. EAR and DA are dynamic reconfiguration methods which are found to be effective in maximum power generation when PV modules are shaded [39, 43]. In this paper, a comprehensive review is carried out on the different configurations of PV modules. These PV configurations are carefully analysed and their benefits and drawbacks are underlined.

2 PV Array Configuration Schemes

A. Series-Parallel (SP)

Figure 1(a) shows a 4×4 SP configuration of PV modules. The PV modules are linked in a series and parallel configuration. In terms of the intended output voltage and current, SP configuration enables the benefits of both series and parallel arrangements to be achieved [8]. Such a topology is straightforward but cost-effective [9]. SP configuration has well balanced performance in terms of efficiency, maximum power peak, fill factor and number of power peaks when more PV modules are connected in parallel and less PV modules connected in series [10, 11]. SP exhibited the highest mismatch losses due to its large number of series connected PV strings [12]. Long series string in SP configuration should be avoided for higher power output [13]. Mathematical models for TCT and SP have been developed and analysed in [14]. The study shows that TCT outperforms SP in all cases. However, SP is preferable when it comes to row-wise partial shading pattern because it has fewer connecting wires. Moreover, the redundancy level in SP configuration is lower as compared to TCT because it has no extra number of ties [15].

B. Total Cross-Tied (TCT)

Figure 1(b) illustrates an array of 4×4 TCT connected PV modules. The connection of TCT arrangement is quite complicated. The PV modules are first joined in parallel, and then in series. TCT configuration is intended to compensate for the shortcomings of SP configuration because it is less susceptible to mismatch losses as compared to SP [16].

The voltage across each row equals the open circuit voltage of a single PV module, and the total voltage across all rows equals the output voltage of the PV array. The total current is the sum of the currents from all PV modules in a row [17]. TCT outperforms in most shading conditions because it has more cross links, which provides more current paths and maximises array use [18]. In terms of output performance, TCT reacts and adapts effectively to different partial shading patterns [19]. When various performance factors such as power loss, fill factor, and mismatch loss are considered, TCT outperforms SP and BL [20]. Despite these advantages, TCT configuration tends to create stepped I-V characteristics and multiple peaks in P-V characteristics under row-wise shading [21]. These drawbacks can be mitigated by shade dispersion technique such as SuDoKu [22].

C. Bridge-Linked (BL)

Figure 1(c) shows a BL configuration of PV modules connected in array size of 4×4 . The BL configuration is like the TCT configuration, except that half of the ties are removed [23]. In BL configuration, two PV modules are first linked in series, then these two sets of series-connected modules are linked in bridge rectifier fashion [24]. As a result, installation times and wire losses are reduced as compared to TCT [25]. Output voltage is calculated by adding all the voltages in the series connections, and total current is obtained by adding all the currents in the parallel connections [26]. Due to fewer number of cross ties, BL is less susceptible to mismatch losses than SP configurations [8]. Results have proven that the maximum power output in BL is higher than SP but lower than TCT [27]. In addition, it is investigated that BL under uneven row shading without bypass diodes produces more power than TCT and SP [26].

D. SuDoKu

Figure 1(d) shows a 4×4 TCT PV array with the SuDoKu puzzle pattern arrangement. SuDoKu is a logic-based number placing puzzle. SuDoKu puzzle is solved when every row and column of the $n \times n$ matrix contain every number from 1 to n without repeating. SuDoKu pattern is effective in dispersing the shade across other area of PV array [28]. In [29], PV modules in TCT configuration is rearranged in SuDoKu puzzle pattern without changing the electrical wirings. It produces only single power peak in P-V characteristic during short-wide, long-wide, short-narrow, and long-narrow shading conditions. Besides, the power output in SuDoKu arrangement is higher than TCT, BL, and SP in short-wide and long-wide shading pattern [30]. Nevertheless, it is studied that SuDoKu arrangement requires longer length of wires [31] and shade dispersion is ineffective under sub-array matrix [32]. These drawbacks can be mitigated by Optimal SuDoKu and Improved SuDoKu configurations [31, 33].

E. Electrical Array Reconfiguration (EAR)

Figure 1(e) shows electrical array reconfiguration (EAR) of 4×4 PV array. In [34], switching matrix is needed to reconfigure or change the size of the PV array. Switches of the switching matrix can be turn on and off to add more PV modules to a row or to add more rows of PV modules to the PV array [35]. The output current and output voltage of the PV array can be increased by changing the size of the PV array dynamically using EAR technique [36]. When the PV array is under partial shading, irradiance equalization is achieved by controlling the switching matrix to match the currents in each row equally

[37]. In all partial shading conditions used by [38] in the simulation and experimental works, EAR outperforms SP, TCT, and BL in terms of power output, and mismatch loss, and power loss. Besides, the efficiency of EAR based PV array configuration is higher than TCT and SuDoKu [39].

F. Dragonfly Algorithm (DA)

Figure 1(f) shows a 4×4 PV array size using dragonfly algorithm (DA) dynamic reconfiguration technique [43]. The results in [40] show that DA is an efficient MPPT tracking technique. Besides, DA has fast tracking speed with reduced energy losses [41] and high tracking efficiency under different shading conditions [42]. In [43], the study shows that PV array reconfiguration using DA is proven to be effective in reducing switch counts of switching matrix for optimal reconfiguration under partial shading conditions. Results have proven that DA reconfiguration technique has the maximum power generation under different shading conditions as compared to TCT, SuDoKu, and EAR. Besides, DA reconfiguration technique has lower mismatch losses with a smooth P-V curve during partial shading condition. The smooth P-V curve shows only single power peak during partial shading, reducing mismatch losses caused by MPPT tracking failure.

The summary of pros and cons of the PV configurations is shown in Table 1.

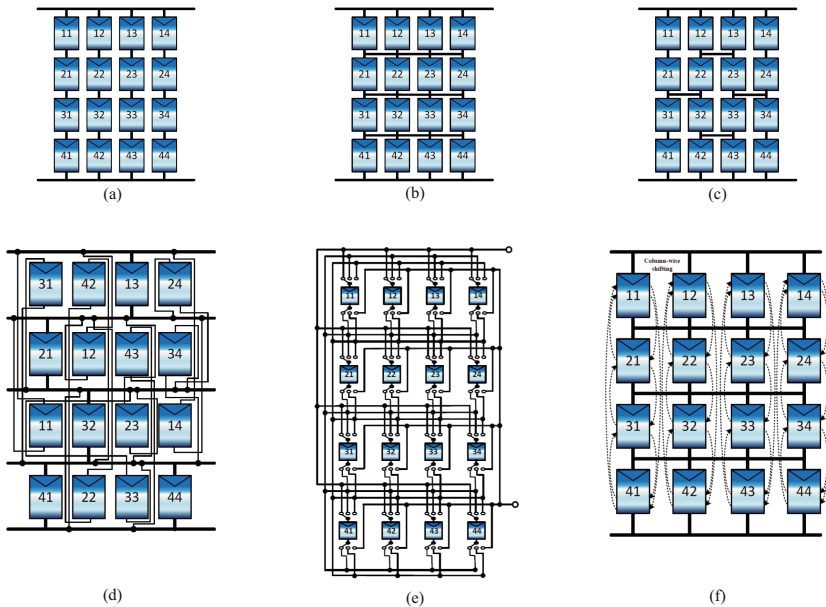


Fig. 1. Different PV configurations (a) Series-Parallel (SP), (b) Total-cross-tied (TCT), (c) Bridge-linked (BL), (d) SuDoKu, (e) Electrical Array Reconfiguration (EAR), (f) Dragonfly Algorithm Reconfiguration (DA)

Table 1. Summary of pros and cons of different PV configurations

Configurations	Pros	Cons
SP	<ul style="list-style-type: none"> • simple with fewer interconnections among modules • reduces complexity, cable loss and wiring time • performs better than TCT under corner and L-shape shading • low redundancy under unshaded condition • low fill factor 	<ul style="list-style-type: none"> • high mismatch loss due to the series connections and when using bypass diodes • malfunctions under partial shading conditions • multi peaks occurs in P-V characteristic under partial shading conditions
TCT	<ul style="list-style-type: none"> • reduces the corresponding partial shading losses • provides alternative current path • provides highest power output under center, right side, frame and diagonal shading patterns over SP, BL and HC PV configurations • superior performance in most of the shading patterns • is preferred for stand-alone and grid connected PV system applications • high fill factor, reliability and efficiency • performed marginally in mismatch loss • more cross ties increase the lifespan 	<ul style="list-style-type: none"> • low output current under row-wise shading condition • more complex interconnections • increase in installation cos, electrical wiring cost, and time • increase losses in cables • high mismatch current when partial shading increases • high redundancy • increase in large size PV system complicity
BL	<ul style="list-style-type: none"> • higher power output than SP and TCT under random shading • low mismatch loss due to lesser series connected PV strings • lower mismatch loss than SP • reduced wiring installation time • generates maximum power under uneven row shading without bypass diode 	<ul style="list-style-type: none"> • higher mismatch loss than TCT • high mismatch loss under L-shape shading pattern • high redundancy

(continued)

Table 1. (continued)

Configurations	Pros	Cons
SuDoKu	<ul style="list-style-type: none"> • PV physical location can be changed without altering electrical connection • suitable for large PV array size • effective in shade dispersion • higher maximum output power compared to SP, TCT, and BL • low mismatch loss • minimum additional wiring requirement • reduces sub-array shading and wiring losses • better performance than SP, TCT, and BL under uneven row shading • high fill factor • increases current entering a node under partial shading • no sensor, switching matrix and complex control algorithm 	<ul style="list-style-type: none"> • low performance under random and long-wide shadings • requires huge manpower • limited to even number of array size • uneven shade dispersion under sub-array matrix • unaltered first column after reconfiguration causing multiple peaks and lower output power • repeated row-numbers in diagonal causing lower output current
EAR	<ul style="list-style-type: none"> • automatic PV array reconfiguration • reduced mismatch loss by dispersing shade equally • higher efficiency improvement compared to SP and TCT 	<ul style="list-style-type: none"> • requires switching matrix, individual current sensors, and complex control algorithm • higher number of switches resulting in extra switching losses • level of control complexity is high • costly • limited to small PV array size • vulnerable to short-circuit fault
DA	<ul style="list-style-type: none"> • PV array can be reconfigured automatically • improves efficiency of PV system • reduces or eliminates multi peaks • higher MPP tracking efficiency • faster convergence rate • applicable for any size of symmetric and asymmetric PV arrays • low complexity • reduces switch counts • low power losses and mismatch losses during partial shading 	<ul style="list-style-type: none"> • complex mathematical operation • requires switches and sensors

3 Conclusion

Different PV configurations exhibit its own advantages and drawbacks. It is important to choose a suitable PV configuration for a specific shading condition. SP configuration is simple to be applied in PV system. TCT is more complicated than SP but it can improve the output power significantly compared to SP. The output power performance for BL configuration is in between SP and TCT. Static cross-ties reconfiguration such as SuDoKu outperform SP, TCT, and BL configuration in terms of maximizing output power. Although EAR is very complex and requires large number of switches and sensors, it can mitigate the problem of huge manpower needed by SuDoKu static reconfiguration. It is found that DA dynamic reconfiguration technique can effectively mitigate the partial shading for higher power output enhancement.

References

1. Saha, A., Nipu, N.N., Khan, M.F.: Effect of partial shading on the performance of solar PV module and impact of bypass diode in performance enhancement. In: 2019 5th International Conference on Advances in Electrical Engineering (ICAEE), pp. 891–896 (2019). <https://doi.org/10.1109/ICAEE48663.2019.8975669>
2. Refaat, A., Elgamal, M., Korovkin, N.V.: A novel photovoltaic current collector optimizer to extract maximum power during partial shading or mismatch conditions. In: 2019 IEEE Conference of Russian Young Researchers in Electrical and Electronic Engineering (EConRus), pp. 407–412 (2019). <https://doi.org/10.1109/EConRus.2019.8657173>
3. Alqaisi, Z., Mahmoud, Y.: Comprehensive approach of estimating power-peaks of partially shaded pv strings with overlapping bypass diodes. In: 2019 IEEE Energy Conversion Congress and Exposition (ECCE), pp. 2033–2038 (2019). <https://doi.org/10.1109/ECCE.2019.8911871>
4. Ben Smida, M., Sakly, A.: Genetic based algorithm for maximum power point tracking (MPPT) for grid connected PV systems operating under partial shaded conditions. In: 2015 7th International Conference on Modelling, Identification and Control (ICMIC), pp. 1–6 (2015). <https://doi.org/10.1109/ICMIC.2015.7409433>
5. Sharma, D.K., Purohit, G.: Advanced perturbation and observation (P&O) based maximum power point tracking (MPPT) of a solar photo-voltaic system. In: 2012 IEEE 5th India International Conference on Power Electronics (IICPE), pp. 1–5 (2012). <https://doi.org/10.1109/IICPE.2012.6450411>
6. Mehiri, A., Hamid, A., Almazrouei, S.: The effect of shading with different PV array configurations on the grid-connected PV system. In: 2017 International Renewable and Sustainable Energy Conference (IRSEC), pp. 1–6 (2017). <https://doi.org/10.1109/IRSEC.2017.8477420>
7. Pradhan, R., Kar, S.: A comprehensive study of partial shading effect on the performance of PV array with different configuration. In: 2020 International Conference on Renewable Energy Integration into Smart Grids: A Multidisciplinary Approach to Technology Modelling and Simulation (ICREISG), pp. 78–83 (2020). <https://doi.org/10.1109/ICREISG49226.2020.9174548>
8. Bonthagorla, P.K., Mikkili, S.: Performance analysis of PV array configurations (SP, BL, HC and TT) to enhance maximum power under non-uniform shading conditions. Eng. Rep. **2**(8) (2020). <https://doi.org/10.1002/eng2.12214>
9. Pareek, S., Chaturvedi, N., Dahiya, R.: Optimal interconnections to address partial shading losses in solar photovoltaic arrays. Sol. Energy **155**, 537–551 (2017). <https://doi.org/10.1016/j.solener.2017.06.060>

10. Ramesh, T., Rajani, K., Panda, A.K.: A novel triple-tied-cross-linked PV array configuration with reduced number of cross-ties to extract maximum power under partial shading conditions. *CSEE J. Power Energy Syst.* **7**(3), 567–581 (2020). <https://doi.org/10.17775/CSEEJPES.2020.00750>
11. Prince Winston, D., Kumaravel, S., Praveen Kumar, B., Devakirubakaran, S.: Performance improvement of solar PV array topologies during various partial shading conditions. *Solar Energy* **196**, 228–242 (2020). <https://doi.org/10.1016/j.solener.2019.12.007>
12. Lappalainen, K., Valkealahti, S.: Effects of PV array layout, electrical configuration and geographic orientation on mismatch losses caused by moving clouds. *Sol. Energy* **144**, 548–555 (2017). <https://doi.org/10.1016/j.solener.2017.01.066>
13. Satpathy, P.R., Jena, S., Sharma, R.: Power enhancement from partially shaded modules of solar PV arrays through various interconnections among modules. *Energy* **144**, 839–850 (2018). <https://doi.org/10.1016/j.energy.2017.12.090>
14. Changmai, P., Nayak, S.K., Metya, S.K.: Mathematical model to estimate the maximum power output of a total cross tied connected PV array during partial shading condition. *IET Renew. Power Gener.* **13**(14), 2647–2655 (2019). <https://doi.org/10.1049/iet-rpg.2019.0279>
15. Satpathy, P.R., Babu, T.S., Shanmugam, S.K., Popavath, L.N., Alhelou, H.H.: Impact of uneven shading by neighboring buildings and clouds on the conventional and hybrid configurations of roof-top PV arrays. *IEEE Access* **9**, 139059–139073 (2021). <https://doi.org/10.1109/ACCESS.2021.3118357>
16. Darussalam, R., Pramana, R.I., Rajani, A.: Experimental investigation of serial parallel and total-cross-tied configuration photovoltaic under partial shading conditions. In: 2017 International Conference on Sustainable Energy Engineering and Application (ICSEEA), pp. 140–144 (2017). <https://doi.org/10.1109/ICSEEA.2017.8267699>
17. Tubniyom, C., Jaideaw, W., Chatthaworn, R., Suksri, A., Wongwuttanasatian, T.: Effect of partial shading patterns and degrees of shading on total cross-tied (TCT) photovoltaic array configuration. *Energy Procedia* **153**, 35–41 (2018). <https://doi.org/10.1016/j.egypro.2018.10.028>
18. Mohammadnejad, S., Khalafi, A., Ahmadi, S.M.: Mathematical analysis of total-cross-tied photovoltaic array under partial shading condition and its comparison with other configurations. *Sol. Energy* **133**, 501–511 (2016). <https://doi.org/10.1016/j.solener.2016.03.058>
19. Rafiq Nazer, M.N., et al.: Scenario-based investigation on the effect of partial shading condition patterns for different static solar photovoltaic array configurations. In: *IEEE Access* **9**, 116050–116072 (2021). <https://doi.org/10.1109/ACCESS.2021.3105045>
20. Bonthagorla, P.K., Mikkili, S.: Performance investigation of hybrid and conventional PV array configurations for grid-connected/standalone PV systems. *CSEE J. Power Energy Syst.* **8**(3), 682–695 (2022). <https://doi.org/10.17775/CSEEJPES.2020.02510>
21. Yu, H., Hou, M., Zhu, Z., Gao, H., Huyan, T.: An improved strategy for reconstruction of PV arrays based on irradiance equalization. In: 2020 5th Asia Conference on Power and Electrical Engineering (ACPEE), pp. 1072–1079 (2020). <https://doi.org/10.1109/ACPEE48638.2020.9136457>
22. Tatabhatla, V.M.R., Agarwal, A., Kanumuri, T.: Performance enhancement by shade dispersion of Solar Photo-Voltaic array under continuous dynamic partial shading conditions. *J. Clean. Prod.* **213**, 462–479 (2019). <https://doi.org/10.1016/j.jclepro.2018.11.015>
23. Jha, V., Triar, U.S.: Experimental verification of different photovoltaic array configurations under partial shading condition. In: 2017 IEEE International WIE Conference on Electrical and Computer Engineering (WIECON-ECE), pp. 43–46 (2017). <https://doi.org/10.1109/WIECON-ECE.2017.8468929>

24. Satpathy, P.R., Jena, S., Jena, B., Sharma, R.: Comparative study of interconnection schemes of modules in solar PV array network. In: 2017 International Conference on Circuit, Power and Computing Technologies (ICCPCT), pp. 1–6 (2017). <https://doi.org/10.1109/ICCPCT.2017.8074185>
25. Krishna, G.S., Moger, T.: Comparative study on solar photovoltaic array configurations under irregular irradiance conditions. In: 2018 8th IEEE India International Conference on Power Electronics (IICPE), pp. 1–6 (2018). <https://doi.org/10.1109/IICPE.2018.8709512>
26. Pendem, S.R., Mikkili, S.: Modelling and performance assessment of PV array topologies under partial shading conditions to mitigate the mismatching power losses. *Sol. Energy* **160**, 303–321 (2018). <https://doi.org/10.1016/j.solener.2017.12.010>
27. Saiprakash, C., Mohapatra, A., Nayak, B., Ghatak, S.R.: Analysis of partial shading effect on energy output of different solar PV array configurations. *Mater. Today Proc.* **39**, 1905–1909 (2021). <https://doi.org/10.1016/j.matpr.2020.08.307>
28. Duc Tuyen, N., Viet Thinh, L., Xuan Son Huu, V.: On the Sudoku-based arrangement in reconfiguring a large-scale photovoltaic array. In: 2020 59th Annual Conference of the Society of Instrument and Control Engineers of Japan (SICE), pp. 1719–1724 (2020). <https://doi.org/10.23919/SICE48898.2020.9240301>
29. Rani, B.I., Ilango, G.S., Nagamani, C.: Enhanced power generation from PV array under partial shading conditions by shade dispersion using Su Do Ku configuration. *IEEE Trans. Sustain. Energy* **4**(3), 594–601 (2013). <https://doi.org/10.1109/TSTE.2012.2230033>
30. Khan, A., Kishor, A., Sharma, S., Varshney, L.: Increasing the efficiency of solar PV array using Sudoku configuration. In: 2021 International Conference on Advance Computing and Innovative Technologies in Engineering (ICACITE), pp. 173–178 (2021). <https://doi.org/10.1109/ICACITE51222.2021.9404696>
31. Sai Krishna, G., Moger, T.: SuDoKu and optimal SuDoKu reconfiguration for TCT PV array under non-uniform irradiance condition. In: 2018 IEEE 8th Power India International Conference (PIICON), pp. 1–6 (2018). <https://doi.org/10.1109/POWERI.2018.8704458>
32. Ye, C.-E., Tai, C.-C., Huang, Y.-P., Chen, J.-J.: Dispersed partial shading effect and reduced power loss in a PV array using a complementary SuDoKu puzzle topology. *Energy Convers. Manag.* **246** (2021). <https://doi.org/10.1016/j.enconman.2021.114675>
33. Sai Krishna, G., Moger, T.: Improved SuDoKu reconfiguration technique for total-cross-tied PV array to enhance maximum power under partial shading conditions. *Renewab. Sustain. Energy Rev.* **109**, 333–348 (2019). <https://doi.org/10.1016/j.rser.2019.04.037>
34. La Manna, D., Li Vigni, V., Riva Sanseverino, E., Di Dio, P.: Reconfigurable electrical interconnection strategies for photovoltaic arrays: a review. *Renewab. Sustain. Energy Rev.* **33**, 412–426 (2014). <https://doi.org/10.1016/j.rser.2014.01.070>
35. Huang, Y.-P., Chen, X., Ye, C.-E.: Implementation of a modified circuit reconfiguration strategy in high concentration photovoltaic modules under partial shading conditions. *Sol. Energy* **194**, 628–648 (2019). <https://doi.org/10.1016/j.solener.2019.10.038>
36. Cadena, F., Munoz, J., Aliaga, R., Rohten, J., Espinosa, E.: Embedded reconfiguration of panels to obtain the maximum power of a PV array. In: 2016 IEEE 16th International Conference on Environment and Electrical Engineering (EEEIC), pp. 1–5 (2016). <https://doi.org/10.1109/EEEIC.2016.7555720>
37. Sugumar, S., Prince Winston, D., Pravin, M.: A novel on-time partial shading detection technique for electrical reconfiguration in solar PV system. *Solar Energy* **225**, 1009–1025 (2021). <https://doi.org/10.1016/j.solener.2021.07.069>
38. Satpathy, P.R., Bhowmik, P., Babu, T.S., Sain, C., Sharma, R., Alhelou, H.H.: Performance and reliability improvement of partially shaded PV arrays by one-time electrical reconfiguration. *IEEE Access* **10**, 46911–46935 (2022). <https://doi.org/10.1109/ACCESS.2022.3171107>

39. Srinivasan, A., et al.: L-shape propagated array configuration with dynamic reconfiguration algorithm for enhancing energy conversion rate of partial shaded photovoltaic systems. *IEEE Access* **9**, 97661–97674 (2021). <https://doi.org/10.1109/ACCESS.2021.3094736>
40. Lodhi, E., et al.: Dragonfly optimization-based MPPT algorithm for standalone PV system under partial shading. In: 2021 IEEE International Conference on Emergency Science and Information Technology (ICESIT), pp. 277–283 (2021). <https://doi.org/10.1109/ICESIT53460.2021.9697000>
41. Raman, G., Raman, G., Manickam, C., Ganesan, S.I.: Dragonfly algorithm based global maximum power point tracker for photovoltaic systems. In: *Advances in Swarm Intelligence*, pp. 211–219. Springer, Cham (2016). https://doi.org/10.1007/978-3-319-41000-5_21
42. Rezk, H., et al.: A novel statistical performance evaluation of most modern optimization-based global MPPT techniques for partially shaded PV system. *Renewab. Sustain. Energy Rev.* **115** (2019). <https://doi.org/10.1016/j.rser.2019.109372>
43. Aljafari, B., Satpathy, P.R., Thanikanti, S.B.: Partial shading mitigation in PV arrays through dragonfly algorithm based dynamic reconfiguration. *Energy* **257** (2022). <https://doi.org/10.1016/j.energy.2022.124795>



A New Method for Image Encryption Using DNA Sequences and Hyper Chaos

Mehrnaz Arian, Morteza Saberi Kamarposhti, and Ali Broumandnia^(✉)

Department of Computer Engineering, Islamic Azad University, South Tehran Branch, Tehran, Iran

Broumandnia@azad.ac.ir

Abstract. In the decade of the significant progress in new communication sciences, digital images with a large amount of information are sent and received many times in different communication networks. Due to the high probability of manipulation and theft of some high-value digital images, as well as digital images that are of high value to the owner, they should be encrypted before transmission to be more secure. Several tools such as chaos functions, DNA coding, evolutionary algorithms, frequency domain transformations and substitution boxes have been used for image encryption. In this research, a new algorithm based on hyper chaotic map and DNA sequences is introduced to improve the security of the state-of-the-arts algorithms. The experimental analyzes show the efficiency of the proposed algorithm.

1 Introduction

With the significant progress of new technologies in communication, digital images with a large amount of information are sent and received many times in different communication networks. Due to the high probability of manipulation and theft of some high-value digital images, as well as digital images that are of high value to the owner, they should be encrypted before transmission to be more secure [1–3]. For the following three reasons, traditional encryption methods are not usable for encryption of the digital image:

1. High volume of digital images
2. Horizontal, vertical and diagonal correlation between adjacent pixels in digital images
3. Redundancy of data in digital images

The two main parts in image encryption algorithms are the permutation part and the diffusion part. Changing the position of the pixels in original image and changing the gray level value of the pixels are done in the permutation and diffusion parts, respectively. Also, in the previously presented algorithms, various tools such as chaos functions, DNA coding, evolutionary algorithms, frequency domain transformations and substitution boxes have been used [4]. In recent years, due to the inherent feature of chaotic signals such as unpredictability and sensitivity to initial values, the use of these signals for image encryption has been greatly developed.

In [4], a new color image encryption algorithm is introduced using hyper-chaotic two-dimensional sinusoidal logistic pair map (2D-LSCM), bit interpolation and propagation

steps, and to initialize the parameters which are needed for cross-channel pixels. Also, based on the SHA-512 hash value, the chaotic map initial values are calculated which is extracted from plain color image. Good performance of the proposed method is shown in experimental analyzes.

Also, a Chebyshev polynomial's generated function with normal to chaotic doubling period is proposed in [5], where it is proved by using Lyapunov exponent and bifurcation diagram. For control parameters with certain values, the introduced production function is a deterministic system which has chaotic behavior. Also, this production function has been employed to present an image encryption method based on the proposed chaotic system. The proposed Chebyshev polynomial generating function in the simulated analysis provides excellent resistance against various attacks.

Furthermore, a novel asymmetric algorithm for optical image encryption based on hyper-chaos and aiming to solve the problem of transmitting and distributing complex keys securely in image encryption system based on optical transform is proposed in [6].

Using the Chen 4D hyper-chaotic system, two random phase masks are generated and in the Fresnel domain, the plain image is encrypted using double random phase encoding. Then, to manage and allocate the system parameters, initial values, and Fresnel diffraction system parameters, the asymmetric cryptosystem is employed to encrypt the image. Efficiency and high performance of the proposed method is proved through several analyses.

In addition, a comprehensive framework for color image encryption is proposed in [7] which has several new features. Furthermore, elliptic curve cryptography, hyper-chaotic system and dynamic DNA encoding are employed. Using row-level encoding rules which is chosen randomly, encoding of the color image into a DNA sequence is performed. Also, to produce pseudo-random sequences, new 4D-Hyperchaotic system is employed for permutation phase. Experimental results show that the proposed algorithm is resists against several different attacks.

In this article, a new algorithm is proposed for image encryption using DNA sequences and hyper chaos. In the first section, the preliminary study is described. Then, proposed method is briefly discussed and its efficiency in evaluated in experimental results section. Finally, the paper in concluded in the last section.

2 Preliminary Study

2.1 Lorenz System

A mathematician named Edward Lorenz presented a system of ordinary differential equations for the first time in the year 1963, which was named the Lorenz system. For certain parameter values and certain initial conditions, this system has chaotic behavior. It could be formulated as:

$$\begin{aligned}\frac{dx}{dt} &= a(y - x) \\ \frac{dy}{dt} &= x(p - z) - y \\ \frac{dz}{dt} &= xy - bz\end{aligned}\tag{1}$$

The above system has chaotic behavior when $p = 28$, $a = 10$ and $b = 8/3$. The behavior of the Lorenz system could be seen at Fig. 1.

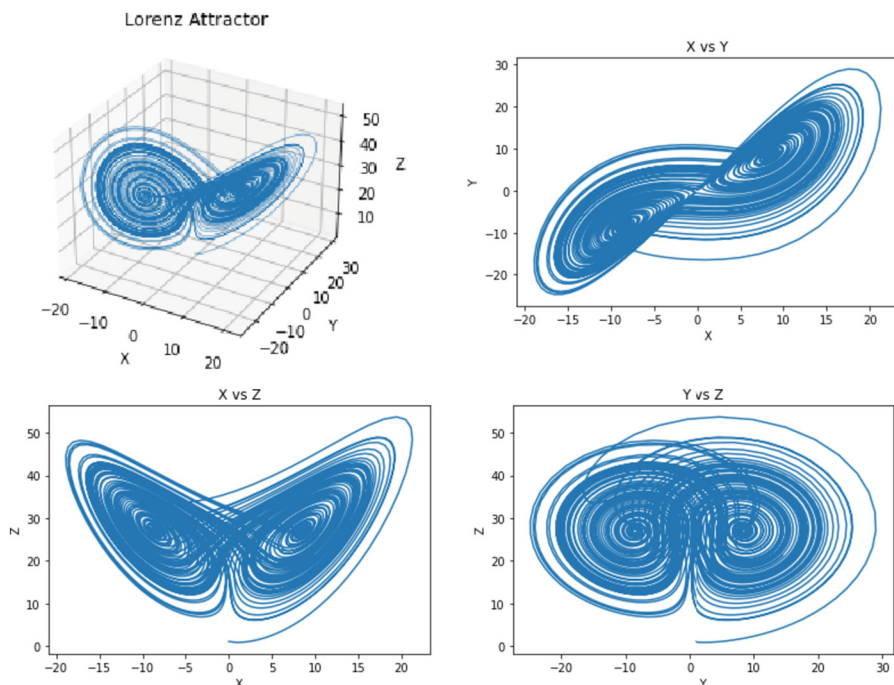


Fig. 1. The behavior of the Lorenz system when $p = 28$, $a = 10$ and $b = 8/3$.

2.2 DNA Sequences

Nucleic acid bases A(adenine), C(cytosine), G(guanine), T(thymine), are four parts of a DNA sequences where C and G are complementary, while A and T are complementary. These bases (A, C, G and T) could be encoded with two bits. Some kinds of coding schemes could satisfy the complement rule that is named Watson-Crick [7], which could be seen in Table 1:

Each pixel grey value is between 0 and 255 which could be represented by 8 bits in binary form and also 4 bases. For example 157 is 10011101 in binary and can be encoded by these acids as “TACA” (with assuming rule three). As it could be seen in Table 2, two algebraic operations could have defined on DNA sequences [7]:

1. Add
2. Subtract

It is worth noting that in each row or column, the base is unique, and as a result, the output of this operation is also unique.

Table 1. All eight coding schemes which satisfy the Watson-Crick complement rule

	Rule1	Rule2	Rule3	Rule4	Rule 5	Rule 6	Rule 7	Rule 8
A	00	00	01	01	10	10	11	11
T	11	11	10	10	01	01	00	00
C	01	10	00	11	00	11	01	10
G	10	01	11	00	11	00	10	01

Table 2. Add and Subtract operations in DNA Sequences

+	A	C	G	T	-	A	C	G	T
A	A	C	G	T	A	A	C	T	G
C	C	G	T	A	C	C	A	G	T
G	G	T	A	C	G	G	T	A	C
T	T	A	C	G	T	T	G	C	A

3 Proposed Method

In this section, the proposed method is described step by step:

1. Secret key as a 256 bits' secret key is converted to binary form:

$$s = s_{255}s_{254} \dots s_1s_0$$

2. It is sliced to 8 parts, each 32 bits:

$$P_7 = s_{255}s_{254} \dots s_{225}s_{224}$$

$$P_6 = s_{223}s_{222} \dots s_{193}s_{192}$$

⋮

$$P_0 = s_{31}s_{30} \dots s_1s_0$$

3. The initial value of x, y and z are calculated using secret key with following formula:

$$x = \frac{P_0 \times P_3 \times P_6 \times P_7}{2^{128}} \in [0.1]$$

$$y = \frac{P_0 \times P_2 \times P_5 \times P_7}{2^{128}} \in [0.1]$$

$$z = \frac{P_0 \times P_1 \times P_4 \times P_7}{2^{128}} \in [0.1]$$

4. For each row and its corresponded column, values of x and y are calculated and the row and column of the plain image pixels are shifted to right circularly x time and y times to scramble the plain image and obtain Imgs.

5. Then, the scrambled image is converted to DNA sequence form using Table 1 and z is used to choose the rule for each pixels.
6. The DNA mask image is created using x, y and z with new initial conditions:

$$x_{new} = \frac{y + z}{2}$$

$$y_{new} = \frac{x + z}{2}$$

$$z_{new} = \frac{x + y}{2}$$

7. x, y is used to locate a pixel in mask image and z is used to prepare a value for that position and obtain *Imgm*.
8. *Img* is obtained using the above formula using Table 2 operators:

$$CipherImage = Imgs + Img_m$$

9. The cipher image is in hand by converting image to original form using Table 1.

4 Experimental Analysis

In the experimental analysis section, the proposed method is analyzed about resistance against several methods for attacking such as statistical, cryptanalytic, brute-force attacks.

4.1 Statistical Analysis

The histogram of the image in three channels and correlation coefficient between adjacent pixels is calculated for several known images to inquire the stability of the proposed algorithm via statistical attacks.

4.1.1 Histogram Analysis

A good encryption method must have a uniform histogram for cipher image to be secure against attackers. As it could be seen in Fig. 2, the proposed method is very efficient and the histogram of cipher image is fully uniform.

4.1.2 Correlation Coefficient

As an inherent specific of digital image, there is high correlation between adjacent pixels in original image. So, in cipher image, these correlations must dramatically have decreased to be resisted against statistical attack. For this analysis, 2048 pairs of adjacent pixels are chosen randomly from the original image and cipher image. Then, following Eq. (2) is used to calculate the correlation coefficients parameter which the results is

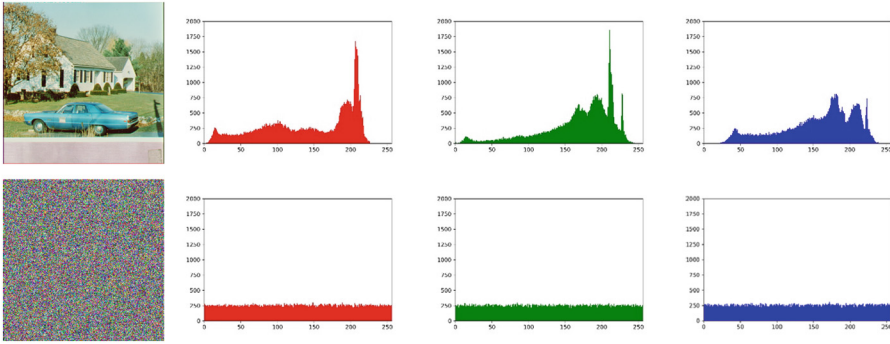


Fig. 2. Histogram of Plain image and cipher image in Red, Green and Blue channel.

illustrated in Table 3.

$$\begin{aligned}
 E(x) &= \frac{1}{N} \sum_{i=1}^N x_i \\
 D(x) &= \frac{1}{N} \sum_{i=1}^N (x_i - E(x_i))^2 \\
 \text{cov}(x, y) &= \frac{1}{N} \sum_{i=1}^N (x_i - E(x_i))(y_i - E(y_i)) \\
 r_{xy} &= \frac{\text{cov}(x, y)}{\sqrt{D(x)}\sqrt{D(y)}}
 \end{aligned}
 \tag{2}$$

Also, these correlations graphically could be seen in Fig. 3.

4.2 Information Entropy

Uncertainty degree in the digital image could be calculated as the information entropy [8]. The ideal value of information entropy is 8. So, if the computed parameter for any image is closer to ideal value, it means that the histogram of the image is more uniform. It could be defined by equation (3):

$$H(S) = \sum_{i=0}^{2N-1} P(s_i) \log\left(\frac{1}{P(s_i)}\right)
 \tag{3}$$

The information entropy of three encrypted test images are reported in Table 3.

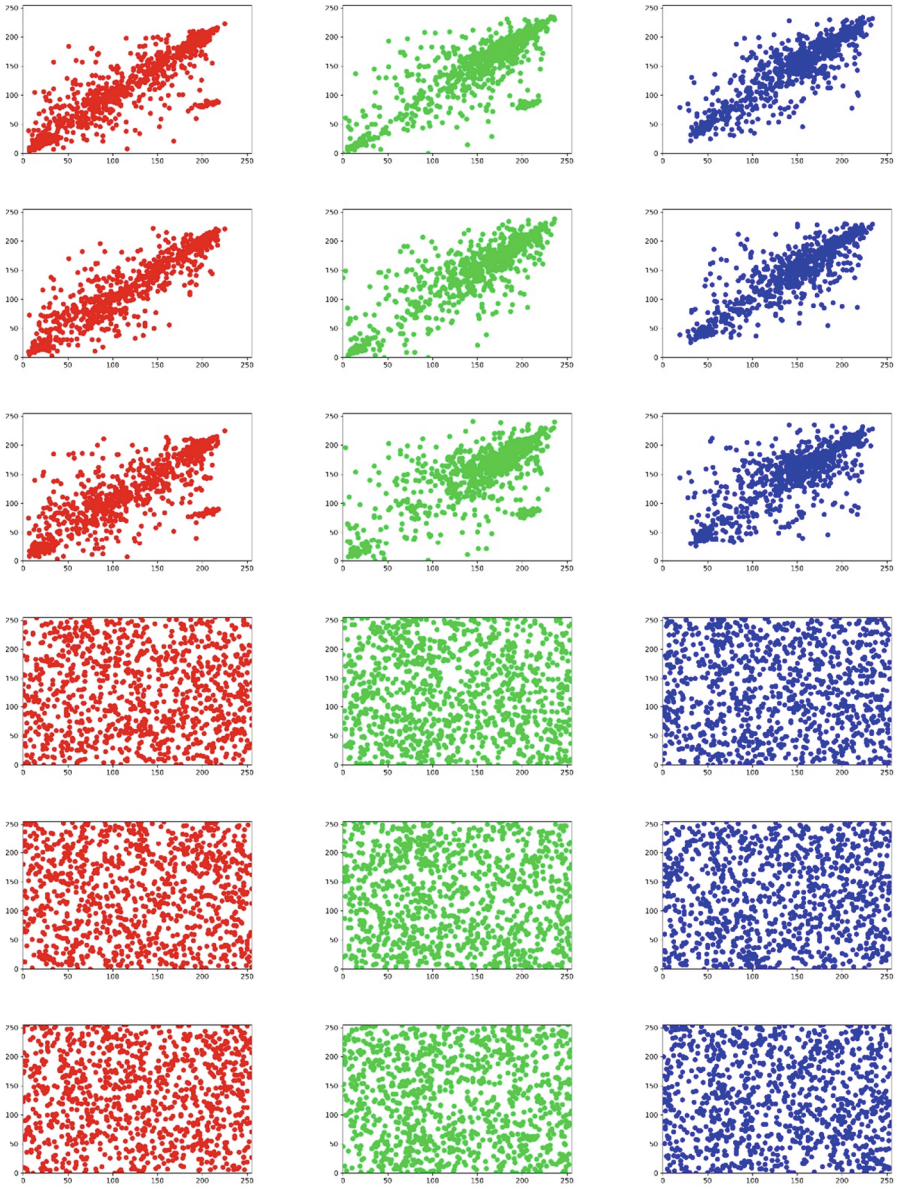

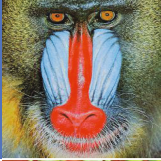



Fig. 3. Correlation coefficient between two adjacent pixels in plain image in horizontal, vertical and diagonal and their equivalent in cipher image in three channels.

Table 3. Correlation coefficient and information entropy of three encrypted test images.

Image	Horizontal Correlation Coefficient	Vertical Correlation Coefficient	Diagonal Correlation Coefficient	Information Entropy
	0.02673	0.03981	0.01294	7.9912
	0.06231	0.01104	0.07321	7.9935
	0.08327	0.07650	0.06671	7.9927

References

1. Asadollahi, H., Saberi Kamarposhti, M., Moosavian Jandaghi, E.: Image encryption using cellular automata and Arnold cat's map. *Aust. J. Basic Appl. Sci.* **5**(8), 587–593 (2011)
2. Jadidy Aval, K., Sabery Kamarposhty, M., Damrudi, M.: A simple method for image encryption using chaotic logistic map. *J. Comput. Sci. Comput. Math.* **3**(3) (2013)
3. Sabery Kamarposhty, M., Yaghoobi, M.: A simple and robust approach for image hiding using chaotic logistic map. In: *International Conference on Advanced Computer Theory and Engineering*. IEEE (2008)
4. Demirtaş, M.: A new RGB color image encryption scheme based on cross-channel pixel and bit scrambling using chaos. *Optik* **265**, 169430 (2022)
5. Louzzani, N., et al.: A novel chaos based generating function of the Chebyshev polynomials and its applications in image encryption. *Chaos Solitons Fractals* **151**, 111315 (2021)
6. Liu, Y., et al.: Optical image encryption algorithm based on hyper-chaos and public-key cryptography. *Opt. Laser Technol.* **127**, 106171 (2020)
7. Jasra, B.H.M., Ayaz: Color image encryption and authentication using dynamic DNA encoding and hyper chaotic system. *Expert Syst. Appl.* **206**, 117861 (2022)
8. Shannon, C.E.: A mathematical theory of communication. *Bell Syst. Tech. J.* **27**, 379–423 (1948)



Cancer Detection in Digital Image Using Machine Learning Algorithms

Yaser Darkaleh¹, Mahta Sadat Mirzazadeh Tekieh²,
and Sima Aboulhassani Khajeh³(✉)

¹ Department of Biomedical Engineering, Rouzbahan University, Sari, Iran

² Department of Environmental Engineering, Islamic Azad University, Science and Research Branch, Tehran, Iran

³ Department of Computer Science, Islamic Azad University, Gheshm International Branch, Gheshm, Iran

S.abolhasani@iraninsurance.ir

Abstract. Every day, a large amount of medical data is being produced in hospitals and medical centers. Using this data to analyze the results can save treatment costs for both patients and the government. Therefore, it is very important to collect medical data about various diseases as well as their appropriate and correct analysis. In recent years, the use of machine learning algorithms to extract and identify patterns from various diseases, including in cancer research, which is a significant challenge for humans with high morbidity and mortality, has attracted much attention. In this article, several machine learning algorithms are employed for cancer detection on UCI standard data. The obtained results show the appropriate accuracy of the proposed method.

1 Introduction

Every day, a large amount of medical data is being produced in hospitals and medical centers. Using this data to analyze the results can save treatment costs for both patients and the government. Therefore, it is very important to collect medical data about various diseases as well as their appropriate and correct analysis. In recent years, the use of machine learning algorithms to extract and identify patterns from various diseases, including in cancer research, which is a significant challenge for humans with high morbidity and mortality, has attracted much attention. Several works are done in this field, in the recent years [1–6].

A correlation-based feature selection method is proposed in [7] where the SMOTE is employed for dataset pre-processing. For balancing the dataset for partitioning, a method which is called The Kennard-Stone is employed. The experiment analysis shows the dramatic improvement than other similar algorithms.

Also, under a dataset from a Korean teaching hospital, of more than six hundred patients who is suffering from breast cancer, a prognostic model is used in [8] for estimation of recurrence and survival. Feature selection phase have done for multiple rounds on around two hundred variables in the dataset, to choose seven variables. Three different algorithms such as artificial neural network, support vector machine and Cox regression is performed for classification where the accuracy results obtained from SVM is the best and around 84.6%. Also, Normalized Mutual Information Index (NMI) is employed in this research to recognize the features' importance.

In [9], comparing several kinds methods for feature selection such as Information gain, DPSORS and Chi-Square are performed and a subset of features are selected to use in the classification instead of the whole dataset. Their concluded, there is a not a best feature selection technique which is suitable for all datasets and it could be selected based on the nature, the number of features and type of the dataset.

Using breast cancer dataset, several machine learning methods are employed with combination of some criteria for feature selection in [10]. Four dataset from UCI machine learning repository, some criteria for feature extraction and feature selection which is combined with some classification techniques are employed. Analysis shows the efficiency of the proposed algorithm.

In this article, several machine learning algorithms are employed for cancer detection on UCI standard data. In the next section, the proposed method is briefly described. Then, in the experimental results section, the proposed method is analyzed and compared to existing methods.

2 Models and Dataset Discussion

The Breast Cancer Wisconsin (Diagnostic) dataset is used in this research as a part of UCI Machine Learning Repository where the features in dataset are calculated using digital captured image of breast mass fine needle aspirate (FNA) as characteristics of the nuclei cell. Heat-map diagram of some selected features in this dataset could be seen in Fig. 1.

Also, these features are shown in comparison together based on the diagnostic (M for malignant and B for benign) in Figs. 2 and 3. In this research, several known classifiers are applied to the Breast Cancer Wisconsin (Diagnostic) dataset and the results are compared to found the best model. These known classifiers are listed as follows:

1. Logistic Regression
2. K-Nearest Neighbor
3. Support Vector Machine
4. Naïve Bayes
5. Decision Tree
6. Random Forest

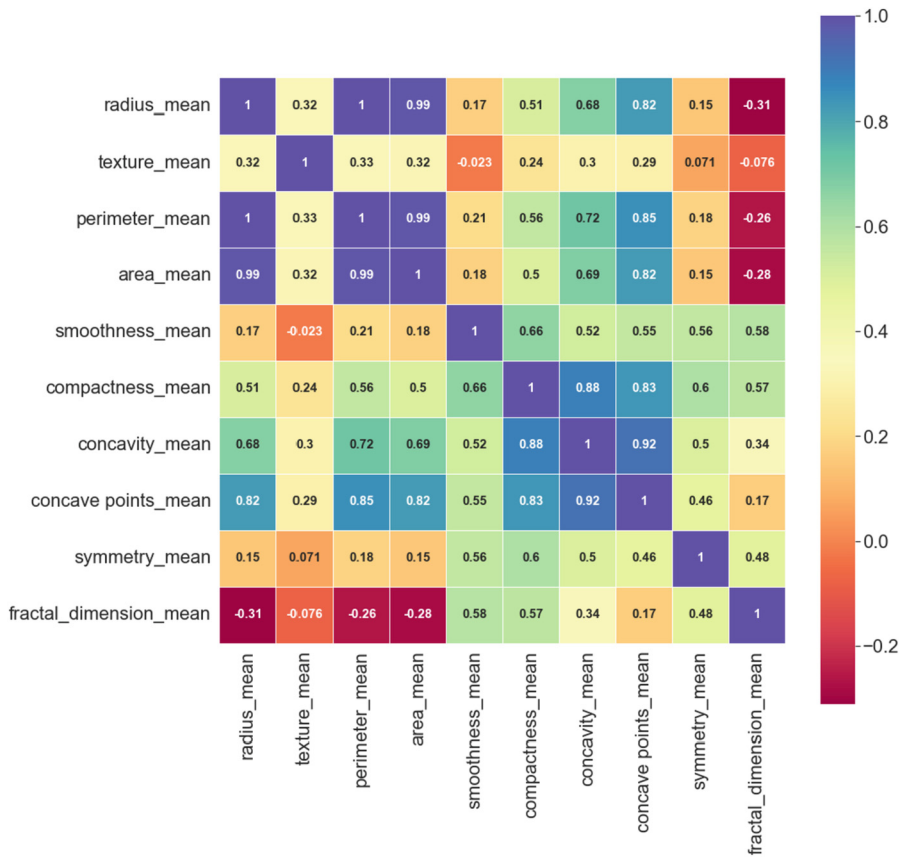


Fig. 1. Heat-map diagram of ten selected features in dataset.

3 Experimental Results

In this section, these models are implemented using Python programming language and five parameters including accuracy, precision, recall, Mean Squared Error (MSE) and F1 measure are calculated as evaluation parameters [11] which is reported in Table 1. Dataset are split to train and test data with three separate percentages as follows:

- 1- 80% Train vs 20% Test
- 2- 75% Train vs 25% Test
- 3- 70% Train vs 30% Test

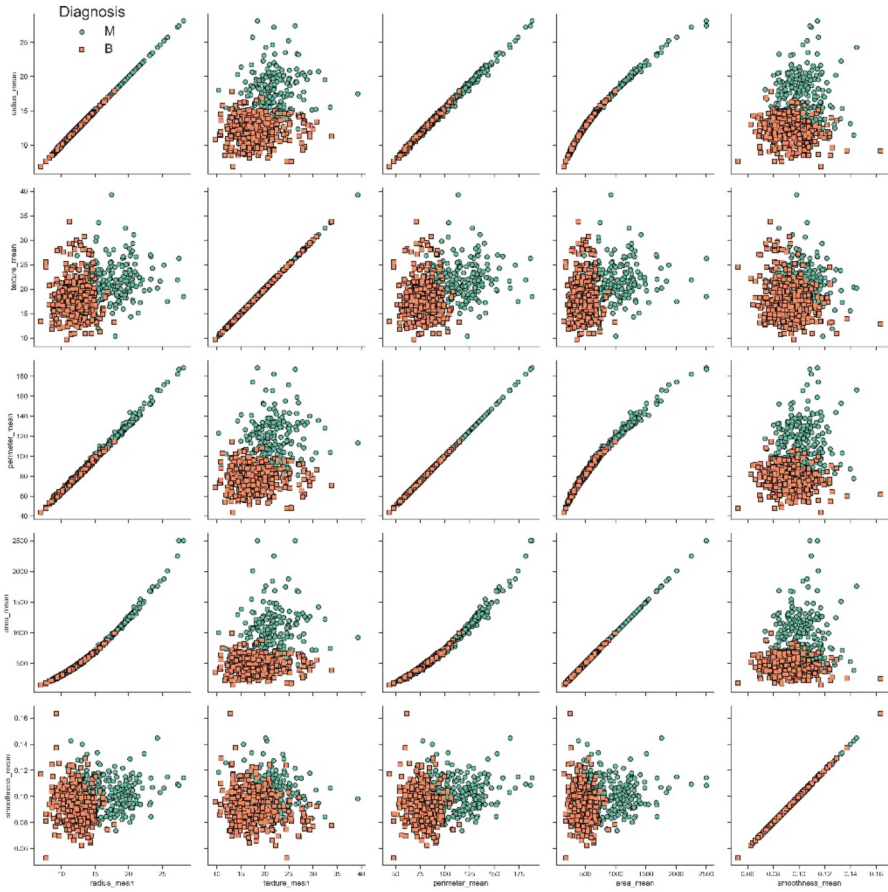


Fig. 2. Five features in comparison together based on the diagnostic (M for malignant and B for benign)

As in could be seen in Fig. 4, the accuracy of all models is good but the random forest has best results.

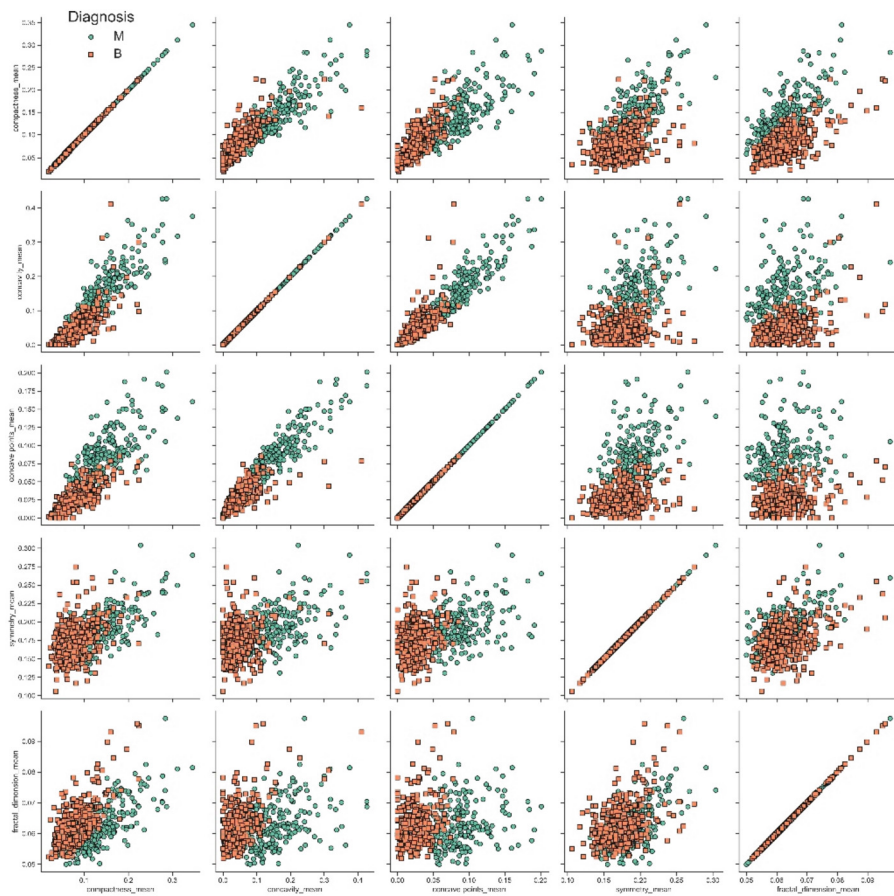


Fig. 3. The accuracy of all models

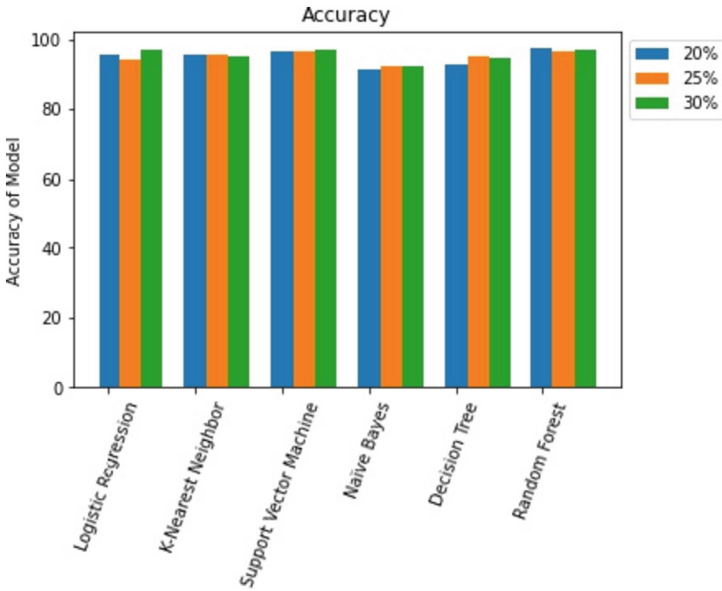


Fig. 4. Remained five features in comparison together based on the diagnostic (M for malignant and B for benign)

Table 1. Experimental Results

No	Model	Scores	Test Data Percentage		
			20%	25%	30%
1	Logistic Regression	<i>Accuracy</i>	95.614	94.406	97.076
		<i>Precision</i>	95.652	92.453	98.333
		<i>Recall</i>	93.617	92.453	93.651
		<i>MSE</i>	0.044	0.056	0.029
		<i>F1 Score</i>	0.946	0.925	0.959
2	K-Nearest Neighbor (K = 5)	<i>Accuracy</i>	95.614	95.804	95.322
		<i>Precision</i>	100.0	97.959	96.61
		<i>Recall</i>	89.362	90.566	90.476
		<i>MSE</i>	0.044	0.042	0.047
		<i>F1 Score</i>	0.944	0.941	0.934
3	Support Vector Machine	<i>Accuracy</i>	96.491	96.503	97.076
		<i>Precision</i>	93.878	94.444	95.312

(continued)

Table 1. (continued)

No	Model	Scores	Test Data Percentage		
			20%	25%	30%
		<i>Recall</i>	97.872	96.226	96.825
		<i>MSE</i>	0.035	0.035	0.029
		<i>F1 Score</i>	0.958	0.953	0.961
4	Naïve Bayes	<i>Accuracy</i>	91.228	92.308	92.398
		<i>Precision</i>	89.362	90.385	89.062
		<i>Recall</i>	89.362	88.679	90.476
		<i>MSE</i>	0.088	0.077	0.076
		<i>F1 Score</i>	0.894	0.895	0.898
5	Decision Tree	<i>Accuracy</i>	92.982	95.105	94.737
		<i>Precision</i>	89.796	89.655	92.188
		<i>Recall</i>	93.617	98.113	93.651
		<i>MSE</i>	0.07	0.049	0.053
		<i>F1 Score</i>	0.917	0.937	0.929
6	Random Forest	<i>Accuracy</i>	97.368	96.503	97.076
		<i>Precision</i>	97.826	94.444	98.333
		<i>Recall</i>	95.745	96.226	93.651
		<i>MSE</i>	0.026	0.035	0.029
		<i>F1 Score</i>	0.968	0.953	0.959

References

1. Doja, M.N., Kaur, I., Ahmad, T.: Current state of the art for survival prediction in cancer using data mining techniques. *Curr. Bioinf.* **15**(3), 174–186 (2020). <https://doi.org/10.2174/1574893614666190902152142>
2. Behera, M., et al.: Statistical learning methods as a preprocessing step for survival analysis: evaluation of concept using lung cancer data. *BioMed. Eng. OnLine* **10**(1) (2011). <https://doi.org/10.1186/1475-925X-10-97>
3. Tai, P., et al.: Diseasespecific survival for limited-stage small-cell lung cancer affected by statistical method of assessment. *BMC Cancer* **7**(1) (2007). <https://doi.org/10.1186/1471-2407-7-31>
4. Ganggayah, M.D., Taib, N.A., Har, Y.C., Lio, P., Dhillon, S.K.: Predicting factors for survival of breast cancer patients using machine learning techniques. *BMC Med. Inform. Decis. Mak.* **19**(1) (2019). <https://doi.org/10.1186/s12911-019-0801-4>
5. Zhao, B., Gabriel, R.A., Vaida, F., Lopez, N.E., Eisenstein, S., Clary, B.M.: Predicting overall survival in patients with metastatic rectal cancer: a machine learning approach. *J. Gastrointest. Surg.* **24**(5), 1165–1172 (2020). <https://doi.org/10.1007/s11605-019-04373-z>

6. Wang, Y., Wang, D., Ye, X., Wang, Y., Yin, Y., Jin, Y.: A tree ensemble-based two-stage model for advanced-stage colorectal cancer survival prediction. *Inform. Sci.* **474**, 106–124 (2019). <https://doi.org/10.1016/j.ins.2018.09.046>
7. Chen, C.-M., Hsu, C.-Y., Chiu, H.-W., Rau, H.-H.: Prediction of survival in patients with liver cancer using artificial neural networks and classification and regression trees. *Seventh Int. Conf. Nat. Comput.* **2011**, 811–815 (2011). <https://doi.org/10.1109/icnc.2011.6022187>
8. Wang, K.-J., Makond, B., Wang, K.-M.: An improved survivability prognosis of breast cancer by using sampling and feature selection technique to solve imbalanced patient classification data. *BMC Med. Inform. Dec. Mak.* **13**(1) (2013). <https://doi.org/10.1186/1472-6947-13-124>
9. Kim, W., et al.: Development of novel breast cancer recurrence prediction model using support vector machine. *J. Breast Cancer* **15**(2), 230 (2012). <https://doi.org/10.4048/jbc.2012.15.2.230>
10. El-Rahman, S.A.: Predicting breast cancer survivability based on machine learning and features selection algorithms: a comparative study. *J. Amb. Intel. Human. Comput.* **12**(8), 8585–8623 (2021). <https://doi.org/10.1007/s12652-020-02590-y>
11. Pradeep, K.R., Naveen, N.C.: Lung cancer survivability prediction based on performance using classification techniques of support vector machines, C4.5 and naive Bayes algorithms for healthcare analytics. *Proc. Comp. Sci.* **132**, 412–420 (2018). <https://doi.org/10.1016/j.procs.2018.05.162>

Author Index

A

Abdalla, Badraan 156
Abdulkareem, Muyideen 156
Abed, Akram H. 285
Adaramola, Bernard A. 230
Adegbenjo, Abayomi 230
Afolalu, S. A. 205
Afolalu, Sunday A. 230
Afrouzi, Hadi Nabipour 322, 361
Ahmed, Jubaer 361
Akintunde, M. A. 205
Al Ezzi, Amged 147
Al Jalil, Arshad A. 285
Ali, Hayder Mohsin 104
Alizadeh, Seyed Morteza 322
Al-Naamee, Muna Kheder Jassim 104
Al-Yacoubi, Ahmad Mahamad 163, 263
Angula, Ester 31, 59, 66, 85, 113, 121, 129
Arian, Mehrnaz 371
Awang, M. 294
Awang, Mokhtar 241, 275
Awani, Oritsetsolayemi O. 214
Ayeronfe, Fadilat 156

B

Balogun, Vincent A. 214
Benjamen, Patrick Guda anak 346
Bodunde, Ojo P. 214
Broumandnia, Ali 371

C

Chaichan, Miqdam T. 39, 50
Chaichan, Miqdam Tariq 104
Che, Hui Xin 312
Cheema, Saeed 156
Chua, Hong Siang 346, 354, 361

D

Darkaleh, Yaser 379
Dhahad, Hayder A. 39

E

Emamian, S. 241, 294
Erinosho, Mutiu 31, 59, 66, 85, 113, 121, 129

F

Fayad, Mohammed A. 39, 50, 104

G

Ganiyu, Abideen 156
Geach, Chen Rui 322

H

Hassan, Ateeb 322
Hassan, M. Z. 177
Hassan, Samatar 156
Heng, Ching Wen 16
Hoh, Chin Yap 9

I

Ikumapayi, O. M. 205
Ikumapayi, Omolayo M. 214, 230

J

Janasekaran, Shamini 312
Janga, Venkata Somi Reddy 275
Jayamani, Elammarran 322
Jen, Tien-Chien 230
Jessam, Raed A. 73, 147
Joharudin, Nurul Farahin Mohd 138
Johnson, Oluwagbenga 85

K

Kamarudin, Kamarul-Azhar 138
Kamarulbahrin, Mohamad Azri bin 163
Kaur, Deshvinder 156
Kazeem, Rasaq A. 214
Kee, Sook 156
Khajeh, Sima Aboulhassani 379
Khlief, Ayad K. 285

Kho, Sarah Jane 346
 Krishna, Shwetank 93

L

Lam, Weng Hoe 1, 9, 16, 332, 339
 Lam, Weng Siew 1, 9, 16, 332, 339
 Latif, Noradila Abdul 138
 Lee, Eric J. 275
 Lee, Hui En 346, 354
 Lee, Pei Fun 1
 Liew, Kah Fai 339
 Liew, M. S. 163, 263
 Lim, Huai Tein 23
 Lim, Jia Wei 346
 Lim, Shun Jinn 332
 Ling, Ting Rang 346

M

Magaril, Elena 73
 Mahdi, Ahmed Sahib 138
 Mahdi, Louay Abd Al-Azez 104
 Mehranzamir, Kamyar 322
 Mercer, Zehnder Jarroop Augustine 354
 Meyghani, Bahman 241, 294
 Mizan, Mohd Farid Bin 263
 Mustapa, Mohammad Sukri 138

N

Ng, Peh Sang 23
 Ng, Sing Muk 354
 Noor Izza, N. H. 198
 Nsien, E. P. 205
 Nyaut, Ashlee Jude Anak 354

O

Ogedengbe, T. S. 205
 Ogedengbe, Temitayo S. 230
 Ogundipe, Adebayo T. 214, 230
 Oluwafemi, Jesutoni R. 214
 Omar, N. 177
 Ooi, Mong How 346

R

Rabiatul Adawiyah, M. A. 198
 Rady, Mohammed Hussein 138
 Rasid, Z. A. 177
 Richard, Rowena 156
 Ridha, Syahrir 93
 Rominiyi, O. L. 205
 Rusli, Muhd Rizuan 138

S

Saberi Kamarposhti, Morteza 371
 Sabo, Umar Nabil 93
 Saliza Azlina, O. 198
 Shaanika, Erasmus 121
 Shaanika, Sam 31, 59, 66, 85, 113, 121, 129
 Shijer, Sameera S. 50
 Sia, Yaw Yoong 312

T

Tai, Vin Cent 312
 Tan, Yong Chai 312
 Tayier, Walisijiang 312
 Tekieh, Mahta Sadat Mirzazadeh 379
 Ting, Lawrence Sii Ying 361
 Tioh, Yen Shuang 16
 Tsen, Xin Hui 346

U

Utomo, Wahyu Mulyo 138

W

Wahhab, Hasanain A. Abdul 39, 50, 73, 104,
 147
 Wong, Shann Ying 9

Y

Yam, Hok Chai 156
 Yeong, Wai Chung 23
 Yong, Irene Seok-Ching 23
 Yusuf, Mohammad 93

Z

Zhang, Shuai 312